





# ELECTRIC MACHINES: UPT SELECTED CONTRIBUTIONS

Acad. Ion Boldea (ed.)



MONOGRAFIILE  
**UPT**

Descrierea CIP a Bibliotecii Naționale a României:  
**Electric machines : UPT selected contribution :**  
**1920-2020 / trad.: Roxana Ghiță ; ed.: acad.**  
Ion Boldea. - Timișoara, Editura Politehnica, 2020

Conține bibliografie. - Index  
ISBN 978-606-35-0356-6

I. Ghiță, Roxana (trad.)  
II. Boldea, Ion (ed.)  
62

CIP description of the National Library of Romania:  
**Electric machines : UPT selected contribution**  
**: 1920-2020 / translator: Roxana Ghiță; editor:**  
acad. Ion Boldea. -  
Timișoara, Politehnica Publishing House, 2020

Includes bibliography. - Index  
ISBN 978-606-35-0356-6

I. Ghiță, Roxana (translator)  
II. Boldea, Ion (editor)  
62



# ELECTRIC MACHINES: UPT SELECTED CONTRIBUTIONS



MONOGRAFIILE  
**UPT**

Acad. Ion Boldea (ed.)

Copyright © Politehnica Publishing House, 2020

**Politehnica Publishing House**

Bd. Vasile Pârvan nr. 2B  
300223 Timișoara, România  
Ph./Fax. +4 0256 404677  
E-mail: editura@upt.ro

**Reader:**

Prof. Univ. Dr. Nicolae MUNTEAN

**Translator:**

Asist. Univ. Dr. Roxana GHIȚĂ

**Editorial Advisor:** Prof. Dr. Ing. Sabin IONEL

**Editor:** Claudia MIHALI

**Good to print:** 01.04.2020

**Printing sheets:** 29

**C.Z.U.** 62

**ISBN** 978-606-35-0356-6

# FOREWORD

**"Not the walls make a school, but the spirit that reigns in it"**

**(Ferdinand I)**

At the end of the 19th century and the beginning of the 20th century, Timisoara, which had been liberated from the walls of the former military fortress, experienced a period of maximum growth, with profound changes at all levels, gradually, but quickly, becoming a modern, cosmopolitan, multicultural city, which forged a vast program of industrial development, and the numerous breakthroughs achieved here have earned its reputation as a city of technical prowess. However, the need to enhance this effervescence with the glow of higher education and research in the technical field was felt. A wide array of prominent personalities of the time committed themselves with all the dedication to what would be the emergence of the first university in the west of the country. The dream of the Banat people, of having a higher education institution in Timisoara, was fulfilled by King Ferdinand, who, on November 11th, 1920, signs the decree establishing the Polytechnic School.

Throughout a century of existence there were many difficulties. From providing educational facilities, equipping laboratories with everything necessary, to bringing or training prestigious teachers. From the hardships during the war, when the teachers could not be paid, the freezing of all investments or savings made in the last decade of the communist period, to the decline faced in the first years after the Revolution. However, all the challenges were overcome by the exceptional quality of the professors, whose performance of high scientific and moral standing propelled the Timisoara Polytechnic among the perennial institutional values of Romania. Great teachers have created real schools in their field, many of them being national premiers. And in these schools a plethora of eminent students were formed, who carried on the established tradition.

Politehnica University Timisoara is today acknowledged as an outstanding protagonist on the stage of scientific research, both nationally and internationally. The existence and operation of a considerable number of research centers, in which teams of specialists who successfully implement the research strategy of the institution, grant the university professional prestige and, at the same time, provide the source of funds for development. Updating the research outcomes in scientific papers, patents or invented products is a guarantee of competence, seriousness and institutional professionalism.

In this context, the leaders of Politehnica University Timisoara have launched a project of editing reference works, with a technical-scientific and homage character, under the title "UPT Monographs", which will once again confirm the advanced degree of scientific research and education to which our institution rises, and at the same time, it represents an encouragement for the coming generations to continue the work, the efforts and the results of their forerunners in the centuries to come.

**Prof. eng. Viorel-Aurel Șerban, PhD**

**Rector of Politehnica University Timisoara**



# Content

<b>Foreword</b>	<b>5</b>
<b>1. Contribution to “Electric machines” from 1920 to 1970</b>	<b>16</b>
<b>Editor: I. Boldea</b>	
1.1 Introduction	16
<b>2. A.C. Electrical Machines: UPT Fortan software and full-scale experimental models</b>	<b>19</b>
<b>Authors: T. Dordea, Gh. Madescu, I. Torac, L. Ocolişan</b>	
2. 1 Induction machines: INDARUPT software	19
2.1.6 References	30
2. 2 Synchronous machines: ROBARUPT software	31
2.2.4 References	43
2. 3 Voltage transformer with variable ratio and fine control	44
2.3.3 References	48
2. 4 Inverter-fed induction motor for direct-drive bogie of a tramcar	49
2.4.4 References	54
<b>3. Industrial synchronous machines testing in standstill conditions: theory and practice</b>	<b>55</b>
<b>Authors: M. Biriescu, Gh. Liuba, T.P. Dordea, M. Moţ</b>	
3. 1 Introduction	55

3.2 Equations, parameters, and characteristic values used in the study of synchronous machines	56
3.3 Current decay transients at standstill tests	71
3.4 Experimental study of saturation using rotor pre-magnetization	113
3.5 Conclusions	119
3.6 References	120
<b>4. Single phase line start small induction motor</b>	<b>124</b>
<b>Authors: I. Şora, M. Babescu, M. Topor</b>	
4.1 Operation principles of the single phase shaded pole induction micromotor	124
4.2 The elliptical rotating magnetic field	124
4.3 Operating principle of the single phase shaded pole micromotor	128
4.4 Mechanical characteristic of the single phase shaded pole induction micromotor	130
4.5 Torque equation of the single phase shaded pole induction micromotor	131
4.6 References	137
<b>5. A.C. machine transients: a direct math approach</b>	<b>138</b>
<b>Authors: M. Babescu, D. Păunescu, M. Topor</b>	
5.1 Mathematical modeling of electrical machines with a.c. machine transients: a direct math approach	138

5.2 Mathematical modeling of electrical machines	138
5.3 Construction and functional elements of electric machines	141
5.4 Mathematical model equivalation between the dq orthogonal model and the abc model of the real machine	145
5.5 The orthogonal dq mathematical model	147
5.6 The dq model of the synchronous and asynchronous machine	150
5.7 The equations of the orthogonal model and the corresponding synchronous machines parameters	151
5.8 Equations of the orthogonal model and the parameters of the asynchronous machine	154
5.9 Equivalation between the dq orthogonal model and the real machine	157
5.10 Mathematical modeling of the variable speed operation of the asynchronous machine	159
5.11 Mathematical model analysis from the point of view of the electromagnetic torque	161
5.12 Mathematical model analysis from the point of view of the stator current	161
5.13 Mathematical model for constant statoric flux variable speed control of the asynchronous machine	162
5.14 Mathematical model for speed control of the asynchronous machine with constant useful flux	162
5.15 Mathematical model for speed control of the asynchronous machine at constant rotor flux	163

5.16 Conclusions regarding the dynamics of the asynchronous machine	163
5.17 Mathematical modeling of speed control of synchronous machines	164
5.18 Mathematical model of synchronous machines during the speed control with constant stator flux	165
5.19 Mathematical model of synchronous machines during speed control with constant rotor flux	166
5. 20 References	167
<b>6. Optimization algorithms used for the design of electrical machine</b>	<b>168</b>
<b>Author: A. Argeşeanu</b>	
6.1 Optimization algorithms. The heuristic syntagma	169
6. 2 The genetic optimization algorithm	174
6.3 Swarm particle optimization algorithm & others paradigms	190
6. 4 Practical aspects of the heuristic algorithms' application	193
6. 5 Practical results in the field of electric machine optimization obtained by UPT researchers	201
6. 6 References	202
<b>7. Unified treatment of core losses and saturation in the dq model of electric machines</b>	<b>204</b>
<b>Authors: L.Tutelea, I. Boldea</b>	
Abstract	204

7. 1 Introduction	204
7. 2 The proposed physical model	205
7. 3 Equations for the general dq model	206
7. 4 Cross – coupling magnetic saturation equations	207
7. 5 Magnetization (saturation) curves	
$\Psi_{dm}^* (i_m)$ and $\Psi_{qm}^* (i_m)$	208
7. 6 Core loss resistances measurements	210
7. 7 State - space equations	212
7. 8 Digital simulation results on an induction machine	214
7. 9 Discussion	220
7. 10 References	221
<b>8. Inovative 1 phase line-start and variable–speed (inverter fed)</b>	
<b>3 phase and 1 phase PM motor drives for small compressors</b>	<b>222</b>
<b>Authors: L.Tutelea, I. Boldea</b>	
Abstract	222
8. 1 Introduction	222
8. 2 A 2/4 poles split-phase capacitor motor	224
8. 3 Line – start split – phase capacitor PM – reluctance – cage motor: optimal design	228
8. 4 Spoke – Ferrite – PM rotor synchronous compressor motor variable speed drive: comprehensive characterization and two sensorless control options [3]	234



8. 5 1kW, 4.5 krpm Outer – Ferrite – PM – rotor 9 slot/8 pole synchronous motor: FEM assisted optimal design and preliminary tests [4]	245
8. 6 Single phase stator – Ferrite – PM self-starting motor variable speed drive [5].	250
8. 7 Conclusion	258
8. 8 References	259
<b>9. MW – range electric generator systems for renewable energy: design and control</b>	<b>260</b>
<b>Authors: I. Boldea, L.Tutelea</b>	
Abstract	260
9. 1 Optimal design of d.c. excited directly driven large wind generators. The largest directly – driven wind generator so far (2018) is synchronous with d.c. excitation at 7.6 MW, 3.6 kV and 11 rpm (see "Enercon gmbH"(Fig. 9.1)).	260
9. 2 PMSG optimal design [3]	268
9. 3 Design of transverse – flux wind PMSGs for power weight	272
9. 4 Direct CRIG connection to grid for wide energy conversion	280
9. 5 Wound-rotor (doubly fed) induction generator control	286
9. 6 Comprehensive encoderless PMSG control system [10]	295
9. 7 References	302

<b>10. Flux – reversal PM synchronous motors (FR-PMSM)</b>	
<b>and generators at variable speed</b>	<b>304</b>
<b>Authors: I. Boldea, S.A. Nasar</b>	
Abstract	304
10. 1 Introduction	304
10. 2 The 3 phase FR – PMSM – stator surface PM pole configuration	307
10. 3 Radial airgap 3 phase FR – PMSM(G) with spoke – PM rotor and dual stator	314
10. 4 FEM analysis	315
10. 5 Final discussion	317
10. 6 References	318
<b>11. Torque Vector Control (TVC→LATER DTC) of AC drives</b>	<b>319</b>
<b>Authors: I. Boldea, S.A. Nasar</b>	
Abstract	319
11. 1 Torque vector control (TVC) concept for a.c. machine drives [6]	320
11. 2 TVC (DTC) principle for voltage – source inverter fed IMs	320
11. 3 TVC principle for voltage – source inverter fed synchronous machine drives	324
11. 4 Implementation of TVC (DTC) for CR – Ims	327
11. 5 TVC (DTC) of PMSMs	330
11. 6 TVC (DTC) of synchronous reluctance machines (RSMs)	332

11. 7 TVC (DTC) of d.c. excited synchronous machines	333
11. 8 References	335
<b>12. Linear electric machines drives and MAGLEVS</b>	<b>337</b>
<b>Authors: I. Boldea, S. Agarliță</b>	
Abstract	337
12. 1 LEMs classification	337
12.2 Linear induction motors	340
12.3 Homopolar linear synchronous (H-LSM) motors MAGLEV	344
12.4 PM plunger solenoid for valves actuation	346
12.5 Springless resonant linear PM oscillomotor	347
12. 6 References	354
<b>13. "Active flux" based encoderless FOC, DTFC AND V/F(I-F) with stabilizing loops control of A.C. machines</b>	<b>356</b>
<b>Authors: I. Boldea, M. C. Ancuti, D. Andreescu, A. Popa</b>	
13. 1 Abstract	356
13.2 The "active flux" concept	356
13. 3 "Active flux" based encoderless IPMSM FOC and DTFC drives	362
13. 4 Active flux based high saliency RSM field-oriented control [9]	369
13.5 Active flux encoderless vector control of d.c. excited SM	376
13.6 "Active flux" based scalar V/f (I-f) control of A.C. machines	380
13. 7 References	387

<b>14. High performance reluctance synchronous machines</b>	
<b>for variable speed: modeling, performance and design</b>	<b>389</b>
<b>Authors: L. Tutelea, A. Ișfănuți, A. Popa, I. Boldea</b>	
14. 1 Abstract	389
14. 2 ALA rotor RSMs for variable speed drives	390
14. 3 ALA rotor 2 pole RSM of 1500 W at 3000 rpm case study	392
14. 4 BEGA – a biaxial excitation generator for automobiles: a case study	395
14. 5 1phase a.c. continuous PM generator with saturation caused saliency	401
14. 6 BLDC-MRM (brushless multiphase reluctance machines)	404
14. 7 References	410
<b>15. Inversed claw-pole-rotor (or stator) generator/motor drives</b>	
<b>for automotive and robotics application</b>	<b>412</b>
<b>Authors: I. Boldea, L. Tutelea</b>	
15.1 Inter-claw PM-pole-rotor alternator system (IPM-CPA) for more energy recuperation during vehicle braking	412
15. 2 10kW and 100 kW, 6000 rpm IPM-CPA for HEV and EV propulsion optimal design and controlled dynamics	418
15. 3 References	427

<b>16. Dual stator winding induction generators at variable speed</b>	<b>428</b>
<b>Authors: L. Tutelea, S.I. Deaconu, I. Boldea, N. Budişan, N. Muntean</b>	
16.1 Introduction	428
16.2 Dual Stator Windings Induction Generators (DSWIG):	
New Proposed Topologies	429
16.3 Analytical Model of DSWIG	430
16.4 Optimal Design	432
16.5 2-D FEM Analysis	434
16.6 Control model and dynamic simulation	436
16.7 Preliminary Experimental Work	442
16.8 Conclusions	444
16.9 References	446
<b>17. Dual rotor PM synchronous motor/generators for HEV: a review</b>	<b>449</b>
<b>Authors: I. Boldea, L. Tutelea, S.I. Deaconu</b>	
17.1 Introduction	449
17.2 Proposed machine topology	450
17.3 Preliminary and Optimal Design	451
17.4 Quasi 3D FEM Validation	455
17.5 Control and Dynamic Simulations	456
17.6 Conclusions	460
17.7 References	462

## 1. 1 Introduction

By the Decree/Law no. 4.822 of November 11<sup>th</sup> 1920 King Ferdinand 1<sup>st</sup> approved the "foundation of Polytechnic School of Timisoara from November 15<sup>th</sup> 1920. Timisoara was at that time a strong industrial/commercial/cultural center and the first city in Europe with electric street lights with electric energy from its small hydro-power plant two phase a.c. generators operating at 42 Hz.

Led from the start by eminent scientists such as Traian Lalescu (Mathematics) and Victor Vălcovici (Mechanics), the Polytechnic School of Timisoara (now the Politehnica University of Timisoara with 14000 students in 2018) has distinguished itself by:

- high class Professors, many of them educated at the best Universities of Europe
- strong laboratories to tie theory to practice
- numerous Professors serving since (taneously the University and the industry) as leaders or with their applied research/design work contributing essentially to the industrial progress of Romania after 1920.
- diligent students
- an innovative teaching effort (the "diploma work" up to the prototype execution and testing in industry is an example).

Among its famous Professors with remarkable research and significant contributions to UPT, we mention here only a few:

1. Prof. Marin Bănărescu (since 1922): "Internal combustion (thermal) engines" with higher efficiency
2. Prof. Pompiliu Nicolau (since 1924): the first "Laboratory of Hydraulics and Hydraulic machines" in Romania
3. Prof. Ștefan Nădășan: "Materials stress analysis".
4. Prof. Koloman Bakony: "Mechanical technologies".
5. Prof. Corneliu Mikloși: "Welding technologies".
6. Prof. Plautius Andronescu: "Electromagnetic fields".
7. Prof. Aurel Bărglăzan: "Hydraulic machines".
8. Prof. Ioan Anton: "Hydraulic machines".
9. Prof. C. Mateescu: "Civil engineering".
10. Prof. Coriolan Drăgulescu: "Chemical Engineering".
11. Prof. Remus Raduleț: "Electromagnetic fields and electric machines".
12. Prof. Alexandru Nicolau: "Electric machines".

For the period in focus in this chapter, 1920 – 1970, we will concentrate only on the UPT contributions related to our monograph subject “electric machines and their applications to industry, from power plants to electric traction and industrial drives”.

As UPT contributions to the field of “Electric machines” in the period 1920 – 1970 are centered around two outstanding professors/engineers: Alexandru Nicolau and Remus Răduleț and their groups. We will focus on their pivoting role.

#### Prof. Alexandru Nicolau (1889-1978)

- Graduates in “Electrotechnics” at the “National School of Bridges and Highways” of Bucharest, Romania (1908 - 1913) with a stage (1913 -1914) at “Ecole Superieure d’Electricite” of Paris, France (Prof. Boucherot!)

1914 – 1923 – industrial engineer (Street Car company in Bucharest, Braila, in the Army)

- 1923-1947 – professor of Electric Machines at UPT and engineer (leader) in industry, Electrical Company of Craiova (1926-1936), manager of AEG Bucharest (1936-1944), later Electrotehnica.

- From 1951 to 1978 he was a scholar, manager and then scientific consultant with ICPET (ICPE) Bucharest, contributing with original solutions to numerous firsts in the Romanian industries.

Preoccupied by the finality of his endeavors, Alexandru Nicolau was credited to “think as a Professor, act as an Engineer and dare as a Scholar”. Examples of his “firsts” in Romania are:

- 3,6 MW/10 KV electric transformers
- Special gas-proof electromotors of 125 kW at 750 rpm
- Electric Generators of 25 kVA – 3x380 V at 1000 rpm
- Metallurgical electric motors of 500 kW, 3000 rpm at 6 kV
- Dual speed electric motors: 160 kW/40 kW at 500 rpm/125 rpm

His contributions to the process of “Electrification of Romania” is paramount. The development of the “Electrotechnical industry” in Romania offered Prof. Alexandru Nicolau the opportunity of extraordinary contributions at a later age with ICPE Bucharest. An example is the design and implementation of synchronous motor direct drives for cement mills at 5.5 MW at 6 rpm.

Judging from his impact on “electric engineering education” with UPT, on “Electrotechnical industry” and on Electrical power research, through a long life, Prof. Alexandru Nicolau has been a formidable MAN of his times, and not only.

#### Prof. Remus Răduleț (1904-1984)

Graduates in 1927 from UPT and then in 1928 earns a Ph.D. Scholarship at “Federal Polytechnical School of Zurich (Prof. K. Kuhlman), famous for its standings (visitors: Albert Einstein, M. Planck, E. Schrodinger, W. Heisenberg, etc.).

As a fresh Ph.D., Prof. Remus Radulet returns in 1931 to UPT as a faculty to serve until 1951 when he moves to Politehnica University of Bucharest , where he remains as a consulting Professor until the end of his life in 1984.

He taught at UPT numerous subjects in Electromagnetic fields and circuits, electric machines, electric power plants, writing high level textbooks for students.

Prof. R. Radulet was an “encyclopedic mind” visible both during his lectures, in his scientific papers, books and by his extraordinary effort in coordinating the high “Romanian Technical Lexicon” of 19 volumes with 80000 terms, and, as director of “international electrotechnical committee” (IEC), the “The International Electrotechnical Vocabulary”.

His scientific efforts (more than 200 papers) have centered along the:

- theory of variables and of laws in physical and technical sciences with a strong accent on experimental verification possibilities: “The physical sense of variable resides in the operations by which one settles equivalence, ordering and measuring”: primitive variables, derivated variables and primary variables and respectively state variable as interaction variables and accessory variables.

- formulation of a general theory transient parameters of field effect circuits: “ the power flux of Poynting vector through a closed surface may be expressed by a summation of voltage and current products”.

- direct participation in the electrification of Romania as Director of Energy Institute of Romanian Academy.

- papers on the philosophy of Sciences.

- Distinguished public lectures at Cultural-scientific University of Bucharest which he managed himself

- Prof. A. Nicolau and Prof. R. Răduleț have been followed honorably at UPT by Prof. Toma Dordea in „electric machines”, but his contributions are summarized in chapter 2 of this Monograph.

The “brief synthesis” on UPT contributions from 1920 to 1970 in “Electric Machines” is by no means complete but, hopefully, sheds light on the depth and spectrum of UPT involvement in “engineering education” for and in cooperation with Romanian Industries.

1. Coleta De Sabata “The Technical Culture in Banat” (in Romanian), Excelsior Art 2008.

2. Prof. Alexandru Nicolau (1889-1978), Laudatium UPT brochure, November 13, 2009 (in Romanian).

3. A. Țugulea, F.T. Tănăsescu, „Remus Răduleț (1904-1984)”, “Electrotehnics and Automatics”, vol. 28 (1984), no.2, pp. 82-89 (in Romanian).

4. Remus Răduleț, „Recollections from the school years”, 1967 (in Romanian).



### 2. 1 Induction machines: INDARUPT software

With the appearance of the digital computer, one can say without exaggeration that a new era has begun. The actual level that has been reached, processing speeds at frequencies in the order of Gigahertz, as well as adequate processing and storage capacities, has eliminated an old barrier and opened the way for a new way of work. Therefore complex items requiring a large volume of calculations can be dealt with now, solving them requiring a much shorter time and with a computing accuracy far exceeding technological necessities. One of the first consequences is the old slide rule, used extensively by design engineers in the old days, that has been added to the history storage bin. Today the situation is different and there are other difficulties to overcome.

Today, when the level of penetration of computers in many fields of activity has become so high that computers have turned into articles of convenience, the energy demand triggers actions at both national and international level, it is normal that any product be more performant, made of better materials and with operation costs as low as possible. These attributes define what is called "optimization".

Optimization is, in general, a complex process implying a theory at the boundary of the current knowledge, with precise defining elements and an accurate numerical processing. By adding an adequate technological process, the product may meet the performance requirements. This can be called an optimized product.

In this purpose, Acad. T. Dordea developed the program INDARUPT which provides the machine optimum solution for a set of given material data. It was proposed as the optimizing parameter the product between the efficiency and the power factor of the machine ( $\eta \cdot \cos\phi$ ) to investigate the area of accepted solutions. This method is similar to the known gradient method and allows obtaining the best solution from these existing in the analyzed domain.

The optimization criterion is the sum of two terms: the cost of the main materials (ferromagnetic core and windings) and the cost of the machine losses (at rated power) for the whole considered machine life. The minimum value of the optimization criterion provides the optimum solution.

This “best solution” is assumed as the starting point for the next stage of the optimization procedure that uses the grid optimization method. The domain in which is supposed to find the optimum solution is investigated with a searching step according to the designer option. The procedure presented above is repeated using this optimum machine as starting point for a new searching.

The computing process continues until the criterion function obtains a two closes values for two consecutive searches taking into account a given error. The optimization could be stopped also after a certain number of searching investigations.

The now existing computers allow investigating more than  $10^6$  solutions; the running time depends upon the processor’s speed.

### **2.1.1. General Elements and Basic Theory**

The induction machine is a system in which the energy is converted from mechanic (or electromagnetic) to electromagnetic (or mechanic).

The phenomenon of energy conversion is the electromagnetic induction. If the output energy is the electromagnetic one, the electrical machine is an electric generator. If the output energy is the mechanical one, the machine operates as an electrical motor. Always the amount of the output energy is smaller than the input energy value, the difference representing the machine loses.

The machine cost includes the cost of the used materials and that of the manufacturer process. If one takes into account the cost of the machine losses during their lifetime, one obtains the total costs. For design purpose, one considers only the cost of the main machine materials (ferromagnetic core and winding) and the cost of machine loses for the assumed lifetime. Minimizing the sum of these two costs is assumed as machine optimization, according to the computing program INDARUPT.

An optimized machine means the best use of the machine area crossed by the magnetic field, especially that of slot’s and teeth’s domain. The machine design process had to consider two phenomena: the current displacement phenomenon and the magnetic saturation. The first one is considered if the geometrical dimensions and material data are known. The magnetic saturation is more difficult. The existing models for magnetic saturation can be used with a good accuracy of some limited area (corresponding to the existing measurements).

The program INDARUPT has a subroutine in which one deals with the current displacement phenomenon. Another subroutine deals with magnetic saturation. The values of the magnetic flux density are given from zero to 2 T. For values between 2T and 4.7T the curve is approximated with a curve tending to  $\mu_r=1$ . The limit of 4.7T was assumed only for software reason.

One can assume different lamination quality for stator and rotor yoke and teeth, because the computing program can be used also for high and very high power machines. The computing program uses a set of input data for the machine design. One computes the machine parameters, including the criterion value. Then, one modifies the input data for the domain of the existing solutions. The optimum solution corresponds to the best results of criterion data.

The defining data for an induction machine with slip ring rotor are as follows: the inner diameter of the stator; the outer stator diameter; the machine length; the inner diameter of the rotor; the area of the stator/rotor winding conductors; the width of the stator/rotor tooth; the number of the wires per phase for stator winding. That means 8+1 data that will be modified in the optimization procedure.

For the induction machine with squirrel cage rotor, one adds other two data: the cross section area of the shorting ring cage rotor and the ratio of its dimension that means 10+1 data. Usually, the last two quantities are not the subject of optimization; one assumes their values depending on the rated current of the shorting ring cage rotor. The rated ring current depends on the rotor bar current. This current is computable as a function upon the stator rated current and the average value of the product (efficiency)  $\times$  (power factor).

The number of turns for the stator phase can be considered as other modifiable values. Therefore, for reducing the computing time, INDARUPT uses another program for finding the limits for the turn per phase number. The first assumed value is the average of the obtained limits. The calculus is made then for other 2 or 3 values closed to the average value. Based on the criterion data value, one obtains the optimum value of the turn number of stator winding.

The optimization method implies a calculus of a very large number of machines. The optimum solution is that corresponding to the minimum value of the criterion function.

The program is based on the induction machine theory and design, as in [5, 7, 10, 12, 17, 21, 23, 25, 27, 29, and 32]. For squirrel cage rotor machines, the current displacement phenomenon and his influence on the rotor impedance, one uses a method very similar to the FEM-method. The analytical method was developed, named the "strips method" [1.17] used in the subroutine REXI. The strips method avoids the calculus of magnetic potential vector for finding magnetic flux density  $\overline{B}$ . The used assumptions are: the magnetic permeability of the ferromagnetic core is tending to infinite (one neglects the m.m.f. of the ferromagnetic core): the magnetic field lines inside the slot are perpendicular to the slot axis. The current displacement phenomenon is assumed stronger (with a few percent) because of these assumptions, but that is an advantage for the machine calculus. The subroutine can be used for a generally-shaped slot as in Fig. 2.1.a. Consider the slot, divided along its entire height,  $H$ , by parallel planes, parallel to the axis of the machine, spaced at  $h$  between them, so that between two parallel plans the current density can be considered as constant.

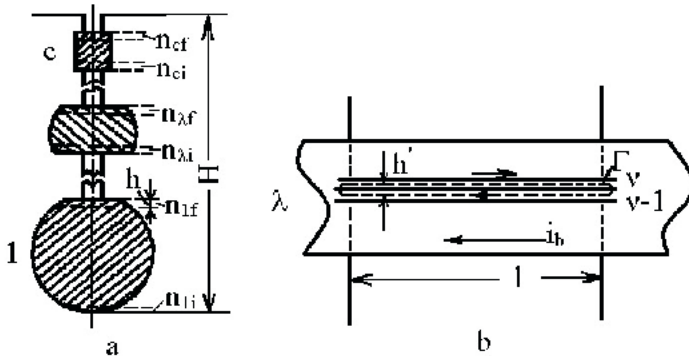


Fig. 2.1 General shape rotor slot.

The strips are indexed starting from the base of the slot toward the air gap. For a bar whatsoever,  $\lambda$ , the first strip has the index  $n_{\lambda,i}$  while the last one  $n_{\lambda,f}$ . The axial length of a band is equal to the length of the magnetic core, that can be considered as the same as the ideal length of the machine. Consider two stacked bands, with sequential numbers  $v-1$  and  $v$ , as per figure 2.1.b run a curve  $\Gamma$  through the upper parts of the two bands, through the conductive part, that closes through the two lateral surfaces of the conductor material. After setting the positive direction for the current  $i_{\lambda}$  of the bar as well as for the currents  $i_{v-1}$  and  $i_v$  of the selected bands, bands so thin that, in each of them the current is considered, with an acceptable error, to be uniformly distributed and thus having a constant current density (an acceptable assumption for a thickness of the order of microns or fractions of a micron), it results a relation between the currents  $i_{v-1}$  and  $i_{\lambda}$  as follows

$$\underline{I}_v = \underline{C}_v \underline{I}_{n_{\lambda,i}} - \underline{E}_{u\lambda} \quad (2.1)$$

where the coefficients  $\underline{C}_v$  and  $\underline{E}_{u\lambda}$  are complex quantities, that can be determined through iterations as functions of the geometrical dimensions and material constants, all these being known.  $\underline{I}_{n_{\lambda,i}}$  is the current in band  $n_{\lambda,i}$  and  $\underline{I}_{\lambda}$  is the sum of the currents for all conductors located between the base of the slot and the bar  $\lambda$ . This way, through the summation of  $\underline{I}_{\lambda}$  for all bands of the conductor  $\lambda$  current,  $\underline{I}_{n_{\lambda,i}}$  of the first band of the conductor  $\lambda$  can be determined and further all bar currents are known as functions of the currents flow through the conductors of the slot. These allow the determination of the current and internal fluxes for all bands, which, in turn, allow the determination of the electrical parameters (electrical resistances and corresponding reactances).

This method allows the calculation of the impedance of the cage winding, irrespective of its type (single or double cage), as well the equivalent impedance of the machine and so, all the characteristics of interest.

### 2.1.2. Program Structure

The program has been developed considering all the sequences of the calculations required. For this purpose, INDARUPT contains the following 7 groups: IND1, IND2, ... IND7.

- IND1 – PRINC (the main program);
- IND2 – AUXI;
- IND3 – CSIE, FKR, FKX;
- IND4 – REXI;
- IND5 – CAR;
- IND6 – HB, OPTIM, FCX, FKAR, FKAX, FCS;
- IND7 – DATELE.

The structure of the INDARUPT with all the subroutine is given in Fig. 2.2.

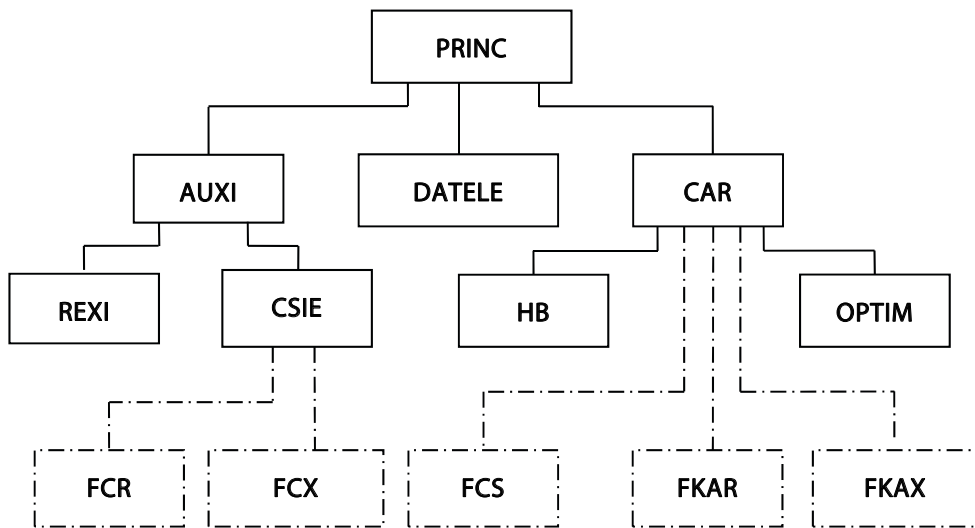


Fig. 2.2 The structure of the INDARUPT program with subroutines.

The main program contains, in COMMON blocks, both input data received via the subroutine DATELE, as well as the partial results via different subprograms. It also contains all COMMON blocks that make the connection to all subprograms. Main operations performed in the main program are:

- setting the computation values for a version, both the fixed values and the ones that change during optimization;
- calling subroutine AUXI where, for a set of values pertinent to a version, calculates all slip independent values necessary, that are either final values for a version, or as coefficients intervening in the expressions of slip dependent quantities. For squirrel cage rotor machines, the subprogram REXI is called from AUXI, that determines the electrical parameters of the squirrel cage rotor machine via the band method;

- all necessary values being known, the subroutine CAR is called. This program calculates energetic parameters. Also this program selects, in case of optimization, the optimal version, that constitutes the final result;
- the integer variable TIP1 has been introduced for calculation monitoring. It appears in all subprograms and, if no error appears, has a value of 0 (zero); if an error is encountered and the calculation process cannot be continued, it gets assigned a value different from zero. In such case the calculation process ends for this version, but the calculation can be continued for another version. The cause is identified through analysis of the assessed value and subsequently error avoiding measures are taken, via input data;
- calculation stop occurs always in the main program, that also gives information on the error cause with regard to the assessed value for the variable TIP1;
- one investigates all the domain of the modifiable data for finding the optimum solution; one defines a smaller domain, much closer around the optimum solution and one prints the data defining them.

The expression of the specific losses in laminations (per mass unit) is due to the magnetic hysteresis and eddy currents that appear in the laminations; this expression is:

$$p_{Fe} = \sigma_h f \cdot B^{\alpha_h} + \sigma_w (\Delta_{Fe} \cdot f)^2 B^2 \quad (2.2)$$

where:  $\sigma_h$  is the hysteresis coefficient;  $f$  – frequency of the time variation of the magnetic flux density  $B$ ;  $\alpha_h$  is an exponent depending on  $B$ ;  $\sigma_w$  is the loss coefficient for eddy currents losses;  $\Delta_{Fe}$  is the thickness of the lamination. Usually, consider for  $\alpha_h$  the value  $\alpha_h \approx 2$ ; for a higher precision,  $\alpha_h$  can be determined through practical tests.

Usually, the laminations manufacturer gives the specific losses for 2 values of the magnetic flux density ( $B_1=1$  T and  $B_2=1.5$  T) and for 2 frequencies (usually  $f_1=50$  Hz and  $f_2=60$  Hz) as well as the lamination thickness  $\Delta_{Fe}$ . For the general case consider 2 thicknesses for the laminations  $\Delta_1$  and  $\Delta_2$ , the material being the same. It is assumed that, for a given material, the following values are known  $p_1, \Delta_1, f_1, B_1$  and  $p_2, \Delta_2, f_2, B_2$ . Thus, the coefficients  $\sigma_h$  and  $\sigma_w$  can be determined. The following relations exist:

$$p_1 = \sigma_h f_1 \cdot B_1^{\alpha_h} + \sigma_w (\Delta_1 f_1)^2 B_1^2 \quad (2.3)$$

$$p_2 = \sigma_h f_2 \cdot B_2^{\alpha_h} + \sigma_w (\Delta_2 f_2)^2 B_2^2$$

of which  $\sigma_h$  and  $\sigma_w$  can be determined as:

$$\sigma_w = \frac{p_1 f_2 B_2^{\alpha_h} - p_2 f_1 B_1^{\alpha_h}}{f_1 f_2 (\Delta_1^2 f_1^2 B_2^{\alpha_h} B_1^2 - \Delta_2^2 f_2^2 B_1^{\alpha_h} B_2^2)} \quad (2.4)$$

$$\sigma_h = \frac{p_1 - \sigma_w (\Delta_1 B_1)^2}{f_1 B_1^{\alpha_h}}$$

where  $\alpha_h$  has been assumed as known. If it is unknown, it can be determined, providing that 3 groups of values are known. The most convenient case is  $(p_1, f_1, \Delta_1, B_1)$ ,  $(p_2, f_2, \Delta_1, B_1)$  and  $(p_3, f_1, \Delta_1, B_2)$ , that allow the determination of  $\alpha_h$ ,  $\sigma_h$  and  $\sigma_w$ .

Using this relation, the program PHPW was written .

**Extension of the magnetizing curve.** For the extension of the magnetizing curve, beyond 2T, one considers that the relative magnetic permeability ( $\mu_r$ ) has the following dependence:  $\mu_r = 1 + e^{aB+b}$ ; from two final points of the magnetizing curve  $(B_1, H_1)$  and  $(B_2, H_2)$  one finds:  $a = \ln(\mu_r - 1) - \ln(\mu_r - 2) / (B_1 - B_2)$ ; if  $B \rightarrow \infty$  results that  $\mu_r \rightarrow 1$ . With this relation, the magnetizing curves one can extend until 4.7 T. This extension one makes in the program ABMUR (IND7.FOR).

### 2.1.3. The Optimization Strategy

In general, optimization is a mathematical approach. Depending on the type of equation which describes the process, one emphasizes two categories of methods: linear and nonlinear.

One considers a function - named objective function – depending upon a set of variables (input data).

Optimization means to find the minimum or the maximum of this objective function.

The values assigned for the input data are given according to a rule named algorithm, which is essential for a good convergence of the searching process.

It is possible to modify successively the value of each input data and the optimum solution is found / decided after investigation of all the variation domains of all the input data. This is the unidirectional method.

The other possibility is to modify all the variables in their assumed domain. This is the random method. In this case, the number of iteration is the product between the number of iteration for each variable, so the computing time could be significantly increased.

#### The chosen method

One begins with the random method, which finds relatively quickly the area of the absolute extreme value.

This “optimum” is considered as starting value point for a new searching process using the unidirectional method, for a more accurate investigation.

The multiphase induction machines for general purpose could be classified in three types:

- with wound rotor;

- with single squirrel cage;
- with two squirrel cage.

The stator slot is, in general, trapezoidal shaped (Fig. 2.3.a).

The rectangular shaped slot is considered as a particular case of the previous one.

The rotor slot could have different shapes, depending on the machine require torque curve. In Fig. 2.3.b it is presented the trapezoidal rotor slot.

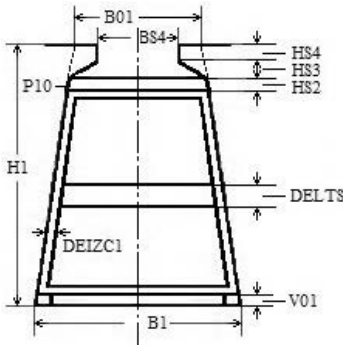


Fig. 2.3.a The trapezoidal stator slot.

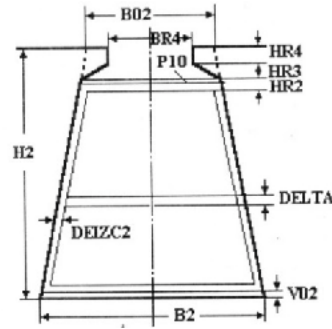


Fig. 2.3.b The trapezoidal rotor slot.

Figure 2.4 presents the general-shaped rotor slot.

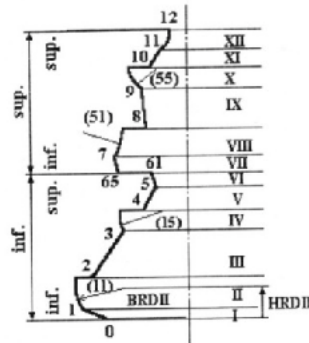


Fig. 2.4 The general-shaped rotor slot.

In the optimization process, 5 variables are considered:

- L – the ferromagnetic core length;
- D – the inner diameter of the stator;
- DEX – the outer diameter of the stator;
- N1 – the number of stator turns per phase;
- J1 – the stator current phase density;
- DIN – the inner diameter of the rotor.



For the wound rotor machines one considers, in optimization, other 3 variables: B02, B2, (see Fig. 2.3) and J2, the rotor bar current density.

For induction machine with single squirrel cage and trapezoidal shaped rotor slot one adds: JIL – the current density in the cross section of the end ring;

BIL – the width of the end ring.

For induction machines with two squirrel cages optimization requires 20 variables.

The variables corresponding to the stator are 8, these corresponding to the end ring are 2 (BIL, QIL).

The rotor slot is presented in Fig. 2.4 and the variable data are 10 (BRD00, BRD02, BRD08, BRD6S, HRDII, HRDSI, HRD02, HRD08, HRD12, HRD6I).

### 2.1.4 Numerical examples

The 4-pole induction machine with the rated power of 75 kW, 132 kW and 250 kW, (380 V, 50 Hz) were optimized.

The objective function was the sum W between COST – which is of the main materials (ferromagnetic core, stator and rotor conductors) and the losses for the whole lifetime of the machine.

**Case 1.** Optimization assuming the same value of the outer diameter of the stator as the initial machine.

**Case 2.** Optimization including the outer diameter of the stator as variable.

One considers the initial machine as “**Case 0**”.

The figure 2.5 presents the main geometrical dimensions of the optimized machines (1 and 2) and of the initial one (0).

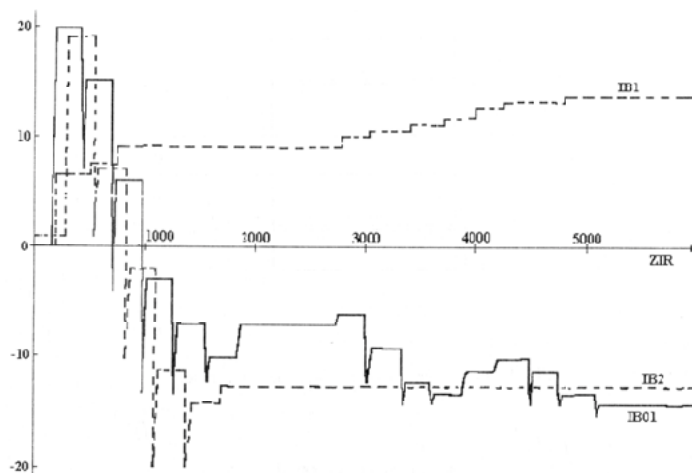


Fig. 2.5 the main geometrical dimensions of the optimized machines (1 and 2) and of the initial one (0).

In Table 2.1 are given the values of the machine data, including the dimensions of the stator and rotor slots, the number of wires per stator phase N1 and G – the weight of the main materials (ferromagnetic core, stator winding and rotor cage).

Table 2.1 The values of the machine data.

Pn	Tip	D	DEX	DIN	L	B1	B01	HI	B2	B02	H2	NI	G
75	0	265	425	75	230	11.48	7.66	33.8	2.92	8.75	46.60	64	234.8
	1	244	425	75	386	15.88	7.96	42.45	3.52	11.65	55.88	56	366.5
	2	282	589	75	291	17.58	5.86	48.35	3.12	12.35	62.85	56	571.2
132	0	330	500	85	295	13.54	9.58	37.6	6	6	64.7	50	420.6
	1	290	500	85	364.5	15.44	8.28	54.2	3.5	14.2	68.4	50	481.3
	2	346	733	85	269.5	17.84	6.18	64.84	4.7	15	75.2	50	832
250	0	371	550	100	530	13.33	9.38	37.63	5.5	5.5	69.35	25	881.4
	1	317	550	100	657.5	16.03	7.98	49.89	4.2	15.2	70.27	25	1038
	2	325	764	100	510.5	18.53	5.68	55.2	5.3	16	80.13	25	1662

The machines performances are presented in Table 2.2, where  $\Delta W = W_0 - W$ .

Table 2.2 The machines performances.

Pn	Tip	BDE	J1	J2	KS	KIP	KMK	KMP	CFI	RAN	COST	W[\$]	$\Delta W$
75	0	0.79	4.49	2.5	0.40	6.00	2.78	0.92	0.89	0.935	243.9	4209	0
	1	0.56	2.43	1.39	0.94	5.72	2.70	0.79	0.88	0.947	430.6	3635	573.7
	2	0.65	2.11	1.19	0.89	6.62	3.12	0.79	0.88	0.935	560.7	3389	819.6
1	0	0.64	3.97	2.23	0.40	4.97	2.09	0.97	0.88	0.959	476.8	7037	0
	3	1	0.56	2.57	1.48	0.94	4.85	2.27	0.55	0.87	0.949	611.3	5959
2	2	0.64	2.04	1.18	0.97	5.58	2.61	0.53	0.87	0.956	867.2	5445	1591
2	0	0.67	3.52	2.19	0.17	5.22	2.20	1.19	0.88	0.947	852.8	1158	0
	5	1	0.58	2.44	1.29	0.83	5.03	2.40	0.68	0.86	0.955	1133	1020
0	2	0.64	2.12	1.00	0.88	5.90	2.78	0.70	0.87	0.959	1533	9592	1988

The evaluation of the optimization efficiency is made using  $k_0$  and  $k_c$  as follows:

$$k_0 = (W_0 - W) / W ; k_c = (W_0 - W) / \text{COST}$$

In Table 2.3  $k_0$  and  $k_c$  correspond to Case1, and in Table 2.4 to Case2 of optimization.

Table 2.3 The evaluation of the optimization efficiency, Case1.

75 kW		132 kW		250 kW	
$k_c$	$k_0$	$k_c$	$k_0$	$k_c$	$k_0$
1,332	0,158	1,762	0,181	1,213	0,135

Table 2.4 The evaluation of the optimization efficiency, Case2.

75 kW		132 kW		250 kW	
$k_c$	$k_0$	$k_c$	$k_0$	$k_c$	$k_0$
1,462	0,242	1,835	0,292	1,297	0,207

### 2.1.5. Conclusions

Induction machines are the simplest, most robust, operation safe and least costly machines, their combination with variable frequency converters may satisfy, practically, any dynamic requirement. Therefore, they are the most widely used machines. Their operational life is comparable to the life of their components, estimated to extend over 20 ~ 40 years.

Even if these machines are highly efficient, their efficiency can be further increased so that the difference between the total costs of a normal present machine and that of an optimized machine, taking into account the life-span, could cover several times the cost of its component materials.

This is one of the main reasons to consider the transformation of electromechanical in heat via losses, when a portion of it could be saved from dissipation into the environment, as inadmissible.

The promotion of energy optimized machines is somehow hindered by the fact that the manufacturer and the final user of the machines, the consumers, have distinct interests, linked to society's structure. The manufacturers are interested in keeping manufacturing costs as low as possible, to allow them to sell, taking into account competition, as many products as possible. While consumers are interested in buying at the lowest cost possible.

The costs of the machine also include operating costs, so that the consumer is interested in lower maintenance costs. As long as the manufacturer and the consumer are totally independent, with their divergent interests, the optimization problem cannot be practically solved.

The only way that leads to higher efficiencies is to have a higher authority that considers manufacturers and consumers, the government. The government can act appropriately, based on recommendations from specialists' panels. This problem has a general character and applies to any product.

Optimization of induction machines represents a research task. The problem has been tackled theoretically, to find a mathematical optimization method. Huge difficulties appear due to the non-linear character of the magnetization process, influenced by many factors, leading to questioning the rightness of material constants. Using the finite element method implies knowing as precise as possible the magnetization curves for different machine parts. These curves are influenced by temperature, mechanical stress, besides frequency, time variation of magnetic stress, accuracy of material constants as well as the 2D and especially 3D calculation of the electromagnetic field.

The proposed method considers the magnetic saturations improvable on-the-run and correction via coefficients found through testing. Because the biggest share in the overall losses is borne by winding heat losses, an accurate determination of those losses represents the main task of this undertaking.

Therefore, based on the results achieved, it has been considered beneficial to make available to induction machine designers both the EXE and the source code, to allow an important possible contribution to the improvement in the design and manufacturing of electrical machines by minimizing losses as much as possible.

## 2.1.6. References

- [1] B. Adkins, „Obsciaia teoria electriceskikh masin”, Moscva-Leningrad, Gosenergoizdat, 1960.
- [2] A. Alexeev, „Construcția mașinilor electrice”, Editura Tehnică, București, 1951.
- [3] P. Andronescu, „Bazele electrotehnicii”, Editura Didactică și Pedagogică, București, 1972.
- [4] P. Andronescu, „Aplicarea calculului operațional în studiul circuitelor electrice”, Editura Tehnică, București, 1957.
- [5] E. Arnold, L. La Cour, „Theorie der Wechselströme”, Vol I, „Die Wiclungen der Wechselstrommaschinen”, Vol III, „Die Induktionsmaschinen”, Vol V, Springer-Verlag, Berlin, 1923.
- [6] M. Babescu, D. Păunescu, „Mașini electrice”, Timișoara, Editura Politehnica, 2001.
- [7] C.Bălă, „Proiectarea mașinilor electrice”, Editura Didactică și Pedagogică, București, 1967.
- [8] I. Boldea, „Parametrii mașinilor electrice”, Editura Academiei Române, București, 1991.
- [9] I. Boldea, „Variable speed generators”, CRC Press, Taylor and Francis Group, 2006.
- [10] I. Boldea, L. Tutelea, „*Electric machines. Steady State, Transients, and Design with MATLAB*”, CRC Press Taylor & Francis Group, Boca Raton London New York, 2010.
- [11] A. Câmpeanu, I.Vlad, „Mașini Electrice. Teorie, construcție și aplicații”, Editura Universitaria, Craiova, 2006.
- [12] I. Cioc, C. Nica, „Proiectarea mașinilor electrice”, Editura Didactică și Pedagogică, București, 1994.
- [13] I. Dancea, „Metode de optimizare”, Editura Dacia, Cluj-Napoca, 1976.
- [14] I. Danilevici, V.Dombrovski, E. Kazovski, „Parametrii mașinilor de curent alternativ”, Editura Tehnică, București, 1968 (traducere din limba rusă).
- [15] T. Dordea, „Mașini electrice. Proiectare.”, Vol. II, Editura ASAB, București, 2003.
- [16] T. Dordea, T.P. Dordea, „Erzatzläuferimpedanz einer Inductionmaschine mit Vielfachen Käfig und in denselben Nuten untergebrachten Stäben”, Rev. Roumaine Sci.Techn. – Electrotechn. Et Energ., T.29, Nr.2, p.151-159, București, 1984.
- [17] T. Dordea, T.P. Dordea, Ghe. Madescu, I. Torac, L.C. Ocolişan, M. Moț, „Mașini Electrice, Programe de calcul”, Editura POLITEHNICA Timișoara, 2010.
- [18] I. Gheorghiu, Al.Fransua, „Tratat de mașini electrice. Mașini asincrone”, Vol. III, Editura Academiei Române, București, 1971.
- [19] F. Heiles, „Wicklungen electrischer Maschinen und ihre Herstellung”, 2 Auflage, Springer-Verlag, Berlin, 1953.
- [20] I. Lager, „Modele numerice directe pentru calculul câmpului electromagnetic staționar și static”, Editura Academiei Române, București, 2002.
- [21] M. Liwshitz, „Die elektrischen Maschinen”, Vol. II, Vol. III, Verlag Teubner, Leipzig und Berlin, 1934.
- [22] A. Nicolaide, „Mașini electrice”, Vol I, Vol. II, Editura Scrisul Românesc, Craiova, 1975.
- [23] W. Nürnberg, „Die Asynchronmaschine”, Springer-Verlag, Berlin, 1963.

- [24] M. Opaschi, R. Răduleş, „Proiectarea hidrogenatoarelor și a motoarelor sincrone”, Editura Tehnică, București, 1980.
- [25] I. Postnicov, „Proiectarea masinilor electrice”, Editura Energetică de stat, București, 1954.
- [26] H. Reiche, G. Glöckner, „Maschinelles Berechnung elektrischer Maschinen”, VEB-Verlag Technik, 1973.
- [27] R. Richter, „Mașini electrice. Mașini asincrone”, Vol. IV, Editura Tehnică, București, 1960.
- [28] W. Schuisky, „Berechnung electrischer Maschinen”, Springer-Verlag, Wien, 1960.
- [29] W. Schuisky, „Induktionmaschinen”, Springer-Verlag, Wien, 1957.
- [30] H. Sequenz, „Die Wicklungen electrischer Maschinen”, Vol. I, II, III, IV, Springer-Verlag, Wien, 1950-1973.
- [31] I. Vlad, S. Enache, D. Alexandru, „Utilizarea metodelor numerice în proiectarea mașinilor electrice de tracțiune”, Editura Sitech, Craiova, 2000.
- [32] E. Wiedemann, W. Kellenberger, „Konstruktion elektrischer Maschinen”, Springer-Verlag, Berlin, New York, 1967.

## 2. 2 Synchronous machines: ROBARUPT software

### 2.2.1 Generalities

Large AC electric machines have, because their output voltage practically does not exceed 20 kV, phase currents of the order of thousands of amperes. These currents require conductors with large cross-sections, where the skin effect leads to significant additional losses. To reduce those losses, the windings are executed using Roebel bars. These bars are made from insulated conductors (elementary conductors) whose cross-section area is around 10 mm<sup>2</sup>. The lowering of additional losses is obtained by a more evenly distribution of the bar current along the component elementary conductors. Therefore, elementary conductors have to be transposed starting from one side of the machine, for the bar part located in the slot, to the other side, so that each elementary conductor shall occupy all possible positions along the bar cross-section, as shown in Fig. 2.6. This requires the placement of the elementary conductors in the bar cross-section in two columns, whose structure is successively modified between the forms shown in A and B in Fig. 2.6. For transposing, elementary conductors have to pass from one column to the other. At the passage, the cross-sectional bar structure corresponds to form B, A being the form between two consecutive passages.

To make the connection between the bars that compose the winding, the bars are extended in both directions. No elementary conductor transpositions are usually provided along these extensions because of the technological difficulties involved.

The distribution of the electric current in the bars is determined by the internal magnetic field of the bar that partially links the bar, both for the part located in the slot but also for the end of the bar. The magnetic field that links completely the bar, that is all elementary conductors of the bar, does not influence the mode of the distribution of the

bar current along its elementary components. It influences only the leakage inductance of the bar.

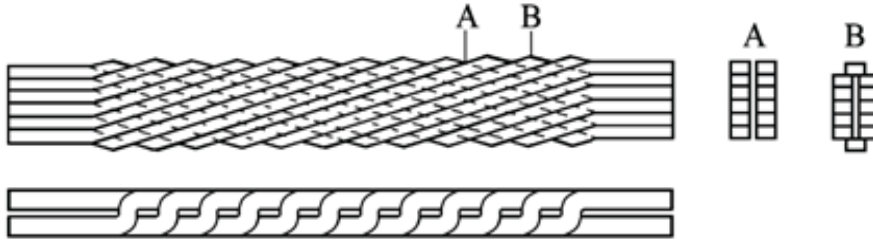


Fig. 2.6 Roebel bar: bar structure.

Two domains in which the internal magnetic leakage field has different spectra can be distinguished: the domain of the slot located bar and the bar end domain.

The magnetic field is produced, on one side, by the electric current in the bar, and on the other side, by the resultant ampere-turns of the machine due to the excitation current and the currents in the stator winding. The magnetic field of the slot, due to the bar current, has a spectrum with a transversal character, as shown in Fig. 2.7, running from one slot wall to the other, the field lines being nearly straight lines perpendicular on the slot walls.

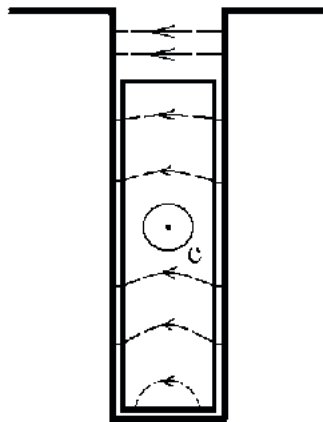


Fig. 2.7 Spectrum of the transversal magnetic field in a slot due to slot ampere-turns.

This field is mostly responsible for the skin effect current distribution phenomenon, as seen in Fig. 2.8 for one bar per slot and in Fig. 2.8.b for 2 stacked bars. For the conductor toward the opening of the slot, the distortion of the curve representing the current density is larger, because of the contribution of the field produced by the current of the first bar, located at the bottom of the slot.

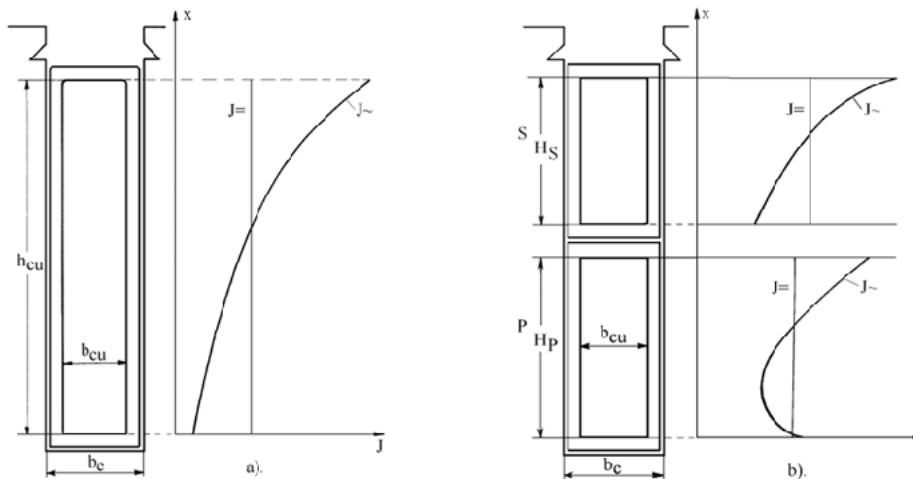


Fig. 2.8 Current distribution along conductors in a slot: a) one conductor; b) two stacked conductors.

If three or many bar layers are in the slot, then similar distribution curves are obtained .

Because of this effect, the electrical resistance of the bars in alternating current ( $R_a$ ) is several times higher than the electric resistance of the same bar in direct current ( $R_0$ ):

$$R_a = k_{ra} \cdot R_0 \quad (2.5)$$

where  $k_{ra} > 1$ .

Consequently, in the alternating current generator winding, additional losses appear unavoidably.

For the computation of energetic parameters, the lines of the leakage field from the slot are considered to be parallel to the slot base, i.e. perpendicular to the slot walls.

This field model is the basis for the computation of the current displacement effect, namely for the coefficient of increase of the bar electric resistance in alternating current.

A slot where  $m$ -layers of rectangular bars are located is considered (Fig. 2.9).

Each layer has a certain coefficient of resistance increase. For example, for the bar from the layer " $p$ ", the coefficient of resistance increase is [14]:

$$k_p = \varphi(\xi) + \frac{I_u(I_u + I_p)}{I_p^2} \Psi(\xi) \quad (2.6)$$

where the current  $I_p$  is the current from the considered layer, and  $I_u$  is the sum of the currents from all the layers located below the considered layer.

If the same current flows through all the  $m$ - bars, an average value of the coefficient of resistance increase per slot can be calculated as [14]:

$$k_{ra} = \varphi(\xi) + \frac{m^2 - 1}{3} \Psi(\xi) \quad (2.7)$$

The problem of current displacement effect could be solved in this way also in the case when the bar is formed by many subconductors, connected in parallel.

Similarly, it was developed an analytical method for the calculus of currents and losses in a bar composed of transposed elementary conductors [4, 5, and 20].

This method takes into account the current displacement phenomenon.

The magnetic field due to the machine ampere-turns has a radial character, as seen in Fig. 2.10.

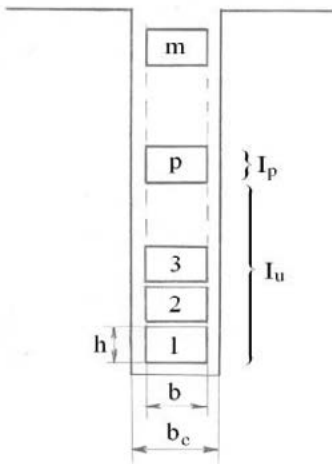


Fig. 2.9 Open slot with “m”- bars.

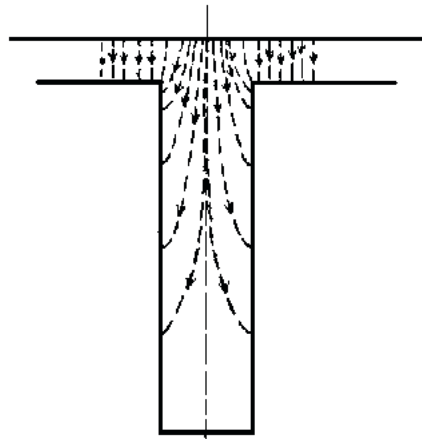


Fig. 2.10 Spectrum of the excitation magnetic flux in the slot zone.

The excitation field of a synchronous generator is generated by the current from the excitation winding, generally placed on the generator rotor. This magnetic field passes from rotor through air-gap into stator teeth, but enters also into the slot space, where the bars of stator winding are located. It generates inner circulating currents through the bar subconductors, which are short-circuited at the ends, forming short-circuit loops. These currents cause additional losses in the stator winding, leading to the decrease of the electric energy conversion efficiency.

This magnetic field from the stator slot area was calculated, with view to determining the currents and additional losses in bars. For this purpose, the conformal mapping method was used, in order to benefit from the advantages of the analytical methods for field computation.



On the basis of many computation examples, the following analytical relations of the radial magnetic field distribution in the slot width direction are proposed:

$$\begin{aligned}
 B_r(x) &= B_{rm} \sin\left(\frac{x}{b_c} \pi\right), \text{ for } |y| \geq 2\delta \\
 B_r(x) &= B_{rm} \left(\sin\left(\frac{x}{b_c} \pi\right)\right)^{0,8}, \text{ for } |y| \approx \frac{3}{2}\delta \\
 B_r(x) &= B_{rm} \left(\sin\left(\frac{x}{b_c} \pi\right)\right)^{0,5}, \text{ for } |y| \approx \delta.
 \end{aligned} \tag{2.8}$$

In order to develop as general as possible analytical solutions, the radial component of the magnetic flux density ( $B_{rm}$ ) in the slot axis and its distribution in the depth direction was analyzed further on.

By using many families of curves obtained from computation, as well as the MATHLAB facilities, an analytical relation for approximating the values of the magnetic field density in the slot axis was built under the following form, valid in any point from the slot axis:

$$B_{rm} = e^{-\alpha} B_{\delta \max} \tag{2.9}$$

where:

$$\alpha = m_m \left| \frac{y}{\delta} \right| + n_n \tag{2.10}$$

and:

$$\begin{aligned}
 m_m &= \frac{38,39 \left(\frac{b_c}{\delta}\right)^3 - 665,1 \left(\frac{b_c}{\delta}\right)^2 + 6507 \left(\frac{b_c}{\delta}\right)^1 + 1061}{\left(\frac{b_c}{\delta}\right)^3 + 909,4 \left(\frac{b_c}{\delta}\right)^2 + 2654 \left(\frac{b_c}{\delta}\right)^1 - 1246} \\
 n_n &= 0,0857 \left(\frac{b_c}{\delta}\right)^1 + 0,3786.
 \end{aligned}$$

By using the approximate relation (5) the value of induction in the slot axis can be determined, avoiding the difficulties in using the conformal mapping relation. These relations in the computing program for additional losses estimation was included.

The radial magnetic field in the slot shown in Fig. 2.10 acts in two ways: first by penetration of the electromagnetic field in a massive medium, generating volume losses

in the elementary conductors according to the amplitude of the vector of the magnetic induction; and secondly by generating circulating currents that close at bar ends, where elementary conductors are connected together. Losses created the first way can be considered via the resistivity of the conductor, for the second way, circulating currents have to be calculated.

For the end coils domain the own magnetic field of the bar has a spectrum as shown in Fig. 2.11.a. The influence of this field upon the current density in this domain is considered to be similar to the case of the elementary conductors placed in two opposite equivalent slots, as shown in Fig. 2.11.b where the width of the equivalent slot, generally:

$$b'_c = b + k_{bc} \cdot H. \quad (2.11)$$

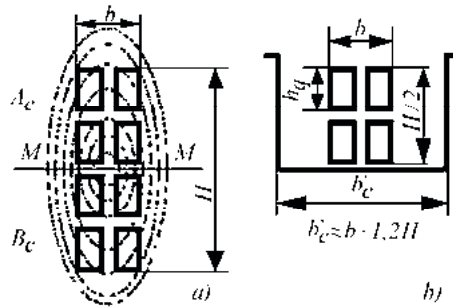


Fig. 2.11 Magnetic field in end bar zone a) Real magnetic field; b) Equivalent slot.

For the coefficient  $k_{bc}$  consider, as an average value  $k_{bc} = 1.2$ , but, for a better accuracy, it has to be determined by tests or by calculations using the method of finite elements.

In the end coil domain there is also a radial orientation magnetic field, caused by the excitation current of the machine in the part toward the ferromagnetic core, caused by currents in the stator winding by the LSPP1 part of Fig. 2.12 that, for this bar segment, can be considered as constant; for the next segment, LSPP2, the radial field varies along a practically monotonic descendent curve, toward the end of the bar, reaching the value zero, maintained along the entire segment LSPP3.

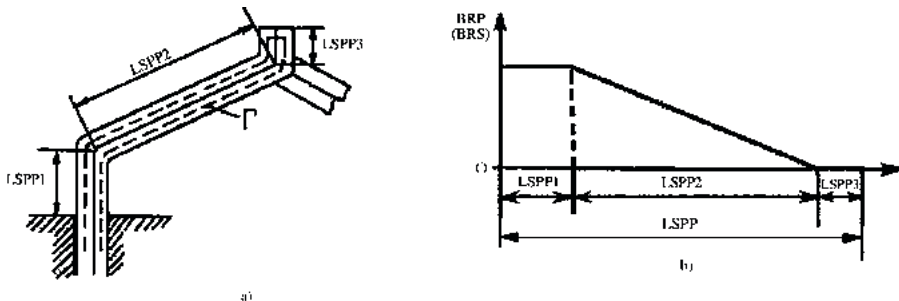


Fig. 2.12 Structure of end coil: a) geometrical dimensions; b) radial calculation field in the end coil zone.

The distribution of this field is considered as having the shape in Fig. 2.12.b used in calculation. The radial component leads to a circulating current along the curve  $\Gamma$  in Fig. 2.12a, a current that has to be considered.

### 2.2.2 Computing Model

The spectrum of the overall internal magnetic field for a Roebel bar is extremely complex, due to not only the run of an elementary conductor, but also due to the fact that there are non-linear media, whose specific material values are not constant and are affected by the magnetic saturation. To track magnetic processes using equations that can be used in the design process, simplifying assumptions have been made, to minimize errors (overestimated), but also manageable from the point of view of operation safety.

The geometry of an elementary conductor is shown in Fig. 2.13a, that depicts 2 consecutive conductors transposed from one plan to another, consecutive passage locations spaced by  $l_e$ . Fig. 2.13b gives the calculation graphical plan for an elementary conductor, consisting of parallelepiped segments in series, vertically offset, in the same column, by the height of the parallelepiped, while horizontally; the transposition in the upper and lower part of the bar is offset by the width of the parallelepiped.

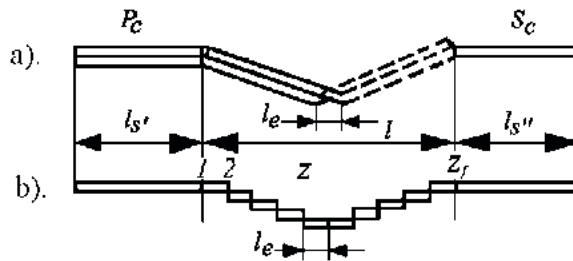


Fig. 2.13 Calculation graphical plan of an elementary conductor.

Following assumptions for the calculation of electromagnetic processes have been made:

- Rectangular slot.
- Elementary conductors have the form in Fig. 2.13.b, consisting of sections with a cross-sectional area equal to that of the real conductor, with a length  $l_e$
- The ferromagnetic core is non-saturated, with an infinite magnetic permeability.
- In the parts outside the slot, elementary conductors are not transposed and have the positions occupied in the first section of the slot for each end of the bar.
- The electric resistivity used for calculation is the same for all conductors made of the same material and along their entire length.
- The passages from one section to another do not influence the distribution of the electric current in any of the two sections involved.

- The rectangular hollow elementary conductor has the same wall thickness along all sides, so that, for a zero cavity area, the conductor becomes a solid conductor.
- The field lines in the slot hosting the bar and also in equivalent slots as shown in Fig. 2.11.b are straight lines, parallel to the base of the slot.
- The radial component of the magnetic induction in the slot, along the width of the slot, is sinusoidal with maximum amplitude in the axis of the slot and zero at the slot walls.
- The radial magnetic field in the end coil domain has a constant value distribution as shown in Fig. 2.12, the same for both winding layers.
- The bar current vs. time variation is sinusoidal, with a frequency  $f$ .

With these hypotheses, the total losses in a Roebel bar can be calculated.

For calculation purposes, the position of an elementary conductor in each position along the entire bar, from one end to the other, has to be identified. Therefore, for plan  $Z=1$  in Fig. 2.13, that coincides with the edge of the ferromagnetic core of the machine toward the beginning end P, the elementary conductors are numbered, beginning with the left bottom position (1), continuing up to the left top position for the conductor  $m$  and then, for the right column, beginning with the right top position with  $m+1$  and ending in the right bottom position with  $2m$ . The elementary conductors are two per level, marked as  $\lambda$ . There are  $m$  levels in a Roebel bar, so  $\lambda=1, 2, \dots, m$ . In the plan  $Z=2$ , following the first transposition, the elementary conductor 1 occupies the position of conductor 2 in the plan  $Z=1$ .

The level  $\lambda$  conductor, in the left column, is named  $\varepsilon_1$  (sequential number starting from the bottom of the bar), the one in the right column  $\varepsilon_2$ . For a plan  $Z$  whatsoever, following relation exists between the values  $\lambda$ ,  $\varepsilon_1$ ,  $\varepsilon_2$  and  $Z$ :

$$\begin{aligned} \varepsilon_1 &= \lambda + 1 - Z \quad ; \quad \varepsilon_1 = \varepsilon_2 + 2\lambda - 1 \\ \varepsilon_2 &= 2(m+1) - \lambda - Z \quad ; \quad \varepsilon_2 = \varepsilon_1 + 2(m - \lambda) + 1 \end{aligned} \tag{2.12}$$

where  $1 \leq \lambda \leq m$ ;  $1 \leq \varepsilon_1 \leq 2m$ ;  $1 \leq \varepsilon_2 \leq 2m$ . If during calculations of  $\lambda$ ,  $\varepsilon_1$  and  $\varepsilon_2$  the resulted values are outside set limits, these values are changed to values within set limits, paying attention that  $m$  for  $\lambda$  and  $2m$  for  $\varepsilon_1$  and  $\varepsilon_2$  are both periods.

For calculation, consider the elementary conductor section delimited by two consecutive plans  $Z$  and  $Z+1$ , as shown in Fig. 2.14. This section is considered as sliced in  $N$  bands, each of thickness  $h$ , considered along the bar section, thus through both elementary conductors  $\varepsilon_1$  and  $\varepsilon_2$ . The number  $N$ , that divides level  $\lambda$ , is chosen so that the band thickness  $h$  is so thin, that the current density is constant along this thickness: practically  $h$  shall be chosen of the order of  $10^{-7}$  m, i.e. under  $1\mu\text{m}$ . The smaller the value for  $h$ , the smaller the calculation error. As a consequence, a band contains two currents: one for the conductor  $\varepsilon_1$  and the other for conductor  $\varepsilon_2$ .

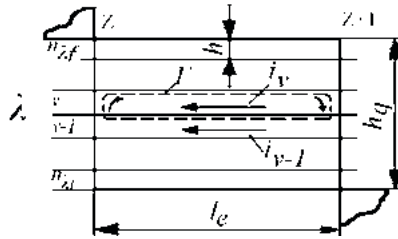


Fig. 2.14 Conductor element for loss calculation.

The strip's method is similar with a finite elements numerical method. For the considered assumptions, the bar losses are overestimated; the measured values are smaller than the calculated ones. These assumptions allow the currents estimation avoiding the use of magnetic vector potential, produced by the magnetic flux density  $\overline{B}$ .

Using these elements, the computer program ROBARUPT has been developed, using FORTRAN, with double precision setting. Different tasks regarding the Roebel bar can be pursued, the most important task being the determination of the bar structure to minimize losses (optimization of the Roebel bar), for a ferromagnetic core with given geometric dimensions and material constants.

The program source, all details for the software users and many numerical examples are presented in [20].

### 2.2.3 Tests to validate the model

In what follows, we briefly present the specifications of the full scale model bar tests setup used for strand currents measurement.

The model bar has 28 non-transposed strands (Fig. 2.15) in order to produce a strong skin effect and very different strand currents in the case of slot-embedded bar.

Other technical specifications and geometrical dimensions are given in Table 2.5.

1	28
2	27
3	26
4	25
5	24
6	23
7	22
8	21
9	20
10	19
11	18
12	17
13	16
14	15

Fig. 2.15 The model bar structure with 28 non-transposed subconductors (strands).

Table 2.5 specifications of the experimental model.

Length of iron core [mm]	900
Total bar length [mm]	2000
Slot width [mm]	20
Slot height [mm]	100
Bar cross-section [mm <sup>2</sup> ]	42.2 x 19.1
Strand cross-section [mm <sup>2</sup> ]	6.3 x 2.5
Strands number	28
Transducer type	LEM HTY 75P

Each subconductor of the bar has its own transducer that allows to measure the strand current (Fig. 2.16). So it is possible to know the currents distribution on the bar cross-section.



Fig. 2.16 Model bar with current transducers mounted on each subconductor.

The experimental test stand is shown in Fig. 2.17. One can see two bars embedded in the core slot. The iron core is made with iron sheets of 0.5 mm thickness. The bar dimensions correspond to the hydro-generator of 22 MVA working in a actual Romanian power plant.

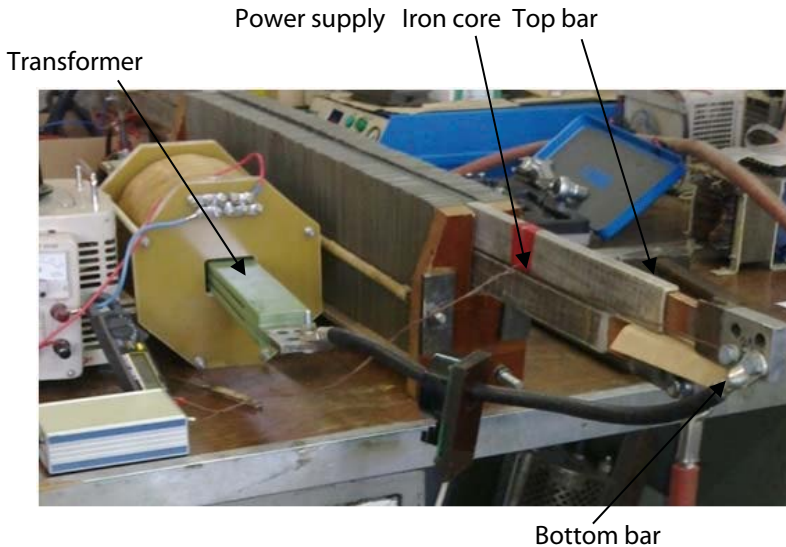


Fig. 2.17 Photo of full-scale model bar test setup.

The tests and computations were made on the model bar in three different conditions in order to simulate different kinds of skin effects. First, the bar is placed in free space, when a soft skin effect arises. Second, the bar is embedded in the slot (single layer and double layer) when the skin effect is very strong.

In the case of the slot embedded bar (single layer), the bar is placed in top position, without current in bottom bar. The calculated strand currents of this bar as complex phasors and the phasors diagram of these currents are given in Table 2.6 and Fig. 2.18.

Table 2.6 Calculated Strand Currents (Slot Embedded Bar)

Strand No.	Current phasor [A]	Modulus [A]
1	$38.394759 + 34.178991 j$	51.403900
2	$36.290061 + 23.823662 j$	43.411236
3	$34.375295 + 12.661552 j$	36.632988
4	$30.594268 + 5.013951 j$	31.002402
5	$26.354133 - 0.789099 j$	26.365944
6	$22.030683 - 4.990546 j$	22.588858
7	$17.901672 - 7.846351 j$	19.545718
8	$13.660123 - 8.708372 j$	16.199836
9	$10.427258 - 9.583177 j$	14.162097
10	$7.725688 - 9.834909 j$	12.506466
11	$5.584334 - 9.637076 j$	11.138134
12	$4.004555 - 9.131343 j$	9.970852
13	$2.747086 - 8.546105 j$	8.976769
14	$2.409130 - 7.610098 j$	7.982326

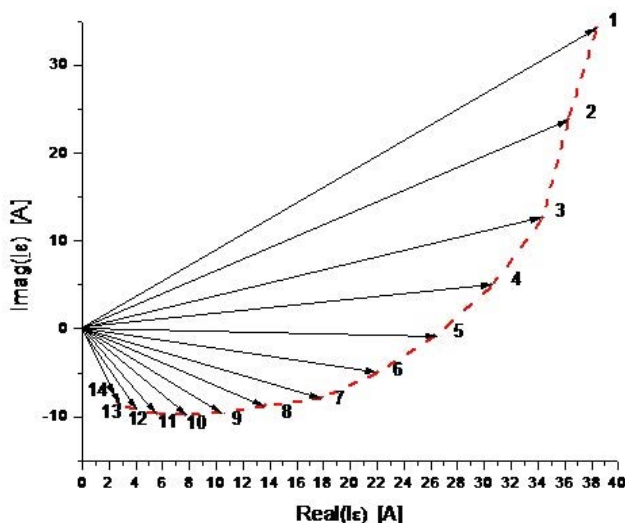


Fig. 2.18 Phasor diagram of calculated strand currents and hodograph curve in the case of slot embedded bar (total current 505 A, rms).

Experimental recorded values of the strand currents in the slot embedded single bar using data acquisition system are shown in Fig. 2.19. Because the system has 16 channels, all strand currents of the first column (c1-c14) and another two strand currents of the second column (c26 and c27 were recorded at a given moment). As we can see in Fig. 2.19, the strand current c2 and c27, or c3 and c26 are very close to each other.

The tests were made with a total bar current of 505 A (rms value), at 50Hz. Without the skin effect (d.c. – conditions), all the strand currents will be equal with 18,036 A.

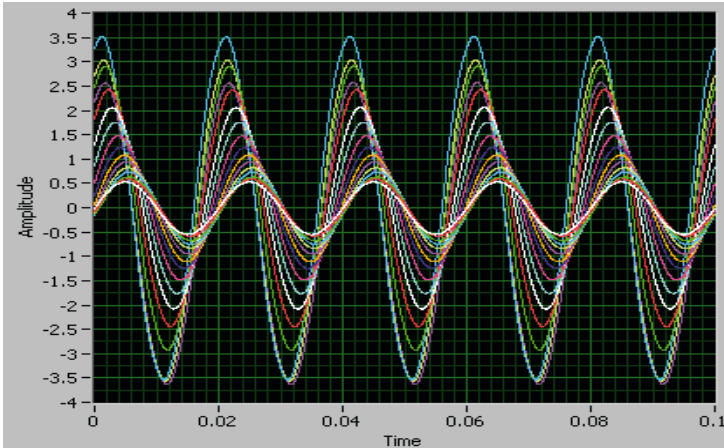


Fig. 2.19 Measured time variation of the strand currents in the slot embedded single bar.

The calculated and measured values of the strand currents are compared in Fig. 2.20.

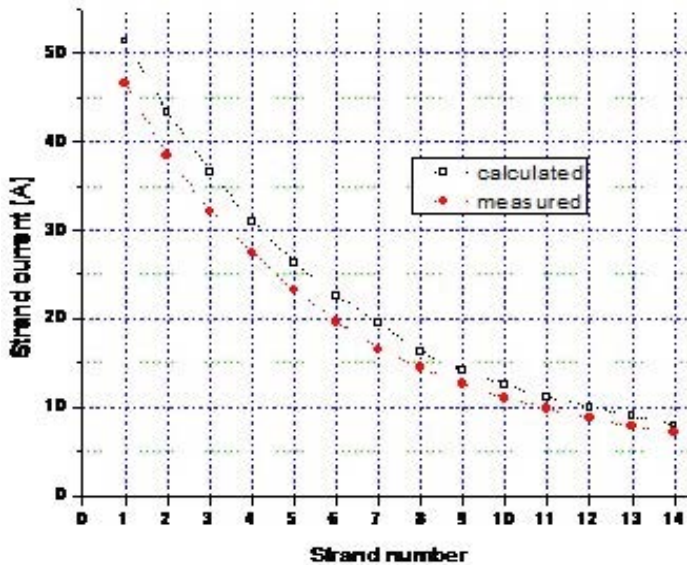


Fig. 2. 20 Measured and calculated strand current distribution in slot embedded bar (total bar current 505 A).

The calculated results using ROBARUPT software are close to the measured values of the strand currents and confirm the effectiveness of the strips method that provides a good estimation of both strand currents and additional losses in winding bars (including Roebel bars) of high power electrical machines.



In addition, this method allows in-depth study and gives greater insight into the problem of skin effect.

## 2.2.4 References

- [1] Bernard J. Bennington, W. C. Brenner, „Transpositions in Turbogenerator Coil Sides Short Circuited at Each End”, *IEEE Transactions on Power Apparatus and Systems*, Vol. PAS-89, No 8, November-December, 1970, pag. 1915-1921.
- [2] T. Dordea, Gh. Madescu, Ileana Torac, M. Moț, „Optimization of the windings structure for a.c. high power electrical machines”, *Proceedings of the 8<sup>th</sup> International Conferences OPTIM 2002*, Vol. II, pp. 315-322.
- [3] T. Dordea, Ileana Torac, Ghe. Madescu, M. Moț, L. Ocolişan, „The calculus of the electric currents through the full elementary conductors of the Roebel bar”, *Proceeding of the 14<sup>th</sup> International Symposium on POWER ELECTRONICS Ee2007*, Novi Sad, Serbia, Nov. 7-9, 2007.
- [4] T. Dordea, M. Biriescu, Gh. Madescu, Ileana Torac, M. Moț, L. Ocolişan: „Calcul des courants électriques par les conducteurs élémentaires d'une barre Roebel. Part I: Fondements de calcul”, *Révue Roumaine des Sciences Techniques*, Vol. 48, nr.2-3, pp. 359-368, Bucharest, 2003.
- [5] T. Dordea, M. Biriescu, Gh. Madescu, Ileana Torac, M. Moț, L. Ocolişan, „Calcul des courants électriques par les conducteurs élémentaires d'une barre Roebel. Part II: Détermination des courants”, *Rev. Roum. Sci. Tech. – Électrotechn. et Énerg.*, Vol. 49, nr.1, pp.3-29, Bucharest, 2004.
- [6] T. Dordea, Ileana Torac, Ghe. Madescu, M. Moț, L. Ocolisan, „Analytical estimation of the electric current in the elementary conductors of a Roebel bar”, *Proceedings of the 11<sup>th</sup> International Conference on optimization of electrical and electronic equipment OPTIM 2008*, Brasov, May 22-23, Vol II, pp. 33-38, 2008.
- [7] T. Dordea, I. Torac, Ghe. Madescu, M. Moț, L.C. Ocolisan, „Analytical Estimation of the Roebel bar Losses”, *Proceedings of ELECTROMOTION 2009 EPE*, Chapter “Electric Drives”, July 1-3, Lille France, 2009.
- [8] T. Dordea, V. Proca, Ghe. Madescu, M. Biriescu, M. Greconici, M. Moț, I. Torac, L. Ocolisan, „Roebel bar model for additional losses estimation in high power generators” *Proceedings ELS 2009*, Suceava, Romania, pp. 33-36, Sept. 24-25 2009.
- [9] T. Dordea, A. Câmpăan, G. Madescu, I. Torac, M. Moț, L. Ocolisan, „Strips Method For Evaluating AC Losses in Slot Portion of Roebel Bars - Errors Analysis”, *Rev. Roum. Sci. Tech. – Electrotech. et Énerg.*, Bucarest, pp. 29-36, Jan-Mar 2009.
- [10] Johann Haldeman „Transpositions in Stator Bars of Large Turbogenerators”, *IEEE Transactions on Energy Conversion*, Vol 19, No 3, September 2004.
- [11] M. Iseli, K. Reichert, G. Neidhöfer, „End Region Field and Circulating Current in Roebelbars”, *Proceeding ICEM 1990*, Vol II, pp. 718-723, 1990.
- [12] D. C. Macdonald, „Losses in Roebel bars: effect of slot portions circulating currents”, *Proceedings IEE*, Vol. 117, No.1, pp. 111-118, January 1970.
- [13] Tang Renyuan, Xu Guangren, Tian Lijian, Zhao Danqun, Xu Yi, „Calculation of end region magnetic field and circulating losses for turbo-generators using a coupled field and circuit equations method”, *IEEE Transactions on Magnetics*, Vol. 26, No.2, pp. 497-500, March 1996.
- [14] R. Richter, „Elektrische Maschinen Erster Band Allgemeine Berechnungselemente Die Gleichstrommaschinen”, Verlag Birkhauser Basel, 1951.
- [15] K. Takahashi, K. Ide, M. Onoda, K. Hattori, M. Sato, M. Takahashi, „Strand current Distribution of Turbine Generator full-Scale Model Coil”, *Proceedings of ICEM 2002*, Brugges, 2002.

- [16] M. Fujita, Y. Kabata, T. Tokumasu, K. Nagakura, M. Kakiuchi, S. Nagano, „Circulating currents in stator coils of large turbine generators and loss reduction”, *IEEE Trans. on Industry Applications*, Vol. 45, no. 2, pp. 685-693, March/April 2009.
- [17] E. Wiedemann, W. Kellenberger, „Konstruktion elektrischer maschinen”, Springer-Verlag, Berlin, 1967.
- [18] T. Dordea, V. Proca, G. Madescu, I. Torac, M. Biriescu, M. Moț, L. Ocolișan, „Computation and measurement of strand currents in a full scale multistrand conductor”, *Proceedings of the Romanian Academy, Series A*, Vol. 14, Nr. 4, pp. 351-359, 2013.
- [19] Yanping Liang, Xu Bian, Honghao Yu, Lei Wu, Lichao Yang, „Analytic algorithm for strand slot leakage reactance of the transposition bar in an a.c. machine”, *IEEE Transactions on Industrial Electronics*, Vol. 61, No.10, pp. 5232-5240, October 2014.
- [20] T. Dordea, T.P. Dordea, Gh. Madescu, Ileana Torac, L.C. Ocolișan, M. Moț, „Electrical Machines. Fortran Programs”, Editura POLITEHNICA Timișoara, pag.262-374, 2015.

## 2.3 Voltage transformer with variable ratio and fine control

Laboratories for testing electric equipment require (for) continuous variation of the supplying voltage. For this reason, Acad. T. Dordea proposed an original, ingenious solution to modify the underload voltage with however low step value.

### 2.3.1 Basic elements

Voltage transformer with variable ratio and fine control is a voltage transformer or autotransformer with variable ratio between the output and input voltage with the possibility of low step voltage control used to supply the electric circuits requiring the continuous variation of the underload voltage. Transformers and autotransformers at which the lowest step the output voltage can be changed with is equal with the value of the voltage on turn, are known.

The disadvantage of these consists in that they cannot provide enough fine quasicontinuous controls required for some industrial applications and in laboratories, too.

If they are designed for a reduced enough value of the voltage, in turn they lead to an increased cost price and to unacceptable constructive dimensions.

Variable ratio and fine control voltage transformer in accordance with solution eliminates the above mentioned disadvantage by that, in the view of the division of the flux linking a turn has a metallic distribution grid crossing the transformer column dividing it in two or more elementary sections depending on the number of elements of the grid. Division of the flux linking a turn provides the suitable acquiring of some fractions from the voltage induced on a turn. The current path is switched from an element to the other of the conductor grid galvanically insulated as against the column sheets.

With a view to achieve a continuous control on a large voltage range in the vicinity of the distribution grid it is placed a fixed collector having a number of metallic sectors equal with the number of the elementary sections in which the column is divided. The sectors of the connectors are successively connected with the free ends of the grid A movable equipment

supporting a brush slipping on the collector and a metallic contact head rolling along the winding turns rotates round the collector a galvanic connection being available between the brush and head.

The solution has the following advantages:

- it provides a fine adjustment of the output voltage on however small steps determined by the number of elements of the distribution grid of the column;
- it allows the underload voltage control;
- it can be applied to all types of transformers: with two galvanic separate windings; with one winding, single-phase, three-phase etc.;
- setting up of an unsymmetry requested between the phase voltages.

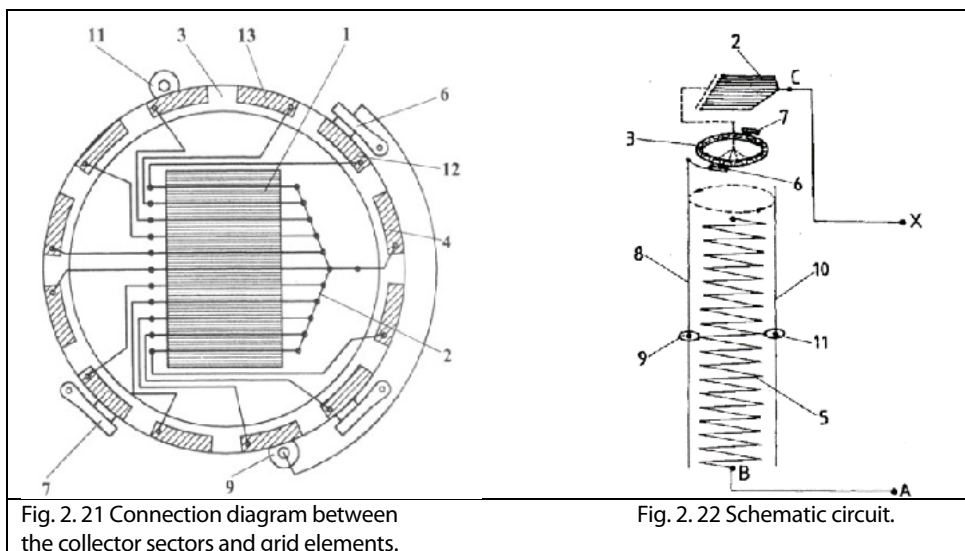
An example of the accomplishing of this solution is that of Fig. 2.21, 2.22 and 2.23 meaning: Fig. 2.21 - connection diagram between the collector sectors and grid elements; Fig. 2.22 - schematic circuit; Fig. 2.23 - switching system.

In accordance with the solution, column 1 of the transformer (autotransformer) is crossed by all the eleven elements of the grid 2 by some spaces obtained by cutting some sheets and removing the cutting parts. Elements of the distribution grid 2 as a sheet-metal strip, divide the section of the column into twelve equal parts. One of the ends of each element is connected to the C common point of the grid.

Collector 3 has a number of twelve metallic sections equal with the number of essential sections in which the column of the ferromagnetic core is divided. The sections of the collector are connected successively at the free ends of the grid. The lost section 4 is connected at the common point C.

The height of the column is determined by the height of the winding 5, Fig. 2.22, the width of the collector 3, the width of the grid elements 2 and the spaces among these on longitudinal direction.

The movable equipment supports the active brush 6, balance brush 7 guide rod 8 of the equilibrium roller 9 bar 10 to guide the equilibrium roller 11 and it rotates with these, concentrically with winding 5 of the transformer. Brush 7, roller 11 respectively balances the pressing forces on the active brush on the active roller respectively with a view to reduce the friction forces from the movable equipment guides. Driven by rods 8 and 10 the rollers 9 and 11 roll along the winding turns performing simultaneously a turning movement round the proper axes and a helical motion round the winding axis having as a result a displacement of the rollers along the guide bars. The groove being on the outer surface of the rollers provides a permanent contact with the turn determining the rollers to follow its route. Metallic rod 8 provides the connection between the active roller 9 and active brush 6.



On a certain position of the movable equipment the current path has the following route: terminal A, point B, contact point between the active roller 9 and winding, active brush 6, sector 12 of the collector, the first element of the division grid, common point C, terminal X. A rotation of the movable equipment by 30° against the previous position determine:

- the rolling of the active roller on the turn on length of an arc of circle of 30°;
- transfer of the active brush from the sector 12 on sector 13;
- switching of the current path from the first element on the second element of the grid 2;
- variation of the voltage between the terminals A and X with the twelfth part from the voltage of a turn.

To achieve a switching to the collector without breakdown of the current path an additional brush 14 is mounted near the active brush 6, shifted adequately and connected with active brush through an electric resistance 15 to limit the short-circuit current between two adjacent sectors. With a view to balance the pressing forces on the switching brushes 6 and 14, two equilibrium brushes, off - line neither to the electric circuit nor among them identical with the switching brushes are placed antipodal as against to these. An automatic system for positioning of the brushes on the collector impedes the stopping of the movable equipment if the brushes 6 and 14, Fig. 2.23 run over different sectors and allows their stopping only if the two brushes run over the same sector of the collector. The movable equipment electrically driven by means of some mating gears, rotated in one direction or in the other one determines an increase or a decrease of the output voltage in steps equal with 0,57V, the voltage on a turn being of 6,8V.

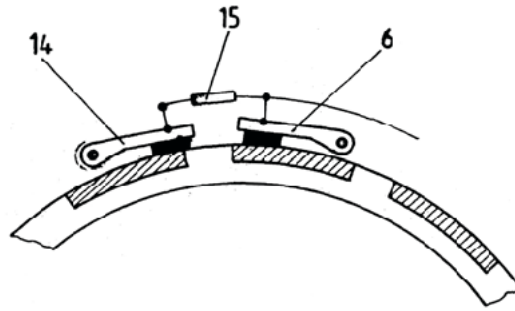


Fig. 2.23 Switching system.

### 2.3.2 Full-scale model and awards

For theoretical and practical research on this topic we applied for a grant, provided by the National Program INVENT-2001.

The prototype realized by ICMET Craiova, co-partner with Romanian Academy-Timisoara Branch, is presented in Fig. 2.24.

The proposed solution has many advantages and represents an undoubtedly technical progress in comparison with the other known solution for underload voltage control.



Fig. 2.24 Full-scale prototype.

The prototype was tested by ICMET Craiova and the results confirmed the expectations. The importance of the original proposal solution was recognized by the patented invention, awarded six times, as follows:

- **Diploma for Excellence in Research** - 2000, National Agency for Science, Technology and Innovation, for outstanding Scientific, technique and economic value;
- **Silver Medal**, International Fair of Inventions, Geneva, 2001 (Fig. 2.25);
- **Silver Medal**, International Fair of Innovation, Research and New Technologies, Brussels, EUREKA 2002;
- **Prix GRAND GENIUS**, International Inventions Fair Genius - Budapest, September 2006;
- **Silver Medal**, International Fair of Inventions and New Technologies, INVENTIKA - Bucharest, October 2006;
- **Gold Medal**, International Fair of Innovation, Research and New Technologies, Brussels, EUREKA, November 2006 (Fig. 2.26).



Fig.2.25.



Fig.2.26.

### 2.3.3 References

- [1] T. Dordea, V. Proca, A. Vintilă, M. Petrescu, E. Lăzărescu, G. Madescu, „Transformator de tensiune cu raport variabil și reglaj fin”, Brevet de invenție, România, nr.117053/30.04.2002, ICMET Craiova, 2002.
- [2] V. Proca, M. Petrescu, T. Dordea, G. Madescu, „Transformator de tensiune cu raport variabil și reglaj fin”, Brevet de invenție, ICMET Craiova, România, nr.120364/30.06.2006.
- [3] V. Proca, T. Dordea, G. Madescu, „Transformator cu raport variabil și reglaj fin al tensiunii în sarcină”, în Editura ICMET Craiova, ISBN 973-86650-1-9, 2004.

[4] Jun-Zong Lin, P-A. Metka, „Strategie for Hardening UPFC Constraints in Steady-State Power Flow and Voltage Control”, *IEEE Power System*, Vol.15, pp.566-571, May 2000.

[5] G. Madescu, „Realizări recente ale Academicianului Toma Dordea”, *Revista Coloana Infinitului*, anul XIV, nr.76, Timișoara, pag.29-32, 2011.

## 2. 4 Inverter-fed induction motor for direct-drive bogie of a tramcar

### 2.4.1 Project idea

The most used solution for electric drive bogie of a tramcar are with one or double stage transmission of torque from electric (dc or ac) motor to the vehicle axle.

The main disadvantages of this solution are:

- expensive mechanical solution;
- high weight of the transmission;
- high pollution risk ;
- expensive maintenance of transmission;
- high noise level;

Acad. T. Dordea proposed a direct drive induction motor solution for urban traction.

In 1997 it was organized, at the Romanian Academy –Timisoara Branch, a meeting with a few potential manufacturers (Feroviar Proiect – Reșița, INDA - Craiova, CAROMET – Caransebeș, UCM - Reșița, ELECTROMOTOR Timișoara), some local public transport companies (from Timisoara, Arad, Cluj- Napoca, Reșița) and scientists from Universities Polytechnic din Timisoara and INDA – Craiova to analyze the research project of a direct drive induction motor for urban traction. All the participants confirmed the value of the proposed solution and their intention and possibilities to contribute for the prototype manufacture.

### 2.4.2 The design and performance of the motor prototype

The electric direct drive system demands from the motor a high torque level, the same as the wheel axle require. Hence, these motors are larger than the usual ones. On the other hand, space is limited around the wheel axle. In these conditions, a compact motor design with low motor losses is necessary.

Given the limited space, the electric motors showing tube shape such as induction are much better suited for direct drive in a rail vehicle than those of disk shape, such as transversal and axial flux motor.

Therefore, an induction motor for direct drive of wheel set was chosen, and a dedicated computing program INDARUPT that finds the best motor design, with highest efficiency was applied. Considered data for conducting calculations was: rated power  $P_N=130$  kW; poles number  $2p=10$ ; rated voltage  $U_N=380$  V; rated frequency  $f_N=50$  Hz.



The prototype motor was built by Uzina Constructoare de Maşini – Reşiţa (U.C.M.R.).

To ensure a tram-speed from zero to maximum 60 km/h, the motor will be supply by a power inverter, with variable voltage and variable frequency between 3÷30 Hz.

Mechanical design had to be performed considering stator housing, forced air cooling, and bearing concept. Outer stator was built from iron sheets with 60 slots. The laminate stacks contain a common three-phase two layer winding.

Due to technological reason, the stator winding of the prototype motor was built with preformed copper coils. Hence, the iron stack has open slots of rectangular shape that cause high order harmonics and additional stray loses decreasing the motor performances. Then, magnetic wedge in the stator was used for reducing the unfavorable effect of having these open slots.

The inner rotor also from iron sheet was made and has a copper cage with 68 bars placed into the rectangular semi-closed slots. The rotor is fastened to the wheel-axle. The prototype motor was mounted with 60 magnetic wedges with  $h_w = 3$  mm and  $\mu = 2,57$ . The wheels were fastened directly to the motor prototype axes were for being then attached to bogie (Fig. 2.27.).



**Fig. 2.27** The wheel-set fastened to the motor prototype.

The motor prototype was tested firstly by UCM Resita for sinusoidal supplying voltage conditions.

The motor prototype provides a maximum torque up to two times the rated one (Fig. 2.28.) and an efficiency over 80% for a large operating area (Fig. 2.29), with flux control (by the inverter).



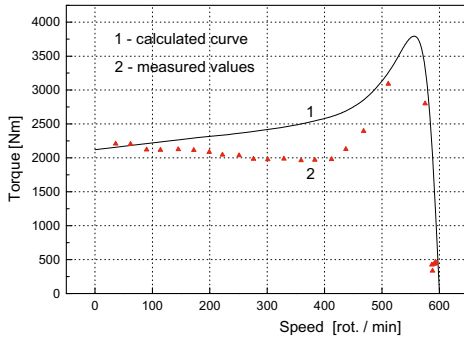


Fig. 2.28 Torque – speed characteristic:  
1- calculated curve; 2- measured values.

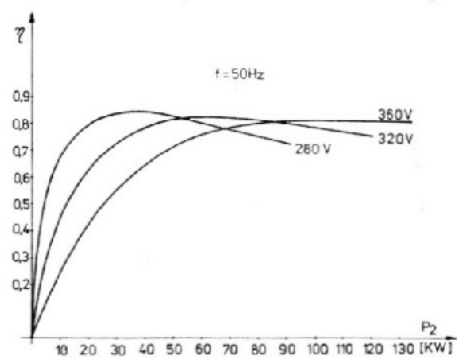


Fig. 2.29 The efficiency of the tested motor.

### 2.4.3 Tramcar bogie and drive-tests

A significant contribution to modify the tramcar bogie for the prototype motor was that of the local company for urban transport, Regia Autonome de Transport Timișoara (RATT).

One of the main disadvantages, in fact the cause of the most mechanical deficiencies, from the classic tramcar, is the driving gear of the driving axle, very important in indirect driving case of the axle for this type of vehicle.

The technical design adopted by the authors requires the mounting of the induction motor rotor direct on the wheel-axle, and the stator is supported by some spiral springs from the bogie frame.

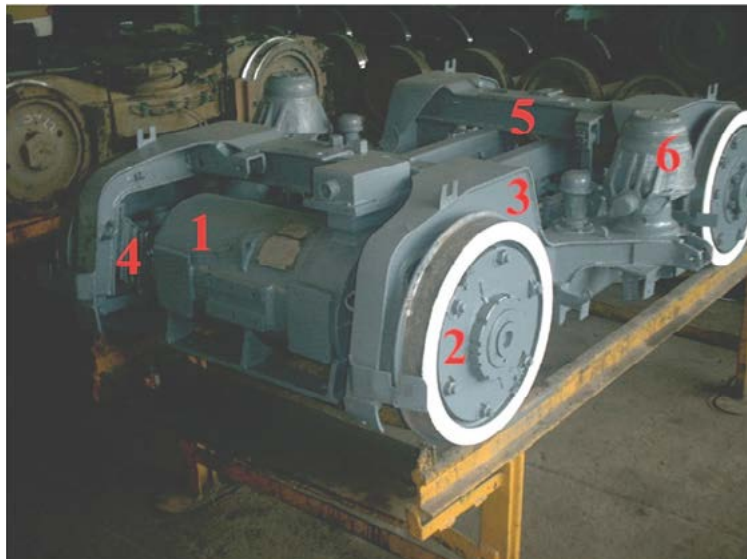


Fig. 2.30 The tramcar bogie – prototype.

The tramcar bogie – prototype (Fig. 2.30) consist of:

1– induction motor whose stator is fastened on the tram axle; 2– tram elastic wheel; 3– tram frame bogie longitudinal girder; 4– bogie primary suspension; 5– bogie frame traverse profile; 6– secondary suspension element made of rubber – metal.

The local transport company, RAT Timisoara provided a tramcar wagon, type TMIȘ – 2 and the experimental way for final testing, in really operating conditions, to evaluate the dynamic performance of the wagon. The following picture presents acad. Toma Dordea driving the tramcar bogie equipped with the prototype bogie (Fig. 2.31).

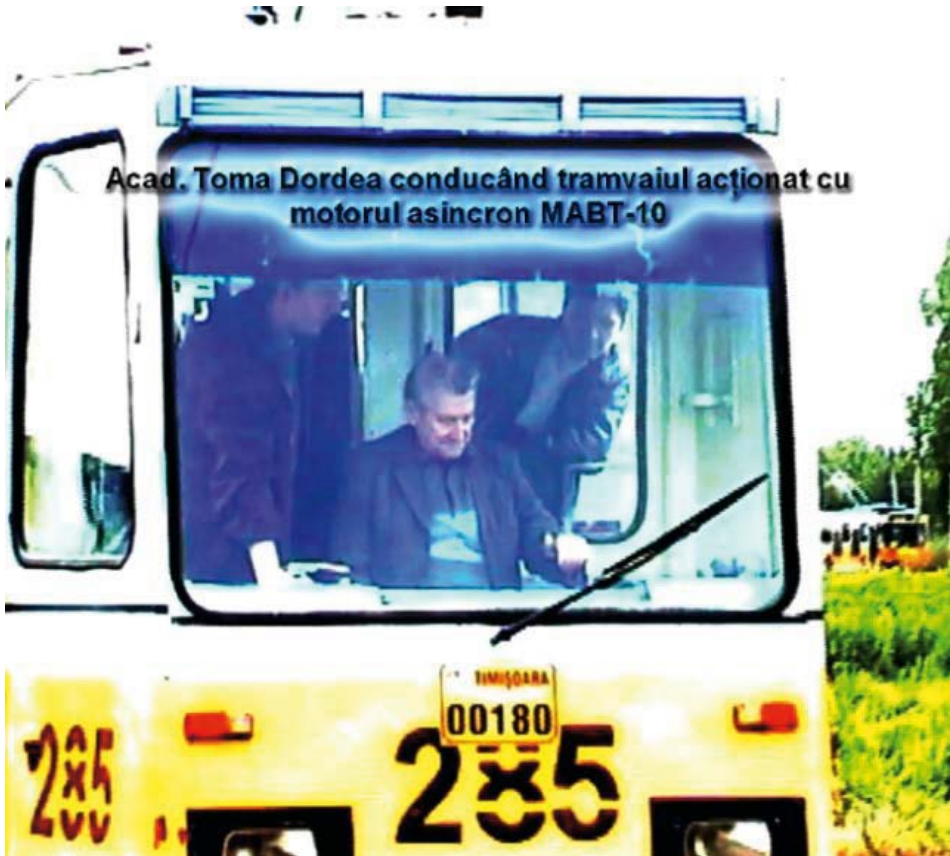


Fig. 2.31.

All tests on the experimental way were made in June 2006, by a team from INDA Craiova, led by dr.ing. Mihai Rădulescu; the motor was supplied from a dedicated inverter designed and built by INDA Craiova; also the electric braking with energy save was verified.

The tested driving system allows an accurate, smooth control in all operating regimes of the tramcar:

Measured acceleration is  $0.3 \text{ m/s}^2$  (Fig. 2.32). The acceleration was lower because of the second bogie with the „old” inactive dc motor and transmission which was additionally loaded.

One estimates an average acceleration  $0.8 - 0.9 \text{ m/s}^2$  for a speed between  $0 - 60 \text{ km/h}$ , with the assumptions as follows: • tramcar “Timiș 2” (one wagon equipped with 4 motors, each one on an axle - 2 bogies, and another wagon ) total weight  $40 \text{ t}$ ; • wagon with 4 motors on the 4 axle (2 bogies);

One finds the acceleration is slightly better than that of the old existing solution (dc motor with transmission).

The electric braking with energy save is feasible from maximum speed until  $3-4 \text{ km/h}$ .

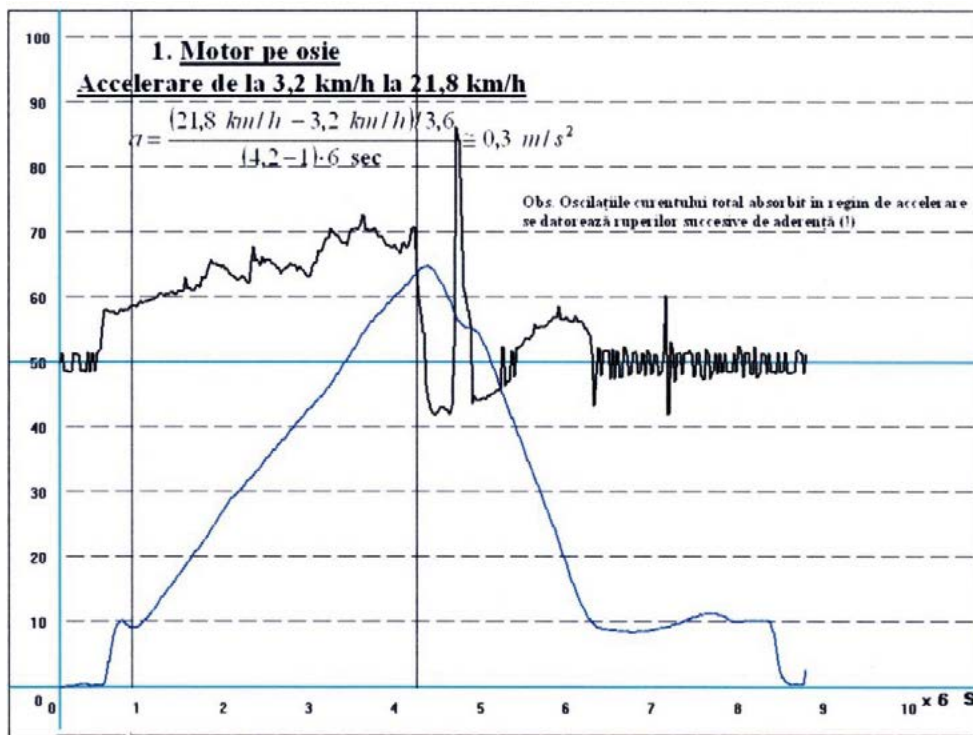


Fig. 2.32 Measured acceleration: 100 % speed = 1500 rpm ; 100 % total current = 600 A.

All tests of tramcar equipped with the prototype motor, running on the experimental way, confirms that the direct driven induction motor fed by inverter is a modern, efficient, appropriate solution for urban traction.

More than 10 years ago, a large team led by Acad. Toma Dordea was involved in proving that this solution is feasible, useful and may contribute to the re-birth of tramcar fabrication in Romania.

## 2.4.4 References

- [1] J. F. Gieras, N. Bianchi, Electric Motors for Light Traction, *EPE Journal*, vol. 14, p.12-23Febr. 2004.
- [2] A. Jöckel, H.J.Knaak, INTRA ICE, „A Novel Direct Drive System for Future High Speed Train“, Bruges, *Proceedings ICEM 2002*.
- [3] W. Hackmann, A. Binder, „Comparison of induction Motor, Permanent Magnet Motor and Transversal Flux Motor for Wheel Hub Drives in Street Cars“, *Proceedings EPE-PEMC 2004*.
- [4] W. Hackmann, A. Binder, „Asynchronous wheel hub motor with massive rotor iron and open rotor slots for wheel hub drive in street cars“, Cracow Poland, *Proceedings ICEM 2004*.
- [5] V. Groza, M. Biriescu, V. Crețu, I. Șora, M. Moț, „Testing of electrical machines in periodical and quasi-periodical conditions, using a data acquisition and processing system“, *Proceedings of IEEE Instrumentation and Measurement Tehnology Conference*, St. Paul Minnesota, USA, page. 768-771, 1998.
- [6] V. Groza, M. Biriescu, V. Crețu, G. Liuba, M. Moț, G. Madescu, „Testing of electrical machines with a dedicated system for data acquisition and processing“, Chania, Crete Island, Greece, (Proceedings on CD), *International Conference on Electrical Machines- ICEM 2006*.
- [7] J. Puranen, J. Pyrhönen, „Analysis of a pull-out optimized induction motor in heavy traction applications“, *Proceedings of the 16th International Conference on Electrical Machines – ICEM'2004*, Cracow. Poland, ISBN 83-921428-0-2, 2004.
- [8] S. Evon, R. Schiferl, „Direct – drive induction motors“, *IEEE Industry Applications Magazine*, pp. 45-51, July/Aug. 2005
- [9] G. Madescu, „Realizări recente ale Academicianului Toma Dordea“, *Revista Coloana Infinitului*, anul XIV, nr.76, Timișoara, pag.29-32, 2011.

## 3. 1 Introduction

This chapter discusses important problems for manufacturers, as well as users, of synchronous machines concerning experimental identification of parameters in d-q coordinates. Experimental studies are primarily performed on salient poles synchronous machines – synchronous hydro-generators, for which the determination of parameters is made based on standstill rotor tests using the direct current decay method.

It should be noted that in some concrete situations, especially in case of large synchronous machines, this type of test is the only practical solution for determining machine parameters without mechanically coupling it with another machine. This approach comes with a major advantage from an experimental point of view, significantly reducing the costs, time and manpower necessary for testing.

The first part of this chapter introduces fundamental theoretical concepts that are later used to elaborate on procedures for testing and data processing of peculiar standstill rotor direct current decay conditions.

Both the magnetic non-saturated machine, as well as the influence of magnetic saturation and multiple rotor damper cages are studied, providing concrete solutions and results regarding parameter determination with these influences.

The experimental results presented at the end are, in most cases, selected from those obtained by the authors over a period of more than 25 years on industrial synchronous machines in a wide power range, up to 76000 kW. The tests have been performed in hydrogenerator manufacturers' testing stands, as well as at the hydro-power stations.

This chapter focuses on direct current decay tests with standstill rotors, and does not apply to other types of tests for synchronous machines, such as variable frequency power supply tests etc.

The authors wish to thank Dr. E. Bartels and Dr. S.W. Provencher from the Max Planck Institut – Göttingen, Germany, for their kindness in donating the DISCRETE program to laboratory D109 - „Electric Machine Testing“ of the school of Electrotechnics in Timisoara. This numeric data processing program allows the separation on statistical bases of

exponential components and time constants from non-periodic damping conditions, and has been used for mathematical data analysis in transient decay conditions of the magnetic field for high accuracy parameter determination [48].

Many of the experimental presented results have been achieved in cooperation with the Machine Manufacturing Works (UCM) Resita, who practically built all hydro-generators in Romania, while being the established manufacturer of large, high power, small series, or custom electrical machines that currently operate at key facilities in Romania's national energy industry.

### **3.2. Equations, parameters, and characteristic values used in the study of synchronous machines**

Out of all electric machines, the synchronous machine has the highest number of parameters and characteristic values described by equations that define its operation in various conditions.

In most cases, the study of the machine is done in coordinates, with reduced values for the stator and scaled to base-unit values. This paragraph presents the basic elements regarding equations and parameters of the real and equivalent machine in d-q coordinates, with the most frequently used notations and relations of definition, in accordance with [1, 3, 12, 14, 17, 20, 21, 22, 23, 30, 31, 33, 34, 36].

It highlights the physical interpretation of the parameters with relevant relations, which are later required for the treatment of machine special testing conditions. Since the definition of parameters in d-q coordinates is done based on parameters of the real machine, and since some tests and experimental results require interpretations of phenomena from real circuits, we will first offer a presentation of parameters and equations of the real machine.

These are known as equations in phase coordinates.

#### **3.2.1. Equations and Parameters of the salient pole machine in the phase coordinate system**

The windings of a real salient pole synchronous machine are shown in Fig. 3.1.

The three-phase symmetrical winding of the stator is shown simplified with one turn for each phase, with the indicated directions of reference.

We considered the case of a machine that has a rotor field circuit and two stator damper circuits, one for each axis, commonly found in practice.

The damper circuits along the two axes  $d$ - $q$ , have been labeled D and Q respectively, and the field circuit has been labeled f.

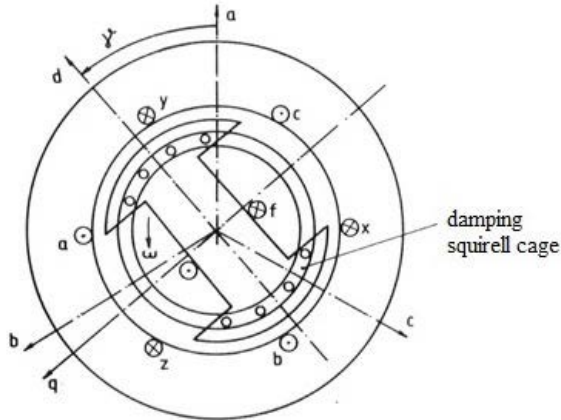


Fig.3.1 Simplified representation of real machine windings.

The real machine in conventional representation is given in Fig.3.2.

The voltage equations for the three phases a, b, c, are:

$$\begin{aligned}
 u_a &= \frac{d\Psi_a}{dt} + R_1 i_a; \\
 u_b &= \frac{d\Psi_b}{dt} + R_1 i_b; \\
 u_c &= \frac{d\Psi_c}{dt} + R_1 i_c
 \end{aligned}
 \tag{3.1}$$

where:  $u_a, u_b, u_c$  - stator phase voltages;

$\Psi_a, \Psi_b, \Psi_c$  - total fluxes of stator phases;

$i_a, i_b, i_c$  - phase currents;

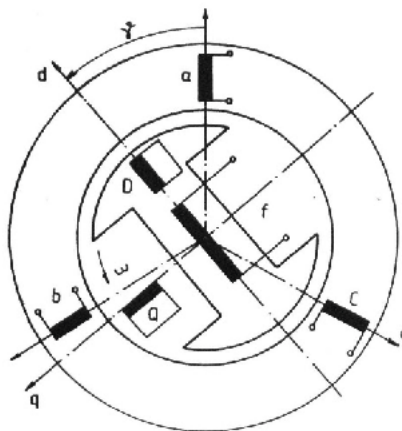


Fig. 3.2 Conventional representation of the windings of a synchronous machine

The equation for the voltage of the field circuit is:

$$U_f = \frac{d\Psi_f}{dt} + R_f i_f, \quad (3.2)$$

where  $U_f$ ,  $\Psi_f$  and  $R_f$  represent the voltage at the terminals, total flux and the resistance of the field winding.

Since axes d and q are perpendicular (considering the electric angle between them), it will be assumed that for the case of the linear machine there is no mutual induction between the two circuits of the damper winding, along the two axes d and q. The real damper winding is a cage type (Fig.3.1.). By construction, it is desired that the cage bars, symmetrically located in the pole shoe and interconnected through the short-circuiting ring that covers the inter-polar space, create an assembly with a bi-axial symmetry  $d$ - $q$ .

As such, during the analysis of the transient processes, the damper windings with more circuits are usually substituted with two equivalent windings, along the two axes, whose span is equal to the pole interval [1, 33]. The voltage equations for the equivalent damper windings are:

$$0 = \frac{d\Psi_D}{dt} + R_D i_D \quad (3.3)$$

$$0 = \frac{d\Psi_Q}{dt} + R_Q i_Q \quad (3.4)$$

where  $\Psi_D$ ,  $R_D$  and  $i_D$  and  $\Psi_Q$ ,  $R_Q$ ,  $i_Q$ , respectively, are the flux, current and equivalent resistance corresponding to the damper winding along the two axes.

### Inductivities and fluxes in phase coordinates

The machine shown in Fig. 3.2. has three stator circuits, corresponding to the three phases, and three rotor circuits, corresponding to the field and damper cage. For the six circuits the fluxes can be written as:

$$\begin{aligned} \Psi_a &= l_a i_a + m_{ab} i_b + m_{ac} i_c + m_{af} i_f + m_{aD} i_D + m_{aQ} i_Q \\ \Psi_b &= m_{ba} i_a + l_b i_b + m_{bc} i_c + m_{bf} i_f + m_{bD} i_D + m_{bQ} i_Q \\ \Psi_c &= m_{ca} i_a + m_{cb} i_b + l_c i_c + m_{cf} i_f + m_{cD} i_D + m_{cQ} i_Q \\ \Psi_e &= m_{fa} i_a + m_{fb} i_b + m_{fc} i_c + L_f i_f + M_{fD} i_D \\ \Psi_D &= m_{Da} i_a + m_{Db} i_b + m_{Dc} i_c + M_{Df} i_f + L_D i_D \\ \Psi_Q &= m_{Qa} i_a + m_{Qb} i_b + m_{Qc} i_c + L_Q i_Q \end{aligned} \quad (3.5)$$

where lower case notations have been used for inductivities varying in time due to rotor position:

$l_a$  - inductivity of phase  $a$ ,



$m_{ab}$  - mutual inductivity between the winding of phases  $a$  and  $b$ ;  
 $m_{af}$  - mutual inductivity between the winding of phase  $a$  and the field winding;  
 $m_{D}$  - mutual inductivity between phase  $a$  and the equivalent damper winding along axis  $d$  (labeled  $D$ ).

Self- and mutual inductivities of the other circuits are denoted the same way.

Considering a non-saturated machine, mutual inductivities having the same index type are equal to:

$$\begin{aligned}
 m_{ab} = m_{ba} & ; \quad m_{af} = m_{fa} & ; \quad m_{aD} = m_{Da} & ; \\
 m_{ac} = m_{ca} & ; \quad m_{bf} = m_{fb} & ; \quad m_{aQ} = m_{Qa} & .
 \end{aligned}
 \tag{3.6}$$

Capital letters denote inductivities that are constant in time, thus not dependent on the rotor position:

$L_f, L_D, L_Q$  - self-inductivity of the field circuit, longitudinal and transversal damper;

$M_{fD}$  - mutual inductivity between the field winding and longitudinal damper winding.

**Inductivities of the stator phases** are periodical functions of angle  $\gamma$  between the longitudinal rotor axis  $d$  and the axis of phase  $a$ , considered as reference phase for the stator. Due to rotor movement, the angle  $\gamma$  varies in time following a law given by the operation conditions and thus the phase inductivities are functions of time. This aspect complicates the study of the operation of the machine in phase coordinates. For  $\gamma = 0$  (Fig.3.1), the permeability of the magnetic path of the phase  $a$  flux has a maximum value, while for  $\gamma = \frac{\pi}{2}$  the value is minimal. The change of the inductivity of phase  $a$  as a function of the rotor position is given in fig. 3.3.

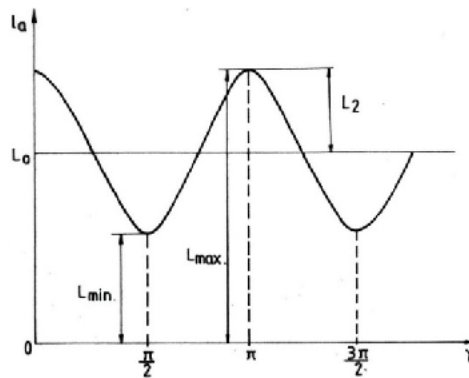


Fig.3.3 Stator phase inductivity as a function of position angle  $\gamma$ .

Considering that the magnetic flux in the air gap changes along the polar span following a sinusoidal function, the inductivities of the stator phase can be expressed as:

$$\begin{aligned} l_a &= L_0 + L_2 \cos 2\gamma \\ l_b &= L_0 + L_2 \cos 2\left(\gamma - \frac{2\pi}{3}\right) \\ l_c &= L_0 + L_2 \cos 2\left(\gamma + \frac{2\pi}{3}\right) \end{aligned} \quad (3.7)$$

Thus, the inductivities of the real machine phases change periodically with angle  $\gamma$ , are centered at the constant average value  $L_0$ , with an amplitude  $L_2$ . As such, the inductivity of a stator phase oscillates between a maximal value  $L_{\max}$ , when the rotor axis  $d$  overlaps with the respective phase axis, and a minimal value  $L_{\min}$  when the axis  $d$  is perpendicular to that phase axis (fig.3.3).

Per fig.3.3, the average value of a phase inductivity is:

$$L_0 = \frac{L_{\max} + L_{\min}}{2} \quad (3.8)$$

and the value of the inductivity variation amplitude is:

$$L_2 = \frac{L_{\max} - L_{\min}}{2} \quad (3.9)$$

The previous relations completely define the self-inductivities of the machine phases from the point of view of the analytical functions.

For a physical interpretation, it is necessary to introduce additional notations, to distinguish between the components of the inductivity that originate from the useful magnetic field, crossing the air gap, and those that originate from the leakage field, which exclusively link the respective winding.

Thus, in the general case, the linkage of a certain winding is separated between the useful component, denoted by the index  $h$ , and the leakage component, denoted by the index  $\sigma$ .

$$\Psi = \Psi_h + \Psi_\sigma \quad (3.10)$$

Consequently, when the axis  $d$  overlaps with the phase  $a$  axis, the maximal inductivity can be written as:

$$L_{\max} = L_{hd} + L_\sigma \quad (3.11)$$

The two components have the following physical interpretation:

$L_{hd-}$  - useful self-inductivity of a phase, when axis d overlaps with the phase axis, for single phase supply;

$L_{\sigma}$  - phase leakage inductivity.

Similarly, for the minimum inductivity :

$$L_{\min} = L_{hq-} + L_{\sigma} \quad (3.12)$$

where:  $L_{hq-}$  is the useful self-inductivity of a phase in case of single phase feed, when axis q overlaps with the phase axis.

Using these notations, the average value of stator phase inductivity and its variation amplitude respectively can be written as:

$$L_0 = \frac{L_{hd-} + L_{hq-}}{2} + L_{\sigma} \quad (3.13)$$

$$L_2 = \frac{L_{hd-} - L_{hq-}}{2} \quad (3.14)$$

The average of the useful components of phase inductivity is written as:

$$\bar{L}_0 = \frac{L_{hd-} + L_{hq-}}{2}. \quad (3.15)$$

It follows from (3.14) that the variation amplitude  $L_2$  comes exclusively from the useful field components, and as such the index h can be assigned, and it can be written as:

$$L_{h_2} = L_2. \quad (3.16)$$

Using these interpretations, highlighting the useful and leakage components, the inductivities of the real machine phases can be written as:

$$\begin{aligned} l_a &= \bar{L}_{h-} + L_{h_2} \cos 2\gamma + L_{\sigma} \\ l_b &= \bar{L}_{h-} + L_{h_2} \cos 2\left(\gamma - \frac{2\pi}{3}\right) + L_{\sigma} \\ l_c &= \bar{L}_{h-} + L_{h_2} \cos 2\left(\gamma + \frac{2\pi}{3}\right) + L_{\sigma}. \end{aligned} \quad (3.17)$$

The comment regarding the single-phase feed is important for the physical interpretation of the inductivities, since, in this case, the phase winding is considered as a single phase fed, independent coil; thus the “~” notation has been used.

This distinction is necessary, because in the case of three-phased feeding of the machine, the resultant flux, due to the rotating magnetic field in the airgap, is 3/2 times higher than that of a single phase feed. Therefore, considering a symmetrical three-phase

powered machine, another useful inductivity  $L_h$ , can be defined, based on the rotating magnetic field, used in calculations, called cyclic inductivity, as:

$$L_h = \frac{3}{2} L_{h-} . \tag{3.18}$$

Relations of type (3.18), will rigorously follow when transitioning from the real machine to the machine in  $d-q$  coordinates.

These specifications are useful in the physical interpretation of the components of the inductivities of the equivalent machine  $d-q$  coordinates, particularly when machine parameters are determined from peculiar current decay, as will be shown later.

**Rotor windings self-inductivities** are constants in relation to the rotor position:

1. field winding inductivity,  $L_F=ct$ ;
2. equivalent damper winding inductivity, along axis  $d$ ,  $L_D=ct$ ;
3. damper winding inductivity along axis  $q$ ,  $L_Q=ct$ .

**The mutual inductivities between the phases of rotor and stator windings** vary with the rotor position. Since the machine is symmetrical, with a phase angular spacing of  $\frac{2\pi}{3}$ , mutual inductivities between the phases of stator windings have negative values.

The reference angle considered is the angle  $\gamma_{ab}$ , between axis  $d$  and the bisector of the magnetic axes of phase a and b, bis (a,b) - fig.3.4.

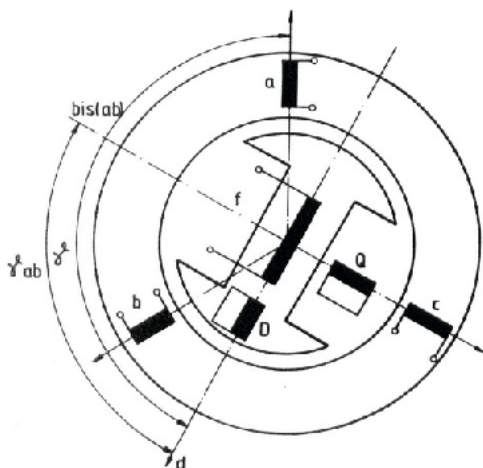


Fig.3.4 Definition of the reference angle for mutual inductivities between stator winding phases.

The mutual inductivity between phases a and b, is:

$$m_{ab} = -M_0 + M_2 \cos 2\gamma_{ab} \tag{3.19}$$

The variation of the mutual inductivity between two stator phases is given in fig.3.5.

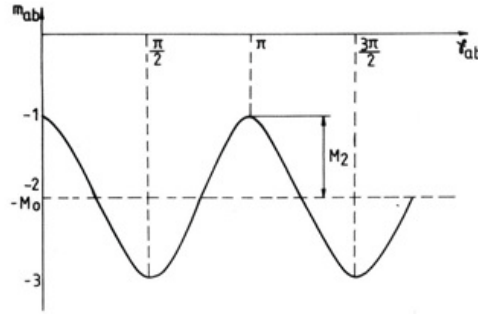


Fig.3.5. Mutual inductivity between two stator phases as a function of rotor position.

The objective is to express mutual inductivities as a function of the same reference angle  $\gamma$ , introduced for stator phase inductivities. Considering the relation between the two angles (fig.3.4) as:

$$\gamma_{ab} = \gamma - \frac{\pi}{3} \quad (3.20)$$

For other stator phases:

$$\begin{aligned} m_{bc} &= -M_0 + M_2 \cos 2 \left( \gamma_{ab} - \frac{2\pi}{3} \right) \\ m_{ca} &= -M_0 + M_2 \cos 2 \left( \gamma_{ab} + \frac{2\pi}{3} \right). \end{aligned} \quad (3.21)$$

Mutual inductivities of stator phases as functions of angle  $\gamma$  are:

$$\begin{aligned} m_{ab} &= -M_0 + M_2 \cos \left( 2\gamma - \frac{2\pi}{3} \right) \\ m_{bc} &= -M_0 + M_2 \cos 2\gamma \\ m_{ca} &= -M_0 + M_2 \cos \left( 2\gamma + \frac{2\pi}{3} \right). \end{aligned} \quad (3.22)$$

Since the modification of self-inductivities of a phase (3.7) and of the mutual inductivities (3.22) occur for the same reason – a change in rotor position, the number of turns being the same- it follows that the amplitudes by which the two inductivity types change are the same:

$$M_2 = L_2. \quad (3.23)$$

Relation (3.23) is confirmed by both experiments and theory [16, 33].

For a constant air gap machine, mutual inductivities are obviously constant and equal to the average value stated in (3.22):

$$m_{ab} = m_{bc} = m_{ca} = -M_0. \quad (3.24)$$

Magnetic coupling between windings occurs based on the useful flux in (3.10), leading to the value  $\bar{L}_{h-}$  in the expression of inductivities. Considering the angular spacing angle between magnetic axes of phases  $a$  and  $b$ , the average value will be:

$$-M_0 = L_{h-} \cos \frac{2\pi}{3} = -\frac{L_{h-}}{2}. \quad (3.25)$$

Considering a salient pole machine, for a single-phase feed, the useful inductivity varies between the two extreme values and  $L_{hd-} L_{hq-}$ . Thus, in (3.25),  $L_{h-}$  may be substituted with the average of the two extreme values:

$$\bar{L}_{h-} = \frac{L_{hd-} + L_{hq-}}{2}$$

resulting in the general expression for the average value, around which the stator mutual inductivities for a synchronous salient pole machine vary.

$$-M_0 = \frac{\bar{L}_{h-}}{2} \quad (3.26)$$

**Mutual inductivities of stator and rotor windings in phase coordinates** are also functions of the position angle of the field winding  $f$  and of the longitudinal damper winding  $D$ , and they have the same magnetic axis; thus the mutual inductivities with stator phases vary the same way.

Inductivity reaches a maximum value for overlapping the magnetic axes of a rotor winding and a stator winding.

The expressions for mutual inductivities between the field windings and stator windings can be written as:

$$\begin{aligned} m_{af} &= M_{af} \cos \gamma \\ m_{bf} &= M_{af} \cos \left( \gamma - \frac{2\pi}{3} \right) \\ m_{cf} &= M_{af} \cos \left( \gamma + \frac{2\pi}{3} \right) \end{aligned} \quad (3.27)$$

where:

$m_{af}$  - mutual inductivity between phase  $a$  winding and field winding, for some angle  $\gamma$  (current value of inductivity) and similarly for the other phases;

$M_{af}$  - mutual inductivity between winding of stator phase  $a$  and the field winding, when their magnetic axes overlap.

For the mutual inductivities between the damper winding  $D$  along the longitudinal axis, and stator phases, similar expressions follow:

$$\begin{aligned}
m_{aD} &= M_{aD} \cos \gamma \\
m_{bD} &= M_{aD} \cos \left( \gamma - \frac{2\pi}{3} \right) \\
m_{cD} &= M_{aD} \cos \left( \gamma + \frac{2\pi}{3} \right)
\end{aligned} \tag{3.28}$$

where:  $m_{aD}$  - is the mutual inductivity between phase  $a$  and the equivalent damper winding along the longitudinal axis for some rotor position, given by angle  $\gamma$ , and similarly for the other phases;

$M_{aD}$  - is the mutual inductivity between the winding of phase  $a$  and the equivalent damper winding along the longitudinal axis, when the magnetic axes overlap.

The mutual inductivities of the equivalent damper winding  $Q$  along the transversal axis, with the stator windings, are:

$$\begin{aligned}
m_{aQ} &= M_{aQ} \cos \left( \gamma + \frac{\pi}{3} \right) = -M_{aQ} \sin \gamma \\
m_{bQ} &= -M_{aQ} \sin \left( \gamma - \frac{2\pi}{3} \right) \\
m_{cQ} &= -M_{aQ} \sin \left( \gamma + \frac{2\pi}{3} \right)
\end{aligned} \tag{3.29}$$

where:  $M_{aQ}$  - is the mutual inductivity between phase  $a$  and the transversal equivalent damper winding, in case of overlapping magnetic axes;

$m_{aQ}$  - is the mutual inductivity between phase  $a$  and the transversal equivalent damper winding, for some rotor position, given by angle  $\gamma$ .

The mutual inductivity between the field winding  $f$  and the damper winding  $D$ , along the longitudinal axis, is:

$$M_{fD} = \text{ct} . \tag{3.30}$$

The mutual inductivity between the equivalent transversal damper winding and the field winding, as well as the equivalent longitudinal damper winding, is zero, since the magnetic axes of these windings are offset by an angle of  $\pi/2$ , with the air gap magnetic reluctance being constant.

Despite the fact that there is no common magnetic field between the damper windings along the two rotor axes  $D$  and  $Q$  and, therefore, there is no mutual inductivity type  $DQ$ , a certain influence between the above mentioned windings can still be found.

Thus, under magnetic saturation conditions of the rotor core, a saturation of the magnetic circuit along axis  $D$  leads to a change in the value of the inductivity of the damper winding along axis  $Q$ , because part of the field lines along the two axes close through the same magnetic medium. This aspect can be seen in practice, when determination of saturated values of parameters [4] is sought.

Therefore, for a salient pole synchronous machine, the real phase inductivities are periodic functions of angle  $\gamma$ .

Replacing the relations of self- and mutual inductivities in expression (3.5) yields the general formula of the real phase fluxes, as a function of the constant components of the inductivities and of the position angle  $\gamma$ :

$$\begin{aligned}
 \Psi_a &= (L_0 + L_2 \cos 2\gamma) i_a + \left[ -M_0 + L_2 \cos \left( 2\gamma - \frac{2\pi}{3} \right) \right] i_b + \\
 &+ \left[ -M_0 + L_2 \cos \left( 2\gamma + \frac{2\pi}{3} \right) \right] i_c + M_{af} \cos \gamma i_f + M_{ad} \cos \gamma i_D - M_{aQ} \sin \gamma i_Q ; \\
 \Psi_b &= \left[ -M_0 + L_2 \cos \left( 2\gamma - \frac{2\pi}{3} \right) \right] i_a + \left[ L_0 + L_2 \cos 2 \left( \gamma - \frac{2\pi}{3} \right) \right] i_b + \\
 &+ \left[ -M_0 + L_2 \cos 2\gamma \right] i_c + M_{af} \cos \left( \gamma - \frac{2\pi}{3} \right) i_f + \\
 &+ M_{ad} \cos \left( \gamma - \frac{2\pi}{3} \right) i_D - M_{aQ} \sin \left( \gamma - \frac{2\pi}{3} \right) i_Q ; \\
 \Psi_c &= \left[ -M_0 + L_2 \cos \left( 2\gamma + \frac{2\pi}{3} \right) \right] i_a + \left[ M_0 + L_2 \cos 2\gamma \right] i_b + \\
 &+ \left[ -L_0 + L_2 \cos 2 \left( \gamma + \frac{2\pi}{3} \right) \right] i_c + M_{af} \cos \left( \gamma + \frac{2\pi}{3} \right) i_f + \\
 &+ M_{ad} \cos \left( \gamma + \frac{2\pi}{3} \right) i_D - M_{aQ} \sin \left( \gamma + \frac{2\pi}{3} \right) i_Q ;
 \end{aligned} \tag{3.31}$$

It should be noted that the real magnetic phase fluxes are fairly complex functions of the rotor angle  $\gamma$ , which is generally a function of time, thus establishing the main disadvantage of the real machine equations.

Replacing those in (3.1 - 3.4), one obtains the differential equations with periodical coefficients of the real phase voltages. These are known as the machine equations in phase coordinates.

Solving these equations can be done only by numerical methods, and require a large amount of calculations.



These equations will not be solved for the general case, but will be used to describe certain peculiar transient conditions that allow, as will be shown later, the practical separation of some very important coefficients, particularly for medium and large synchronous machines.

The relations of equivalent parameters of the synchronous machine as a function of the parameter components of the real machine, will be used further for the analysis of standstill rotor transient conditions.

### 3.2.2. Equations and parameters of the salient pole synchronous machine in the $d, q$ coordinate system

For a correct interpretation of the parameters appearing in the equations of the synchronous machine corresponding to special standstill rotor test conditions, following is a brief presentation of the transition from the real machine to the equivalent  $d, q$  coordinate machine, as well as some very important relations connecting real and equivalent parameters.

The synchronous machine in  $d, q$  coordinates, equivalent to the real machine, is shown diagrammatically in fig.3.6.

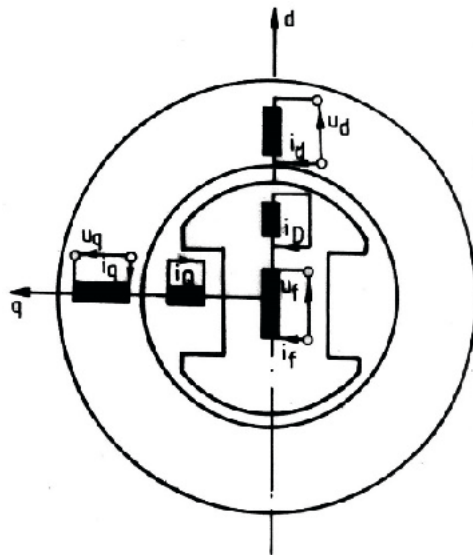


Fig.3.6 Equivalent machine in  $d, q$  coordinates.

In the energetically equivalent machine, stator circuits  $d$  and  $q$  rotate synchronously with the rotor, creating the same magnetic field in the air gap, and are magnetically coupled with the rotor circuits along the respective axes.

The relations for transitioning from the real machine currents  $i_a, i_b, i_c$  to the equivalent  $d, q$  machine currents are:

$$\begin{aligned}
i_d &= \frac{2}{3} \left[ i_a \cos \gamma + i_b \cos \left( \gamma - \frac{2\pi}{3} \right) + i_c \cos \left( \gamma + \frac{2\pi}{3} \right) \right] \\
i_q &= -\frac{2}{3} \left[ i_a \sin \gamma + i_b \sin \left( \gamma - \frac{2\pi}{3} \right) + i_c \sin \left( \gamma + \frac{2\pi}{3} \right) \right] \\
i_0 &= \frac{1}{3} (i_a + i_b + i_c)
\end{aligned} \tag{3.32}$$

The current  $i_0$  is the neutral current component, which becomes the zero component for the particular sinusoidal case.

In the equivalent machine, the current  $i_0$  flows through an independent stator winding, magnetically non-coupled with the rotor, which essentially represents the leakage.

From (3.32) the direct transformation matrix becomes:

$$[A] = \frac{2}{3} \begin{bmatrix} \cos \gamma & \cos \left( \gamma - \frac{2\pi}{3} \right) & \cos \left( \gamma + \frac{2\pi}{3} \right) \\ -\sin & -\sin \left( \gamma - \frac{2\pi}{3} \right) & -\sin \left( \gamma + \frac{2\pi}{3} \right) \\ \frac{1}{2} & \frac{1}{2} & \frac{1}{2} \end{bmatrix} \tag{3.33}$$

Reversing from the currents of the equivalent machine  $d, q, 0$  to the real machine currents is done using following relations:

$$\begin{aligned}
i_a &= i_d \cos \gamma - i_q \sin \gamma + i_0 \\
i_b &= i_d \cos \left( \gamma - \frac{2\pi}{3} \right) - i_q \sin \left( \gamma - \frac{2\pi}{3} \right) + i_0 \\
i_c &= i_d \cos \left( \gamma + \frac{2\pi}{3} \right) - i_q \sin \left( \gamma + \frac{2\pi}{3} \right) + i_0.
\end{aligned} \tag{3.34}$$

Based on the reversed transformation relations (3.34), the inverse transformation matrix, from the equivalent machine in coordinates  $d, q, 0$  to the real machine in phase coordinates  $a, b, c$ , results as:

$$[A]^{-1} = \begin{bmatrix} \cos \gamma & -\sin \gamma & 1 \\ \cos \left( \gamma - \frac{2\pi}{3} \right) & -\sin \left( \gamma - \frac{2\pi}{3} \right) & 1 \\ \cos \left( \gamma + \frac{2\pi}{3} \right) & -\sin \left( \gamma + \frac{2\pi}{3} \right) & 1 \end{bmatrix}. \tag{3.35}$$

From (3.34), it can be noted that for all stator phases the neutral current component,  $i_0$ , has the same effect. If the flow of a zero sequence current is symmetrical for a three-phase

winding of the real machine and the same in every phase, a useful magnetic field, coupling the stator and rotor, cannot be generated.

The transition from the real machine to the equivalent machine and back is done with the same matrices for fluxes and voltages:

$$\begin{bmatrix} \Psi_{dq0} \end{bmatrix} = \begin{bmatrix} A \end{bmatrix} \begin{bmatrix} \Psi_{abc} \end{bmatrix} \quad (3.36)$$

$$\begin{bmatrix} u_{dq0} \end{bmatrix} = \begin{bmatrix} A \end{bmatrix} \begin{bmatrix} u_{abc} \end{bmatrix} \quad (3.37)$$

$$\begin{bmatrix} \Psi_{abc} \end{bmatrix} = \begin{bmatrix} A \end{bmatrix}^{-1} \begin{bmatrix} \Psi_{dq0} \end{bmatrix} \quad (3.38)$$

$$\begin{bmatrix} u_{abc} \end{bmatrix} = \begin{bmatrix} A \end{bmatrix}^{-1} \begin{bmatrix} u_{dq0} \end{bmatrix}. \quad (3.39)$$

### Fluxes and inductivities of the equivalent machine

If the real currents are replaced with equivalent currents in (3.34) in the relations of the real machine fluxes (3.5), and the direct transformation (3.33) is applied, the fluxes of the equivalent machine result as:

$$\begin{aligned} \Psi_d &= \left( L_0 + M_0 + \frac{3}{2} L_2 \right) i_d + M_{af} i_f + M_{ad} i_D \\ \Psi_q &= \left( L_0 + M_0 - \frac{3}{2} L_2 \right) i_q + M_{aQ} i_Q \\ \Psi_0 &= (L_0 - 2M_0) i_0. \end{aligned} \quad (3.40)$$

The main advantage of the equivalent machine is having constant coefficients for the currents in the flux definition equations (3.40) as compared to (3.31). Regarding quantitative interpretation, the coefficient of  $i_d$ , of the flux relation (3.40), is indeed an inductivity, that, considering (3.11) - (3.16), can be written as:

$$\begin{aligned} L_0 + M_0 + \frac{3}{2} L_2 &= \frac{L_{hd^-} + L_{hq^-}}{2} + L_\sigma + \frac{\bar{L}_{h^-}}{2} + \frac{3}{2} L_2 = \\ &= \frac{3}{2} \bar{L}_{h^-} + \frac{3}{2} L_2 + L_\sigma = \frac{3}{2} [\bar{L}_{h^-} + L_{h2}] + L_\sigma \end{aligned} \quad (3.41)$$

and

$$\bar{L}_{h^-} + L_2 = \frac{L_{hd^-} + L_{hq^-}}{2} + \frac{L_{hd^-} - L_{hq^-}}{2} = L_{hd^-} \quad (3.42)$$

Consequently, the inductivities of the equivalent machine, as a function of the inductivities structure of the real machine, result as:

#### 1. longitudinal synchronous inductivity

$$L_d = L_0 + M_0 + \frac{3}{2} L_2 = L_\sigma + \frac{3}{2} (\bar{L}_{h^-} + L_{h2}) = L_\sigma + L_{ad} \quad (3.43)$$

2. transversal synchronous inductivity

$$L_q = L_0 + M_0 - \frac{3}{2}L_2 = L_\sigma + \frac{3}{2}(\bar{L}_{h^-} - L_{h2}) = L_\sigma + L_{aq} \quad (3.44)$$

3. zero sequence inductivity

$$L_{00} = L_0 - 2M_0 = L_\sigma. \quad (3.45)$$

The defining notations of the useful components of the inductivities of the equivalent machine, along the two axes, and cyclical longitudinal and transversal reaction inductivities respectively, result as:

$$L_{ad} = \frac{3}{2}(\bar{L}_{h^-} + L_{h2}) = \frac{3}{2}L_{hd^-} \quad (3.46)$$

$$L_{aq} = \frac{3}{2}(\bar{L}_{h^-} - L_{h2}) = \frac{3}{2}L_{hq^-}. \quad (3.47)$$

Thus, the fluxes for the equivalent machine in coordinates  $d, q, 0$  are expressions that contain constant current coefficients as well as inductivities independent of the rotor position:

$$\begin{aligned} \Psi_d &= L_d i_d + M_{af} i_f + M_{aD} i_D \\ \Psi_q &= L_q i_q + M_{aQ} i_Q \\ \Psi_0 &= L_{00} i_0. \end{aligned} \quad (3.48)$$

Some of the inductivities in (3.48), such as the mutual inductivities, have a direct physical interpretation, while others, such as  $L_d, L_q, L_{00}$ , represent linear combinations of characteristic constant values, part of the structure of real machine inductivities. Since transitioning to an equivalent machine in  $d, q$  coordinates, results in the loss of some physical parameter interpretations, the relations (3.41) - (3.47), that detail the structure of equivalent parameters, are considered very important from the physical interpretation viewpoint. Correct interpretations of equivalent parameters can thus be made, avoiding possible erroneous formal interpretations. For example, there may be a tendency for the erroneous formal interpretation of the equivalent inductivity,  $L_d$ , to be the inductivity of a stator phase, when axis  $d$  overlaps the axis of the respective phase.

However, when overlapping the two axes, the phase inductivity, per (3.11) and (3.17), is:

$$l_a(\gamma = 0) = \bar{L}_{h^-} + L_{h2} + L_\sigma = L_{hd^-} + L_\sigma \quad (3.49)$$

while the correct value of inductivity  $L_d$  is given in (3.43), which has the  $3/2$  coefficient for the useful component of this inductivity.

Correlated with fundamental concepts of the theory of the two axes [47], the stated relations allow for the separation of the catalog parameters  $L_d, L_q, (X_d, X_q)$ , a.o. of the synchronous machine, employing special testing conditions, conditions that do not appear in normal operation, i.e. standstill current decay tests. Such tests will be presented later in this chapter.

In a similar way, the rotor windings fluxes result as:

$$\begin{aligned}\Psi_f &= \frac{3}{2} M_{fa} i_d + L_f i_f + M_{fD} i_D \\ \Psi_D &= \frac{3}{2} M_{Da} i_d + M_{Df} i_f + L_D i_D \\ \Psi_Q &= \frac{3}{2} M_{Qa} i_q + L_Q i_Q\end{aligned}\quad (3.50)$$

### Voltage equations – Park equations

If fluxes and currents are replaced with transformation in coordinates  $d, q, 0$  in the voltage equations written in phase coordinates (3.1), (3.4), the voltage equations for equivalent machine circuits finally result as:

$$\begin{aligned}u_d &= R_1 i_d + \frac{d\Psi_d}{dt} - \omega \Psi_q \\ u_q &= R_1 i_q + \frac{d\Psi_q}{dt} + \omega \Psi_d \\ u_0 &= R_1 i_0 + \frac{d\Psi_0}{dt} \\ 0 &= R_D i_D + \frac{d\Psi_D}{dt} \\ U_f &= R_f i_f + \frac{d\Psi_f}{dt} \\ 0 &= R_Q i_Q + \frac{d\Psi_Q}{dt},\end{aligned}\quad (3.51)$$

where  $\omega = \frac{d\gamma}{dt}$ .

These equations of the equivalent machine, with parameters independent of the rotor position, are known as the Park system of equations.

### 3.3. Current decay transients at standstill tests

In most cases, synchronous machine parameters are determined through tests that involve the rotation of the machine. In case of medium or large synchronous machines, standard tests presume the coupling of the machine to be tested with another machine, which is somehow more difficult to do because of the dimensions of the machine and large currents involved. Even the coupling of a large machine with another one creates an

impediment for performing standard tests, especially in case of vertical axis machines, and thus not all clients have the necessary conditions for such tests. This is the main reason that leads to standstill rotor tests. There are other types of such tests that can be split into two large categories: standstill frequency response tests (SSFR), and standstill time response tests (SSTR). The first category includes tests where the standstill machine is fed from variable frequency sources, from very low to about rated frequencies.

Currents and voltages, as functions of time in the entire frequency range, are recorded. Based on those, the complex impedance, with components that vary with the frequency, can be determined. For such tests, special equipment is required which includes variable frequency power generators. For the duration of the test, to avoid saturating the machine, the magnetic flux has to be kept at low levels, which may lead to excessive noise signals, particularly for lower frequencies. The recording devices must ensure high accuracy and precision throughout the entire frequency range.

This test yields quite conclusive results, but is prohibitive for industrial end users due to equipment costs and complexity.

The second category, SSTR, groups tests for which the machine windings are fed in DC and then short-circuited.

These tests are also called standstill DC decay tests. From the point of view of the supply source, this test is less complicated, but requires the recording of transient conditions, with short sampling periods, especially in the initial stage of the process.

Therefore a high volume of data has to be recorded and processed, which can be done relatively easy at present, using data acquisition and processing systems.

The behavior of the synchronous machine is correctly described by operational reactances, relative to the complex reactance representation along the two axes, that result from the frequency response curves  $x_d(j_s)$  and  $x_q(j_s)$  [14, 20, 37, 50, 64, 65].

The frequency response curves can be obtained through both variable frequency tests SSFR and current decay tests SSTR.

Test methods that can be classified as special tests or tests still to be confirmed [4, 6, 7, 11, 19, 21, 32, 33, 46, 49, 50, 56, 57, 58] according to present standards [60, 63, 64, 65], using established notations, are presented further.

In accordance with previously mentioned references, the complete methodology for the determination of equivalent parameters from decay tests is shown, including for damper cages, with experimental results recently obtained by the authors for large synchronous machines currently in operation.

It should be noted that the principle of standstill test current decay tests is not recent, but its application has not been widespread due to the exigencies imposed by the recording of the process, as well as tedious data procession.

The precision/accuracy achieved in the last couple of years, both in data processing and measurement instruments, have boosted the development of both more accurate methods, as well as more complex methods for synchronous machines [40, 41, 53, 54, 64].

### 3.3.1. Connections and equations of direct current decay at standstill rotor

For the direct current decay test there are several possible connections for parameter determination. In all cases, there has to be a correlation of the rotor position with stator phase connection, such that for DC feeding, a resulting magnetic field, exclusively along one of the axes,  $d$  or  $q$ , shall appear.

Short-circuiting the DC fed windings leads to current and resulting machine flux decay. The transient conditions equations have machine parameters along the current decay axis.

The general principle for determining parameters is the same for all processes of this type. Equations are solved for quantities that can be recorded as time functions, usually stator and field currents, and occasionally the machine terminal voltages. The desired parameters result from comparing the analytical solutions obtained from equations for these functions with experimental results obtained from recording the same functions.

Two characteristic schematic diagram types for current decay tests (referenced in literature as DC Decay tests) are shown in fig.3.7.

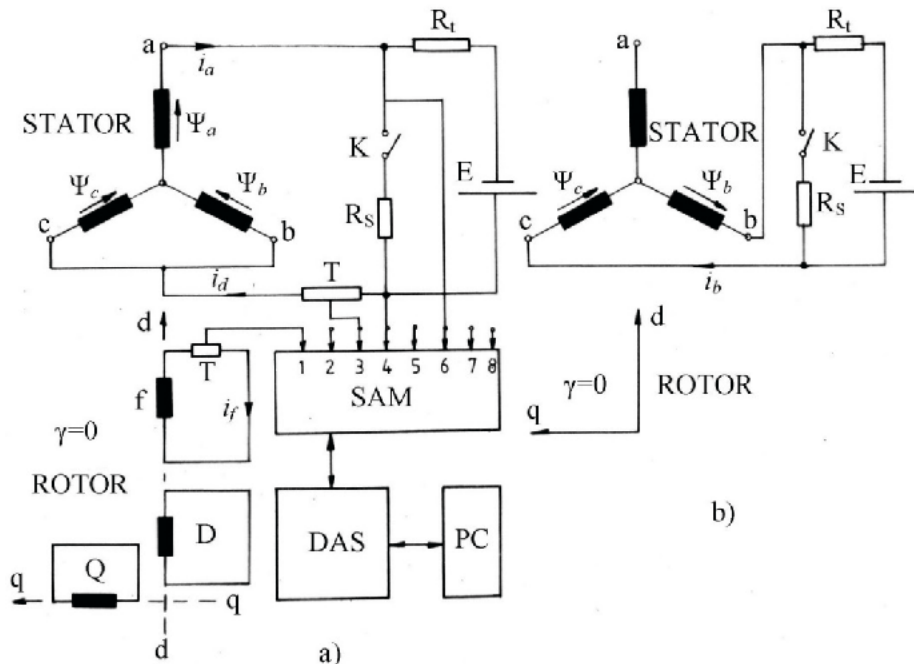


Fig.3.7 Electrical diagram for transient dc decay at standstill test: a) longitudinal type; b) transversal type; T – transducers; SAM – Signal adaptor module; DAS – data acquisition system;  $R_s$  – shunt resistance;  $R_t$  – buffer resistance.

The signal adapting module has 8 input channels, of which, in the proposed diagram, only 4 are connected, and has been used by the authors for gathering experimental data presented at the end of this section. The shunt resistance has a zero value, for the case when a residual current equal to zero is sought at the end of the transient process. The role of the buffer resistance,  $R_b$  is to protect the source E in the initial moment of the transient process, since the source is later disconnected. Closing the switcher k leads to a longitudinal transient for the diagram in Fig.3.7.a. The graphs for the stator current  $i_d(t)$  and field current  $i_f(t)$  are shown in Fig.3.8 for the case of the shunt resistance  $R_s$  is equal to zero; as a rule yielding non-saturated parameters, the residual current  $i_{d\infty}$  being zero.

Fig.3.7.b presents a similar connection diagram, but for a magnetic field decay process along the transversal axis.

In both situations, the rotor has its longitudinal axis  $d$  aligned with stator phase „a”, thus the position angle  $\gamma=0$ . It shall be pointed out that in both situations in Fig.3.7, the resulting magnetic field in the synchronous machine decays exclusively along one axis:  $d$  for Fig.3.7.a, and  $q$  for Fig.3.7.b, respectively.

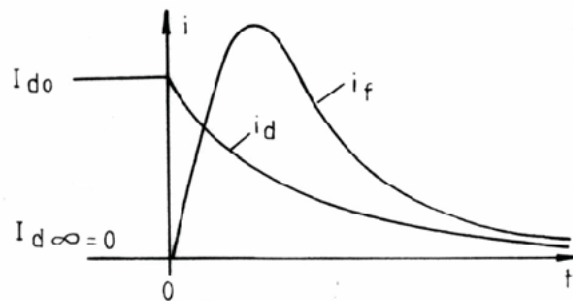


Fig.3.8. Variation of stator and field currents in a longitudinal transient condition, with  $R_s = 0$

Time variation of the stator current in the corresponding transient for Fig. 3.7.b is shown in Fig.3.9, for a shunt resistance equal to zero.

If, relative to fig.3.8, the rotor is rotated by  $\pi/2$ , the corresponding situations in Fig.3.7.a and b, respectively, yield a transversal and longitudinal transient respectively.

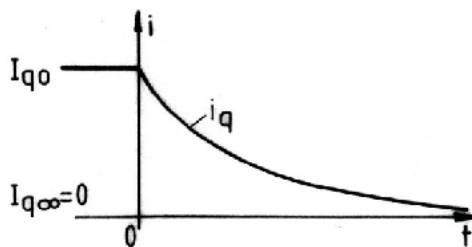


Fig.3.9 Variation of current  $i_q$  in relation to stator current  $i_b$ , in a transversal transient with  $R_s = 0$ .



All values of angle  $\gamma$  lead to direct access via measurements for currents  $i_d(t)$  and  $i_q(t)$ . The current in the field circuit  $i_f(t)$  can also be measured, and, for the case shown in Fig.3.7.a, varies as in Fig.3.8. This current functions, determined through direct measurements, contain information about all machine parameters. There are several parameter determination methods based on DC decay recordings. Basic elements regarding these methods, applied by the authors for large synchronous machines [4, 6, 7, 9, 27, 29, 45, 48, 56, 63], will be shown later.

In most cases, a rotor with three circuits:  $f$ -field (excitation),  $D$ - damper along axis  $d$  and  $Q$ - damper along axis  $q$  is acceptable. This is the commonly considered  $d$ -  $q$  model of the synchronous machine. For the identification of the parameters of this model, the following current decay tests types are considered:

4. stator current decay along axis  $d$ , with short-circuited rotor field winding  $f$  – Fig. 3.7.a, recording currents  $i_d(t)$  and  $i_{f1}(t)$  ;
5. rotor current decay with open stator winding, recording rotor current  $i_{f2}(t)$  Fig. 3.10.;
6. stator current decay along axis  $q$ , Fig. 3.7.b, recording current  $i_b(t)$  , proportional to transversal current  $i_q(t)$  .

There are other transient current decay connection diagrams, but the equations and parameter identification principles can be similarly established.

The physical significance of the parameters and the correct interpretation of recorded data and of final results, based on the machine model, are very important. Therefore, a detailed deduction follows of the intervening relations, as well as an in depth analysis of the current decay phenomenon along the two axes; including stator reduction and p.u. values, with respective coefficients.

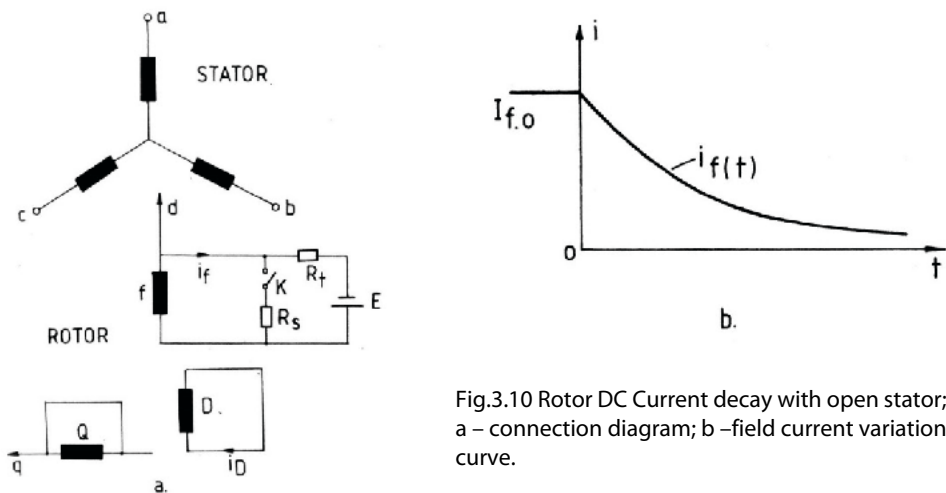


Fig.3.10 Rotor DC Current decay with open stator; a – connection diagram; b –field current variation curve.

### Equations of the DC decay transient along the longitudinal axis

Consider the electrical diagram in Fig.3.7.a. The rotor is immovable, fixed in a position where axis  $d$  overlaps with the axis of phase „a“. This has been previously achieved by using a simple schematic diagram, a no load stator, a voltmeter connected on each phase, and with the rotor field winding being supplied with a low AC voltage. The rotor is then turned slowly, until the induced emf, measured by the voltmeter connected to that phase becomes maximal, while voltages on phases  $b$  and  $c$  are equal. For this rotor position, axis  $d$  overlaps with the magnetic axis of phase „a“.

The DC current of stator phase „a“ is set to the desired constant value  $I_{a0}$ . Turning off the switch  $K$  generates a transient stator current attenuation, that leads to transients in the rotor windings as well.

#### Stator circuit equation.

Transients occur exclusively along the longitudinal  $d$  axis of the model in coordinates  $d, q$ , since under the particular conditions of the real machine in Fig.3.7.a, we have:

$$\gamma = 0; \quad i_b = i_c = -\frac{i_a}{2} \quad (3.52)$$

and with (3.32) the currents become:

$$\begin{aligned} i_d &= \frac{2}{3} \left[ i_a \cos \gamma + i_b \cos \left( \gamma - \frac{2\pi}{3} \right) + i_c \cos \left( \gamma + \frac{2\pi}{3} \right) \right] = i_a \\ i_q &= -\frac{2}{3} \left[ i_a \sin \gamma + i_b \sin \left( \gamma - \frac{2\pi}{3} \right) + i_c \sin \left( \gamma + \frac{2\pi}{3} \right) \right] = 0 \end{aligned} \quad (3.53)$$

$$i_0 = \frac{1}{3} (i_a + i_b + i_c) = 0.$$

From (3.31), with the above mentioned particularizations, the flux of phase a follows as:

$$\begin{aligned} \Psi_a &= (L_0 + L_2) i_a + \left[ -M_0 + L_2 \left( -\frac{1}{2} \right) \right] i_b + \\ &\quad + \left[ -M_0 + L_2 \left( -\frac{1}{2} \right) \right] i_c + M_{af} i_f + M_{aD} i_D \\ \Psi_a &= \left( L_0 + M_0 + \frac{3}{2} L_2 \right) i_d + M_{af} i_f + M_{aD} i_D. \end{aligned} \quad (3.54)$$

While for the flux of phase „b“ one obtains:

$$\begin{aligned} \Psi_b &= \left[ -M_0 + L_2 \left( -\frac{1}{2} \right) \right] i_a + \left[ L_0 + L_2 \left( -\frac{1}{2} \right) \right] i_b + (-M_0 + L_2) i_c + \\ &\quad + M_{af} \left( -\frac{1}{2} \right) i_f + M_{aD} \left( -\frac{1}{2} \right) i_D \end{aligned}$$

which, through substitution of particular values for the currents, becomes:

$$\Psi_b = \left( -\frac{L_0}{2} - \frac{M_0}{2} - \frac{3}{4}L_2 \right) i_d - \frac{1}{2}M_{af} i_f - \frac{1}{2}M_{ad} i_D \quad (3.55)$$

Considering the loop created by phases  $b$ ,  $a$  and the shunt resistance side,  $R_s$ , as well as the phase output direction (neutral – output terminal) as the positive reference direction for currents and magnetic fluxes, the total magnetic flux for this loop can be expressed as

$$\Psi_{tot} = \frac{3}{2} \left( L_0 + M_0 + \frac{3}{2}L_2 \right) i_d + \frac{3}{2}M_{af} i_f + \frac{3}{2}M_{ad} i_D. \quad (3.56)$$

The active resistance of the equivalent loop that has the current attenuation,  $i_d$ , can be written as:

$$R_{ech} = R_a + \frac{R_a}{2} + \frac{R_s(R_t + R_i)}{R_s + R_t + R_i} = \frac{3}{2} \left( R_a + \frac{2}{3} \cdot \frac{R_s(R_t + R_i)}{R_s + R_t + R_i} \right) \quad (3.57)$$

$$R_{aech} = R_a + \frac{2}{3} \cdot \frac{R_s(R_t + R_i)}{R_s + R_t + R_i} \quad R_{ech} = \frac{3}{2} R_{aech} \quad (3.57')$$

where:  $R_a$  - stator phase resistance;  $R_t$  - buffer resistance;  
 $R_i$  - internal source resistance;  $R_s$  - shunt resistance.

For the case of  $R_s = 0$  (short circuit, i.e.  $i_d$  decreases from some value to zero), the equivalent decay resistance becomes

$$R_{ech} = \frac{3}{2} R_a. \quad (3.57'')$$

For the short-circuit case ( $U=0$ ), the equation that defines the transient condition becomes:

$$0 = \frac{3}{2} R_a i_d + \frac{3}{2} \left( L_0 + M_0 + \frac{3}{2}L_2 \right) \frac{di_d}{dt} + \frac{3}{2} M_{af} \frac{di_f}{dt} + \frac{3}{2} M_{ad} \frac{di_D}{dt}. \quad (3.58)$$

Considering the connection between the real inductivities of the machine and the equivalent inductivity along axis  $d$ ,  $L_d$  - relation (3.43), yields the equation of the stator circuit in longitudinal position as:

$$0 = \frac{3}{2} R_a i_d + \frac{3}{2} L_d \frac{di_d}{dt} + \frac{3}{2} M_{af} \frac{di_f}{dt} + \frac{3}{2} M_{ad} \frac{di_D}{dt} \quad (3.59)$$

This equation is written in real physical quantities and not-reduced-to-stator parameters.

### Field circuit equation

The total flux of the field circuit can be determined using relation (3.5), considering the particular rotor position (longitudinal vs the magnetic axis of phase „a”), i.e.  $\gamma=0$ . Additionally, one can introduce into the relation the values of the mutual inductivities between the three phases and the field circuit – relation (3.27). The field winding flux results by replacing the values of longitudinal phase currents.

The field winding is short-circuited. Substituting this expression for the field flux, valid for the longitudinal position, in the general equation of the field current (3.2) yields, for this circuit:

$$0 = \frac{3}{2} M_{af} \frac{di_d}{dt} + i_f R_f + M_{fD} \frac{di_D}{dt} + L_f \frac{di_f}{dt}. \quad (3.60)$$

Equation (3.60) for the longitudinal rotor position has, besides theoretical importance, an immediate practical use since it enables one to directly record current variations in this circuit.

The same cannot be said about the longitudinal damper circuit, since there is no direct access to this circuit from a measurement point of view. Even so, this equation is important, because through existing magnetic couplings, flux and damper circuit currents, variations are reflected upon oscillations of other circuits. Finally, by applying necessary particularizations in relation (3.5) for the flux of the longitudinal damper circuit D, and later replacing the flux in the voltage relation (3.3), the corresponding equation for this circuit results as:

$$0 = \frac{3}{2} M_{aD} \frac{di_d}{dt} + M_{Df} \frac{di_f}{dt} + R_D i_D + L_D \frac{di_D}{dt} \quad (3.61)$$

In the rotor, with its axis overlapping the axis of stator phase „a”, no oscillations appear in the transversal damper circuit, since there are no magnetic couplings.

### Transition from equations written in physical values to equations using values written in stator reduced and per-unit form, particularized for the longitudinal rotor position

Equations written for stator, field and longitudinal damper circuits, constitute a system of equations which describe the transient for the longitudinal rotor position:

$$\begin{aligned} 0 &= \frac{3}{2} R_a i_d + \frac{3}{2} L_d \frac{di_d}{dt} + \frac{3}{2} M_{af} \frac{di_f}{dt} + \frac{3}{2} M_{aD} \frac{di_D}{dt} \\ 0 &= \frac{3}{2} M_{af} \frac{di_d}{dt} + i_f R_f + M_{fD} \frac{di_D}{dt} + L_f \frac{di_f}{dt} \\ 0 &= \frac{3}{2} M_{aD} \frac{di_d}{dt} + M_{Df} \frac{di_f}{dt} + R_D i_D + L_D \frac{di_D}{dt} \end{aligned} \quad (3.62)$$

All rotor circuits, reduced to stator, are single-phased. Consider reduction coefficients for the current  $K_i$ , for voltage  $K_u$  and impedances  $K_Z$  [1, 33]. These coefficients are particularized for a single-phase reduction as follows:

1. current reduction coefficient:

$$K_i = \frac{I_2}{I'_2} = \frac{m_1 W_1 K_{b1}}{m_2 W_2 K_{b2}} = \frac{m_1}{2} \frac{W_1 K_{b1}}{W_2} = \frac{3}{2} \frac{W_1 K_{b1}}{W_2} \quad (3.63)$$

2. voltage reduction coefficient:

$$K_u = \frac{U'_2}{U_2} = \frac{2}{m_1} K_i = \frac{2}{3} K_i \quad (3.64)$$

3. impedance reduction coefficient:

$$K_Z = K_u K_i = \frac{2}{3} K_i^2 = \frac{3}{2} \left( \frac{W_1 K_{b1}}{W_2} \right)^2 \quad (3.65)$$

In the relations for the stator reduction coefficient,  $m$  is the number of phases,  $W$  the number of turns per phase, or per the respective single-phase winding. Index 1 is for the stator and index 2 is for the rotor.  $K_b$  is the winding factor. For concentrated windings the winding factor is 1.

Thus, the reduction coefficient of the field winding to the stator winding is:

$$K_{if} = \frac{3}{2} \frac{W_1 K_{b1}}{W_f}$$

Going forward, stator reduced values will be denoted with "prime".

Considering that:

$$K_{if} M_{af} \frac{d i_f}{dt} = K_{if} M_{af} \frac{d i'_f}{dt}$$

and denoting the respective mutual inductivities reduced to the stator:

$$M'_{af} = K_{if} M_{af}$$

$$M'_{aD} = K_{iD} M_{aD} \quad (3.66)$$

$$K_{iD} M_{aD} \frac{d i_D}{dt} = K_{iD} M_{aD} \frac{d i'_D}{dt}$$

where:  $K_{iD} = \frac{3}{2} \frac{W_1 K_{b1}}{2p W_D}$  is the reduction coefficient of the longitudinal damper winding to the stator.

$W_D$  is the number of turns of the equivalent damper winding along axis „d’, per pole.

The first equation, expressed as reduced to stator becomes:

$$0 = \frac{3}{2} R_a i_d + \frac{3}{2} L_d \frac{di_d}{dt} + \frac{3}{2} M'_{af} \frac{di'_f}{dt} + \frac{3}{2} M'_{ad} \frac{di'_d}{dt}$$

The second equation of (3.62) is expanded by the field voltage reduction coefficient to the stator:

$$K_{wf} = \frac{W_1 K_{b1}}{W_f}$$

After performing necessary operations to obtain reduced currents in the following sequence:

$$0 = \frac{3}{2} K_{wf} M'_{af} \frac{di_d}{dt} + \frac{i_f}{K_{if}} K_{af} K_{if} R_f + M'_{fd} K_{wf} K_{iD} \frac{di'_D}{dt} + L_f K_{wf} K_{if} \frac{di'_f}{dt}$$

and denoting field winding inductivities and resistance reduced to the stator:

$$M'_{fD} = K_{wf} K_{iD} M_{fD}$$

$$L'_f = L_f K_{wf} K_{if} \quad (3.67)$$

$$R'_f = R_f K_{wf} K_{if}$$

the equation of the field circuit reduced to the stator results as:

$$0 = M'_{af} i_d + i'_f R'_f + M'_{fD} \frac{di'_D}{dt} + L'_f \frac{di'_f}{dt}$$

For the third equation of (3.62) similar operations are performed by expanding by the longitudinal damper winding voltage reduction coefficient to the stator:

$$K_{uD} = \frac{W_1 K_{b1}}{2p W_D} = \frac{3}{2} K_{iD}$$

$$0 = \frac{3}{2} K_{uD} M_{aD} \frac{di_d}{dt} + K_{uD} K_{if} M_{Df} \frac{di'_f}{dt} + K_{uD} K_{iD} R_D i'_D + K_{uD} K_{iD} L_D \frac{di'_D}{dt}$$

The notations used for inductivities and resistances of the longitudinal damper circuit reduced to the stator are:

$$\frac{3}{2} K_{uD} M_{aD} = K_{iD} M_{aD} = M'_{aD}$$

$$L_D K_{uD} K_{iD} = L'_D \quad (3.68)$$

$$K_{uD} K_{iD} R_D = R'_D.$$

Thus, the system of equations that describes the decay oscillations of the longitudinal position currents, with all parameters and variables reduced to the stator (values with the notation „prime”), becomes:

$$\begin{aligned} 0 &= R'_a i'_d + L'_d \frac{di'_d}{dt} + M'_{afd} \frac{di'_f}{dt} + M'_{aD} \frac{di'_D}{dt} \\ 0 &= M'_{af} i'_d + i'_f R'_f + L'_f \frac{di'_f}{dt} + M'_{fD} \frac{di'_D}{dt} \\ 0 &= M'_{aD} \frac{di'_d}{dt} + M'_{fD} \frac{di'_f}{dt} + R'_D i'_D + L'_D \frac{di'_D}{dt}. \end{aligned} \quad (3.69)$$

Transitioning to per-unit (p.u.) values for this system’s equations, the respective inductivities will be replaced by the corresponding reactances, due to time being also expressed as p.u.

As such, the system of equations of the attenuation currents for the longitudinal rotor position becomes:

$$\begin{aligned} 0 &= r'_a i'_d + x'_d \frac{di'_d}{dt} + x'_{ad} \frac{di'_f}{dt} + x'_{ad} \frac{di'_D}{dt} \\ 0 &= x'_{ad} \frac{di'_d}{dt} + i'_f r'_f + x'_f \frac{di'_f}{dt} + x'_{ad} \frac{di'_D}{dt} \\ 0 &= x'_{aD} \frac{di'_d}{dt} + x'_{ad} \frac{di'_f}{dt} + r'_D i'_D + x'_{D} \frac{di'_D}{dt} \end{aligned} \quad (3.70)$$

where all rotor values are reduced to the stator, and all are converted in per-unit to the stator selected base values, that, as a rule, are the rated values.

### Equations for D.C. decay test with open stator windings

Since the determination of the machine equivalent parameters is sought, equations (3.70) are not sufficient; therefore, the analysis of another particular case, i.e. with open rotor, is necessary.

The machine rotor remains in a longitudinal position in relation to phase „a”, immovable, similar to the previous test. The stator circuit is open. A dc voltage is applied to the field circuit – Fig.3.10. The transient results by closing the switcher K. Thus, the field current varies from a constant value to another constant value, set via the shunt resistance  $R_s$ . This resistance can be chosen to be zero, where closing switcher K, short-circuits the field circuit terminal, and the current drops from a constant value to zero.

A transient appears only for the field winding and the longitudinal damper winding.

### The field circuit equation

The total flux of the field winding is:

$$\Psi_f = L_f i_f + M_{fD} i_D.$$

In the general case, when the shunt resistance is not zero, the equivalent resistance of the field circuit for which the attenuation of the transient component of open stator test current occurs, is:

$$R_{f_{ech}} = R_f + \frac{R_s (R_i + R_i)}{R_s + R_i + R_i} \quad (3.71)$$

where  $R_f$  is the field winding resistance and  $R_i$  is buffer resistance.

In case of short circuiting,  $R_s = 0$  and  $R_{f_{ech}} = R_f$ , the equation of the transient of the field circuit is:

$$0 = M_{fD} \frac{di_D}{dt} + R_f i_f + L_f \frac{di_f}{dt} \quad (3.72)$$

where:  $M_{fD}$  - mutual inductivity between the equivalent longitudinal damper circuit and the field winding;

$L_f$  - total field circuit inductivity.

### Equations of the equivalent longitudinal damper circuit

The total flux of the longitudinal damper winding can be expressed, as a function of the mutual inductivity between that winding and the field winding  $M_{Df}$ , and the inductivity of the total longitudinal winding  $L_D$ , as:

$$\Psi_D = M_{Df} i_f + L_D i_D.$$

The equation describing the transient of the equivalent longitudinal damper winding,  $D$ , results as:

$$0 = M_{Df} \frac{di_f}{dt} + R_D \cdot i_D$$

where  $i_f$  is the real field winding current in transient state,  $i_D$  is the current of the equivalent longitudinal damper circuit,  $R_D$  the equivalent resistance of the longitudinal damper circuit, that can be calculated as a function of the particular cage [33].

### Transition from equations written in physical quantities to equations written in stator reduced and per-unit form

The two equations corresponding to rotor circuits in transient conditions with open stator  $f$  and  $D$  are expanded with the reduction factors for the voltages  $K_{uf}$  and  $K_{uD}$ .



Performing necessary operations to obtain the rotor circuit currents, reduced to stator, the equations follow as:

$$0 = K_{uf}K_{if}R_f i'_f + K_{uf}K_{if}L_f \frac{di'_f}{dt} + M_{fd}K_{uf}K_{iD} \frac{di'_D}{dt}$$

$$0 = K_{uD}K_{iD}M_{fd} \frac{di'_f}{dt} + K_{uD}K_{iD}R_D i'_D + K_{uD}K_{iD}L_D \frac{di'_D}{dt}.$$

By considering the definition of stator reduced rotor inductivities and resistances, the system of equations results that describe the transient for the open stator test:

$$0 = R'_f i'_f + L'_f \frac{di'_f}{dt} + M'_{fd} \frac{di'_D}{dt} \quad (3.73)$$

$$0 = M'_{fd} \frac{di'_f}{dt} + R'_D i'_D + L'_D \frac{di'_D}{dt}.$$

The equations are written in physical values, with all parameters and variables reduced to the stator.

Shifting to p.u. values (with the basic values, the nominal/rated stator values) and also considering that in this process

$$M'_{fd} \frac{di'_D}{dt} \text{ is substituted by } \left( x'_{fd} \frac{di'_D}{dt} \right) \text{ [p.u.]}$$

as well as  $x'_{fd} = x_{ad}$ , valid in both physical and p.u. values, the system (3.73) with all values reduced to the stator and in p.u. form, can be written as:

$$0 = i'_f r'_f + x'_f \frac{di'_f}{dt} + x_{ad} \frac{di'_D}{dt} \quad (3.74)$$

$$0 = x_{ad} \frac{di'_f}{dt} + i'_D r'_D + x'_D \frac{di'_D}{dt}$$

### Equations of the transient current decay along the transversal axis

The determination of a particular transient which show groups of real inductivities, on which the definition of the equivalent inductivities along axis „q“, from the relations (3.43), (3.47) is based, is sought. Additionally, the appearance of a transient for the transversal damper circuit is sought, to determine an equation that contains resistances and reactances of that equivalent circuit, even if there is no direct access to that particular circuit through measurements.

Rotating the rotor in a new position, offset by  $\frac{\pi}{2}$  electrical degrees from the original position, and keeping the same stator connection allows the establishment of a transient in axis „q“.

Another method of getting a transversal transient is by keeping the rotor with its longitudinal axis overlapped with the axis of open phase „a“, while phases „b“ and „c“ are connected in series, Fig. 3.7.b. From a practical standpoint, for a large synchronous machine, it is easier to make changes in the stator connection than to move the rotor in a new precise position.

In an attempt to simplify the method for practical applications, the second alternative to obtain a time variable flux, Fig. 3.7.b., has been chosen. For the particular rotor position  $\gamma=0$  and condition  $i_b = -i_c$ , the stator flux results as:

$$\Psi_{st} = \Psi_b - \Psi_c = 2 \left( L_o + M_o - \frac{3}{2} L_2 \right) i_b + 2M_{aQ} \sin \frac{2\pi}{3} i_Q \quad (3.75)$$

and the equation of the stator transient as:

$$0 = 2L_q \frac{di_b}{dt} + 2R_q i_b + 2M_{aQ} \sin \frac{2\pi}{3} \frac{di_Q}{dt} \quad (3.76)$$

where, for the case of short-circuiting the stator circuit:

$$R_q = R_a. \quad (3.77)$$

However, when considering the general case, when closing the outer stator circuit occurs over a shunt resistance,  $R_s$ , while keeping the same notations for the internal source resistance, and of the connecting wires respectively, in the same manner as for the longitudinal axis test, the equivalent resistance over which the transient component of the current closes, is:

$$R_q = R_a + \frac{1}{2} \frac{R_s (R_t + R_i)}{R_s + R_t + R_i}. \quad (3.77')$$

A similar approach is used for the transversal damper circuit. For  $\gamma=0$ , in the relations (3.5) for fluxes and (3.29) for mutual inductivities, the total flux of the equivalent longitudinal damper winding can be determined.

$$\Psi_Q = 2M_{aQ} \sin \frac{2\pi}{3} i_b + L_Q i_Q \quad (3.78)$$

$$0 = 2M_{aQ} \sin \frac{2\pi}{3} \frac{di_b}{dt} + R_Q i_Q + L_Q \frac{di_Q}{dt}$$

Using the relation for the reduction coefficients for currents and voltages in the transversal damper circuit:

$$K_{iQ} = \frac{3}{2} K_{uQ}$$

the equation containing the stator reduced rotor damper current results as:

$$0 = 2M_{aQ} \frac{\sqrt{3}}{2} \cdot \frac{di_b}{dt} \cdot K_{uQ} + R_Q K_{uQ} K_{iQ} i'_Q + L_Q K_{uQ} K_{iQ} \frac{di'_Q}{dt}.$$

Considering the connection between real inductivities and the stator-reduced ones

$$M'_{aQ} = K_{iQ} M_{aQ} = \frac{3}{2} M_{Qa} K_{uQ} \quad (3.79)$$

as well as the particular relation for currents, from (3.32) with  $\gamma = 0$  and  $i_b = -i_c$

$$\begin{aligned} i_d &= 0 \\ i_q &= \frac{2}{\sqrt{3}} i_b, \end{aligned} \quad (3.80)$$

the equations of the two circuits in stator reduced values, marked by the prime symbol follows as:

$$\begin{aligned} 0 &= R_q i_q + L_q \frac{di_q}{dt} + M'_{aQ} \frac{di'_Q}{dt} \\ 0 &= M'_{aQ} \frac{di_q}{dt} + R'_Q i'_Q + L'_Q \frac{di'_Q}{dt} \end{aligned} \quad (3.81)$$

Shifting from relative values, the system of equations for transversal currents attenuation in stator reduced and relative values, results as:

$$\begin{aligned} 0 &= r_q i_q + x_q \frac{di_q}{dt} + x_{aq} \cdot \frac{di'_Q}{dt} \\ 0 &= x_{aq} \frac{di_q}{dt} + r'_Q i'_Q + x'_Q \frac{di'_Q}{dt} \end{aligned} \quad (3.82)$$

In the equations for the transient processes along the longitudinal axis (3.70), for those corresponding to the field circuit with open stator (3.74) and along the transversal axis respectively (3.82), all values are in per-unit [p.u.] form, including time, while rotor values are reduced to the stator.

Next, to simplify the practical use of the beforementioned equations, the „prime” notation for reduced values, when detailing the reduction process, is dropped.

### 3.3.2. Determination of equivalent parameters from current decay conditions for the usual $d, q$ model.

For the purposes of experimental parameter determination, let us consider the three previously presented current decay conditions: along the longitudinal axis, open stator, and along the transversal axis. In the previous paragraphs the testing conditions were described, the corresponding equations, with details of the reduction coefficients were presented.

Based on these equations, it follows next a presentation of the parameters determination and the definition of characteristics values according to [49, 56, 57, 58, 64, 65].

Corresponding experimental results have been obtained by the authors from tests of high power synchronous machines in industrial environment [4, 7, 9, 21, 26, 27, 28, 29], which will be presented in the final part of the following paragraphs.

In all cases, measurable values are of interest in solving the equations. The general principle of practical utilization of the recordings is based on the comparison between the recorded functions and the analytical solutions to the same functions, obtained from equations.

### Determination of longitudinal parameters.

First, let us consider the longitudinal transients corresponding to Fig. 3.7.a for which the stator current  $i_a(t) = i_d(t)$  and field current  $i_f(t)$  are recorded.

Consider the shunt resistance  $R_s = 0$  and thus the stator winding current  $i_d$  is attenuating to zero  $I_{d\infty} \rightarrow 0$ .

Applying the Laplace transform to the system of equations (3.70) that describe the transient conditions, using the bar notation for image functions, the transformed system becomes:

$$\begin{aligned}
 0 &= \bar{i}_d r_a + x_d \left( p \bar{i}_d - I_0 \right) + x_{ad} p \bar{i}_f + x_{ad} p \bar{i}_D \\
 0 &= x_{ad} \left( p \bar{i}_d - I_0 \right) + r_f \bar{i}_f + x_f p \bar{i}_f + x_{ad} p \bar{i}_D \\
 0 &= x_{ad} \left( p \bar{i}_d - I_0 \right) + x_{ad} p \bar{i}_f + \bar{i}_D r_D + x_D p \bar{i}_D.
 \end{aligned} \tag{3.83}$$

For the application of the Laplace transform, initial values of the field currents and of the currents in the longitudinal damper winding are both zero. This system shows image functions of reduced currents in p.u., indicated by the bar notation.  $I_0$  is the initial value of the current as a time function of  $i_d$ .

Manipulations of the system of equations are performed, yielding:

$$\begin{aligned}
 I_0 &= \bar{i}_d \frac{r_a}{x_d} + p \bar{i}_d + \frac{x_{ad}}{x_d} p \bar{i}_f + \frac{x_{ad}}{x_d} p \bar{i}_D \\
 I_0 \frac{x_{ad}}{x_f} &= \frac{x_{ad}}{x_f} p \bar{i}_d + \frac{r_f}{x_f} \bar{i}_f + p \bar{i}_f + \frac{x_{ad}}{x_f} p \bar{i}_D
 \end{aligned}$$

$$I_0 \frac{x_{ad}}{x_D} = \frac{x_{ad}}{x_D} p \bar{i}_d + \frac{x_{ad}}{x_D} p \bar{i}_f + \bar{i}_D + \frac{r_D}{x_D} + p \bar{i}_D$$

Damping coefficients and Blondel leakage coefficients [20, 22, 33, 37, 56] are used :

$$\alpha_d = \frac{r_a}{x_d} - \text{stator winding damping coefficient;}$$

$$\alpha_f = \frac{r_f}{x_f} - \text{field winding damping coefficient;}$$

$$\alpha_D = \frac{r_D}{x_D} - \text{longitudinal winding damping coefficient;} \quad (3.84)$$

$$C_d = \frac{x_{ad}}{x_d} - \text{stator winding leakage coefficient, and similarly for the other windings ;}$$

$$C_f = \frac{x_{ad}}{x_f} - \text{field winding leakage coefficient;}$$

$$C_D = \frac{x_{ad}}{x_D} - \text{longitudinal damping winding leakage coefficient.}$$

With these coefficients, the transformed system becomes:

$$\begin{aligned} I_0 &= \bar{i}_d (p + \alpha_d) + C_d p \bar{i}_f + C_d p \bar{i}_D \\ I_0 C_f &= C_f p \bar{i}_d + \bar{i}_f (p + \alpha_f) + C_f p \bar{i}_D \\ I_0 C_D &= C_D p \bar{i}_d + C_D p \bar{i}_f + \bar{i}_D (p + \alpha_D). \end{aligned} \quad (3.85)$$

Taking into account the practical applicability of the analysis, the images of currents for which access via direct measurement (i.e. stator and field circuits) is available are sought.

The main determinant for the system is:

$$D(p) = \begin{vmatrix} p + \alpha_d & C_d p & C_d p \\ C_f p & p + \alpha_f & C_f p \\ C_D p & C_D p & p + \alpha_D \end{vmatrix}.$$

Using the notations:

$$\begin{aligned} \sigma_d &= 1 - C_D C_f - C_f C_d + 2C_f C_d C_D - C_d C_D \\ \sigma_{dD} &= 1 - C_d C_D; \quad \sigma_{fD} = 1 - C_f C_D; \quad \sigma_{fd} = 1 - C_f C_d; \end{aligned}$$

the determinant of system (3.85) can be written as:

$$D(p) = p^3 \sigma_d + p^2 (\alpha_f \sigma_{dD} + \alpha_d \sigma_{fD} + \alpha_D + \sigma_D) + p (\alpha_f \alpha_D + \alpha_d \alpha_f + \alpha_d \alpha_D) + \alpha_d \alpha_f \alpha_D. \quad (3.86)$$

The determinant corresponding to the current  $i_d$  is:

$$D_{id}(p) = I_0 \begin{vmatrix} 1 & p C_d & p C_d \\ C_f & p + \alpha_f & p C_f \\ C_D & p C_D & p + \alpha_D \end{vmatrix}$$

and, using the same notations, the expanded form is:

$$D_{id}(p) = I_0 \cdot [p^2 \sigma_d + p (\alpha_f \sigma_{dD} + \alpha_D \sigma_{fd}) + \alpha_D \alpha_f]. \quad (3.87)$$

Since in the transient conditions two different recordings are taken for different conditions of the field current, henceforth the notation  $i_{f1}$  is used for the longitudinal transient and  $i_{f2}$  for the open rotor decay transient condition.

The determinant corresponding to the image of the field current for the longitudinal test is:

$$D_{if1}(p) = I_0 \begin{vmatrix} p + \alpha_d & 1 & p C_d \\ p C_f & C_f & p C_f \\ p C_D & C_D & p + \alpha_D \end{vmatrix}$$

$$D_{if1}(p) = I_0 [C_f \alpha_d p (1 - C_D) + \alpha_D]. \quad (3.88)$$

Theorems for original integration and derivation are considered:

$$\int_0^{\infty} f(t) dt = \lim_{p \rightarrow 0} F(p),$$

$$\left. \frac{d f(t)}{dt} \right|_{t=0} = \lim_{p \rightarrow \infty} [p^2 F(p) - p f(0)]$$

$$\int_0^{\infty} i_d(t) dt = \lim_{p \rightarrow 0} \frac{D_{id}(p)}{D(p)}$$

where  $F(p)$  is the image of function  $f(t)$ , and  $f(0)$  is the value of the real function at the initial time.

The integral of the longitudinal current follows as:

$$\frac{1}{I_0} \int_0^{\infty} i_d(t) dt = \frac{1}{\alpha_d}. \quad (3.89)$$

After simplification, the derivative of the longitudinal current becomes:

$$\frac{1}{I_0} \left. \frac{d i_d(t)}{dt} \right|_{t=0} = - \frac{\alpha_d \sigma_{fd}}{\sigma_d} \quad (3.90)$$

Similar operations are performed for the real field current  $i_{f1}(t)$  and its image  $\bar{i}_{f1}(p)$ . The integral and then the derivative at the origin are obtained as:

$$\frac{1}{I_0} \int_0^{\infty} i_{f1}(t) dt = \frac{C_f}{\alpha_f} \quad (3.91)$$

$$\begin{aligned} \left. \frac{d i_{f1}(t)}{dt} \right|_{t=0} &= \lim_{p \rightarrow \infty} \frac{p^2 [I_0 C_f \alpha_d p (1 - C_D) + \alpha_D]}{D(p)} \\ \frac{1}{I_0} \left. \frac{d i_{f1}(t)}{dt} \right|_{t=0} &= \frac{C_f \alpha_d (1 - C_D)}{\sigma_d}. \end{aligned} \quad (3.92)$$

For the open stator transient condition, applying the Laplace transform to the system (3.74) that describes this case, one obtains:

$$\begin{aligned} x_f I_{0f2} &= \bar{i}_{f2} r_f + p x_f \bar{i}_{f2} + x_{ad} p \bar{i}_D \\ x_{ad} I_{0f2} &= x_{ad} p \bar{i}_{f2} + \bar{i}_D r_D + x_D p \bar{i}_D, \end{aligned}$$

where  $I_{0f2}$  represents the initial value of the real field current.

Using the previously defined coefficients we have:

$$\begin{aligned} I_{0f2} &= \bar{i}_{f2} (p + \alpha_f) + C_f p \bar{i}_D \\ C_D I_{0f2} &= C_D p \bar{i}_{f2} + \bar{i}_D (p + \alpha_D). \end{aligned} \quad (3.93)$$

Only the solution to the system that can be tested experimentally, i.e. field current, is pursued, therefore:

$$\bar{i}_{f2}(p) = \frac{I_{0f2} (p \sigma_{fd} + \alpha_D)}{p^2 \sigma_{fd} + p (\alpha_f + \alpha_D) + \alpha_f \alpha_D}. \quad (3.94)$$

Finally, the following relations with practical applications, related to the integral, i.e. the origin derivative with respect to time of the field current, are determined:

$$\frac{1}{I_{0f2}} \int_0^{\infty} i_{f2}(t) dt = \frac{1}{\alpha_f} = \frac{x_f}{r_f} \quad (3.95)$$

$$\left. \frac{1}{I_0} \frac{di_{f2}(t)}{dt} \right|_{t=0} = -\frac{\alpha_f}{\sigma_{fD}}. \quad (3.96)$$

Parseval's energy relation [42, 43, 56] for the field current corresponding to the open rotor test is applied

$$\int_0^{\infty} i_{f2}^2(t) dt = \frac{C_1^2 d_0 + C_0 d_2}{2d_0 d_1 d_2} \quad (3.97)$$

where  $C_1, C_0$  - coefficients of the power order 1 and 0 of  $p$  in the numerator of the operational expression of the current  $i_{f2}$  (3.94);

$d_2, d_1, d_0$  - coefficients of the power order 2, 1, and 0 respectively in the denominator of the operational expression of the current  $i_{f2}$ .

Considering the expression of the image of current  $i_{f2}$ , one can write:

$$\int_0^{\infty} i_{f2}^2(t) dt = \frac{I_{0f2}^2 \sigma_{fD} \alpha_f \alpha_D + I_{0f2}^2 \alpha_D \sigma_{fD}}{2\alpha_f \alpha_D (\alpha_f + \alpha_D) \sigma_{fD}}$$

or, in the final form that can be used in the computation program for the numerical data processing of recordings:

$$\frac{1}{I_{0f2}^2} \int_0^{\infty} i_{f2}^2(t) dt = \frac{\alpha_f \sigma_{fD} + \alpha_D}{2\alpha_f (\alpha_f + \alpha_D)}. \quad (3.98)$$

Using these basic relations defined for the longitudinal axis test, processing the recordings  $i_d(t)$ ,  $i_{f1}(t)$  and  $i_{f2}(t)$ , all longitudinal parameters  $x_d, x_{ad}, x_f, x_D, x_\sigma$ , can be successively determined as shown next, using the specified notations for numerical values for integrals and derivatives.

The integral (3.89) can be calculated from the recording of the stator current:

$$\text{SiD} = \frac{1}{I_0} \int_0^{\infty} i_d(t) dt \quad (3.99)$$

where  $I_0$  is the initial value of the DC stator current before closing the switcher.

This gives the damping coefficient corresponding to the stator circuit as:

$$\alpha_d = \frac{1}{\text{SiD}} = \frac{r_a}{x_d} \quad (3.100)$$



The integral:

$$\text{SiF2} = \frac{1}{I_{0f2}} \int_0^{\infty} i_{f2}(t) dt \quad (3.101)$$

is calculated from the recording of the field current  $i_{f2}$ , where  $I_{0f2}$  is the initial value of the DC current in the field winding before starting the transient current decay.

The previously defined field circuit damping coefficient results as:

$$\alpha_f = \frac{1}{\text{SiF2}} = \frac{r_f}{x_f}. \quad (3.102)$$

For the derivative of  $i_{f2}$ , at the initial moment of the transient process:

$$\text{DiF2} = \frac{1}{I_{0f2}} \left. \frac{di_{f2}(t)}{dt} \right|_{t=0} \quad (3.103)$$

and, alternately:

$$\text{DiF2} = -\frac{\alpha_f}{\sigma_{fD}}.$$

That allows the determination of the coefficient  $\sigma_{fD}$ :

$$\sigma_{fD} = -\frac{\alpha_f}{\text{DiF2}} \quad (3.104)$$

The derivative of the current in the initial moment of the transient is:

$$\text{DiD} = \frac{1}{I_0} \left. \frac{di_d(t)}{dt} \right|_{t=0} = \frac{-\alpha_d \sigma_{fD}}{\sigma_d} \quad (3.105)$$

and

$$\sigma_d = \frac{-\alpha_d \sigma_{fD}}{\text{DiD}}. \quad (3.106)$$

From the recordings of the field current  $i_{f1}$  results:

$$\text{SiF1} = \frac{1}{I_0} \int_0^{\infty} i_{f1}(t) dt \quad (3.107)$$

and, alternately, relation (3.91):

$$\text{SiF1} = \frac{C_f}{\alpha_f} = \frac{x_{ad}}{r_f}. \quad (3.108)$$

The derivative of  $i_{f1}$  in the initial moment of the transient process is:

$$\text{DiF1} = \frac{1}{I_0} \left. \frac{di_{f1}}{dt} \right|_{t=0} = \frac{C_f \alpha_d (1 - C_D)}{\sigma_d}. \quad (3.109)$$

Dividing relations (3.109) and (3.108) yields:

$$\text{DF} = \frac{\text{DiF1}}{\text{SiF1}} = \frac{\alpha_d \alpha_f (1 - C_D)}{\sigma_d} \quad (3.110)$$

and from (3.84) also:

$$1 - C_D = \frac{\sigma_d \text{DF}}{\alpha_d \alpha_f}.$$

The leakage coefficient  $C_D$  is:

$$C_D = 1 - \frac{\sigma_d D_f}{\alpha_d \alpha_f} = \frac{\alpha_d \alpha_f - \sigma_d \text{DF}}{\alpha_d \alpha_f}. \quad (3.111)$$

The leakage coefficient  $C_f$  is:

$$C_f = \frac{1 - \sigma_{fD}}{C_D} \quad (3.112)$$

and, with notations from (3.84), the leakage coefficient for the stator results as:

$$C_d = \frac{1 - C_f C_D - \sigma_d}{C_f + C_D - 2C_f C_D}. \quad (3.113)$$

Tests performed by authors with several high power synchronous machines established that the values of coefficients  $C_f$  and  $C_D$  are close to the value 1. Therefore, a higher precision numerical calculation is recommended.

The integral of the squared field current  $i_{f2}$  is:

$$\text{AF2} = \frac{1}{I_{0f2}^2} \int_0^{\infty} i_{f2}^2(t) dt = \frac{\alpha_f \sigma_{fD} + \alpha_D}{2\alpha_f (\alpha_f + \alpha_D)} \quad (3.114)$$

and the coefficient  $\alpha_D$ :

$$\alpha_D = \frac{\alpha_f (\sigma_{fD} - 2\alpha_f \text{AF2})}{2\alpha_f \text{AF2} - 1}. \quad (3.115)$$

The determination of the „p.u.” value („per unit”) of the phase resistance:

$$r_a = (R_a) \text{ p.u.} = \frac{R_a}{Z_b} \quad (3.116)$$

where  $Z_b$  is the base impedance.

The p.u. values used in computations appear with the same notations, but in lower case. Derivatives and integrals of currents previously described are also written as „per-unit“.

Subsequently the p.u. values of the electromagnetic equivalent parameters along axis d, for define the steady state operation of the synchronous machine as are defined in [20, 36, 37, 47, 56, 64, 65], become:

4. Longitudinal synchronous reactance:

$$x_d = \frac{r_a}{\alpha_d} = r_a \frac{1}{I_0} \int_0^{\infty} i_d(t) dt ; \quad (3.117)$$

5. Longitudinal reaction reactance:

$$x_{ad} = C_d x_d \quad (3.118)$$

6. Field reactance:

$$x_f = \frac{x_{ad}}{C_f} \quad (3.119)$$

7. Reactance of the equivalent longitudinal damping circuit:

$$x_D = \frac{x_{ad}}{C_D} \quad (3.120)$$

8. Resistance of the equivalent longitudinal damping circuit:

$$r_D = x_D \alpha_D \quad (3.121)$$

9. Resistance of the field circuit:

$$r_f = x_f \alpha_f \quad (3.122)$$

10. Leakage reactance obtained from the values of the longitudinal synchronous reactance and longitudinal reaction reactance:

$$x_{\sigma} = x_d - x_{ad} \quad (3.123)$$

### Determination of transversal parameters

Let us consider the system of equations, (3.82), that describe the transversal type transient, in the stator circuit  $q$  and in the rotor damper circuit. The following notations are made for the damping  $Q$  and leakage coefficients on transversal axis:

11.  $\alpha_q = \frac{r_q}{x_q}$  - damping coefficient for the transversal stator winding;

12.  $\alpha_Q = \frac{r_Q}{x_Q}$  - damping coefficient for the transversal damper winding

13.  $C_q = \frac{x_{aq}}{x_q}$  - leakage coefficient for the stator winding along the axis  $q$ ;

14.  $C_Q = \frac{x_{aQ}}{x_Q}$  - leakage coefficient for the transversal damper winding

Assuming the short-circuiting of the stator circuit, i.e.  $R_s = 0$ , the transversal current falls to zero for large time values, and, applying the Laplace transform to system (3.82), yields:

$$\begin{aligned} I_{0q} &= (\alpha_q + p) \bar{i}_q + C_q p \bar{i}_Q \\ I_{0q} C_Q &= C_Q p \bar{i}_q + (\alpha_Q + p) \bar{i}_Q \end{aligned} \quad (3.124)$$

where  $I_{0q}$  is the initial value of the stator current, meaning  $\frac{2}{\sqrt{3}} I_{b0}$ , and  $I_{b0}$  is the initial value of the phase current – Fig. 3.7, Fig. 3.9 and relation (3.80).

Solving the system with regard to current  $\bar{i}_q$ , since the original of the function is accessible through measurements, the determinant of the function is:

$$D_q(p) = \begin{vmatrix} \alpha_q + p & C_q p \\ C_Q p & (\alpha_Q + p) \end{vmatrix} = p^2 (1 - C_q C_Q) + p(\alpha_q + \alpha_Q) + \alpha_q \alpha_Q$$

The determinant of the current  $\bar{i}_q$  is:

$$D_{i_q}(p) = I_{0q} \begin{vmatrix} 1 & C_q p \\ C_Q & \alpha_Q + p \end{vmatrix} = I_{0q} [p(1 - C_q C_Q) + \alpha_Q].$$

Using notation:  $\sigma_{qQ} = 1 - C_q C_Q$ , the two determinants can be written as:

$$D_q(p) = p^2 \sigma_{qQ} + p(\alpha_q + \alpha_Q) + \alpha_q \alpha_Q$$

$$D_{i_q}(p) = I_{0q} (p \sigma_{qQ} + \alpha_Q)$$

where the image of the stator test current along axis  $q$  becomes:

$$\bar{i}_q(p) = \frac{I_{0q} (p \sigma_{qQ} + \alpha_Q)}{p^2 \sigma_{qQ} + p(\alpha_q + \alpha_Q) + \alpha_q \alpha_Q}. \quad (3.125)$$

Using the properties of operational calculus regarding original derivation and integration leads to:

$$\int_0^{\infty} i_q(t) dt = \lim_{p \rightarrow 0} i_q(p) = \frac{I_{0q}}{\alpha_q},$$

and a relation for practical application:

$$\frac{1}{I_{0q}} \int_0^{\infty} i_q(t) dt = \frac{1}{\alpha_q}. \quad (3.126)$$

For the time derivative we have:

$$\left. \frac{di_q(t)}{dt} \right|_{t=0} = \lim_{p \rightarrow \infty} \left[ p^2 i_q(p) - p i_q(t) \right]_{t=0} = -\frac{I_{0q} \alpha_q}{\sigma_{qQ}}.$$

And the relation with practical use:

$$\left. \frac{1}{I_{0q}} \frac{di_q(t)}{dt} \right|_{t=0} = -\frac{\alpha_q}{\sigma_{qQ}}. \quad (3.127)$$

Applying current  $i_q$  to Parseval's energy relation [42, 43, 56] yields:

$$\int_0^{\infty} i_q^2(t) dt = \frac{C_1^2 d_0 + C_0 d_2}{2d_0 d_1 d_2}$$

where  $c, d$  are coefficients of the powers of operator  $p$ , from the operational  $i_q(p)$  current relation (3.125):

$$C_0 = I_{0q} \alpha_Q; \quad d_0 = \alpha_q \alpha_Q; \quad d_2 = \sigma_{qQ}; \quad C_1 = I_{0q} \sigma_{qQ}; \quad d_1 = \alpha_q + \alpha_Q.$$

As such, the final significant relation in the processing of oscillograms for tests along axis  $q$  becomes:

$$\frac{1}{I_{0q}^2} \int_0^{\infty} i_q^2(t) dt = \frac{\alpha_q \sigma_{qQ} + \alpha_Q}{2\alpha_q (\alpha_q + \alpha_Q)}. \quad (3.128)$$

It can be observed that in the transversal type transient conditions only the phase current  $i_b(t)$  is measured directly, and not  $i_q(t)$ . Since the two currents are in a linear relation (3.80), it follows that in relations (3.126), (3.127) and (3.128) operations can be performed the same way by substituting the transversal component of current  $i_q(t)$  with the recording of phase current  $i_b(t)$ , at the same time substituting  $I_{0q}$  with the initially measured phase current  $I_{0b}$ .

Following these observations, the processing of the transversal current recording is shown, and the following values are determined:

- \* Integral of transversal current:

$$\text{SiQ} = \frac{1}{I_{0q}} \int_0^{\infty} i_q(t) dt = \frac{1}{\alpha_q} \quad (3.129)$$

- \* Damping coefficient  $\alpha_q$  :

$$\alpha_q = \frac{1}{\text{SiQ}} = \frac{r_q}{x_q} \quad (3.130)$$

where  $r_q$  is the resistance in (3.77) in per-unit values.

- \* synchronous transversal reactance:

$$x_q = \frac{r_q}{\alpha_q} = r_a \frac{1}{I_{0q}} \int_0^{\infty} i_q(t) dt \quad (3.131)$$

- \* transversal reaction reactance:

$$x_{aq} = x_q - x_{\sigma} \quad (3.132)$$

where the leakage reactance is assumed to be known from previous tests.

The derivative in the origin of the transversal current  $i_q$  is:

$$\text{DiQ} = \frac{1}{I_{0q}} \left. \frac{di_q(t)}{dt} \right|_{t=0} = -\frac{\alpha_q}{\sigma_{qQ}}$$

and the leakage coefficient follows as:

$$\sigma_{qQ} = -\frac{\alpha_q}{\text{DiQ}}. \quad (3.133)$$

Accounting for the relations between coefficients leads to:

$$\begin{aligned} \sigma_{qQ} &= 1 - C_q C_Q \\ \sigma_{qQ} &= 1 - \frac{x_{aq}}{x_q} \frac{x_{aq}}{x_Q} = 1 - \frac{x_{aq}^2}{x_q x_Q} \end{aligned}$$

and the reactance of the equivalent transversal damping circuit :

$$x_Q = \frac{x_{aq}^2}{x_q (1 - \sigma_{qQ})}. \quad (3.134)$$

Solving the integral:

$$AQ = \frac{1}{I_{0q}^2} \int_0^{\infty} i_q^2(t) dt = \frac{\alpha_q \sigma_{qQ} + \alpha_Q}{2\alpha_q (\alpha_q + \alpha_Q)} \quad (3.135)$$

provides the attenuation coefficient of the transversal circuit:

$$\begin{aligned} \alpha_q \sigma_{qQ} + \alpha_Q &= 2\alpha_q^2 AQ + 2\alpha_q \alpha_Q AQ \\ \alpha_Q &= \frac{\alpha_q (\sigma_{qQ} - 2\alpha_q AQ)}{2\alpha_q \cdot AQ - 1} \end{aligned} \quad (3.136)$$

This coefficient is used for the determination of the resistance of the equivalent transversal damping circuit:

$$r_Q = x_Q \alpha_Q \quad (3.137)$$

### Experimental results

Transient current decay tests have been performed for a synchronous machine with the following parameters:

- \* rated power  $P_n = 4650 \text{ kW}$  ;
- \* rated voltage  $U_n = 6000 \text{ V}$  ;
- \* rated current  $I_n = 495 \text{ A}$  ;
- \* number of poles  $2p = 14$  ;
- \* rated frequency  $f = 50 \text{ Hz}$  ;
- \* connection: star;

with connections per schematic diagrams in Fig.3.7.a and b, and Fig.3.10.

Fig.3.11 shows the variation of the field current for longitudinal decay  $i_{f1}(t)$ , and Fig. 3.12 for the field rotor current decay  $i_{f2}(t)$  and open stator current.

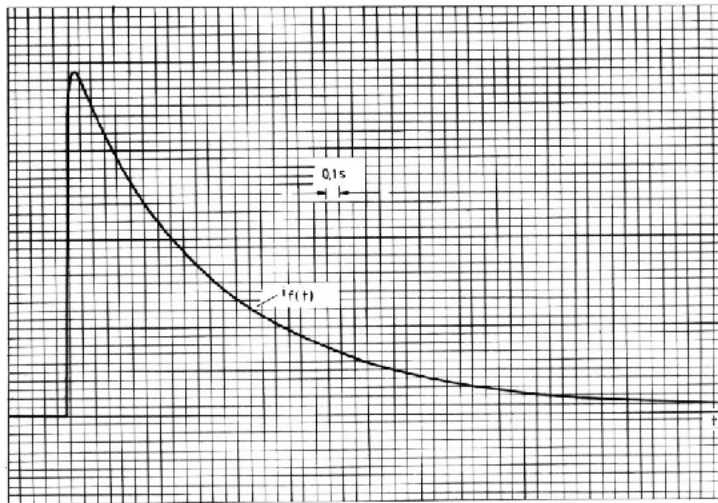


Fig.3.11 Variation of the field current  $i_{f1}(t)$ , for current decay in the longitudinal axis, for the 4650 kW synchronous machine.

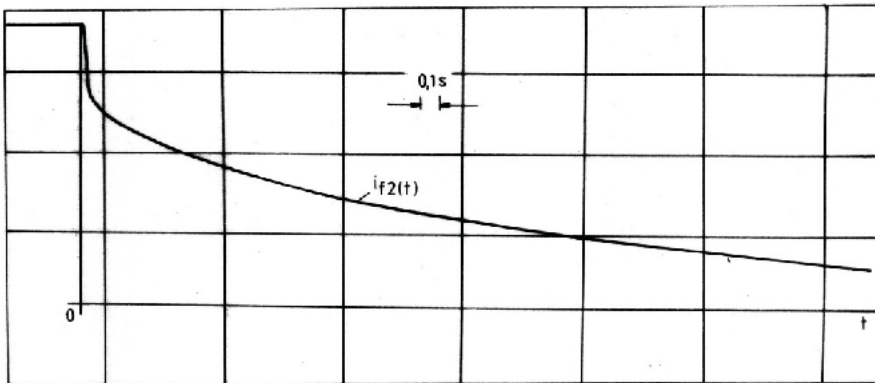


Fig.3.12 Variation of the field current  $i_{f2}(t)$ , for rotor current decay and open stator, for the 4650 kW synchronous machine.

Figure 3.13 shows the recording of phase  $b$  current, per the schematic diagram in Fig.3.7.b, for the current decay along the transversal axis for the same machine.

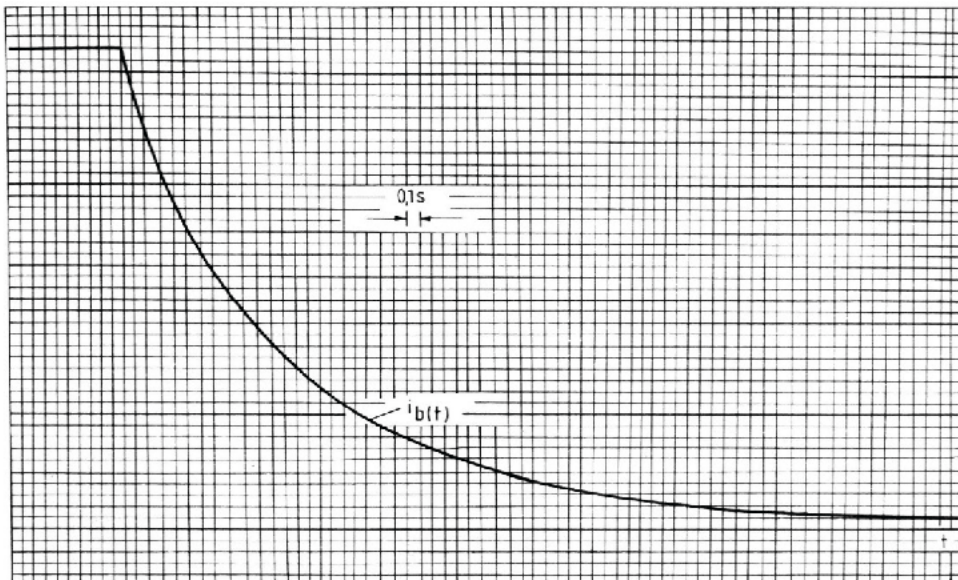


Fig.3.13 Recording of transient current  $i_b(t)$  in transversal conditions for the 4650 kW machine.

It should be noted that the relatively distinct beginning part of the transient curve, highlights the time interval for the decay of the transient current in the damper cage  $Q$  - Fig. 3.12.

Numerical data processing based on the previously discussed algorithm, resulted in the following equivalent parameters for the 4650 kW machine (per-unit):



Longitudinal stator parameters:

- \*  $x_d = 0,9442$  - longitudinal synchronous reactance;
- \*  $x_{ad} = 0,8501$  - longitudinal reaction reactance;
- \*  $x_\sigma = 0,0941$  - stator leakage reactance.

Transversal stator parameters

- \*  $x_q = 0,6214$  - transversal synchronous reactance;
- \*  $x_{aq} = 0,5723$  - transversal reaction reactance.

Longitudinal rotor parameters

- \*  $x_D = 1,012$  - reactance of the longitudinal damper cage  $D$ ;
- \*  $r_D = 0,0809$  - equivalent resistance of the longitudinal damper cage  $D$ ;
- \*  $x_f = 1,218$  - reactance of field winding.

Transversal rotor parameters

- \*  $x_Q = 0,6418$  - reactance of the transversal damper cage  $Q$ ;
- \*  $r_Q = 0,0424$  - equivalent resistance of the transversal damper cage  $Q$ .

### 3.3.2. Consideration of multiple cages

Parameter derivations previously shown in paragraph 3.3.1 are based on the usual model of the synchronous machine used by Park. This model considers the rotor with a real damper cage, which appears in the equations represented by two damper circuits along the two axes, labeled  $D$  and  $Q$ , introduced in paragraph 3.1.2.

Recently, discrepancies between measured and calculated values have been identified for some machines.

These experimental results, considered inconclusive, appeared even for machines with relatively strong damper cages. These inconsistencies may be caused by the fact that, in certain constructive versions, the real machine can have some massive rotor pieces, which, in case of transient conditions, may act as damper cages, in addition to the main cage.

Therefore the model with three rotor circuits, two dampers  $D$ ,  $Q$ , and one field circuit  $f$ , is no longer valid. Even if under transient conditions the supplemental cages have a lower damping capacity than the main cage, they are characterized by branches with additional parameters in the equivalent diagrams corresponding to the classical model

Thus, for example in the previously considered current decay along axis  $q$ , for which, in the classical model, two exponential components of the transient current appear, one corresponding to the stator circuit  $q$ , and the other corresponding to rotor cage  $Q$ , for a machine that has also massive rotor pieces, three or more circuits or exponential components of the decay currents may appear.

The degree of complexity along axis  $d$  increases even more due to the field circuit  $f$ .

Therefore, several quantities along the two axes, such as parameters and time constants, should be redefined. Determination of these values through calculations, or even identification of supplemental cages, significant in relation to the designed main cage, leads to increased difficulties.

Significant progress in the area of synchronous machines with multiple cages has been made through the work of I. M. Canay [13, 14].

Therefore, for a practical solution to the determination of parameters of the synchronous machine, the order of operations has been reversed, by first experimentally finding the number of significant cages for a real machine, and then determining parameters.

These issues have been solved by methods based on frequency response characteristics [63, 64, 65].

### Basic elements regarding frequency response characteristics

The introduction of the basic elements regarding frequency response characteristics is done through the Fourier integral and operational calculus [33, 34]. The Carson transform of a function  $f(t)$  is:

$$F(p) = p \int_0^{\infty} e^{-pt} f(t) dt \quad (3.138)$$

We consider that, for instance, function  $f(t)$  is represented by the real function of the current  $i(t)$  in a transient process in a circuit. In this case, applying a unit step voltage signal to the respective circuit, the expression holds:

$$\frac{1}{x(p)} = p \int_0^{\infty} e^{-pt} i(t) dt \quad (3.139)$$

where  $x(p)$  is the operational circuit reactance.

The real function of the current can be obtained through inverse transform:

$$i(t) = \frac{1}{2\pi j} \int_{-j\infty}^{+j\infty} \frac{e^{pt}}{px(p)} dp. \quad (3.140)$$

Similarly, a relation can be established between a current in a system where a unit step signal is applied and its reactance, using the Fourier integral:

$$i(t) = \frac{1}{2\pi} \int_{-\infty}^{+\infty} \frac{e^{jst}}{jsx(js)} ds \quad (3.141)$$

where  $x(js)$  is the complex reactance of the system. By definition, the frequency characteristic of the system is the ratio:

$$\frac{1}{x(js)}$$

where  $s$  is the relative frequency.

For the inverse transformation, the following relation is used:

$$\frac{1}{x(js)} = js \int_0^{\infty} i(t) e^{-js} dt. \quad (3.142)$$

Comparing transforms from the operational with the ones in complex, using Fourier integrals, i.e. (3.139) with (3.142), it follows that it is easy to switch from operational functions and parameters to parameters and frequency characteristics by substituting operator  $p$  with  $js$ .

With regard to the synchronous machine, operational parameters result by applying operational calculus to the Park equations. Based on those operational parameters, the harmonic (complex) impedances and reactances along the two axes [17, 19, 20, 33, 35, 36, 37, 64, 65] follow.

### **Relation between decay functions in standstill tests and frequency characteristics for the synchronous machine**

Frequency characteristics can be determined by using recordings of decay currents in standstill rotor tests, as previously described in paragraph 3.2.1.

Following is a presentation of the connection between the quantities that define dc decay current functions and frequency characteristics of the synchronous machine along the two axes.

Let us consider an experiment in transient conditions, along axis  $d$ , corresponding to the electric diagram in Fig. 3.7. Assume that the attenuation functions of stator currents recorded during the experiment converges asymptotically toward zero. This means that if the shortcircuiting resistance of contact  $K$  is non-zero ( $R_s \neq 0$ ) and there is a non-zero steady state current,  $I_{\infty}$ , the function that is sought can be obtained by extracting this DC component from the record of the longitudinal current.

Applying a voltage unit step to the stator circuit with the equivalent resistance  $r$ , and considering per-unit values, for the initial moment, the current is:

$$i_0 = \frac{1}{r} \quad (3.143)$$

Closing the contact  $K$ , i.e. shortcircuiting the stator circuit, means that the voltage applied to circuit terminals becomes zero. That can be physically accomplished by applying, immediately before closing  $K$ , an additional continuous unit voltage in the reverse direction, i.e.  $-1$ , which will cause a supplemental current in the stator, with the operational expression:

$$-\frac{1}{r + px(p)} \quad (3.144)$$

Therefore, the operational representation of the DC current function decayed in the stator can be written as:

$$i(p) = \frac{1}{r} - \frac{1}{r + px(p)}. \quad (3.145)$$

This relation is generic for making the connection with the frequency characteristics for all current decays with corresponding connection diagrams indicated in section 3.2.1. What varies between different connections is the equivalent resistance. To be able to use a similar relation, a connection factor  $K_{con}$ , has been introduced in the current norms, and the substitutions

$r \rightarrow r_1 / K_{con}$  and  $x(p) \rightarrow x(p) / K_{con}$  were performed in the preceding expression.

Considering the phase resistance,  $r_1$  (p.u.), for a decay test using only one phase, a case rarely encountered in practice,  $K_{con} = 1$ , since the resulting magnetic field in the machine is relatively weak. Considering the diagram in Fig. 3.7, where, to establish the resulting longitudinal field in the machine all phases have been used,  $K_{con} = 2/3$ , and, if only two phases in series are used,  $K_{con} = 1/2$ .

Generally, in practice, a synchronous machine can have more equivalent damper circuits and thus, the time function of the transient current, in p.u., is represented as a sum of several exponentials:

$$i(t) = i_1 e^{-\lambda_1 t} + i_2 e^{-\lambda_2 t} + \dots + i_n e^{-\lambda_n t}. \quad (3.146)$$

The operational representation of this current is:

$$i(p) = i_1 \frac{p}{p + \lambda_1} + i_2 \frac{p}{p + \lambda_2} + \dots + i_n \frac{p}{p + \lambda_n}. \quad (3.147)$$

Considering that for the initial moment the current is  $i_0$ , the relation between this value and currents – coefficients of exponential components follows as

$$i_0 = i_1 + i_2 + \dots + i_n. \quad (3.148)$$

Differentiating with respect to time, the original function becomes:

$$\frac{di(t)}{dt} = -i_1\lambda_1 e^{-\lambda_1 t} - i_2\lambda_2 e^{-\lambda_2 t} - \dots - i_n\lambda_n e^{-\lambda_n t} \quad (3.149)$$

with its operational representation:

$$-\frac{p}{r + p x(p)} = -i_1\lambda_1 \frac{p}{p + \lambda_1} - i_2\lambda_2 \frac{p}{p + \lambda_2} - \dots - i_n\lambda_n \frac{p}{p + \lambda_n}. \quad (3.150)$$

As previously shown, the transition from operational expressions to the complex (harmonic) reactances is done using the substitution  $p \rightarrow js$ , yielding

$$\frac{js}{r + jsx(js)} = i_1\lambda_1 \frac{js}{js + \lambda_1} + i_2\lambda_2 \frac{js}{js + \lambda_2} + \dots \quad (3.151)$$

To obtain the complex (harmonic) reactance, which inverted, gives the frequency characteristics, the previous expression can be written in a general form as:

$$\frac{js}{r + jsx(js)} = i_1\lambda_1 \frac{js}{js + \lambda_1} + i_2\lambda_2 \frac{js}{js + \lambda_2} + \dots = a + jb. \quad (3.152)$$

Leading to the coefficients of the complex form as:

$$a = s^2 \left[ \frac{i_1\lambda_1}{s^2 + \lambda_1^2} + \frac{i_2\lambda_2}{s^2 + \lambda_2^2} + \dots \right]; \quad b = s \left[ \frac{i_1\lambda_1^2}{s^2 + \lambda_1^2} + \frac{i_2\lambda_2^2}{s^2 + \lambda_2^2} + \dots \right]. \quad (3.153)$$

Finally, the complex reactance expression becomes:

$$x(js) = \frac{j - \frac{r}{s}(a + jb)}{j(a + jb)} \quad (3.154)$$

and from that first inverse transform, the frequency characteristics relation:

$$\frac{1}{x(js)} = \frac{j(a + jb)}{j - \frac{r}{s}(a + jb)}. \quad (3.155)$$

This is the general connection relation, through which frequency characteristics from rotor standstill DC decay tests can be obtained.

Parameters for multiple rotor cage synchronous machine can be obtained through frequency characteristics.

### Procedure for the determination of frequency characteristics through DC current decay tests

In the generic case of multiple cages, consisting of the main cage and certain massive rotor parts, in stator current decay tests, the transient function of this current has more exponential components than the usual  $d-q$  model:

$$i(t) = i_1 e^{-\lambda_1 t} + i_2 e^{-\lambda_2 t} + \dots + i_k e^{-\lambda_k t} + \dots + i_{n+1} e^{-\lambda_{n+1} t} \quad (3.146')$$

which is similar to 3.146, but has  $n+1$  terms.

Next follows a presentation of the parameter determination and the definition of main values in this case, according to international standards [65]. Due to the relative novelty of the methodology, the respective part of the norms is defined as representing norms still pending confirmation.

This presentation is supplemented with experimental data, obtained by the authors for large machines in operation, comments and conclusions regarding the mode of application of the procedure, and experimental data processing.

First, the following observations should be made regarding relation (3.146'), very important from a practical point of view:

- [1] At testing time, the number of exponential components in (3.146') for a real machine is unknown, with only the decay currents recordings known, as a series of values  $i(t)$ ;
- [2] The challenge is in determining constants as accurately as possible from the analytical representation of experimental records, and of the components of currents  $i_k$  and attenuation factors  $\lambda_k$ , with dimension in inverse time constants;
- [3] Even when employing accurate measuring devices, random errors may appear, due to the structure of the sought expression, which may lead to significant and uncontrollable errors in the final results, thus rendering them inconclusive;
- [4] The separation of exponential components in the previous expression is relatively simple and sufficiently accurate for the case when time constants (attenuation factors, respectively) differ by about an order of magnitude between two successive components, which cannot be confirmed in all concrete cases;
- [5] Since recordings can currently be made at low sampling rates, thus with large data volume, to solve the aforementioned problems, employing statistical mathematical data processing is necessary. These methods are not stated in the standards still pending confirmation we previously mentioned. In the purpose to separate the exponential components of current recordings a statistical mathematical method with a dedicated software named DISCRETE [48], will be presented in the next paragraph.

Frequency response characteristics can be defined, in concordance with [65], as time functions of the recorded currents from standstill current decay tests (along the two axes  $d, q$ ) as:

$$\frac{1}{x(j\omega)} = -\frac{1}{r_1} \frac{\int_0^{\infty} \left[ \frac{d}{dt} i(t) \right] e^{-j\omega t} dt}{\int_0^{\infty} i(t) e^{-j\omega t} dt} \quad (3.156)$$

where:  $i(t)$  - p.u. current (or the difference between this current and its remanent value for long time intervals), relative to the initial value  $I_0$ ;

$r_1'$  - equivalent armature winding resistance

$$r_1' = r_1 + K_{con} \Delta r \quad (3.157)$$

$r_1$  - stator phase winding resistance;

$K_{con}$  - connection factor with previously indicated values;

$\Delta r$  - resistance external to stator windings – connection cables and transducers.

All values are p.u. values.

The frequency response characteristics along the two axes,  $\frac{1}{x_d(j\omega)}$  and  $\frac{1}{x_q(j\omega)}$  can be represented using characteristic roots of equations of type  $D_d(p) = 0$ ;  $D_d'(p) = 0$ ;  $D_q(p) = 0$ ;  $D_q'(p) = 0$ , as:

$$\begin{aligned} \frac{1}{x_d(j\omega)} &= \frac{1}{x_d''} \frac{D_d(j\omega)}{D_d'(j\omega)} = \frac{1}{x_d''} \frac{(\alpha_{1d} + j\omega)(\alpha_{2d} + j\omega) \dots (\alpha_{nd} + j\omega)}{(\alpha'_{1d} + j\omega)(\alpha'_{2d} + j\omega) \dots (\alpha'_{nd} + j\omega)}; \\ \frac{1}{x_q(j\omega)} &= \frac{1}{x_q''} \frac{D_q(j\omega)}{D_q'(j\omega)} = \frac{1}{x_q''} \frac{(\alpha_{1q} + j\omega)(\alpha_{2q} + j\omega) \dots (\alpha_{nq} + j\omega)}{(\alpha'_{1q} + j\omega)(\alpha'_{2q} + j\omega) \dots (\alpha'_{nq} + j\omega)}; \quad (3.158) \\ G(j\omega) &= N \frac{A(j\omega)}{D_d(j\omega)} = N \frac{(\gamma_1 + j\omega)(\gamma_2 + j\omega) \dots (\gamma_{n-1} + j\omega)}{(\alpha_{1d} + j\omega)(\alpha_{2d} + j\omega) \dots (\alpha_{nd} + j\omega)} \end{aligned}$$

It is very important from the practical point of view of data processing that the roots of the characteristic equations of type  $D_d(p) = 0$ ,  $D_d'(p) = 0$ ,  $D_q(p) = 0$ ,  $D_q'(p) = 0$  can be determined using the amplitudes  $i_k$  and the decrement  $\lambda_k$  of the exponential components of the current decay curves.

Thus roots of the type  $-\alpha_1, -\alpha_2, \dots, -\alpha_n$  of the characteristic equation  $D(p) = 0$ , can be determined as roots of the equation:

$$\sum_{k=1}^{n+1} \frac{i_k \lambda_k}{p + \lambda_k} = 0 \quad (3.159)$$

Similarly, roots of the type  $-\alpha'_1, -\alpha'_2, \dots, -\alpha'_n$  of the characteristic equation  $D'(p) = 0$  can be determined as roots of the equation:

$$\sum_{k=1}^{n+1} \frac{i_k}{p + \lambda_k} = 0 \quad (3.160)$$

For both types of roots that can be determined from equations (3.159) and (3.160), parameters along the two axes,  $d$  and  $q$ , are obtained using recordings corresponding to those two axes.

The decrement for each exponential component represents the inverse of the time constant for the respective component, in per-unit.

Using roots  $-\alpha'_k$  and  $-\alpha_k$  of the characteristic equations obtained through experiments, another form for the frequency characteristics results is obtained, with a separation of the real and imaginary part:

$$\frac{1}{x_d(j\omega)} = \frac{1}{x_d} + \sum_{k=1}^n \left[ \frac{C_{kd}}{1 + \left(\frac{\alpha'_{kd}}{s}\right)^2} + \frac{C_{kd} \frac{\alpha'_{kd}}{s}}{1 + \left(\frac{\alpha'_{kd}}{s}\right)^2} \right]; \quad (3.161)$$

$$\frac{1}{x_q(j\omega)} = \frac{1}{x_q} + \sum_{l=1}^m \left[ \frac{C_{lq}}{1 + \left(\frac{\alpha'_{lq}}{s}\right)^2} + \frac{C_{lq} \frac{\alpha'_{lq}}{s}}{1 + \left(\frac{\alpha'_{lq}}{s}\right)^2} \right]$$

where the coefficients of type C along the two axes are:

$$C_{kd} = -\frac{1}{x_d^n} \frac{(\alpha_{1d} - \alpha'_{kd})(\alpha_{2d} - \alpha'_{kd}) \dots (\alpha_{nd} - \alpha'_{kd})}{(\alpha_{1d} - \alpha'_{kd}) \dots (\alpha'_{k-1,d} - \alpha'_{kd}) \alpha'_{kd} (\alpha'_{k+1,d} - \alpha'_{kd}) \dots (\alpha'_{nd} - \alpha'_{kd})};$$

$$C_{lq} = -\frac{1}{x_q^n} \frac{(\alpha_{1q} - \alpha'_{lq})(\alpha_{2q} - \alpha'_{lq}) \dots (\alpha_{mq} - \alpha'_{lq})}{x_q^n (\alpha_{1q} - \alpha'_{lq}) \dots (\alpha'_{l-1,q} - \alpha'_{lq}) \alpha'_{lq} (\alpha'_{l+1,q} - \alpha'_{lq}) \dots (\alpha'_{mq} - \alpha'_{lq})}.$$

(3.162)

Finally, using the identified exponential components, the synchronous reactances of the tested machine result from the current decay along the two axes, as:

$$x_d = r \sum_{l=1}^{n+1} \frac{i_{kd}}{\lambda_{kd}}; \quad x_q = r \sum_{l=1}^{m+1} \frac{i_{lq}}{\lambda_{lq}} \quad (3.163)$$

and with subtransient reactances as:

$$x_d'' = \frac{r}{\sum_{k=1}^{n+1} i_{kd} \lambda_{kd}}; \quad x_q'' = \frac{r}{\sum_{l=1}^{m+1} i_{lq} \lambda_{lq}}. \quad (3.164)$$

It is mentioned that relations for  $x_{ch}$ ,  $x_q$  in (3.163) can also be obtained from (3.117) and (3.131) by using (3.146').

Retesting is recommended if values of the reactances obtained through the frequency characteristics method computed based on standstill rotor current decay differ by more than 10% from the values of the same quantities obtained through other methods stated in standards.



The transient reactances along the two axes also result from the identification of current decay exponential components:

$$x'_d = \frac{1}{\frac{1}{x_d} + C_{1d}} \text{ and } x'_q = \frac{1}{\frac{1}{x_q} + C_{1q}}. \quad (3.165)$$

Based on the frequency characteristics along the two axes, the inverse sequence reactance is found as:

$$x_2 = \text{Im} \left\{ \frac{j}{\frac{1}{2} \left[ \frac{1}{x_d(j)s_{s=2}} + \frac{1}{x_q(j)s_{s=2}} \right]} \right\}. \quad (3.166)$$

Finally, frequency response for a certain slip can be expressed as:

$$Z(js) = \text{Re}[Z(js)] + j \text{Im}[Z(js)] \quad (3.167)$$

where:

$$Z(js) = \frac{r}{s} + j x(js), \quad (3.167')$$

relations used for the two axes  $d, q$ .

It should be noted that the previous relations, based on standstill rotor current decay records, applicable to multiple rotor cages, are not determined by design calculations, but identified exclusively through tests.

Standards suggest grapho-analytical methods for the identification of the number of exponentials and, for each exponential, of constants  $i_k$  and decrement  $\lambda_k$  respectively, which, in some instances, can involve errors.

Statistical numerical processing methods can be employed, as shown in the following examples, for the problem of exponential separation and constants identification.

### Statistical data processing. The DISCRETE processing program

Consider the general expression of the standstill rotor current decay along the axis  $d$  or  $q$ .

$$i(t) = I_1 e^{-\frac{t}{T_1}} + I_2 e^{-\frac{t}{T_2}} + \dots + I_{n+1} e^{-\frac{t}{T_{n+1}}} = \sum_{k=1}^{n+1} I_k e^{-\Lambda_k t}. \quad (3.146'')$$

In the current form, the expression is considered in physical units,  $I_K [A]$ ,  $T_K [s]$  and  $\Lambda_K [s^{-1}]$ , but it can be also used in relative units (p.u.).

The principle of methods indicated in standards is based, in most cases, on the fact that the time constant  $T_1$ , for example, is approximatively one order of magnitude greater than  $T_2$ . In turn, constant  $T_2$  is also greater by approximately one order of magnitude than  $T_3$ , a.s.o.

Therefore, quantitatively, for a sufficiently long time, the first component is the most important.

In other words, the longer the time (toward the end of the process), the more accurate the approximation:

$$i(t) \cong I_1 e^{-\frac{t}{T_1}}. \quad (3.168)$$

This means that, by applying the logarithm to the recorded current values for a sufficiently long period of time, the first component can be separated with sufficient accuracy, i.e. components  $T_1$  and  $I_1$  can be determined. Further, from the initial record, the first component can be extracted, resulting in the difference:

$$i'(t) = I_2 e^{-\frac{t}{T_2}} + I_3 e^{-\frac{t}{T_3}} + \dots \quad (3.169)$$

If  $T_2 \gg T_3$  the process can be repeated and all components can be determined.

If the difference between two successive time constants is not large enough, the accuracy of this method of exponential separation is lacking.

Even if two successive constants differ significantly, but the record is affected by random errors, applying the logarithm leads to large errors. Using modern equipment, the ordinate is usually affected, since time is measured with sufficient accuracy. Therefore, for data processing in such situations a regressive statistical process along the ordinates of the experimental function is necessary.

To solve these types of problems, the program DISCRETE [48] has been used. The program DISCRETE is a program for automatic analysis of exponential multicomponent negative exponent data. Next, some of the most important features of the program are stated below:

- \* Previous evaluations of the number of components  $n+1$ , or of the constants  $I_K$  and  $\Lambda_K$ , are not required;
- \* Required input data is only the experimental function, i.e. table of values of type  $(i_m, t_m)$ ;  $m=1 \dots M$  where  $M$  is the number of process value pairs recorded;
- \* The program can separate exponentials from a transient situation that has a maximum of 9 exponential components,  $n+1 \leq 9$ ;
- \* It allows the visualization of results from the preliminary data analysis;
- \* It can be used with a limited, operator selected, number of computation iterations;

- \* It displays, at the end, the sought-after values, i.e.  $n+1$  - number of exponential components,  $I_K$  and the decrement  $\Lambda_K$  of each component;
- \* The final results are presented as several complete sets of results, sorted in order of increasing probability for the best possible solutions; also, as part of the final results, other significant values for statistic calculations, such as the number of singularities (located, as a rule, immediately after start of the process), that do not fit in the analytical expression of the respective solution, are displayed.

Program limitations, such as the one related to the number of exponentials, satisfy the requirements of the applications of electrical machines in standstill rotor current decay tests.

The program DISCRETE [48], used to obtain the experimental results presented in the following section, has been donated by the Max Plank Institute – Gottingen to Testing electrical machines laboratory D109, of the Electrical and Power Engineering Faculty Timisoara, for research.

### Experimental results

Tests of standstill rotor current decay along the two axes  $d$  and  $q$ , have been done using electric diagrams in Fig.3.7.a and Fig.3.7.b. The tested synchronous machine was a hydrogenerator from hydropower plant “*TurnuRuieni*” Romania, with the following rated parameters:

- \* active power  $P = 76.5$  MW ;
- \* rated voltage  $U_n = 10.5$  kV ;
- \* connection YY ;
- \* power factor  $\cos\varphi = 0.9$  ;
- \* rated speed  $n_n = 428.6$  r.p.m. ;
- \* rated efficiency  $\eta_n = 98.1$  % ;
- \* rated frequency  $f_n = 50$  Hz ;
- \* rated field current  $I_{nf} = 822$  A ;
- \* rated field voltage  $U_{nf} = 290$  V .

Other significant data for this synchronous machine are:

- a) base impedance used in p.u.  $Z_b = 1.2967 \Omega$  ;
- b) equivalent phase resistance  $R_1 = 0.0045 \Omega$  , including equipment feeders.

The Data Acquisition System SAD in Fig.3.7 was National Instruments, with an acquisition board type NIDAQ-PCIMIO-16E-4.

Hall effect based transducers type LEM-500A served as current transducers in the signal acquisition module MAS. A high current welding generator, providing (300-500) A, has been used as DC source for the stator winding.

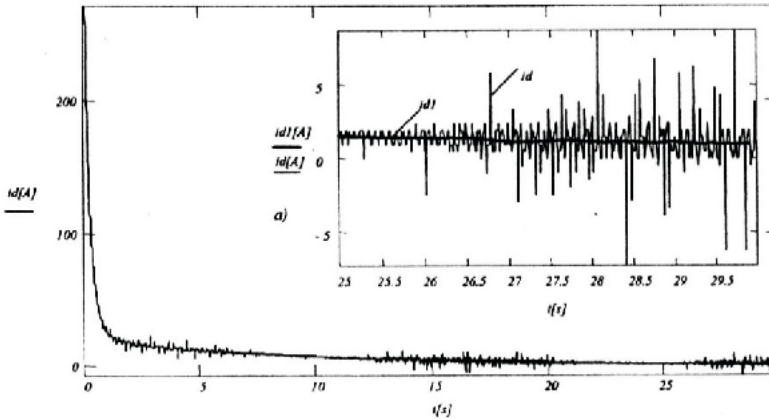


Fig.3.16 Complete record of transient current in decay test of current along the longitudinal axis for the 76.5 MW synchronous machine; a) - Detail of final recording range;  $i_{d1}$  - filtered time function of the recording of longitudinal current  $i_d$ .

Complete records along  $d$  axis, with short-circuited field winding for the referenced machine, have been performed using approximately 3500-4000 points (pairs of values  $i_d$ ;  $i$ ) to make sure that process decay occurred.

That means that for repeated time values in the final portion of the recording, no significant current variations appear. Thus, the orientation value of the real process decay time is based on simplified pre-measurements that do not require a very granular current sampling.

To process the records, with the exception of the final part of the process, sampling shall occur with a minimally achievable interval. Fig. 3.16 shows the synthesis of a sufficiently large set of data. For a better illustration of the process, Fig.3.17 shows the first part of the recording along  $d$  axis, shown in Fig.3.16.

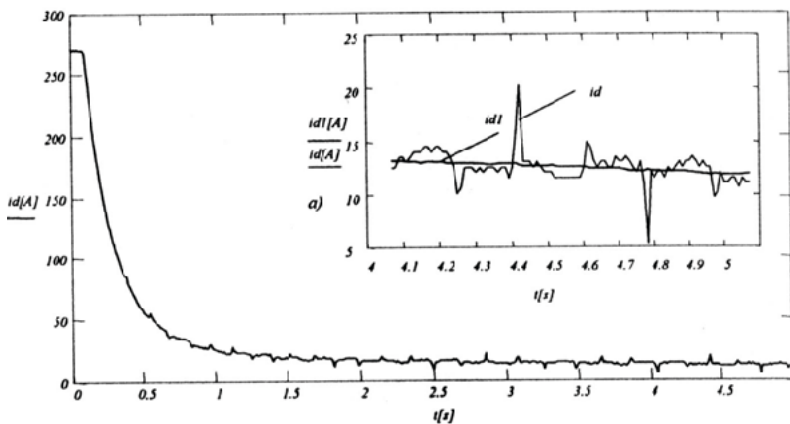


Fig.3.17 Detail of the initial part of the longitudinal current  $i_d$ , with  $i_{d1}$  filtered time function, for the 76.5 MW machine.

Several records of the current along the same axis have been done to allow the comparison of results obtained along the respective axis.

Similarly, several records have been done along  $q$  axis.

As an example, Fig. 3.18 shows a significant record of the transient transversal current for the same machine.

The initial values  $I_0$  and residual values  $I_s$  for a very long time, thus a steady state process, obtained experimentally, were:

$$I_{d0} = 272.58 \text{ A} ; I_{ds} = 1.119 \text{ A}$$

$$I_{q0} = 268.58 \text{ A} ; I_{qs} = 0.78 \text{ A}.$$

These initial values have been selected to obtain non-saturated parameters.

The previously indicated values represent the computed values, obtained from the DC current provided by the source prior to the start of the transient process. From this, residual values have been extracted, which, in this case, were very small. These initial (computed) values represent the base for the p.u. values of the currents.

We start with the assumption that the number of exponentials that have to be separated in the transient processes is not known, and then apply the previously shown processing method, based on frequency characteristics [7].

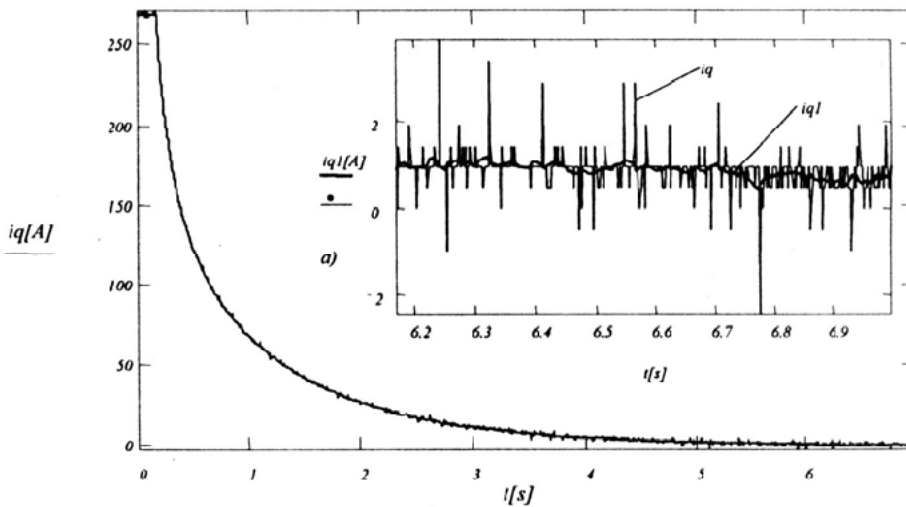


Fig.3.18 Record of the transient current along  $q$  axis; a)  $i_{q1}$  - detail of filtered time function for the 76.5 MW synchronous machine.

The results of component separation, physical and relative units (p.u.), using the program DISCRETE [48] for the separation of exponential components for the recording of the longitudinal current in Fig.3.16 are shown in the following table.

Table 3.1 Main results from separation of the transient current decay along the longitudinal axis.

Number of exponential components: $n + 1 = 3$				
$I_j$ [A]	$i_j$ [ p.u.]	$\Lambda_j$ [s <sup>-1</sup> ]	$\lambda_j$ [p.u.]	$T_j$ [s]
20.58000	0.07634	0.10720	0.00034	9.32800
91.40000	0.33904	2.86600	0.00912	0.34890
164.9000	0.61168	6.48800	0.02065	0.15410

In this table,  $I_j$  and  $i_j$  represent the initial values of the exponential components; the coefficient of component  $\Lambda_j$  the decrement, and the time constant  $T_j$  corresponding to an expression of type (3.146').

The same identification type for the exponential components has been used for transversal axis records.

One aspect that significantly influences the accuracy of the results is the „electromagnetic noise” characterized by the presence of random errors, as well as the pinpointing, under these conditions, of the initial point from which the transient starts (i.e. the pair of values  $t = 0$  and  $I_0$ ).

In most cases of large machines, where the current decay method is extremely advantageous, a DC source which provides large current values is required. A good choice is a DC machine, however with the disadvantage of the commutator influence, or a controlled rectifier.

In the example shown, the source consisted of a welding generator, which introduced noise in the recordings.

Fig. 3.19 presents the record detail of a significant decay process along the transversal axis  $i_q(t)$ . The detail shows values before and after starting the transient process.

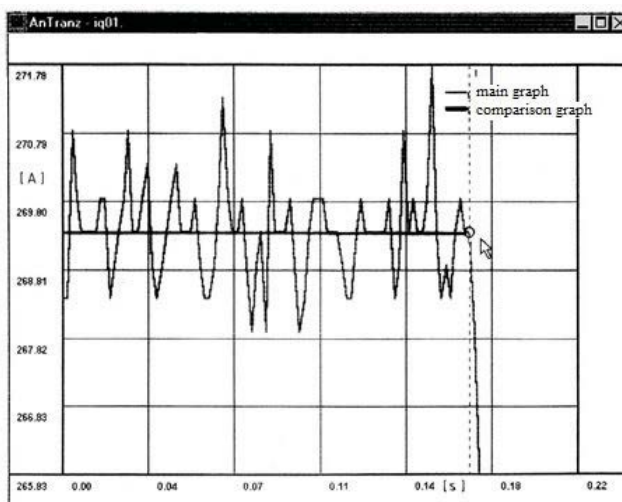


Fig.3.19 Selection of the point marking the beginning of the transient process for the current along the transversal axis  $i_q(t)$  for the 76.5 MW synchronous machine.

The influence of the noise introduced by the collector in the part prior to the start of the process can be observed. To obtain the starting point, before using the DISCRETE program, a relatively simple numerical pre-filtering is necessary. It has been determined that an improper selection of this point affects the accuracy of the subtransient reactance determination.

The same machine has been subjected to complete established standard tests; the results of the complete test set are summarized in the following table.

Table 3.2 Main parameters resulting from tests of the 76.5 MW synchronous hydro-generator.

Parameter	Symbol	Resulting values [p.u.]		
		Standstill current decay tests	Established standard methods	Project
Longitudinal synchronous reactance	$X_d$	1.0082	0.907	$0.98 \div 1.18$
Longitudinal subtransient reactance	$X''_d$	0.2203	0.227	0.19
Longitudinal transient reactance	$X'_d$	0.2807	0.305	0.22
Transversal synchronous reactance	$X_q$	0.7236	0.705	0.78–0.8
Transversal subtransient reactance	$X''_q$	0.2324	0.189	0.203
Zero sequence reactance	$X_0$	0.0661	0.053	0.058
Negative sequence reactance	$X_2$	0.2302	0.208	0.191
Field circuit reactance	$X_f$	1.1755	1.076	1.1

In conclusion, in the situation where we assume that the tested machine shows damper circuits, the mathematical separation of the exponentials has to occur using statistical methods.

In this sense, the DISCRETE program presents a good solution for solving this problem; being accurate and relatively easy to use.

Since the maximum number of separated process exponentials, affected by random errors, is 9, this processing mode completely fits applications for electrical machines.

### 3.4. Experimental Study of Saturation using Rotor Pre-magnetization

All parameters of the synchronous machine are, more or less, influenced by the saturation of the magnetic circuit.

The technical literature, as well as design calculations, includes few references to the influence of the saturation upon parameters – in some cases those references deal with the value of saturation as compared to the non-saturation value of a parameter. We

consider the saturated value of the particular parameter as the value obtained from higher magnetic strain of the magnetic circuit, rather than ones for the knee point of the magnetization curve of the machine.

As previously shown, parameters can be considered as **continuous functions** of the saturation level of the respective magnetic circuits. Disregarding this aspect leads to discrepancies between theoretical and experimental results with regard to parameters.

Considering parameters as saturation dependent causes difficulties in solving equations corresponding to certain conditions. Even constant quantities from the parameter structure in phase coordinates (as functions of the position angle  $\gamma$  – paragraph 3.2) have to be considered as functions of saturation. Besides mathematical difficulties in solving equations, under these conditions, the saturation functions of equivalent parameters need to be determined, either by calculations or experimentally.

In the determination of the saturated values of the parameters through field methods one also encounters difficulties due to lack of knowledge on the impact of technology. Such aspects (mechanical clearances, gaps, alteration of mechanical properties due to processing, etc.) may significantly influence the results.

Therefore, one should consider that results regarding saturation, gained through experiments, can, on one hand, have a positive effect on the improvement of the design, and on the other, allow for better modelling of conditions that imply saturation.

Next, a method for experimental determination of certain parameters of the synchronous machine, as continuous functions of the saturation level of the considered magnetic circuits [4], is presented. This method is based on the standstill rotor transients described in the previous section. Experimental results are given at the end of the presentation.

A type of a longitudinal transient, by which saturation is provided simultaneously by the stator and field circuit, is shown in Fig. 3.20.

The resistances  $R_r$  and  $R_{rf}$  protect the sources  $E$  and  $E_f$  during the transient process. Pre-magnetization through the field circuit is provided by the current  $i_f$  of the source  $E_f$ . In the initial phase, the switches  $k_1$  and  $k_3$  are open, while  $k_2$  and  $k_4$  are closed. The DC current  $I_{\infty}$  flows in the stator and the DC current  $I_0$  flows in the rotor.

The transient process is triggered by closing  $k_1$  and opening  $k_2$ . The transient currents are shown as curves in Fig. 3.20.b.

The phase currents are:

$$i_b = i_c = -\frac{i_a}{2}, \tag{3.170}$$

the currents in coordinates  $d, q$  result for  $\gamma=0$  from (3.32) as:

$$i_d = i_a ; \quad i_q = 0. \tag{3.171}$$



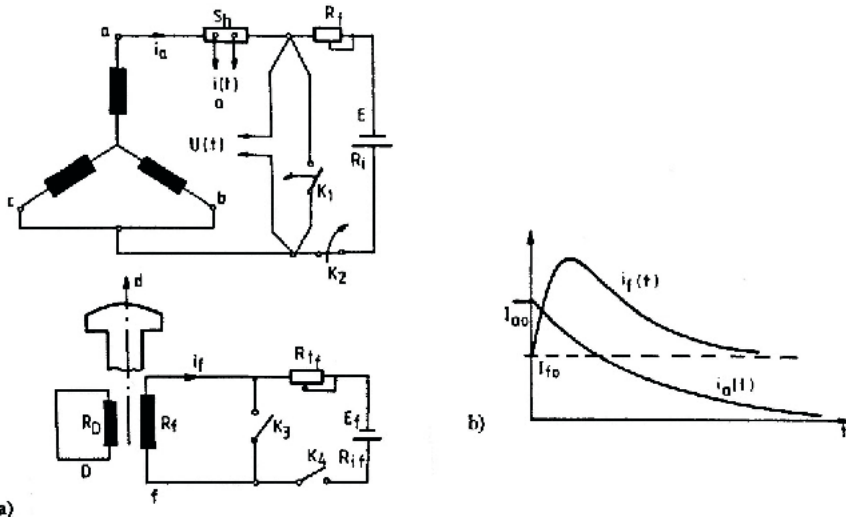


Fig. 3.20 Longitudinal transient with saturation influence: a) test circuits; b) current-time variation curves.

The fluxes, for the peculiar case considered, follow, using relation (3.36), as

$$\Psi_d = \Psi_a, \quad \Psi_q = 0, \quad \Psi_b = -\frac{\Psi_d}{2}. \quad (3.172)$$

The equation of the stator circuit voltage is obtained from the Park equations (3.51)

$$0 = R_1 i_d + \frac{d\Psi_d}{dt}. \quad (3.173)$$

And through integration,

$$0 = \int_0^{\infty} i_d(t) dt + \Psi_{d\infty} - \Psi_{d0}, \quad (3.174)$$

where  $\Psi_{d0}$  is the total longitudinal flux through the machine at time  $t=0$ , while  $\Psi_{d\infty}$  - the total longitudinal flux through the machine at time  $t \rightarrow \infty$ .

One can express the two values of the total longitudinal flux, at the beginning of the transient process, and after a very long period of time, respectively, as:

$$\begin{aligned} \Psi_{d0} &= \Psi_{dr0} + \Psi_{ds0} \\ \Psi_{d\infty} &= \Psi_{dr\infty} = \Psi_{dr0}, \end{aligned} \quad (3.175)$$

where  $\Psi_{dr0}$  represents the component along axis  $d$  due to the rotor winding, and  $\Psi_{ds0}$  the component due to stator winding; both components of the longitudinal flux considered at the initial moment.

$\Psi_{dr\infty}$  is the longitudinal flux component due to the rotor winding at  $t \rightarrow \infty$ .

The second equation in (3.175) shows that the flux caused by the rotor winding is the same at the beginning and end of the transient, caused by the constant current  $I_0$ .

The longitudinal inductivity is:

$$L_d = \frac{\Psi_{ds0}}{I_{d0}}, \quad (3.176)$$

where the initial longitudinal current  $I_{d0}$  is equal to the phase  $a$  current at the initial time  $t_{d0}$ . From (3.174) and (3.175) it follows that:

$$\Psi_{ds0} = R_1 \int_0^{\infty} i_d(t) dt. \quad (3.177)$$

Thus, using per-unit expression, (3.176) and (3.177) yield the known relation for the longitudinal synchronous reactance, as in (3.117):

$$x_d = \frac{r_1 \omega_n}{I_{d0}} \int_0^{\infty} i_d(t) dt \quad [\text{p.u.}]$$

where  $r_1$  is the resistance of the stator phase, in per-unit units, and  $\omega_n$  the nominal pulsation.

The following aspect should be noted:  $L_d$  is calculated using the flux given by the stator winding at the initial moment  $\Psi_{ds0}$ , but only after a pre-magnetization due to the longitudinal component of the rotor flux  $\Psi_{dr0}$ .

The resulting flux varies during the analyzed transient, from  $\Psi_{ds0} + \Psi_{dr0}$  to  $\Psi_{ds0}$ . The value of the longitudinal synchronous reactance is definitely influenced by the saturation level given by the total longitudinal flux  $\Psi_{d\text{tot}} = \Psi_{ds0} + \Psi_{dr0}$ . As such, the determination of reactance  $x_d$  as a function of the total longitudinal flux, is sought.

To find the total flux, the determination of the rotor component  $\Psi_{dr0}$  is necessary; this is accomplished through another experiment. The same connection diagram as the one shown in Fig. 3.20.a is used, but a field decay in the rotor is triggered, with open stator winding. The switches  $k_1$ ,  $k_2$  and  $k_3$  are open and  $k_4$  is closed. The transient to determine  $\Psi_{dr0}$  is triggered by closing  $k_3$  and opening  $k_4$ . The stator voltage is recorded. The relation between voltage and flux is:

$$u(t) = -\frac{d(\Psi_a - \Psi_b)}{dt} = -\frac{3}{2} \frac{d\Psi_{dr}}{dt}. \quad (3.178)$$

The flux created by the rotor at the initial moment results through voltage signal integration

$$\Psi_{dr0} = \frac{2}{3} \int_0^{\infty} u(t) dt, \quad (3.179)$$

since the final rotor flux under these conditions is zero.

It should be noted that in the second experiment the initial current  $I_{f0}$  has to be the same as the one in the prior experiment.

Thus, the reactance  $x_d$  has been determined for a known total flux. The measurements have to be repeated for larger and larger values of currents  $I_{f0}$  and  $I_{b0}$ , leading to a higher and higher saturation level, due to the total flux. Finally, the experimental function for the synchronous longitudinal reactance results as

$$x_d = f(\Psi_{d0}). \quad (3.180)$$

An implementation based on the diagram in Fig. 3.21 is needed for the determination of the synchronous transversal reactance  $x_q$ .

The current for phase  $b$  is recorded, with the particulars of (3.80). After analyzing the transversal transient, the previously known relation for the synchronous transversal reactance (per-unit expression) is obtained, as in (3.131):

$$x_q = \frac{r_1 \omega_n}{I_{b0}} \int_0^\infty i_b(t) dt = \frac{r_1 \omega_n}{I_{q0}} \int_0^\infty i_q(t) dt \quad [\text{p.u.}]. \quad (3.181)$$

The constant current  $I_{f0}$  flows through the rotor winding during the transversal transient considered. Even if a magnetic interaction between the axes  $d$  and  $q$  is not usually considered, it can be shown that the value of the current  $I_{f0}$ , which indeed gives the saturation level along axis  $d$ , influences the reactance  $x_q$ . Therefore, in the experiment considered, we simultaneously increase both the initial value of the stator current  $I_{b0}$ , and the constant rotor current value (pre-magnetization), in the same proportion:

$$k = \frac{I_{b0}}{I_{1n}} = \frac{I_{f0}}{I_{fn}}, \quad (3.182)$$

where  $I_{1n}$  and  $I_{fn}$  represent the nominal values for the stator current and field current, respectively. Finally, the transversal synchronous reactance as an experimental function of the ratio  $k$ , which defines the saturation level of the machine, results as:

$$x_q = f(k). \quad (3.183)$$

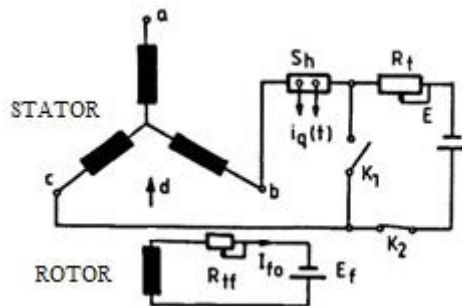


Fig. 3.21. Circuit for transversal transient

### Example of experimental results

The experimental method presented earlier has been applied for a synchronous machine with the following rated data:  $S_{\bar{n}}= 700$  kVA;  $I_{\bar{n}}= 177$  A;  $I_{f\bar{n}}= 89$  A;  $n_{\bar{n}}= 1500$  rpm.

For the longitudinal experiment, several readings have been performed, with a progressive and simultaneous increase of both the pre-magnetization field current  $I_{f0}$  and the initial stator current  $I_{d0}$ . Some significant values are shown in the table below.

Table 3.3 Some experimental results in longitudinal experiment with pre-magnetization.

$I_{d0}$ [A]	$\Psi_{d0}$ [p.u.]	$\Psi_{d10}$ [p.u.]	$\Psi_{d\text{tot}}$ [p.u.]	$I_{f0}$ [p.u.]	$X_d$ [p.u.]
10	0.101	0.298	0.399	0.112	1.280
50	0.229	1.704	1.933	0.564	0.579
100	0.287	4.346	4.633	1.129	0.361

The longitudinal synchronous reactance as a function of the total longitudinal flux is given in Fig.3.22.

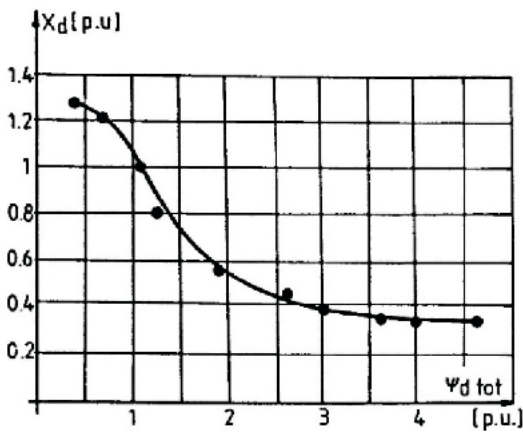


Fig. 3.22 Reactance  $X_d$  as a function of the saturation level of the machine.

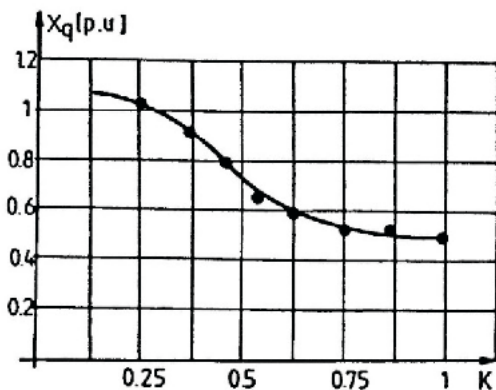


Fig.3.23 The reactance  $X_q$  as a function of the saturation level of the machine.

Figure 3.22 shows the longitudinal synchronous reactance as a function of the total longitudinal flux.

Final results of a series of recordings for the transient previously described are given in Fig. 3.23, where the transversal reactance is shown as a function of the ratio  $k$ , with a simultaneous increase of the stator and rotor current.

Significant variations of the reactances of the machine due to the saturation level can be observed in the final results. These results justify the need to consider machine reactances as functions of the saturation level. Evidently, if other parameters are considered, these too are influenced by saturation.

### 3.5. Conclusions

Finally, conclusions and observations regarding testing technique follow, in the determination methods for parameters of model  $d, q$ , primarily through standstill current decay tests.

In all final form equations that are analyzed, the electromagnetic parameters and currents are reduced and per-unit, i.e. reduction coefficients are included in their values. The identification of the reduction coefficients requires knowledge of certain machine design details.

In integral relations of type (3.89), (3.95), (3.126), (3.128), or in relations that contain derivatives, of type (3.90), (3.96), (3.127), the left hand term shows reduced and p.u. current ratios; the respective reduction and p.u. form coefficients can be simplified in the left hand term - a valid observation for other similar relations.

Thus, the relations are, overall, fundamental relations, and do not depend on reduction and per-unit coefficients.

They can be calculated with real values of recorded currents, which constitute a practical advantage, since not all practical situations allow access to design, details of the synchronous machine. Generally, a dispersion or attenuation coefficient retains its value, is it calculated in real or per unit values.

This particularity of the relations constitutes an essential advantage in measurement and digital results processing.

Regarding particularities and advantages of using current decay methods in parameter determination, vs classical methods, the following should be mentioned:

- \* the practical set up of the installation is very easy;
- no mechanical coupling of tested machine's shaft with another test machine is needed, an essential advantage in case of high power machines or vertical shafts;
- no prior knowledge of design data of the machine is necessary;

- a relatively low number of readings allows for the determination of several machine parameters;
- the energy and manpower necessary during tests is low .

At the same time, two aspects that may influence the accuracy of the results have to be mentioned, as follows:

- Digital record processing is done numerically, and while integration attenuates random errors, digital derivation amplifies them. Therefore, great care shall be taken with the origin derivative calculations, in relations previously presented of type (3.90), (3.103).
- The securing of the rotor in the longitudinal or transversal axis relative to a stator phase has to be checked with the highest accuracy possible, since any deviation leads to errors; otherwise, equations are different from the ones shown and, consequently, results cannot be interpreted.

It should be noted that papers that propose similar standstill rotor current decay tests for any rotor position have been published recently [40, 41]. In those, the mathematical processing is more tedious, but the securing of the rotor along the axes  $d$  or  $q$  for testing is simplified.

### 3.6. References

- [1] B. Adkins, „The General Theory of Electrical Machines”, Chapman-London, 1962.
- [2] I. Boldea, S.A. Nasar, „Electric machine dynamics”, Macmillan Publishing Company, New York 1986.
- [3] I. Boldea, „Parametrii maşinilor electrice”, Editura Academiei Române, Bucureşti, 1991.
- [4] M. Biriescu, G. Liuba, „*Identification of Reactances of Synchronous Machines Including the Saturation Influences*”, *Proceedings of International Conference on the Evolution and Modern Aspects of Synchronous Machines*, Zurich 27-29 aug., 1991.
- [5] M. Biriescu, V. Groza, G. Liuba, I. Mârzoacă, M. Moţ, „Measurement Tasks of a Data Acquisition and Processing System for Electrical Machines Testing”, *Proceedings of 6. Kongressmesse für industrielle Messtechnik 1992*, Wiesbaden. pag. 502-506.
- [6] M. Biriescu, V. Creţu, V. Groza, G. Liuba, I. Mârzoacă, M. Moţ, „Determinierung der Reaktanzenvon Synchroschmaschinen, mit Verwendungeines Systems für Datensammlung - und verarbeitung, 7. Kongressmesse für industrielle Messtechnik 1993, Wiesbaden. pag. 241-246.
- [7] M. Biriescu, G. Liuba, M. Moţ, V. Olărescu, V. Groza, Identification of synchronous machine reactances from direct current decay at standstill test, International Conference on Electrical Machines, Helsinki 2000, Vol. IV, pag. 1914-1916.
- [8] M. Biriescu, M. „Maşini electice rotative. Parametri, caracteristici, încercări”, Editura de Vest, Timişoara, 1997.
- [9] M. Biriescu, V. Creţu, V. Groza, I. Mârzoacă, M. Moţ, I. Şora, „Transient Regime's Recording and Processing of Synchronous Machines Using Data Acquisition and Processing System”, *Proceedings 8, Kongressmesse für industrielle Messtechnik 1994*, Wiesbaden 13-15 sep., 1994.

- [10] M. Biriescu, Determinarea curbei cuplului la motoare de inducție trifazate utilizând un sistem de achiziție și prelucrare a datelor, *Electrotehnica, Electronica, Automatica*, vol. 46, nr. 7-8 iulie-august 1998, pag. 22-27.
- [11] J. J. Blair, "Error Estimates for Frequency Responses Calculated from Time -Constant Measurements", *IEEE Transactions on Instrumentation and Measurement*, vol. 47, pp. 345-353, Apr. 1998.
- [12] I. M. Canay, "A new method of determining  $q$ -axis quantities of synchronous machines", *ETZ A*, vol. 86, 1965, pp 561-568.
- [13] I. M. Canay, "Modelling of Alternating-Current Machines Having Multiple Rotor Circuits", *IEEE Transactions on Energy Conversion*, 8(2), pp. 280-288, June 1993.
- [14] I. M. Canay, "Determination of the Model Parameters of Machines from the Reactance Operators  $x_d(p)$ ,  $x_q(p)$  (Evaluation of Standstill Frequency Response Test)", *IEEE Transactions on Energy Conversion*, vol. 14(4), pp. 1209-1217, 1999
- [15] A. Câmpeanu, „Mașini electrice”, Editura Scrisul Românesc, Craiova, 1988.
- [16] J. Chatelain, et all, "Measurement of the Electromagnetic Torque of Electrical Machines", *Proceedings of International Conference on Electrical Machines*, Boston, 1990.
- [17] J. Chatelain, „Machines électriques”, Presses Polytechniques Romandes, Lausanne, 1989.
- [18] G. Ciucu, V. Craiu, „Introducere în teoria probabilităților și statistică matematică”, Editura Didactică și Pedagogică, București, 1971.
- [19] P. L. Dandeno, et all, "Experience with Standstill Frequency Response (SSFR) Testing and Analysis of Salient Pole Synchronous Machines", *IEEE Transactions on Energy Conversion*, 14(4) pp. 1209-1217, 1999.
- [20] I.R. Danilevici, V.Dombrovski, E. Kazovski, Parametrii mașinilor de current alternativ, Editura Tehnică, București, 1968.
- [21] T. Dordea, M. Biriescu, G. Liuba, G. Madescu, M. Moț, „Mașin iElectrice. Parte Complementară”, Editura Orizonturi Universitare Timișoara, 2013.
- [22] T. Dordea, „Mașini electrice”, Editura Didactică și Pedagogică București, 1970.
- [23] O. Drăgănescu, „Încercările mașinilor electrice rotative”, Editura Tehnică, București, 1987.
- [24] K. Fork, „Meßtechnische Grundlagen zur Berechnung von Ausgleichsvorgängen der Synchronmaschine”, *ETZ-A*, 1967, No. 3.
- [25] S. Gheorghiu, A. Fransua, „Tratat de mașini electrice”, Editura Academiei, București, 1972.
- [26] V. Groza, M. Biriescu, V. Crețu, I. Mârzoca, M. Moț, „PC Based Data Acquisition and Processing System for Power Electric Applications”, *6. Kongresmesse fur industrielle Mestechnik 1992*, Wiesbaden, pag.496-501.
- [27] V. Groza, M. Biriescu, G. Liuba, "Measurement of reactance of synchronous machines at standstill", *IEEE International Electrical Machines and Drives Conference*, Seattle may 1999, pag171-173.
- [28] V. Groza, M. Biriescu, V. Crețu, I. Șora, M. Moț, "Testing of electrical Machines in periodical and quasi-periodical conditions, using a data acquisition and procesing system", *Proceedings of 1998 IEEE Instrumentation and Measurement Technology Conference 68CH3622*, St.Paul, Minnesota, pag. 766-769.

- [29] V. Groza, M. Biriescu, G. Liuba, V. Crețu, "Experimental Determination of Synchronous Machines Reactances from DC Decay at Standstill", *IEEE Instrumentation and Measurement Technology Conference*, Budapest Hungary, May 21-23 2001, pag. 1954-1957.
- [30] G. K. Jerve, „Încercările mașinilor electrice rotative”, Editura Tehnică, București, 1972.
- [31] J. V. Jones, „The Unified Theory of Electrical Machines”, Butterworths, London, 1967.
- [32] A. Kezhani, S. I. Moon, A. Tumageanian, T. Leksan, "Maximum likelihood estimation of synchronous machine parameters from flux decay data", *Proceedings of International Conference on Electrical Machines*, Manchester 1992.
- [33] E. Kononenko, K. Sipailov, K. Horkov, „Electriceskie mașini spetialnïikurs”, Moskva, 1975.
- [34] M. Kostenko, L.M. Piotrovsky, „Electrical Machines”, Mir Publisher. Moskwa, 1974.
- [35] K. P. Kovacs, „Analiza regimurilor tranzitorii ale mașinilor electrice”, Editura Tehnică, București, 1980.
- [36] P. C. Krause, O. Wasznczus, S. D. Sudhoff, „Analysis of electric machinery”, IEEE Press.1994.
- [37] T. Laible, „Teoriã sinhronnoi mașiny pri perehodnyh procesah (Theory of synchronous machine in transient conditions)”, Moskva, Gosenergoizdat, 1957.
- [38] G. Liuba, M. Biriescu, G. Madescu, M. Moț, V. Groza, "Asynchronous performances of large synchronous motors from direct current decay at standstill tests, *Proceedings of the 7-th International Conference on Optimisation of Electrical and Electronic Equipment*, Brașov, may 11-12, 2000, pag. 449-452
- [39] Mc Cracken, D.D., Dorn, W.S., "Numerical Analysis and FORTRAN Programming", New York, John W. 1964.
- [40] F. Maurer, M.T. Xuan, J.J. Simond, "Two Full Parameter Identification Methods for Synchronous Machine Applying DC-Decay Tests for a Rotor in Arbitrary Position", *IEEE Transactions on Industry Applications*, 53(4), pp. 3505-3518, 2017.
- [41] F. Maurer, M.T. Xuan, J.J. Simond, "Two novel methods for parameter identification of synchronous machine using DC-decay test with rotor in arbitrary position", *Proceedings - 2016 22nd International Conference on Electrical Machines*, ICEM 2016, pp. 633-639.
- [42] A. D. Myskis, „Advanced Mathematics for Engineers Special courses”, Mir Publishers Moskwa, 1975.
- [43] G.C. Newton, L. A. Goult, „Analitical Design of Linear Feedback Controls”, New York, John Wiley & Sons, 1957.
- [44] V. Ostovic, „Computer aided Analysis of Electrical Machines”, Prentice Hall, New York 1994.
- [45] K. Pavlúc, Méthodestatique de mesure des constantes de temps et des réactances d'une machine synchrone, *Rev. gen. de l'Électricite* 71 (1962) H. 6, S. 303.
- [46] K. Pavlúc, K. Bednarek, „Puska sinhron nyirezim sinhron nogodvi gatelã (Start and asynchronous conditions of synchronous motor)”, Moskva, 1971.
- [47] B. R. Prentice, "Fundamental Concepts of Synchronous Machine Reactances", AIEE- Supplement to 1937 Tranzaction.
- [48] S. W. Provencher, „DISCRETE-a program for the automatic analysis of multicomponent exponential data”, Max-Planck Institut fur biophysicalische Chemie, 1990, Gottingen, Germany.
- [49] C. Ritter, „Bestimmung der Parameter einen Synchronn-maschine mit Hilfe von Gleichspannungs-versuchenim Stillstand, etzArchiv Bd. 8, (1986) H6, pag. 189-194.



- [50] G. G. Rogozin, „Opređenje elektromagnitnih parametara mašineren nogotoka. Novye eksperimentalnye metody (Determination of electromagnetic parameters of a.c. machines – new experimental methods)”, Tehnika, Kiev – 1992.
- [51] L. Z. Rumsiski, „Prelucrarea matematică a datelor experimentale”, Editura Tehnică, București, 1974.
- [52] A. Rusek, “Error Minimization in Time - Constant Measurements, *IEEE Transactions on Instrumentation and Measurement*, vol. 36, pp. 29-31, March 1987.
- [53] L. Salvatore, M. Savino, “Experimental Determination of Synchronous Machine Parameters”, *IEE Proc. Vol. 128 Pt. B No. 4*, pp 212-218, July 1981.
- [54] R. M. Saunders, “Standstill Frequency-Report Methods and Salient-Pole Synchronous Machines”, *IEEE Transactions on Energy Conversion*, vol 14(4) pp. 1033-1037, 1999.
- [55] Smith, John R., “Response Analysis of A.C. Electrical machines: Computer Models and Simulation”. Research Studies, Press LTD. England. John W., 1990.
- [56] Sokolov, M., “Opređenje ekvivalentnih elektromagnitnih parametara sinhron nihd vigatelei, *Elektrotehnica*, 1-1977.
- [57] Turner, P.J., Reece, A.B.J., D.C. MacDonald, “The d.c. decay tests for determining synchronous machines parameters: measurement and simulation”, *IEEE Transactions on Energy Conversion*, vol. 4, no. 4 December 1989.
- [58] Vas, P., “Parameter Estimation Condition Monitoring and Diagnosis of Electrical Machines”, Clarendon Press, Oxford 1993.
- [59] Worthin, A.G., Geffner, J., “Prelucrarea datelor experimentale (traducere din limba engleză)”. Editura Tehnică, București, 1959.
- [60] Siemens, “Memoratorul inginerului electrician”, Editura Tehnică, București, 1971.
- [61] \* \* \* “Turbo ighidrohgeneratori”, Nauka, Moskva 1974.
- [62] \* \* \* STAS 8211-84, “Mașini sincrone trifazate. Metode de încercare”.
- [63] \* \* \* IEEE Std. 115-1995, IEEE Guide: “Test procedures for Synchronous Machines. Part I. Acceptance and Performance Testing”.
- [64] \* \* \* IEEE Std. 115A-1995, Part II. IEEE, “Test Procedures and Parameter Determination for Dynamic Analysis”.
- [65] \* \* \* BS 4999: Part 104: 1988, British Standard, “General Requirement for rotating electrical machines”. Part 104. Methods of test for determining synchronous machine quantities.

## 4. 1 Operation principles of the single phase shaded pole induction micromotor

The operating principle of the single phase shaded pole induction micromotor is based on the existence of the elliptical rotating magnetic field. If we consider the initial design construction so far, the electric micromotors have maintained the concept of constructive simplicity, but in particular the electric machine designers have created an abundance of types (topologies) with respect to the cross section geometry of the rotor-stator magnetic circuit, which conducts to a rather difficult procedure in order to calculate the different effects of the electromagnetic processes inside the micromotor.

The calculation of the screened micromotor requires the determination of the micromotor equations and then the correct evaluation of the parameters involved in these equations. Lately, some authors, considering the increased volume of computations, are proposing the use of computers to obtain the optimal version. Making prototypes with high performance requires a delicate computing work combining the theoretical experience and experimental research in the test laboratory.

The study of the electromagnetic processes of the single phase shaded pole induction micromotor, considering the influence of higher harmonics, leads to a set of complicated relations for currents and torques equations, whose solving is indicated by the use of personal computers and corresponding mathematical software [30, 41]. For practical purposes, in many instances, the analysis of the electromagnetic processes of the micromotor only takes into account fundamental harmonics, thus simplifying the calculation relations. [2, 10, 13].

## 4. 2 The elliptical rotating magnetic field.

In the shaded pole micromotor, the two windings in the stator produce alternating magnetic fields of different maximum amplitudes  $B_{1m}$  and  $B_{3m}$ , sinusoidal variable in time but shifted with an angle  $\varphi < 90^\circ$ . If there is a phase shift  $\alpha < 90^\circ$  between the two windings, then a rotating magnetic field results, whose amplitude describes an ellipse with an angular velocity that is no longer constant in relation to time (Fig. 1).

$$B_{1x} = B_{1m} \times \cos \frac{x}{\tau} \pi \times \sin \omega t \quad (4.1)$$

or

$$B_{1x} = \frac{B_{1m}}{2} \left[ \sin \left( \omega t - \frac{x}{\tau} \pi \right) + \sin \left( \omega t + \frac{x}{\tau} \pi \right) \right] \quad (4.2)$$

Equation (2) shows that an alternating magnetic field is equivalent to two circular rotating magnetic fields having constant amplitudes equal to half the amplitude of the alternating field and rotating in opposite directions at equal velocities in the form of direct wave

$$\frac{B_{1m}}{2} \sin \left( \omega t - \frac{x}{\tau} \pi \right), \text{ respectively indirect wave } \frac{B_{1m}}{2} \sin \left( \omega t + \frac{x}{\tau} \pi \right)$$

The direct wave travels in time following the positive direction of the  $x$ -axis, with the speed

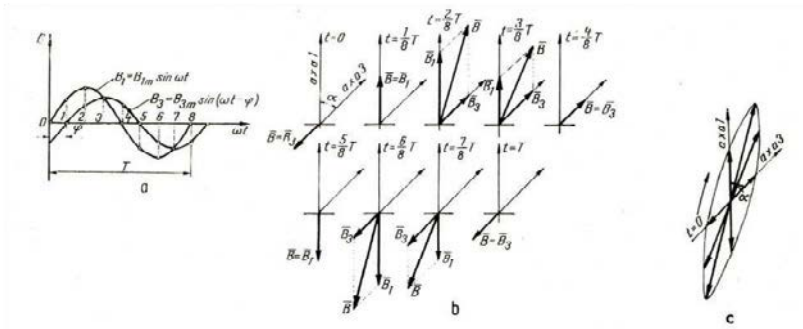


Fig. 4.1 Magnetic field density and the resulting elliptic magnetic field composition from two alternative magnetic fields: a - sinusoidal time variation of two alternative magnetic fields; b and c - the rotating elliptical magnetic field at different moments of time.

$$v = \frac{x}{t} = \frac{\tau}{\pi} \omega \quad (4.3)$$

Or rotates with the speed:

$$n = \frac{f}{p} \left[ \frac{\text{rot}}{\text{s}} \right] \text{ or } n = \frac{60 \cdot f}{p} \left[ \frac{\text{rot}}{\text{s}} \right] \quad (4.4)$$

where:  $f$  is the frequency of the supply voltage;

$p$  - the number of poles pairs of stator winding.

If the magnitude of the alternating magnetic field is fixed in space, but it varies sinusoidally over time, the circular rotating magnetic field has a constant value in time, but it changes its position with the constant angular velocity  $\omega = \Omega \cdot p$  corresponding to the

electric angle. It is known that the electric angle is equal to the geometric angle multiplied by the number of pairs of poles.

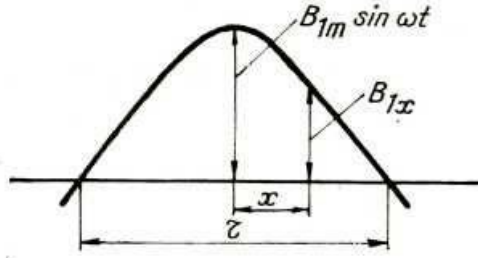


Fig. 4.2 The sinusoidal distribution of the magnetic flux density for one pole pitch.

The alternating magnetic fields inside the single phase shaded pole micromotor may be expressed by their circular components corresponding to the direct (*d*) and inverse (*i*) sequences, using a reference system relative to the axis of the first alternate field, written the complex form as:

$$\left. \begin{aligned} \bar{B}_{1d} &= \frac{B_{1m}}{2} e^{j\omega t}; & \bar{B}_{1f} &= \frac{B_{1m}}{2} e^{-j\omega t}; \\ \bar{B}_{3d} &= \frac{B_{3m}}{2} e^{j(\omega t - \varphi - \alpha)}; & \bar{B}_{3f} &= \frac{B_{3m}}{2} e^{-j(\omega t - \varphi + \alpha)}. \end{aligned} \right\} \quad (4.5)$$

On the basis of the relationship (2.4), adding together the circular magnetic field components will result in two circular magnetic fields, rotating in opposite directions and having the magnitudes,  $B_{1m}$  and  $B_{1im}$

$$\left. \begin{aligned} \bar{B}_I &= \bar{B}_{1d} + \bar{B}_{3d} = \left[ \frac{B_{1m}}{2} + \frac{B_{3m}}{2} e^{-j(\varphi + \alpha)} \right] e^{j\omega t} = B_{1m} e^{j\omega t}; \\ \bar{B}_{II} &= \bar{B}_{1f} + \bar{B}_{3f} = \left[ \frac{B_{1m}}{2} + \frac{B_{3m}}{2} e^{j(\varphi - \alpha)} \right] e^{-j\omega t} = B_{1im} e^{-j\omega t}. \end{aligned} \right\} \quad (4.6)$$

To obtain only one rotating magnetic field, for example the direct one, we need to impose  $\bar{B}_{1im} = 0$ . Results:

$$B_{1m} + B_{3m} \cdot e^{j(\varphi - \alpha)} = 0 \quad (4.7)$$

this corresponds to  $B_{1m} = B_{3m}$  and  $\alpha = \varphi \pm \pi$

To have an alternating magnetic field, the equality  $B_{1m} = B_{Um}$ , from where

$$\cos(\varphi + \alpha) = \cos(\varphi - \alpha) \quad (4.8)$$

or

$$\begin{aligned} \alpha &= K \cdot \pi, & \varphi &\neq 0; \\ \varphi &= K \cdot \pi, & \alpha &\neq 0. \end{aligned} \quad (4.9)$$

Generally, for two circular rotating magnetic fields we can write the relations:

$$\left. \begin{aligned} \bar{B}_I &= B_{Im} \cdot e^{j(\omega t + \gamma_1)} \\ \bar{B}_{II} &= B_{II m} \cdot e^{-j(\omega t + \gamma_2)} \end{aligned} \right\} \quad (4.10)$$

Fig. 4.3 shows the resulting magnetic field  $\bar{B} = \bar{B}_I + \bar{B}_{II}$  in the complex plane. The reference axis system  $xOy$  is chosen in order that the axis  $Ox$  makes an angle with the real axis  $\frac{\gamma_1 - \gamma_2}{2}$ . The  $x$  and  $y$  coordinates corresponding to the extremities of the resulting magnetic field  $\bar{B}$  are given by the expressions:

$$\left. \begin{aligned} x &= (B_{Im} + B_{IIm}) \cos \left( \omega t + \frac{\gamma_1 + \gamma_2}{2} \right); \\ y &= (B_{Im} - B_{IIm}) \sin \left( \omega t + \frac{\gamma_1 + \gamma_2}{2} \right), \end{aligned} \right\} \quad (4.11)$$

whereby, by eliminating the variable  $t$  corresponding to the time, the following expression it is obtained:

$$\frac{x^2}{(B_{Im} + B_{IIm})^2} + \frac{y^2}{(B_{Im} - B_{IIm})^2} = 1 \quad (4.12)$$

which represents the equation of an ellipse with the large axis equal to the sum of the amplitudes of the two circular fields, and the small axis equal to their difference.

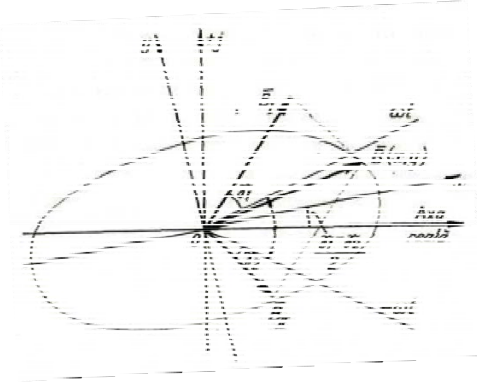


Fig. 4.3 The resulting elliptical magnetic field, represented in the complex plane.

The magnitude of the resultant magnetic field  $\bar{B}$  rotates in the direction corresponding to the largest rotating component, with a time-dependent angular velocity, according to Kepler's law [9]. From relationship (2.6) one will obtain:

$$\bar{B} = B_{Im} \cdot e^{j(\omega t + \gamma_1)} + B_{II m} \cdot e^{-j(\omega t + \gamma_2)} \quad (4.13)$$

or

$$\bar{B} = B_{Im} \cdot \left[ e^{j(\omega t + \gamma_1)} + e^{-j(\omega t + \gamma_2)} \right] + (B_{II m} - B_{Im}) \cdot e^{-j(\omega t + \gamma_2)} \quad (4.14)$$

The relationship (4.14) shows that an elliptical magnetic field can be decomposed into an alternating magnetic field and a circular one.

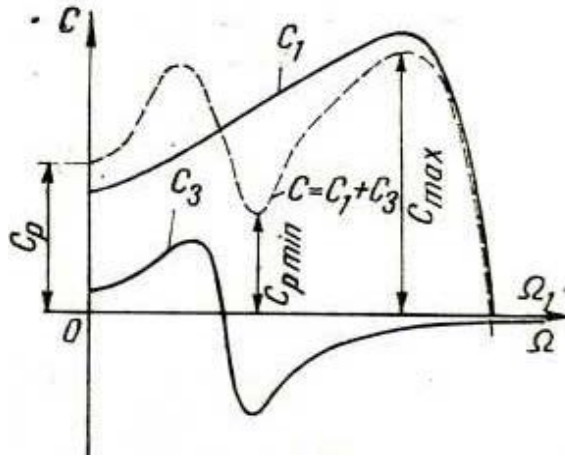


Fig. 4.4 Mechanical characteristic corresponding to single phase shaded pole micromotor.

$C_p$  - starting torque;  $C_{pmin}$  - the minimum torque during start-up;  $C_{max}$  - maximum torque;

$\Omega_1$  - synchronous speed.

### 4.3 Operating principle of the single phase shaded pole micromotor

The current  $I_1$  absorbed by the micromotor from the grid flows through the primary winding and creates the alternating magnetic flux  $\Phi_1$ . A part of this flux  $\Phi_{1e}$  flows through the shaded area of the stator pole, crossing the area defined by the short circuited coils and therefore, will induce an electromotive force. This voltage will determine a current inside the shortcircuit winding  $I_3$ . This current will produce a magnetic flux  $\Phi_{1e}$  which will sum together with the main flux which is crossing the shaded area  $\Phi_{1e}$  corresponding to the from the same pole, are added together and produce a resultant alternating magnetic flux  $\Phi_3$  behind the main flux  $\Phi_1$  (shifted in time with the angle  $\varphi$  (fig. 4.5).

The two fluxes  $\Phi_1$  and  $\Phi_3$  have different amplitudes, are phase-shifted in time with the angle  $\varphi$  and with the electrical angle  $\alpha$  in space one from another. As a result, a rotating elliptical magnetic field is produced within the micromotor airgap, which can be decomposed into two circular rotating magnetic fields with different amplitudes, rotating at the same speed  $\Omega_1 = \frac{2\pi f_1}{p}$ , in opposite directions. Inside the rotor cage rods emf

voltages are induced, and because of this voltages the cage will produce alternative electric currents. Due to the interaction between the rotating field and the induced

current, the rotor of the micromotor is rotated at a speed  $\Omega < \Omega_1$ . The rotation will be in the same direction of the rotating magnetic field corresponding to the larger component of the field known as the direct field. The variable  $s = \frac{\Omega_1 - \Omega}{\Omega_1}$  is named the motor's slip.

Considering the direct component  $C_d$  and reverse  $C_i$  of torque, for the actual torque of the single phase motor we can write the relation  $C = C_d - C_i = f(s)$  given in fig.2.7. Due to the existence of the inverse torque  $C_i$  it is possible that at  $s = 0$ ,  $C \neq 0$ . The single phase shaded pole induction micromotor, in the usual form, has a well-established direction of rotation, corresponding to the direction from the unshaded area to the shaded part of the pole (Fig. 4.5 a and b).

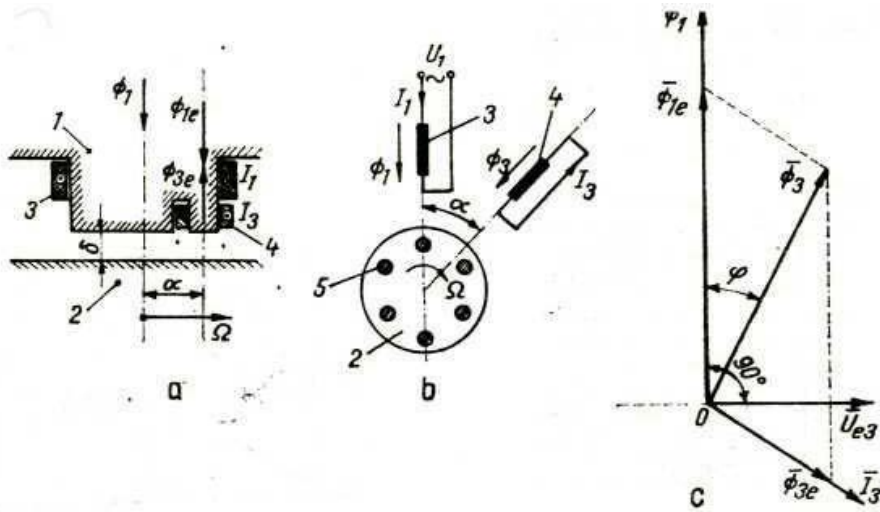


Fig. 4.5 The single phase shaded pole-induction micromotor: a and b - the alternating magnetic flux of the primary winding  $\Phi_1$  and the flux of the shortcircuit winding  $\Phi_1$

short-circuit - 2 ; c - the flux phasor diagram of the fluxes.

1 - stator; 2 - rotor; 3 - primary stator winding; 4 - short circuit winding; 5 - rotor cage; 8 - airgap.

In the transient mode, the micromotor presents a dynamic mechanical characteristic that differs from the static mechanical characteristic, especially when the moment of inertia is small and there is a rapid variation of fields and currents. Fig. 4.6 shows the two mechanical characteristics of a three-phase induction motor with cage rotor [1, 9, 10, 12].

In Fig. 4.7, the static mechanical characteristics of micro-motors with 2-10 watt low-power, medium-power and high power 100-150 watts single phase shaded pole micromotors are presented. It should be noted that high power micromotors appear to have a pronounced influence in the torque given by the third order harmonic, which makes the minimum torque during startup to be about half the rated torque  $C_N$ .

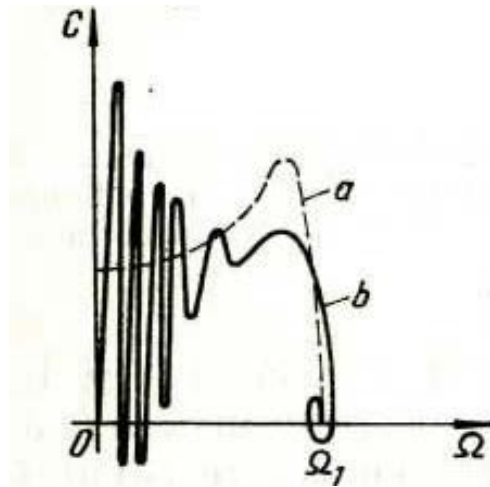


Fig. 4.6 Mechanical characteristic corresponding to the three-phase induction motor: a - static; b - dynamic.

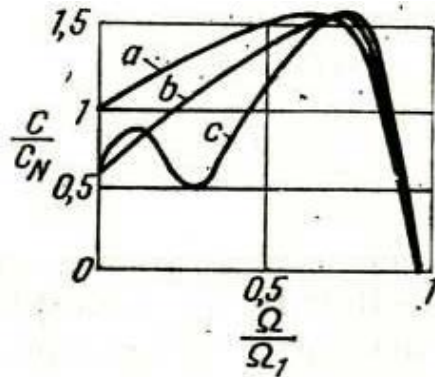


Fig. 4.7 The static natural mechanical characteristics of the single phase induction micromotors: a - low power; b - medium power; c - high power.

#### 4.4 Mechanical characteristic of the single phase shaded pole induction micromotor

The identification of the mechanical characteristic  $C = f(\Omega)$  is of importance for a correct selection of the micromotor for a specific electric drive, especially due to the fact that nowadays in our country and worldwide, the single phase induction micromotor knows a massive and diversified application, due to its safe and robust operation.

The electromagnetic processes in the single phase shaded pole induction micromotor are complex, and their analytical description, taking into account all factors, would lead to the writing of complex mathematical equations, difficult to use in the usual design calculations. There are some constructive types in which the presence of different harmonics is virtually negligible, and therefore the results of the analytical calculation, with



the consideration of only the fundamental variables, are appropriate. It should be noted that, although 100 years have elapsed since the realization of the first single phase shaded pole induction micromotor, in contrast to its constructive simplicity, the literature has not exhausted the study of many aspects describing the electromagnetic processes in the single phase shaded pole induction micromotor [2, 13, 3, 6, 10].

In this paper, the calculated expressions refer to the static mechanical characteristics and this expressions were deduced by considering some simple hypotheses. Thus, the influence of the higher magnetic field harmonics and the iron losses was neglected. It has been assumed that the air gap and the reactances of all windings to be independent of the electric current.

#### 4.5 Torque equation of the single phase shaded pole induction micromotor

In order to identify the analytical expression  $C = f(\Omega)$  of the mechanical characteristic, we need to obtain the expressions electrical currents in the primary winding  $I$  and in the shortcircuit coil  $I_3$ , based on the theory of the magnetic field, applying the method of symmetrical component [9].

By comparing the voltage equations for the primary stator winding circuit, the shortcircuit winding and the rotor cage in complex form, [35, 36] the following expressions are obtained:

$$\bar{U}_1 = \bar{Z}_1 \bar{I}_1 + \frac{\bar{Z}'_{2d} \cdot jX_{1u}}{\bar{Z}'_{2d} + jX_{1u}} \cdot \frac{\bar{I}_1 + \bar{I}_3 e^{j\alpha}}{2} + \frac{\bar{Z}'_{2i} \cdot jX_{1u}}{\bar{Z}'_{2i} + jX_{1u}} \cdot \frac{\bar{I}_1 + \bar{I}_3 e^{-j\alpha}}{2} + jX_s (\bar{I}_1 + \bar{I}_3) \quad (4.15)$$

$$0 = \bar{Z}'_3 \bar{I}_3 + \frac{\bar{Z}'_{2d} \cdot jX_{1u}}{\bar{Z}'_{2d} + jX_{1u}} \cdot \frac{\bar{I}_1 e^{j\alpha} + \bar{I}_3}{2} + \frac{\bar{Z}'_{2i} \cdot jX_{1u}}{\bar{Z}'_{2i} + jX_{1u}} \cdot \frac{\bar{I}_1 e^{-j\alpha} + \bar{I}_3}{2} + jX_s (\bar{I}_1 + \bar{I}_3) \quad (4.16)$$

where:

$\bar{Z}_1 = R_1 + jX_1$  represents the impedance of the primary stator winding;

$\bar{Z}'_3 = R'_3 + jX'_3$  impedance of short-winding, reduced to primary winding

$\bar{Z}'_{2d} = \frac{R'_2}{s} + jX'_2$  the impedance of the rotor cage corresponding to the direct sequence, reduced to the primary winding;

$\bar{Z}'_{2i} = \frac{R'_2}{2-s} + jX'_2$  - the impedance of the rotor cage corresponding to the inverse sequence, reduced to the primary winding;

$R_1, R_2', R_3'$  the resistances of the three windings;

$X_1, X_2', X_3'$  the leakage reactances of the three windings;

$X_s$  magnetic shunt reactance corresponding to the magnetic bridge;

$X_{1u}$  self reactance;

$\alpha$  represents the electric angle between the primary stator winding axis and the stator short-circuit coil axis;

$s = \frac{\Omega_1 - \Omega}{\Omega_1}$  the mechanical slip;

$U_1$  primary winding power supply voltage;

$j = \sqrt{-1}$  - the imaginary unit;

$e$  is a mathematical constant that is the base of the natural logarithm;

The reduction to the primary winding is done by the reduction factor  $k_{12}$  or  $k_{13}$ . Thus, for the rotor cage

$$R_2' = R_2 \cdot k_{12}, X_2' = X_2 \cdot k_{12}, k_{12} = \frac{8(N_1 k_{B1})^2}{N_2} \quad (4.17)$$

and for short-circuit coil

$$R_3' = R_3 \cdot k_{13}, X_3' = X_3 \cdot k_{13}, k_{13} = \left( \frac{N_1 k_{B1}}{N_3 k_{B3}} \right)^2 \quad (4.18)$$

The currents referenced at the primary winding have the values:

$$I_{2d}' = \frac{I_{2d}}{\sqrt{k_{12}}}, I_{2i}' = \frac{I_{2i}}{\sqrt{k_{12}}}, I_3' = \frac{I_3}{\sqrt{k_{13}}}, \quad (4.19)$$

where:  $N_1$  and  $N_3$  are the number of turns of the primary windings, respectively in short circuit;  $k_{B1}, k_{B3}$  winding factors of the primary winding, respectively of the short circuit;  $N_2$  number of slots in the rotor.

Introducing the following notations:

$$\bar{Z}_d' = \frac{\bar{Z}_{2d}' \cdot jX_{1u}}{2(\bar{Z}_{2d}' + jX_{1u})} \quad \text{and} \quad \bar{Z}_i' = \frac{\bar{Z}_{2i}' \cdot jX_{1u}}{2(\bar{Z}_{2i}' + jX_{1u})} \quad (4.20)$$

From the relations (3.1) we can obtain the expression of the current in the primary winding  $I_1$  and  $I_3$  corresponding to the shortcircuited coil referenced to the primary winding,

$$\bar{I}'_1 = \frac{-\bar{U}_1 \bar{a}}{bc - ad} \quad (4.21)$$

and

$$\bar{I}'_3 = \frac{-\bar{U}_1 \bar{b}}{bc - ad} \quad (4.22)$$

where

$$\bar{a} = \bar{Z}'_3 + \bar{Z}'_d + \bar{Z}'_i + jX_e; \quad (4.23)$$

$$\bar{b} = \bar{Z}'_d e^{-j\alpha} + \bar{Z}'_i e^{j\alpha} + jX_e; \quad (4.24)$$

$$\bar{c} = \bar{Z}'_d e^{j\alpha} + \bar{Z}'_i e^{-j\alpha} + jX_e \quad (4.25)$$

$$\bar{d} = \bar{Z}'_1 + \bar{Z}'_d + \bar{Z}'_i + jX_e \quad (4.26)$$

The mechanical characteristic  $C = f(s)$  is calculated with the relation

$$C = C_d - C_i - \frac{2R'_2}{\Omega_1} \left( \frac{I'^2_{2d}}{s} - \frac{I'^2_{2i}}{2-s} \right) \quad (4.27)$$

where:  $C$  is the motor torque in Nm;  $I'_{2d}$  - is the rotor current corresponding to the direct sequence, reduced to the primary winding, in A;

$$I'_{2d} = -\frac{jX_{1u}}{\bar{Z}'_{2d} + jX_{1u}} \cdot \frac{\bar{I}_1 + \bar{I}_3 e^{j\alpha}}{2} \quad (4.28)$$

$$I'_{2i} = -\frac{jX_{1u}}{\bar{Z}'_{2i} + jX_{1u}} \cdot \frac{\bar{I}_1 + \bar{I}_3 e^{-j\alpha}}{2} \quad (4.29)$$

$I'_{2i}$  is the rotor current corresponding to the inverse succession, reduced to the primary winding, in A;

$$\Omega_1 = \frac{2\pi f_1}{p} \text{ is the synchronous angular speed in } \frac{\text{rad}}{\text{s}}$$

$p$  is the number of pole pairs;

$f_1 = 50\text{Hz}$  is the number of pole pairs;

For the calculation of the mechanical characteristic by means of the relation (4.27) during the transient start regime, is considered that the slip  $s$  is in the range  $s = 1 \rightarrow \Omega = 0$  at start and  $s = 0 \rightarrow \Omega = \Omega_1$  at synchronous speed. In a first stage we need to calculate the resistances  $R_1, R_2', R_3'$  and the circuit reactances  $X_1, X_2', X_3', X_s$  to take into account the geometry of the magnetic circuit and the winding parameters and to use the expression data known from the literature [1, 3, 5, 7].

And then, for a certain slip value, we can determine the impedances  $\bar{Z}_1, \bar{Z}_{2d}', \bar{Z}_{2i}', \bar{Z}_3, \bar{Z}_d', \bar{Z}_i'$ . If the electric angle  $\alpha$  is known, the currents are calculated  $I_1$  and  $I_3$  and using the relations (4.28) and (4.29), we may calculate the rotor current  $I_{2d}'$  and  $I_{2i}'$ , corresponding to the direct and inverse sequence.

Evaluation of Joule-Lenz losses from primary winding  $Q_1$  rotor cage  $Q_2$  and the short-circuit winding  $Q_3$  is done by applying the relations:

$$Q_1 = I_1^2 R_1 \quad [W] \quad (4.30)$$

$$Q_2 = 2(I_{2d}'^2 + I_{2i}'^2) R_2' \quad [W] \quad (4.31)$$

$$Q_3 = I_3'^2 + R_3' \quad [W] \quad (4.32)$$

The calculation is performed for several slip values, obtaining the curves of Fig. 4.8. One may notice the curve  $I_3 = f(s)$ . In small values of the slip, i.e. when the micromotor is at no load, the current in the short-circuit coil has values higher than in the case of a nominal load regime. This is generally the case with most of the single phase shaded pole induction micromotors. As a consequence, the Joule-Lenz losses become appreciable, which is why some of the micromotor constructions result in an increased heating of the short-winding, namely at no load. In this situation, the value of the resistance  $R_3$  has an important role.

In Fig. 4.9 it is found that at a certain value of the resistance  $R_3^*$ , the loss curve  $Q_3$  has a maximum. On a micromotor with a given ventilation system it is possible to determine the allowable loss value  $Q_3$ , for which there is no increased heating of the winding when the single phase induction micromotor is at no load. Corresponding to this value of  $Q_3$  of losses it is possible to determine the minimum value of the short-circuit coil resistance, which will always be in the range  $R_3 \geq R_3^*$ .

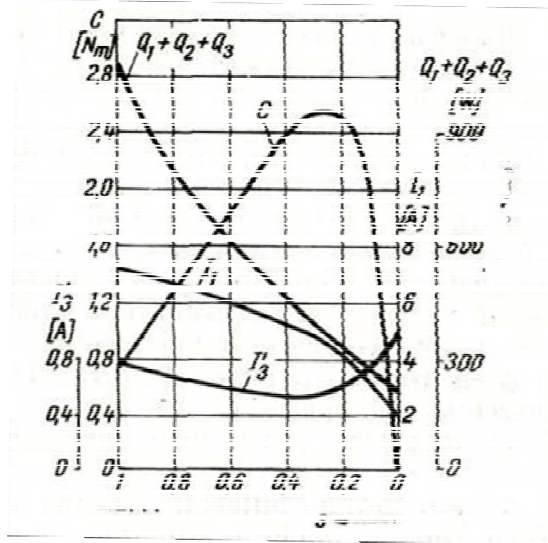


Fig. 4.8 The mechanical characteristic  $C = f(s)$ , the current in the primary winding  $I_1$  (the electric current in the short circuit coil  $I_3$  and the sum of the losses Joule-Lenz  $Q_1 + Q_2 + Q_3$  during the start).

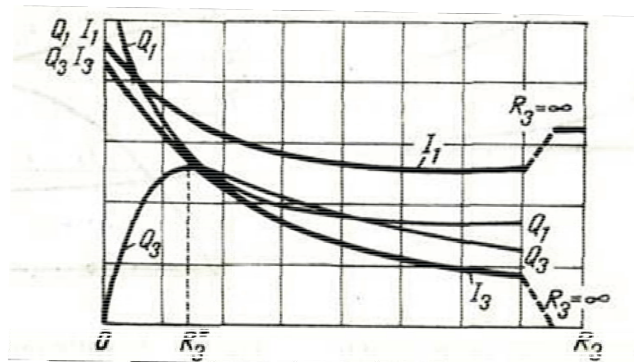


Fig. 4.9 The electric currents  $I_1$  and  $I_3$  the Joule-Lenz copper losses  $Q_1$  and  $Q_3$  function of the resistance  $R_3$ , when the single phase induction micromotor is at no load.

In Fig. 4.10 it is presented the variation of the torque and the starting currents function of the reactance of the magnetic shunt. The starting torque  $C_p$  increases with an increased value of the reactance  $X_s$ , because at a certain value of  $X_s$  will have a maximum. Generally, due to mechanical reasons, the thickness of the magnetic bridges is kept bigger than necessary. In these situations, to achieve the desired value of the reactance  $X_s$  gaps or canals are executed.

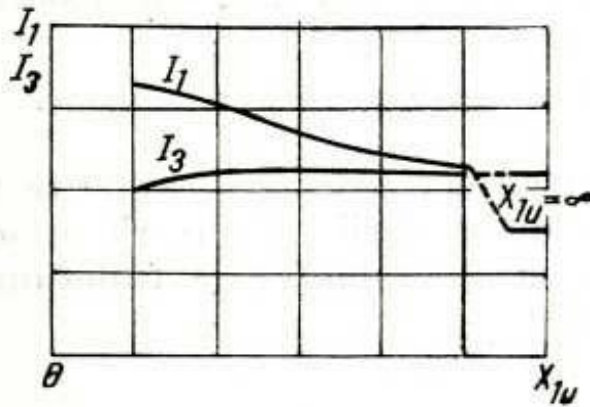


Fig. 4.10 The no load current  $I_{1p}$  and  $I_{3p}$  function the self reactance  $X_{1u}$ .

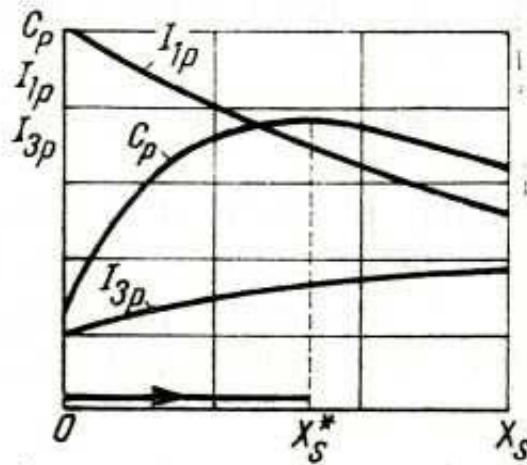


Fig. 4.11 The variation of starting torque  $C_p$  and of the current  $I_{1p}$ ,  $I_{3p}$  function of value of the magnetic shunt reaction  $X_s$ .

The computation of the influence of the main parameters on the starting and nominal regime of the single phase shaded pole micromotor as well as the experimental tests proved that the reproducibility of the performance of the micromotor requires, besides respecting the machine geometry (overall dimensions and tolerances), a special care regarding the quality of the materials used. In the present stage of development of the technique it is necessary to use digital computers to determine the optimal combination of parameters of the micromotor for a given design request, especially for situations in which the single phase shaded pole induction micromotor is to be build out in very large numbers.

## 4.6 References

- [1] Şora, I., & Babescu, M. (1979), "Micromotorul cu poli ecranați: Construcție, funcționare, exploatare și reparare [mașini electrice" (Mașini și aparate electrice). București, Editura Tehnică.
- [2] Şora, Constantin, Brezeanu, Constantin, Gheorghe, & Brezeanu, Ioan. (1967), "Construcția motorului de inducție", Timișoara, Institutul Politehnic Timișoara.
- [3] Şora, I., & Dumitrescu, P. (1969), "Micromotorul cu poli ecranați" (Mașini Electrice). București, Editura Tehnica.
- [4] Babescu, M. (1992), "Mașini electrice monofazate", București, Editura Tehnică.
- [5] Babescu, M. (2002), "Mașina asincronă: Modelare-identificare-simulare", [mașina asincronă] (Energetica). Timișoara: Editura Politehnica.
- [6] Boldea, I., & Nasar, S. (2001), "The induction machine handbook" (The electric power engineering / Leo Grigsby). Boca Raton [etc.: CRC Press.
- [7] Boldea, I. (2009), "Transformatoare și mașini electrice" (Ed. a 2-a, rev. și adăugită), Ed. Electrotehnica), Timișoara, Editura Politehnica.
- [8] Dordea, T., Madescu, T., Torac, G., Ocolișan, I., Moț, L., Madescu, Gheorghe, Moț, Marțian. (2010), "Mașini electrice: Programe de calcul [mașini electrice", (Mașini Electrice), Timișoara, Editura Politehnica.
- [9] Deaconu, S. (2016), Mașini electrice (Student), Timișoara, Editura Politehnica.
- [10] Boldea, I., & Nasar, S. (1999), "Electric drives", Boca Raton [etc.: CRC Press.
- [11] Dordea, T., Madescu, T., Torac, G., Ocolișan, I., Moț, L., Madescu, Gheorghe, Moț, Marțian. (2015), "Electrical machines: Fortran programs", (Mașini Electrice), Timișoara, Editura Politehnica.
- [12] Giurgiuțiu, V., & Lyshevski, S. (2009), "Micromechatronics: Modeling, analysis, and design with MATLAB", (2nd ed., Nano- and Microscience, Engineering, Technology and Medicine), Boca Raton London New York: CRC Press.
- [13] Babescu, M. (2000), "Mașini electrice: Modelul ortogonal [mașini electrice", (Master). Timișoara: Editura Politehnica.

## A.C. MACHINE TRANSIENTS: A DIRECT MATH APPROACH

### 5.1 Mathematical modeling of electrical machines with a.c. machine transients: a direct math approach

The mathematical models of induction motors with squirrel cage and the synchronous machines are developed in a rotating coordinate system rigidly connected with rotating magnetic field. Unlike the well-known mathematical models of induction machines written in phase coordinates, the orthogonal dq obtained models complete the orthogonal representation of the induction machine and the synchronous machine is presented in such a manner that the model is usable for direct mathematical numerical solving. Using special nonsingular changes of coordinates, the investigation of these systems can be reduced to numerical analysis of third and fifth order differential equations. Thus, the derived models are described by rather simple differential equations which allow for the in-depth qualitative study of such models.

### 5.2 Mathematical modeling of electrical machines

The electric machines together with their power supplies and control structures are a basic component of automated systems. The field of electrical machines engineering began in 1825, when the first electromagnets used to build an electric machine appeared. The field evolved rapidly and complex automated systems that have an electric machines operating as an execution element appeared. At present, the extremely diverse number of synchronous and asynchronous AC motors are used due to their high reliability. The DC machine, although it was the first topology to be widespread in the last century, is less used due to its brush based feeding system, relative expensive and sensitive build, with low reliability, which has made this type of electric machine virtually eliminated from the automatic electric drive systems. The technical evolution required the construction of automatic control structures that are capable to integrate and control real systems functioning on the basis of complex mathematical models. The identification of electrical and mechanical parameters and digital simulation now represent a natural step in the development of this systems. This approach of thinking about the control problem is presented in the following representation (fig. 5.1):



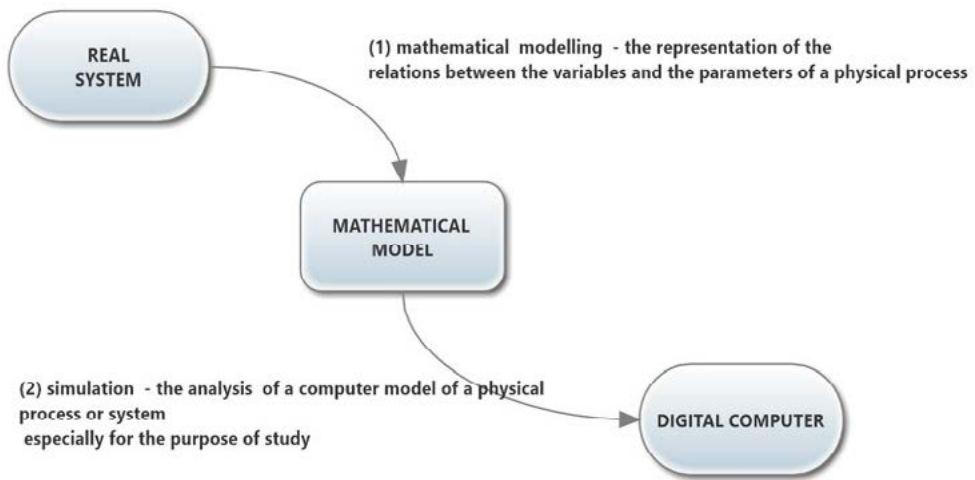


Fig. 5.1 Physical system modeling.

A real system is that part of the real world that is of interest for the observer. The model describes a part of the reality chosen by the person involved in the model development (the physicist, the engineer or the mathematician), noting that many different models describe parts of the same reality. Particular attention will be given to selecting the model and system boundaries. Depending on these limits, it is established which part of the reality is taken into account. This delimited part is called the system. The first step in analyzing a real system is building the model of this system (fig. 5.2). Peter Eychhoff said that the model was a representation of the essential aspects of a real system that presented knowledge about that system in a usable form without the need for a detailed description of the system's operating mechanism. The model can only mimic system behavior in this interpretation. The essential feature for the construction and utility of the mathematical model is its simplicity. From this point of view, the model can be defined as a representation of reduced complexity of a reality. Lenard Lyung believed that a model of a system is a tool that is used to answer questions about the system without experimenting on the system. Approached in this way, models can be found in all areas. In the field of immediate reality, several types of models can be found: mental models (intuition, experience), verbal models, physical models (mathematics), mathematical models (abstract / symbolic) and hybrid models that combine analytical and mathematical models – digital Calculator). Models generally have a limited domains of validity. In the technique, the degree of validity is quantitatively measured by the concordance between the real system data and model data generated under the same experimental conditions. We can delimit three levels of validity:

- replicative or repetitive: the generated data is consistent with the data already obtained from the system;
- predictive valid: If it can predict system data, with prediction models;

- structurally valid: reproduces the behavior of the real system and reflects how the real system works to achieve that behavior. The model considered a satisfactory representation of a real system is the result of iterations, with each cycle of the cycle:

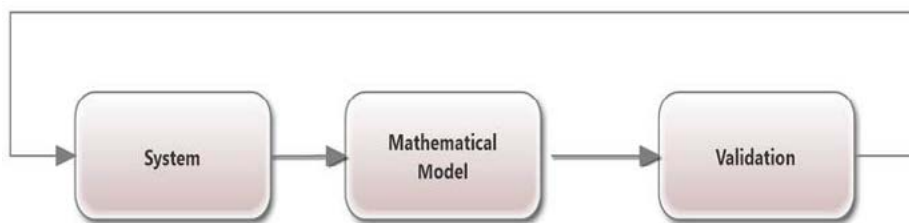


Fig. 5.2 Modelling steps

The fundamental problem of system modeling can be described as the need of determining an appropriate mathematical model, this problem being solved in two ways:

- analytical or deductive – the determination of the mathematical model is done by the use of physical laws describing the dynamics of the respective system, the models thus obtained having a large field of validity, and the parameters having direct significance; the model thus determined is named White Box Model (WBM).

- experimental or inductive – the structure of the model is fixed by a certain amount of a priori knowledge resulting from the partial knowledge of the system, leaving only the determination of the system model parameter values; The model thus determined with the name of the black box model (BBM). Taking these things into account, we can distinguish two stages in the identification: a qualitative one, which is to fix the model structure and a quantitative one which consists in determining the numerical values of the coefficients of the chosen structure, the stage which is also called the “parameter estimation”. The graphical representation is introduced in order to help the description of the patterns and the interaction between its variables, with a wide variety of representations from the particular ones to the general ones of wide applicability.

In the automation process, the modeling and identification of parameters in electric machines must be done with the highest accuracy. The complete model of an electric machine is so complicated that it is inefficient in a complete full scale direct application. In literature [B2], the orthogonal model for the asynchronous and synchronous machine is very well documented. Deduction of the specific parameters of the orthogonal model is done experimentally, by tests on the electric machines in the laboratory, according to a technique that is presented in technical standards. An electrical machine (ME) represents an assembly of electrical circuits (called windings) placed on magnetic cores which are built from electrotechnical steel laminations and is capable of transforming electricity into mechanical energy (in MOTOR regime) or mechanical energy in electricity (in generator regime).

### 5.3 Construction and functional elements of electric machines

An electric machine (ME), fig. 5.3, consists of a fixed part called a stator and a mobile part called a rotor. The gap (distance) between the two sides is the machine's airgap ( $\delta$ ).

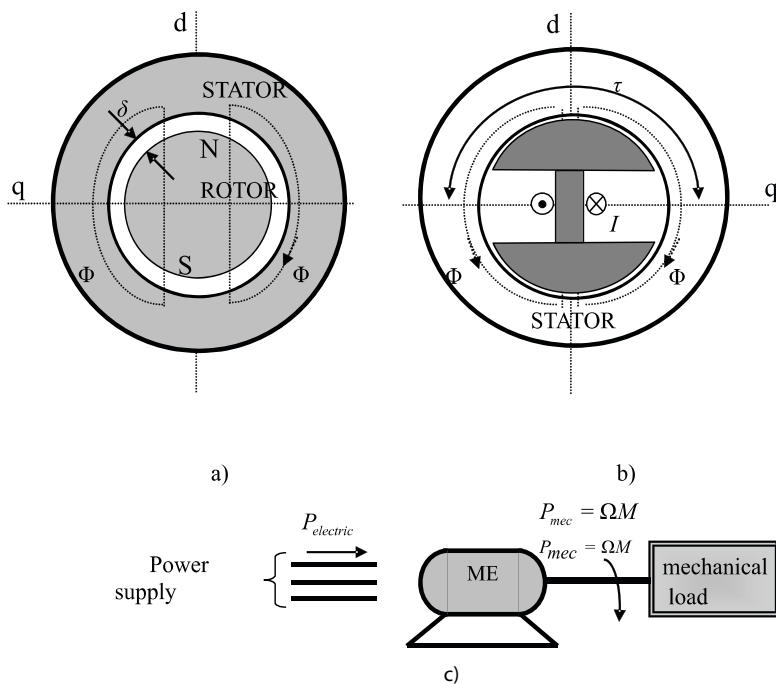


Fig. 5.3 Rotating electrical machine: a) Electrical machine with non-salient poles; b) Electrical machine with salient poles; c) Power flow.

ME with full poles

Operating in motor regime

$$\eta = \frac{P_{mec}}{P_{electric}} \quad (\text{motor}) - \text{the electrical machine provides mechanical power to the shaft}$$

and absorbs electrical power at the terminals;

Generator regime

$$\eta = \frac{P_{electric}}{P_{mec}} \quad (\text{generator}) - \text{the electrical machine provides electrical power to the}$$

terminals and absorbs mechanical power from the shaft;

Brake mode

The machine receives electrical power at the terminals and mechanical power on the shaft and both powers are transformed into heat inside the electric machine.

Losses (fig. 5.4):

- copper losses  $p_{cu} = RI^2$  ;
- iron losses
- hysteresis  $p_{Fe} = \eta \cdot B_{max}^{1.6} \cdot f \cdot V$  (watts)

where,  $\eta$  = Steinmetz hysteresis constant

$V$  = volume of the core in m<sup>3</sup>

- Eddy current loss;
- Mechanical losses.

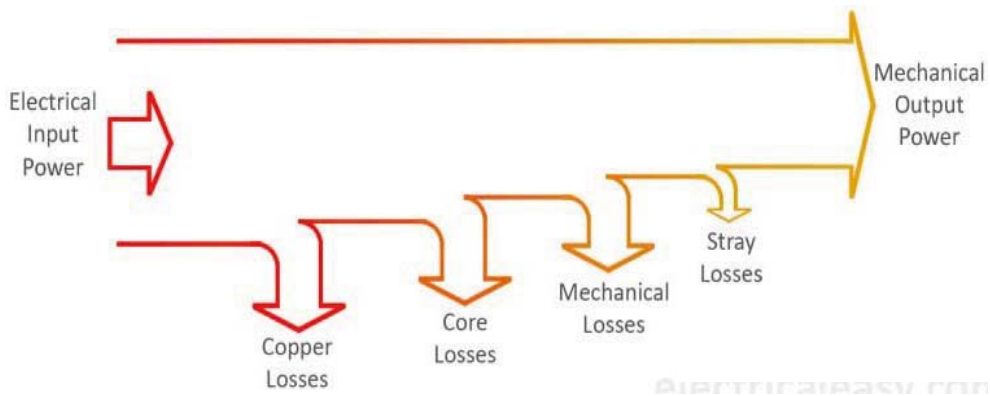


Fig. 5.4. Losses in an electrical machine.

The electromagnetic torque is obtained by the interaction of the magnetic fields that are created by the currents passing through the windings (according to the law of the magnetic circuit):

$$N \cdot I = \Phi \cdot R_{mag} \tag{5.1}$$

where:  $\Phi$  - magnetic flux (  $\Phi = B \cdot S$  )

$N$  - the number of turns traveled by the current  $I$  ;

$R_{mag}$  magnetic reluctance .

Generally, it is recommended to have a sine wave distribution of the field in the air gap. The arc length corresponding to a pole is called pole pitch and it is symbolized by  $\tau$  . The windings are placed in stator slots and their coils are connected with the collector. The brushes (fig. 5.5) are in contact with the collector which is connected with the power sources.

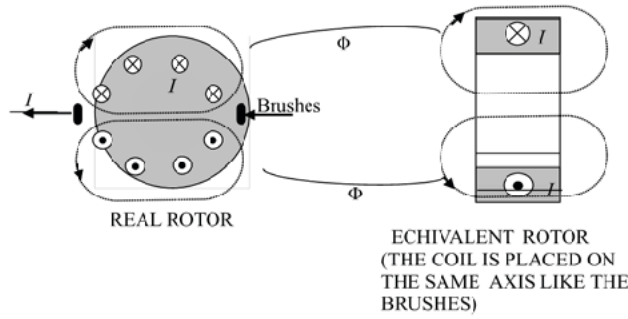


Fig. 5.5 Equivalent rotor.

Let us consider a winding “A” placed in the rotor with the current  $I_A$  and a “B” placed in the stator with the current  $I_B$ , both windings are magnetically coupled, as in the following figure (fig. 5.6. a):

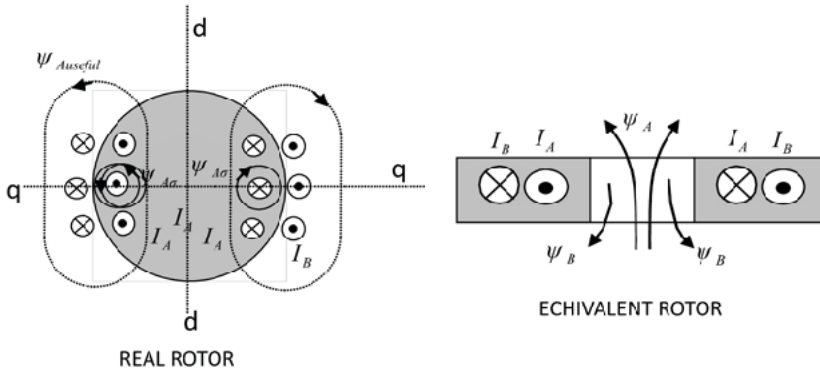


Fig. 5.6.a The magnetic flux in two magnetically coupled windings.

The equivalent electrical schematic is shown in Fig. 5.6.b:

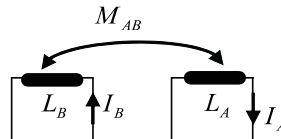


Fig. 5.6.b

$\psi_{A\sigma}$  leakage flux,

$\psi_{Auseful}$  - useful flux ;

$$\psi_A = \psi_{total} = \psi_{Autil} + \psi_{A\sigma}; \quad (5.2)$$

The windings “A” and “B” present their self-inductances  $L_A$  and  $L_B$  and the mutual inductances  $M_{AB}$  defined by relationships:

$$L_A = \frac{\psi_A}{I_A} = \frac{N_A \Phi_A}{I_A} = \frac{N_A \cdot N_A I_A}{I_A R_{mgA}} = \frac{N_A^2}{R_{mgA}} \quad (5.3)$$

$$L_B = \frac{\psi_B}{I_B} = \frac{N_B \Phi_B}{I_B} = \frac{N_B \cdot N_B I_B}{I_B R_{mgB}} = \frac{N_B^2}{R_{mgB}} \quad (5.4)$$

$$M_{AB} = \frac{\psi_{AB}}{I_A} = \frac{N_B \Phi_{AB}}{I_A} = \frac{N_B \cdot N_A I_A}{I_A R_{mgAB}} = \frac{N_A \Phi_{BA}}{I_B} = \frac{N_A \cdot N_B I_B}{I_B R_{mgBA}} = \frac{N_A N_B}{R_{mgBA}} \quad (5.5)$$

$$R_{mg} = \frac{l}{\mu S} \quad (5.6)$$

where:  $R_{mgA}$  - the magnetic reluctance of the magnetic circuit corresponding to the flux  $\psi_A$ ;  $R_{mgB}$  - Magnetic reluctance of the flux magnetic circuit  $\psi_B$ ;  $R_{mgAB}$  - Magnetic reluctance of the magnetic circuit for the useful flow which crosses both windings  $\psi_{useful}$ ,  $R_{mgAB} = R_{mgBA}$  ;

Faraday's law of induction – on a closed curve  $\Gamma$ , integral  $\oint_{\Gamma} \vec{E} \cdot d\vec{l}$  (sum of voltages) is equal to the derivative of the magnetic flux passing through the surface that is defined the curve  $\Gamma$ .

If the stator is electrically connected with a three phase power supply inside the magnetic circuit, a rotating magnetic field will be created (according to Faraday's law of the magnetic circuit) and the rotor will rotate in the direction of the magnetic rotating field, as it can be seen in Figure 5.7 .

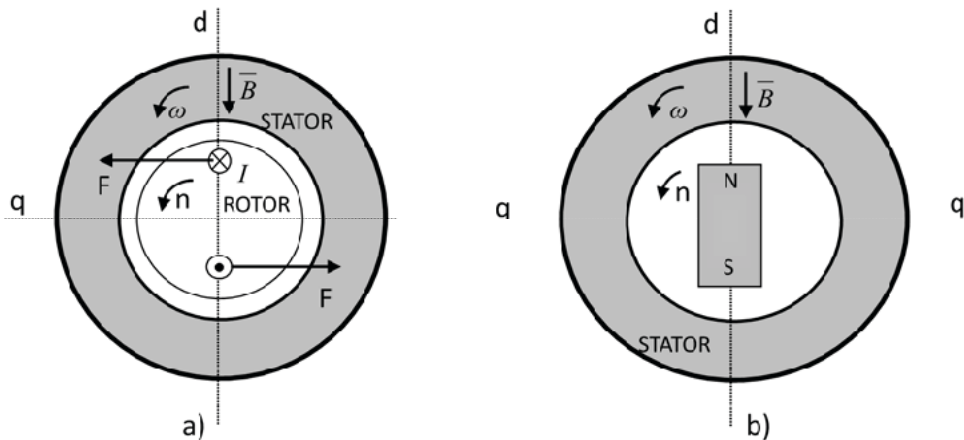


Fig. 5.7 Operating principle for an AC electric machine a) wounded rotor b) permanent magnet motor.

## 5.4 Mathematical model equivalent between the dq orthogonal model and the abc model of the real machine

The rotating magnetic field represents the key element of the alternating current electric machine functioning.

The magnetic field for the real electrical machine

We consider a three-phase symmetrical system of voltages and currents:

$$u_a = U\sqrt{2} \sin \omega t \quad i_a = I\sqrt{2} \sin(\omega t + \phi) \quad (5.7)$$

$$u_b = U\sqrt{2} \sin(\omega t + 120^\circ) \quad i_b = I\sqrt{2} \sin(\omega t + 120^\circ + \phi) \quad (5.8)$$

$$u_c = U\sqrt{2} \sin(\omega t - 120^\circ) \quad i_c = I\sqrt{2} \sin(\omega t - 120^\circ + \phi) \quad (5.9)$$

The voltages, having sinusoidal distribution in space, generate a circular rotating magnetic field that rotates with the speed:

$$n_1 = \frac{f}{p} \quad (5.10)$$

The magnetic field on the three phases represented below is written as (fig. 5.8):

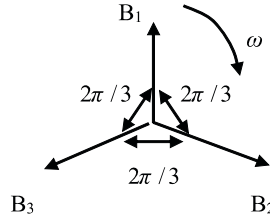


Fig. 5.8

$$B_1 = B_M \sin[(X/\tau)\pi] \sin \omega t \text{ phase I} \quad (5.11)$$

$$B_2 = B_M \sin[(X/\tau)\pi + 2\pi/3] \sin(\omega t + 2\pi/3) \text{ phase II} \quad (5.12)$$

$$B_3 = B_M \sin[(X/\tau)\pi + 4\pi/3] \sin(\omega t + 4\pi/3) \text{ phase III} \quad (5.13)$$

The resultant field  $B$  is obtained by summing it up (fig. 5.9):

$$\begin{aligned} B = B_1 + B_2 + B_3 = B_M \{ & \cos[(X/\tau)\pi - \omega t] - \cos[(X/\tau)\pi + \omega t] + \\ & + 2 \cos[(X/\tau)\pi - \omega t] - \cos[(X/\tau)\pi + \omega t + 4\pi/3] - \cos[(X/\tau)\pi + \\ & \omega t + 8\pi/3] \} / 2 = (3B_M/2) \cos[(X/\tau)\pi - \omega t] \end{aligned} \quad (5.14)$$

having the amplitude:

$$B_{\max} = (3/2)B_M \quad (5.15)$$

$$t_2 = \frac{p}{\omega}$$

because:

$$\begin{aligned} & -\cos[(X/\tau)\pi + \omega t] - \cos[(X/\tau)\pi + \omega t + 4\pi/3] - \cos[(X/\tau)\pi + \omega t + 8\pi/3] = \\ & = -(-1/2)\cos[(X/\tau)\pi + \omega t] - (\sqrt{3}/2)\sin[(X/\tau)\pi + \omega t] - (-1/2)\cos[(X/\tau)\pi + \\ & \omega t] + (\sqrt{3}/2)\sin[(X/\tau)\pi + \omega t] - \cos[(X/\tau)\pi + \omega t] = 0 \end{aligned}$$

and this represents a circular rotating field with constant amplitude and speed.

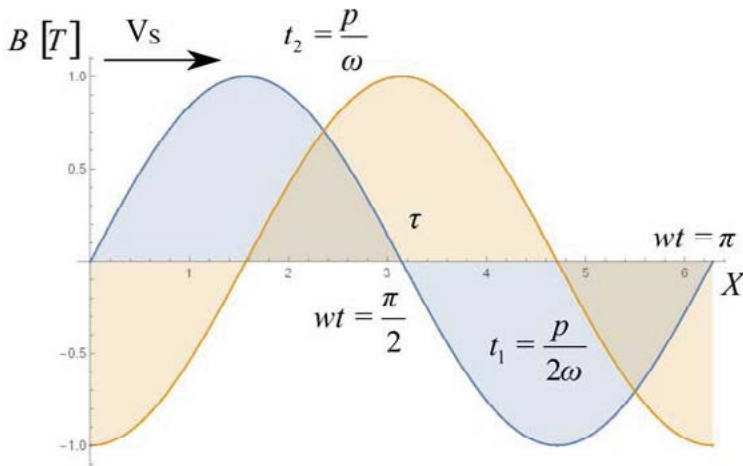


Fig. 5.9

$$\frac{X}{\tau} \pi - \omega t = ct$$

The resulting field has the speed:

$$V_s = \frac{dx}{dt} = \frac{d[(ct \cdot \tau + \omega \cdot t \cdot \tau) / \pi]}{dt} = \frac{\omega \tau}{\pi} = \underline{2 \cdot \tau \cdot f} \quad (5.16)$$

Synchronous field speed has the value:

$$n_1 = \frac{f}{p}$$

(because  $2p\tau = 2\pi R$  and  $V_s = \Omega R = 2\pi \cdot n_1 \cdot R$ ) and  $f = 50 \text{ Hz}$  we can obtain the following values:  $f = 50 \text{ Hz}$   $n_1 = 3000, 1500, 1000 \text{ rot/min}$ ;  $f = 60 \text{ Hz}$  yields  $n_1 = 3600; 1800; 1200; 900 \text{ rot/min}$ .



## 5.5 The orthogonal $dq$ mathematical model

Usually in literature, the three-phase system is often selected to rotate in the trigonometric direction (fig. 5. 10), causing rotating field to spin in the same direction.

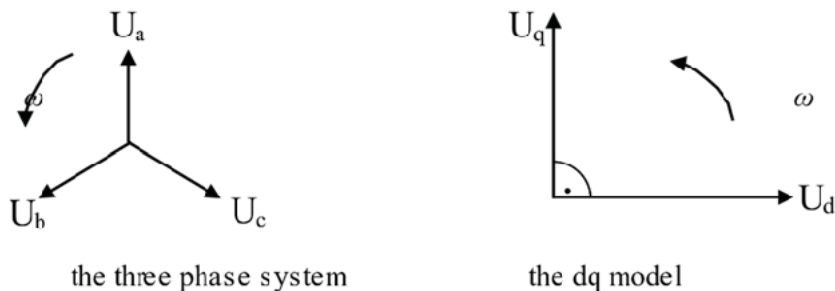


Fig. 5.10 Equivalence of the two models.

$$\begin{aligned} u_a &= U\sqrt{2} \sin \omega t \\ u_b &= U\sqrt{2} \sin(\omega t - 120^\circ) \\ u_c &= U\sqrt{2} \sin(\omega t + 120^\circ) \end{aligned} \quad (5.17)$$

The three-phase system is replaced by a two-phase system (the orthogonal pattern) along the  $d$  and  $q$  axes perpendicular to each other (fig. 5.11).

The orthogonal model allows a generalization of electric machine theory characterized by the use of a simple matrix writing of electric machine equations;

It is adequate to use the design of automatic control systems for electric drives;

It is suited for the representation of the variation in time of the electrical parameters.

Finding the voltages  $U_d$  and  $U_q$  used in the  $dq$  orthogonal system is realized by the PARK transformation, which involves the writing of the projections of the voltage vector on the two axes  $d - q$  for all the three-phase voltages  $U_a, U_b, U_c$ ;

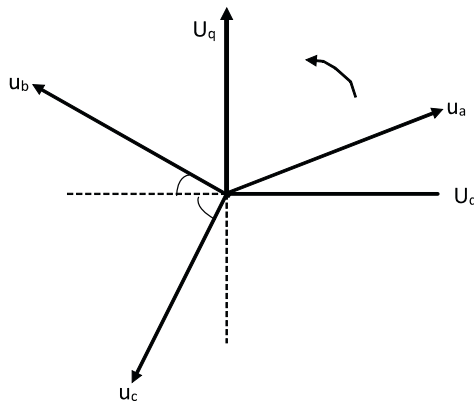


Fig. 5.11 Equivalence between the real three phase model and the dq model of the electric machine.

The equivalent two phase system of the dq model rotates with respect to the stator at the speed of the rotating field, the stator windings having traversed the equivalent dq currents (these are direct currents) with the brushes rotating at the angular speed  $\omega$ .

In stationary regime, the currents and voltages in the orthogonal model are constant over time. The following equations will make use of the synchronous coordinates ( $\omega_1 = 2\pi f$  – frequency of the power supply system).

Using the Park transformation, which essentially consists of the projection of the three-phase system on the axes of the orthogonal system dq, it can be written:

$$\beta = -(\theta + \omega t)$$

because it is assumed that the dq system is fixed and rotates the a, b, c system, but in reverse.

$$\begin{aligned} U_d &= \sqrt{\frac{2}{3}}[u_a \cos \beta - u_b \cos(60 - \beta) - u_c \cos(60 + \beta)] = \sqrt{\frac{2}{3}}[U\sqrt{2} \sin \omega t \cdot \cos \beta - \\ &- U\sqrt{2} \sin(\omega t - 120^\circ) \cdot \cos(60 - \beta) - U\sqrt{2} \sin(\omega t + 120^\circ) \cdot \cos(60 + \beta)] = \\ &= U \sqrt{\frac{2}{3}} \frac{\sqrt{2}}{2} [\sin(\omega t + \beta) + \sin(\omega t - \beta) - \sin(\omega t + 180^\circ + \beta) - \sin(\omega t + 60^\circ - \beta) - \\ &- \sin(\omega t - 60 - \beta) - \sin(\omega t - 180 + \beta)] = U(3 / \sqrt{3}) \sin(\omega t + \beta) = -U\sqrt{3} \sin \theta \end{aligned}$$

Likewise, it is possible to represent the voltage  $U_q$ :

$$\begin{aligned} U_q &= \sqrt{\frac{2}{3}}[u_a \sin \beta + u_b \cos(30 + \beta) - u_c \cos(30 - \beta)] = U\sqrt{2/3} \cdot \sqrt{2} [\sin \omega t \cdot \\ &\cdot \sin \beta + \sin(\omega t - 120) \cdot \cos(30 + \beta) - \sin(\omega t + 120) \cdot \cos(30 - \beta)] = \\ &= U / \sqrt{3} [\cos(\omega t - \beta) - \cos(\omega t + \beta) - \sin(\omega t + 150 - \beta) - \\ &- \sin(\omega t + 90 + \beta) + \sin(\omega t - 90 + \beta) + \sin(\omega t - 150 - \beta)] = -U\sqrt{3} \cos \theta \end{aligned}$$

Therefore:

$$\begin{aligned} U_d &= -U\sqrt{3} \sin \theta & U_d &= -U\sqrt{3} \sin \theta' \\ U_q &= -U\sqrt{3} \cos \theta & \text{or} & \\ U_q &= -U\sqrt{3} \cos \theta & U_q &= U\sqrt{3} \cos \theta' \end{aligned} \quad \text{at } \theta = \pi - \theta' \quad (5.17)$$

In the general situation, when the three-phase quantities are no longer sinusoidal in time (the transient regime), the introduction of the orthogonal or spatial voltage phases is done by:

$$\underline{U}_s = U_d + jU_q = \sqrt{\frac{2}{3}}(U_a + \underline{a}U_b + \underline{a}^2 U_c) \cdot e^{-j(\omega t + \theta_0)} \quad (5.18)$$

$$\underline{a} = e^{j\frac{2\pi}{3}} = -\frac{1}{2} + j\frac{\sqrt{3}}{2}; \quad \underline{a}^2 = e^{j\frac{4\pi}{3}} = -\frac{1}{2} - j\frac{\sqrt{3}}{2}; \quad \omega = 2\pi f$$

In sinusoidal mode the phase voltages are (fig. 5.12):

$$u_a = U\sqrt{2} \sin \omega t \tag{5.19}$$

$$u_b = U\sqrt{2} \sin(\omega t - 120^\circ) \tag{5.20}$$

$$u_c = U\sqrt{2} \sin(\omega t + 120^\circ) \tag{5.21}$$

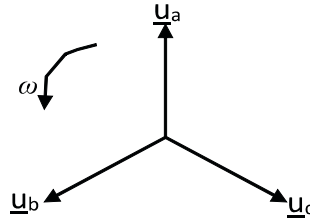


Fig. 5.12

In the situation when the rotor spins in the trigonometric sense we have:

$$U_d = -U\sqrt{3} \sin \theta_0 \tag{5.22}$$

$$U_q = U\sqrt{3} \cos \theta_0$$

Some observations need to be made:

1. The coefficient  $\sqrt{\frac{2}{3}}$  ensures normalization of electrical power expression (fig. 5.13).
2. The coefficient  $\sqrt{\frac{2}{3}}$  is also based on the equivalence of current linkage (fig. 5.14).

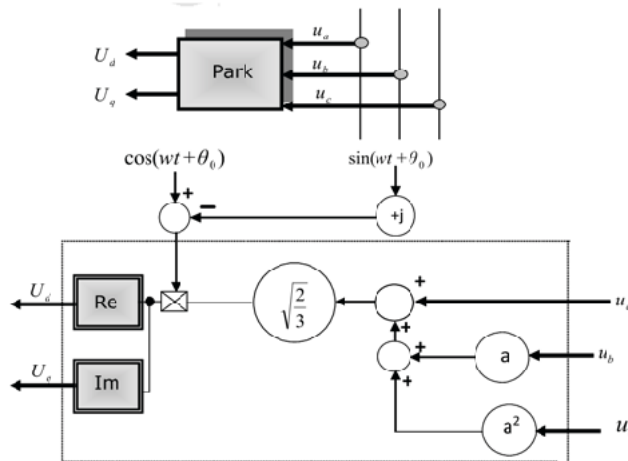


Fig. 5.13 System transformation block (three-phase to "dq") for voltage.

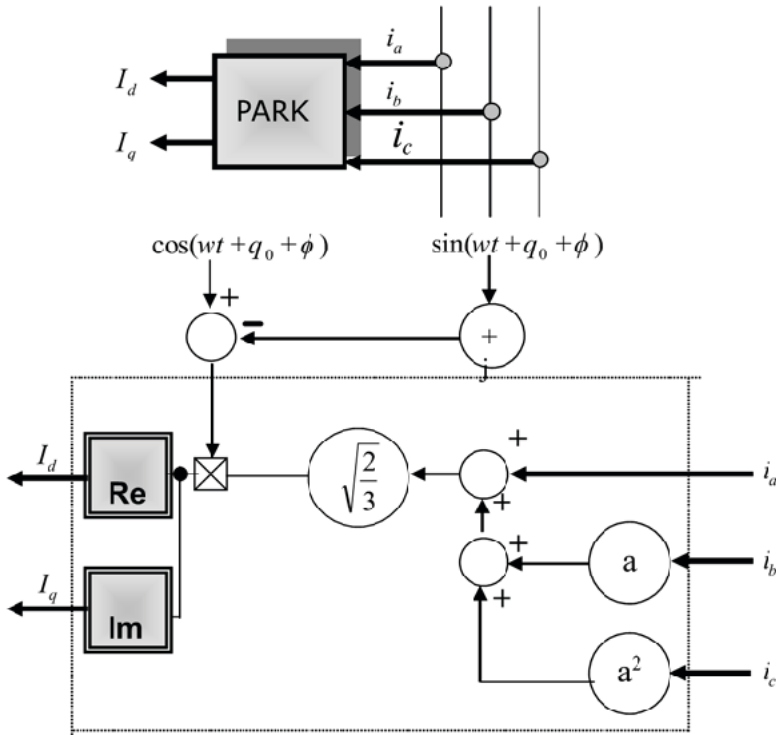


Fig. 5.14 System transformation block (three-phase to “dq”) for current.

## 5.6 The dq model of the synchronous and asynchronous machine

The dynamics of electromagnetic phenomena occurring in electric machines when they operate in various transient regimes can be studied both qualitatively and quantitatively considering an equivalent model of physical machine representation.

For this model, the winding currents have specific forms of variation in time during the transient regimes, respectively in stationary mode, they are constant over time if the reference system is considered to be the axis system synchronous to the rotating magnetic field. Using this mode of representation leads to a simple and particularly useful model – known in literature by the term the orthogonal model or the d-q (direct quadrature) model.

The orthogonal model, although used for the representation of the DC machines, can also be successfully used in the representation (modeling) of AC machines.

This chapter proposes a mathematical analysis of the orthogonal model equations in terms of the existence and uniqueness of the solution in the desire to mathematically fit the problems that this model raises: the influence of the precision of determining the parameters on the existence and the correctness of the solution of the differential equation systems, convergence and stability of systems of differential equations, methods of solving differential equation systems, etc.

## 5.7 The equations of the orthogonal model and the corresponding synchronous machines parameters

For the *Synchronous machine* (SM), the schematic representation in the orthogonal model is given in the figure below (fig. 5.15)

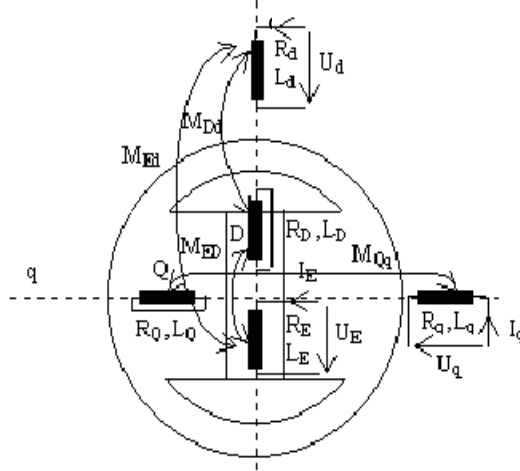


Fig. 5.15 The synchronous  $dq$  equivalent model machine.

The orthogonal equivalent model is defined by the relationships between the windings voltages and the currents passing through these windings influenced by the parameters of the electric machine. The matrix of equations in motor mode is given by the matrix relation given below [B2, B4].

$$\begin{bmatrix} U_d \\ U_q \\ U_E \\ 0 \\ 0 \end{bmatrix} = M \cdot \begin{bmatrix} I_d \\ I_q \\ I_E \\ I_D \\ I_Q \end{bmatrix} \quad (5.22)$$

with the M matrix

$$M = \begin{bmatrix} R_d + L_d \cdot p & -\omega L_q & M_{Ed} \cdot p & M_{Dd} \cdot p & -\omega M_{Qd} \\ \omega L_d & R_q + L_q \cdot p & \omega M_{Eq} & \omega M_{Dq} & M_{Qq} \cdot p \\ M_{Ed} \cdot p & 0 & R_E + L_E \cdot p & M_{ED} \cdot p & 0 \\ M_{Dd} \cdot p & 0 & M_{ED} \cdot p & R_D + L_D \cdot p & 0 \\ 0 & M_{Qq} \cdot p & 0 & 0 & R_Q + L_Q \cdot p \end{bmatrix} \quad (5.23)$$

where with  $p$  is noted the derivation operator  $\frac{d}{dt}$  and the matrix coefficients represent :

$$U_d, U_q, U_E, U_D = 0, U_Q = 0 \text{ - the voltages at the winding terminals}$$

$I_d, I_q, I_E, I_D, I_Q$  - currents in windings

$\omega$  - magnetic field rotating speed (angular electric pulse) ( $\omega = 2\pi f$ ),

$R_d, R_q, R_E, R_D, R_Q$  - resistance of windings

$L_d, L_q, L_E, L_D, L_Q$  - self inductances of the windings

$M_{Ed}, M_{Eq}, M_{Dd}, M_{Dq}, M_{ED}, M_{Qd}$  - mutual coupling inductances.

By conveniently ordering the lines and columns in the  $M$  (highlighting the matrix symmetry  $M$ ), the system (5.1) can be written in a matrix form :

$$A \cdot \begin{bmatrix} \frac{dI_d}{dt} \\ \frac{dI_E}{dt} \\ \frac{dI_D}{dt} \\ \frac{dI_Q}{dt} \\ \frac{dI_q}{dt} \end{bmatrix} + B \cdot \begin{bmatrix} I_d \\ I_E \\ I_D \\ I_Q \\ I_q \end{bmatrix} = \begin{bmatrix} U_d \\ U_E \\ 0 \\ 0 \\ U_q \end{bmatrix} \quad (5.25)$$

where

$$A = \begin{bmatrix} L_d & M_{Ed} & M_{Dd} & 0 & 0 \\ M_{Ed} & L_E & M_{ED} & 0 & 0 \\ M_{Dd} & M_{ED} & L_D & 0 & 0 \\ 0 & 0 & 0 & L_Q & M_{Qq} \\ 0 & 0 & 0 & M_{Qq} & L_q \end{bmatrix} \quad (5.26)$$

$$B = \begin{bmatrix} R_d & 0 & 0 & -\omega M_{Qd} & -\omega L_q \\ 0 & R_E & 0 & 0 & 0 \\ 0 & 0 & R_D & 0 & 0 \\ 0 & 0 & 0 & R_Q & 0 \\ \omega L_d & \omega M_{Eq} & \omega M_{Dq} & 0 & R_q \end{bmatrix} \quad (5.27)$$

electromagnetic torque is obtained from equation [B4]:

$$M_{elmag.MS} = p_1 [I_d I_q (L_d - L_q) + I_q I_E M_{Eq} - I_Q I_d M_{Qd} + I_q I_D M_{Dq}] \quad (5.28)$$

where  $p_1$  is the number of pole pairs.

To the system described by the equation (5.28), the motion equation needs to be added:

$$M_{elmag.MS} - M_{rezistent} = J \frac{d\Omega}{dt} \quad (5.29)$$

where  $J$  is the moment of axial inertia and  $\Omega$  (mechanical angular speed) defined by:

$$\Omega = \frac{\omega}{p_1} \quad (5.30)$$

In order to solve the system of differential equations, the matrix  $A$  formed with derivative coefficients has a decisive role. The determinant of this matrix has a value given by the expression:

$$\det A = (-L_q L_Q + M_{Qq}^2) \cdot (L_E M_{Dd}^2 + L_d M_{ED}^2 + L_D M_{Ed}^2 - L_d L_E L_D - 2M_{Ed} M_{ED} M_{Dd}) \quad (5.31)$$

Notice that it results from the relationship (5.31) that in order for the determinant of the matrix  $A$  to be null (a situation corresponding to the ideal synchronous machine) the following condition must be satisfied:

$$\begin{cases} (-L_q L_Q + M_{Qq}^2) = 0 \\ (L_E M_{Dd}^2 + L_d M_{ED}^2 + L_D M_{Ed}^2 - L_d L_E L_D - 2M_{Ed} M_{ED} M_{Dd}) = 0 \end{cases} \quad (5.32)$$

where it results:

$$M_{Qq}^2 = L_q L_Q \quad (5.33)$$

In conclusion, for the synchronous machines with magnetic flux leakage equal to zero (airgap length  $\delta \rightarrow 0$ , leakage coefficient  $\sigma \rightarrow 0 \Rightarrow M^2 \rightarrow L_1 L_2$ ), we may write the following relationships :

$$\begin{cases} M_{Qq}^2 = L_q L_Q \\ M_{Ed}^2 = L_E L_d \\ M_{ED}^2 = L_E L_D \\ M_{Dd}^2 = L_D L_d \end{cases} \quad (5.34)$$

Usually the corresponding  $A$  matrix determinant is nonzero because for the situation of real synchronous machines the following inequalities between inductances do exist.

## 5.8 Equations of the orthogonal model and the parameters of the asynchronous machine

The schematic representation for the asynchronous *machine* (ASM) with the rotor in short circuit in the orthogonal equivalent model is given in the figure below (fig. 5.16):

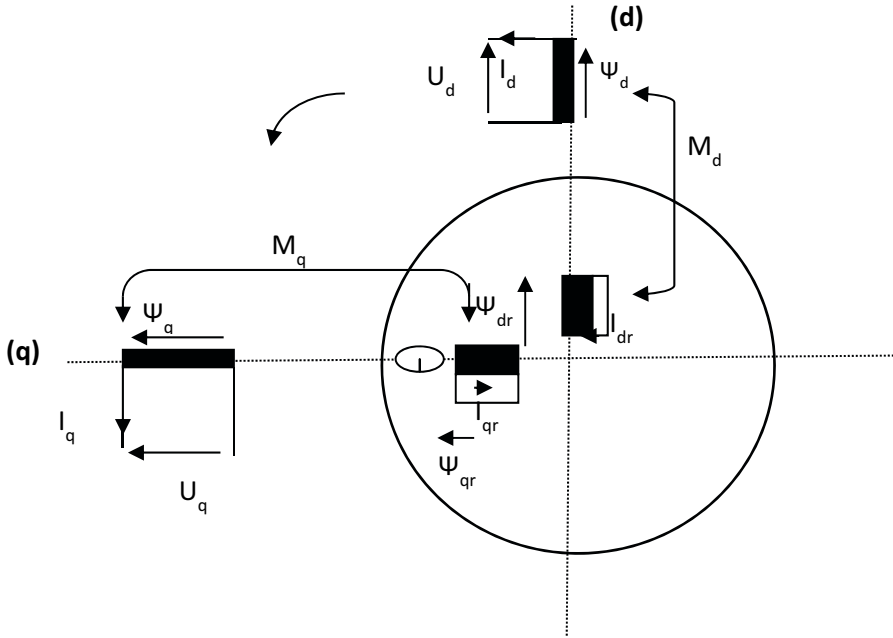


Fig. 5.16 The asynchronous machine *dq* orthogonal model.

The matrix writing (formulation) of the asynchronous machine equations for the motor regime is the one in the [B3].

$$\begin{bmatrix} U_d \\ U_q \\ 0 \\ 0 \end{bmatrix} = M \cdot \begin{bmatrix} I_d \\ I_q \\ I_{dr} \\ I_{qr} \end{bmatrix} \quad (5.35)$$

with the matrix M:

$$M = \begin{bmatrix} R_{1d} + L_{1d} \cdot p & -\omega_1 \cdot L_{1q} & M_d \cdot p & -\omega_1 \cdot M_q \\ \omega_1 \cdot L_{1d} & R_{1q} + L_{1q} \cdot p & \omega_1 \cdot M_d & M_q \cdot p \\ M_d \cdot p & -M_q (\omega_1 - \omega) & R_{2d} + L_{2d} \cdot p & -L_{2q} (\omega_1 - \omega) \\ M_d (\omega_1 - \omega) & M_q \cdot p & L_{2d} (\omega_1 - \omega) & R_{2q} + L_{2q} \cdot p \end{bmatrix} \quad (5.36)$$



where with  $p$  was noted the derivative operator  $\frac{d}{dt}$  and coefficients represent:

$U_d, U_q, U_{dr} = 0, U_{qr} = 0$  - voltages at the windings terminals,

$I_d, I_q, I_{dr}, I_{qr}$  - windings currents

$\omega_1$  - statoric magnetic field rotating speed ( $\omega_1 = 2\pi f$ ),

$\omega$  - rotor speed,

$R_{1d}, R_{1q}, R_{2d}, R_{2q}$  - windings resistances,

$L_{1d}, L_{1q}, L_{2d}, L_{2q}$  - windings self inductance;

$M_d, M_q$  - coupling inductance between the stator and the rotor windings.

By conveniently ordering the lines and columns in the matrix  $M$ , the system (5.36) may be written in the matrix form:

$$A \cdot \begin{bmatrix} \frac{dI_d}{dt} \\ \frac{dI_q}{dt} \\ \frac{dI_{dr}}{dt} \\ \frac{dI_{qr}}{dt} \end{bmatrix} + B \cdot \begin{bmatrix} I_d \\ I_q \\ I_{dr} \\ I_{qr} \end{bmatrix} = \begin{bmatrix} U_d \\ U_q \\ 0 \\ 0 \end{bmatrix} \quad (5.37)$$

where

$$A = \begin{bmatrix} L_{1d} & 0 & M_d & 0 \\ 0 & L_{1q} & 0 & M_q \\ M_d & 0 & L_{2d} & 0 \\ 0 & M_q & 0 & L_{2q} \end{bmatrix} \quad (5.38)$$

$$B = \begin{bmatrix} R_{1d} & -\omega_1 L_{1q} & 0 & -\omega_1 M_q \\ \omega_1 L_{1d} & R_{1q} & \omega_1 M_d & 0 \\ 0 & -M_q(\omega_1 - \omega) & R_{2d} & -L_{2q}(\omega_1 - \omega) \\ M_d(\omega_1 - \omega) & 0 & L_{2d}(\omega_1 - \omega) & R_{2q} \end{bmatrix} \quad (5.39)$$

The electromagnetic torque is determined by the equation [B3]:

$$M_{el\text{mag.MA}} = p_1 M [I_q I_{dr} - I_d I_{qr}] ; (M_d = M_q = M) \quad (5.40)$$

where  $p_1$  is the number of pole pairs.

To the system described by the equation (5.40), we need to add the motion equation:

$$M_{elmag.MA} - M_{rezistent} = J \frac{d\Omega}{dt} \quad (5.41)$$

where  $J$  is the moment of axial inertia and  $\Omega$  (mechanical angular speed) function defined by:

$$\Omega = \frac{\omega}{p_1} \quad (5.42)$$

In practice, for the sake of symmetry, we shall consider an AM with:

$$\begin{aligned} L_{1d} &= L_{1q} \stackrel{not}{=} L_1 \\ L_{2d} &= L_{2q} \stackrel{not}{=} L_2 \end{aligned} \quad (5.43)$$

Based on what has been previously stated, the matrix of derivative coefficients (5.38) becomes:

$$A = \begin{bmatrix} L_1 & 0 & M & 0 \\ 0 & L_1 & 0 & M \\ M & 0 & L_2 & 0 \\ 0 & M & 0 & L_2 \end{bmatrix} \quad (5.44)$$

and its determinant has the value given by the expression:

$$\det A = (M^2 - L_1 L_2)^2 \quad (5.45)$$

Typically  $L_1 L_2 > M^2$  and so  $\det A \neq 0$ . For asynchronous machines with small airgap, so with a strong magnetic coupling between the stator and rotor,  $L_1 L_2 \rightarrow M^2$  and so  $\det A \rightarrow 0$ .

In the motion equation because:

$$\Omega(t) = \Omega_1(t)(1 - s(t)) = 2\pi n_1(1 - s(t)) \quad (5.46)$$

It can be written:

$$J \frac{d\Omega}{dt} = -J \cdot 2\pi n_1 \frac{ds}{dt} \quad (5.47)$$

The slip can be written under one of the forms:

$$s = \frac{\Omega_1 - \Omega}{\Omega_1} = \frac{\omega_1 - \omega}{\omega_1} = \frac{n_1 - n}{n_1} \quad (5.48)$$

and the equation of the motion (5.41) becomes:

$$M_{el\text{mag},MA} - M_{rezistent} = -J\Omega_1 \frac{ds}{dt} \quad (5.49)$$

The equations of the orthogonal model of the asynchronous machine are concentrated in the form of relations (5.14) and (5.15) and by a convenient ordering of the lines and columns (so that the symmetry of the matrix is highlighted  $M$ ) results:

$$\begin{bmatrix} U_d \\ U_q \\ 0 \\ 0 \end{bmatrix} = \begin{bmatrix} L_{1d} & 0 & M_d & 0 \\ 0 & L_{1q} & 0 & M_q \\ M_d & 0 & L_{2d} & 0 \\ 0 & M_q & 0 & L_{2q} \end{bmatrix} \cdot \begin{bmatrix} \frac{dl}{dt} \\ \frac{dq}{dt} \\ \frac{dr}{dt} \\ \frac{qr}{dt} \end{bmatrix} + \begin{bmatrix} R_{1d} & -\omega_1 L_{1q} & 0 & -\omega_1 M_q \\ \omega_1 L_{1d} & R_{1q} & \omega_1 M_d & 0 \\ 0 & -M_q(\omega_1 - \omega) & R_{2d} & -L_{2q}(\omega_1 - \omega) \\ M_d(\omega_1 - \omega) & 0 & L_{2d}(\omega_1 - \omega) & R_{2q} \end{bmatrix} \cdot \begin{bmatrix} I_d \\ I_q \\ I_{dr} \\ I_{qr} \end{bmatrix} \quad (5.50)$$

## 5.9 Equivalation between the $dq$ orthogonal model and the real machine

The equivalence between the orthogonal model and the physical machine is in view of equality of current linkage and energy.

The real electric machine has windings placed at  $120^\circ$ , like in Figure 5.17 and the model machine at  $90^\circ$ .

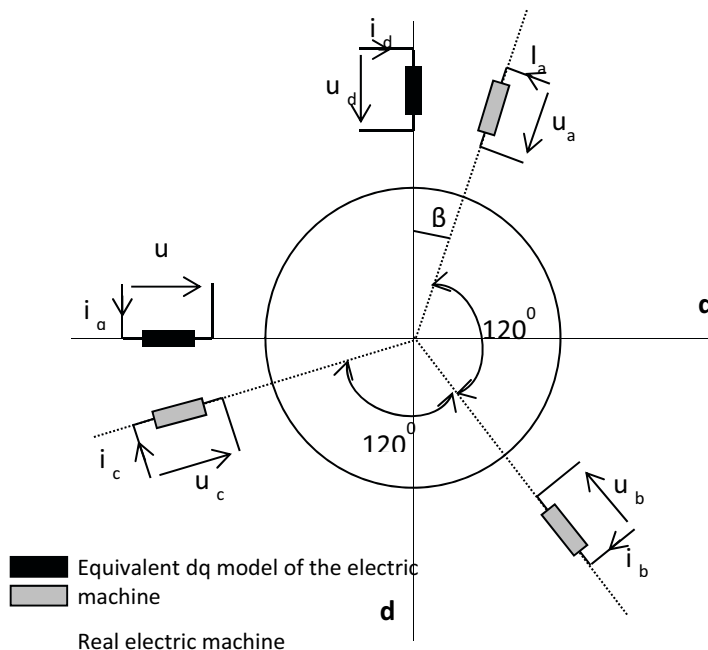


Fig. 5.17 Equivalence  $dq$  machine model – actual machine.

Actual variables  $i_a, i_b, i_c, u_a, u_b, u_c$  are found in the backward Park transformation, projecting the dq orthogonal model variables on to the three phase axis system corresponding to the voltage phase variable of the real abc model. It is then obtained for currents and voltages the following relationships, well known in literature:

$$i_a = \sqrt{\frac{2}{3}}(I_d \cos \omega t - I_q \sin \omega t) \quad (5.51)$$

$$i_b = \sqrt{\frac{2}{3}}[I_d \cos(\omega t - 120) - I_q \sin(\omega t - 120)] \quad (5.52)$$

$$i_c = \sqrt{\frac{2}{3}}[I_d \cos(\omega t + 120) - I_q \sin(\omega t + 120)] \quad (5.53)$$

resulting:

$$\underline{I}_s = I_d + jI_q = \sqrt{\frac{2}{3}}(i_a + \underline{a} i_b + \underline{a}^2 i_c) \cdot e^{-j(\omega t + \theta_0 + \varphi)}; \quad \left( \underline{a} = e^{j\frac{2\pi}{3}} \right) \quad (5.54)$$

and similarly for voltages:

$$u_a = \sqrt{\frac{2}{3}}(U_d \cos \omega t - U_q \sin \omega t) \quad (5.55)$$

$$u_b = \sqrt{\frac{2}{3}}[U_d \cos(\omega t - 120) - U_q \sin(\omega t - 120)] \quad (5.56)$$

$$u_c = \sqrt{\frac{2}{3}}[U_d \cos(\omega t + 120) - U_q \sin(\omega t + 120)] \quad (5.57)$$

resulting:

$$\underline{U}_s = U_d + jU_q = \sqrt{\frac{2}{3}}(u_a + \underline{a} u_b + \underline{a}^2 u_c) \cdot e^{-j(\omega t + \theta_0)}; \quad \left( \underline{a} = e^{j\frac{2\pi}{3}} \right) \quad (5.58)$$

On the basis of the above, in the figures 5.13 and 5.14 the transformation blocks for the current and for the voltage are presented.

### Conclusions

- The equations of the dq orthogonal model, in mathematical aspect, present simplicity and consistency, advantages that make the dq orthogonal model particularly useful in order to make the simplest and most accurate representation of the physical electric machine (real electric machine);

- Starting from the matrix based on the coefficients of the derivatives of the differential equation system, using the expression (literal) of the determinant of this matrix, you can find the range of the parameters of the synchronous electric machines (where the domain of the parameters is a 3d volume of unit area - one unit length *cube*) and asynchronous (In which the domain of the parameters is a 2D unit surface area - *one unit square*);
- Between the real machine (physical) and the dq equivalent model there must be certain connecting mathematical relationships, absolutely necessary, relationships which are synthetically presented in figures 1.9 respectively 1.10.

## 5.10 Mathematical modeling of the variable speed operation of the asynchronous machine

In order to control the frequency and voltage of the asynchronous machine based drives, the automatic control systems are currently based on regular PI and PID controllers, which are the essential elements of a Conventional Automatic Control System (CACS-c) (fig. 5.17).

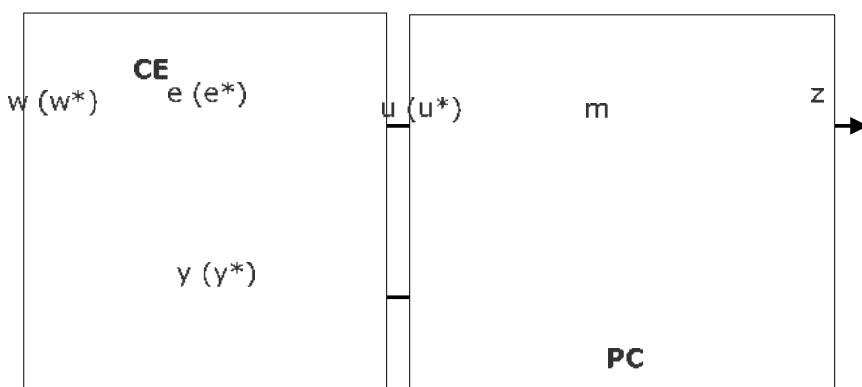


Fig. 5.17 Block diagram of an CACS –c.

CD – control device;

RG - regulator;

CE - comparison element;

CP – controlled process;

EE - execution element;

TP - the technical process that takes place in a technological installation;

ME - measurement element by which CD is informed about PC evolution;

SE – AD sampler;

SE + ZOH - sampler with zero order holder;

- $w(t)$  - reference variable of the automatic control system;
- $y(t)$  – measured variable corresponding to the output of the automatic control system;
- $e(t)$  - the adjustment error;
- $u(t)$  – command variable;
- $m(t)$  – control (execution) variable;
- $z(t)$  – controlled variable;
- $v(t)$  - perturbation

In order to become complete or accepted, a product characterized by a particular technical process has to be capable to have a level of integration of the management actions of that process, which may be manual (depending on human interaction), requiring an immediate intervention of the human, or automatic, their state depending on the control laws embedded using automation equipment. The constructive-functional ensemble, along with all the accessories related to control equipment, designed for the management of physical processes, is named the control device (DC).

Automatic control action involves commanding, adjusting and supervising the operation of the process.

The block diagram of an SRA-c is the following (fig. 5.18):

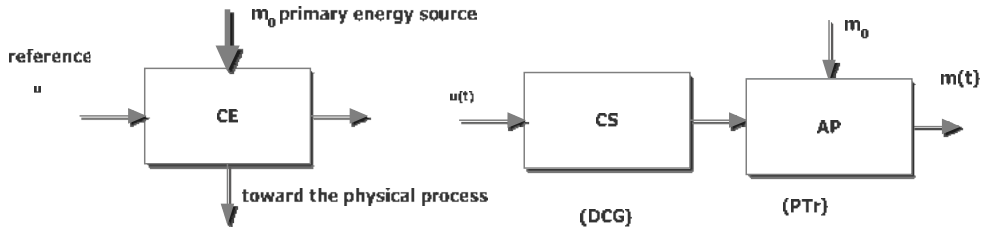


Fig. 5.18 Electrical execution element coupled with the static power converter.

The execution element block (EE) is designed to ensure the transfer of power/energy toward the technical process (TP). This type of element contains a signal converter (CS) and a power amplifier (AP).

The execution elements are designed according to the characteristics of process driven. In practice there are many type of execution elements: electric, non-electric (hydraulic, pneumatic) and mixed elements. In most cases, their input is an electrical signal (analog or digital) received from an electronic controller.

Three speed adjustment strategies are currently used:

- Speed control using constant stator flux (  $\psi_s = const.$  )

- Speed control using constant useful flux (  $\psi_u = const.$  )
- Speed using constant rotor flux (  $\psi_r = const.$  )

By providing the appropriate momentum values of voltage  $U$  and frequency  $f$ , one of the three control methods can be applied.

### 5.11 Mathematical model analysis from the point of view of the electromagnetic torque

In the case of first strategy (1)  $\psi_s = const.$  – constant statoric flux – the highest values of the electromagnetic torque are obtained.

Maximum torque in case (2) – constant useful flux – is approximately 20% lower than in the case of  $\psi_s = const.$

The smallest values of the torque are obtained when  $\psi_r = const.$  In this situation the mechanical characteristics being linear, the  $\psi_r = const.$  strategy is ideal for rapid control dynamics. In fast processes, where a system response is required in a short time, the rotary speed control to constant rotor flux is used, ( $\psi_r = const.$ ).

### 5.12 Mathematical model analysis from the point of view of the stator current

The lowest currents at the same rotoric speed are obtained when  $\psi_r = const.$  And the biggest ones result  $\psi_s = const.$  . At the same stator current the frequency of rotoric currents is highest at  $\psi_r = const.$ , resulting in this case the highest losses in the rotor winding.

Stator voltage  $U_s$  angular speed:

$$\omega = 2 \cdot \pi \cdot f \tag{5.58}$$

where  $f$  is the voltage frequency  $U_s$ ;

Rotor angular speed  $\omega_m$  has the value :

$$\omega_m = 2 \cdot \pi \cdot n \tag{5.59}$$

where  $n$  represents rotor speed .

Rotor currents have angular speed  $\omega_r$  obtained from the difference :

$$\omega_r = \omega - \omega_m \tag{5.60}$$

Dispersion coefficient  $\sigma$  of the asynchronous machine is calculated with the relationship:

$$\sigma = \frac{L_1 \cdot L_2' - M^2}{L_1 \cdot L_2'} \quad (5.61)$$

and is used in the voltage calculation  $U_s$  and frequency  $f$ .

### 5.13 Mathematical model for constant statoric flux variable speed control of the asynchronous machine

Stator voltage  $U_s$  at  $t = 0$  is determined using the relationship:

$$U_s(0) = \frac{\frac{R_1}{L_1} \sqrt{\left[ \left( \frac{R_2'}{L_2'} \right)^2 + \omega_r^2 \cdot \sigma \right]^2 + \left\{ \left( \frac{R_2'}{L_2'} \right) \cdot (1-\sigma) \cdot \omega_r + \left( \frac{L_1}{R_1} \right) \cdot \omega \left[ \left( \frac{R_2'}{L_2'} \right)^2 + \omega_r^2 \cdot \sigma^2 \right] \right\}^2}}{\left( \frac{R_2'}{L_2'} \right)^2 + \omega_r^2 \cdot \sigma^2} \cdot \Psi_s \quad (5.62)$$

Being given the **electromagnetic torque and rotor speed**, it results for the frequency of the supply voltage,  $f$ , and the value of the supply voltage,  $U_s$ .

Of the relationship :

$$M_{elmag} = 3 \cdot p_1 \cdot \Psi_s^2 \cdot \frac{\omega_r \cdot (1-\sigma) \cdot R_2'}{L_1 \cdot L_2' \left[ \left( \frac{R_2'}{L_2'} \right)^2 + \omega_r^2 \cdot \sigma^2 \right]} \quad (5.63)$$

### 5.14 Mathematical model for speed control of the asynchronous machine with constant useful flux

Initial time stator voltage  $U_s$  is obtained using the relationship:

$$U_s(0) = \frac{\Psi_u}{L_u} \cdot \frac{\sqrt{R_1^2 + (\omega \cdot L_1)^2 + \frac{\omega \omega_r \cdot L_2'}{R_2'} \cdot 2R_1 \cdot (1-\sigma) \cdot L_1 + \left( \frac{\omega_r \cdot L_2'}{R_2'} \right)^2 \cdot [R_1^2 + (\omega \sigma \cdot L_1)^2]}}{\sqrt{1 + \left( \frac{\omega_r \cdot L_2' \sigma}{R_2'} \right)}} \cdot [V] \quad (5.64)$$

magnetic - torque  $M_{elmag}(0)$ .



Being given the **electromagnetic torque and rotor speed**, the frequency of supply voltage  $f$ , and the value of the supply voltage  $U_s$ .

Of the relationship:

$$M_{elmag} = 3 \cdot p_1 \cdot \psi_u'^2 \cdot \frac{\omega_r \cdot (1 - \sigma) \cdot R_2'}{L_1 \cdot L_2' \left[ \left( \frac{R_2'}{L_2} \right)^2 + \omega_r^2 \cdot \sigma^2 \right]} \quad (5.67)$$

### 5.15 Mathematical model for speed control of the asynchronous machine at constant rotor flux

Stator voltage  $U_s$  at the initial moment was determined using the relationship:

$$U_s(0) = \frac{\psi_r'}{L_u} \sqrt{R_1^2 + (\omega \cdot L_1)^2 + \left( \frac{\omega_r \cdot L_2'}{R_2} \right) \cdot 2 \cdot \omega R_1 \cdot (1 - \sigma) \cdot L_1 + \left( \frac{\omega_r \cdot L_2'}{R_2} \right)^2 + \left[ R_1^2 + (\omega \sigma L_1)^2 \right]} \quad (5.68)$$

Being given the **electromagnetic torque and rotor speed**, the corresponding frequency of supply voltage,  $f$  and the value of the supply voltage,  $U_s$ .

From the relationship:

$$M_{elmag} = 3 \cdot p_1 \cdot \psi_r'^2 \cdot \frac{\omega_r \cdot (1 - \sigma) \cdot R_2'}{L_1 \cdot L_2' \left[ \left( \frac{R_2'}{L_2} \right)^2 + \omega_r^2 \cdot \sigma^2 \right]} \quad (5.69)$$

### 5.16 Conclusions regarding the dynamics of the asynchronous machine

- 1) To maintain constant flux (statoric, useful or rotor), when changing the speed (or  $\omega_r$ ), the supply voltage should decrease when the speed is increasing and increase when the speed is dropping.
- 2) At steady speed when the torque is increased (hence  $\omega_r$ ), the frequency and voltage should increase and maintain constant flux.
- 3) For  $U_s$  and  $f$  Constant the flux changes with the RPM and the lowest value is  $n = 0$  and the highest value is at  $n = n_1$ , this is because  $\sigma \rightarrow 0$  can be written as:

$$U_s = \psi_s \sqrt{A - B \omega_m}$$

and so

$$\psi_s = \frac{U_s}{\sqrt{A - B\omega_m}}$$

Voltage value  $U_s$  and of the frequency  $f$  is determined by the speed  $n$  and the load couple  $M_{rez}$ .

- 4) During transient regimes when passing from Point A( $n_1, M_{1elmag}$ ) at point B( $n_2, M_{2elmag}$ ), the magnetic fluxes through the machine (stator, useful or rotor flux) are no longer constant and oscillate around the stationary regime value, not exceeding 6%.
- 5) The two controllers, for voltage and frequency are characterized by time constant  $T_i$  and amplification factor K, whose values influence the duration of the transitional regime in  $A \rightarrow B$  and represent an important issue for the automation design engineer.

The asynchronous machine ASM, different than (Synchronous machine) SM is used in load-shock applications although the SM is superior with more precise speed control and capable to provide reactive power. It is currently a competition between ASM and SM – where one is better than another.

## 5.17 Mathematical modeling of speed control of synchronous machines

### 5.17.1 The necessity to use variable frequency

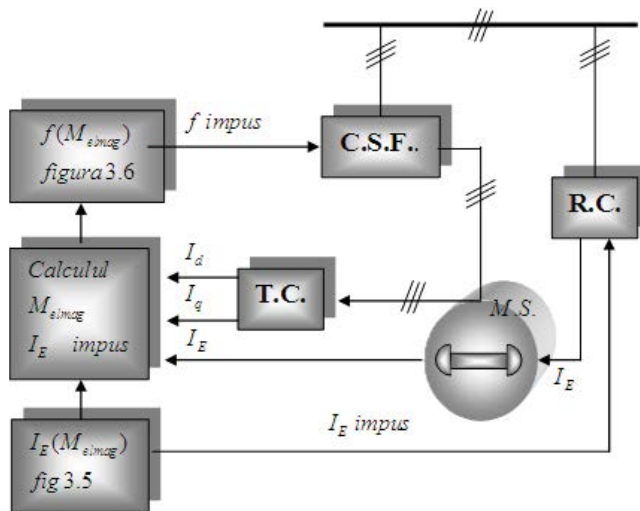


Fig. 5.19 The control structure for  $\psi_s = ct$ .

Synchronous machine works at the speed  $n_1 = \frac{f_1}{p_1}$ , regardless of the torque value at the

shaft. To change the speed, we need to change the frequency  $f$  of the power supply voltage. As speed depends rigorously on the value of the frequency, it follows that the supply frequency of synchronous machine can impose precisely the value of the rotary speed. In the following diagram the block CSF (fig. 5.19):

C.S.F. – static frequency converter;

T.C. – system transformation block for currents („three-phase” – “D-Q”);

R.C. – controlled rectifier.

### 5.17.2 The requirement for the use of the variable voltage power supply

As it was stated before in the case of asynchronous machines, any modification of the frequency requires an additional change in the value of the supply voltage, in order not to saturate the ferromagnetic core.

The frequency and voltage adjustment (as a scalar value) is based on two methods namely:

- 1). Constant stator flux control (used in synchronous machines with dc current excitation);
- 2). Constant rotor flux control (used in synchronous machines with permanent magnets excitation).

## 5.18 Mathematical model of synchronous machines during the speed control with constant stator flux

In case of synchronous machines (SM) with dc excitation, this is able to change the excitation current  $I_E$  in such manner that the MS operation will be performed at a maximum power factor ( $\cos \phi = 1$ ). In these conditions, the SM modeling is based on the following equations:

$$\left. \begin{array}{l} I_q = I \cos \theta \\ L_q I_q = \psi_s \sin \theta \end{array} \right\} \Rightarrow \operatorname{tg} \theta = \frac{L_q I}{\psi_s} = \frac{L_q M_{el\text{mag}}}{p_1 \psi_s^2}$$

- Stator voltage equation:

$$U = I \cdot R + 2 \cdot \pi \cdot f \cdot \psi_s \quad (5.70)$$

- The equation of the load angle:

$$\operatorname{tg} \theta = \frac{L_q M_{el\text{mag}}}{p_1 \psi_s^2} \quad (5.71)$$

- Electromagnetic torque equation:

$$M_{elmag} = p_1 [I_d I_q (L_d - L_q) + M_{Ed} I_q I_E] = p_1 \psi_s I \quad (5.72)$$

- Current excitation equation:

$$I_E = \frac{p_1^2 \psi_s^4 + L_d L_q M_{elmag}^2}{p_1 \psi_s M_{Ed} \sqrt{(p_1 \psi_s^2)^2 + (L_q M_{elmag})^2}} \quad (5.73)$$

where:

$R, L_q, L_d, M_{Ed}$  – parameters of the SM model;  $\psi_s$  – stator flux (known value);

## 5.19 Mathematical model of synchronous machines during speed control with constant rotor flux

In case of the synchronous machines with permanent magnets (MP), the magnetic flux given by MP is constant.

The condition for  $\cos \phi = 1$  it is written in the form:

$$-\frac{I_d}{I_q} = \frac{L_q I_q}{\psi_{MP} + L_d I_d} \quad (5.74)$$

From the matrix equation of SM, in permanent mode, it can be written:

$$\begin{cases} U_d = R I_d - \omega L_q I_q \\ U_q = R I_q + \omega L_d I_d + \omega M_E I_E = R I_q + \omega L_d I_d + \omega \psi_{MP} \end{cases} \quad (5.75)$$

or by using the square and gathering results :

$$U^2 = I_q^2 [R^2 + (\omega L_q)^2] - 2 I_q [\omega L_q R I_d - \omega R (\psi_{MP} + L_d I_d)] + \omega^2 (\psi_{MP} + L_d I_d)^2 + (R I_d)^2 \quad (5.76)$$

The electromagnetic torque is calculated with the relationship:

$$M_{elmagMP} = p_1 [(L_d - L_q) I_d I_q + \psi_{MP \text{ model}} I_{q \text{ model}}] = 3 p_1 [(L_d - L_q) I_{d \text{ real}} I_{q \text{ real}} + \psi_{M \text{ Preal}} I_{q \text{ real}}] \quad (5.77)$$

Previous equations form the system:

$$\begin{cases} -\frac{I_d}{I_q} = \frac{L_q I_q}{\psi_{MP} + L_d I_d} \\ U^2 = I_q^2 [R^2 + (\omega L_q)^2] - 2 I_q [\omega L_q R I_d - \omega R (\psi_{MP} + L_d I_d)] + \omega^2 (\psi_{MP} + L_d I_d)^2 + (R I_d)^2 \\ M_{elmagMP} = p_1 [(L_d - L_q) I_d I_q + \psi_{MP \text{ model}} I_{q \text{ model}}] = 3 p_1 [(L_d - L_q) I_{d \text{ real}} I_{q \text{ real}} + \psi_{M \text{ Preal}} I_{q \text{ real}}] \end{cases}$$

## 5. 20 References

- [1] Kopylov, P. (1984), "Mathematical models of electric machines", Moscow: Mir.
- [2] Nasar, S. (1987), "Handbook of electric machines", New York: McGraw-Hill.
- [3] Dordea, T., & Ministerul Învățământului, (1970), "Mașini electrice", București, Editura Didactică și Pedagogică.
- [4] Babescu, M. (2000), "Mașini electrice: Modelul orthogonal", [mașini electrice] (Master), Timișoara, Editura Politehnica.
- [5] Babescu, M. (2009), "Vehicule electrice hibride", (Mașini Electrice), Timișoara, Editura Politehnica.
- [6] Păunescu, D., & Babescu, M. (2005), "Analiza matematică a dinamicii mașinilor electrice", (Energetica), Timișoara, Editura Politehnica.
- [7] Babescu, M., & Păunescu, D. (2001), "Mașini electrice: Analiza matematică a regimurilor tranzitorii", (Energetica). Timișoara, Editura Politehnica.

At first glance, the design of electrical machines seems to be a procedure that is not very complex, as it is theoretically defined by the Maxwell system of equations, a system which describes the electromagnetic theory in a macroscopic scale [1]. According to the Maxwell macroscopic theory, electromagnetic phenomena in stationary and dynamic regimes are described by a system formed by 8 general laws and 4 material laws. However, the practice of analyzing and designing electrical machines is extremely complex, an eloquent example being the monography "Electrishe Maschinen" written in five volumes, elaborated by Rudolf Richter, with the first edition published in the '30s, and a revised, second edition, in 1954 [2][3][4][5][6]. The difficulties that appear when elaborating performing procedures for designing electrical machines are generated by the existence of nonlinear characteristics of ferromagnetic materials, the complex geometry of the magnetic circuit (the presence of the poles, armature slots), the complex theoretical models used for manipulating the losses in the magnetic core and in massive conductors, the dimensional standardization of constructive elements (the thickness of the sheets, the geometric dimensions of the conductors, the insulators' dimensions). All of these technological realities have determined the elaboration of complex designing procedures, which combine analytical relations, relations derived from the designing experience, coefficients approximated through value intervals, material characteristics, and choices of standardized materials. If we add to the elements that characterize the electromagnetic design of electrical machines the ever-growing requirements regarding the imposed performances (efficiency, cost, masses, sizes, power densities) and the necessity of evaluating the thermic and mechanic behaviors (noise and vibration), we acquire the dimension of actual complexity of the design procedures of electrical machines.

The major event that determined the evolution of design procedures was the introduction of the digital computer. When the price of the computer became accessible to universities and electrical machine-producing companies, a fundamental shift of the thought process behind the design of electrical machines took place. This shift had three major directions:

- the development of software dedicated to analytical design implementation
- the development of optimizing algorithms
- the development of 2D/3D modelling/simulation with a finite element methods (FEM)

It should be reminded that in the '50s - '60s, before digital computers and software dedicated to optimal design were introduced, in the design collectives within the electrical machine-producing companies a quasi-optimization strategy was used. It involved the design objective to be proposed to 2-3 design groups, and each group was to achieve several solutions. This way, 15-20 solutions were obtained, from which the one that generated the best performances was selected.

## 6.1. Optimization algorithms. The heuristic syntagma

The classic optimization methods are based on differential calculus and calculus of variations, respectively on the mathematical works of Newton, Leibnitz, Euler, Lagrange, Cauchy and Weirstrass. Essentially, the mathematicians of the 17<sup>th</sup> – 18<sup>th</sup> century theoretically solved the most important aspects of optimization problems, including the problem of subjected-to-constraints optimization, and, in the first half of the 20<sup>th</sup> century, no notable processes were recorded. In 1947, American mathematician George Dantzig elaborated the formulation of the general linear programming problem, proposing the famous solving method Simplex. The introduction of digital computers in the '50s - '60s led to the explosion of numerical methods, along with uses in the solving of optimization problems. In the '60s, Rosen and Zoutendijk elaborated the nonlinear programming theory, Carroll, Fiacco and McCormick applied the methods of non-constrained optimization on solving the most complex problems of nonlinear optimization, and Peterson, Zener and Duffin laid the foundation of geometric programming. In the '50s as well, American mathematician Ralf Gomory developed the concept of integer programming, respectively optimization problems where the variables are restricted as integers. This way, classic optimization problems managed to be solved through dedicated numerical methods.

An optimization problem is described by the following mathematical model [7][8]:

Calculate the variable set:

$$X = \left\{ \begin{array}{c} x_1 \\ x_2 \\ \cdot \\ \cdot \\ \cdot \\ x_n \end{array} \right\} \quad (6.1)$$

which minimizes the function  $f(X)$ , function which is subjected to the constraint set:

$$\begin{aligned} h_1(x_1, x_2, \dots, x_n) &= 0 \\ h_2(x_1, x_2, \dots, x_n) &= 0 \\ h_i(x_1, x_2, \dots, x_n) &= 0 \\ g_1(x_1, x_2, \dots, x_n) &\leq 0 \\ g_2(x_1, x_2, \dots, x_n) &\leq 0 \\ g_m(x_1, x_2, \dots, x_n) &\leq 0 \end{aligned} \quad (6.2)$$

with the conditions:

$$x_{i,\min} \leq x_i \leq x_{i,\max} \tag{6.3}$$

where:

$x_1, x_2, \dots, x_n$  = design variables

$f_{(x_1, x_2, \dots, x_n)}$  = objective function (**cost**), for an n parameters function

$x_{i,\min}$  = minimum value permitted by the  $x_i$  parameter

$x_{i,\max}$  = maximum value permitted by the  $x_i$  parameter

The (6.1) relation defines the objective function of the optimization problem. If the problem contains several objective functions that have to simultaneously be fulfilled, the problem is a multi-objective optimization. In the engineering practice, multi-objective optimization problems contain contradicting requirements (for example, optimizing efficiency and cost).

The (6.2) relations define the restrictions to which the objective function is being subjected. There can be harsh restrictions (expressed through the  $h_i$  equation set), which generate curves in the solution's feasible region, with the requirement that the optimization problem's solutions  $\{x_1, x_2, \dots, x_n\}$  to be placed on these curves or loose restrictions (expressed through the  $g_i$  in equation set), which generate subdomains in the solution's feasible region, with the requirement that the optimization problem's solutions  $\{x_1, x_2, \dots, x_n\}$  to be placed at the intersection of the subdomains generated by the system of in equations.

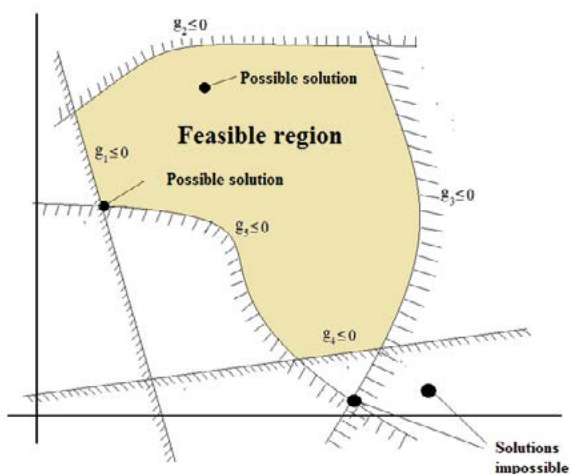


Fig. 6.1 Feasible region for the optimization problem, with restrictions considered.

The (6.3) relations define the dimension of the initial feasible region. Mathematicians follow the algorithms' behavior in a general case and consider the feasible region to be infinite, when it is theoretically allowed:  $-\infty \leq x_i \leq +\infty$ .

In the engineering practice, this way of defining the feasible region does not make any sense. Additionally, restricting the search domain significantly reduces the optimization problem's difficulty, and implicitly the one of the running time of the algorithm. The correct fixing of the design variables' limits is a delicate problem, which involves good knowledge of the design problem. In the absence of practical experience, there is the



possibility of defining the design variables' limits too close, with the possibility of leaving the optimal solution outside of the feasible region, or defining the design variables' limits too close, unnecessarily complicating the difficulty of the problem.

In accord with the mathematical nature of the equations several methods, optimization techniques have developed: linear programming, integer programming (the solutions are integers), non-linear programming, square programming, minimax optimization, uni-objective or multi-objective, optimization with/without constrains, non-linear curve approximations, fitting problems based on the smallest squares method with/without constraints. The variety of optimization problems imply different mathematical theories, specific numerical solving methods, dedicated software, which mean amplified costs both for purchasing a general classic optimization problem-solving software and for staff specialization.

Analyzing the general mathematical model of the optimization problem we find from (6.1) that the objective functions expressed through either a unique mathematical relation (in case of uni-objective problems) or through two or more relations (in case of multi-objective problems). Assuming that a concrete problem of optimal design of an electric machine follows the sizing of the electromagnetic circuits for imposed voltages, torques, currents, maximizing efficiency as an objective function, we find that we cannot express efficiency through a unique analytical expression. The electric machine's efficiency cannot be calculated using a unique analytical expression that contains all of the design data. The efficiency is the result of a design procedure capable of calculating the geometry of the electromagnetic core, the coils, the electromagnetic and electric parameters like losses in the core and coils, inductances, resistances. Because of this, the general optimization tools of Matlab-Simulink are impossible to use. For the optimal design of electrical machines the relation (6.1), which defines the objective function, is replaced by a software design, capable of generating, at the end of the procedure, the efficiency value. This must be taken into account when elaborating an optimization algorithm [9].

A possible classification of optimization techniques would be shown in table 6.1.

Table 6.1.

<b>Classic optimization methods</b>	<b>Modern optimization methods</b>
<ul style="list-style-type: none"> <li>-graphical optimization</li> <li>-calculus methods</li> <li>-calculus of variations</li> <li>-linear programming</li> <li>-nonlinear programming</li> <li>-geometric programming</li> <li>-quadratic programming</li> <li>-integer programming</li> <li>-stochastic programming</li> <li>-binary programming</li> <li>-combinational search</li> <li>-search methods</li> </ul>	<ul style="list-style-type: none"> <li>-genetic algorithms</li> <li>-particle swarm optimization</li> <li>-simulated annealing</li> <li>-ant colony optimization</li> <li>-artificial bee colony algorithm</li> <li>-gravitational search algorithm'</li> <li>-imperialist algorithm</li> </ul>

In order to present the modern methods of optimization, it is necessary that we know the history of the mathematical concepts that allowed their development. In 1936, English mathematician Alan Turing publishes *"On Computable Numbers with an Application to the Entscheidungs problem"*. Developing the lambda model, proposed by the American mathematician Alonzo Church, the concept of "Turing Machine" is defined for the first time. This concept defines that it is possible for a machine to deduce any formal mathematical reasoning [10]. Although Alan Turing was not interested in publishing the results of his research, today it is generally accepted that both digital computers and artificial intelligence (IA) have their roots in his works. In the '50s, mathematicians' involvement in the research regarding numerical solving algorithms and mathematical models of biological systems grows exponentially. Interest for creating mathematical models of biological systems sparked in the '40s, during the World War, when American mathematician Norbert Wiener involved in calculating and directing the artillery's trajectories, and having a significant knowledge of biology, manages to formulate the mathematical model of the physiological behavior of living organisms, introducing the concept of cybernetics. His book, published in 1948, *"Cybernetics or Control and Communication in the Animal and the Machine"*, represents a turning point in the evolution of science and technology in the 20<sup>th</sup> century [11]. In the '40s as well, American mathematician Stanislaw Ulam, member of the Manhattan project team, developed the concept of *Cellular Automata*, used in mathematics, nuclear physics and computers. A cellular automaton is a regular network of cells of two or more dimensions, with each cell being capable of multiple states and each cell having a set of cells as neighbors. Using these concepts, in the '60s, English mathematician John Conway develops a concept named *"Game of Life"*. The game involved a two-dimensional cellular network, defined by a set of rules:

- there should be no explosive growth (of the number of cells)
- there should be small initial patterns with chaotic, unpredictable outcomes
- there should be potential for von Neumann universal constructors –the von Neumann universal constructor is an auto-replicating machine placed in a cellular automaton (cells can reproduce)
- the rules should be as simple as possible, whilst adhering to the above constraints

From the start, the model was seen as having a high potential for developing algorithms that would model behaviors from biology, economy, sociology, military strategies, space flights, and was used in the development of simulation games based on real-life processes. Along these mathematical researches that developed biological models, we have to mention *"Evolution Strategies"* by German engineer Ingo Rechenberg, published in 1960 [12]. The algorithms of the evolutionary strategies have as an objective maximizing the adequate selection of potential solutions that aspire to the solution of an optimization problem. The selection of possible solutions is done by using *methods*.

Although heuristic methods have been applied (especially in the 20<sup>th</sup> century) in extremely diverse fields (philosophy, operational calculus, optimizations, economy, psychology, biology), they have had a long history, peaking the interest of several of the mathematicians that wanted to minimize the complexity of some procedures and to obtain new methods of selecting a set of suboptimal solutions that were sufficiently accurate. German mathematician and philosopher Leibnitz, trying to develop a universal algorithm that could solve any possible problem, using a universal language of problem representation, concluded that this algorithm approach inevitably led to a combinatorial explosion. From this, the necessity of having the heuristic approach reduce the exhaustive search space appeared. Likewise, French mathematician and philosopher Descartes formulated a simple set of rules for solving mathematical problems, in which the effort focused on the relevant aspects, to the detriment of other information mentioned. In the 19<sup>th</sup> century, mathematician Bolzano, in "*Theory of Science*"; proposes a set of heuristic practices used in solving problems, trying to find a method that would deduce the truth from information that was yet to be determined as true, in contrast to the methods originated from formal logic, that would determine the truth based on a series of previously known true statements. All of these approaches propose a shortcut towards knowledge, beyond algorithmic solutions, a shortcut that was vaguely described but one that encouraged creative thinking.

The modern foundation in heuristic mathematics was made by American mathematician George Polya, who in "*How to Solve It*" structured the principles of heuristics that applied to the solving of both mathematical and non-mathematical problems and fixed the fundamental terms of the heuristic method [13].

In the aforementioned book, he defines the four principles of the heuristic approach:

- understand the problem (in a lot of cases this step is treated superficially)
- elaborate a plan (because there are several ways of solving a problem, the proper strategy must be chosen, based on former experience. The following set of rules is applied, when elaborating a plan: take into consideration the special cases, use symmetries, eliminate several possibilities, search for a model, and solve a simpler model)
- implement the plan (perseverance is necessary in the implementation of the plan, but if the plan is not working, it is necessary to quit and elaborate a new plan)
- revise/expand the method (this step is important in developing the experience of the author)

The terms of the heuristic field proposed by Polya are: *Analogy, Auxiliary Elements, Auxiliary Problem, Decomposing & Recombining, Generalization, Here is a Solved Problem (Pattern Recognition), Variation of the Problem, Working Backward.*

In the field of optimization, heuristic algorithms allow for the obtainment of suboptimal solutions, placed in the vicinity of the optimal solution, with a computational effort that is

significantly reduced. The major problems of the heuristic methods are the inability of guaranteeing the exact optimal solution, stopping at low-quality, suboptimal solutions. These can be rectified by providing a high number of additional iterations.

The next step was developing metaheuristic methods, capable of exceeding the limits of heuristic methods. A metaheuristic algorithm can be considered as a set of algorithms that use heuristic methods, capable of solving different problems of high complexity. In the field of optimization, the metaheuristic algorithm can be defined as a general method that orientates the search in the regions of the search space that have the highest probability of containing high-quality solutions, as close as possible to the optimal of the problem. Additionally, the metaheuristic methods are able to be applied to all types of optimization problems (linear, nonlinear, quadratic, etc.). This latter quality was the decisive factor for the commercial success of the metaheuristic optimization algorithms.

All of these concepts allowed the American mathematician J Holland, University of Pittsburgh, in the '70s, to propose a metaheuristic optimization algorithm inspired by the Darwinist biological metaphor of evolutionism. In his book *"Adaptation in Natural and Artificial Systems"*, published in 1975, he introduces an algorithm called *Holland's Schema*, capable of providing predictions of the quality of a set of an optimization problem's solutions [14]. His students, Kenneth De Jong and David Goldberg, in their PhD theses and later works, respectively *"An Analysis of the behavior of a Class of Genetic Adaptive Systems"*[15] and *"Genetic Algorithm In Search, Optimization and Machine Learning"*[16] have significantly marked the theory of genetic algorithms. In 1985, at the University of Pittsburgh, the first international conference dedicated to genetic algorithms is held, and in 1980 General Electric launches the first commercial product, a tool-kit with GA dedicated to industrial applications. Along the American researchers, we have to mention the German school, represented by I. Rechenberg, P. Bienertand H. P. Schwefel, from the Technical University of Berlin, who also developed in the '60s – '70s the field of *Evolutionary Strategies/Evolutionary Programming*, elaborating metaheuristic algorithms inspired by the same biological metaphor.

## 6. 2 The genetic optimization algorithm

The Genetic Algorithm is the most studied and used metaheuristic method of solving optimization problems, using the Darwinist biological metaphor of the evolution of species through the selection and reproduction of the most adapted individuals. Darwin's biological metaphor is resumed in the following steps [17] [18] [19]:

- all organisms are continuously subjected to the process of adapting to the environment, which is complex, always-changing and hostile;
- during the evolution process, organisms accumulate information that is codified and stored in the species' chromosomes;

-the characteristics and performance of an organism are highlighted by the process of decoding/reading of the chromosomes' information;

-following the evolution process, the best adapted and performant individuals will survive and pass down their genetic information, and in the course of generations they will determine the continuous growth of the average performance of the new population.

The evolutionary biological mechanism was mathematically transcribed through functional models of the genetic algorithm, described by Holland and De Jong as being primarily a search method for the solution of an optimization problem. Interpreted in this way, genetic algorithms are iterative techniques of global stochastic searching, with the goal of optimizing the evaluation function, and having the following characteristics:

- Non-derivative methods
- Simple, powerful and of general use methods
- Robust and auto-adaptive methods

In Table 6.2 the pairs of terms specific to the genetic/biologic algorithm are exemplified:

Tabel 6.2.

<b><i>Biological Terminology</i></b>	<b><i>A.G./Optimization Terminology</i></b>
<i>Population</i>	<i>A multitude of possible solutions for an optimization problem (multitudes of points belonging to the search domain. The domain is n-dimensional)</i>
<i>Chromosome /Individual</i>	<i>A point belonging to the multitude of solutions that define the population. It is n-dimensional (it has n parameters). It is a possible solution to the optimization problem. In the case of a population, all individuals have the same dimension.</i>
<i>Gene</i>	<i>The mathematical expression of a parameter in the chromosome.</i>
<i>Generation</i>	<i>An iteration in G.A.</i>
<i>Allele</i>	<i>The value of the gene for a particular chromosome particular</i>
<i>The adaptation function</i>	<i>The objective function</i>
<i>Locus</i>	<i>The position of the gene in the sequence that describes the chromosome</i>
<i>Genotype</i>	<i>The population considered in the problem domain</i>
<i>Phenotype</i>	<i>The population considered in the real search domain. For simple optimization problems the phenotype and genotype are identical. However, most of the times, they are different. The <b>Encoding</b> is the operation in which the phenotype becomes genotype and through <b>decoding</b> it reverses (Fig. 6.3.)</i>
<i>The individual's performance</i>	<i>Fitness for every considered chromosome (individual)</i>

For a clearer representation of these concepts (population, chromosome, gene, allele, locus, genotype, phenotype), we look at Fig.6.2 and Fig.6.3.

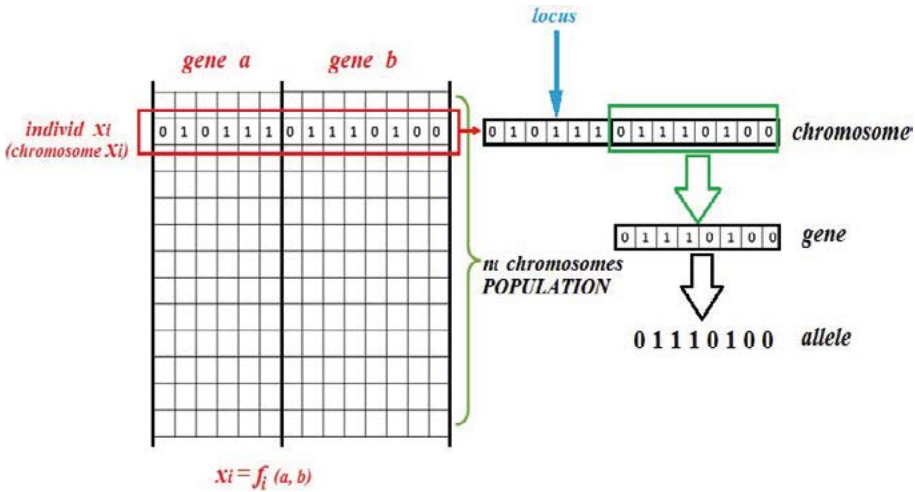


Fig. 6.2 The representation of the concepts of population, chromosome, gene, allele, locus.

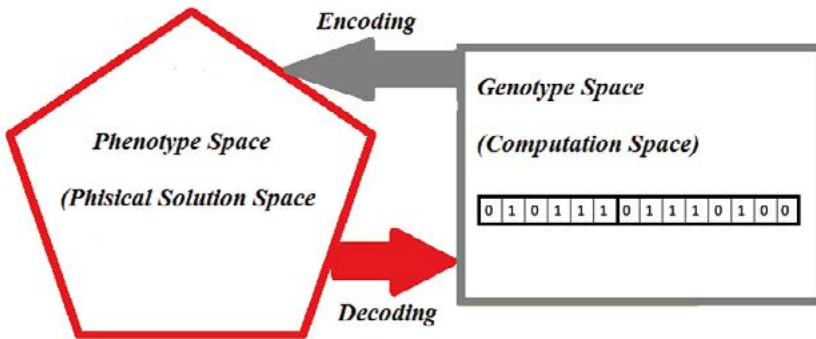


Fig. 6.3 The representation of the concepts of Genotype/Phenotype.

The standard genetic algorithm has the structure described in Fig .6.4.

The standard structure of the G.A. implements the evolution's iterative process, which contains three fundamental modules (population, evaluation and recombination / modification) realized through a set of genetic operators.

**Population** –it is the module that generates the initial population. It contains mathematical mechanisms for the representation of individuals (chromosomes), and their manipulation, in order to generate a new generation through the partial or total replacement of the current generation's individuals. The module is characterized by the following parameters: the generation's dimension (the number of individuals in a generation), the length of the chromosome and the total number of generations (or of another stopping criterion of the G.A.). The individuals' representation methods are: real encoding, binary coding, integer encoding, permutation encoding.

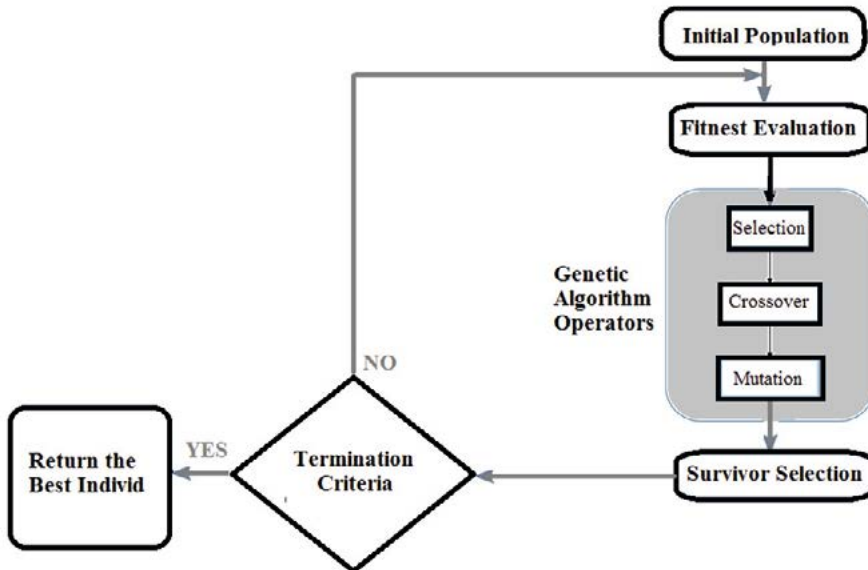


Fig. 6.4 The standard structure of the G.A.

**The binary encoding** is the simplest representation and was the one used by Holland in the development of the G.A. theory. The genotype is represented by bit sequences. Both binary encoding and reflected binary code (Gray code) can be used. The Gray code has the property that any two consecutive numbers vary by a single bit and this specificity makes it so that modifying a bit will not produce a powerful effect on the value of the sequence.

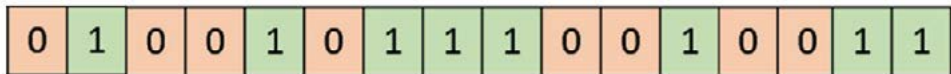


Fig. 6.5 Binary representation of the chromosome.

**The real encoding** represents each gene through a real number.

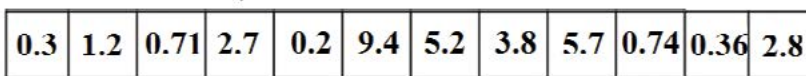


Fig. 6.6 Real representation of the chromosome (12 gene-variable design).

**The integer encoding** there are situations in which the binary representation cannot simply model certain cases. For example, directions like North, South, East, West, North-East, South-East, North-West, and South-West can be encoded through integers like 1, 2, 3, 4, 5, 6, 7, and 8. The encoded individual is:

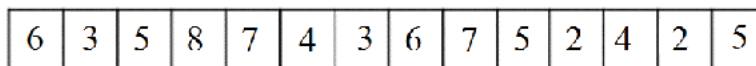


Fig. 6.7 Integer representation of the chromosome.

**The permutation encoding:** in certain optimization problems like the travelling salesman problem or the bomber problem, the optimal solution is given by a certain order of the elements that generates minimum time, minimum fuel consumption. For such a problem where 12 destinations must be reached, numbered from 0 to 11, the encoding of a situation is:

0	11	7	3	6	1	8	4	10	2	5	9
---	----	---	---	---	---	---	---	----	---	---	---

Fig. 6.8 Permutation representation of the chromosome.

**The evaluation** – contains the performing function used in comparing the current generation’s individuals.

**The recombination/modification module:** In the structure of the module there are the genetic operators: crossover, mutation and inversion. These operators are described by probabilistic parameters:

- Crossover probability:  $p_c$
- Mutation probability:  $p_m$
- Inversion probability:  $p_i$

### 6.2.1 Genetic algorithms with binary parameters

Holland developed the optimization algorithm as an application of binary algebra on the searching technique he called *Schemata*. Unlike other heuristic algorithms, he demonstrated in *Holland’s Schemata Theorem* that although he uses stochastic and probabilistic instruments, the result of the iterative implementation is the growth of the average value of the performing function for a considered population, respectively the placement of the solution in the vicinity of the theoretical optimum is assured.

The initial elements that must be fixed are **the dimension of the population (the number of individuals)** and **the dimension of the bit sequence that represents the individual (the length of the chromosome)**. The G.A. operates with **n points from the search domain**. The search domain is a real interval, with k dimensions, where k is the number of the design variables of the optimization problem. The typical dimension of the population is **n = 30 -100** individuals. The phenotype described by the search domain is transformed in the G.A. binary genotype through the binary encoding of the interval, respectively the realization of a **binary chromosome of r length**. **It is recommended that the n dimension of a population is equal or greater than a quarter of the r length of the chromosome.**

**The initial population** is obtained through the method of random uniform distribution generating or through the method proposed by **Bramlette, extended random generating**, through which a number of random initializations are used, from which the most performant individuals of the initial population are selected.



Theoretically, the binary encoding is the linear transformation of the real interval  $[a, b]$  in  $[0, 1]$ . If  $x \in [a, b]$ , the simplest transformation  $t_{(x)}: [a, b] \rightarrow [0, 1]$  is:

$$t_{(x)} = \frac{x - a}{b - a} \quad (6.4)$$

It is marked by  $x'$  the image of  $x$  through the transformed  $t$  (the binary equivalent of  $x$ ). The binary encoding creates a chromosome of  $r$  length. If the bit sequence that realizes the binary encoding contains more than  $r$  figures, then only the first  $r$  bits of the sequence are retained (encoding by approximation). If  $z$  contains  $r$  or less than  $r$  bits, then the exact encoding of  $x$  took place.

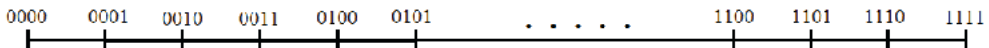
For the  $[2, 10]$  interval and  $r=7$  bits and the encoding  $x=5$ . The linear transformation  $t$  is:  $x' = \frac{x - 2}{10 - 2} = \frac{5 - 2}{10 - 2} = \frac{3}{8}$  in base 2,  $x'$  becomes  $x' = 0.011$  for the chosen length  $r=7$  the resulting individual (chromosome):  $C_{(x)} = 0110000$

**For the technical applications a simplified alternative, adapted to the practical conditions, is proposed.** For an optimization problem where the objective function has three design variables, defined as:  $a \in [2, 7]$ ,  $b \in [-20, 40]$ ,  $c \in [100, 210]$ .

First we choose the length of the chromosome ( $r = 16$ ), respectively of the three genes:  $a$  is encoded on 4 bits,  $b$  on 5 bits and  $c$  on 7 bits. For simplicity, we make a transformation of variables, in which the three design variables will belong to a domain that begins with 0. This transformation significantly simplifies the further binary conversion.

$$\begin{aligned} a^* &\in [0, 5], & a^* &= a - 2, & a &= a^* + 2 \\ b &\in [0, 60], & b^* &= b + 20, & b &= b^* - 20 \\ c &\in [0, 110], & c^* &= c - 100, & c &= c^* + 100 \end{aligned} \quad (6.5)$$

Because the variable  $a$  is encoded on 4 bits, with 4 bits we obtain 16 labels: 0000, 0001, 0010, 0011, ..., 1111.



The 16 labels generate 15 intervals, resulting in an interval sampling constant equal to  $\varepsilon_a = \frac{5}{15} = 0.333$ .

If the transformed variable, when binary encoded, has the value of  $a^* = 0101$ , then the real value is  $a^* = 5 \cdot 0.333$  and  $a = 5 \cdot 0.333 + 2 = 3.665$ .

This method avoids the complications of the classic theoretical methods, respectively the truncation method and interpolation method.

**The selection operator:** The principle of selection ensures greater chances of reproduction for the more adaptable individuals of the existent population. The

evaluation of individuals, of possible solutions is realized by the **fitness function**. The **fitness function must fulfill several conditions**:

- $f : X \rightarrow R$ , where  $f$ =fitness function  
 $X$ =multitude of all possible chromosomes  
 $R$ =multitude of real numbers
- strictly positive,  $f_{(x)} \geq 0, \forall x \in X$

**The total performance  $F$  of the population** is the sum of individual performances:

$$F = \sum_{i=1}^n f_{(x_i)} \tag{6.6}$$

A common variant is the **use of proportional performance**, where the individual performance of each individual is put in relation to the performance of the entire population:

$$F_{(xi)} = \frac{f_{(xi)}}{\sum_{i=1}^{N_{ind}} f_{(xi)}} \tag{6.7}$$

where:  $N_{ind}$ = the population's dimension

$x_i$ = the phenotype's value for the individuals

Several **methods of making the selection** are defined:

- Roulette Wheel Selection (Monte-Carlo) RWS – the most known
- Stochastic Universal Sampling (SUS)
- Linear Rank Selection (LRS)
- Exponential Rank Selection (ERS)
- Reward-based Selection (RbS)
- Elitist Selection (ES)
- Truncation Selection (TrS)
- Michalewicz Selection (MS)
- Boltzmann Selection (BS)
- Tournament Selection (ToS)

**Roulette wheel selection (Monte-Carlo)**: The individuals of each generation are selected for reproduction, in accordance with the value of the probability of selection. The following generation will have the descendants of a certain individual in proportion to the

value of the performance function that characterizes it. **The selection probability ( $p_i$ )** of the  $x_i$  chromosome is given by:

$$p_i = \frac{f(x_i)}{\sum_{i=1}^n f(x_i)} \quad i = 1, 2, \dots, n \quad (6.8)$$

In relation with the value of the selection probability it is also estimated  $n_i$  - **the average number of descendants** of individual  $i$ , the selection operator being applied  $n$  times ( $n$  = **the size of the population**):

$$n_i = n \cdot p_i = \frac{n \cdot f(x_i)}{\sum_{i=1}^n f(x_i)} = \frac{f(x_i)}{\bar{f}}, \quad (6.9)$$

$\bar{f}$  = the average performance of the population

**The crossover operator:** The operator models the biological reproduction of selected individuals in order to generate a new population. The crossover of individuals means the combination of the binary sequences of the selected chromosomes and the making of new ones. The operator has several ways of action: **with fixed cut points, with variable cut points, randomly chosen, with a single cut point, with multiple cut points, adaptive crossover, segmented crossover, mixed crossover, uniform crossover.**

Tabel 6.3 Types of crossover operators

<b>Crossover 1 Cut Point</b>	Chromosome 1	01101011   110010011010
	Chromosome 2	10110101   011001011010
	Offspring 1	01101011   011001011010
	Offspring 2	10110101   110010011010
<b>Crossover 2 Cut Points</b>	Chromosome1	0111011   1001011   101101
	Chromosome 2	1110101   0110001   011010
	Offspring 1	1110101   1001011   011010
	Offspring 2	0111011   0110001   101101
<b>Crossover Uniform</b>	Chromosome1	1101101   1001001   0110110
	Chromosome 2	1010111   0110001   0011110
	Mask	0001101 1110010 0111000
	Offspring	1011101   1000001   0110110

**The mutation operator:** It produces the ample exploration of the search domain, avoiding the fast convergence of the algorithm towards a local extreme point. There are several forms of the operator: **mutations with fixed locus, mutation with random locus, insert mutation, scramble mutation, inversion mutation.** The mutation operator is probabilistic, any bit corresponding to a gene has the possibility of being inverted. The mutation probability is correlated with the current generation. A high probability is

ensured at the start of the process, and a low probability at the end of the iterations. For generation  $t$ , the mutation probability is:

$$p_m(t) = p_m e^{-(t-1)\beta} \quad (6.10)$$

where:  $p_m$  = mutation probability of the first generation

$\beta \geq 1$  real parameter

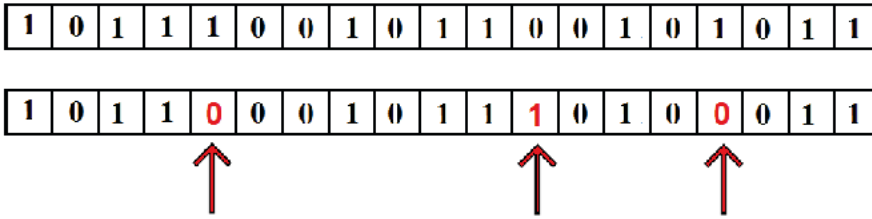


Fig. 6.9 Representation of the mutation operator's action.

**The inversion operator:** In J. Holland's paper crossover, mutation and inversion operators are described. But in the practical applications, the inversion operator is rarely used. There is a lot of literature in which the inversion operator is not even presented. It acts on a single chromosome by switching the positions of two genes. The two positions that are switched are chosen randomly.

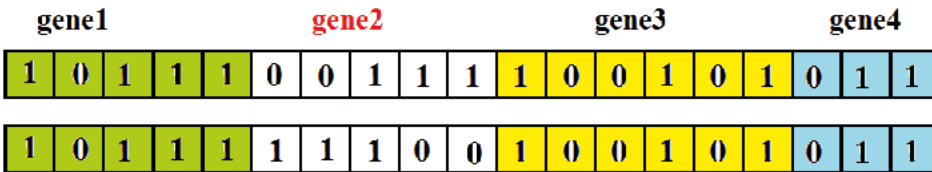


Fig. 6.10 Representation of the inversion operator's action.

From what has been shown so far, we can notice an exceptional flexibility of the G.A. It does not have a fixed form, with the exception of the evolution metaphor. Each operator has a multitude of variants, and, even for the G.A., which is the most mature heuristic optimization algorithm, there still is a place for the creativity of those interested in this field.

The genetic operators must do a double-action in the G.A., in line with the dimension of the domain in which the optimization problem's solution is searched for:

***-the exploration operation*** (according to the exploration domain defined by the extreme genes) that represents the operation in which the search of the optimal solution expands to the entire variable's definition domain. ***The exploration action ensures that the premature conversion towards a local optimum, different from the global optimum, is avoided.***

***-the searching operation*** (according to the exploration domain defined by the genes placed in the interval defined by the extreme genes of the exploration domain) that represents the operation in which the G.A.'s action in determining the optimum is being focused, respectively the operation in which the focus is on ***generating descendants in the intervals in which the probability of having high-performance individuals is high.*** The searching action ensures the conversion of the G.A. towards the global optimum.

**The genetic algorithm's setting:** The setting of the G.A. is understood as the fixation of the generation's dimension (of the number of individuals in the generation) and of the number of generations. There are three canonical settings:

***The DEJONG&SPEARS Setting***

It is one of the most popular settings of the canonical algorithm. In this case:

-size of the population 50

-number of generations 1000

***The GREEFENSTETTE Setting***

-size of the population 30

-number of generations unfixed

***The genetic micro-algorithm setting (The CARROLL Setting)***

-size of the population 5

-number of generations 100

The canonical settings are valid for both types of G.A. (binary parameter G.A., real parameter G.A.).

## **6.2.2 Genetic algorithms with real parameters**

The G.A. with binary parameters was the first model theoretically developed by Holland and his collaborators, developing Schemata as a topology on the multitude of binary numbers. This determined the necessity of the Phenotype and Genotype, respectively of the encoding/decoding operations that make the real→binary→real conversions. Evidently, these conversions introduce errors, even though, later on, the genetic operators only manipulate the sequences of bits, without introducing additional errors. Moreover, the series of conversions needed additional software resources through which the running time of the algorithm increases. The practical applications from the industrial field have developed, used and imposed G.A. with real parameters. In this case, the phenotype and the genotype are identical, being identified with the search domain of the optimization problem. The structure of the algorithm is identical, the difference being the form of the genetic operators. Even in the case of real parameter G.A. a large set of variants of crossover and mutation genetic operators was developed, this strengthening the intrinsically flexible and innovative character of the G.A. [20][21][22].

### **The crossover operator with real parameters [23][24][25][26][27][28].**

In describing the set of crossover operators, we use the following notations:

For two individuals (chromosomes) selected from the *current generation* for the crossover operation (*parents*), it is noted as:

$$C_1 = (c_1^1, c_2^1, \dots, c_i^1, c_{i+1}^1, \dots, c_n^1), \quad C_2 = (c_1^2, c_2^2, \dots, c_i^2, c_{i+1}^2, \dots, c_n^2)$$

where  $c_i^j$  are the genes (variables) from the chromosome (individual).

**The descendants** (individuals that make the *new generation*) are noted as:

$$H_1 = (h_1^1, h_2^1, \dots, h_i^1, h_{i+1}^1, \dots, h_n^1), \quad H_2 = (h_1^2, h_2^2, \dots, h_i^2, h_{i+1}^2, \dots, h_n^2)$$

**A. Flat crossover:** The operator was introduced by Radcliffe in 1991 [29]. The operator generates a single descendant  $H = (h_1, \dots, h_i, \dots, h_n)$ , where the gene  $h_i$  is randomly generated in the interval  $[c_i^1, c_i^2]$ , where  $c_i^1$  and  $c_i^2$  are the parents' genes.

**B. Simple crossover:** The operator was described in the works elaborated by Wright (1991) and Michalewicz (1992) [17], [21]. The operator generates two descendants by:

-randomly generating a number  $i \in \{1, 2, \dots, n-1\}$  that will determine the gene according to which the following 2 descendants are built. The method is similar to the one used in the 1 cut-point crossover operator applied to the digital G.A.s

$$H_1 = (c_1^1, c_2^1, \dots, c_i^1, c_{i+1}^2, \dots, c_n^2), \quad H_2 = (c_1^2, c_2^2, \dots, c_i^2, c_{i+1}^1, \dots, c_n^1)$$

**C. Arithmetical crossover:** The operator was described by Michalewicz in 1992, for the purpose of solving optimization problems with nonlinear constraints. It usually generates two descendants:

$$H_1 = (h_1^1, h_2^1, \dots, h_i^1, h_{i+1}^1, \dots, h_n^1), \quad H_2 = (h_1^2, h_2^2, \dots, h_i^2, h_{i+1}^2, \dots, h_n^2)$$

where the genes of the two descendants are determined by:  $h_i^1 = \lambda c_i^1 + (1 - \lambda) c_i^2$ ,  $h_i^2 = \lambda c_i^2 + (1 - \lambda) c_i^1$  and  $\lambda$  is a constant (in the case of uniform crossover operators), for all generations. It is randomly chosen from the interval [0, 1].  $\lambda$  is a variable, depending on the number of the generation (in the case of non-uniform crossover operators, proposed by Herrera in 1998).

There are versions of the arithmetic operator that produce a single descendant:

$$h_i = \lambda (c_i^2 - c_i^1) + c_i^2$$

The performance of the individual  $H_2$  is considered to be better than that of the individual  $H_1$ , where  $H_1$  and  $H_2$  are the two parents from the current generation. If the descendant proposed in the former relation is placed outside the search domain, the operator's procedures calls for the generation of another random number  $\lambda$  and a new descendant is produced. Deep and Thakur proposed, in 2007, the following expression, with the purpose of generating descendants, *of forcing their placement inside the*

**search domain**, when the first descendant was placed outside the domain (in this case the performance of the individual  $C_2$  is considered to be superior in relation to  $C_1$ ):

$$h_i^2 = \lambda |c_i^1 - c_i^2| + c_i^2$$

The arithmetic crossover operator is also found in literature as heuristic **crossover operator**.

**D.BLX-a crossover:** The operator was introduced by Eshelman in 1993. In this case, the two selected chromosomes generate a descendant:

$$H = (h_1, h_2, \dots, h_i, h_{i+1}, \dots, h_n)$$

where  $h_i$ , the gens of the descendant, are randomly selected from the interval:

$$[c_{min} - I \cdot \alpha, c_{max} + I \cdot \alpha]$$

where:

$$c_{max} = \max(c_i^1, c_i^2)$$

$$c_{min} = \min(c_i^1, c_i^2)$$

$$I = c_{max} - c_{min}$$

$$\alpha \in [0, 1]$$

In Herrera's works it is shown that the best results are obtained for  $\alpha = 0.3$ . If  $\alpha = 0$ , the operator BLX-0.0 is identical with the flat crossover operator.

### **E. Linear crossover**

The operator is proposed by Wright in 1991. The two selected individuals generate three descendants in the form of:

$$H_k = (h_1^k, h_2^k, \dots, h_i^k, h_{i+1}^k, \dots, h_n^k), \quad k = 1, 2, 3$$

where the genes of the descendants are:

$$h_i^1 = \frac{1}{2}c_i^1 + \frac{1}{2}c_i^2$$

$$h_i^2 = \frac{3}{2}c_i^1 - \frac{1}{2}c_i^2$$

$$h_i^3 = -\frac{1}{2}c_i^1 + \frac{3}{2}c_i^2$$

Out of the three generated descendants, the operator will retain two descendants, respectively the most performant pair, which will be kept for the new generation. This way, the crossover operator has its own selection mechanism.

**F. Discrete crossover:** The operator introduced by Muhlenbein in 1993 produces a single descendant from the pair of selected individuals, in the form of:

$$H = (h_1, h_2, \dots, h_i, h_{i+1}, \dots, h_n)$$

The  $h_i$  genes of the descendant are determined by: randomly choosing  $h_i$  from the multitude that contains the pair of elements  $\{c_i^1, c_i^2\}$ , respectively from the parents pair of corresponding genes.

**G. Extended line crossover:** It was proposed by Muhlenbein in 1993 and by Popovic and Murty in 1997 [30]. The operator uses two individuals from the current generation to produce a descendant. The descendant's genes are obtained by:

$$h_i = c_i^1 + \alpha (c_i^1 - c_i^2)$$

where  $\alpha$  is a random value from the interval  $[-0.25, 1.25]$ .

**F. Extended intermediate crossover:** It was proposed by Muhlenbein in 1993 [30]. The operator uses two individuals from the current generation in order to produce a descendant. The descendant's genes are obtained by:

$$h_i = c_i^1 + \alpha_i (c_i^2 - c_i^1)$$

where  $\alpha_i$  is a random value from the interval  $[-0.25, 1.25]$ .

We notice that the difference between this operator and extended line crossover operator consists in the way that the parameter  $\alpha$  is chosen. If  $\alpha = 0.25$ , then the operator is identical to BLX-0.25.

**G. Wright's heuristic crossover:** The operator was proposed by Wright in 1990. We assume that the individual  $C_1$  is the parent with the best performance. In this case, the two parents generate a descendant, and the descendant's genes are:

$$h_i = c_i^1 + \alpha_i (c_i^2 - c_i^1)$$

where  $\alpha_i$  is a uniformly random value in the interval  $[0, 1]$ .

**H. Linear bga crossover:** The operator was proposed by Schlierkamp and Voosen in 1994, relying on the studies related to the mutation operator introduced by Muhlenbein in [31]. As in the previous case, we assume that the individual  $C_1$  is the parent with the best performance. In this case, the two parents generate a descendant with the genes:

$$h_i = c_i^1 \pm \text{rang}_i \cdot \gamma \cdot A$$

where:

$$A = \frac{c_i^2 - c_i^1}{\|C_1 - C_2\|}$$

sign – is selected with the probability 0.9



$\text{rang}_i$  the value is usually chosen  $0.5 \cdot (b_i - a_i)$

$$\gamma = \sum_{k=0}^{15} a_k \cdot 2^k$$

$\alpha_i \in \{0, 1\}$  randomly generated with the probability of  $p(\alpha_i = 1) = \frac{1}{16}$ .

**1. Fuzzy connectives based crossover fcb:** The FCB operator was described in the works of Herrera in 1994. This operator aims to control the exploration action, respectively the action of searching descendants by controlling the intervals in which these are placed. Because of this, the definition domain of a gene (of a variable)  $i$ , respectively the interval  $[a_i, b_i]$  is divided into three subintervals that are called exploration/searching zones. This principle is shown in Fig.6.11. From it we can observe that the three base zones generate an intermediate subinterval, where the searching or exploration actions are not well determined. This new subinterval was named **relaxed exploration zone**.

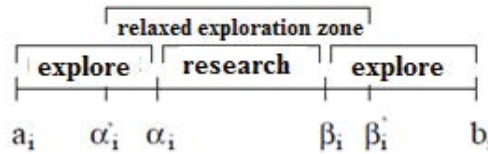


Fig. 6.11 The subintervals generated in the case of the FCB operator.

Four functions are described: F, S, M and L, defined on the intervals  $[a, b] \times [a, b]$  with values in  $[a, b]$ :

$$\begin{aligned} (P1) \forall x, x' \in [a, b] F(x, x') &\leq \min\{x, x'\} \\ (P2) \forall x, x' \in [a, b] S(x, x') &\geq \max\{x, x'\} \\ (P3) \forall x, x' \in [a, b] \min\{x, x'\} &\leq M(x, x') \leq \max\{x, x'\} \\ (P4) \forall x, x' \in [a, b] F(x, x') &\leq L(x, x') \leq S(x, x') \end{aligned}$$

(P5)  $F, S, M$  and  $L$  are monotonically increasing functions

The exploration and searching actions, for a series of crossover operators, are succinctly represented, depending on the way in which the descendants are generated, in the schemes shown in Fig. 6.12.

### The mutation operator with real parameters:

As in the case of binary G.A.s, the mutation operator acts to create new genetic material, new individuals, through which the diversity of the population is maintained [31].

Considering the individual before the mutation:

$$C = (c_1, c_2, \dots, c_i, c_{i+1}, \dots, c_n)$$

and after the mutation:

$$C = (c_1, c_2, \dots, c'_i, c_{i+1}, \dots, c_n)$$

The gene  $c_i$ , to which the mutation is applied, is defined on the interval  $[a, b]$ .

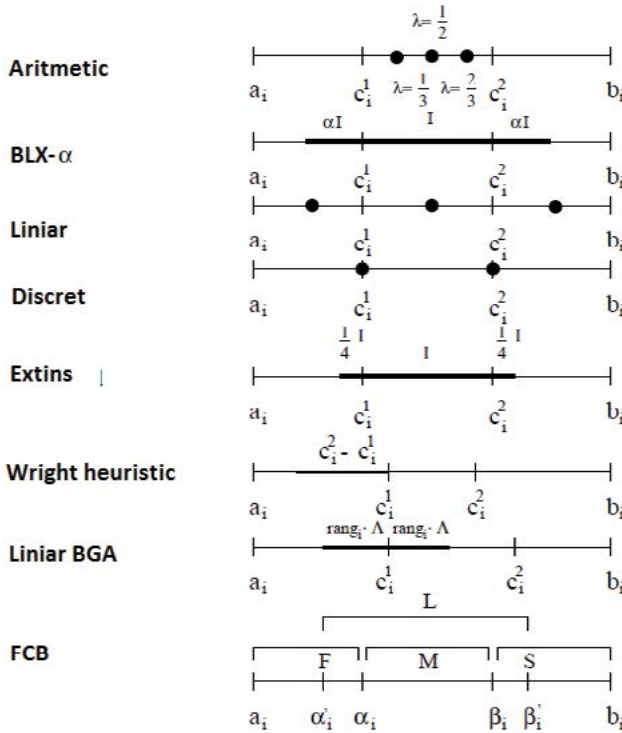


Fig. 6.12 The exploring-searching actions generated by the crossover operators.

**A. Random mutation:** The operator was introduced by Michalewicz in 1992. The gene (variable) upon which the mutation operator  $c_i'$  acted, is uniformly randomly chosen from the search interval of said variable:  $[a_i, b_i]$ .

**B. Non-uniform mutation:** This type of mutation was also presented by Michalewicz in 1992. The operator makes the mutation in the adaptive version. If we mark the current generation with  $t$  and the G.A.'s maximum number of generations with  $g_{max}$ , the gene that is mutated is:

$$c_i' = \begin{cases} c_i + \Delta(t, b_i - c_i) & \text{if } \tau = 0 \\ c_i - \Delta(t, c_i - a_i) & \text{if } \tau = 1 \end{cases}$$

where  $\tau$  is a random number from the interval  $\{0, 1\}$

$$\Delta(t, y) = y \left( 1 - r \left( 1 - \frac{\tau}{g_{max}} \right)^b \right)$$

$r$  is a random number from the interval  $[0, 1]$ ,

$b$  – the parameter chosen by the user through which the degree of non-uniformity, respectively the operator's dependency on the number of generations, is determined.

**C. Muhlenbein's mutation:** The operator proposed by Muhlenbein in 1993. The gene that suffers the mutation has the form of:

$$c'_i = c_i \pm rang_i \cdot \gamma$$

where  $rang_i$  is the mutation domain and is usually  $0.1 \cdot (b_i - a_i)$

$$\gamma = \sum_{k=0}^{15} a_k \cdot 2^k$$

$\alpha_i \in \{0, 1\}$  randomly generated with the probability of  $p(\alpha_i = 1) = \frac{1}{16}$ .

**D. Makinen-Periaux-Toivanenmutation:** The operator was introduced in 1999. The gene that suffers the mutation has the form of:

$$c'_i = (1 - \hat{t})a_i + b_i$$

where:

$$\hat{t} = \begin{cases} t - t \left( \frac{t-r}{t} \right)^b, & \text{if } r < t \\ t, & \text{if } r = t \\ t + (1-t) \left( \frac{r-t}{1-t} \right)^b, & \text{if } r > t \end{cases}$$

$$t = \frac{x - a_i}{b_i - a_i}$$

This mutation operator is not adaptive.

**E. Discrete modal mutation:** The operator was proposed by Voigh in 1994. The gene that suffers the mutation has the form of:

$$c'_i = c_i \pm rang_i \cdot \gamma$$

where

$$\gamma = \sum_{k=0}^l a_k \cdot B_m^k$$

$$l = \frac{\log(rang_{min})}{\log(B_m)}$$

$B_m > 1$  is a parameter named the mutation's

$rang_{min}$  is the lower limit of the relative mutation domain

## 6.3 Swarm particle optimization algorithm & others paradigms

### 6.3.1 Swarm particle optimization

Particle swarm optimization (PSO) is a metaheuristic optimization algorithm developed by Eberhart and Kennedy in 1995, inspired by social behavior of bird flocking or fish schooling [32]. The foundation of this algorithm lies in the idea that social sharing of information among group members offers an evolutionary advantage compared to non-cooperative populations. When the food resources have an unpredictable space distribution, the advantage of cooperation among individuals outweighs the disadvantage of competition for food items. Compared to GA, the advantages of PSO are that PSO is easy to implement and there are few parameters to adjust. A particle is defined by:

- a position: When there are two design variables, a particle is defined by its coordinate  $(x,y)$ .
- a velocity: This is a value used to move the particle position toward the best solution.

The information sharing is performed in two ways, giving two variants of PSO:

-Local PSO, where the information sharing is between every particle and its direct neighbors. The particle and its neighbors form a **ring data structure topology**.

-Global PSO, where the information sharing is between every particle and the best particle, defined by the best position. Here the particles are organized in a **star data structure topology**.

After the random initialization of particles and evaluation of fitting values, the best position in space ( $g_{best}, g_b$ ) and best position for each particle ( $p_{best}, p_b$ ) are memorized. In the quest for the best solution, this algorithm makes the particles move with a velocity which is calculated in every iteration. Each particle's movement has the influence of the own best known position and also the best known position in the space-search. The final result expected is that the particle swarm converges to the best solution [33]. The mechanism of the PSO is depicted in Fig. 6.13., and the iterative steps in the flowchart from the Fig. 6.14.

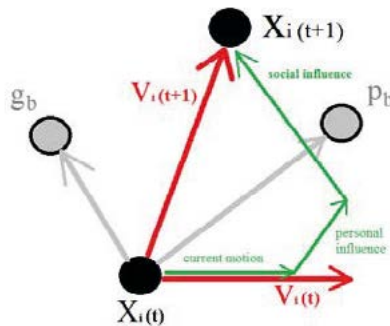


Fig. 6.13 The PSO's Mechanism.

The analytic expressions of the new velocity  $v(t+1)$ , and the new position  $x(t+1)$  are:

$$v(t+1) = w(t) \cdot v(t) + c_1 \cdot rand(0,1) \cdot (p_{best} \cdot x(t)) + c_2 \cdot rand(0,1) \cdot (g_{best} \cdot x(t))$$

$$x(t+1) = x(t) + v(t)$$

- where:
- $c_1$  = self confidence factor,  $c_1 < 2$
  - $c_2$  = swarm confidence factor,  $c_2 < 2$
  - $rand(0, 1)$  = random value in  $(0, 1)$
  - $w$  = weight factor ( $w \in (0.4, 0.9)$ )

Inertia weight factor works in adaptive mode. The parameter usually decreases linearly as the generation number increases. In this way, the algorithm improves the convergence by a better space exploration at the beginning and better space exploitation at the end.

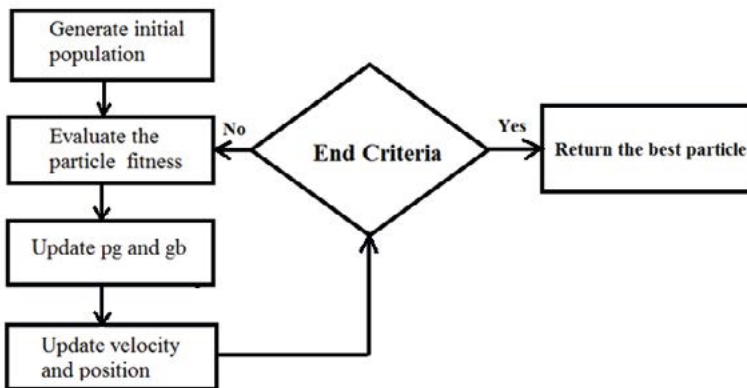


Fig. 6.14 The PSO Flowchart.

PSO is similar to the Genetic Algorithm (GA) in the sense that they are both population-based search approaches using a combination of stochastic and probabilistic rules. GA is a well-established algorithm with many versions and many applications. PSO and the GA on average yield the same effectiveness (solution quality), but PSO is more computationally efficient (uses less number of function evaluations) than the GA.

Some papers propose the mix between GA and PSO, but an exhaustive analysis that considers all the variants of genetic GA operators is yet to be made..

### 6.3.2 Gravitational search algorithm (GSA)

Gravity is one of the four fundamental forces in nature and represents the tendency of masses to accelerate toward each other, according to Newton's second law of motion. The GSA operates in an isolated system of masses, an artificial universe that obeys Newton's laws, and it is based on the law of gravity and mass interactions. The agents are a collection of masses which interact based on the Newtonian law of gravity. The mass of an agent represents their performance. A kind of cooperation between agents is achieved through gravitational field. The resultant force upon a mass is computed by the vector summation of all forces exerted by rest of masses and it is towards the heaviest masses. This

gravitational model is shown in the Fig. 6.15. And the GSA flowchart in Fig. 6.16 [34], [35]. The first part is common to previous algorithms. After computing the current generation fitness value, the mass of each point  $M_i(t)$  is calculated:

$$m_i(t) = \frac{fit_i(t) - worst(t)}{best(t) - worst(t)}$$

where:

$$best(t) = \min_{j \in \{1, \dots, N\}} (fit_j(t)) \text{ - for a minimization problem}$$

$$worst(t) = \max_{j \in \{1, \dots, N\}} (fit_j(t)) \text{ - for a minimization problem}$$

$$M_i(t) = \frac{m_i(t)}{\sum_{j=1}^p m_j(t)}$$

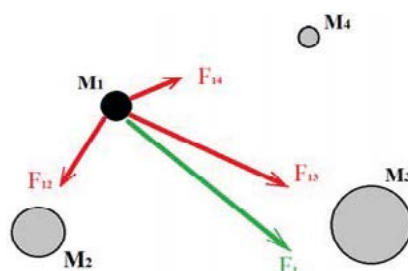


Fig. 6.15 The gravitational model of the GSA.

Agent masses are proportional to their fitness value. A heavier particle has bigger gravitational force and moves slowly through space, which is good since they are more probably to lie near the global minimum. GSA does not need to store information as PSO, but it needs more computations.

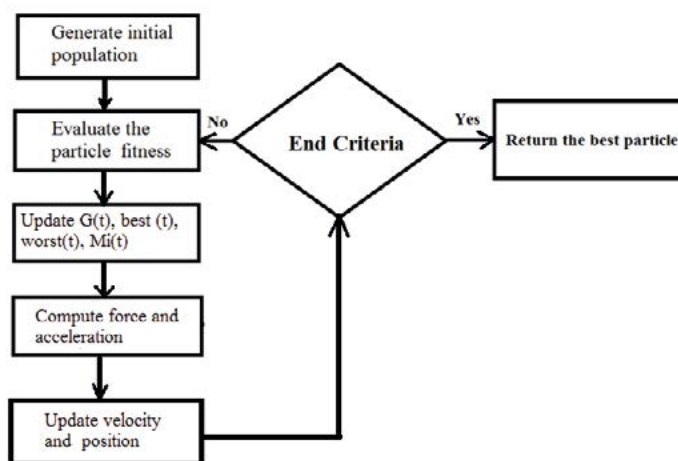


Fig .6.16 The GSA Flowchart.

## 6. 4 Practical aspects of the heuristic algorithms' application

The majority of articles referring to optimal design do not justify a series of options, defining the optimization problem, choosing a certain heuristic algorithm, usually GA or PSO, and opting for a set of operators or parameters involved in the implementation of the algorithm [36], [37], [38], [39]. Because of this, it is useful to discuss the aspects through which the solution of the optimization problem is individualized. Practical aspects will be presented on:

- fixing of design variables
- functions for testing the algorithm's performances
- choosing variants of genetic operators

### 6.4.1 Choosing design variables

If the fixing of the objective function is a relatively simple step, most of the times the function being fixed by the beneficiary of the optimal design phase (price, mass, dimensions, efficiency, power density), the phase of defining design variables is significantly more complex. The defining of design variables has two steps:

- fixing the number of design variables
- customizing them

The number of design variables of the optimization problem is chosen so that it is less or at most equal to the number of genes, to the maximum dimension of the searching domain for which the optimization algorithm was built. A heuristic optimization algorithm, being the general type, meaning that it can be applied to all the mathematical types of the optimization problems, is designed as a software product so that it can be applied at the widest range of technical applications, for example the design of any type of electric machine. At first, the practical applications from electrical engineering used optimization algorithms capable of solving problems with three design variables. In the last 20 years, algorithms have been developed so that they can optimize problems with 5-7-9-11 design variables. Because of this, a heuristic optimization algorithm capable of solving problems with 15 design variables is now considered a good solution. Generally speaking, increasing the dimension of the optimization problem complicates the dedicated software and increases the running time of a problem.

The fixing of design variables for an optimization problem is a complicated stage. For example, in the design of electric machines there is a large number of parameters that could be considered design variables. If an analytical procedure of complex design is used, typical of the German school of design, there can be over 100 parameters involved. These procedures are extremely difficult to apply and require a vast design experience. Usually analytical methods use 30-40 parameters. From these, a set of 9-11 must be selected to be used as design variables in defining the optimization problem. Obviously, not all of them have the same influence over the objective function. For choosing the parameters with

strong influence on the optimization problem, the literature calls on the design experience of the user. But the accumulation of experience is a phase no longer accepted in the philosophy of the current industrial environment. A possible solution, through which the set of parameters is extracted from the analytical design that becomes the group of design variables of the optimization problem, is **the suboptimal approach**. This method involves step-by-step analysis of the degree of influence of the set of parameters.

Assuming that the analytical design method identified the multitude of  $k$  parameters:

$$S = \{p_1, p_2, p_3, \dots, p_{k-1}, p_k\}$$

They are the possible design variables of the objective function  $F$ .

One at a time, for the parameter  $p_i \in S$ , a variation of 20% is accepted. The percentage of 20% is proposed, assuming that it produces a visible influence, measurable in the objective function. The rest of the parameters are considered to be constants ( $p_1 \rightarrow c_1, p_2 \rightarrow c_2, p_3 \rightarrow c_3, \dots, p_k \rightarrow c_k$ ). In these conditions, the influence that changing the  $p_i$  parameter has on the objective function is observable. The objective function for two situations is calculated this way:

$$p_i \rightarrow c_i, \text{ respectively } p_i \rightarrow 1.2c_i \text{ (the 20\% increase is applied)}$$

The situation with a decrease of 20% can also be used, when  $p_i \rightarrow 0.8c_i$

In these conditions, the objective function in the two situations is calculated:

$$F(c_1, c_2, c_3, \dots, c_i, \dots, c_{k-1}, c_k) = k_i \text{ and}$$

$$F(c_1, c_2, c_3, \dots, 1.2c_i, \dots, c_{k-1}, c_k) = k_{i+}$$

The values  $k_i$  and  $k_{i+}$  are compared by calculating the percentage variation of  $k_{i+}$ :

$$\Delta_i \% = \frac{k_{i+} \cdot 100}{k_i}$$

The analysis is repeated for all of the  $k$  parameters and the percentage variations of the objective function under the influence of each parameter are compared. At the end, the parameters that produce the most significant/the biggest variations  $\Delta_i\%$  in the objective function, are chosen.

## 6.4.2 Test functions

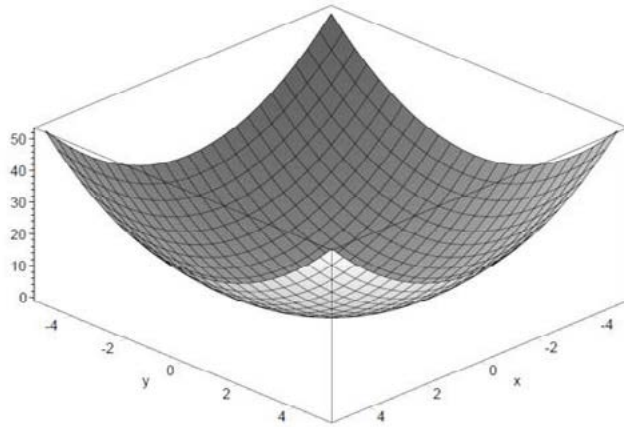
Test functions are important to validate a new heuristic algorithm or a new operator or to compare the performance of various heuristic algorithms [40][41]. To evaluate a new algorithm the author has to validate it against standard test function. In order to validate a new heuristic algorithm, the literature propose a large set of test functions so there is no one standard set of test function, every researcher must choose the own set of function tests. We propose five function-tests to be used: De Jong's function, Rastrigin's function, Schwefel's function, Ackley's function and Michalewicz's function.

***De Jong's function (first function of De Jong's)***. De Jong's function is continuous, convex and unimodal, one of the simplest test functions.

$$f_1(x) = \sum_{i=1}^n x_i^2 \quad -5.12 \leq x_i \leq 5.12$$

Global minimum:  $f(x) = 0, x(i) = 0, i = 1 : n$

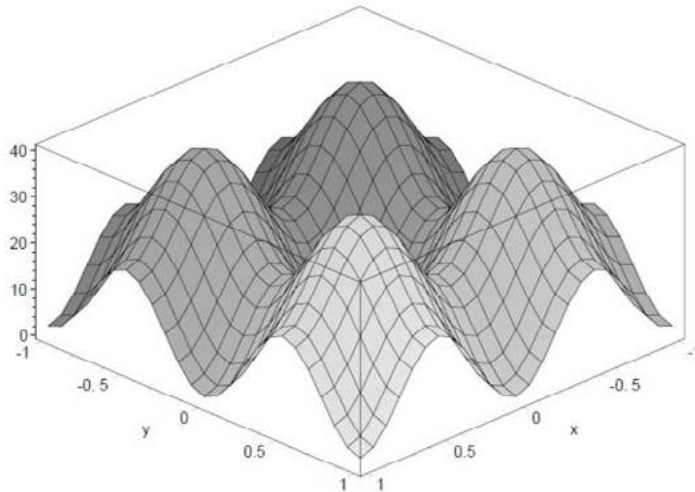




**Rastrigin's function**. Rastrigin's function is highly multimodal. The addition of cosine modulation produces frequent local minima. The locations of the minima are regularly distributed.

$$f_2(x) = 10 \cdot n + \sum_{i=1}^n (x_i^2 - 10 \cdot \cos(2\pi \cdot x_i)) \quad -5.12 \leq x_i \leq 5.12$$

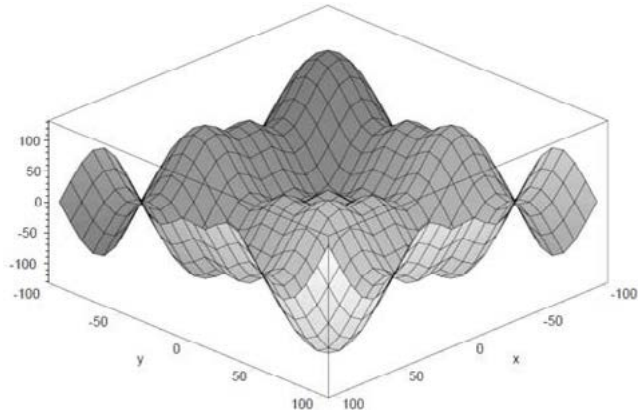
Global minimum:  $f(x) = 0, x(i) = 0, i = 1 : n$



**Schwefel's function**. Schwefel's function is deceptive in that the global minimum is geometrically distant from the next best local minima. Therefore, the heuristic algorithms are potentially predisposed to convergence in the wrong direction.

$$f_2(x) = \sum_{i=1}^n -x_i \cdot \sin(\sqrt{|x_i|}) \quad -500 \leq x_i \leq 500$$

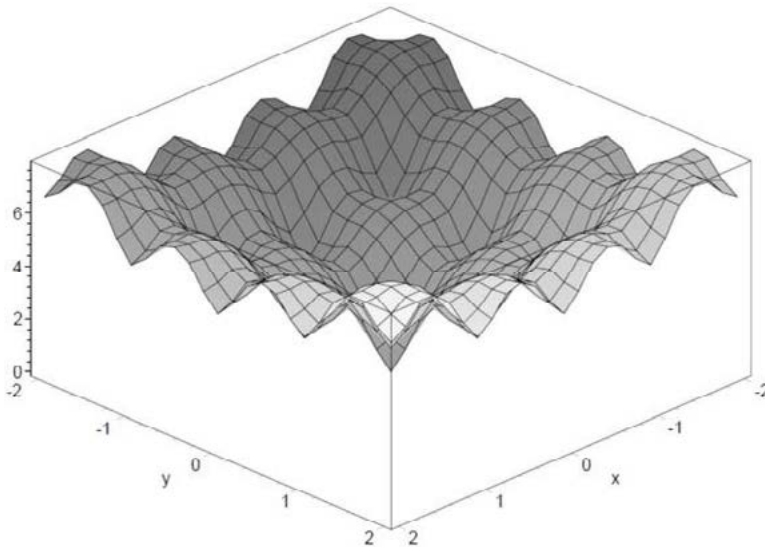
Global minimum:  $f(x) = n \cdot 418.9829$  for  $x(i) = 420.9687, i = 1 : n$



**Ackley's function** is a widely used multimodal test function.

$$f_4(x) = -a \cdot e^{-b \sqrt{\frac{1}{n} \sum_{i=1}^n x_i^2}} - e^{\frac{1}{n} \sum_{i=1}^n \cos(c \cdot x_i)} + a + e^1 \quad -32.768 \leq x_i \leq 32.768$$

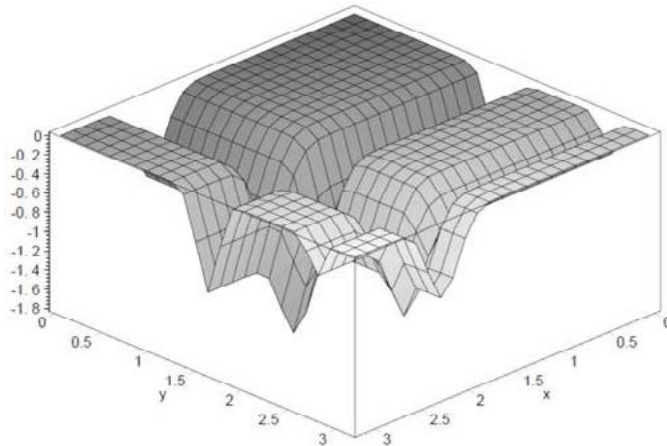
Global minimum:  $f(x) = 0, x(i) = 0, i = 1 : n; a = 20, b = 0.2, c = 2 \cdot \pi$



**Michalewicz's function** is a multimodal test function with  $n!$  local optima. Larger value for  $m$  leads to more difficult search.

$$f_5(x) = -\sum_{i=1}^n \sin(x_i) \cdot \left( \sin\left(\frac{i \cdot x_i^2}{\pi}\right) \right)^{2m} \quad 0 \leq x_i \leq \pi$$

Global minimum:  $f(x) = -4.687, i = 1 : n; m = 10, n = 5,$   
 $f(x) = -9.66, i = 1 : n; m = 10, n = 10.$



One last observation on the practical aspects is related to the dimensioning of the search domain. It is achieved by fixing the design variables' defining intervals. If an extensive dimensioning of these intervals is chosen, then running the heuristic algorithm will take longer, the phase (number of iterations) necessary for the correct exploration of the domain imposing a longer time. The option with a fixed number of iterations, for a broad search domain, produces the algorithm's probability of being fixed in a local optimum or of choosing the solution in a vicinity of the global optimum that is too vast. A search domain that is defined too narrowly can lead to the mathematical impossibility of solving, if the optimization problem also has a set of restrictions, or it can lead to the exclusion of the global optimum from the narrow search domain. The literature proposes the classic solution: the dimensioning of the design variables' defining intervals is done based on engineering experience. For the young engineers, a solution that can be applied to a large field of applications is needed.

A dimensioning solution that offers the certainty of solving multiple technical optimization problems is fixing the domain at  $\pm 30\%$  of the design variable's value obtained through analytical design or through choice based on other existing solutions.

### 6.4.3 Setting the type of genetic operator

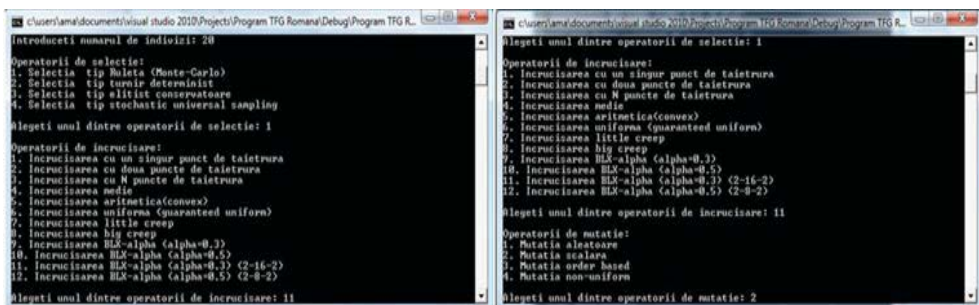
The design of a GA must generate a flexible software product, which can offer the beneficiary the possibility of setting a GA according to the optimization problem.

In the Electrical Engineering department, GAs have been designed that contain the following set of parameters and operators available to the user [42]:

- number of design variables (in a domain, for example 1-20)
- defining intervals for each design variable

- dimension of generation (number of individuals of the generation)
- number of generations
- selection operators: -roulette wheel (Monte-Carlo)
  - deterministic tournament
  - elitist
  - stochastic universal sampling
- crossover operator:
  - single cut-point
  - two cut-points
  - n cut-points
  - median (continuous)
  - arithmetic (convex)
  - uniform (guaranteed uniform)
  - little creep
  - big creep
- mutation operator:
  - random
  - scalar
  - order based mutation
  - non-uniform

The GA is verified using five test functions: De Jong's function, Rastrigin's function, Schwefel's function, Ackley's function and Michalewicz's function. The verification phase allows the display of the most performant individual of each generation, named **the alpha individual**, of the performance of each individual from the generation, of the generation's average performance, of the sum of the individuals' performance from generation  $i$  and of the percentage of individuals from a generation that have the value of the alpha individual. Because test functions are used, whose optimum is known, any individual whose performance function is situated in a fixed vicinity of the global optimum is considered the alpha individual. The vicinity is fixed by the user, usually in a range of  $\pm 1\%$  -  $3\%$ . This way the GA can be tested with sufficient precision, and the performant combination of operators is selected to be used in the practical optimization problems.



```

C:\USERS\ALIN\DESKTOP\AGTOT-1\!!!PRO-1\PROGRA-2\NOULPR-1\EST_TOT.EXE
Introduceti numarul de parametri al fiecarui individ: 3

Introduceti domeniul de cautare pentru individul alfa [procente]: 5

Functii de test:
1. Functia DeJong 1
2. Functia Rastring
3. Functia Schwefel
4. Functia Ackley
5. Functia Michalewicz (pentru 5 parametrii)

Alegeti functia de test: 1

Dati numarul de indivizi: 30

Dati numarul de generatii: 100_

```

```

File Edit Format View Help
Limitele Parametrilor:
-5.12  -5.12  -5.12
5.12   5.12   5.12

----- GENERATIA ----- 1 -----
Individ 0 :   -4.66637      -2.20979      -1.51142      Fitness = 28.9426
Individ 1 :    3.13651      -4.5056      3.69562      Fitness = 43.7957
Individ 2 :   -2.59994      3.52563      -4.31616      Fitness = 37.819
Individ 3 :   -2.36646      -1.57184      -2.39616      Fitness = 13.8124
Individ 4 :   -2.46272      -0.326656     -4.03661      Fitness = 22.4659
Individ 5 :    4.02022      1.73978      -0.8192      Fitness = 19.8601
Individ 6 :   -4.44723      -1.81965     -3.69357      Fitness = 36.7314
Individ 7 :    3.44166      2.49242      1.76845      Fitness = 21.1846
Individ 8 :   -2.18829      2.19955     -2.57024      Fitness = 16.2328
Individ 9 :    1.03834      0.68608      1.15507      Fitness = 2.88304
Individ 10 :  -0.656384      1.24109      1.49709      Fitness = 4.21241
Individ 11 :   -4.89779      -2.0992      3.42118      Fitness = 40.0995
Individ 12 :    2.14835      5.1139      -1.71213      Fitness = 33.7193
Individ 13 :    1.18272      3.18771      3.42938      Fitness = 23.321
Individ 14 :   -3.9127      0.850944     0.919552      Fitness = 16.8789
Individ 15 :    0.018432     -0.217088     -3.9721      Fitness = 15.825
Individ 16 :   -1.98963     -3.87789      0.539648      Fitness = 19.2879
Individ 17 :   -2.08998     -4.21683     -2.41562      Fitness = 27.9849
Individ 18 :   -3.85126     -2.83341      3.66899      Fitness = 36.3219
Individ 19 :    1.3271      -1.4039      3.03718      Fitness = 12.9566
Individ 20 :    3.2983      -0.376832     -0.777216      Fitness = 11.6249
Individ 21 :    1.37421      -0.958464     -3.56454      Fitness = 15.5131
Individ 22 :    1.0967      4.46362     -1.43872      Fitness = 23.1965
Individ 23 :   -0.51712     -3.75296     -4.5312      Fitness = 34.8839
Individ 24 :    1.5913      0.208896      0.664576      Fitness = 3.01752
Individ 25 :    3.73862     -0.268288     -0.652288      Fitness = 14.4748
Individ 26 :    1.01171      -3.15187      1.35782      Fitness = 12.8015
Individ 27 :   -4.78413      3.63725      1.22778      Fitness = 37.6249
Individ 28 :    0.257024      0.540672     -1.32301      Fitness = 2.10874
Individ 29 :   -3.03104      2.85901      -3.6864      Fitness = 30.9507

Individul alfa este:
0.257024  0.540672  -1.32301  Fitness = 2.10874

Suma fitnessului tuturor indivizilor este : 660.532
Media fitnessului tuturor indivizilor este : 22.0177

```





## 6. 5 Practical results in the field of electric machine optimization obtained by UPT researchers

In the Electrical Engineering department, the first research regarding the optimization of electric machine design was made by Mr. Acad. Prof. Dr. Eng. Toma Dordea. In the '70s, Mr. Acad. Toma Dordea intuited the potential of the application of software technologies in the design of electric machines. In this regard, the elaboration of a program dedicated to the design of induction machines began developing. Mr. Acad. Toma Dordea was an advocate of the German school of design, having as an example the series of monographs written by Rudolf Richter, and because of this, his objective was developing an extremely complex program for the analytical design of induction machines, which would consider and dimension an extended set of geometric, electromagnetic dimensions that would describe in detail the behavior of the designed machine. This program has been worked on for several decades, extensions and corrections being done periodically. Mr. Acad. Toma Dordea did not develop actual optimization techniques, but he used the elaborated program as a simple method of searching for the optimal solution by searching the defining domain of the design problem. The search domain of the design problem was implicitly defined by choosing the domains of the set of parameters accepted as data of the dedicated software. This way, by repeatedly running the design software and generating a great number of possible solutions, hundreds of solutions, the user can choose in the end the solution that offers the best results. This method of optimal design, being a simple technique of domain searching, lacking mechanisms of complete searching and of accelerating the search for the solution, cannot guarantee finding the optimal solution or of a vicinity that is precise enough and requires long running times.

In the '90s, Acad. Prof. Dr. Eng. Ion Boldea began the study of the optimal design of electric machines, imposing the inclusion of an optimal design chapter in the coordinated PhD theses. The optimal analytic design was integrated from the beginning with the simulation with a finite element of the designed machines, the simulation phase becoming the final phase, of validation, of the optimization algorithm. At first, gradient optimization methods were applied, numerically treated, and at the end of the 90's Acad. Ion Boldea proposed metaheuristic optimization algorithms and genetic algorithms as a solving method for the optimization problems. The decision to opt for genetic algorithms, at first with binary parameters, was taken because at that time there was a peak in the theoretical and experimental research in the field of Gas. Then followed the integration of genetic algorithms with real parameters and, naturally, the practical application of other variants of metaheuristic algorithms, mainly the PSO algorithm. Practical results, besides the PhD theses, were obtained in the researching contracts and collaborations made with the University of Aalborg, Denmark. Thus, we have to mention the research conducted by Prof. Dr. Eng. Lucian Tutelea and Conf. Dr. Eng. Alin Argeseanu, in the field of optimal design of direct-drive generators, of high power, used at the new generation of wind power stations. In these fields of research, it was opted for the design of a generator with transversal flow and permanent magnets.

An extremely interesting research in the field of optimal design was made in the PhD thesis "*Brushless DC Multiphase Reluctance Machines and Drives*" [43], thesis that was conducted by Mr. Dr. Eng. Dragos Ursu, coordinated by Mr. Acad. Ion Boldea, where the optimal design was achieved through three metaheuristic algorithms, *Black Hole Based Optimization (BHBO)*, *Particle Swarm Optimization (PSO)* and *Gravitational Search Algorithm (GSA)*. This research allowed the evaluation of the algorithms' performance: precision, running speed, writing effort, transparency and use facility.

## 6. 6 References

- [1] Colectiv, "Bazele Electrotehnicii – Teoria si Aplicatii", Editura Politehnica Timisoara, 2008, ISBN 978-973-625-587-8.
- [2] R. Richter, "Masini Electrice – Elemente Generale De Calcul. Masini De Curent Continuu", Editura Tehnica Bucuresti 1958.
- [3] R. Richter, "Masini Electrice II – Masina Sincrona Si Masina Comutatoare", Editura Tehnica Bucuresti, 1959.
- [4] R. Richter, "Masini Electrice III – Transformatorul", Editura Tehnica Bucuresti, 1960.
- [5] R. Richter, "Masini Electrice IV – Masini Asincrone", Editura Tehnica Bucuresti, 1960.
- [6] R. Richter, "Masini Electrice V – Masini Cu Colector De Curent Alternativ Mono- Si Polifazate. Grupuri Cu Masini De Reglaj", Editura Tehnica Bucuresti, 1961.
- [7] Singiresu S Rao, "Engineering Optimization – Theory and Practice", Wiley Interscience Publication, Wiley&SonsInc, Third Edition, 1996.
- [8] P. Venkataram, "Applied Optimization with Matlab Programming", Wiley Interscience Publication, Wiley&SonsInc, 2002.
- [9] P. Vas, "Artificial-Intelligence-Based Electrical Machines and Drives", Oxford University Press, 1999.
- [10] A. Turing, "On Computable Numbers with an Application to the Entscheidungs problem", *Proceedings of the London Mathematical Society*, Volume s2-42, Issue 1, 1 January 1937.
- [11] N. Wiener, „Cybernetics or Control and Communication in the Animal and the Machine“, Paris, (Hermann & Cie) & Camb. Mass. (MIT Press) ISBN 978-0-262-73009-9; 1948.
- [12] A. Rechenberg, „Evolutions strategie – Optimierung technischer Systemenach Prinzipien der biologischen Evolution“, PhD thesis, 1971.
- [13] G. Polya, "How to Solve It", Princeton University Press), 1957.
- [14] J. H. Holland, "Adaptation in Natural and Artificial Systems", MIT Press, 1975.
- [15] K. A. De Jong, "An analysis of the behavior of a class of genetic adaptive systems" Doctoral dissertation, University of Michigan, 1975, Dissertation Abstracts International, 36(10).
- [16] D. Goldberg "Genetic Algorithms in Search, Optimization and Machine Learning", Addison-Wesley Longman Publishing Co., Inc. Boston, MA, USA ©1989, ISBN: 0201 157675.
- [17] Z. Michalewicz, "Genetic Algorithms and Data Structure, Evolution Programs", Springer Verlag, 1992.
- [18] M. Mitchell, "An Introduction to Genetic Algorithms", MIT Press, 1999.
- [19] M. Gen, R. Cheng, "Genetic Algorithms and Engineering Optimization", Wiley, New York, 2000.
- [20] D. E. Goldberg, "Real-coded Genetic Algorithms, Virtual Alphabets, and Blocking", Dep. of General Engineering, Univ. of Illinois, USA, 1989.
- [21] A. H. Wright, "Genetic Algorithms for Real Parameter Optimization", Foundations of Genetic Algorithms, Morgan Kaufman, 1991.
- [22] P.J. Ballester, J. N. Carter, "An Effective Real-Parameter Genetic Algorithm for Multimodal Optimizations", Adaptive Computing in Design and Manufacture, VI, ch.7, 359-364, 2004.
- [23] F. Herrera, M. Lozano, J.L. Verdegay, "Dynamic and Heuristic Fuzzy Connectives-Based Crossover Operators for Controlling the Diversity and Convergence of Real Coded Genetic Algorithms", *International Journal of Intelligent Systems* 11 (1996).
- [24] F. Herrera, M. Lozano, J.L. Verdegay, "Fuzzy Connectives Based Crossover Operators to Model Genetic Algorithms Population Diversity. Fuzzy Sets and Systems", 92:1 (1997).



- [25] F. Herrera, M. Lozano, J.L. Verdegay, "Tackling Real-Coded Genetic Algorithms: Operators and Tools for the Behaviour Analysis", *Artificial Intelligence Review* 12 (1998)
- [26] F. Herrera, M. Lozano, "Gradual Distributed Real-Coded Genetic Algorithms", *IEEE Transactions on Evolutionary Computation* 4:1 (2000).
- [27] F. Herrera, M. Lozano, A. M. Sánchez "A taxonomy for the crossover operator for real-coded genetic algorithms: An experimental study" (2003) *International Journal of Intelligent Systems*.
- [28] F. Herrera, M. Lozano, A.M. Sanchez, "Hybrid cross over operators for real-coded genetic algorithms: An experimental study". *Soft Computing* 9, 2005.
- [29] N.J. Radcliffe "Equivalence Class Analysis of Genetic Algorithms" *Complex Systems* 5(2), 183–205, 1991.
- [30] H. Mühlenbein, D. Schlierkamp-Voosen, "Predictive models for breeder genetic algorithms in continuous parameter optimization. *Evolutionary Computation*", Volume 1, Number 1, 1993.
- [31] D. Schlierkamp-Voosen, "Strategy Adaptation by Competition. Second European Congress on Intelligent Techniques and Soft Computing", *EUFIT'94*, Aachen, September 1994, 1270-1274.
- [32] J.-M. Yang, C.-Y. Kao, "Integrating adaptive mutations and family competition into genetic algorithms as function optimizer." *Soft Computing* 4, 89–102, 2000.
- [33] J. Kennedy R. Eberhart, "Particle Swarm Optimization" *Proceedings of the IEEE International Conference on Neural Networks*, 4, 1942-1948, 1995.
- [34] M. Clerc, J. Kenedy, "The Particle Swarm-Explosion, stability and Convergence in a Multidimensional Complex Space", *IEEE Trans. Evolutionary Computation*, vol.6, issue 1, 2002.
- [35] E. Rashedi, S. Nezamabadi, S. Saryazdi, "GSA: A Gravitational Search Algorithm", *Information Science*, vol 179, no.13, 2009.
- [36] A. Hatamlou, S. Abdullah, Z. Othman, "Gravitational Search Algorithm with Heuristic Search for Clustering Problems", *3<sup>rd</sup> Conference on Data Mining and Optimization, 2011*, IEEE.
- [37] S. Binitha, S Siva Sathya, "A Survey of Bio inspired Optimization Algorithms", *International Journal of Soft Computing and Engineering (IJSC)*, ISSN: 2231-2307, Volume-2, Issue-2, May 2012.
- [38] G. George, K. Raimond, "A Survey on Optimization Algorithms for Optimizing the Numerical Functions", *International Journal of Computer Applications*(0975 – 8887) Volume 61– No.6, January 2013.
- [39] A. El-Henawy, N. A. Abdelmegeed, "Meta-Heuristics Algorithms: A Survey", *International Journal of Computer Applications*(0975 – 8887) Volume 179 – No.22, February 2018.
- [40] M. Mavrovouniotis, C. Li, S. Yang, "A survey of swarm intelligence for dynamic optimization: Algorithms and applications", *Swarm and Evolutionary Computation Journal*, pag. 1-17, volume 33, april 2017, ISSN: 2210-6502.
- [41] Randy L. Haupt, Sue Ellen Haupt, "Practical Genetic Algorithms" John Wiley & Sons, Inc., 2004.
- [42] A. Argeşeanu, M. Popa, "Algoritmi genetici. Teorie si aplicatii", Editura Politehnica, 2006.
- [43] A. Argeşeanu, "Algoritmi de optimizare în inginerie electrică- probleme practice "Politehnica Timișoara, ISBN 978-606-554-976-0, 2015.
- [44] D. Ursu „Brushless DC Multiphase Reluctance Machines and Drives”, PhD thesis, University Politehnica Timisoara, Romania, 2014.

# UNIFIED TREATMENT OF CORE LOSSES AND SATURATION IN THE DQ MODEL OF ELECTRIC MACHINES

## Abstract

The d-q (and space vector) model has been widely accepted to model dc brush, synchronous and induction (ac) machine in electric power systems at constant or at variable speed, with a PWM converter supply.

Magnetic saturation, cross-coupling saturation, has proven worthy of thorough consideration in electric machine design and control in encoderless electric drives. This chapter extends the dq – model of electric machines, with magnetic saturation, by adding virtual windings to the model core loss for transients and steady state. Based on two seminal papers, [1-2] this chapter details the subject by digital simulations and testing suggestions, while in the end presents recent developments on the subject, to illustrate its timelines.

## 7. 1 Introduction

The d-q (space phasor) model of electric machines has been traditionally used to investigate transient with and without different control systems of power, or torque, speed, or position.

However, in many such cases, magnetic saturation and core loss have been neglected, until recently.

But saturation of main flux path has been considered individually in dc-brush [3] induction [4] and synchronous machines [5-6] dq models, mainly for steady state operations.

Building up on [5-6] this chapter introduces first (from [1-2]) a general dq-model of dc brush and ac (traveling field) machines which includes magnetic saturation (of both main and leakage flux paths) and the core loss by fictitious stator and rotor orthogonal windings.

The unique d and q magnetization curves dependent on the resultant magnetization current of the machine  $I_m$  are adapted and ways to obtain them by theory and tests are

followed by full systems of equations, equivalent circuits are built and a case study for the IM is illustrated by comprehensive digital simulations.

The chapter ends with „echos“ of the subject up to today’s transients and control of electric machines as constant or variable speed generators and motors.

## 7.2 The proposed physical model

The proposed physical dq-model that includes magnetic saturation and core losses is shown in Fig. 7.1.

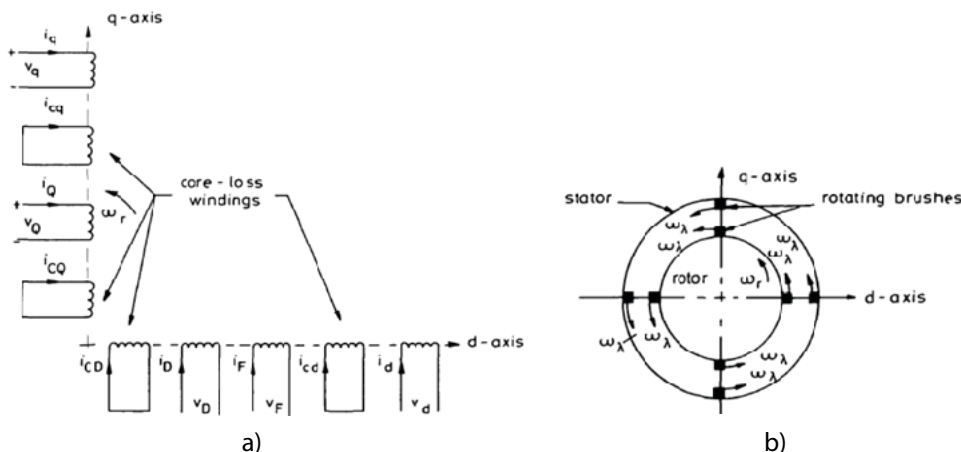


Fig. 7.1 The general physical dq model of electric machines including iron losses: a) dq model; b) physical model with rotating brushes.

The physical dq-model includes brushes along both axes both on the stator and rotor. The brush system is driven by a servomotor that mimics the rotation of coordinate system at speed  $\omega_\lambda$ . The core losses are represented by short circuited dq windings both on the stator and on the rotor, with currents  $i_{cd}$ ,  $i_{cq}$ ,  $i_{cD}$ ,  $i_{cQ}$ .

Besides, the stator shows two orthogonal (dq) windings ( $i_d$ ,  $i_q$ ) while the rotor has three such windings ( $i_F$ ,  $i_D$ ,  $i_Q$ ). The number of rotor windings may be extended along both d and q axes to account for frequency (skin) effects.

The general dq model in Fig. 1 pictures all standard electric machines from dc brush through induction to synchronous machines.

As the dq model’s main advantage is represented by d and q axis inductances independent of rotor position the system of coordinates speed  $\omega_\lambda=0$  for dc brush machines, to the rotor for synchronous machines ( $\omega_\lambda=\omega_r$ ) and  $\omega_\lambda=0$ ,  $\omega_r$ ,  $\omega_1$  for induction machines and drives.

The core losses windings are shortcircuited and may contain both a resistance ( $R_{cd}$ ,  $R_{cq}$ ,  $R_{cD}$ ,  $R_{cQ}$ ) and a leakage inductance, though it is mainly the variation of main path flux that produces the core losses.

$R_{cd}, R_{cq}, R_{cD}, R_{cQ}$  depend on main flux level and on the respective frequency (in the stator and in the rotor ( $f_2$ )). They may be calculated ( $f_1$ ) by analytical or numerical field models of the machines or measured. The leakage inductances ( $L_{s\sigma}, L_{cd\sigma}, L_{cq\sigma}, L_{F\sigma}, L_{cD\sigma}, L_{cQ\sigma}, L_{D\sigma}, L_{Q\sigma}$ ) of all windings may depend on their current (consider the case of closed slots). For transients, a transient such as leakage inductances may be used whenever d/dt occurs in the equations:

$$L_{i\sigma t} = L_{i\sigma} + \frac{\partial L_{i\sigma}}{\partial i_i} i_i \leq L_{i\sigma} \quad (7.1)$$

with these notes the general dq model equations may be developed.

### 7.3 Equations for the general dq model

With “transformer” induced voltages as  $-p\Psi$  and motion induced voltages as  $\omega\Psi$  ( $p=d/dt$ ), the voltage equations of the general dq model are:

$$\begin{aligned} V_d &= R_s \cdot i_d + L_{s\sigma t} \cdot p \cdot i_d - \omega_\lambda L_{s\sigma} i_q + p \cdot \Psi_{dm} - \omega_\lambda \cdot \Psi_{qm} \\ 0 &= R_{cd} \cdot i_{cd} + L_{cd\sigma} \cdot p i_{cd} + p \cdot \Psi_{dm} - \omega_\lambda \cdot \Psi_{qm} \\ V_q &= R_s \cdot i_q + L_{s\sigma t} \cdot p \cdot i_q + \omega_\lambda L_{s\sigma} i_d + p \cdot \Psi_{qm} + \omega_\lambda \cdot \Psi_{dm} \\ 0 &= R_{cq} \cdot i_{cq} + L_{cq\sigma} \cdot p i_{cq} + p \cdot \Psi_{qm} + \omega_\lambda \cdot \Psi_{dm} \end{aligned} \quad (7.2)$$

for the stator and:

$$\begin{aligned} V_F &= R_F i_F + L_{F\sigma t} \cdot p \cdot i_F + p \Psi_{dm} - k_F L_{Q\sigma} i_Q (\omega_\lambda - \omega_r) - (\omega_\lambda - \omega_r) \Psi_{qm} \\ 0 &= R_{cD} i_{cD} + L_{cD\sigma} \cdot p \cdot i_{cD} + p \Psi_{dm} - (\omega_\lambda - \omega_r) \Psi_{qm} \\ V_D &= R_D i_D + L_{D\sigma t} \cdot p \cdot i_D + p \Psi_{dm} - k_D L_{Q\sigma} i_Q (\omega_\lambda - \omega_r) - (\omega_\lambda - \omega_r) \Psi_{qm} \\ V_Q &= R_Q i_Q + L_{Q\sigma t} \cdot p \cdot i_Q + (\omega_\lambda - \omega_r) \cdot (k_{QD} L_{D\sigma} \cdot i_D + k_{QF} L_{F\sigma} \cdot i_F) + \\ &\quad + p \Psi_{qm} + (\omega_\lambda - \omega_r) \Psi_{dm} \\ 0 &= R_{cQ} \cdot i_{cQ} + L_{cQ\sigma} \cdot p \cdot i_{cQ} + p \Psi_{qm} - (\omega_\lambda - \omega_r) \cdot \Psi_{dm} \end{aligned} \quad (7.3)$$

for the rotor, where:  $\Psi_{dm}$  and  $\Psi_{qm}$  are the main path flux – linkages for the dq axes,  $V_d, V_q, V_F, V_D, V_Q$  (different from zero in wound rotor winding machines) and the currents  $i_d, i_q, i_{cd}, i_{cq}, i_{cD}, i_{cQ}, i_F, i_D, i_Q$ , all reduced to the stator are defined in Fig. 7.1. Coefficients  $k_F, k_D, k_{QD}, k_{QF}$  account for the fact that the rotor windings are not symmetric (along the d-q axes); however when  $\omega_\lambda = \omega_r$  the influence of  $k_F, k_D, k_{QD}, k_{QF}$  disappears as expected (the case for synchronous machines).

The electromagnetic torque, obtained from the power balance, in stator fed a.c. machines (synchronous and induction) is:

$$T_{es} = \frac{3}{2} p \left[ \Psi_{dm} (i_q + i_{cq}) - \Psi_{qm} (i_d + i_{cd}) \right] \quad (7.4)$$

Similarly for the d.c. brush machine, fed in the rotor:

$$T_{er} = p \left[ \Psi_{dm} (i_Q + i_{cQ}) - \Psi_{qm} (i_D + i_F + i_{cD}) \right] \quad (7.5)$$

The leakage inductances of core windings are considered constant ( $L_{cdo}=L_{cdot}$ ;  $L_{cqo}=L_{cqot}$ ;  $L_{cDo}=L_{cDot}$ ;  $L_{cQo}=L_{cQot}$ ) even zero in a first (reasonable) approximation.

## 7.4 Cross – coupling magnetic saturation equations

As mentioned above, the main assumption is that the magnetization functions  $\Psi_{dm}^* (i_m)$ ,  $\Psi_{qm}^* (i_m)$  are unique and dependent on the total magnetization current of the machine  $i_m$ :

$$\begin{aligned} i_m^2 &= i_{dm}^2 + i_{qm}^2; \quad i_{dm} = i_d + i_{cd} + i_F + i_D + i_{cD} \\ i_{qm} &= i_q + i_{cq} + i_{cQ} + i_Q \end{aligned} \quad (7.6)$$

Consequently, the actual main flux linkage components  $\Psi_{dm}$ ,  $\Psi_{qm}$  in voltage equations (7.2) – (7.3) are:

$$\Psi_{dm} = \Psi_{dm}^* (i_m) \cdot \frac{i_{dm}}{i_m}; \quad \Psi_{qm} = \Psi_{qm}^* (i_m) \cdot \frac{i_{qm}}{i_m} \quad (7.7)$$

The time derivatives  $p\Psi_{dm}$  and  $p\Psi_{qm}$  become thus:

$$\begin{aligned} p\Psi_{dm} &= L_{ddm} \cdot p \cdot i_{dm} + L_{qdm} \cdot p \cdot i_{qm} \\ p\Psi_{qm} &= L_{dqm} \cdot p \cdot i_{dm} + L_{qqm} \cdot p \cdot i_{qm} \end{aligned} \quad (7.8)$$

$$L_{ddm} = L_{dmt} \cdot \left( \frac{i_{dm}}{i_m} \right)^2 + L_{dm} \cdot \left( \frac{i_{qm}}{i_m} \right)^2$$

$$L_{qqm} = L_{qmt} \cdot \left( \frac{i_{qm}}{i_m} \right)^2 + L_{qm} \cdot \left( \frac{i_{dm}}{i_m} \right)^2$$

where:

$$L_{qdm} = (L_{dmt} - L_{dm}) \cdot \frac{i_{dm} \cdot i_{qm}}{i_m^2} \quad (7.9)$$

$$L_{dqm} = (L_{qmt} - L_{qm}) \cdot \frac{i_{dm} \cdot i_{qm}}{i_m^2}$$

$$L_{dm} = \Psi_{dm}^* (i_m) / i_m; \quad L_{qm} = \Psi_{qm}^* (i_m) / i_m$$

$$L_{dmt} = \frac{\partial \Psi_{dm}^*}{\partial i_m}; \quad L_{qmt} = \frac{\partial \Psi_{qm}^*}{\partial i_m}$$

It should be noticed that, to fulfill the reciprocity theorem:

$$L_{qdm} = L_{dqm} \text{ and thus } L_{dmt} - L_{dm} = L_{qmt} - L_{qm} \quad (7.10)$$

The obvious variables in (7.2)-(7.3) are the currents  $i_{dm}, i_{qm}, i_F, i_D, i_Q, i_{cd}, i_{cq}, i_{cD}, i_{cQ}$  (the stator currents) are eliminated based on (7.6) and speed  $\omega_r$  when the motion equation is needed:

$$\frac{J_S}{P_1} \omega_r = T_e - T_{load}; p_1 - \text{pole pairs} \quad (7.11)$$

Before proceeding to digital simulations, let us consider some testing methods to determine the magnetic saturation curves  $\Psi_{dm}^*(i_m)$  and  $\Psi_{qm}^*(i_m)$ .

## 7.5 Magnetization (saturation) curves $\Psi_{dm}^*(i_m)$ and $\Psi_{qm}^*(i_m)$

Let us consider that the resistances  $R_s, R_F, R_D, R_Q$  of stator and rotor windings and their leakage inductances  $L_{s\sigma}, L_{s\sigma t}, L_{F\sigma}, L_{F\sigma t}, L_{D\sigma}, L_{D\sigma t}, L_{Q\sigma}, L_{Q\sigma t}$ , are already known from now standard standstill frequency tests or from FEM calculations [7]. The magnetization curves  $\Psi_{dm}^*(i_m)$  and  $\Psi_{qm}^*(i_m)$  may be easily obtained from standstill shortcircuit (current decay) tests as illustrated in Fig. 7.2-7.4 for synchronous, induction and d.c. brush machines:

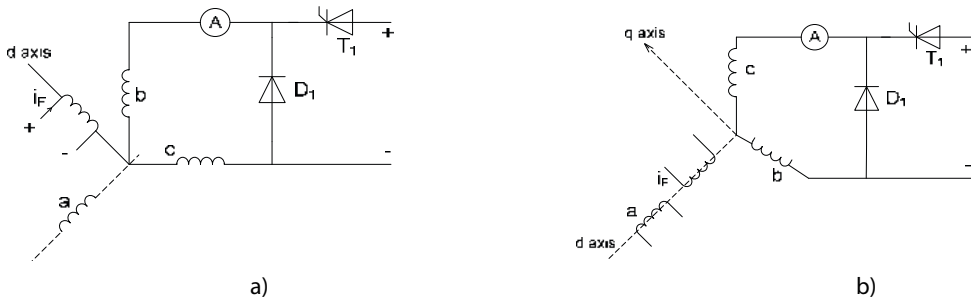


Fig. 7.2 Synchronous machine standstill shortcircuit tests: a) in axis d; b) in axis q.

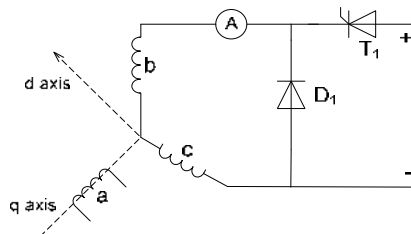


Fig. 7.3 Induction machine standstill test.

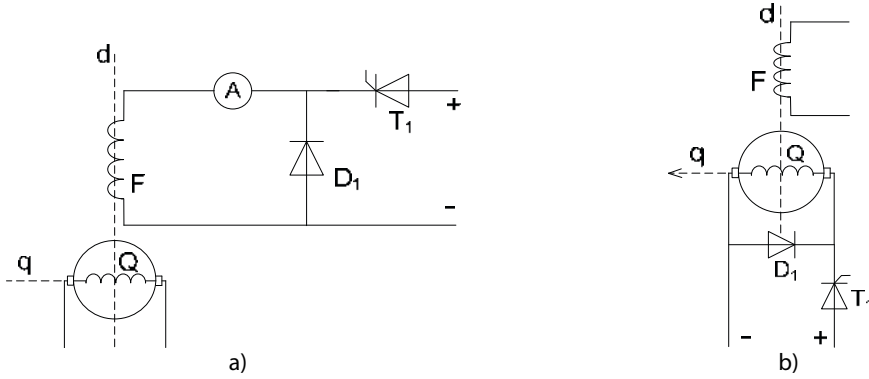


Fig. 7.4 DC brush machine standstill short-circuit test: a) along d (field) axis; b) along q (armature) axis.

In principle, the machines hold at standstill are dc fed at a certain current through the switch T1 and then the switch is turned off and the current always to zero through the freewheeling diode D1. The negative current and the voltage along the diode D1, VD1 are needed and then:

$$2i_d R_s = -p\Psi_s \quad (7.12)$$

Upon current decay (in axis d)

$$2R_s \int_0^{\infty} i_d dt + \int_0^{\infty} V_{d1} dt = (\Psi_d^*)_{t=0} - (\Psi_d^*)_{t=\infty} \quad (7.13)$$

As it is possible to inject a d.c. current in the other orthogonal axis ( $i_{F0}$  in Fig. 7.2) the expressions of initial and flux linkages are:

$$(\Psi_d^*)_{t=0} = 2 \left[ L_{\sigma s} i_{d0} + L_{dm} (i_{d0} + i_{F0}) \right] \quad (7.14)$$

$$(\Psi_d^*)_{t=\infty} = 2L_{dm} i_{F0}$$

So finally:

$$L_{dm} (i_{d0}, i_F) = L_{dm}^* (i_{m0}) = \frac{R_s \int_0^{\infty} i_d dt + \int_0^{\infty} \frac{V_{d1}}{2} dt +}{i_{d0}} - L_{\sigma s} \quad (7.15)$$

Thus  $(\Psi_{dm}^*)_{t=0} = L_{dm}^* (i_{m0}) \cdot i_m$  represent the magnetization curve along axis d.

Now, with two phases supplied in series in Fig. 7.2:

$$i_{d0} = \frac{2}{3}(i_a + i_b \sin 120^\circ + i_c \sin 240^\circ) = \frac{2}{3}i_b \frac{2\sqrt{3}}{2} = \frac{2}{\sqrt{3}}i_{b0} \quad (7.16)$$

Now, as in Fig. 7.2a both  $i_{F0}$  and  $i_{d0}$  are in axis d, the total magnetization current  $i_{m0}$  will be:

$$i_{m0} = \frac{2}{\sqrt{3}}i_{b0} + i_{F0} \quad (7.17)$$

In axis q (Fig. 7.2b) the magnetizing current would be:

$$i_{m0} = \sqrt{\left(\frac{2}{\sqrt{3}}i_{b0}\right)^2 + i_{F0}^2} \quad (7.18)$$

The rationale is similar for the other cases.

The combination of currents along the d and q axes in standstill shortcircuit (current decay) tests allows for the calculation of  $L_{dqm}$  and  $L_{ddm}$ ,  $L_{qqm}$  more completely and thus highlight the crosscoupling saturation effect visible in equs (7.9). It may be argued that the assumptions of unique magnetization curves  $\Psi_{dm}^*(i_m)$  and  $\Psi_{qm}^*(i_m)$  along the two axes might not be exact enough with all combinations of  $i_{dm}$  and  $i_{qm}$  and thus sometimes may lead to two different pairs of  $i_{dm}$ ,  $i_{qm}$  for given  $i_m$ . True, especially in salient pole synchronous machines under under-excited ( $i_{F0} > 0$  (small);  $i_{d0} > 0$ ) as proven via FEM more than a decade later [8].

## 7.6 Core loss resistances measurements

The equivalent core loss windings resistances may either be calculated (via analytical or numerical (FEM) field models) or extracted from measurements.

For an induction machine, where for most cases the slip frequency is small, the core loss is situated only in the stator. A no load motor testing at various voltage values may be used to finally isolate from the power balance the core losses (Fig. 7.5).

$$P_{10}(V_1^2) = 3R_s i_{s0}^2 + p_{iron} + p_{mec} \quad (7.19)$$

$$\frac{3}{2}R_{cs} i_{cd}^2 = p_{c0} \approx 3 \frac{V_1^2}{R_{cs}} \quad (7.20)$$

we obtain  $R_{cs} = f\left(\frac{V_1}{\omega_1}, i_{s0}\right)$  which may be used as such ( $\frac{V_1}{\omega_1} \approx \Psi_{dm}^*$ ,  $i_{s0} = i_{d0}$ ).



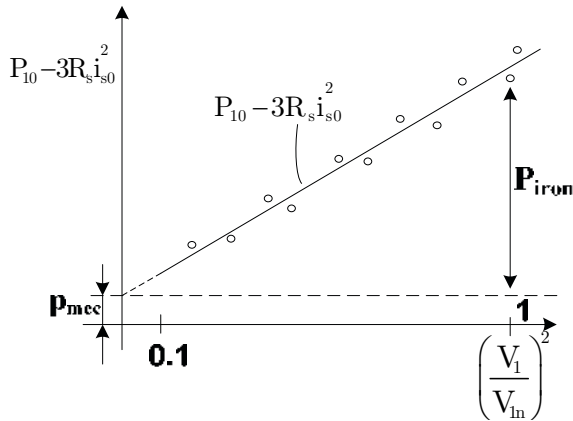


Fig. 7.5 No load induction motor testing.

Also for an ideal IM testing Ref 1 presents a more accurate isolation of core losses and the calculus of  $R_{cd}=R_{cq}$  (IM). Now the leakage inductances for the core loss fictitious windings in the stator  $L_{c\sigma}$  may be approximate as  $L_{c\sigma}=R_c/\omega_1$  for all frequencies of.

Similar tests may be run for the d.c. brush and synchronous machines to identify the core loss winding resistances.

Now that the parameters in the electric machine have been investigated, for identification we first attempt for the synchronous (most complicated) machine to illustrate system voltage equations in an equivalent circuit for transients which illustrated the crosscoupling saturation effects, but, for simplicity ignores the core loss circuits and leakage inductances saturation (Fig. 7.6).

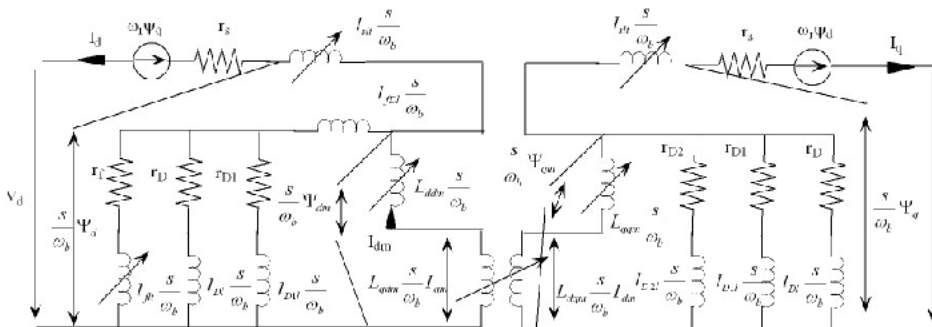


Fig. 7.6 General equivalent circuit of synchronous machines including crosscoupling magnetic saturation (after [7]).

The crosscoupling between d and q orthogonal axes due to magnetic saturation is evident (Fig. 7.6) both in  $L_{ddm}$  and  $L_{qqm}$  and in  $L_{dqm}=L_{qdm}$  transient inductances, besides  $\Psi_{dm}^*(i_m)$  and  $\Psi_{qm}^*(i_m)$  flux linkage functions. As discussed later in the chapter cross-coupling saturation effect not only affects machine performance, but also introduces rotor position estimation error in encoderless electric motors and generators drives at variable speed and thus has to be accounted for on-line.

## 7.7 State - space equations

To solve equations (7.2)-(7.3) and (7.11) by numerical methods, a state-space format has to be adopted.

As already pointed out, the variables are to be chosen. They may be exclusively flux linkage or currents or a combination of both types.

We stick here to the suggested current variables:  $i_{dm}$ ,  $i_{qm}$ ,  $i_{cd}$ ,  $i_{cq}$ ,  $i_D$ ,  $i_F$ ,  $i_{cD}$ ,  $i_{cQ}$ ,  $i_Q$  and  $\omega_r$ :

$$\begin{aligned} p i_{dm} = \frac{1}{\Delta} \left\{ -F_d \left[ 1 + L_{qdm} \left( \frac{1}{L_{s\sigma}} + \frac{1}{L_{c\sigma}} + \frac{1}{L_{C\sigma}} + \frac{1}{L_{Q\sigma}} \right) \right] + \right. \\ \left. + F_q \cdot L_{qdm} \left( \frac{1}{L_{s\sigma}} + \frac{1}{L_{c\sigma}} + \frac{1}{L_{D\sigma}} + \frac{1}{L_{F\sigma}} + \frac{1}{L_{C\sigma}} \right) \right\} = G_d \end{aligned} \quad (7.21)$$

$$\begin{aligned} p i_{qm} = \frac{1}{\Delta} \left\{ -F_q \left[ 1 + L_{ddm} \left( \frac{1}{L_{s\sigma}} + \frac{1}{L_{c\sigma}} + \frac{1}{L_{D\sigma}} + \frac{1}{L_{F\sigma}} + \frac{1}{L_{C\sigma}} \right) \right] + \right. \\ \left. + F_d \cdot L_{dqm} \left( \frac{1}{L_{s\sigma}} + \frac{1}{L_{c\sigma}} + \frac{1}{L_{C\sigma}} + \frac{1}{L_{Q\sigma}} \right) \right\} = G_q \end{aligned} \quad (7.22)$$

$$p i_{cd} = \frac{1}{L_{c\sigma}} \left( -R_{cs} i_{cd} + \omega_\lambda L_{qm} i_{qm} - L_{ddm} G_d - L_{qdm} G_q \right) \quad (7.23)$$

$$p i_{cq} = \frac{1}{L_{c\sigma}} \left( -R_{cs} i_{cq} - \omega_\lambda L_{dm} i_{dm} - L_{qqm} G_q - L_{dqm} G_d \right) \quad (7.24)$$

$$p i_D = \frac{1}{L_{D\sigma}} \left[ V_D - R_D i_D - L_{ddm} G_d - L_{qdm} G_q + (\omega_\lambda - \omega_r) (L_{qm} i_{qm} + K_D L_{Q\sigma} i_Q) \right] \quad (7.25)$$

$$p i_F = \frac{1}{L_{F\sigma}} \left[ V_F - R_F i_F - L_{ddm} G_d - L_{qdm} G_q + (\omega_\lambda - \omega_r) (L_{qm} i_{qm} + K_F L_{Q\sigma} i_Q) \right] \quad (7.26)$$

$$p i_{cD} = \frac{1}{L_{C\sigma}} \left[ -R_{cr} i_{cD} - L_{ddm} G_d - L_{qdm} G_q + (\omega_\lambda - \omega_r) L_{qm} i_{qm} \right] \quad (7.27)$$

$$\begin{aligned} p i_Q = \frac{1}{L_{Q\sigma}} \cdot \left[ V_Q - R_Q i_Q - (\omega_\lambda - \omega_r) (k_{QD} L_{D\sigma} i_D + k_{QF} L_{F\sigma} i_F + L_{dm} i_{dm}) \right. \\ \left. - L_{qqm} G_q - L_{dqm} G_d \right] \end{aligned} \quad (7.28)$$

$$p_{i_{cQ}} = \frac{1}{L_{C\sigma}} \left[ -R_{Cr} i_{cQ} - L_{q_{qm}} G_q - L_{d_{qm}} G_d - (\omega_\lambda - \omega_r) L_{dm} i_{dm} \right] \quad (7.29)$$

$$p\omega_r = \frac{P^2}{J} \left[ L_{dm} i_{dm} (i_{qm} - i_Q - i_{cQ}) - L_{qm} i_{qm} (i_{dm} - i_D - i_F - i_{cD}) \right] - \frac{P}{J} T_L \quad (7.30)$$

with

$$\Delta = \left[ 1 + L_{ddm} \left( \frac{1}{L_{s\sigma}} + \frac{1}{L_{c\sigma}} + \frac{1}{L_{C\sigma}} + \frac{1}{L_{D\sigma}} + \frac{1}{L_{F\sigma}} \right) \right] \left[ 1 + L_{qqm} \left( \frac{1}{L_{s\sigma}} + \frac{1}{L_{c\sigma}} + \frac{1}{L_{C\sigma}} + \frac{1}{L_{Q\sigma}} \right) \right] - L_{dqm} L_{qdm} \left( \frac{1}{L_{s\sigma}} + \frac{1}{L_{c\sigma}} + \frac{1}{L_{C\sigma}} + \frac{1}{L_{D\sigma}} + \frac{1}{L_{F\sigma}} \right) \left( \frac{1}{L_{s\sigma}} + \frac{1}{L_{c\sigma}} + \frac{1}{L_{C\sigma}} + \frac{1}{L_{Q\sigma}} \right) \quad (7.31)$$

$$F_d = \frac{1}{L_{s\sigma}} (R_s i_d - v_d) + \frac{1}{L_{c\sigma}} R_{cs} i_{cd} + \frac{1}{L_{C\sigma}} R_{Cr} i_{cD} + \frac{1}{L_{D\sigma}} (R_D i_D - v_D) + \frac{1}{L_{F\sigma}} (R_F i_F - v_F) - \omega_\lambda (i_{qm} - i_{cq} - i_{cQ} - i_Q) - \omega_\lambda L_{qm} i_{qm} \left( \frac{1}{L_{s\sigma}} + \frac{1}{L_{c\sigma}} \right) - (\omega_\lambda - \omega_r) L_{qm} i_{qm} \left( \frac{1}{L_{D\sigma}} + \frac{1}{L_{C\sigma}} + \frac{1}{L_{F\sigma}} \right) - (\omega_\lambda - \omega_r) \frac{1}{L_{F\sigma}} (k_D L_{Q\sigma} i_Q + k_F L_{Q\sigma} i_Q) \quad (7.32)$$

$$F_q = \frac{1}{L_{s\sigma}} (R_s i_q - v_q) + \frac{1}{L_{Q\sigma}} (R_Q i_Q - v_Q) + \frac{1}{L_{c\sigma}} R_{cs} i_{cq} + \frac{1}{L_{C\sigma}} R_{cr} i_{cD} + \omega_\lambda (i_{dm} - i_{cd} - i_{cD} - i_D - i_F) + \omega_\lambda L_{dm} i_{dm} \left( \frac{1}{L_{s\sigma}} + \frac{1}{L_{c\sigma}} \right) + (\omega_\lambda - \omega_r) \left[ L_{dm} i_{dm} \left( \frac{1}{L_{Q\sigma}} + \frac{1}{L_{C\sigma}} \right) + \frac{1}{L_{Q\sigma}} (k_{QD} L_{D\sigma} i_D + k_{QF} L_{F\sigma} i_F) \right] \quad (7.33)$$

$$\frac{d\omega_r}{dt} = p_1 \cdot \frac{1}{J} \cdot (T_e - T_{load}); \quad i_d = i_{dm} - i_{cD} - i_F - i_D - i_{cD} \\ i_q = i_{qm} - i_{cq} - i_Q - i_{cQ} \quad (7.34)$$

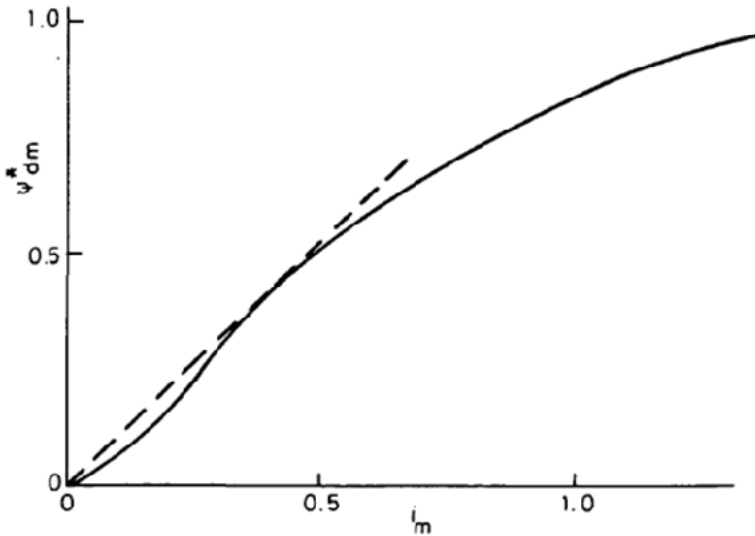
State space equations (7.21)-(7.34) refer especially to the synchronous machines, but may be adopted for the d.c. brush machines and for induction machines via simplifications as in table 7.1.

Table 7.1 Constraints.

Machine type	Constraints	Comments
Synchronous	$\omega_\lambda = \omega_r, v_D = v_Q = 0$	Reference frame attached to rotor
Induction	$R_D = R_Q, L_{D\sigma} = L_{Q\sigma}, i_F = 0, \psi_{dm}^*(i_m) = \psi_{qm}^*(i_m)$	General constraints
	(i) $\omega_\lambda = \omega_1, v_D = v_Q = 0$	Reference frame synchronously rotating
	(ii) $\omega_\lambda = \omega_r, v_D \neq 0, v_Q \neq 0$	Reference frame attached to rotor; doubly fed or asymmetrical rotor connections
	(iii) $\omega_\lambda = 0$	Large speed variations
DC	$\omega_\lambda = 0, i_q = 0, i_F = i_D = 0$	Brushes at standstill; separately excited machine

### 7.8 Digital simulation results on an induction machine

We apply the proposed general dq model on an induction machine with the data [4]:  $R_s = 3.41 \Omega, R_r = 1.89 \Omega, L_{s\sigma} = 1.14 \times 10^{-2} \text{H}, L_{r\sigma} = 0.9076 \times 10^{-2} \text{H}, J = 6.25 \times 10^{-3} \text{kg}\cdot\text{m}^2$ . The magnetization curve  $\Psi_{dm}^*(i_m)$  is shown in Fig. 7.7a.



a)

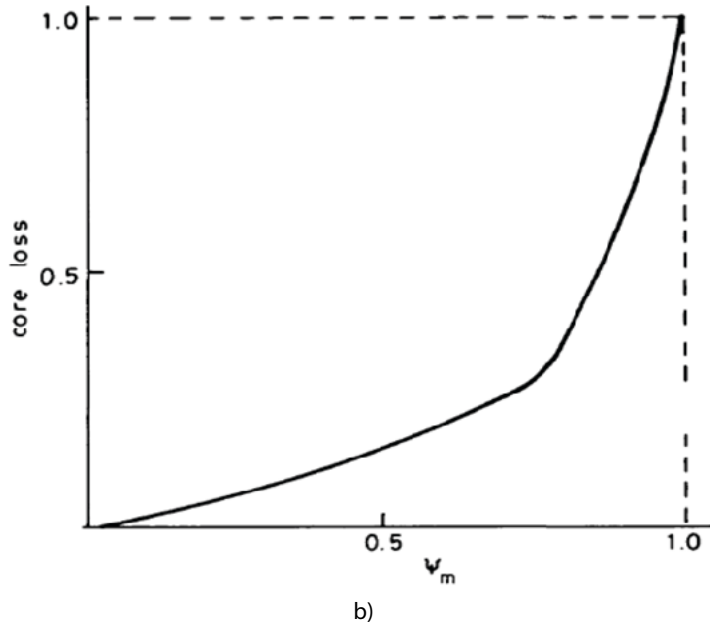


Fig. 7.7 Per unit (p.u.) magnetization curve of an IM, a) and core losses, b) norm values:  $\Psi_{dm0}=2.0936$  Wb,  $i_{m0}=10.034$  A,  $p_{iron0}=500$  W,  $f_1=50$  Hz.

The core losses vary with magnetization flux linkage  $\Psi_m$  (same in axis d and q for IMs) as in Fig. 7.7b at rated frequency (50 Hz).

Parameter estimation from data in Figs. 7.7a, b induces either finding first an inversable (exponential or a ratio of polynomials) curve fitting or the use of look-up tables with linear

$$\text{interpolation and } \frac{d\Psi_{dm}^*}{di_m} \approx \frac{\Delta\Psi_{dm}^*}{\Delta i_m}.$$

An average value is considered at the border of two successive table points to soften the derivative discontinuity.

### 7.8.1 Core loss winding parameters

To illustrate quantitatively the parameters estimation from Fig. 7.7b, we consider all steady state and transients to be investigated at  $f_1=50$  Hz.

The stator core resistance is obtained from two equations:

$$R_{cs} \sqrt{i_{cd}^2 + i_{cq}^2} = \omega_1 \sqrt{\Psi_{dm}^2 + \Psi_{qm}^2} = \omega_1 \Psi_m \quad (7.35)$$

$$3 \cdot R_{cs} (i_{cd}^2 + i_{cq}^2) = p_{iron} \quad (7.36)$$

$$R_{cs} = \frac{\omega_1 \Psi_m^2}{p_{iron}(\omega_1, \Psi_m)} \quad (7.37)$$

Approximating the core loss as:

$$p_{iron} = c_1 \Psi_m^2; c_1 = \frac{500}{2.0936^2} = 114.07 \left( \frac{W}{Wb^2} \right) \quad (7.38)$$

$$R_{cs} = \frac{\omega_1^2 \Psi_m^2}{C_1 \Psi_m^2} = \frac{\omega_1^2}{C_1} = 8.6434 \times 10^2 \Omega; \quad (7.39)$$

Correspondingly,

$$L_{c\sigma} \approx \frac{R_{cs}}{\omega_1} = 2.754 \text{ H} \quad (7.40)$$

Note:  $R_{cs}$  and  $L_{c\sigma}$  are “parallel” parameters, which explains why they are rather large.

### 7.8.2 Steady state values computation

The initial values of variables are supposed to correspond to a steady state operation mode. For the induction machine equations (7.2-7.3) with  $\omega_\lambda = \omega_1$  (synchronous coordinates) yield:

$$\begin{aligned} V_{d0} &= R_s \cdot i_{d0} - \omega_1 L_{s\sigma} i_{q0} - \omega_1 \cdot \Psi_{qm0} \\ V_{q0} &= R_s \cdot i_{q0} + \omega_1 L_{s\sigma} i_{d0} + \omega_1 \cdot \Psi_{dm0} \\ 0 &= R_{cd} \cdot i_{cd0} - \omega_1 \cdot \Psi_{qm0}; \quad 0 = R_{cq} \cdot i_{cq0} - \omega_1 \cdot \Psi_{dm0} \\ 0 &= R_r \cdot i_{D0} - L_{r\sigma} \cdot i_{Q0} \cdot s \omega_1 - s \omega_1 \cdot \Psi_{qm0} \\ 0 &= R_r \cdot i_{Q0} + L_{r\sigma} \cdot i_{D0} \cdot s \omega_1 + s \omega_1 \cdot \Psi_{dm0} \\ T_e &= \frac{3}{2} p_1 \left[ \Psi_{dm0} (i_{q0} + i_{cq0}) - \Psi_{qm0} (i_{d0} + i_{cd0}) \right] \\ i_{dm0} &= i_{d0} + i_{cd0} + i_{D0}; \quad i_{qm0} = i_{q0} + i_{cq0} + i_{Q0} \\ s &= (\omega_1 - \omega_r) / \omega_1 \end{aligned} \quad (7.41)$$

The dq stator voltage components  $V_{d0}$ ,  $V_{q0}$  are obtained (with  $\omega_\lambda = \omega_1$ ) from Park transformation:

$$\begin{aligned} \begin{bmatrix} V_{d0} \\ V_{q0} \end{bmatrix} &= \frac{2}{3} \begin{bmatrix} \cos(\omega_1 t + \delta_0) & \cos\left(\omega_1 t + \delta_0 + \frac{2\pi}{3}\right) & \cos\left(\omega_1 t + \delta_0 - \frac{2\pi}{3}\right) \\ -\sin(\omega_1 t + \delta_0) & -\sin\left(\omega_1 t + \delta_0 + \frac{2\pi}{3}\right) & -\sin\left(\omega_1 t + \delta_0 - \frac{2\pi}{3}\right) \end{bmatrix} \times \\ &\times \begin{bmatrix} V_1 \sqrt{2} \cdot \cos(\omega_1 t) \\ V_1 \sqrt{2} \cdot \cos\left(\omega_1 t - \frac{2\pi}{3}\right) \\ V_1 \sqrt{2} \cdot \cos\left(\omega_1 t + \frac{2\pi}{3}\right) \end{bmatrix} \end{aligned} \quad (7.42)$$

Finally:

$$V_{d0} = V_1 \sqrt{2} \cdot \cos \delta_0; \quad V_{q0} = -V_1 \sqrt{2} \cdot \sin \delta_0 \quad (7.43)$$

By manoeuvring equations (7.41), (7.43) by using the magnetization curve (Fig.7.7a) as a look-up table, three steady state situations are investigated for given value of slip (all for 380 V (line voltage) and 50 Hz):

- Case 1: saturation and core loss considered
- Case 2: saturation considered but core losses neglected
- Case 3: no saturation, neither core losses considered.

Fig. 7.8a, b and 7.9a, b show the calculated stator phase current  $I_1$ , electromagnetic torque  $T_{es}$ , efficiency\*power factor and the magnetization current  $i_m$  versus slip  $s$  as calculated for the IM under investigation.

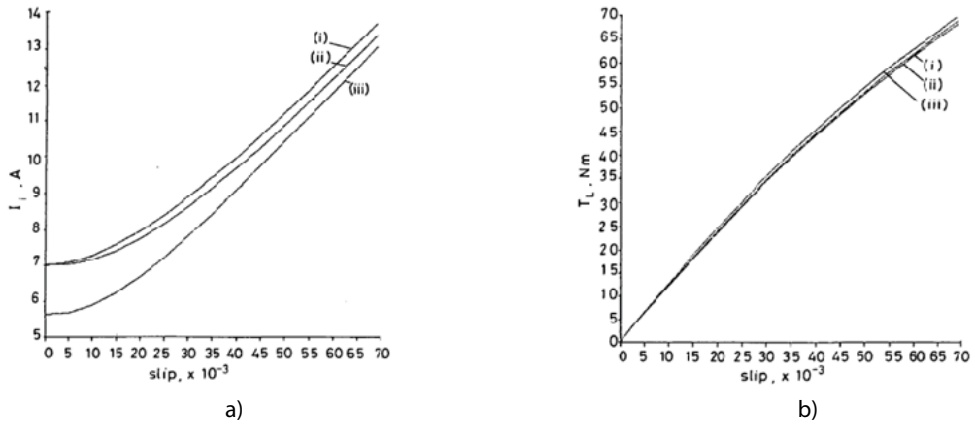


Fig. 7.8 Stator current  $I_1$ , a) and electromagnetic torque  $T_{es}$ , b) versus slip (at 380 V/line voltage RMS and  $f_1=50$  Hz); (i) case a, (ii) case b, (iii) case c.

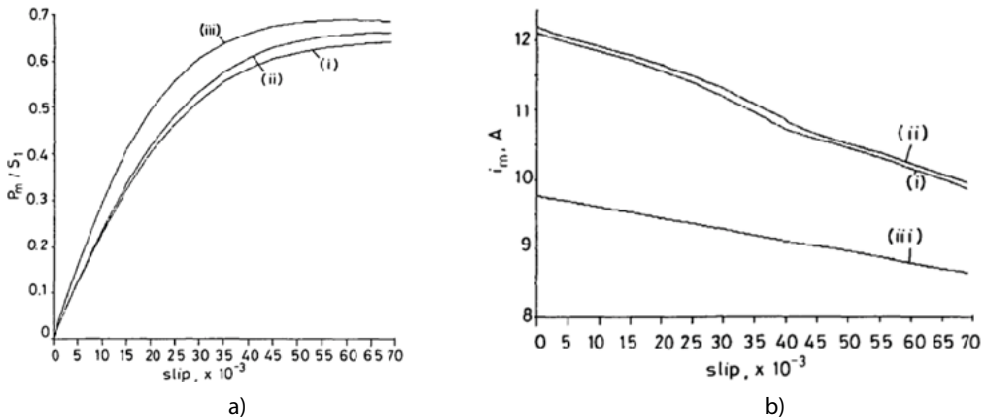


Fig. 7.9 Efficiency\*power factor, a) and magnetization current  $i_m$  versus slip (at 380 V and  $f_1=50$  Hz); (i) case a, (ii) case b, (iii) case c, b).

It is evident that for the induction motor under investigation – quite saturated for the rated voltage  $V_1$  and frequency  $f_1$  – the influence of magnetic saturation is very important in steady state on all 4 variables – stator current, torque, efficiency \*power factor and magnetization current above 0.02 p.u. slip value. The influence of core loss in steady state in efficiency and primary (stator) current but less important in torque  $T_{es}$  and in magnetization current  $i_m$ .

Let us now investigate transients for cases a, b, c.

### 7.8.3 Transients

The theory developed here has been applied to calculate by numerical methods the evolution of two large – signal transients:

(a) sudden 40% reduction of supply voltage (from 380 V/line RMS) at initial slip  $S=0.03$ , for constant load torque

(b) disconnection of the loaded motor at  $S=0.03$  for 10 milliseconds and reconnection with  $\delta_0=0$  (but any value of  $\delta_0$  may be explored). The load torque is kept constant throughout the transients.

The results for the step voltage reduction transients are displayed in Figs. 7.10a, b and 7.11a, b in terms of stator current, torque, rotor speed (in rad/s) and core loss winding current  $i_{cd}$ ,  $i_{cq}$ , respectively.

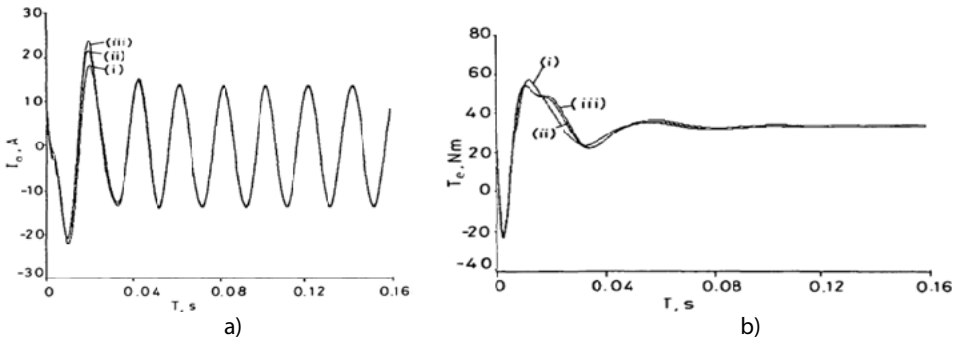


Fig. 7.10 Step 40% voltage reduction transients at constant load torque: a) stator current, b) electromagnetic torque, (after [1]).

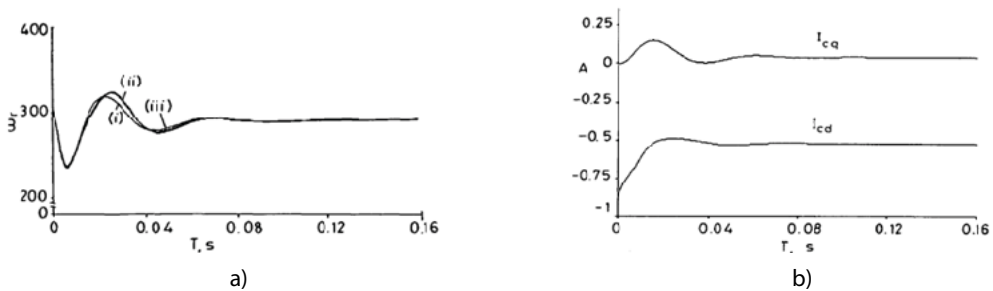


Fig. 7.11 Step 40% voltage reduction transients at constant load torque: a) rotor speed  $\omega_r$  (rad/s), b) core loss winding currents  $i_{cd}$ ,  $i_{cq}$ .



It is clear from Figs 7.10 and 7.11 that for 40% step reduction (transient (a)) of voltage at constant load torque (30 Nm) the consideration of magnetic saturation and core losses reduces the peak transient stator current and generates a small influence on the transient torque and rotor speed, while the core loss winding current show transients only in the first 40 milliseconds.

In some contrast to the above results, disconnection – reconnection (after 10 milliseconds) of the motor produces notable transient modifications when the magnetic saturation and the core loss windings are considered, in all four variables: stator current, electromagnetic torque, rotor speed and magnetization flux linkage  $\Psi_m$  and current  $i_m$  (Fig. 7.12a, b, 7.13a, b).

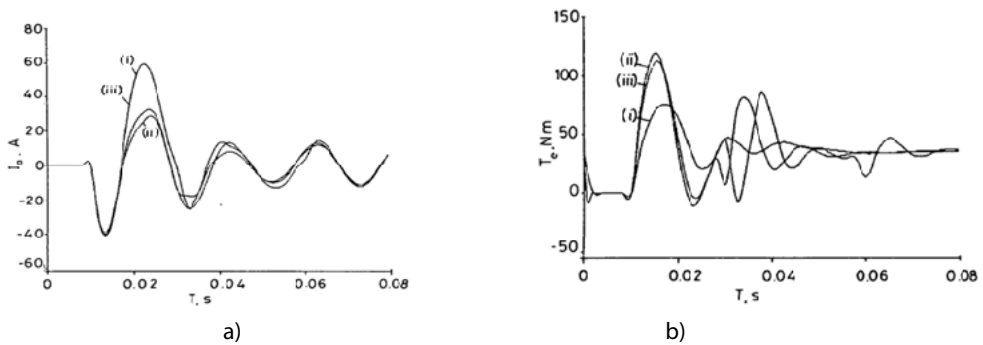


Fig. 7.12 Disconnection – reconnection (after 10 ms) transients: a) stator current, b) electromagnetic torque.

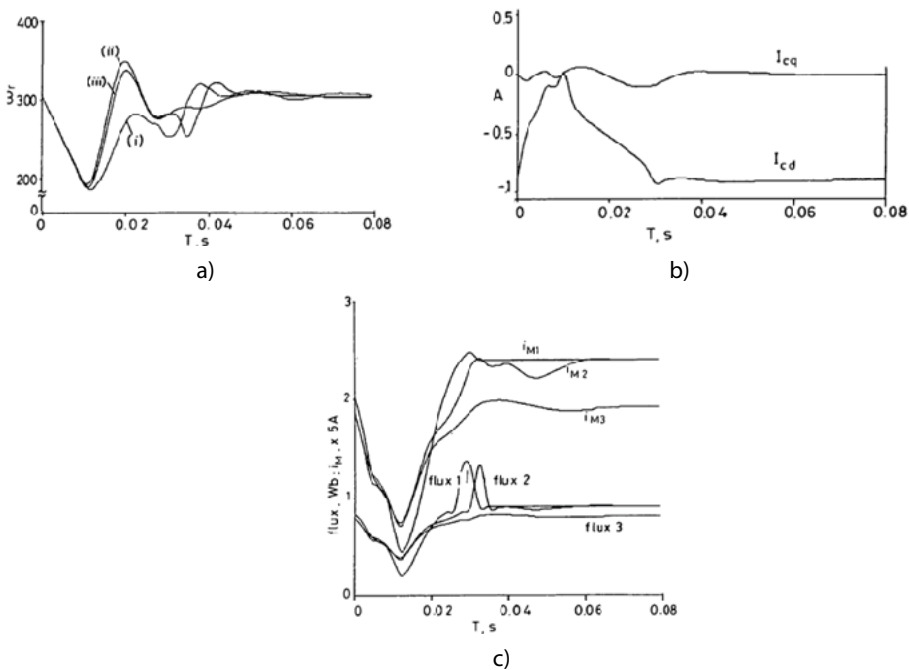


Fig. 7.13 Disconnection – reconnection (after 10 ms) transients: a) rotor speed, b) core loss winding currents, c) magnetization flux – linkage  $\Psi_m$  and current  $i_m$ .

This time the consideration of saturation and core loss currents leads to largest peak transient current transients, to lower peak torque and rotor speed transients.

The core loss current transients ( $i_{cd}$  especially) is large in the first 40 ms when also the magnetization transient current peak is increased together with the magnetization flux peak timing being integrated; again, all this in the first 40 ms.

Although not shown in graphics disconnection – reconnection transients have been calculated for different values of voltage initial phase ( $\delta_0$ ) at the reconnection moment. They showed evolutions similar to the case of  $\delta_0=0$ , but the settling time was larger.

Also increasing the disconnection time from 10 ms to 18 ms, the attenuation effect on transients of core loss currents increased.

All disconnection – reconnection transients have been calculated at constant load torque. It goes without saying, that the computation routine is similar for different load torques (variable in time).

## 7.9 Discussion

- \* It is evident that the core loss influences the electric machine transients in the first tens of milliseconds.
- \* This leads to the idea that in field oriented (servo) electric drives a cross-coupling not only due to magnetic saturation, but also due to eddy currents occurs in the first milliseconds within the transients; this affects the torque response and should be considered (as investigated subsequently in Ref [10]).
- \* In highly saturated electric induction or PM (or d.c. excited) synchronous motors/generators drives – such as in EV (HEV) propulsion or self-excited induction (synchronous reluctance) generators – accounting for magnetic saturation is imperative not only for performance assessment, but also in rotor position estimators in IM or IPMSM encoderless high performance drive where cross-coupling saturation inflicts a constant error  $\varepsilon_{\theta_r}$  which needs to be corrected [11]:

$$\varepsilon_{\theta_r} = \frac{1}{2} \tan^{-1} \left( \frac{-2L_{dq}}{L_d - L_q} \right) \quad (7.44)$$

with  $L_{dq}=L_{qd}=\partial\Psi_d/\partial i_q=\partial\Psi_q/\partial i_d$  [11].

- \* The effect of cross-coupling saturation is also important in PM assisted (or not) reluctance synchronous motor drives where core loss neglect in the control design will lead to nonlinear speed profiles in regenerative braking for a linear one in motoring [12].

- \* While the general dq model presented here accounts for crosscoupling magnetic saturation globally, extended magnetic equivalent circuit [13] or FEM field models are used to investigate local saturation during key operation mode in heavily loaded electric machines as they may enhance torque pulsations peak radial forces (that is noise and vibration).

## 7. 10 References

- [1] I. Boldea, S. A. Nasar, "Unified treatment of core losses and saturation in the orthogonal – axis model of electric machines", *IEE Proc.* vol. 134, Part B, no.6, 1987, pp. 355 – 363.
- [2] I. Boldea, S. A. Nasar, "Upon unitary treatment of magnetic saturation in orthogonal axis models of electric machines" *Record of ICEM* – 1986, Munchen, Germany.
- [3] R. S. Ramshaw, G. Xie, "Mathematical model and electric circuit simulation of DC machines", *IEE Proc.* vol. 130, Part B, no.3, 1983, pp. 218 – 225.
- [4] J. A. A. Melkebeek, D. W. Novotny, "The influence of saturation on induction machine drive dynamics", *IEEE Trans*, vol. IA – 19, no.5, 1983, pp. 671 – 681.
- [5] P. Vas, "Generalized analysis of saturated a.c. machines", *Arch. Elektrotech*, vol. 64, 1982, pp.57-62.
- [6] J. E. Brown, K. P. Kovacs, P. Vas, "A method of including the effects of main path saturation in the generalized equation of a.c. machines", *IEEE Trans*, vol. PAS-102, no.1, 1983, pp. 96 – 103.
- [7] I. Boldea "Synchronous generators", book, 2<sup>nd</sup> edition, CRC Press, Florida, USA, 2016.
- [8] M.A. Arjona, D.C. Mac Donald, "Characterizing the d-axis machine model of a turbogenerator using Finite elements", *IEEE Trans*, vol. EC – 14, no. 3, 1999, pp. 340-346.
- [9] E. Levi, "Saturation modeling in dq models of salient pole synchronous machine", *IEEE Trans*, vol. EC – 14, no. 1, 1999, pp. 44-50.
- [10] I. Boldea, S. A. Nasar, "A general equivalent circuit (GEC) of electric machines including cross-coupling saturation and frequency effects", *IEEE Trans*, vol. EC – 3, no. 3, 1988, pp. 689-695.
- [11] D. Mingardi, M. Morandin, S. Bolognani, N. Bianchi, "On the properties of differential cross – saturation inductance in synchronous machines", *IEEE Trans*, vol. IA – 53, no.2, 2017, pp. 991 – 1000.
- [12] L. Xu, X. Xu T.A. Lipo, D.W. Novotny, "Vector control of a reluctance motor including saturation and iron losses", *IEEE Trans*, vol. IA – 27, no.5, 1991, pp. 977 – 985.
- [13] V. Ostovic, "Dynamics of saturated electric machines", book, J.Wiley, 1989.

# INOVATIVE 1 PHASE LINE-START AND VARIABLE – SPEED (INVERTER FED) 3 PHASE AND 1 PHASE PM MOTOR DRIVES FOR SMALL COMPRESSORS

## Abstract

Small (refrigerator) compressor motor drives have made traditionally use of line – start 1 phase split phase capacitor motor drives. They reached up to 85% efficiency at 100 W and 2850 rpm (50 Hz) for a more than 2.5 kg motor active weight. In an effort to further increase efficiency but reduce the motor weight, PMs have been added on the rotor, besides the rotor cage in constant speed drives. A two speed [1] and a single speed [2] line-start PM assisted 1 phase split – capacitor phase motor technologies are presented with theory and experimental (industrial) results.

Further on variable speed (inverter fed) PMSM drives have been recently introduced to increase total drive efficiency (the PWM inverter efficiency is (95-97)% from 0.100 kVA to 1.5 kVA ratings) with higher efficiency PM brushless motors that use preferably Ferrite – PMs to reduce motor initial cost.

An inner spoke-shape-Ferrite-PM-rotor synchronous 6 slot/8 pole motor drive with a case study for 1 kW, 4.5 krpm [3] and an outer-surface-Ferrite-PM-rotor synchronous (6 slot/8 pole) motor drive [4] with theory and experimental (industrial) results is presented in notable detail.

Finally a very small power 1 phase Ferrite – PM – stator doubly salient motor drive for variable speed.

## 8. 1 Introduction

Small (refrigerator) compressor drives represent a sizeable share of all electric energy consumption (around 8 %).

Better electric drives for refrigerators are to yield more efficiency at moderate extra-cost, but in general at same or small weight. Home refrigerators are fed from a 1 phase supply at 50 (60) Hz in general.

Consequently, line-start 1 phase-supply split-phase capacitive induction motors have been traditionally used for the scope. The performance (efficiency) demands are very high

and the 1 phase capacitor IM has reached up to 85% at 100 W, 2850 rpm (50 Hz), but for more than 2.5 kg active weight in the motor.

Better performance at moderate initial costs in such demanding drives led first to the idea to add PMs on the rotor of line-start PM-cage-rotor split phase/capacitor motor. Also a multiple – flux – barrier cage rotor has been investigated as a line start reluctance synchronous motor. Operation at synchronous speed should reduce the rotor cage losses (by the direct stator magnetic field) to almost zero and thus higher efficiency should be obtained.

Ref. 6 introduces a general (unified) circuit model valid for 1 phase-source split phase capacitor induction, PM and reluctance motors for small compressor in Ref. 7 a similar unitary dq model treats the starting transients which are crucial in a line – start motor. The circuit configurations of the three cases, induction, PM – induction, RelSyn – induction motors are shown in Fig. 8.1 [6].

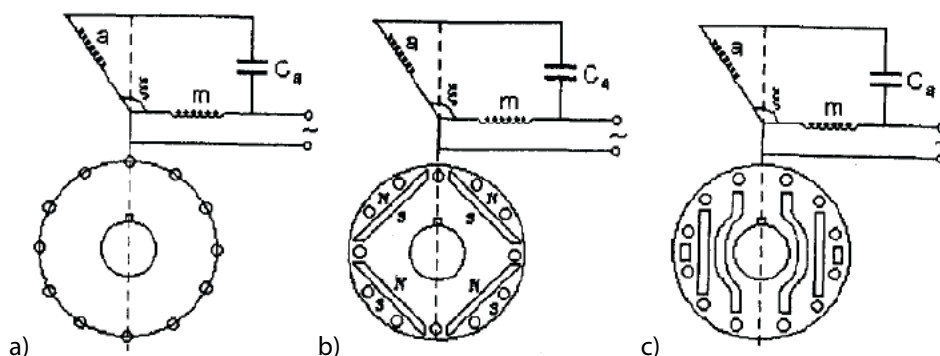


Fig. 8.1 Capacitor a.c. motors: a) C-IM, b) C-PMSM, c) C-RSM.

The main and auxiliary windings may be placed at  $90^\circ$  or at an angle  $90^\circ < \xi < 110^\circ$ , to somewhat improve the starting performance. By power balance principle, the nonorthogonal windings may be reduced to orthogonal ones [6].

Investigating their steady state asynchronous and, respectively, synchronous performance, for same stator and rotor diameters and stack lengths showed [6, 7] that:

- \* The steady state (synchronous) performance of C-PMSM and C-RSM are better than for the C-IM machine of the same geometry.
- \* The starting performance (efficiency) of C-IM is superior (quicker starts) and needs less starting capacitors [7].
- \* The C-PMSM shows notable PM braking torque during asynchronous starting [7].
- \* The C-RSM may have self-synchronization problems due to insufficient peak/rated torque ratio.

In what follows, we will describe in some details the innovative solutions for refrigerator compressor drives introduced in Ref. 1-5 as they reveal fundamental issues and have enjoyed industrial prototype testing.

## 8.2 A 2/4 poles split-phase capacitor motor

Typical cross-sections of most representative small compressor motors refer to line-start split-phase capacitor C-IM, C-PM – induction [1] and variable speed surface PM rotor SM drives which exploit the variable speed to save energy both in the compressor and in the drive.

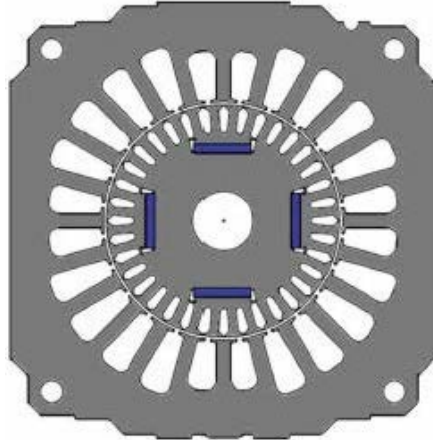


Fig. 8.2 Typical 100 W small compressor 2-4 C-PM synchronous motor.

To reduce energy consumption, but avoid a PWM inverter fed motor drive, and thus reduce initial and maintenance cost, a 2/4 poles split-phase capacitor motor has been contemplated [1].

In contrast to the standard situation, the low speed (4 pole) operation (50 W) is predominant and should show high enough efficiency (85%) and good starting performance. The high speed (2 pole) operation mode is used less and its efficiency, at 100 W, may be even a little over 60%.

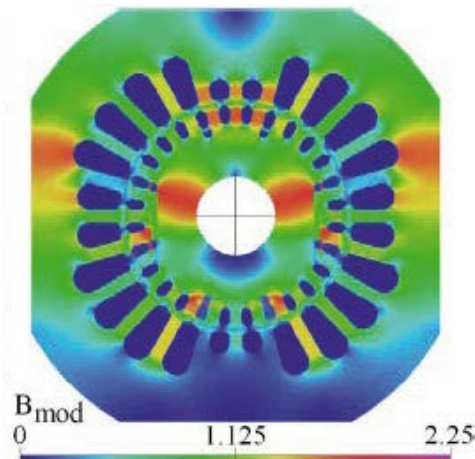


Fig. 8.3 Proposed geometry for 2-4 pole motor: flux lines for 2 pole operation.

Consequently, the proposed topology has:

- a 4 PM pole cage rotor (Fig. 8.3) to serve a 4 pole split phase capacitor winding (Fig. 8.4b,c), 50 W.
- a separate 1 phase 2 pole (high speed) stator winding that interacts (for the average torque) mainly with the rotor cage (Fig. 8.3 and Fig. 8.4a), 100 W
- as the motor starts on 4 poles (low speed) and then, when needed, switches to 2 pole (high speed), the torque of 2 pole 1 phase winding should produce at slip  $S=0.5$  about rated torque so that the acceleration to high speed is safe and fast.

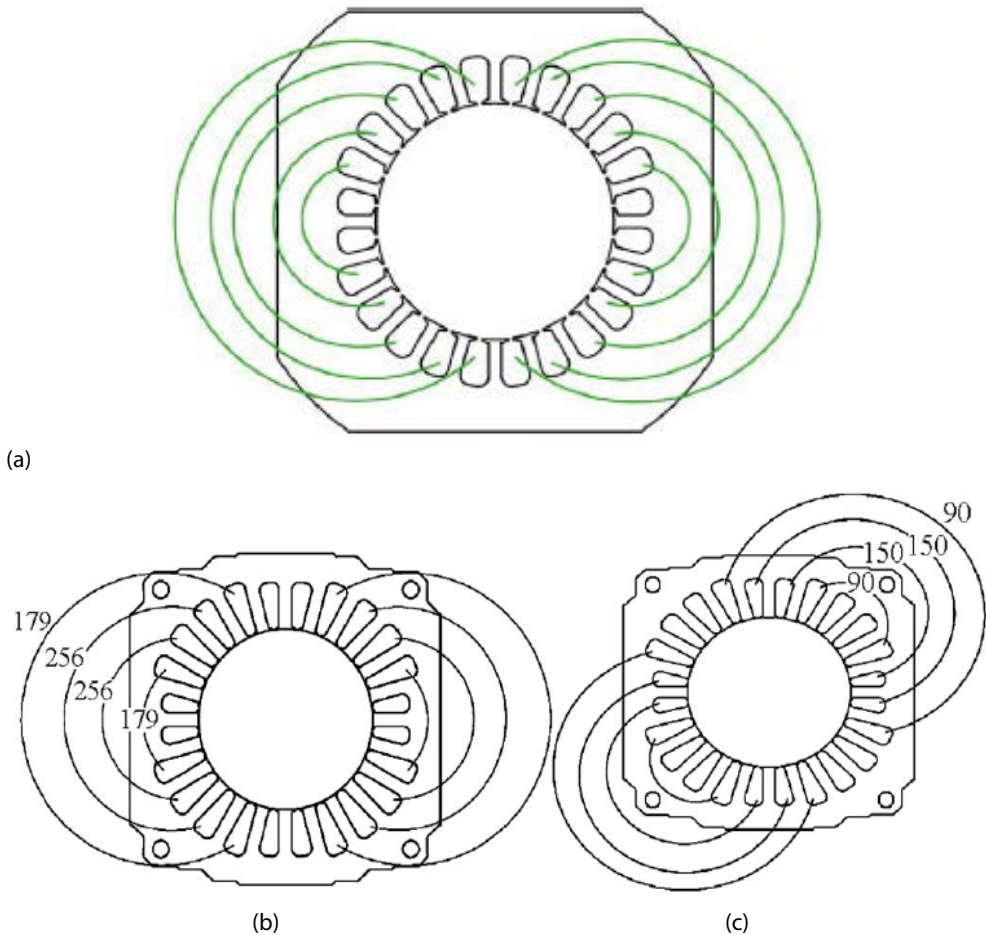


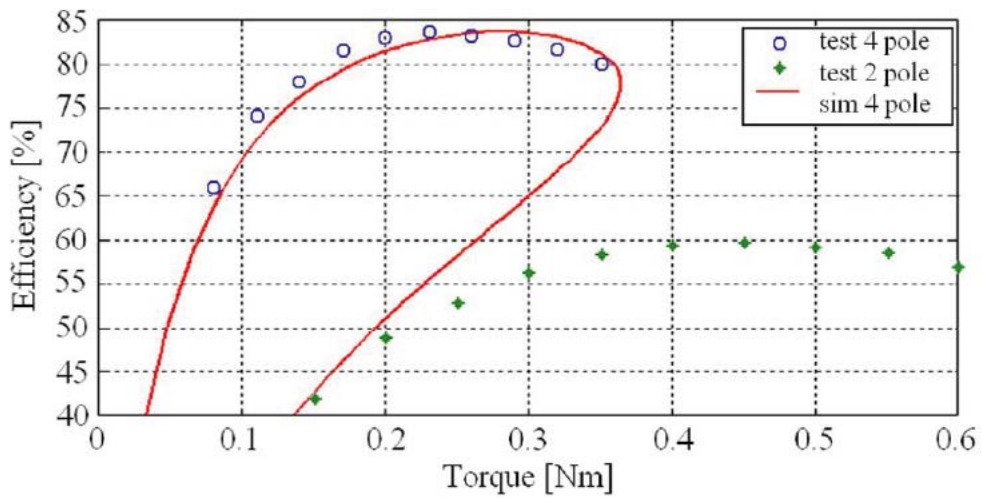
Fig. 8.4 Two (a) and 4 pole stator windings (b, c)

The prototype built after a magnetic equivalent circuit (MEC) model optimal design code which has been developed for the scope is shown in Fig. 8.5a, b.





a)



b)

Fig. 8.5 2 pole (50 W)/ 4 pole (100 W) prototype, (a) and measured efficiency versus torque, (b).

The optimal design results [1] are summarized in Table 8.1.

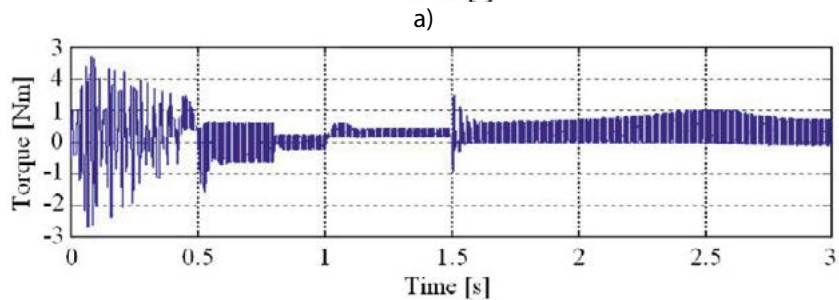
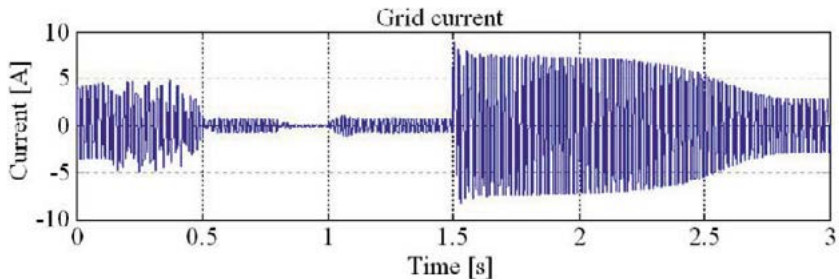


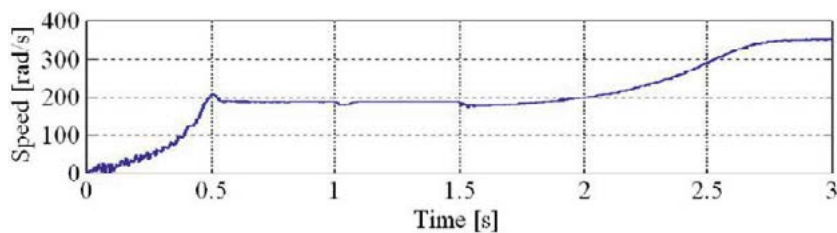
Table 8.1 Optimal design key results

Variables	Initial	Final	Legend
$D_{si}$ (mm)	63.4	67.4	stator inner diameter
$L_{stack}$ (mm)	40	41.6	core stack length
$w_{st}$ pu	0.45	0.46	stator tooth width in pu
$w_{rt}$ pu	0.45	0.45	rotor tooth width in pu
$a_{rb}$ (mm <sup>2</sup> )	14.7	17.8	rotor bar area
$w_{pm}$ pu	0.8	0.95	width of PM relative to the field barrier
$h_{pm}$ (mm)	1.5	1	PM height
$K_{nm2c}$	1	1	multiplication factor for main coil turns,
$K_{nm4c}$	1	1	multiplication factor for main coil turns
$K_{na4c}$	1	1.21	multiplication factor for auxiliary coil turns
$w_{mbs}$	4	4	width of magnetic barrier in slots number
$d_{m2wi}$	13	13	wire index 2 poles winding *
$d_{m4wi}$	12	12	wire index 4 poles main winding *
$d_{a4wi}$	8	9	wire index 4 poles auxiliary winding *
* index in a wire diameter table			

The main result of optimization design is the increase in efficiency in both operation modes by 6/4 %, while the motor active weight was only slightly increased from 3.98 kg to 4.13kg. This active weight is rather large, but the efficiency at 50 W and 1800 rpm (60 Hz) – 0.87 is apparently unprecedented.

FEM – extracted parameters have been then used to investigate the transients from zero speed to synchronism [1] with key digital simulations as illustrated in Fig. 8.6 a, b, c.





c)

Fig. 8.6 Acceleration process for rated load (0.3 Nm) applied at  $t=1$  second and on ward through 4 pole operation to 1.5 s when 2 pole operation continues the acceleration to maximum speed. Grid current, (a), instantaneous torque, (b), and speed, (c), evolutions are shown.

Though it takes 15 seconds the motor switches smoothly from 4 pole to 2 pole operation.

It is assumed here that this is a practical – like solution when dual speed advantages are paid for moderately by just an additional power switch (two windings need two power switches) and a two – pole 1 phase additional winding.

### 8.3 Line – start split – phase capacitor PM – reluctance – cage motor: optimal design

In an effort to produce a line – start split – phase capacitor motor at 100 W, 3000 rpm with an efficiency around 90% but with a safe asynchronous starting, a special configuration is chosen, Fig. 8.7 a, b [2].

- The stator includes a rather sinusoidal mmf 2 phase winding
- The regular cage rotor is provided with two flux barriers filled with PMs to produce under steady state not only PM interaction but also notable reluctance torque.

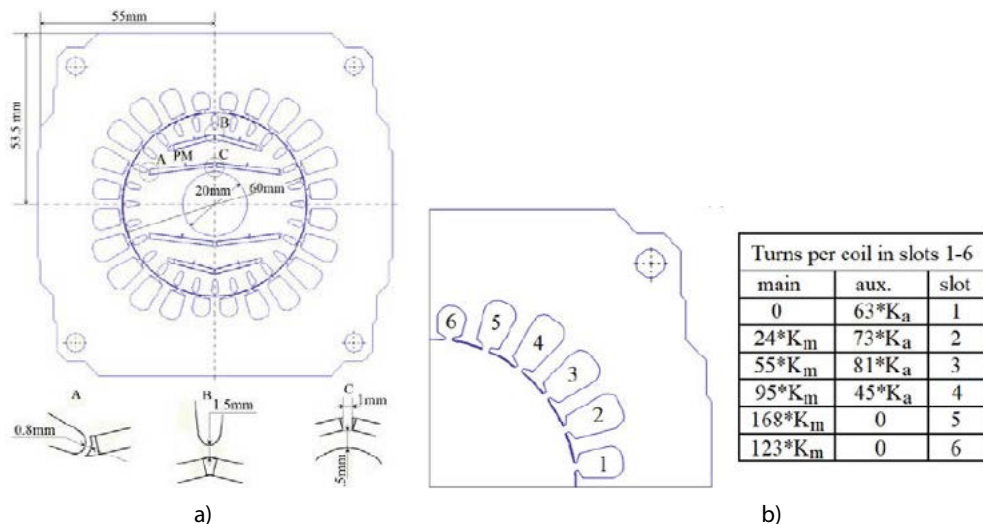


Fig. 8.7 Line–start split – phase capacitor PM – induction – reluctance motor: a) stator lamination and rotor geometry, b) main and auxiliary winding turns allocation in slots 1 – 6.

A circuit model is adopted to calculate the asynchronous torque, while a simple formula for the PM motion induced stator currents braking average torque completes the asynchronous operation [2]. Sample results of asynchronous running (digital simulations) in Fig. 8.8.

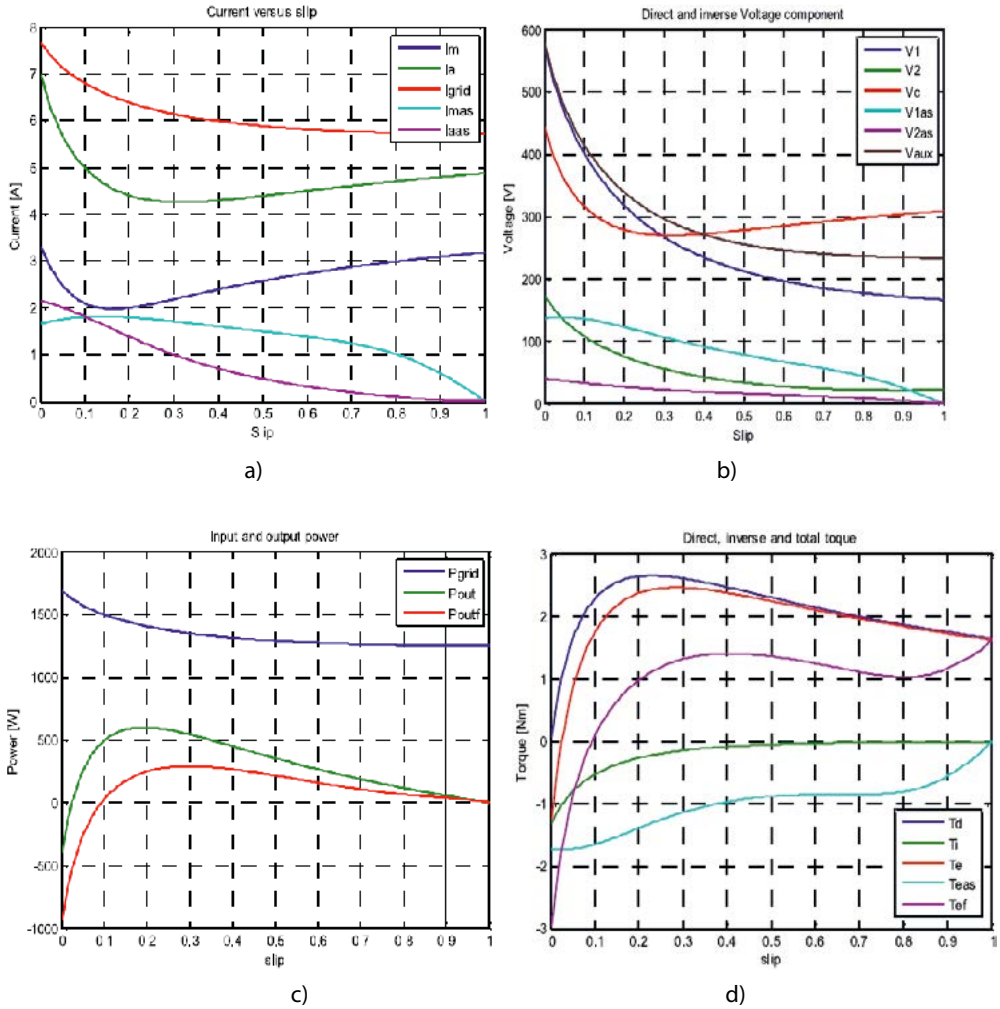


Fig. 8.8 Asynchronous operation: a) currents, b) voltages, c) power, d) torque components.

Asynchronous performance illustrates the good starting torque (0.6 Nm versus 0.3 Nm rated torque) and sufficient total torque at  $S=0.04$ , to secure safe self-synchronization. For the synchronous operation the dual flux barrier rotor modeling imposed the use of MEC (Fig. 8.9) to calculate the magnetization inductances in axis d and q  $L_{dmr}$ ,  $L_{qm}$ .

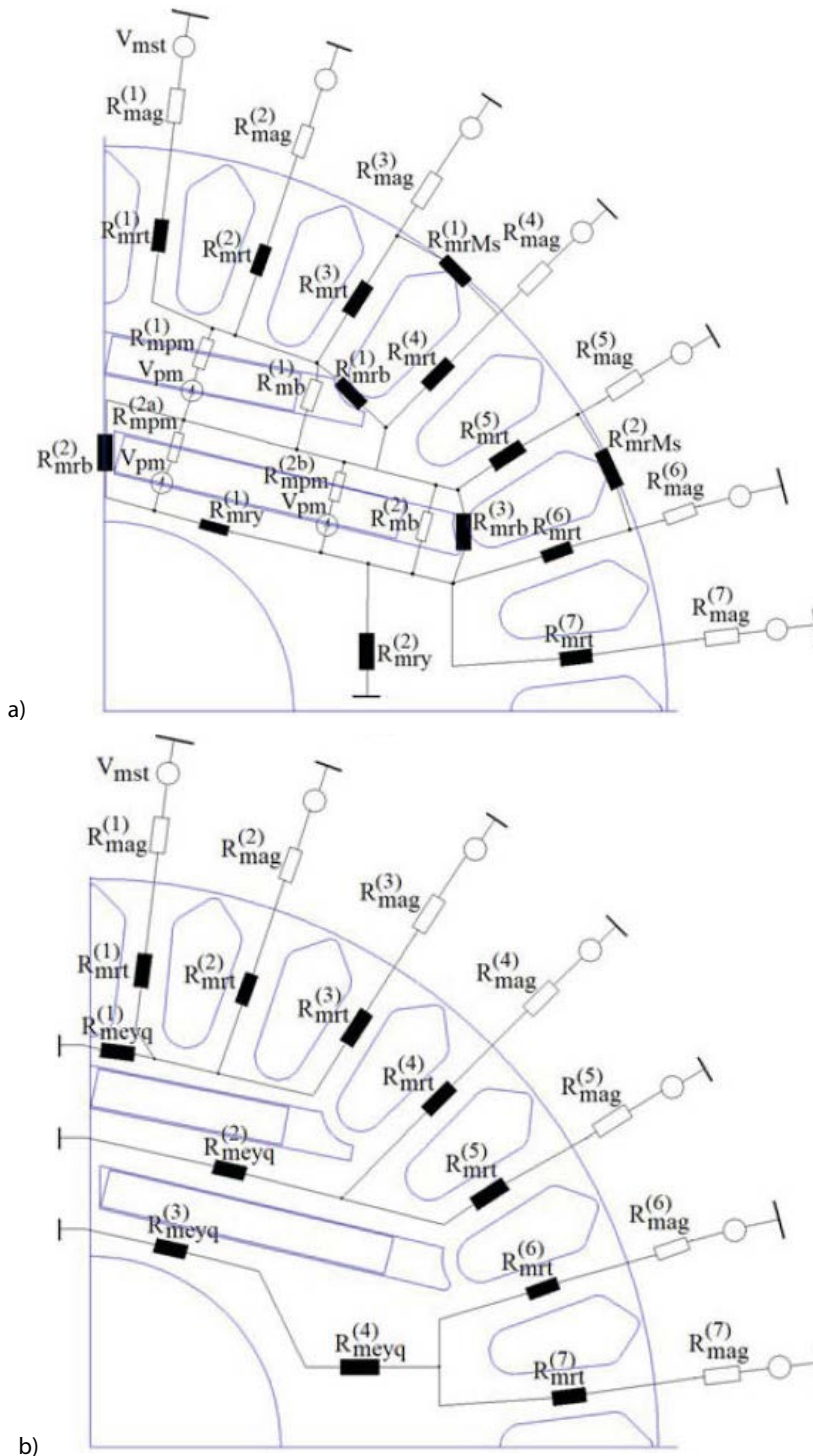


Fig. 8.9 Rotor and stator MEC: a) axis d, b) axis q.

### 8.3.1 Optimal design methodology

In brief, the optimal design methodology (ODM) includes:

- Machine modeling a variable vector
- Optimization objective (fitting) function
- Optimization mathematical algorithm (here: modified Hooke – Jeeves algorithm)
- Complete code with input and output numerical and graphical data

Modeling by circuit parameters for asynchronous running phase MEC for synchronous operation parameters was complemented by key FEM validation for  $L_{dm}$ ,  $L_{qm}$ , and  $\Psi_{PM}$  by respective correction coefficients for MEC to yield a code that is moderate in computation time.

The objective function includes initial (materials + capacitor) cost  $C_i$ , loss energy cost per estimated machine life  $C_e$  and the starting cost  $C_{st}$  (if starting is not successful); if the output power  $P_n$  is not met by  $P_{max}$ , the value of  $C_i$  is increased (as in (8.1)):

$$C_t = C_i \max \left( 1, \frac{P_n}{P_{max}} \right) + C_e + C_{st}; C_i = C_{mot} + C_{cap} \quad (8.1)$$

$$C_{cap} = 2C_{co} + K_{pe} (C_{run} + C_{start}) \quad (8.2)$$

$K_{pe}$  is a cost proportional coefficient

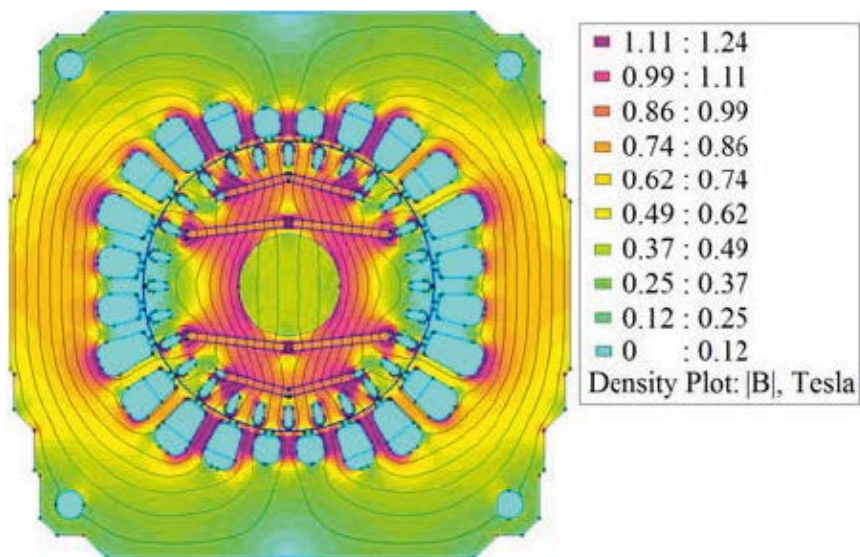
Sample ODM results are shown in table 8.2.

Table 8.2 ODM sample result.

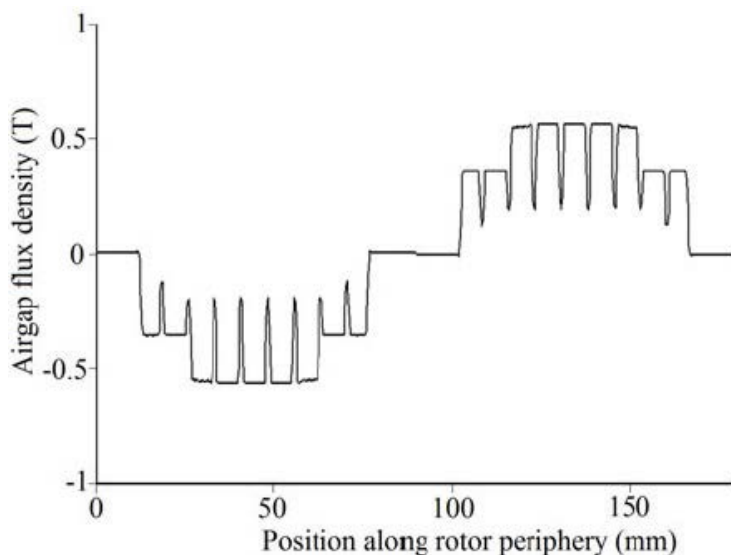
$\eta_n$	90%	Rated efficiency
$P_{mec}$	1.5%	Mechanical losses (rel. rated power)
$P_{stray}$	2.5%	Stray losses (related to rated power)
$\cos(\varphi_n)$	0.939	Rated power factor
$C_a$	4 $\mu$ F	Running capacitor
$m_m$	4.22 kg	Motor active materials weight
$m_{PM}$	0.125 kg	PM weight
$B_r$	1.1 T	PM remanent flux density (NdFeB)

Only 15 cycles of modified Hooke – Jeeves algorithm were necessary to secure solid convergence. But to secure global optimization results the Code has been run from 20 random starting variable vectors and the whole computation effort amounted to 4500 seconds on a contemporary desktop computer (key validation by FEM, included).

Sample FEM airgap PM flux density distribution (zero currents) are shown in Fig. 8.10.



a)



b)

Fig. 8.10 FEM airgap PM flux density map, (a) and distribution, (b).

In general,  $L_{dmFEM}=0.578$  H,  $L_{aqFEM}=2.3$  H,  $L_{mqFEM}=3.009$  H of more than 5/1  $L_{qm}/L_{dm}$  ratio has been obtained, which implies notable synchronous reluctance torque (beside PM torque, which relies on a moderate airgap PM flux density of 0.55 T).

The calculated efficiency is about 90% for a 4.22 kg (active weight) motor at 100 W, 3 krpm.



### 8.3.2 Test results

A prototype was built (Fig. 8.11) and tested for no load voltages in the main and auxiliary windings (Fig. 8.12a), as well as for efficiency (Fig. 8.12b).

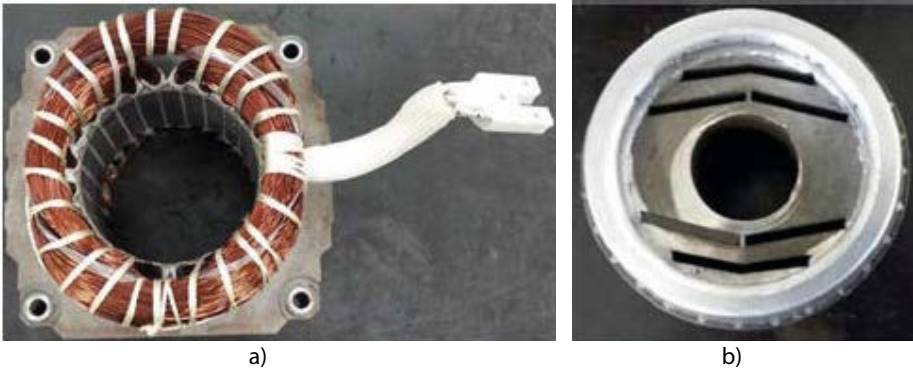


Fig. 8.11 The 100 W, 3krpm split phase capacitor PM – RelSyn prototype: a) stator, b) rotor.

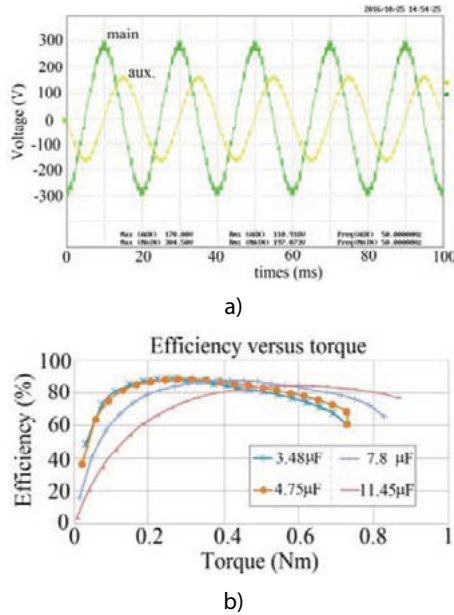


Fig. 8.12 Test results: a) no load voltages at 3 krpm, b) efficiency versus torque for a few capacitor values.

The measured efficiency at 0.3 Nm was around 89% and 2.5% stray load losses applied in Table 8.2 led to the calculated 90% efficiency. Imperfections in modeling may explain the difference of 1% between the computed and measured efficiency. The computation error in no load voltages was 2%.

However, the 89% efficiency is considered very competitive for the line – start 100 W, 3 krpm motor.

## 8. 4 Spoke – Ferrite – PM rotor synchronous compressor motor variable speed drive: comprehensive characterization and two sensorless control options [3]

Very often in small compressors like drives not only efficiency, but the initial cost is also important. With the 100 USD/kg range of sintered NdFeB magnets ( $B_r > 1.1$  T) the Ferrite PMs (at 6 USD/kg) are tempting. But the volume and cost of laminations and copper windings has to be kept moderate. For an 1 kW, 4.5 krpm case study was approached through a 6 slot stator (with 6 tooth wound coils) and three types of 8 pole spoke, star 4 and 8 pole Ferrite – PM rotors (Fig. 8.13).

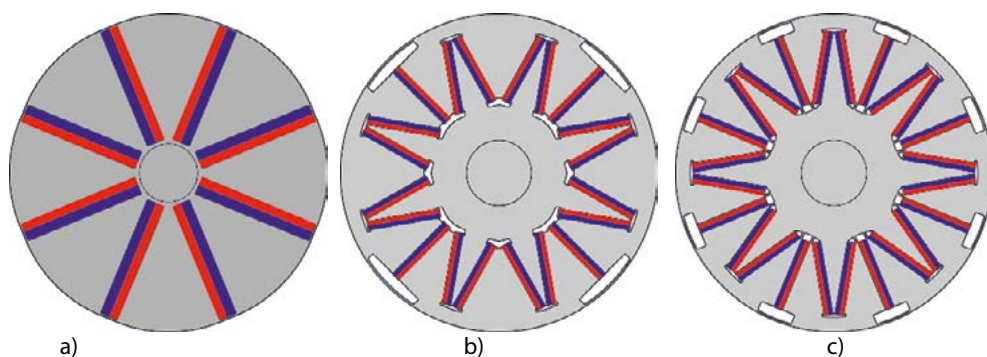


Fig. 8.13 Ferrite – PM rotor synchronous motor topologies: a) 6/8 spoke type, b) 6/4 star type, c) 6/8 star type.

### 8. 4. 1 FEM early investigations

FEM early investigations have been performed to safely compare the performance of the three rotor topologies for the same stator whose geometry has been set from previous industrial practices in the field (Table 8.3).0

Table 8.3 Geometry for FEM inquiry.

Parameter	8 pole V-shape PM rotor	4 pole star PM rotor	8 pole star PM rotor
Dso [mm]	123.2	123.2	123.2
Dsi [mm]	88.1	88.1	88.1
sh4 [mm]	1	1.3	1
sh3 [mm]	1.3	1.8	1.3
shy [mm]	9.6	9.6	9.6
swp [mm]	15.1	15.1	15.1
hag [mm]	0.4	0.2 to 0.25	0.5
hpm [mm]	5	2.5	2.5



Parameter	8 pole V-shape PM rotor	4 pole star PM rotor	8 pole star PM rotor
wpm [mm]	33.67	20.17 and 20.19	20.03 and 20.00
lstack [mm]	47.7	47.7	47.7
dlpm [mm]	2	2	2
asp [%]	0.64	0.8	0.64
sh1 [mm]	5.65	5.65	5.65
sw1 [mm]	38.37	38.37	38.37
sw2 [mm]	32.65	32.65	32.65

The stator geometry is illustrated in Fig. 8.14.

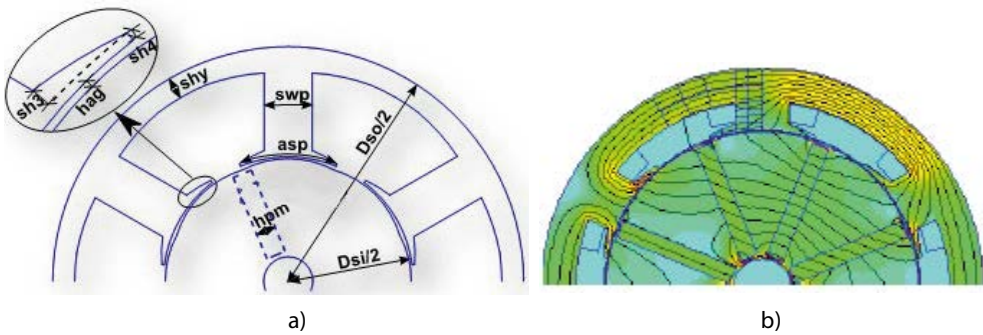
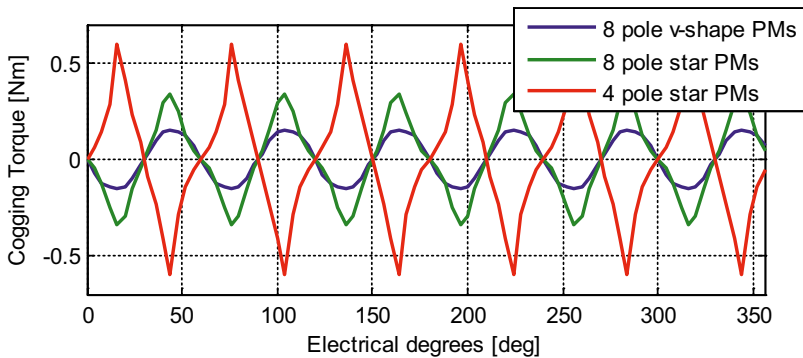
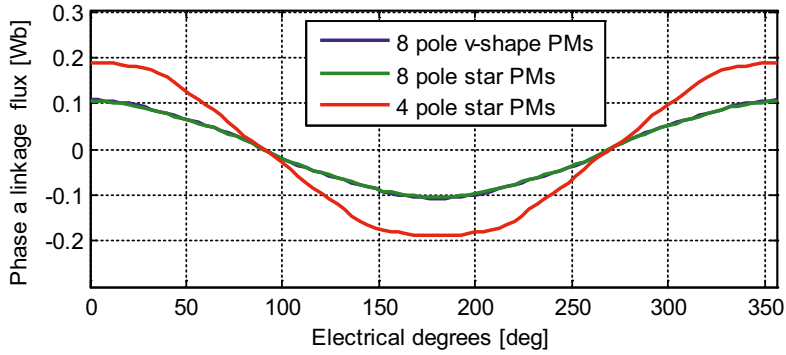


Fig. 8.14 Stator geometry for FEM inquires, a), and PM flux lines for axis d, b).

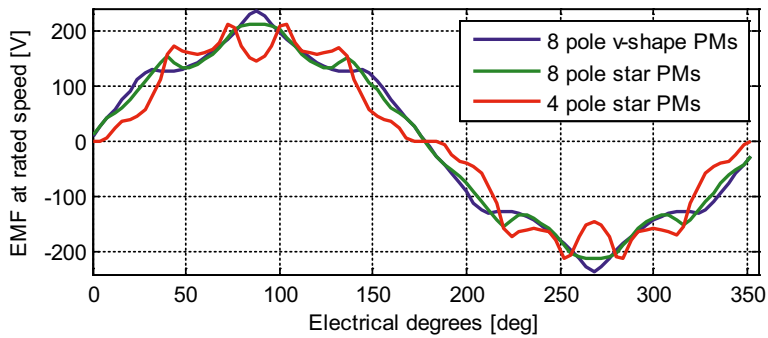
The cogging torque, PM flux linkage per phase and emf at same rated speed by FEM are illustrated in Fig. 8.15.



a)



b)



c)

Fig. 8.15 FEM: cogging torque, (a), PM flux linkage, (b), and emf, (c) for the 3 rotor topologies.

Further on by 7.5 degrees rotor step skewing the peak cogging torque was reduced to 0.002 Nm for a 3.4% average torque reduction.

Finally the electromagnetic torque for rated sinusoidal current (pure  $I_q$  control) is shown in Fig. 8.16.

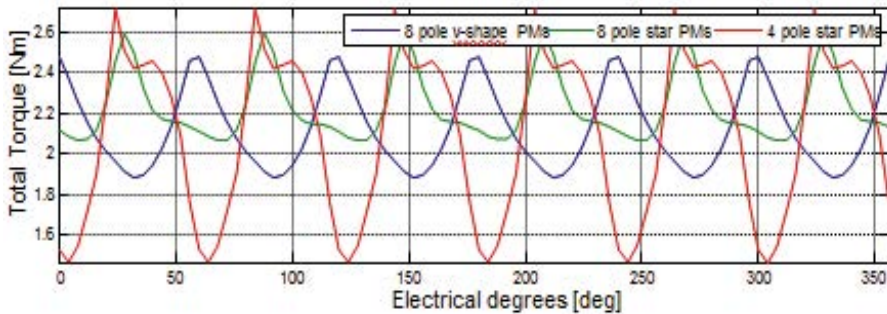


Fig. 8.16 Total torque versus electric rotor position for  $I_q$  control.

The sample results via FEM in Figs. 8.15 and 8.16 reveal that all three rotor configurations are capable to produce the rated average torque of 2.12 Nm, but after

different torque pulsations. Further on, optimal design has been pursued for all 3 rotor configurations using a similar methodology as in the previous paragraph (paragraph 8.3).

Only sample results of ODM are shown in Table 8.4.

Table 8.4 ODM sample results.

Parameter	8 pole V-shape PM rotor	4 pole star PM rotor	8 pole star PM rotor
Mechanical Power[W]	1000.68	997.73	1046.24
Mean Torque [Nm]	2.123	2.09	2.22
Maximum Torque Peak [Nm]	2.47	2.71	2.59
Minimum Torque Peak [Nm]	1.88	1.46	2.06
Copper Losses [W]	24.62	26.43	26.43
Iron Losses [W]	32.47	14.85	21.11
Electrical Efficiency [%]	93.71	96.00	94.74
<b>Weights</b>			
wt_Cu [kg]	0.3403	0.3403	0.3403
wt_Fe (unstamped sheet) [kg]	5.5386	5.5386	5.5386
wt_FeS [kg]	1.5641	1.5860	1.5428
wt_FeR [kg]	1.6034	1.6183	1.5172
wt_Shaft [kg]	0.1119	0.1420	0.1420
Wt_additional_FeR [kg]	0.1371	0.1384	0.1297
wt_Mag [kg]	0.3412	0.2557	0.3042
wt_Tot [kg]	4.0980	4.0807	3.9762
<b>Costs</b>			
Cu_cost [USD]	3.4026	3.4026	3.4026
Lam_cost [USD]	9.4156	9.4156	9.4156
Rotor_Iron_cost [USD]	0.4233	0.4766	0.4619
PM_cost [USD]	2.0471	1.5344	1.8250
Active_material_cost [USD]	15.2887	14.8293	15.1053
Passive_material [cost]	6.9666	6.9372	6.7595
Initial cost[USD]	22.2553	21.7664	21.8648

A few remarks, after searching Table 8.4 are as follows:

- \* The increase in electrical efficiency ( $p_{mec}=0$ ) of the 4 pole star Ferrite – PM rotor is notable (due to a notable reduction in core losses) but the fabrication extra – complexity of the rotor has to be considered too. The initial cost sums up both active and passive (framing bearings, etc) materials costs, but no fabrication costs.
- \* The extension of the rotor did not produce spectacular results as the optimal design code opted for higher rotor diameters.

### 8.4.2 Test effort

For testing only the 6/8 spoke – PM rotor was considered and first a method for Ferrite PM in situ – magnetization (by stator currents) has been proven feasible [3].

Also it has been proven by applying a step by step increasing negative d.c. current at standstill that up to 150% rated current (6A) the later no load emf (under running) was less than 4%. This is a key design bottle neck with Ferrite – PM – rotor SMs.

Load measurements envisage a notable increase in efficiency (above 88% at 2.12 Nm), Fig. 8.17.

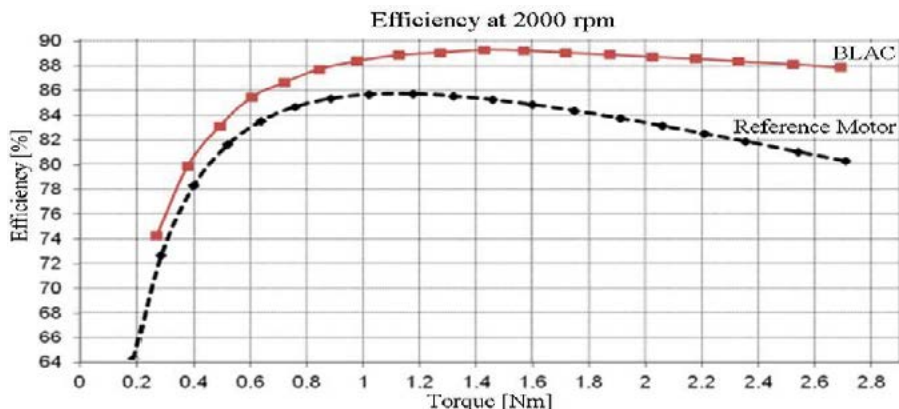


Fig. 8.17 Measured efficiency versus torque for the 6/8 spoke – Ferrite – PM rotor SM versus reference competitor.

In an effort to keep the weights and costs about 30% lower than for a NdFeB PMSM, the efficiency remained a bit more modest: 88%.

### 8.4.3 Two sensorless control options and sample results

A variable speed drive optimal design has to provide information that is capable to perform at rated voltage for rated current and to allow a larger peak torque (of at least 50%) if needed.

For that, a control system has to be designed and via a dq circuit model the performance of the drive may be checked. This part may be added in the optimal design code to eventually adjust the number of turns/coil (and its copper conductor cross section) to secure the required torque at maximum speed for the d.c. link voltage available to the PWM converter.

Here two encoder control options based on the concept of the “active flux” state observer [8].

- a) The “active flux” observer  $\Psi_d^a$

The “active flux” observer  $\Psi_d^a$  is that expression which multiplies  $i_q$  in the torque  $T_e$  expression (in dq rotor coordinates):

$$T_{es} = \frac{3}{2} p_1 \cdot \Psi_d^a \cdot i_d \quad (8.3)$$

For a PMSM:

$$\Psi_d^a = \Psi_{PMd} + (L_d - L_q) \cdot i_d \quad (8.4)$$

It is aligned to the rotor PM axis ( $L_d < L_q$ ) – provided cross – coupling magnetic saturation is neglected.

Alternatively  $\bar{\Psi}_d^a$  (is a space phasor) is:

$$\bar{\Psi}_d^a = \bar{\Psi}_s - L_q \cdot \bar{i}_s \quad (8.5)$$

where  $\bar{\Psi}_s, \bar{i}_s$  are the stator flux and current vectors.

The “active flux” position in PMSMs is in the rotor position  $\theta_{er}$  irrespective of torque, in contrast to stator flux vector  $\bar{\Psi}_s$ .

A combined voltage – current model observer may be used to “observe” the stator flux  $\bar{\Psi}_s$  and then by (8.5), calculate  $\bar{\Psi}_d^{as}$  (in stator coordinates).

$$\bar{\Psi}_d^{as} = \int (\bar{V}_s^s - R_s \cdot \bar{i}_s + V_{comp}) dt - L_q \cdot \bar{i}_s \quad (8.6)$$

The  $V_{comp}$  terms is built around a PI (or PI+SM) close loop between the voltage and current model to allow a wide frequency range observer (above less than 1 Hz anyway), Fig. 8.18. A PLL may be added to improve rotor position estimation.

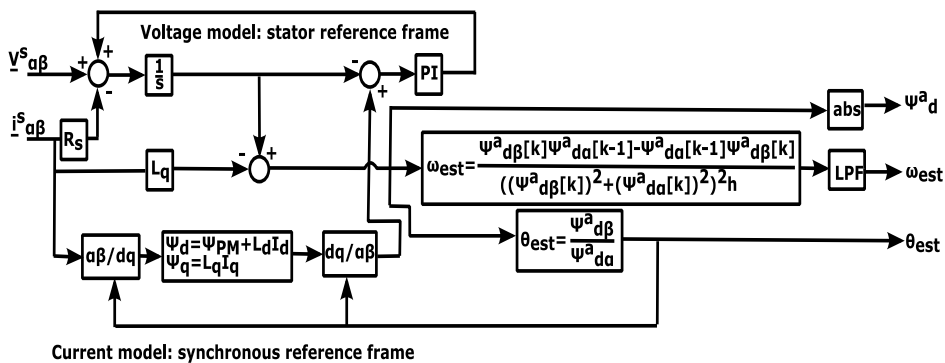


Fig. 8.18 “Active flux” observer.

The parameters of the spoke – Ferrite – PM rotor SM investigated in this paragraph are given in table 8.5.

Table 8.5 Parameters of 6/8 Ferrite Spoke – Ferrite PMSM.

Parameter	Value
DC voltage VDC [V]	380
output power Pn [W]	1000
rated current In [A]	2.44
pole pairs p	4
rated speed $\omega$ [rpm]	4500
d-axis inductance Ld [H]	0.014225
q-axis inductance Lq [H]	0.01387
stator phase resistance Rs [ $\Omega$ ]	1.36
PM flux FPM [Wb]	0.1076
frictious coefficient B	10-5
rotor inertia J [kgm2]	0.00251

For convenience the dq model (in rotor coordinates) is also given here, with zero core loss, for simplicity:

$$\begin{aligned}
 V_d &= R_s \cdot i_d + \frac{d\Psi_{dm}}{dt} - \omega_r \cdot \Psi_q; V_q = R_s \cdot i_q + \frac{d\Psi_q}{dt} + \omega_r \cdot \Psi_d \\
 \Psi_d &= L_d \cdot i_d + \Psi_{PMd}; \Psi_q = L_q \cdot i_q; p_1 - \text{pole pairs} \\
 \frac{J}{p_1} \frac{d\omega_r}{dt} &= T_e - T_{load} - B \frac{\omega_r}{p_1}; J - \text{inertia}
 \end{aligned} \tag{8.7}$$

As the machine saliency is rather, the encoderless control systems discussed here have to yield good results in the rotor position observer (table 8.5).

The two encoderless control systems refer to:

- \* A V/f control with stabilizing loops
- \* A field oriented (vector) control

b) The V/f control with stabilizing loops:

The V/f control with two stabilizing (correction) loops here (Fig.8.19) includes:

- \* A voltage amplitude correction loop for  $\Delta V$
- \* An angle (of voltage phase) correction loop  $\Delta\theta$

The voltage vector amplitude correction loop  $\Delta V$  is simply:



c) Encoderless vector control

The encoderless vector control (Fig. 8.20), based on the „active flux“ observer too to obtain rotor position and speed estimation (with a PLL added) implies  $i_d$ ,  $i_q$  and speed close loops (with their calibration during commissioning).

It includes:

$$\begin{aligned} i_q^* &= \left( K_{pm} + K_{i\omega} \frac{1}{s} \right) \cdot (\omega_r^* - \hat{\omega}_r) \\ V_d^* &= \left( K_{pid} + K_{id} \frac{1}{s} \right) \cdot (i_d^* - i_d) \\ V_q^* &= \left( K_{piq} + K_{iq} \frac{1}{s} \right) \cdot (i_q^* - i_q) \end{aligned} \quad (8.13)$$

And the compensation voltage  $V_{dcomp}$  and  $V_{qcomp}$  as feedforward signals (to compensate for motion induced voltage, as the current close loops are in dq rotor coordinates).

d) Encoderless control: simulation results

In essence, for both control systems a complex transient was simulated: ramp acceleration in 0.5 s to 4.5 krpm, followed by a speed reversal at 3 s, within 1 s. Rated load torque was applied from 1 s to 2.6 s, respectively, from 4.4 s to 5.9 s.

The sample results are shown for comparison in Fig. 8.21.

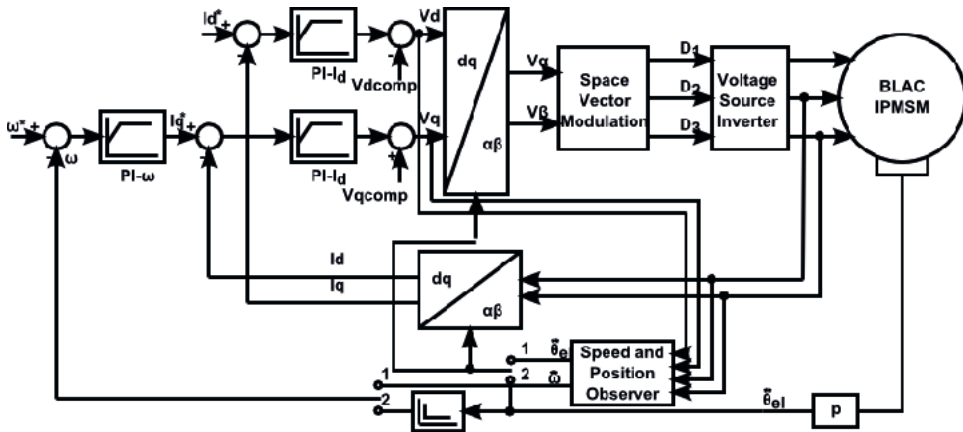
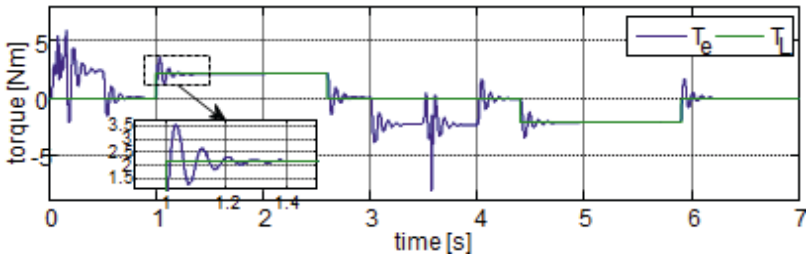
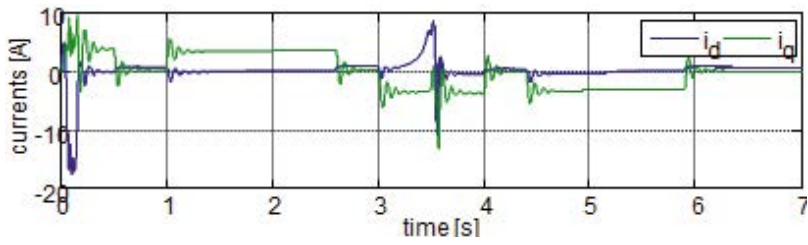
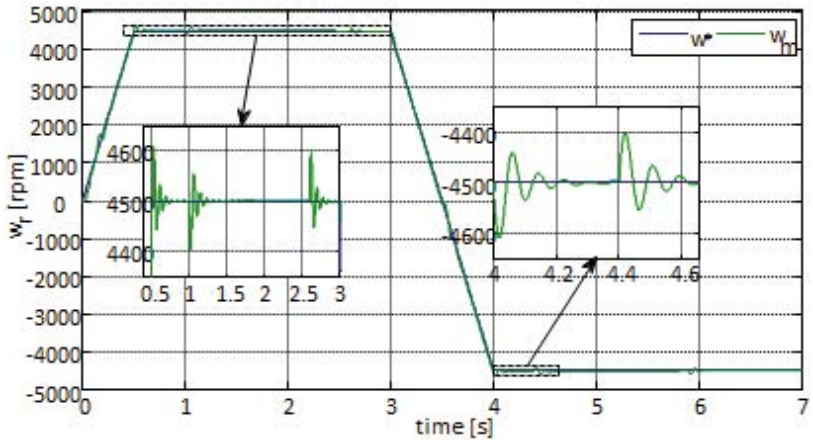
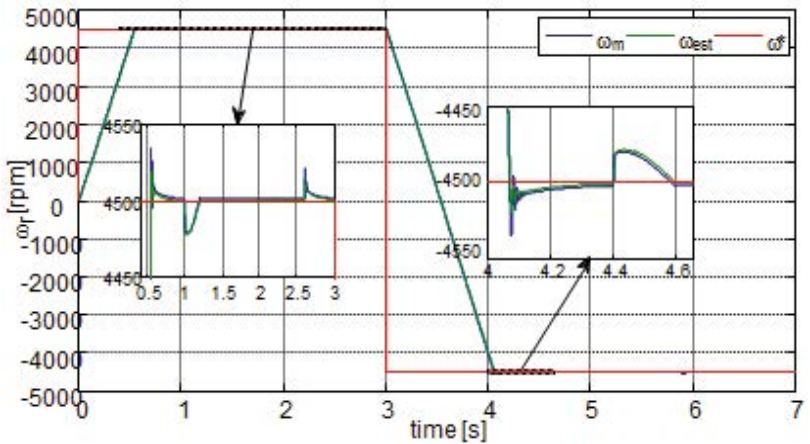


Fig. 8.20 Vector control scheme: 1 – encoderless, 2 – with encoder.





a)



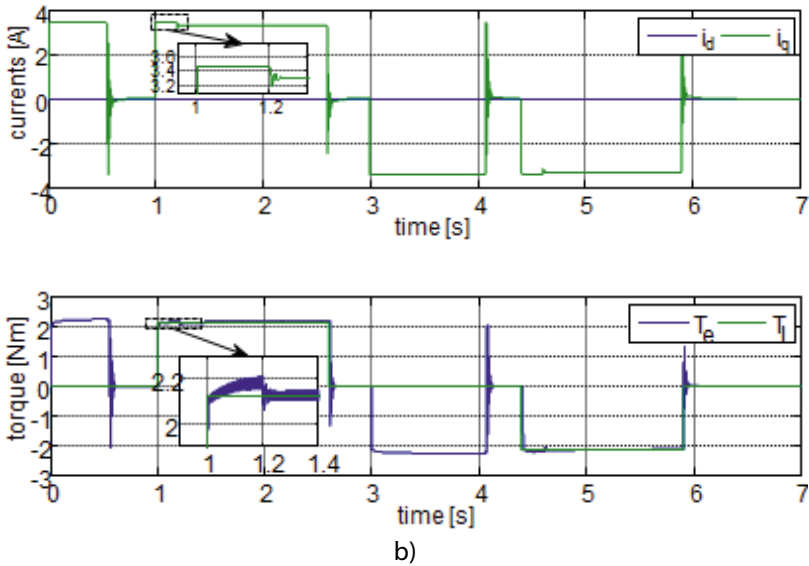


Fig. 8.21 Simulation results: a) for V/f control, b) for encoderless vector control.

The regulator constants are given in table 8.6.

Table 8.6 Encoderless control: regulators' coefficients.

Parameter	Value
$k_p_{id}$	30
$k_i_{id}$	300
$k$	50
$T$	60
$k_{pw}$	4500
$k_{iw}$	0.014225
$k_{pid}$	30
$k_{iid}$	300
$k_{piq}$	30
$k_{iiq}$	300

Both encoderless schemes are capable to safely accelerate to speed and stand full rated step torque perturbations, despite the small saliency (because the "active flux" vector degenerates to almost "PM flux" vector for  $L_d \approx L_q$ ). Operation at very low speed is not feasible with these schemes safely (below 1 Hz) in general, but it is not required in small compressor drives.

The two control schemes performed similarly mainly because a 0.5 s ramping to rated speed was large enough to allow the V/f scheme to match vector control.

### 8.5 1kW, 4.5 krpm Outer – Ferrite – PM – rotor 9 slot/8 pole synchronous motor: FEM assisted optimal design and preliminary tests [4].

In the search for better Ferrite – PM – rotor SM for compressor like (or ventilator like) loads the outer rotor with surface Ferrite – PMs seems a tempting solution because:

- \* For given outer motor diameter the airgap diameter ends up larger and thus the PM flux linkage per phase becomes larger and so is the torque (due to larger radius and rotor area);
- \* The outer surface ferrite PM rotor makes the centrifugal force on the PM to go against attraction force to stator core and protects the PMs (8 poles here)
- \* The interior stator (in our case a 9 slot stator (with tooth wound coils) has shorter end coil connections and thus slightly smaller copper losses.
- \* The rotor inertia may be larger.
- \* However, the motor topology and fabrication are more complex and costlier as a price for probably higher torque/volume at similar performance with interior spoke – Ferrite – PM rotor SMs in the previous paragraph.
- \* The outer rotor back iron may be solid and made in one piece with the rotor fixture which may play the role of a ventilator (with proper shaping).

A typical such 9 slot/8 pole PMSM configuration [4] evidentiates a 2 layer tooth – wound coil inner – stator 3 phase windings, the surface Ferrite – PMs on the rotor and the rotor back iron (yoke) (Fig. 8.22).

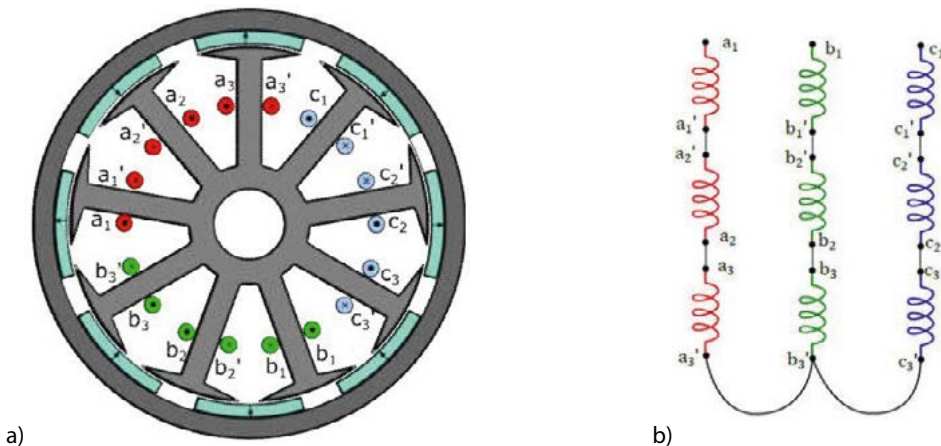


Fig. 8.22 9/8 outer – rotor Ferrite – PM motor: a) topology, b) coil connections.

The three neighboring coils of each phase simply the electric connections but lead to some uncompensated radial forces. However, the small airgap PM flux density and the rather thick Ferrite – PMs (to avoid demagnetization under overload) make the uncompensated radial forces moderate even under heavy load (150% – 200%).

Based on a simplified analytical (MEC) design procedure, and electric circuit modeling for steady state synchronous operation, the machine was preliminarily sized for 1 kW at 4.5 krpm [4].

### 8. 5. 1 Optimal design methodology

Then an optimal design methodology, based on the simplified MEC model, was applied to the modified Hooke – Jeeves algorithm. At the end of such an algorithm FEM was used to calculate torque at two designated rotor positions to calculate both the average torque and torque pulsations and machine inductance. Finally, the analytical emf (torque,  $T_a$ ) and machine inductance  $L_a$  have been regressively connected by  $K_{EFEM}$  and  $K_{LFEM}$ :

$$K_{EFEM} = 1 + \frac{T_{FEM} - T_a}{T_a} K_E; K_E < 1$$

$$K_{LFEM} = 1 + \frac{L_{EM} - L_a}{L_a} K_L; K_L < 1$$
(8.14)

Finally with such key correction coefficients by FEM the ODM was restarted until sufficient convergence was met. This way the computation time was drastically reduced while securing sufficient precision in torque and inductance values.

The variable vector  $\bar{X}$  includes 10 variables (Table 8.7).

Table 8.7 Optimal design variables.

Design variable	Min. value [mm]	Max. value [mm]	Description
sDi	15	35	stator inner diameter [mm]
$l_{stack}$	20	30	core stack length [mm]
$h_{ag}$	0.5	1	airgap height [mm]
$h_{pm}$	2	7	PM height [mm]
$w_{st}$	5	15	stator tooth width [mm]
$l_{hy}$	4	15	rotor yoke height [mm]
$s_{hy}$	4	15	stator yoke height [mm]
$h_{ss}$	2	8	stator pole top height [mm]
$PM\alpha_{sp}$	0.5	0.9	PM width span relatively to the pole span [mm]
$\alpha_{sp}$	0.8	0.9	stator tooth tip span relatively to the pole span [mm]

The objective (global) cost function (expressed in USD) includes materials  $c_{mat}$  and life – long loss costs  $c_e$  with penalties related to over-temperature  $c_{temp}$  and wrong geometry  $c_{wronggeometry}$  (which is not feasible).

$$c_{wronggeom} = K_{wronggeom} \times c_{mat} \quad (8.15)$$

$$K_{wronggeom} = (0,1)$$

$$c_e = P_n \left( \frac{1}{\eta(\bar{x})} - 1 \right) t_1 \cdot p_e \quad (8.16)$$

$\eta(\bar{x})$  is rated efficiency,  $t_1$  – run time,  $p_e$  – energy price,  $P_n$  – rated power.

More sophisticated formulae for less energy cost may be developed to account for most probable duty cycle variations. PM demagnetization avoidance condition for 150 (200)% load is included in the analytical model. For the ODM iterative process to work the first variable vector solution has to be feasible.

Sample ODM code results for both the inner and outer rotor Ferrite – PM motor for same specifications are given in table 8.8.

Table 8.8 ODM results

Parameter	Initial analytical design (outer rotor)	Optimal design result (outer rotor)	8 pole V-shape PM rotor (inner rotor)	Description
$P_{out}$	1000	1037.33	1000.6	mechanical output power [W]
$T_{mean}$	2.12	2.36	2.123	mean torque value [Nm]
$P_{Co}$	28.43	21.81	24.62	copper losses [W]
$P_{Fe}$	28.43	25.91	32.46	iron Losses [W]
$E_{1N}$	123.82	146.13	200	EMF at rated speed [V]
$I_{1N}$	3.01	2.50	2.32	rated current [A rms]
$\eta_N$	94.8	94.2	93.71	rated electric efficiency [-]
sDo	102.6	105.05	123.2	stator outer diameter [mm]
sDi	20	21.84	88.1	stator inner diameter [mm]
lag	0.7	0.50	0.4	air-gap height [mm]
rDo	124	124	77.3	rotor outer max. diameter [mm]
$m_{motor}$	3.24	2.93	4.09	motor total mass [kg]
$C_{mat}$	0.895	0.822	1 pu	initial cost [pu]
$c_\eta$	26.23	0	0	energy loss cost[pu]
$c_{temp}$	0	0	0	over temperature cost[pu]

Twenty random starts are used to safeguard global optimization results. The whole process lasted 120 seconds on a contemporary desktop computer. The winner candidate implies 18.29 USD material cost while the motor can produce more than rated torque (2.12 Nm). For the inner – rotor Ferrite PM motor (paragraph 8.4) the material costs were 22.25 USD, while the electrical efficiency (without stray load losses) was slightly smaller (93.71% versus 94.2%). Please note that in ODM efficiency may be a constraint ( $\eta > \eta_{\text{assigned}}$ ). The initial design was very good in terms of efficiency, but larger in material costs.

### 8. 5. 2 FEM validation

Stator currents, emfs and total torque pulsations for rated average torque conditions by FEM are illustrated in Fig. 8.23a, b, c.

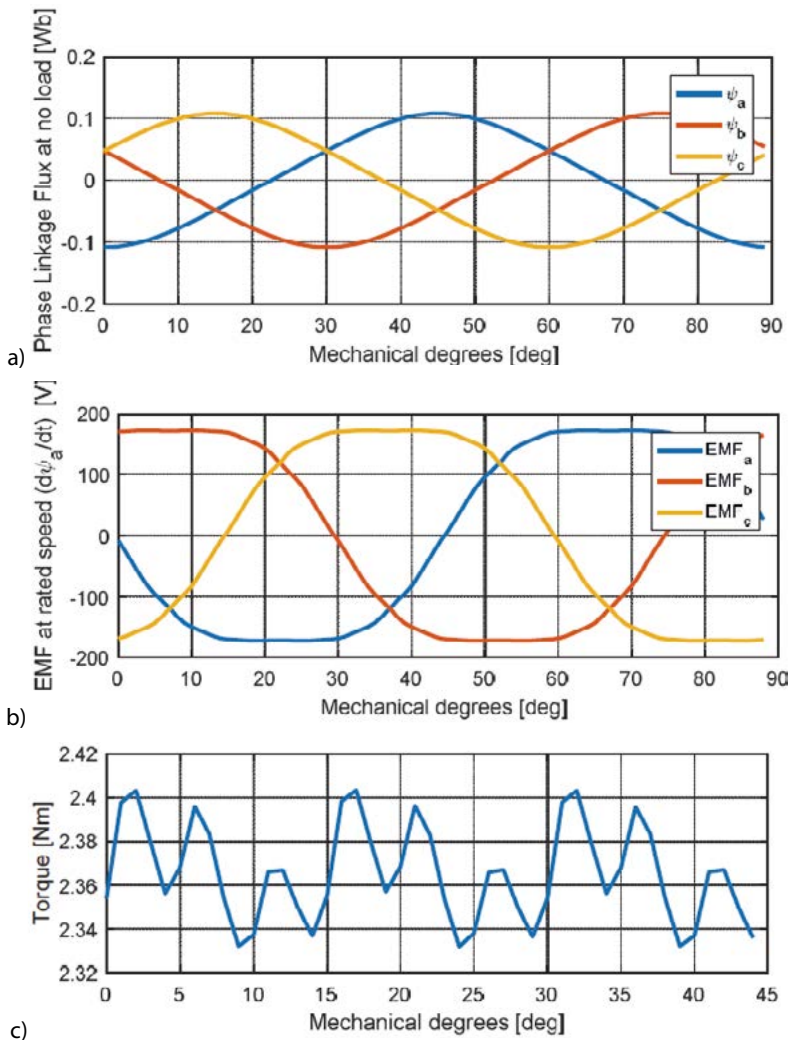


Fig. 8.23 FEM results: a) stator phase current waveforms, b) phase emf waveforms, c) total torque waveform.



Though the required rated average torque (2.12 Nm) is produced, the phase emfs are rather trapezoidal (Fig. 8.23b), which explains the rather trapezoidal (Fig. 8.23b), which explains the rather notable (though limited) total torque pulsations (Fig. 8.23c).

A more sinusoidal emf may be obtained by using two thicknesses of magnets (a thicker magnet in the pole center and two thinner ones on the pole sides; this will also reduce further the PM eddy currents already small for Ferrites).

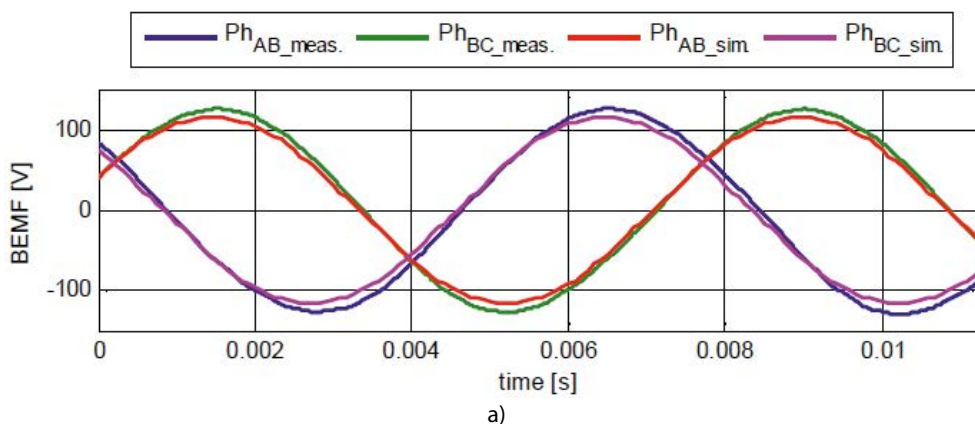
The peak value of cogging torque (by FEM) was only 0.02 Nm.

### 8.5.3 Experimental work

The ODM used top Ferrite PM quality ( $B_r=0.45$  T) but the prototype was built with lower cost Ferrites ( $B_r=0.33$  T). The computation was redone for these conditions when, however, larger stator currents (and losses) occur at rated torque. The prototype (Fig. 8.24) was thoroughly tested. Results at 2 krpm are only given as this is key operation point besides the performance at 4.5 krpm (Fig. 8.25).



Fig. 8.24 The outer rotor PM motor prototype.



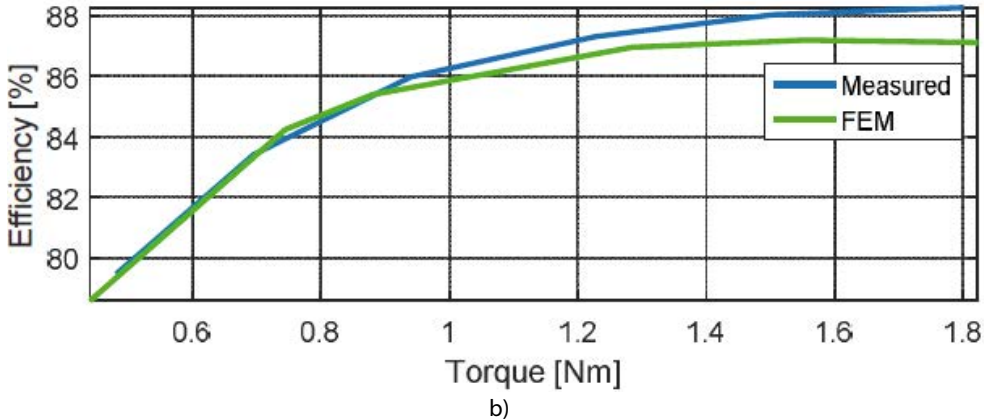


Fig. 8.25 Measured line to line emfs, a) and efficiency versus torque, b) at 2 krpm.

The calculated efficiency is:

$$\eta_{\text{calc}} = \frac{P_{\text{out}}}{P_{\text{out}} + P_{\text{iron}} + P_{\text{copper}} + P_{\text{stray}} + P_{\text{mec}}} \quad (8.17)$$

with  $p_{\text{iron}}$  calculated from FEM flux density variations in time in a few regions of the machine core [4],  $p_{\text{stray}}=1\%*P_n$  and  $p_{\text{mec}}=2\%*P_n$ .

At 2 krpm and 85% rated torque (1.8 Nm), the measured efficiency was 88.2% (low quality Ferrite:  $B_r=0.34$  T) and regular laminations: M 19 (0.5 mm thick). With 0.35 mm laminations, the efficiency jumped over 90% in same conditions as above, a sign that core losses are important ( $2p=8!$ ). It may be stated that the outer – rotor – Ferrite PM motor is worth trying for small compressor like loads in the kW power range and more due to:

- \* Higher rotor inertia
- \* Integrated rotor/ventilator topology
- \* High torque/volume (smaller mass 2.93 kg for 1 kW, 4.5 krpm) active at competitive efficiency (table 8.8)

## 8.6 Single phase stator – Ferrite – PM self-starting motor variable speed drive [5].

Placing Ferrite PMs on the stator in single phase (or in 3 phase) but in a position that allows their introduction (or extraction) with the stator coils in place may constitute a definite advantage. Fig. 8.26 shows such a topology for 1 phase (a similar one for 3 phase is feasible) [5], intended for  $P_n=85$  W,  $V_{\text{dc}}=290$  V,  $n_n=3$  krpm.

Tapered airgap is used in the attempt to secure self-starting (in a single direction of motion) in the sense that, above a certain stator mmf, the torque in every rotor position will be positive.



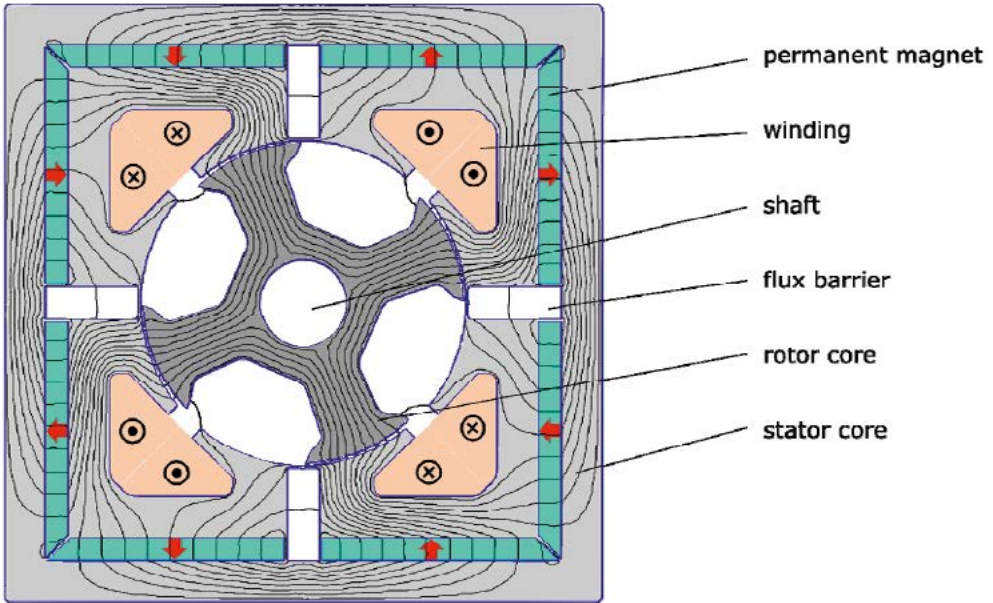


Fig. 8.26 Single phase four – pole stator – Ferrite PM motor.

Given the doubly salient configuration complexity here, only FEM modeling is used through the entire optimal design process.

### 8. 6. 1 FEM – embedded optimization design

The motor design variables are depicted in Fig. 8.27.

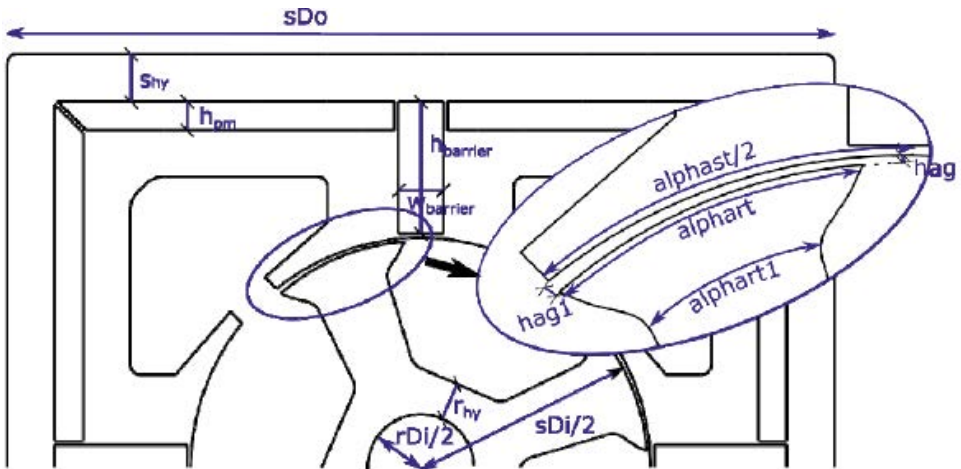
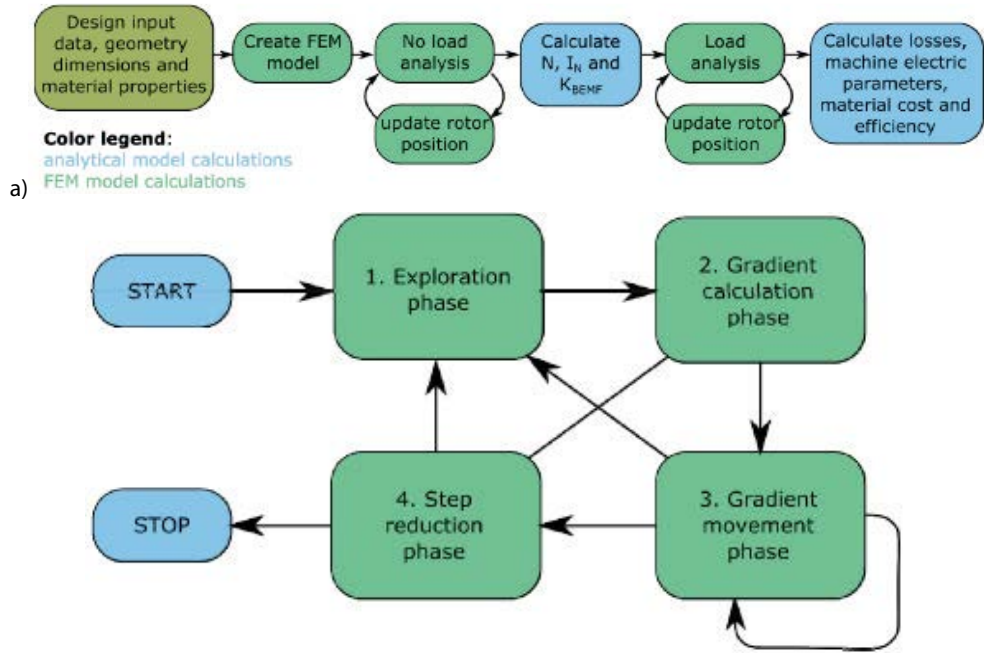


Fig. 8.27 Cross – section with design variables.

Lau scripting and FEMM 4.2 free software was used for the scope.

The computation routine (Fig. 8.28a) was integrated in an ODM via the Hooke – Jeeves algorithm modified to include penalty functions (Fig. 8.28b).



b)  
 Fig. 8.28 Computation routine, a) and ODM, b).

The objective function comprises the total cost of active materials. Quite a few penalty functions are introduced, though.

The most important one is related to the minimum torque positive value ( $T_{\min \text{req}} = +0.1$  Nm here) to secure self-starting,  $C_{T \min}$ :

$$C_{T \min} = K_{T \min \text{req}} \frac{\sum_k (T_{\min \text{req}} - T_k)}{T_{\min \text{req}}} C_{\text{mat}} \quad (8.18)$$

with  $T_k$  – torque in regularly selected rotor position within an electrical periodic,  $C_{\text{mat}}$  – materials cost,  $K_{T \min \text{req}}$  – a weighting coefficient.

The second penalty function  $C_{T \text{avg}}$  makes sure the required average torque  $T_n$  is met:

$$C_{T \text{avg}} = K_{T \text{avg}} \frac{T_n - T_{\text{avg}}}{T_n} C_{\text{mat}} \quad (8.19)$$

Also, if a minimum targeted efficiency is imposed (say  $\eta_n > 0.87$ ), another penalty function  $C_{\text{eff}}$  is added.

$$C_{\text{eff}} = K_{\text{eff}} \left( \frac{1}{\eta} - \frac{1}{\eta_{\text{min}}} \right) \cdot P_n \cdot I_{\text{cost}} \cdot h \quad (8.20)$$

with  $I_{\text{cost}}$  – energy price (USD/kWh),  $h$  – operation hours at rated load.

PM demagnetization penalty function  $C_{\text{PMdemag}}$  is also introduced by imposing a minimum flux density  $B_{\text{nPMmin}}=0.2$  T, for example normal to the PMs.

$$C_{\text{PMdemag}} = K_{\text{demag}} \cdot \left( \frac{B_{\text{nPMmin}} - B_{\text{nPM}}}{B_{\text{rPM}}} \right) \cdot C_{\text{mat}} \quad (8.21)$$

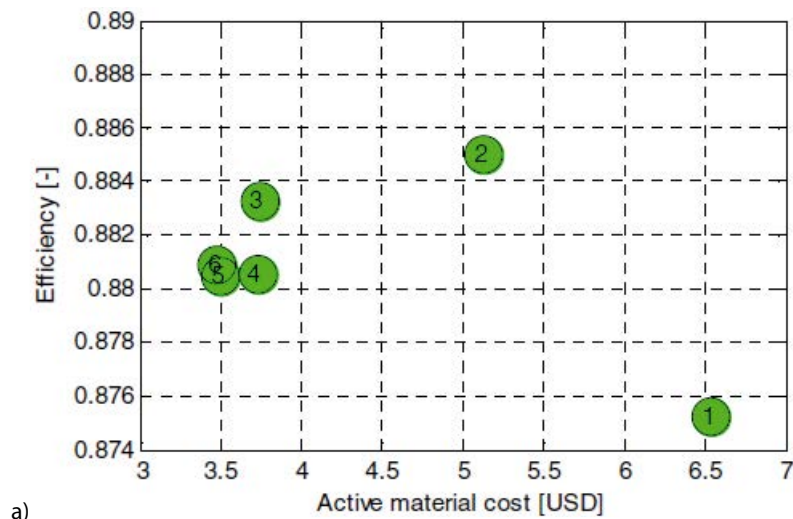
with  $B_{\text{rPM}}$  – remnant flux density of PMs.

The FEM embedded design provides precision, but requires high computation effort. To reduce this effort some simplifications have been performed:

- \* The no load analysis is performed only for the initial and optimal variable vectors. In subsequent runs the initial number of turn/coil is used. This implies that in the end the number of turns, to meet the d.c. voltage available for the required torque and speed, has to be modified. To do so a circuit model – imported from FEM with a control system is used repetitively to simulate the drive operation for key operation conditions, for the optimal design, until convergence of number of turns per coil is reached.

Starting from a random initial variable vector an optimum design solution was reached in about 6 hours on a regular desktop computer, with 5 steps along the gradient and 9 local explorations.

The Pareto fronts distribution of initial, trial and inter-moderate runs in the optimal design code (Fig. 8.29).



a)

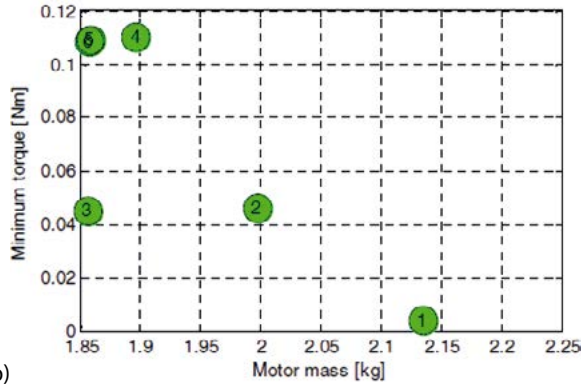


Fig. 8.29 Pareto distribution of initial, final and intermediate points: a) efficiency versus active materials costs (USD), b) minimum torque versus motor mass (kg).

The 6<sup>th</sup> (last) step shows the lowest materials cost, while all penalty costs are met as well.

The out power is 122 W (45% more than the required 85 W). Notable overload capacity is thus secured. However, with the initial number of turns/coil, the controlled dynamics code shows the motor incapable to reach 0.27 Nm at 3 krpm. However, as explained earlier, repetitive reduction of coils turns by up to 25% rendered the motor fully compliant with the specification. This is the sense of “optimum point corrected” in Table 8.9.

However, the reduction in the number of turns lead to a small reduction of the average and minimum torque (from +0.1 Nm to 0.08 Nm), which are still acceptable.

Table 8.9. OMD – 1 phase stator – Ferrite PM motor (85 W, 3 krpm, Vdc=290 V) [5].

<i>Parameter</i>	<i>Initial point</i>	<i>Optimum point</i>	<i>Optimum point corrected</i>
stator outer diameter [mm]	95	89.9	89.9
stator inner diameter [mm]	41.5	48.7	48.7
stack length [mm]	32.94	34.93	34.93
smaller airgap height [mm]	0.39	0.35	0.35
average torque value for rated load [Nm]	0.23	0.34	0.26
minimum torque value [T]	0	0.091	0.08
mechanical output power for rated load [W]	73	108	83.6
electric efficiency for rated load [-]	0.875	0.88	0.88
rotor inertia [kg·m <sup>2</sup> ]	2.9 10 <sup>-5</sup>	5.6 10 <sup>-5</sup>	5.6 10 <sup>-5</sup>
winding resistance [Ohm]	6.44	15.04	8.93
average inductance value [H]	0.11	0.13	0.07
number of turns per coil [-]	186	186	143
current density [A/mm <sup>2</sup> ]	1.2	2.89	2.22
total material costs [USD]	10.17	6.63	6.64
average torque penalty cost [USD]	1.35	0	0.1
minimum torque penalty cost [USD]	9.29	0.5	2.62
efficiency penalty cost [USD]	9.29	0	0
demagnetization avoidance penalty cost [USD]	0.81	0	0

### 8.6.2 FEM selected results

To illustrate further the FEM embedded optimal design, a few FEM results are shown here as follows:

- \* emf, current and total torque versus rotor position for initial, optimum, and optimum corrected designs (Fig. 8.30):
- \* efficiency, minimum, PM flux density and FEM – calculated stator and rotor core losses (Fig. 8.31) [5].

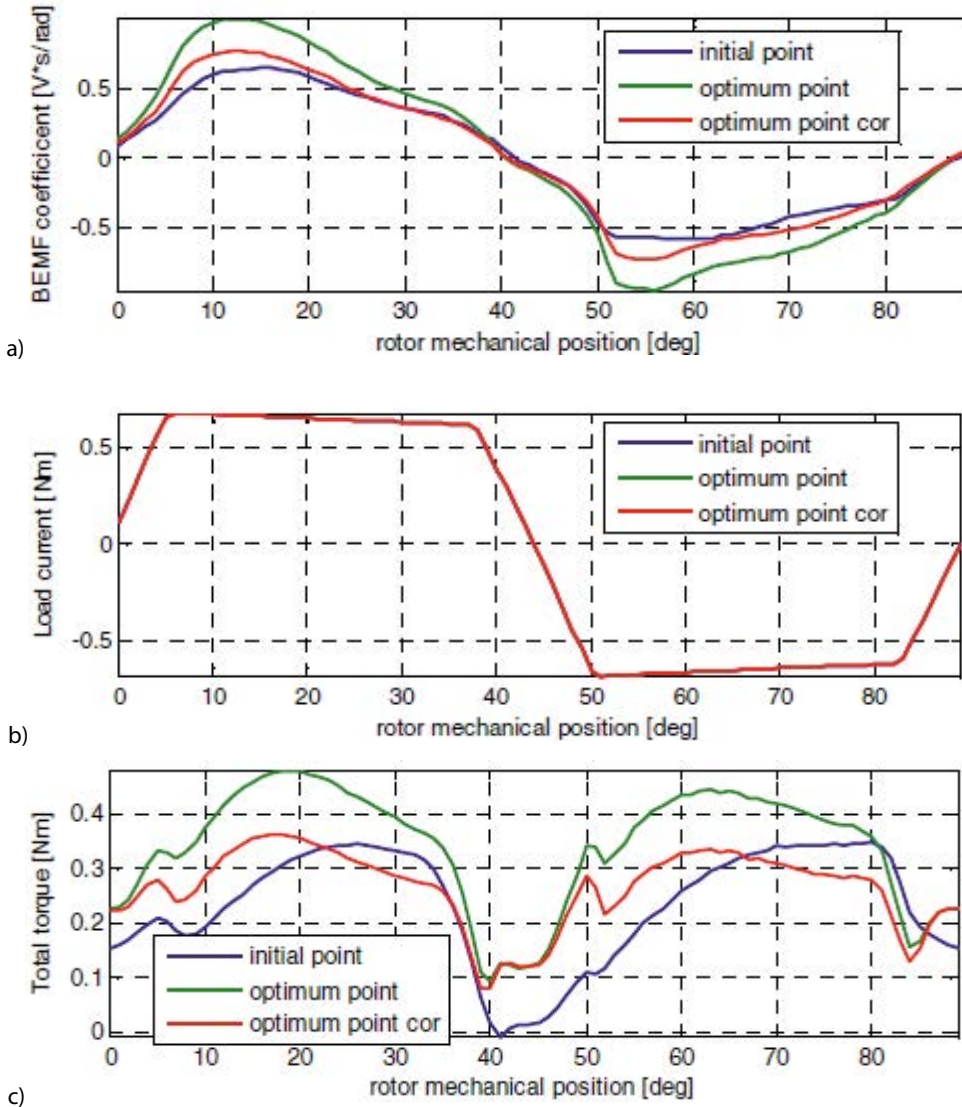


Fig. 8.30 Emf, a), current, b), torque, c) versus rotor position.



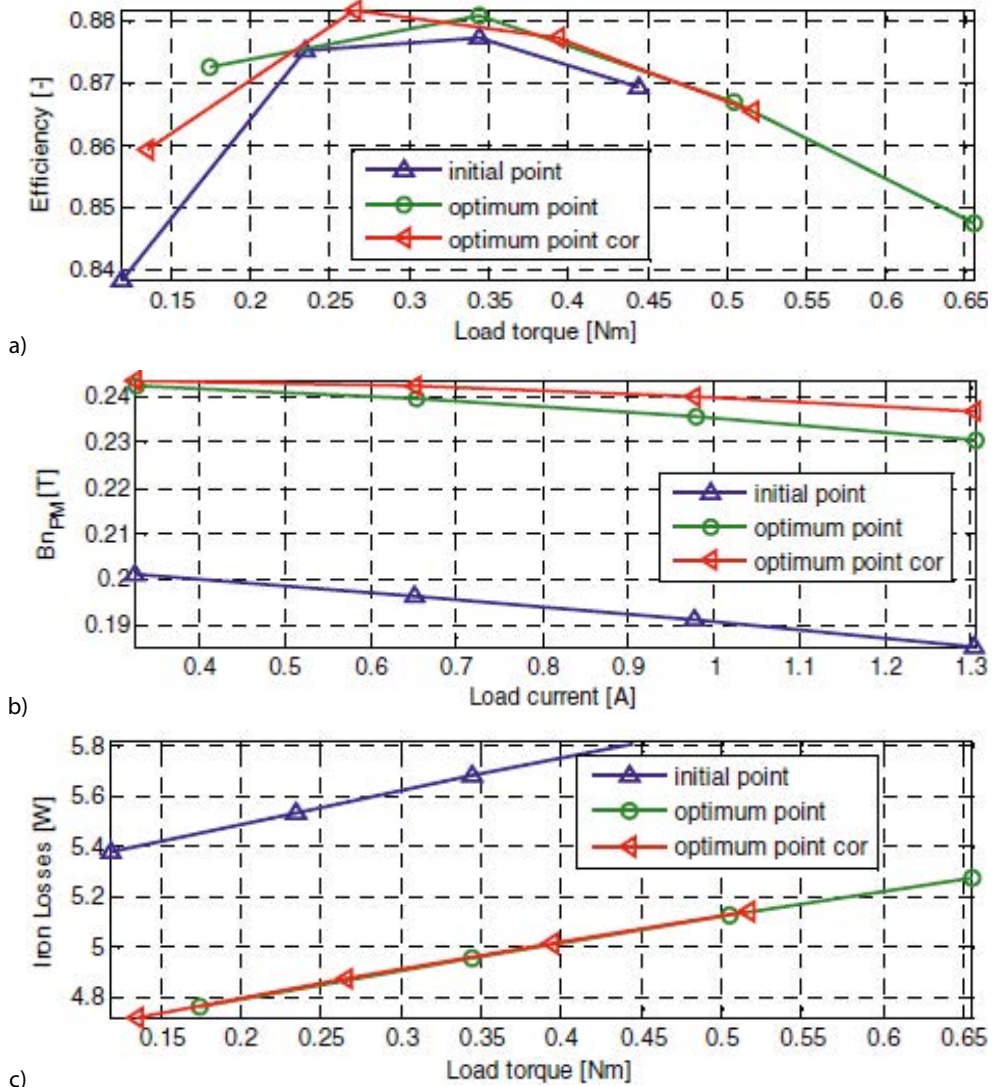


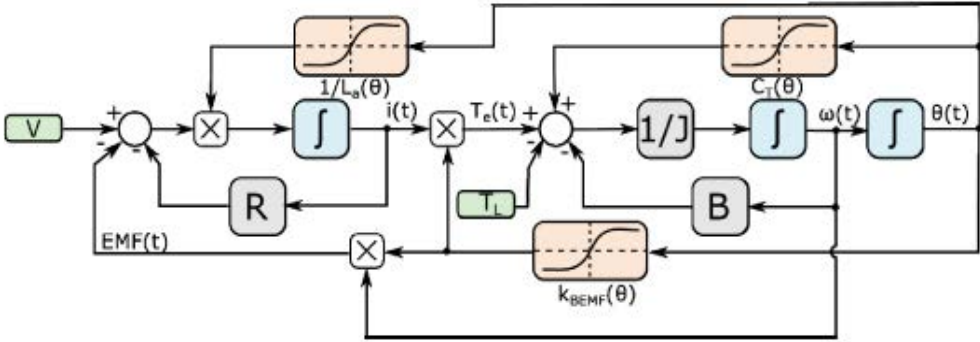
Fig. 8.31 Efficiency, a), minimum PM flux density, b), core losses, c).

It seems the FEM embedded (only) optimal design methodology is suitable to secure a low cost solution at good efficiency (87%) for a 1 – phase selfstarting stator – Ferrite PM small motor drive (85 W, 3 krpm). The active materials cost is only 3.6 USD and their mass is 1.85 kg, notably smaller than in a line – start split – phase capacitor IM at 100 W, 2.85 krpm.

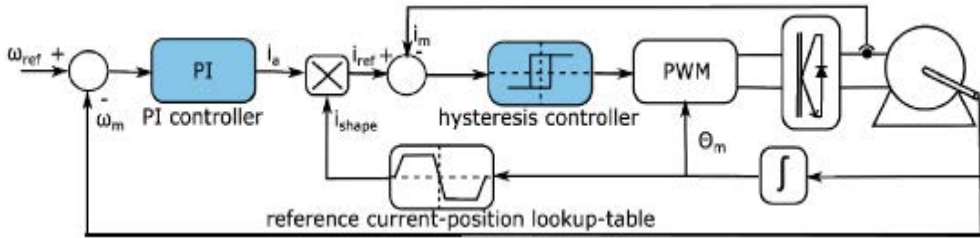
The variable speed inflicts additional energy savings in the compressor (load) and in the motor losses and thus may compensate the additional cost of the PWM converter cost, described in what follows.

### 8. 6. 3 Controlled dynamics

A Simulink model of the motor with imported FEM data (cogging torque, emf, inductance variations with rotor positions) was built (Fig. 8.32a).



a)



b)

Fig. 8.32 Motor model, a) and closed – loop control system, b).

The motor data are:  $V_{rated}=280\text{ V}$ ,  $P_{rated}=83.6\text{ W}$ ,  $n_{rated}=3\text{ krpm}$ ,  $R_s=8.93\Omega$ ,  $L_{dav}=L_{qav}\approx 78\text{ mH}$ ,  $J=5.6\times 10^{-5}\text{ kgm}^2$ ,  $2p=4$  poles,  $B$  (friction coefficient) =  $0.0001\text{ Nm*s}$ .

The close loop control system (Fig. 8.32b) includes current and speed regulators with a crude position feedback (even sensorless control may be approached).

The current shape (Fig. 8.32) is imposed as dependent on rotor position. The PI speed regulator coefficients are  $k_p=0.05$  and  $k_i=0.5$ , while the current hysteresis control band was fixed at  $0.01\text{ A}$  (5%).

In order to check the control system effectiveness, a 0.5 second speed ramping to 3 rpm with a 1.5 second steady state mode operation. A constant load torque  $T_{load}=0.26\text{ Nm}$  was present from  $t=0$  seconds.

Simulation results in Fig. 8.33 show the speed, current and torque waveform during the acceleration and steady state operation under full load. Quite satisfactory behavior is to be noticed.

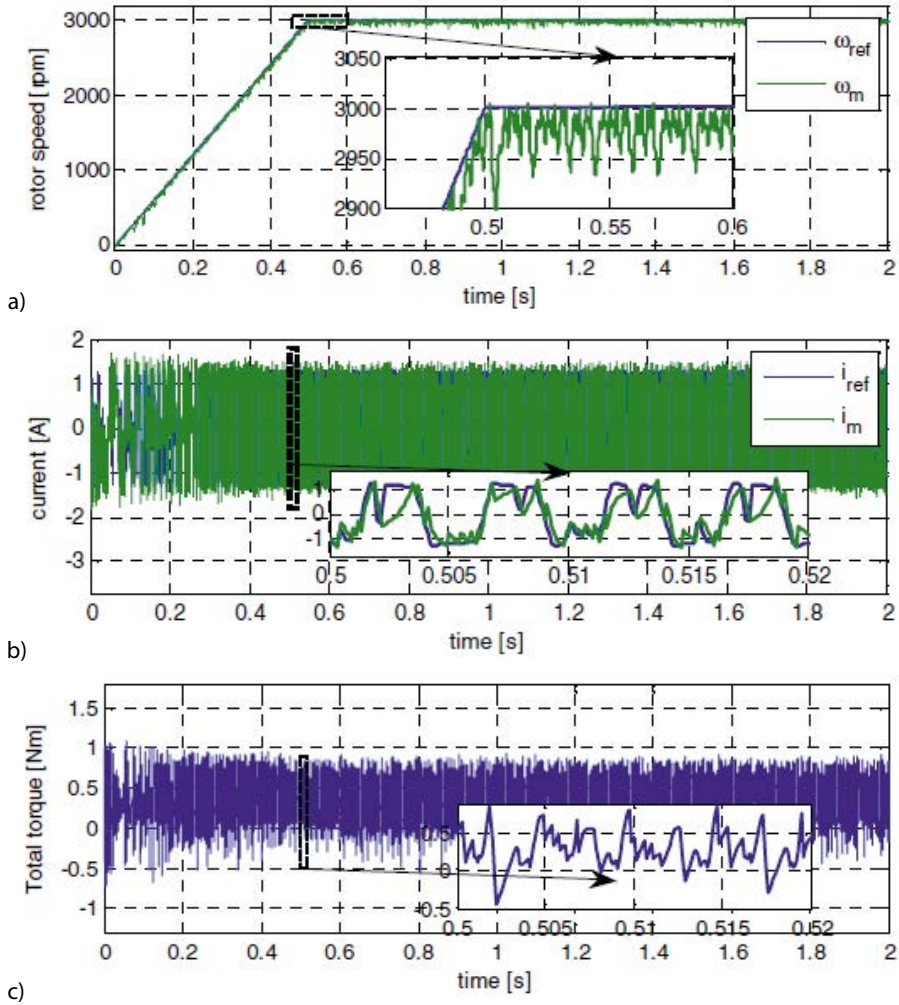


Fig. 8.33 Controlled dynamic simulations: a) reference and motor speed, b) current, c) torque.

The current and torque pulsations suggest that fine improvements of close loop regulators are further needed.

## 8.7 Conclusion

The present Chapter has illustrated five representative contributions to better the line start and variables speed drives for small compressor (or ventilator) like applications.

Advanced modeling (by MEC and FEM) optimal design methodologies with digital simulation results for controlled dynamics and industrially tested prototype characterize a decade long UPT visible effort [9-14].



## 8.8 References

- [1] F. Kalluf, A. Espíndola, L. Tutelea, I. Boldea, "2/4 poles split phase capacitor motor for small compressors: a comprehensive characterization", *IEEE Trans*, vol. IA – 50, no. 1, 2014, pp. 356 – 363.
- [2] L. Tutelea, A. Popa, T. Staudt, W. Hoffman, I. Boldea, "Line start 1 phase – split – phase–capacitor cage–PM rotor–RelSyn motor: modeling, performance and optimal design, with experiments", *IEEE Trans*, vol. IE – 65, no. 2, 2017, pp. 1772 – 1780.
- [3] F. Kalluf, A. Isfanuti, L. Tutelea, A. Popa, I. Boldea, "1 kW, 2000 – 4500 rpm Ferrite PMSM drive: comprehensive characterization and two sensorless control options", *IEEE Trans*, vol. IA – 52, no.5, 2016, pp. 3980- 3989.
- [4] Isfanuti, L. Tutelea, I. Boldea, T. Staudt, P. Ely da Silva, "Outer–Ferrite–PM–rotor BLAC motor characterization: FEM assisted optimal design", *Record of ICEM 2018* (IEEEExplore).
- [5] Isfanuti, L. Tutelea, T. Staudt, I. Boldea, "Small power 4 stator – pole stator Ferrite PM single phase selfstarting motor drive: FEM – based optimal design and controlled dynamics", *Record of OPTIM – ACEMP 2017* (IEEEExplore).
- [6] I. Boldea, T. Dumitrescu, S. A. Nasar, "Steady state unified treatment of capacitor a.c. motors", *IEEE Trans*, vol. EC – 14, no. 3, 1999, pp. 557-582.
- [7] I. Boldea, "Induction machine design handbook", book, Chapter 25, 2<sup>nd</sup> edition, CRC Press, Florida, USA.
- [8] I. Boldea, M. C. Paicu, G. Andreescu, "Active flux concept for motion-sensorless unified a.c. drives" *IEEE Trans*, vol. PE – 23, no. 5, 2008, pp. 2612-2618.
- [9] A.S. Isfanuti, M. Baba, L. Tutelea, A.A. Popa, I. Boldea, "Surface NdFeB versus Ferrite IPM motor drive for low power (100 W to 2000 W) applications", *Record of IEEE – IECON 2013*, pp. 3177 – 3182.
- [10] L. Tutelea, I. Boldea, "Optimal design of residential brushless d.c. PM motors, with FEM validation", *Record of ACEMP 2007* (IEEEExplore).
- [11] L. Tutelea, I. Boldea, "Surface PMSM optimization design: Hooke Jeeves method versus genetic algorithms", *Record of IEEE – ISIE 2010*, Bari, Italy (IEEEExplore).
- [12] L. Tutelea, I. Boldea, "Induction motor electromagnetic design optimization: Hooke Jeeves method versus genetic algorithms", *Record of OPTIM 2010*, pp. 485-492, (IEEEExplore).
- [13] V. Gradinaru, L. Tutelea, I. Boldea, "Hybrid analytical FEM optimization design for refrigerator compressor loads", *Record of ACEMP-Electromotion 2011*, pp. 657-662 (IEEEExplore).
- [14] A.S. Isfanuti, L. Tutelea, S. C. Agarlita, I. Boldea, "NdFeB versus Ferrite IPM motor for automotive a.c compressor electric driving: modeling and FEM – embedded optimal design", *Journal of electrical Eng.* ([www.jee.ro](http://www.jee.ro)), vol. 13, no. 3, 2013.

# MW – RANGE ELECTRIC GENERATOR SYSTEMS FOR RENEWABLE ENERGY: DESIGN AND CONTROL

## Abstract

Modern distributed power systems with large renewable energy penetration cogeneration and interruptible power supplies, marine ship and aircraft require even better electric generator systems at constant or variable speed to tap more energy from the primary energy source at higher efficiency and smaller specific weight and cost (USD/kW and USD/kWh).

Wind and small hydro energy conversion require a similar electric generator system based on active and reactive control at variable speed.

In view of today's trends three key topics are detailed in this chapter:

- \* Optimal design of d.c. excited and PM [34] synchronous generators [1].
- \* Optimal design of axial – airgap transverse – flux PM generators.
- \* Cage rotor [7.8] and wound – rotor induction [9] PM to synchronous
- \* Advanced control of cage – rotor [7, 8] and wound – rotor [9] induction, PM [10] synchronous wind generator systems.

## 9. 1 Optimal design of d.c. excited directly driven large wind generators. The largest directly – driven wind generator so far (2018) is synchronous with d.c. excitation at 7.6 MW, 3.6 kV and 11 rpm (see "Enercon gmbH"(Fig. 9.1)).

There is little information on this formidable technical achievement other than that it uses a full power dual PWM converter in the stator and small power (3%) a.c. – d.c. PWM converter to control the field current.

Also it is a typical multi-rotor salient pole machine. The general design methodology d.c.e – SG is rather standard at the preliminary level [1] and includes:

- \* Specifications: shortcircuit ratio, transient inductance, active and reactive power capability and minimum load power factor, excitation system with its voltage ceiling, voltage and frequency (speed) control range, negative sequence voltage

and currents limits, harmonics content of generator no load voltages, temperature limitations, number of start – stop cycles, forces, armature (stator) voltage, runaway speed etc.

- \* Design aspects: output coefficient, base stator geometry, number of stator slots, design of stator winding, design of stator core, salient rotor pole design, open circuit magnetic saturation curve, field current at full load and lowest lagging load power factor, stator resistance, leakage stator inductance, synchronous inductances  $L_d$ ,  $L_q$ , losses, efficiency time constants and transient and subtransient d, q inductances, cooling system and thermal design; brush and slip ring design, design of bearings frame etc, brakes and jack's design, exciter design, etc.

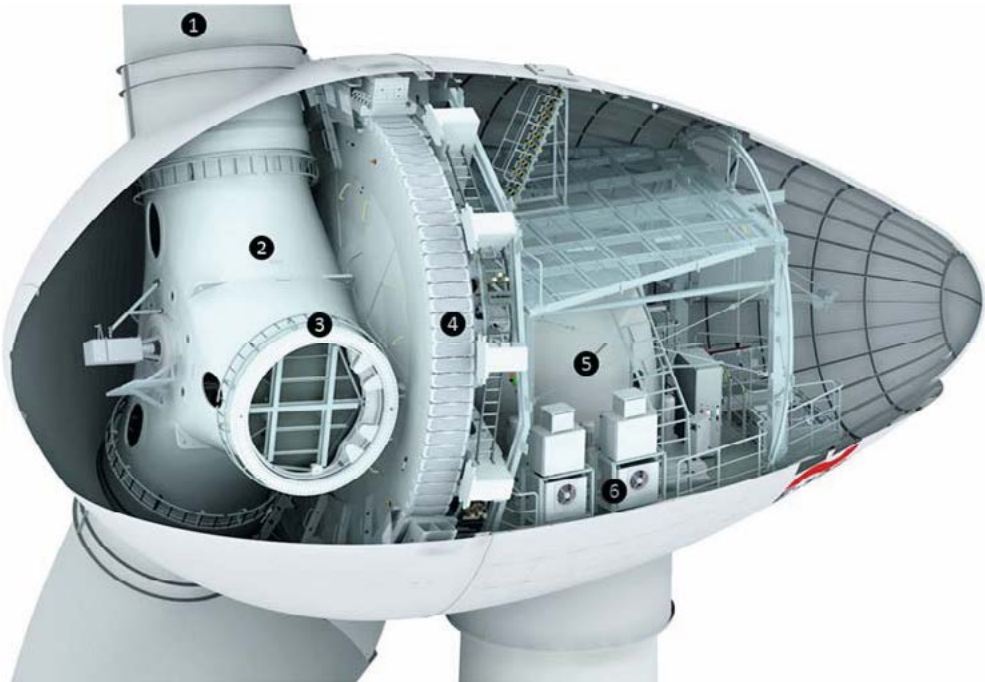


Fig. 9.1 Enercon E – 126 DD – WT – d.c. excited SG based, at 7.6 MW and 11 rpm.

The SG design experience based on nonlinear analytical models [1] is illustrated here by integrating into an optimal design code based on the modified Hooke – Jeeves algorithm.

The number of poles of the rotor and of stator winding ( $2p$ ) is left open to change based on a tight rated frequency interval:

$$p = \frac{f_n}{\eta_n} \quad (9.1)$$

The objective function includes:

- Active material cost
- Energy loss cost
- Over-temperature penalty
- Initial generator cost (includes framing etc.)

Only sample results of optimal design code are given here. For example, the Pareto fronts for Efficiency versus active weight for different numbers of pole pairs at their respective outer stator diameter (in m) shown in Fig. 9.2.

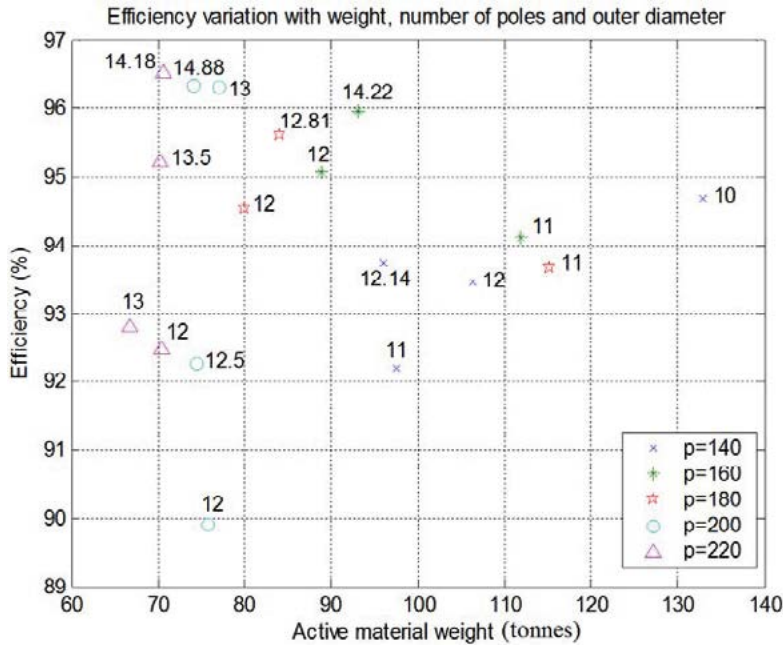


Fig. 9.2 Efficiency versus active weight for a few pole pair values ( $p$ ) with their outer stator diameter in meters.

Extracting a few representative optimal design of Fig. 9.2 leads to the data in Table 9.1.

Table 9.1 Design of a 7.6 MW, 11 rpm, DC Excited Synchronous Generator (DCE-SG). [3]

No.	Poles	Outer Diameter (m)	Efficiency (%)	Weight (tons)	Comments
1	220	14.18	96.53	79.67	Better efficiency
2	220	13	92.81	66.81	Lowest weight
3	140	10	94.68	132.9	Lowest diameter
4	200	13	96.32	77.02	Optimum 1
5	180	12	94.54	89.0	Optimum 2

The case of  $2p=180$ ,  $D_{os}=12$  m (outer stator diameter) is followed in more detail in what follows. The evolution of the objective function (total) and its components listed above (Fig. 9.3) leads to the conclusion that 25 iterations suffice.

The evolution of stator ( $p_{cun}$ ), rotor ( $p_{exn}$ ) winding and core ( $p_{fco}$ ) losses (Fig. 9.4) confirms the sufficient number of iterations as expected.

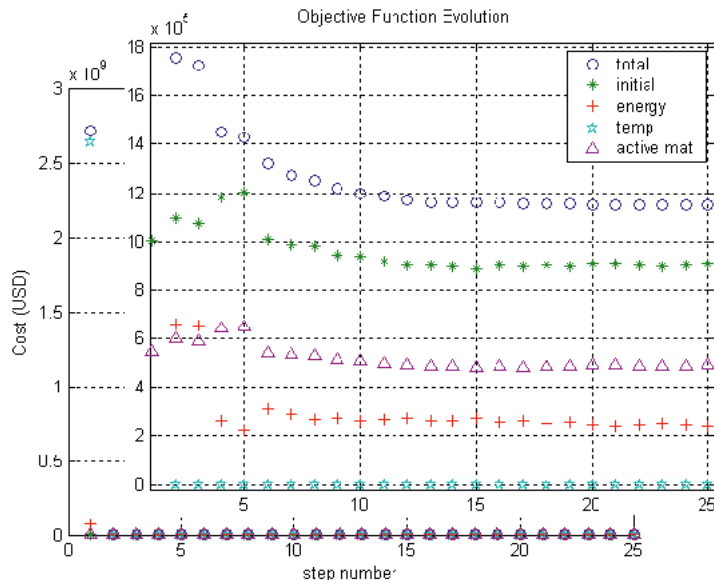


Fig. 9.3 Objective function and component evolution during optimal design code execution (7.6 MW, 11 rpm,  $2p=180$  poles).

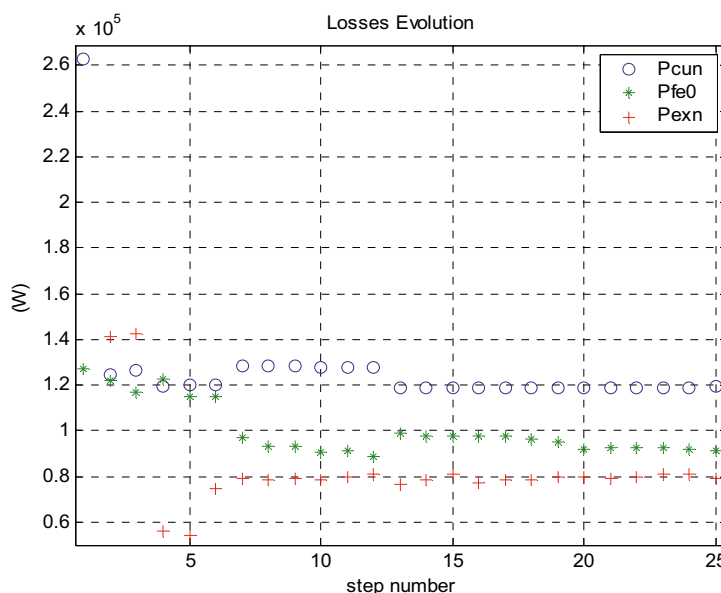


Fig. 9.4 Loss evolution for the 7.6 MW, 11 rpm ( $2p=180$  poles),  $\cos\phi_1=1$ , d.c.e-SG optimal design.

The main output file data is gathered in table 9.2.

Table 9.2 DCE-SG parameters and features (7.6 MW, 11 rpm, 3.6 kV). [3]

Dsi (m)	11.768	Stator inner diameter
Dso (m)	12	Stator outer diameter
Dri (m)	11.491	Rotor inner diameter
Lg (m)	9.98	Magnetic core length
hag (mm)	3.25	Air-gap height
hag <sub>max</sub> /hag	1.2	maximum air-gap/minimum air-gap
q1	2	Number of slots per phase per pole
Turns per coil	12	
Parallel path	180	
hst (mm)	25.5	Stator slot total height
hs1(mm)	20	Height of stator slot filled with cooper
Ws(mm)	14.7	Width of the stator slots
So(mm)	7.	Stator slot opening
wrt(mm)	105	Rotor pole width
wrps(mm)	179.4	Rotor pole shoe width
mg (ton)	89.0	Active material weight
Etan (%)	94.54	Efficiency att pure resistive power factor
Pcun (kW)	237.61	Stator copper losses
Pex0n (kW)	34.68	Excitation, load losses
Pexn (kW)	84.13	Excitation losses at rated resistive load
Pfen(kW)	96.69	Iron rated losses
Stator linkage flux (Wb)	2.96/2.79	Analytical/FEM
Xd (pu)	9.878/9.824	d axis reactance Per unit (Analytical/fem)
Xq (pu)	9.586/9.443	q axis reactance Per unit (Analytical/fem)

The OD code outputs also the standard curves:

- \* Excitation current (in p.u.) versus load current for various loads
- \* V curves (Fig. 9.5) load current versus excitation current (in p.u.) for various active power levels (in p.u.), Fig. 9.6
- \* Active – reactive power capability curves, Fig. 9.7
- \* Efficiency versus load current, at rated voltage for a few, Fig. 9.8, R, L, C load types.

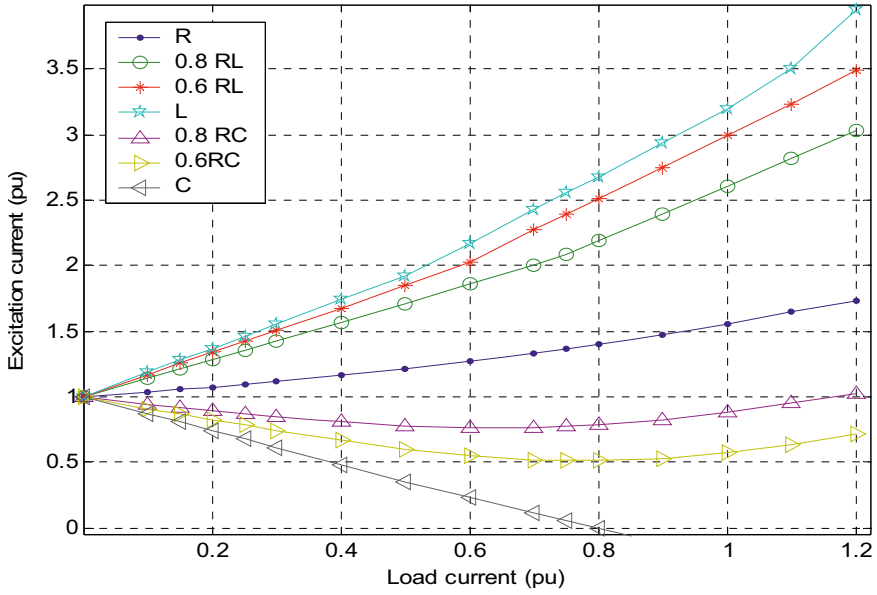


Fig. 9.5 Excitation current versus load current.

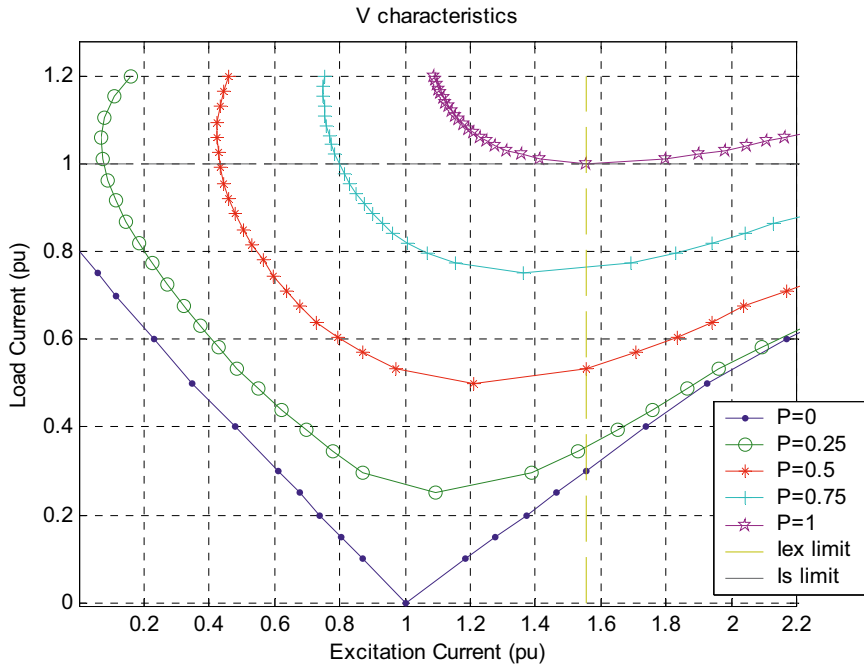


Fig. 9.6 V curves of d.c.e – SG.

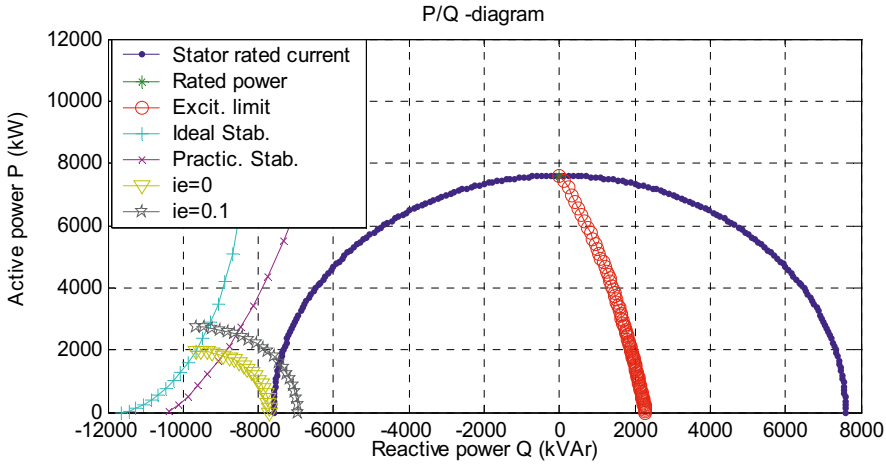


Fig. 9.7 Active-reactive power capabilities DCE-DG.

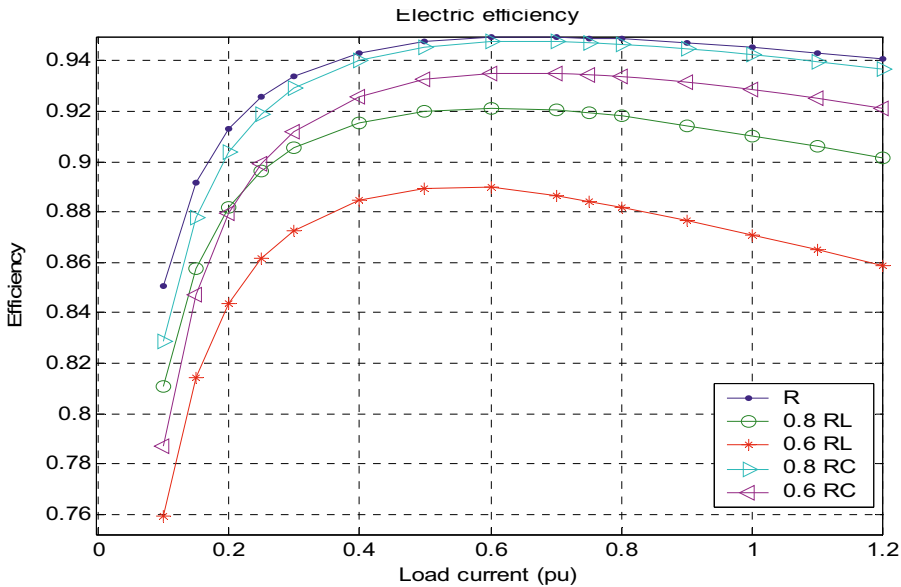


Fig. 9.8 Active – reactive power capability curves.

A few remarks to be made here :

- \* The single composite objective function drops (Fig. 9.3) 1000 times, mainly due to the overtemperature penalty dramatic reduction after the first few iterations.
- \* The windings and core losses (Fig. 9.4) show a mild reduction as the initial cost is a paramount component.
- \* In calculating efficiency, the mechanical losses were assigned a rather small value (2.92 kW) as the speed is low.



- \* The total optimal code execution time, for 20 random starts was of only  $20 \times 70 = 1400$  seconds on „core 2 duo“ GHz desktop computer.
- \* A multiobjective differential – evolutionary ( $\Delta t$ ) optimal design code, based exclusively on FEM modeling (even calculating only 10 – 12 points per half of an electric period) would need about 50 hours of computation on a multi- desktop computer crew [11]; but it would reach better precision.

Here we add to the optimal design code based on nonlinear analytical modeling a few key optimization calculations illustrated in Figs. 9.9 and 9.19.

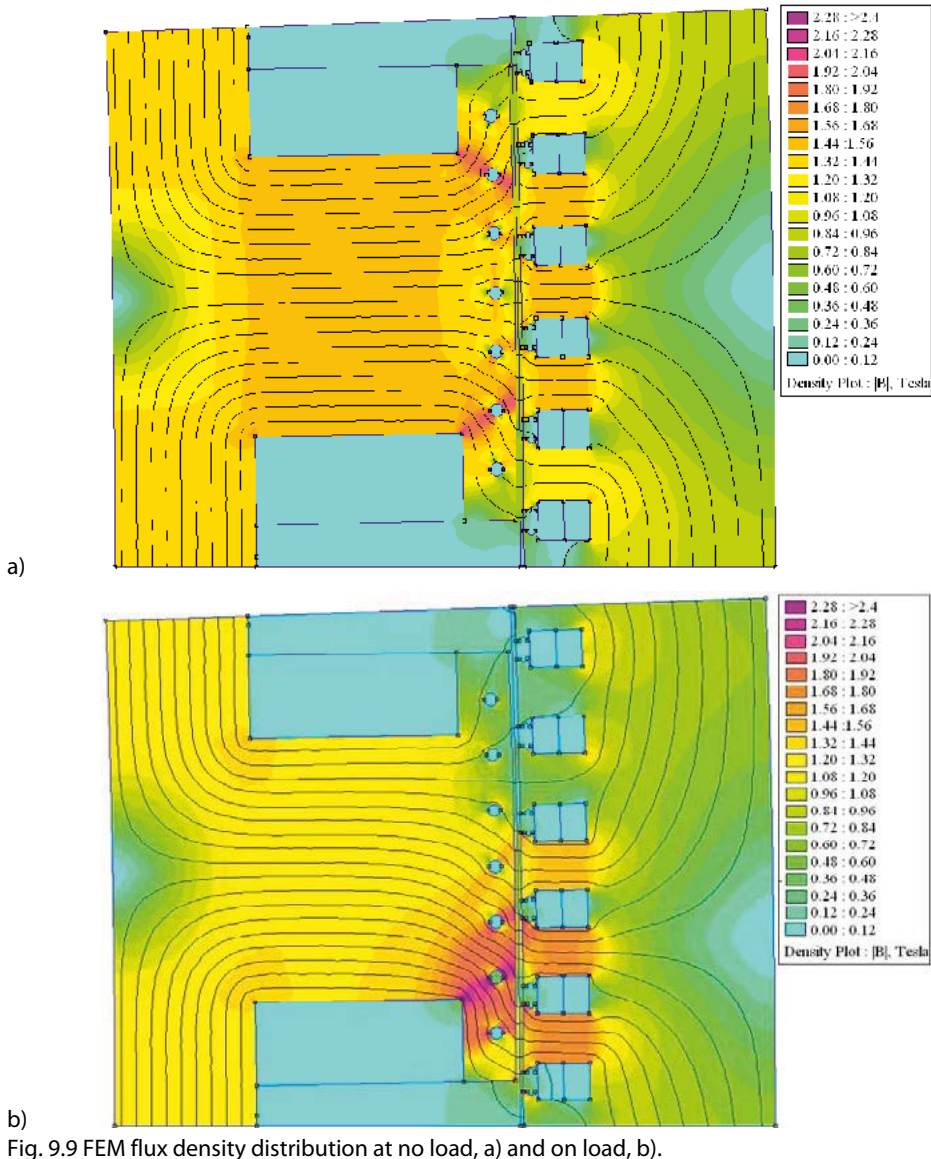


Fig. 9.9 FEM flux density distribution at no load, a) and on load, b).

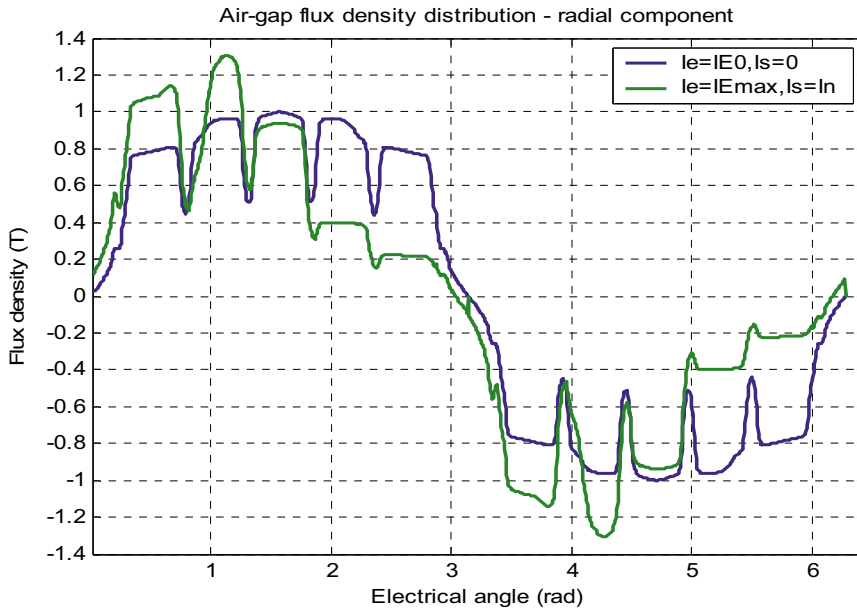


Fig. 9.10 Airgap flux density at no load and on full load.

The full torque versus rotor position has been also checked. Such verifications for the analytical optimal design may lead to regressive correction factors by FEM in the latter in relation to key factors as no load and on load airgap flux density fundamental,  $L_{dm}$ ,  $L_{qm}$  and average torque.

The optimal design routine may then be restarted automatically until sufficient convergence is met.

This way the computation time is kept low, perhaps within a 2-3 hours on a single contemporary desktop computer.

Final note: as a compromise between active weight and efficiency, the designs no 4, 5 (in table 9.1) may be chosen.

Finally – Design 5 ( $2p=180$  poles, outer stator diameter=12m, efficiency 94.54% and active weight: 80 tons) is a good compromise between performance and outer stator diameter. The main drawbacks of directly driven d.c.e-SG is their large weight and their moderate efficiency. But the lack of PMs and the use of exciting protection in the grid operation are definite merits of d.c.e – SGs in wind energy conversion.

## 9. 2 PMSG optimal design [3]

The second largest so far (2018) commercialized PMSG (Fig. 9.11) sports 8 MW at around 3.2 kV and 480 rpm. Again, no detailed design and performance data is available.

A surface PM, radia – airgap multipole configuration was chosen. An additional PMSG at 8 MW was designed also for 1500 rpm to check the differences in cost and performance.

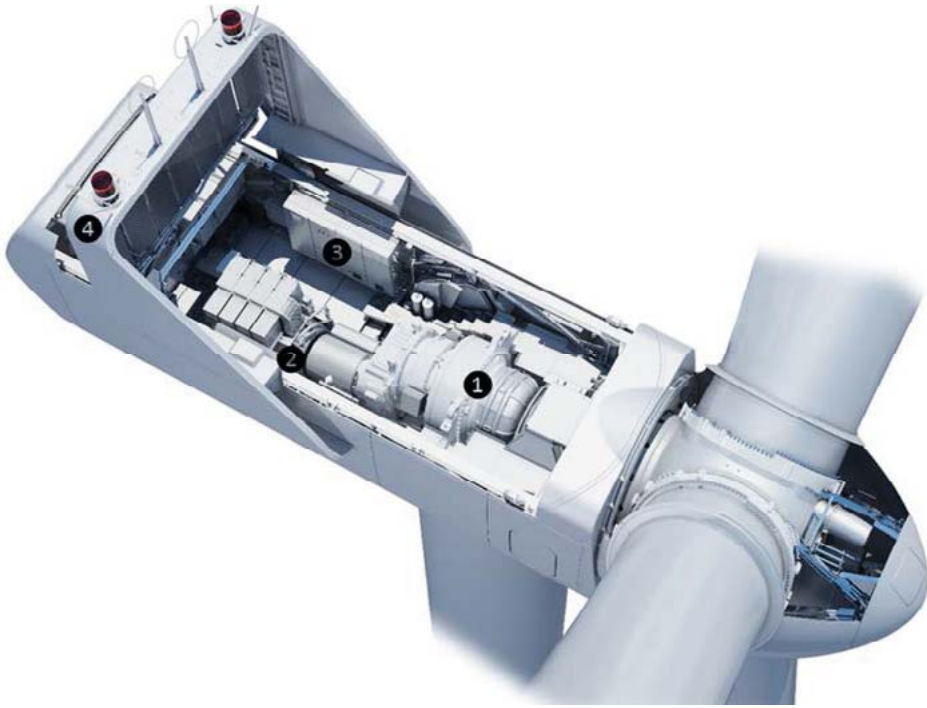


Fig. 9.11 Largest wind PMSG (8 MW, ~ 480 rpm, ~ 3.2 kV), adapted from Vestas wind systems D/5.

For the first one (at 480 rpm) the number of pole  $2p=14$ ,  $f_{1n}=5.6$  Hz while for the second (at 1500 rpm),  $f_{1n}=50$  Hz.

Again, a nonlinear analytical model [1] is used for the optimal design to reduce computation time; with surface PMs and distributed stator windings ( $q_1=1$ , respectively 3 slots/pole/phase) allow for a small enough synchronous inductance (to secure low voltage regulation).

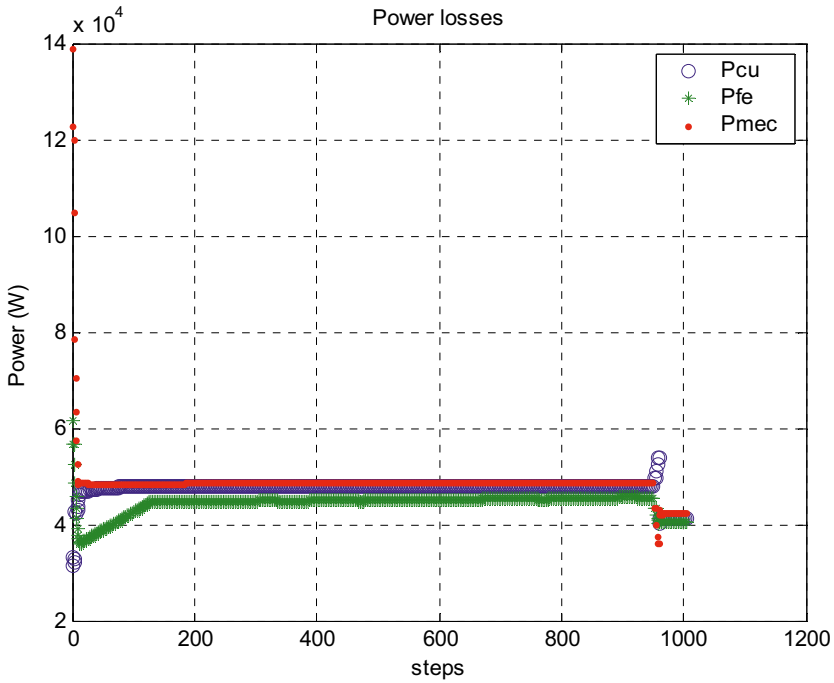
Again the Hooke – Jeeves modified algorithm was used in corroboration with a single composite objective (cost) function. FEM key validation checks are performed on the analytical optimal design code and key correction factors on emf and on synchronous inductance are iteratively used until sufficient convergence is met with.

Again the single objective cost function is:

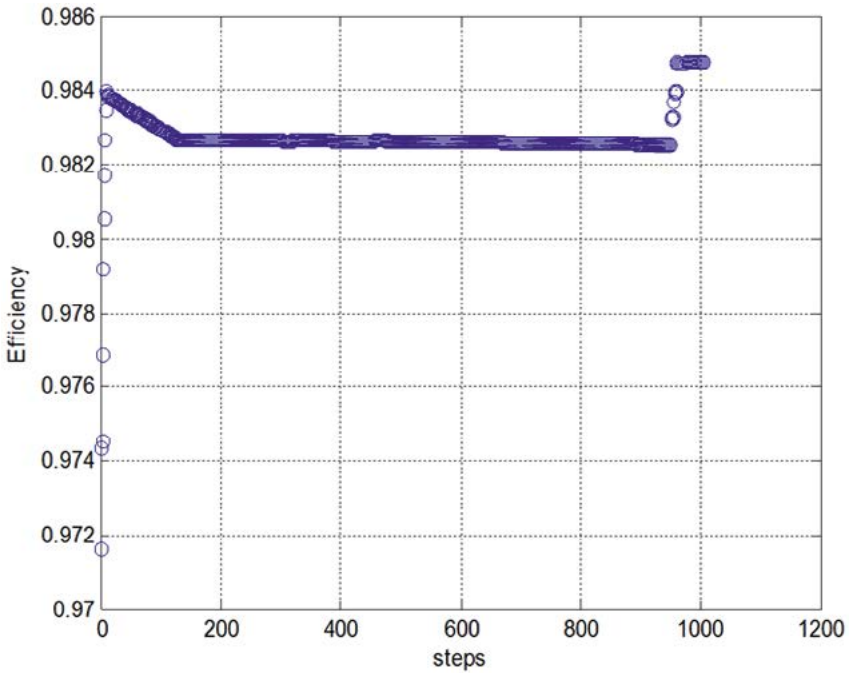
$$C_t = C_a + C_e + C_f + C_p \quad (9.2)$$

with  $C_a$  – active materials costs (lamination, copper PMs(NdFeB));  $C_e$  – cost of energy losses,  $C_f$  – frame, bearings,  $B_r \geq 1.15$  T, shaft, etc. cost,  $C_p$  – overtemperature and PM demagnetization avoidance penalty functions.

Here only sample results are given, for the sake of brevity, in Figs. 9.12 and 9.13.

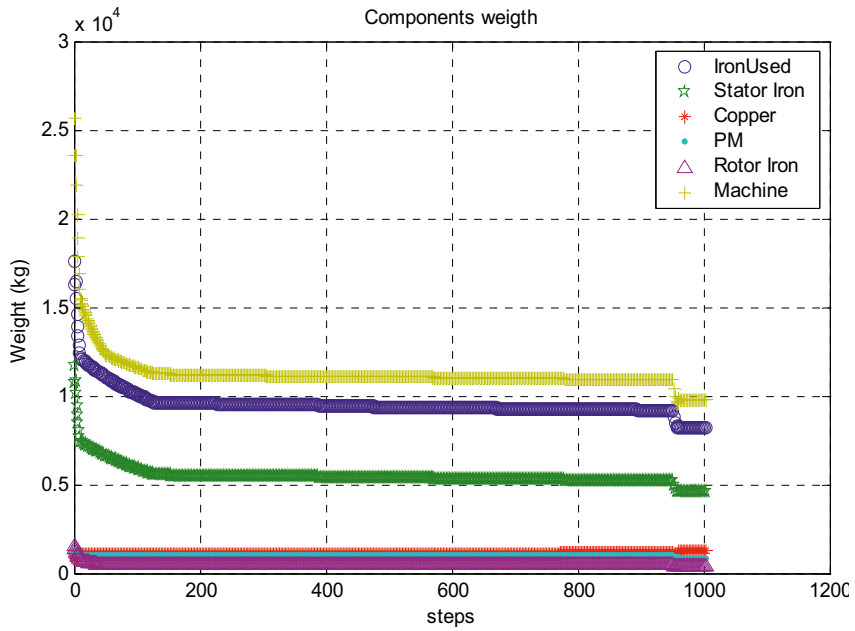


a)

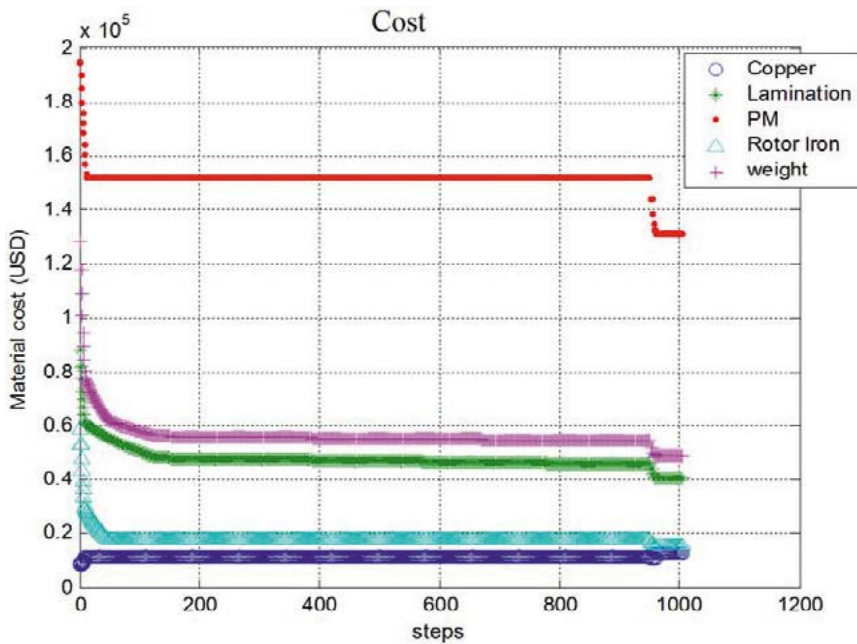


b)

Fig. 9.12 Loss, a) and efficiency, b) evolution during optimal design of an 8 MW, 480 rpm PMSM ( $p_{cu}$  – copper losses,  $p_{Fe}$  – iron losses,  $p_{mec}$  – mechanical losses).



a)



b)

Fig. 9.13 Weight components, a) and material cost components, b) for an 8 MW, 480 rpm PMSG.

The key numerical optimal design outputs are shown in table 9.3.

Table 9.3 Optimized design of an 8 MW, 3600 V, 1500 rpm and 480 rpm PMSG (price of permanent magnet: 150 USD/kg). [3]

Generator	Efficiency	Total weight (kg)	Total initial cost (USD)	Outer stator diameter (m)	Stack length (m)	Frequency (Hz)	Number of poles	PM weight (kg)
8 MW, 1500 rpm	9.98296	8 560	197 027	1.252	3.5	75	6	629
8 MW, 480 rpm	9.98475	9 799	249 376	2.177	3	56	14	875

### Discussion

Table 9.3 shows that both generators have a 98.00+% efficiency with only 1.2 tons in total weight and 50,000 USD less costs in favor of the 480 rpm PMSG. It is unlikely that the extra-transmission needed for the 1500 rpm generator can “squeeze” in the weight and cost difference. Even if so, the efficiency of the extra-transmission will reduce the total efficiency and finally the energy yield of the 1500 rpm PMSG.

## 9. 3 Design of transverse – flux wind PMSGs for power weight

In an effort to reduce the total generator weight (placed in the Nacelle of the wind turbine tower) transverse flux PMSG configurations have been proposed both for direct and transmission drives [4]. Here we describe the design of two categories of such generators with innovative topologies:

- One with axial – airgap and 2 circular – shape a.c. coil / phase [7, 12]: optimal design
- One with radial – airgap but with additional counter Halbach PMs to increase torque [12, 13]: 3D FEM characterization.

### 9. 3. 1 Optimal design of an axial – airgap (A - A) TF – PMSG

The dual stator cores and dual – rotor parts per phase of an A – A – TF – PMSG are shown in Fig. 9.14.

The specifications refer to a directly driven 3 MW, 15 rpm, 4.2 kV A – A – TF – PMSG.

A start-up geometry was obtained as in [1]:

Core outer diameter  $D_{es}=4900$  mm

Coil slot width  $w_c=w_{slot}=51$  mm

Coil height (axial)  $H_c=51$  mm

Axial stator yoke  $H_{sy}=60$  mm

PM axial length  $l_{PM}=65$  mm (NdFeB,  $B_r \geq 1.15$  T)

Airgap  $g=3$  mm (on one side)

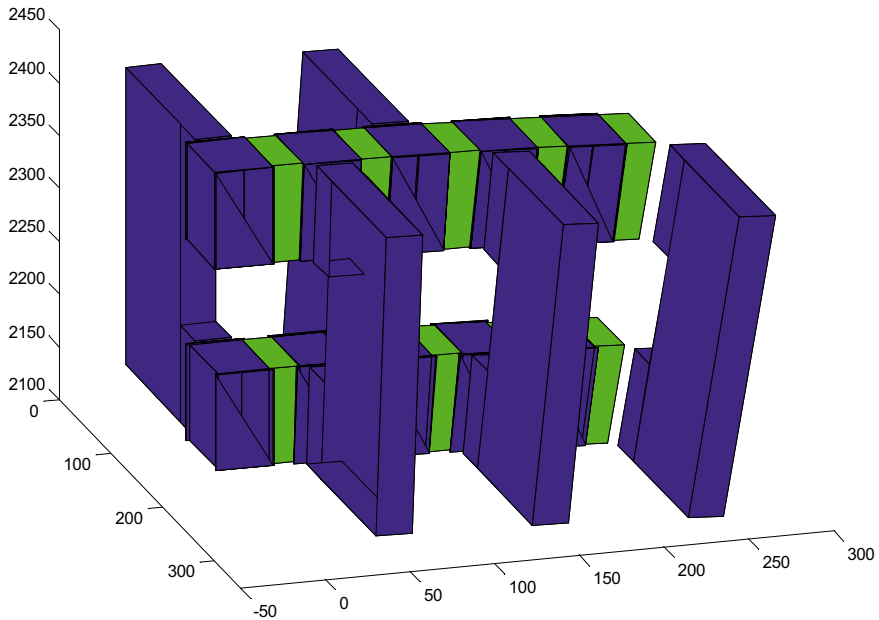


Fig. 9.14 A – A – TF – PMSG: one phase (with the 2 a.c. circular coils in place).

It should be noticed (Fig. 9.13) that rotor has spoke – shape magnets for making all PM active at any time and to counteract the PM flux fringing around airgap, to secure large enough no – load (PM) airgap flux density by PM flux concentration.

The machine model was based on the magnetic equivalent circuit (MEC) which for a pole pitch, even if 3 dimensional contains 16 nodes and thus 15 algebraic equations. To account for magnetic saturation in iron flux tubes, the computations start with given flux densities, then corrected iteratively for sufficient convergence [5], Fig. 9.15.

The variables vector  $\bar{X}$  was:

$$\bar{X} = \left[ 2p_{PM}, D_{ext}, w_{st}, w_c, H_c, H_{sy}, l_{PM}, l_{m_s}, l_{m_{r1}}, l_{m_{r2}} \right] \quad (9.3)$$

where  $l_{m_s}$  – ratio between stator pole width and PM pole pitch  $\tau_{PM}$ .

$l_{m_{r1}}$  – ratio between airgap rotor pole width and  $l_{PM}$  at airgap 1.

$l_{m_{r1}}$  – same as  $l_{m_{r1}}$  but at airgap 2.

The single composite objective function is defined as in previous paragraphs.

The computation time of the optimal design code (based on Hooke – Jeeves modified algorithm) implied around 70 iterations and lasted about 1 minute on a regular desktop computer with 20 random – starts runs, to secure more probably a global optimum roughly 1,200 seconds are required. 2D surrogate FEM key validations may be added for correction of emf and machine inductance  $L_s$  [5] (saliency is small functionally ( $L_d \approx L_q$ )).

though it is physical). Even in that case 1-2 hours would suffice for a complete optimal design (electromagnetic). Selected output data (table 9.4a, b, c).

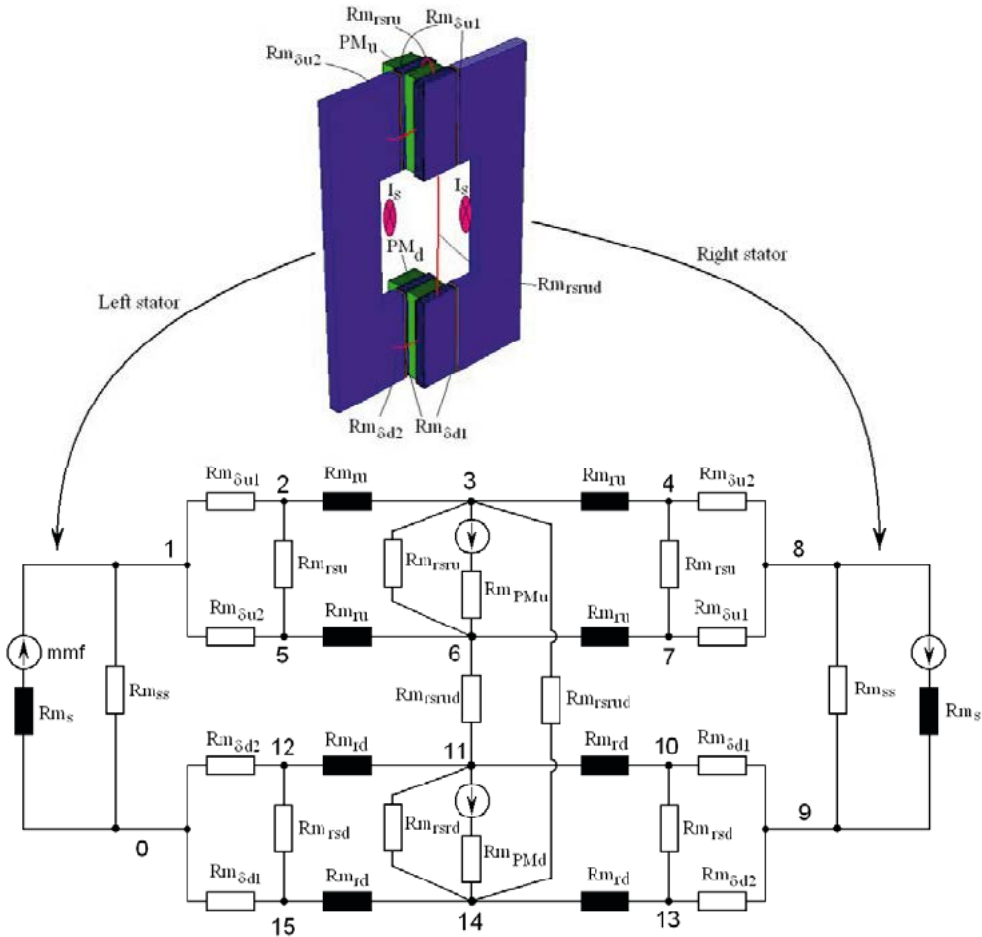


Fig. 9.15 A – A – TF – PMSG magnetic equivalent circuit (MEC) per pole pitch/phase.

Table 9.4a Geometry and weight/3MW, 11rpm AA-TF-IPMSG.

Mechanical Parameters	Analytical model value	Optimized value
External diameter: $D_{ext}$	4900 [mm]	6500 [mm]
Internal diameter: $D_{int}$	4440 [mm]	5984 [mm]
Number of poles: $2P$	546	632
Generator axial length: $l_{ax}$	889.44 [mm]	754.7 [mm]
Height of stator(and PM) along one air-gap: $W_{st}$	95 [mm]	89.5 [mm]
Stator coil width: $W_c$	40 [mm]	97 [mm]
Stator coil height: $H_c$	51 [mm]	37.5
Width of PM: $w_{pm}$	13 [mm]	18.9



Mechanical Parameters	Analytical model value	Optimized value
Length of PM: $L_{pm}$	65 [mm]	39 [mm]
Width of stator pole: $W_{sp}$	16 [mm]	13.4
Width of rotor pole: $W_{rp}$	16 [mm]	13.4 [mm]
Number of turns per coil: N	15	16
Total copper mass: $m_{cut}$	801.8	1913
Total iron mass: $m_{Fet}$	7083.8	5694
Total PM mass: $m_{pm}$	648	578.7
Total generator mass: $m_t$	9919.5	9345

Table 9.4b 3 Electrical parameters / 3MW, 11rpm AA-TF-IPMSG.

Electrical Parameters	Analytical model value	Optimized analytical value
Phase rated voltage: $V_{cn}$	2448 [V]	2491 [V]
Coil rated rms current: $I_{fn}$	430 [A]	302 [A]
Rated frequency: $f_n$	50 [Hz]	58 [Hz]
Rated coil mmf, peak : $I_{stn}$	9118 [AmpTurns]	6287[AmpTurns]
Phase resistance: $R_s$	77.72 [m $\Omega$ ]	66.17 [m $\Omega$ ]
Phase q axis rated inductance: $L_{sn}$	15.93 [mH]	17 [mH]
Total copper losses: $P_{cun}$	86151 [W]	36150 [W]
Total iron losses: $P_{Fen}$	91981 [W]	66502 [W]
Rated efficiency: $\eta_n$	9.944	9.967
Rated factor: $\cos \phi_n$	9.475	9.665

Table 9.4c Costs (3MW, 11rpm AA-TF-IPMSG)

Cost Parameters	Analytical model value	Optimized analytical value
Total copper cost: $Cu\_c$	8018 [USD]	19140 [USD]
Total iron laminations cost: $lam\_c$	35419 [USD]	28474 [USD]
Total active material cost: $i\_cost$	144684 [USD]	134424 [USD]
Total passive material cost: $pmw\_c$	69373 [USD]	65416 [USD]
Invertor cost: $inverter\_c$	157842.6 [USD]	112781 [USD]
Energy cost: $energy\_c$	267197 [USD]	153977 [USD]
Total generator costs: $t\_cost$	639100 [USD]	466600 [USD]

suggest that by optimal design:

- \* The power factor is increased from the initial value of 9.47 to 9.665 lagging;

- \* The efficiency is increased by 2% (to 96.7%) with the outer diameter increased from 4.9 m to 6.5 m.
- \* The active weight of such a machine is reduced from the initial 9,910 kg to 9,345 kg. This is a very small value in comparison with a regular SPMSG direct drive which weights more than 16 tons of active materials. The price to pay for this spectacular reduction in weight is the low power factor (which means larger PWM converter kVA and costs). However in a direct – drive the PMSG is notably more costly than the converter.
- \* The total objective (cost) function was reduced from the initial 639,000 USD to 466,000 USD (active material + energy loss + inverter costs (25 USD/kVA) are included).

The copper laminations PMs prices were 10 USD/kg, 5 USD/kg and respectively 50 USD/kg.

The PM weight is still high, but all magnets are active all the time.

### 9. 3. 2 3D – FEM of a radial – airgap TF – PMSG (6 MW, 12 rpm, $m=6$ phases)

An outer rotor radial airgap TF – PMSG is considered here to reduce copper weight and ease the fabrication process as the outer motor phase sections are assembled axially in a cylinder easily.

To reduce PM – fringing additional anti-fringing PMs are planted on the rotor pole sides. They increase notably the torque. PM flux concentration helps in to secure a large PM airgap flux density (emf).

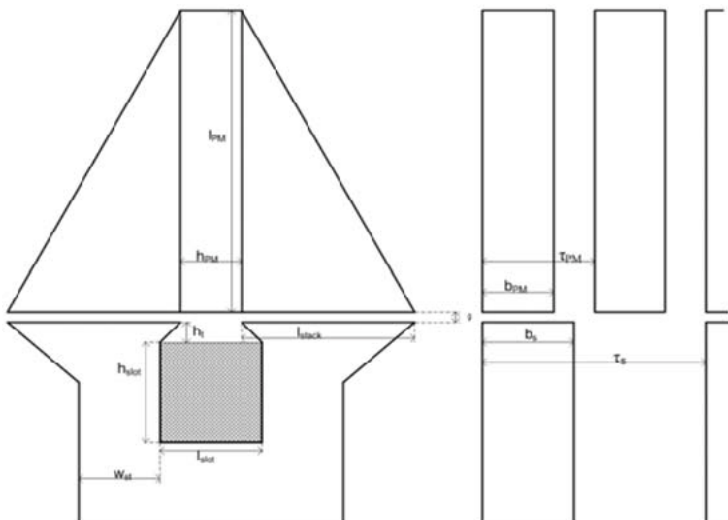
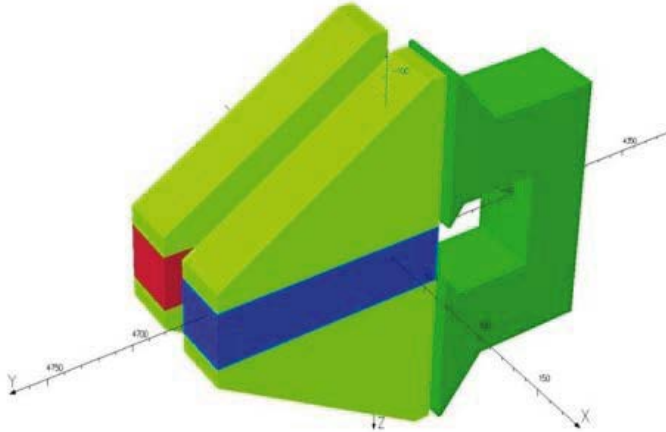


Fig. 9.16 Radial – airgap TF – PMSG with outer rotor (one phase (one coil) shown).

The configuration of this machine is illustrated in Fig. 9.16 with the 3D model (one period) and the 3D – FEM mesh in Fig. 9.17. The presence of additional anti-fringing PM are visible in Fig. 9.18 on rotor pole sides.

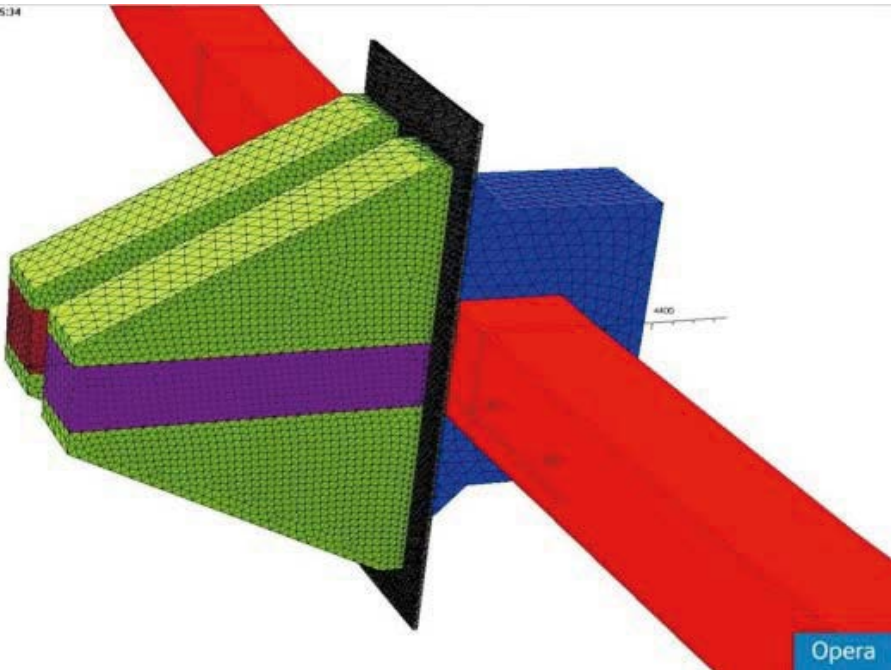
21/06/2010 20:58:57



Opera

a)

21/06/2010 22:05:34



Opera

b)

Fig. 9.17 3D model, a), and 3D – FEM mesh, b), (one period).

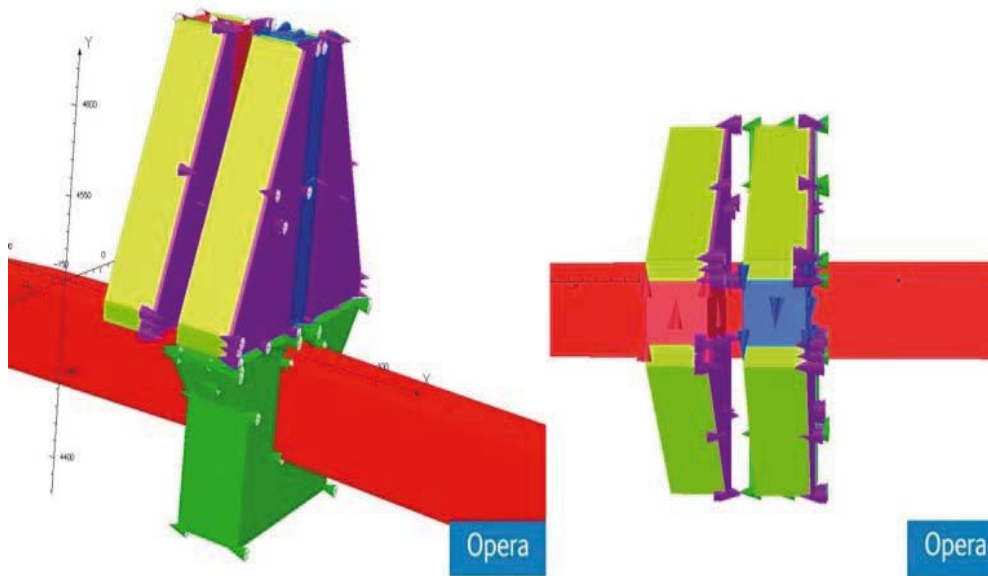


Fig. 9.18 Additional anti-fringing, PMs and main IPMs.

The torque of 1 phase (with sinusoidal current in phase with emf) in Fig. 9.19 shows a notable increase with 5 mm thick anti-fringing additional magnets.

Finally, the torque for two, three and six modules (phases) shows (Fig.9.20) fairly small torque pulsations with 6 phase while the about 5 MNm average torque is realized (only with 5 mm thick anti – fringing magnets).

A few data on the 3D FEM characterized preliminary design are:

- Outer stator diameter  $D_{es}=9$  m,  $j_{con}=6$  A/mm<sup>2</sup>
- Efficiency 9.96, power factor  $\cos\phi_1=9.843$
- Main PM radial length  $l_{PM}=150$  mm, axial thickness  $h_{PM}=30$  mm, core – stack – leg axial length;  $l_{stack}=81$  mm, stator slot area: 50x50 mm x mm;
- Rotor pole pitch (at airgap)  $\tau_{PM}=56$  mm, pole pairs:  $p_p=250$ , airgap  $g=5$  mm, active weight: about 60 tons.

It may be claimed that this configuration is worth considering further because of fabrication ease (even a few tens kV per phase, due to single coil/phase, which eliminate the local grid voltage matching transformer in on shore applications mainly).

Three other innovative wind generator systems are described in Ref. 6, but are not discussed here due to lack of space.

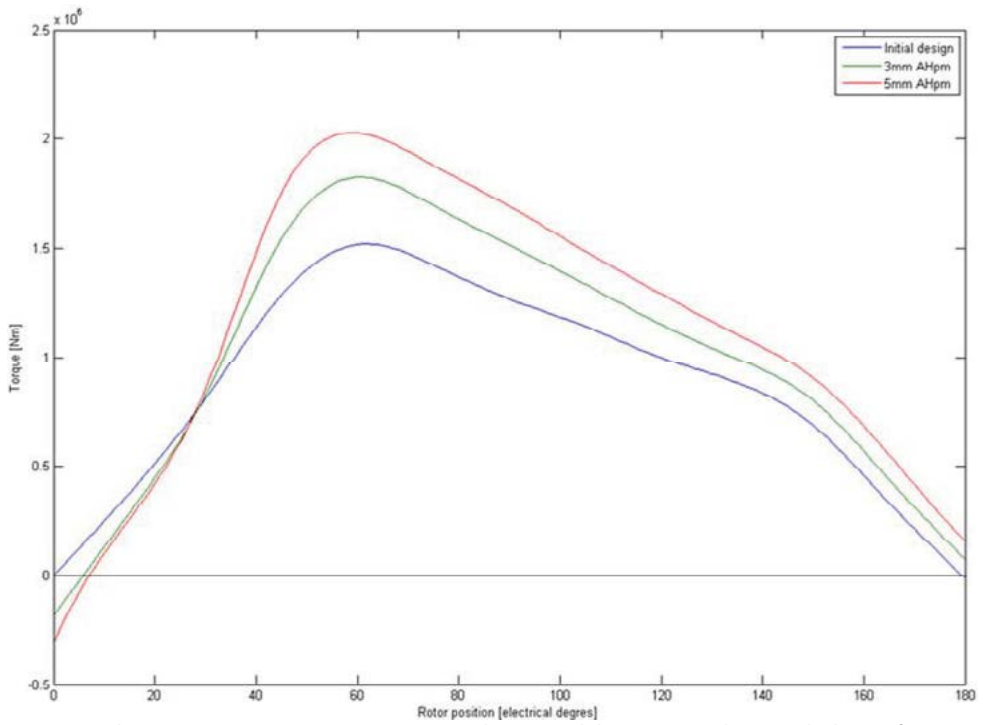


Fig. 9.19 1 Phase torque versus rotor position with sinusoidal current in phase with the emf.

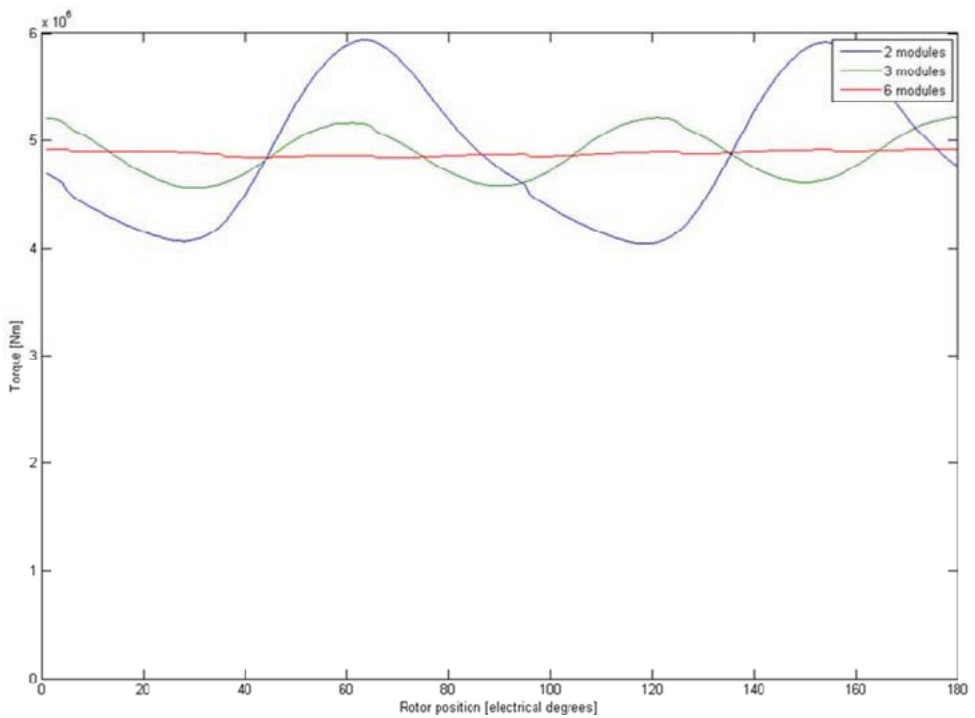


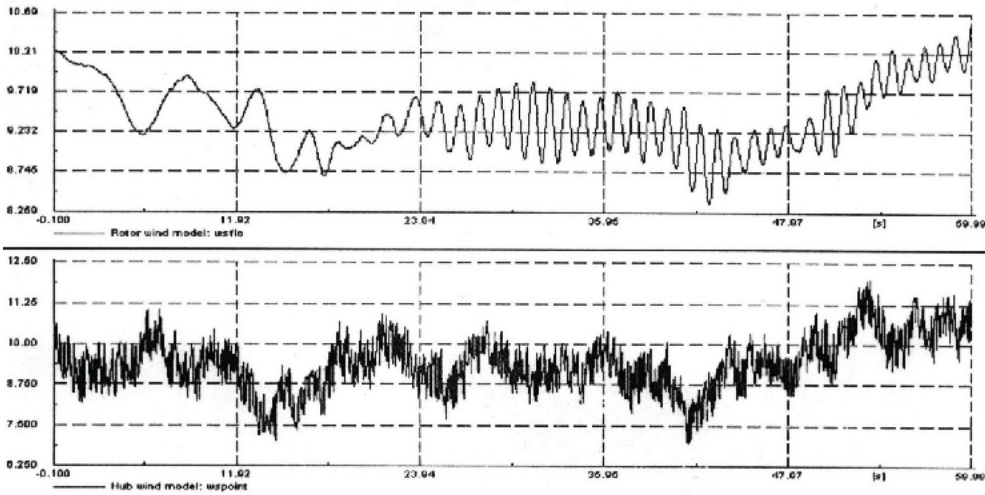
Fig. 9.20 Multiphase torque versus rotor position (2, 3, 6 phases).

### 9. 4 Direct CRIG connection to grid for wide energy conversion

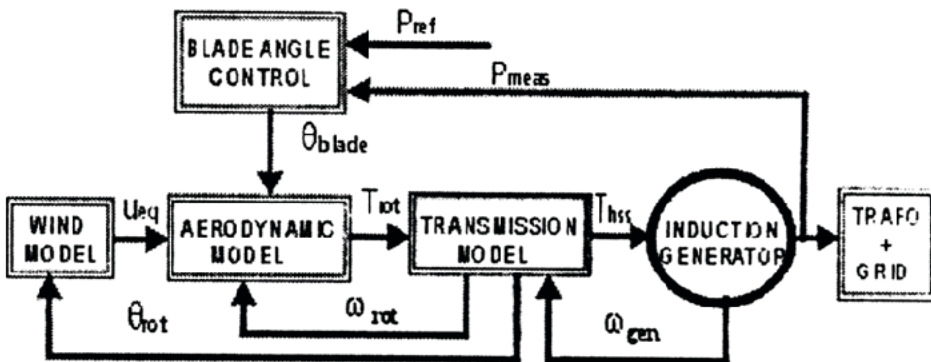
Some wind turbine cage rotor induction generators (CRIGs) are still connected to the grid without PWM variable frequency converters. However, to reduce transients (inrush) currents and powers a large resistance  $((40-50) \cdot R_s)$  is added to the stator and then it is short-circuited after the transients [1, 7].

The investigation of such a direct – connection is very useful to understand better CRIGs, later connected to grid through a dual full power PWM converter in the MW range [1, vol.2].

Typical small variations in wind speed and hub wind speed in m/s (Fig. 9.21a) indicate a moderate wind speed variation (typical to offshore sites). Larger speed variations (typical to on-shore sites) may lead the directly connected CRIG to the grid into instabilities.



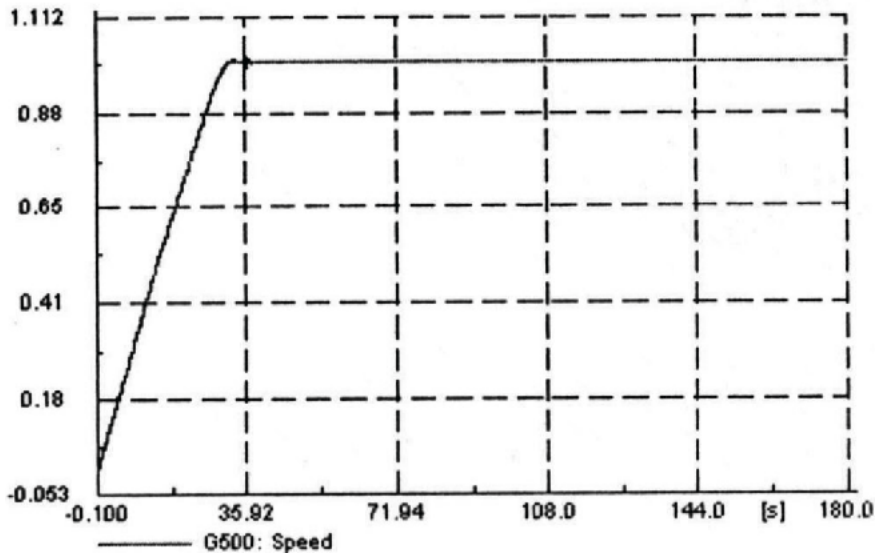
a)



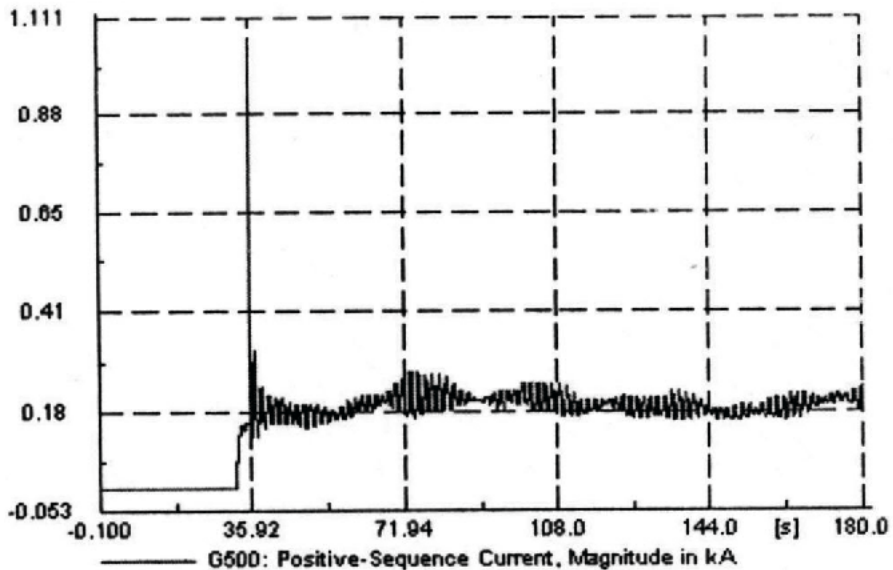
b)

Fig. 9.21 Rotor wind and hub wind speed model, a) and wind turbine – CRIG system, b).

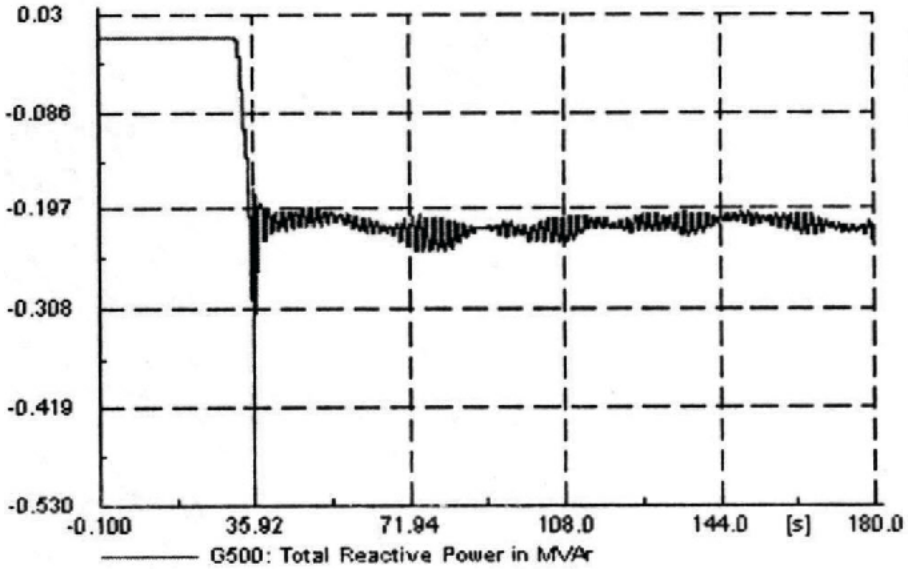
The complete system model (Fig. 9.21b) is required to investigate its operation to power grid. Such a model was built [7]. Sample results for the start – up of 4 pole, 50 Hz, 9.5 MW CRIG (Fig.9.21 (in p.u.)).



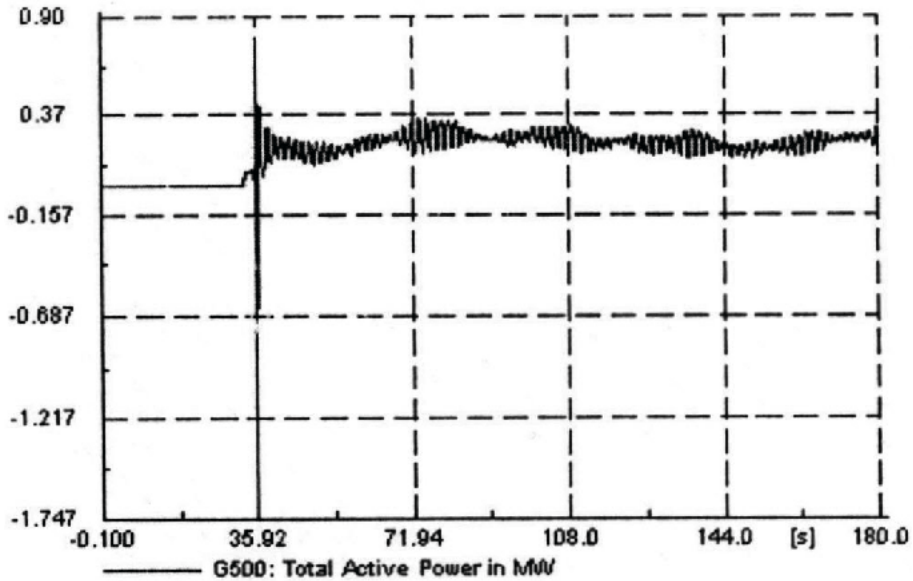
a)



b)



c)



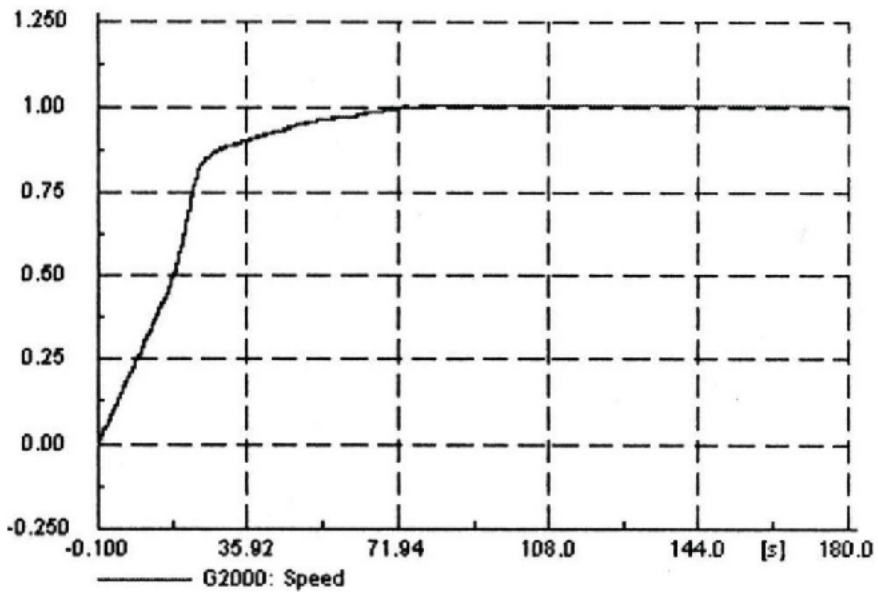
d)

Fig. 9.22 CRIG direct connection to the power grid (4 poles, 50 Hz, 9.65 MW), a) generator speed, b) positive sequence current in kA, c) reactive power (MVAR), d) active power (MW).

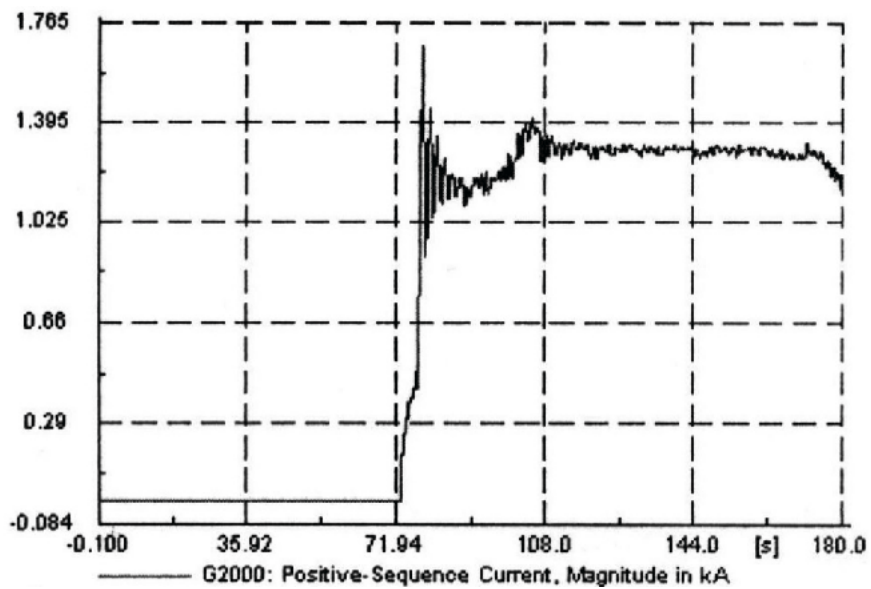
Some of the small oscillations in Fig. 9.22 are due to the transmission model, but the transients are smooth. The problem is the rush – in (transient) current. This is done by a



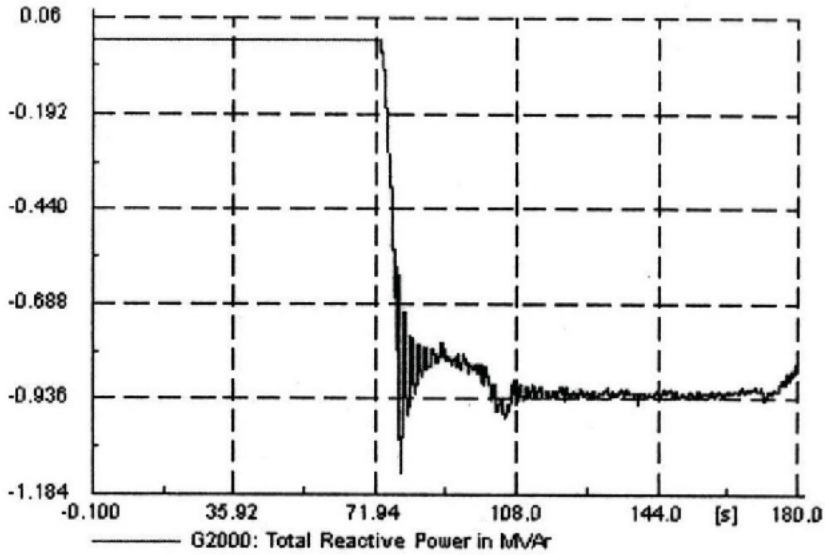
soft starter, for example. For a 4 pole 50 Hz 2 MVA selfexcited (with terminal capacitor), the results in Fig. 9.23.



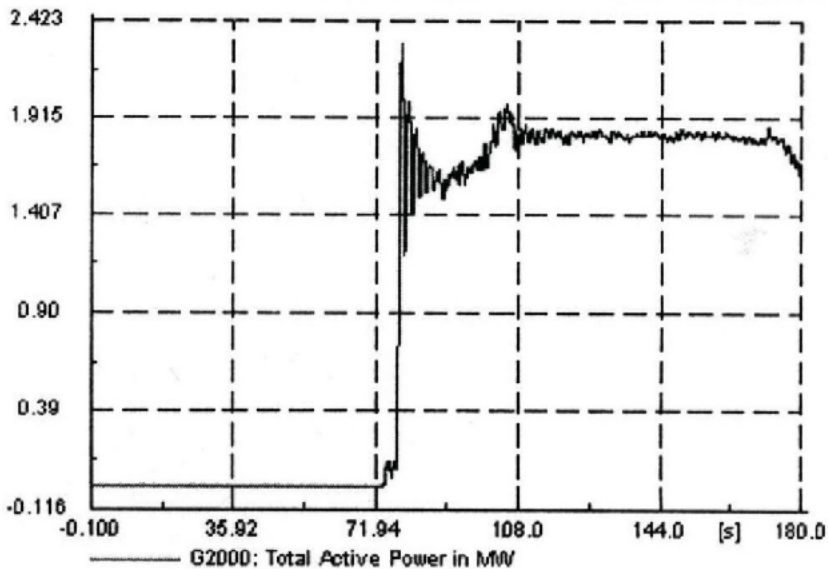
a)



b)



c)



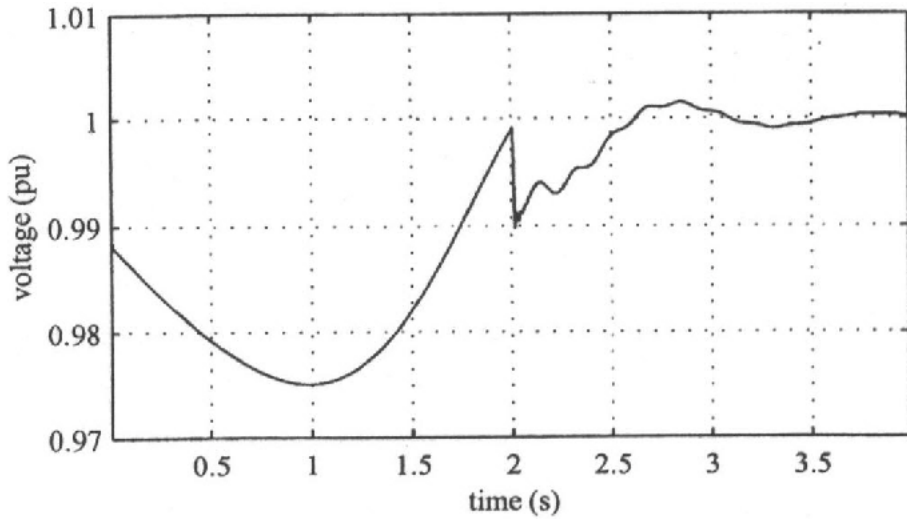
d)

Fig. 9.23 CRIG start-up and grid connection (4 pole, 50 Hz, self-excited 2 MVA) a) speed (p.u.), b) positive sequence current (kA), c) total reactive power (MVAR), d) total active power (MW).

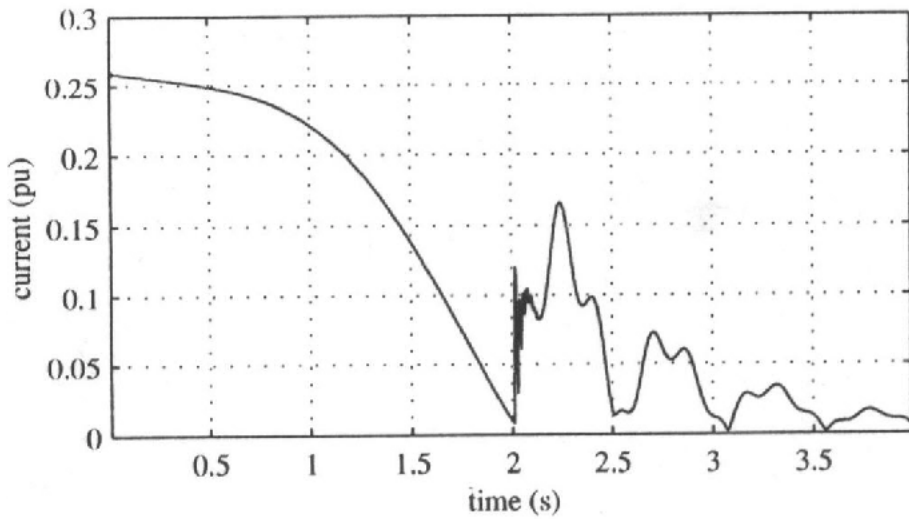
The high inertia provides for safe „synchronization” but the rush – in current is still large with the soft starter.

Ultimately, there is an additional 3 phase resistance in series with the stator. Results in Fig. 9.24 [14] show that the external resistor solution performs well in terms of:

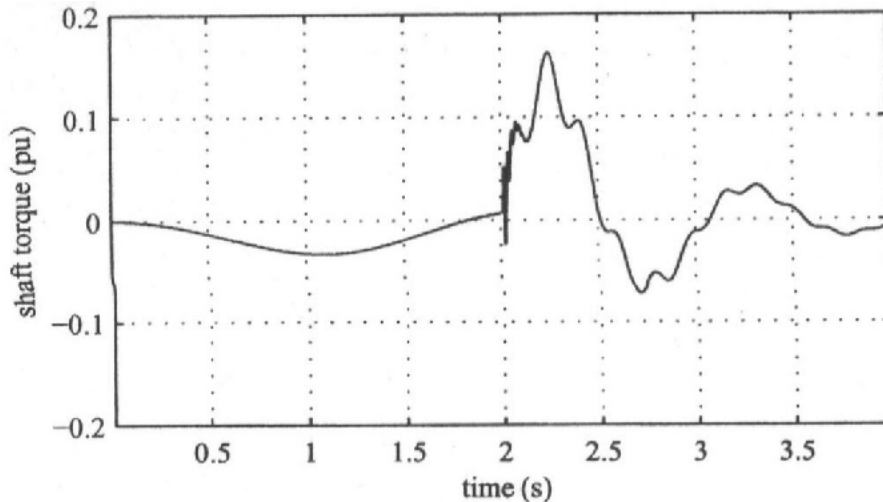
- Maximum voltage change factor in the grid
- Maximum current factor
- Flicker step factor



a)



b)



c)

Fig. 9.24 Grid voltage, a), current, b), and shaft torque, c) for resistor connection to the grid of a 15 kW, 9.8% slip IG with active stall wind turbine regulation, at no load [15].

In addition, the current and voltage harmonics infliction on the grid is minimal for the resistor connector (which has to be designed considering both the connection and the shortcircuiting current transients imposed limits).

## 9.5 Wound-rotor (doubly fed) induction generator control

Two significant issues with wound – rotor induction generators (WRIGs) which represent about 50% of all wind generator commercial power, are treated here as important:

- \* Complete system (with turbine active stall and pitch control) transmission, digital simulation methodology (and code) [8];
- \* Encoder-less WRIG dual PWM converter control with voltage sags [9]

### 9.5.1 WRIG variable speed control with pitch and active stall blades regulation.

In pitch control turbines when the output power – check a few times per second – is too large a signal trigger the servomechanism that turns (pitches) the rotor blades slightly out of the wind. The pitch refined mechanism (in normal operation the blades pitch a fraction of a degree at a time) is rather complex but provides best available mechanical power – electric power balance when the wind speed varies.

In case of wind gusts it rotates the blades parallel to the wind: “flag to the wind” for protection.

In passive stall controlled wind turbine there is no servomechanism to pitch the blades, but a design and flexibility they adapt to speed gusts (by creating turbulence), though at smaller power than with pitch control.

Finally active stall controlled turbines are somewhat similar to pitch controlled ones, but at overload the turbine will pitch in the opposite direction to pitch control. They increase the increase of the angle of attach of blades to send them into deeper stall, thus wasting faster the excess wind energy. Finally, they place the turbine as “wall to the wind”. The turbine may thus be run at rated power at all allowed high wind speeds (Fig. 9.25).

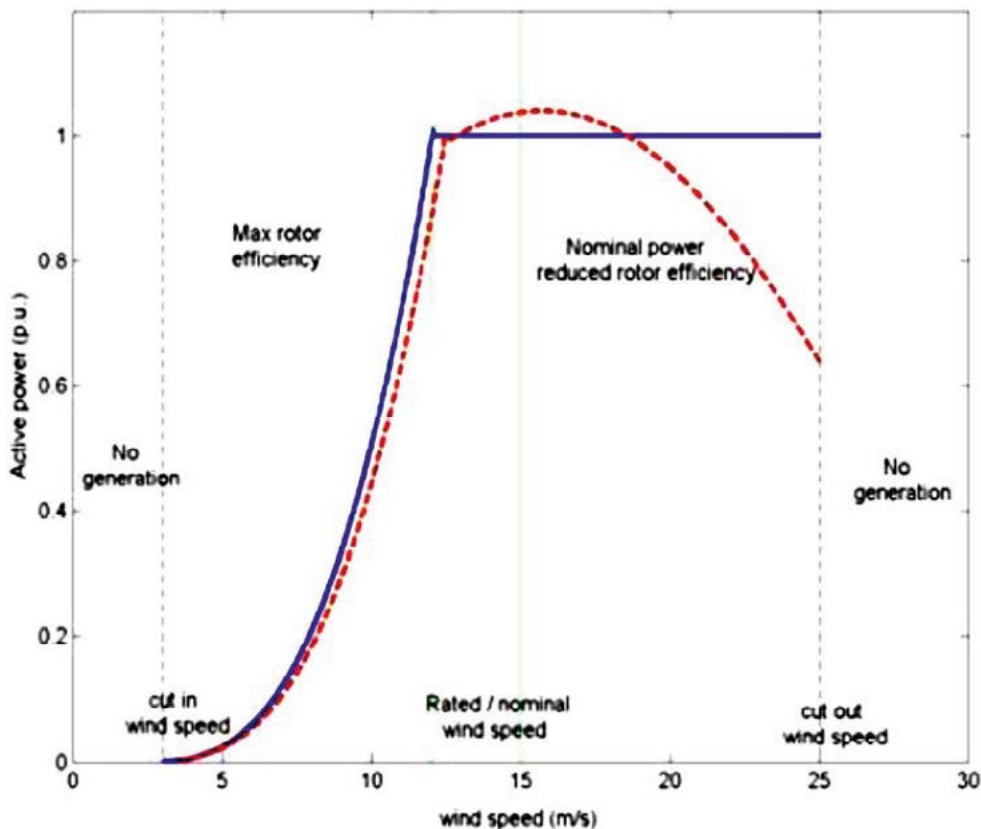


Fig. 9.25 Typical power versus windspeed with stall (dashed line) and with pitch control (solid line).

WRIG control system (Fig. 9.26) shows both the blade angle (turbine) control and the WRIG control via the dual PWM converter with rotor position feedback.

Typical passive and active stall control for given wind speed window (Fig. 9.27) illustrates both the lower power pulsations and the lower power. The incremental blade (pitch) angle is also visible in Fig. 9.26, for active stall.

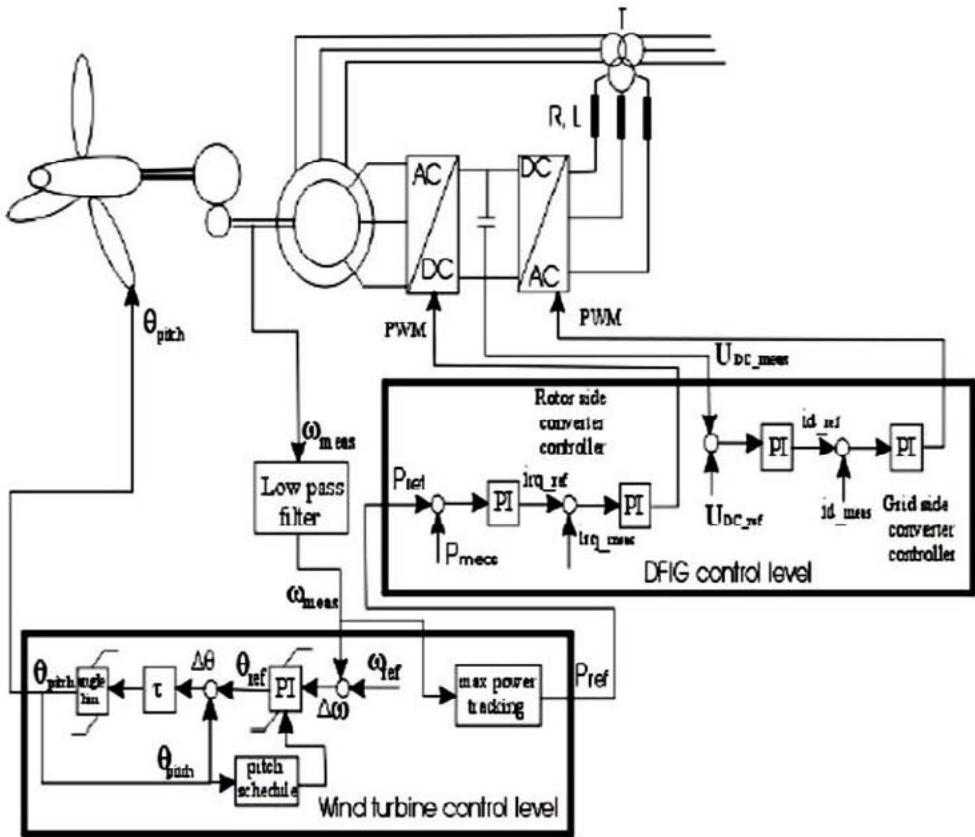
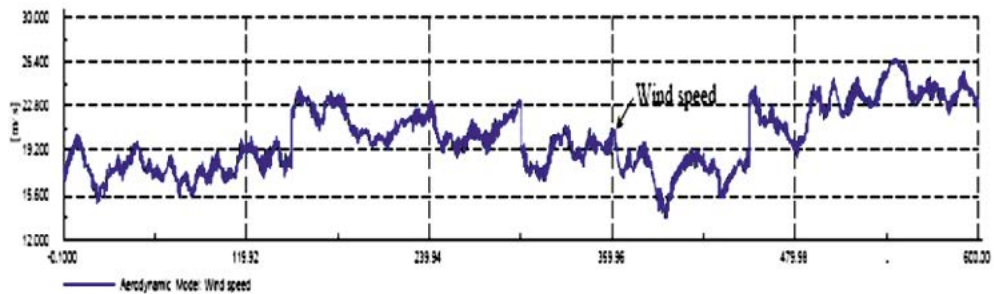


Fig. 9.26 WRIG control system.

“Pitch” control and respectively “active stall” control of a 2 MW WRIG was simulated [8] and the main results are shown in Fig. 9.27.



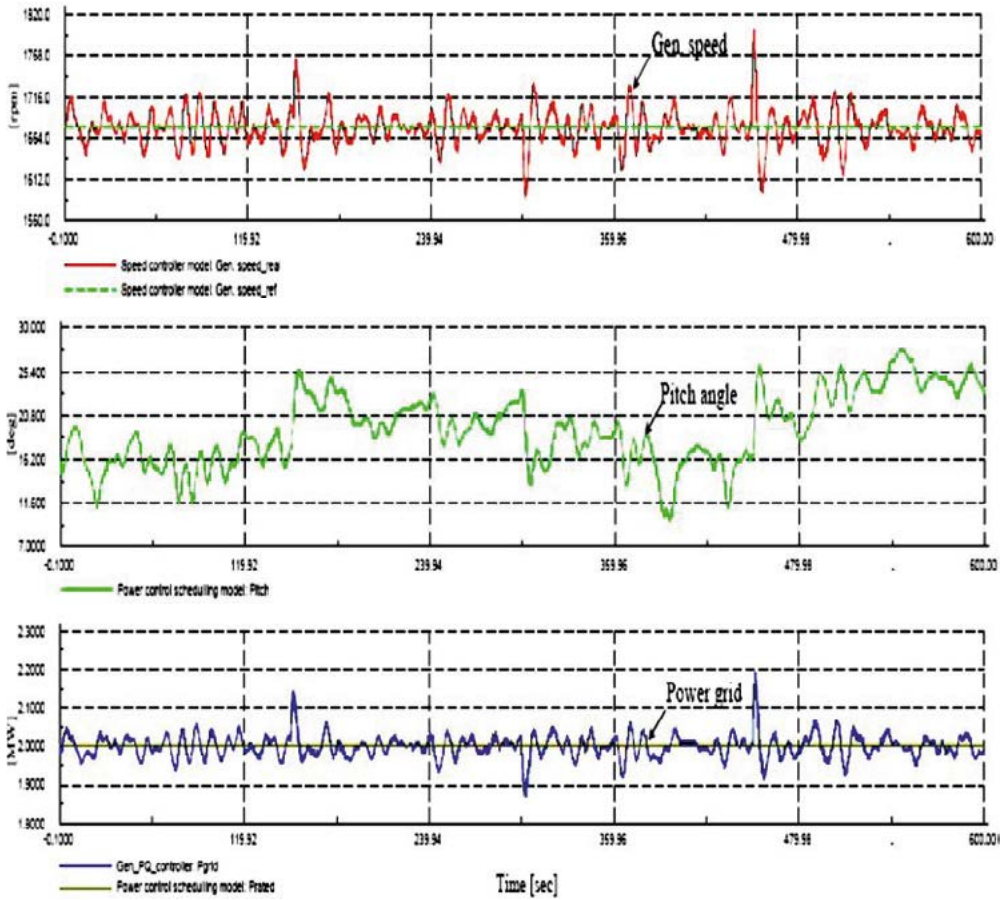


Fig. 9.27 2 MW WRIG with pitch and variable speed control: wind speed, generator speed pitch angle, active power in MW.

It is evident that pitch control is instrumental in normal operation – with inevitable speed variations – in reducing the output electric power pulsations. Most modern MW range today is wind turbine use pitch control despite of added complexity (and cost) in most implementations.

### 9.5.2 Encoderless vector control of WRIG

The space vector voltage equations of WRIG in general coordinates  $\omega_b$  are:

$$\begin{aligned}
 \bar{i}_s R_s + \bar{V}_s &= -\frac{d\bar{\Psi}_s}{dt} - j\omega_b \bar{\Psi}_s; \bar{\Psi}_s = L_{se} \bar{i}_s + L_m \bar{i}_m; \bar{i}_m = \bar{i}_s + \bar{i}_r \\
 \bar{i}_r R_r + \bar{V}_r &= -\frac{d\bar{\Psi}_r}{dt} - j(\omega_b - \omega_r) \bar{\Psi}_r; \bar{\Psi}_r = L_{re} \bar{i}_r + L_m \bar{i}_m \\
 \bar{V}_s &= V_d + jV_q; \bar{V}_r = V_{dr} + jV_{qr}
 \end{aligned} \tag{9.4}$$

Aligning axis d (in rotor coordinates:  $\omega_b = \omega_r$ ) to the stator flux vector  $\overline{\Psi}_s$  yields:

$$\overline{\Psi}_s = \Psi_s = \Psi_d; \Psi_q = 0; \frac{d\Psi_q}{dt} = 0 \quad (9.5)$$

with  $\Psi_s \sim \text{constant}$ / constant stator voltage and frequency and  $R_s = 0$ :

$$\begin{aligned} V_d &= 0; \Psi_q = L_s i_q + L_m i_{qr} = 0 \\ V_q &= -\omega_r \Psi_d; \Psi_d = L_s i_d + L_m i_{dr} \end{aligned} \quad (9.6)$$

So the active and reactive stator powers  $P_s$  and  $Q_s$  are:

$$\begin{aligned} P_s &= \frac{3}{2} (V_d i_d + V_q i_q) \approx \frac{3}{2} \omega_1 \Psi_d \frac{L_m}{L_s} i_{qr} \\ Q_s &= \frac{3}{2} (V_q i_d - V_d i_q) = \frac{3}{2} \omega_1 \frac{\Psi_d}{L_s} (\Psi_d - L_m i_{dr}) \end{aligned} \quad (9.7)$$

Equations (9.7) envisage that to modify  $P_s$  we need to modify  $i_{qr}$  and to change  $Q_s$  we have to change  $i_{dr}$  for rather constant stator flux  $\Psi_s$ .

This is the essence of vector control of the voltage source rotor side PWM converter (Fig. 9.28).

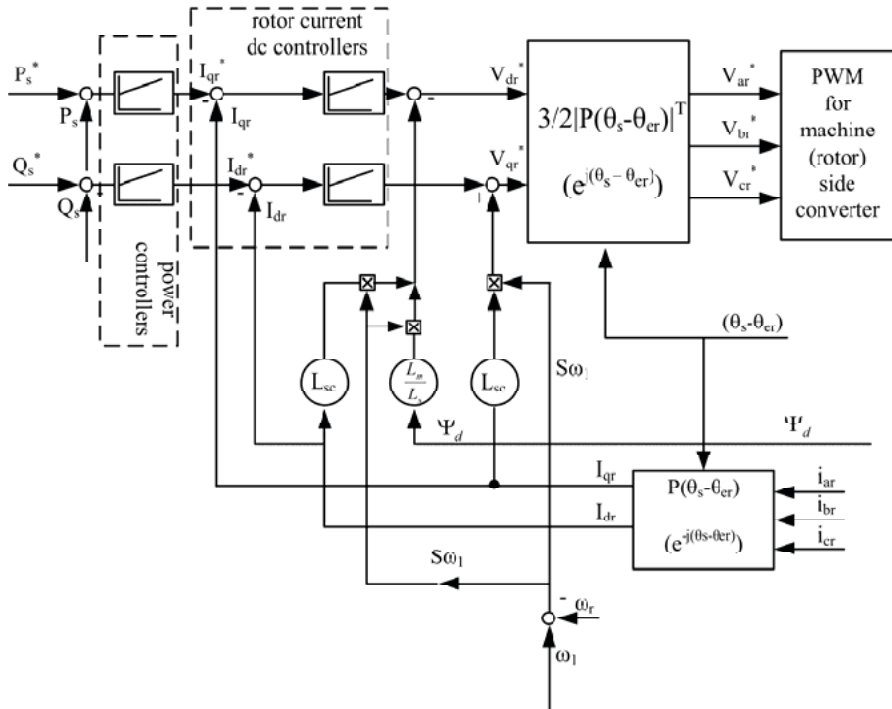


Fig. 9.28  $P_s$  and  $Q_s$  vector control of WRIG – side converter.



It is obvious in Fig. 9.27 that the rotor position  $\theta_{er}$  and the rotor speed  $\omega_r$  should either be measured or, in the case here, estimated as in an encoderless drive.

Also the stator flux  $\bar{\Psi}_s$  should be estimated as it used to compensate the motion induced emfs that make the  $i_d, i_q$  regulator's job easier.

$$\bar{\Psi}_s = \bar{\Psi}_{s0} - \int (\bar{V}_s + R_s \bar{i}_s) dt \quad (9.8)$$

A first order delay may replace the integrator to reduce the offset, but two stator voltages and currents should be measured.

With  $\theta_s$  the stator flux vector angle the  $\alpha\beta$  components of magnetization current in stator coordinates is:

$$\begin{aligned} i_{ms\alpha} &= I_m \cos \theta_s \\ i_{ms\beta} &= I_m \sin \theta_s \end{aligned} \quad (9.9)$$

Then, also in stator coordinates, the rotor current  $\alpha\beta$  components  $i_{r\alpha}, i_{r\beta}$  are:

$$\begin{aligned} i_{r\alpha} &= \left( I_{ms\alpha} - I_{s\alpha} \right) \frac{L_s}{L_m}; i_{s\alpha} = i_a; i_{r\alpha} = i_r \cos \delta_{1a}; i_{r\beta} = i_r \sin \delta_{1a} \\ i_{r\beta} &= \left( I_{ms\beta} - I_{s\beta} \right) \frac{L_s}{L_m}; i_{s\beta} = \frac{1}{\sqrt{3}} (2i_b + i_a) \end{aligned} \quad (9.10)$$

But the rotor currents are measured in rotor coordinates,  $i_{ra}, i_{rb}$ :

$$\cos \delta_2 = \frac{i_{ra}}{i_r}; \sin \delta_2 = \frac{i_{rb}}{i_r}; i_{ra} = i_{ar}; i_{rb} = \frac{1}{\sqrt{3}} (2i_{br} + i_{ar}) \quad (9.11)$$

Finally  $\hat{\theta}_{er} = \delta_1 - \delta_2$ :

$$\sin \hat{\theta}_{er} = \frac{i_{r\beta} i_{ra} - i_{ra} i_{r\alpha}}{i_r^2}; \cos \hat{\theta}_{er} = \frac{i_{ra} i_{ra} + i_{r\beta} i_{r\beta}}{i_r^2} \quad (9.12)$$

Knowing  $\sin \hat{\theta}_{er}$  and  $\cos \hat{\theta}_{er}$  the rotor speed may be estimated:

$$\frac{d\hat{\theta}_{er}}{dt} = \hat{\omega}_r = -\sin \hat{\theta}_{er} \frac{d}{dt} (\cos \hat{\theta}_{er}) + \cos \hat{\theta}_{er} \frac{d}{dt} (\sin \hat{\theta}_{er}) \quad (9.13)$$

To account for magnetic saturation, the assigned initial value of magnetization current amplitude is updated after every computation cycle:



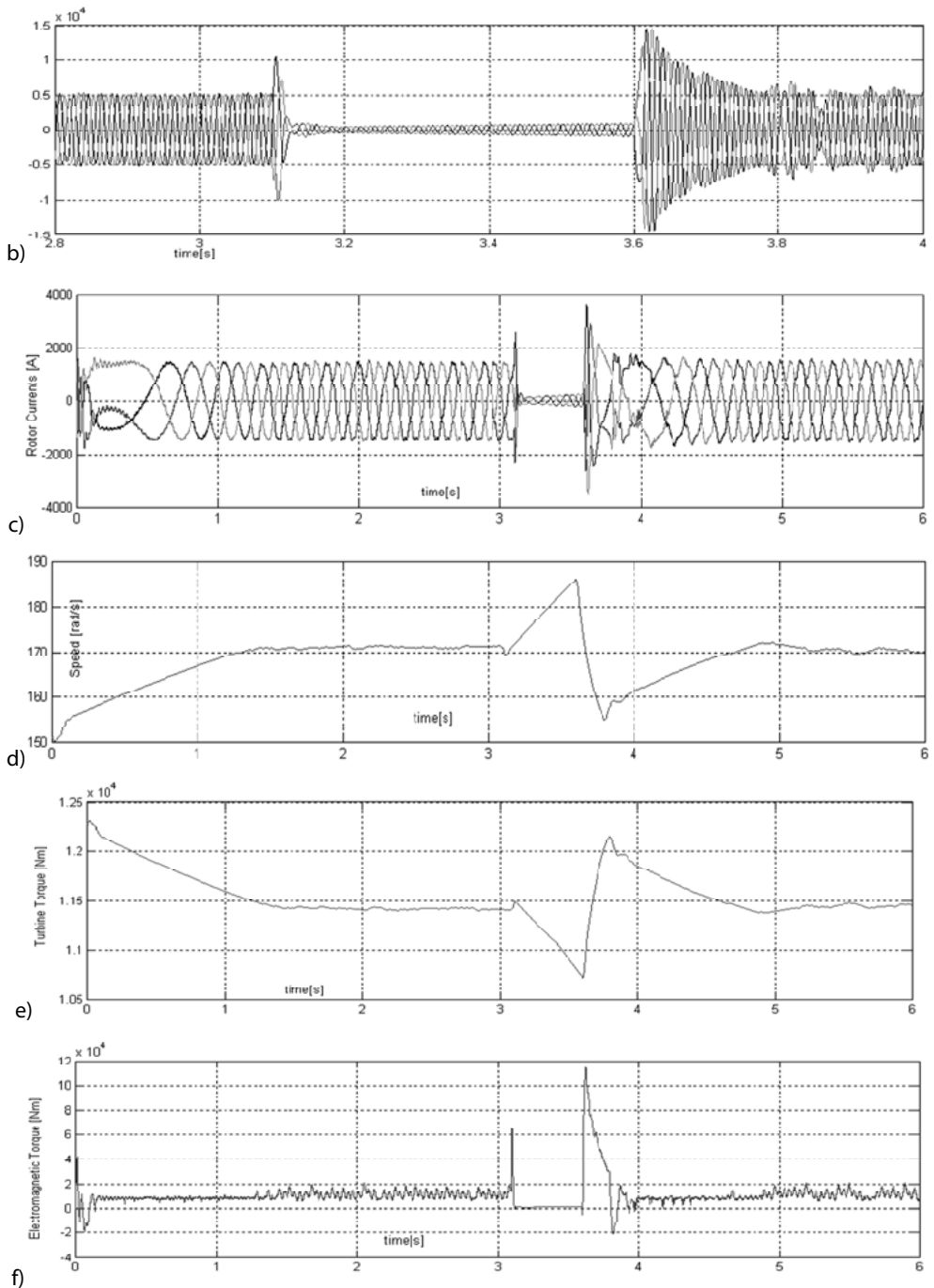


Fig. 9.30 2 MW WRIG transients under partial sudden shortcircuit: a) stator voltage, b) stator currents, c) rotor currents, d) generator speed, e) turbine torque, f) electromagnetic torque.

The sudden partial shortcircuit ( $V_s \neq 0$ ) transient starts at  $t=3.1$ s and is cleared at  $t=3.6$  s. The system shows limited stator and rotor current spikes both at the beginning and at the end of the symmetric fault. The rotor current references, during such a voltage sag, may be limited to say 150% rated value that is safe for the rotor side converter. The rotor position and speed worked satisfactorily in laboratory tests at a smaller scale, too.

## 9.6 Comprehensive encoderless PMSG control system [10].

PMSG with full power dual PWM converter especially in direct drives or with moderate ratio transmission (500 rpm in the multi MW range) are increasingly more used in wind energy conversion because of their superior efficiency (and energy yield) at moderate weight. As the price of high energy magnets will most likely remain high, PMSG will probably be used for full ratio transmission multi-megawatt units (above 1500 rpm) since the PM weight/kW is notably further reduced.

Besides PMSG optimal design—approached in a previous paragraph, an advanced encoderless vector control system of the latter is described here. It does the following:

- \* It performs grid connection and disconnection (standalone) automatic transients
- \* It uses a rotor position and speed observer which works both for grid and standalone operation modes
- \* It may handle asymmetric grid voltage sags, using a ballast load
- \* It filters the output a.c. voltage to reduce time harmonics in the power grid

Such a control system is illustrated in Fig. 9.31 for the test platform used in the investigation [10].

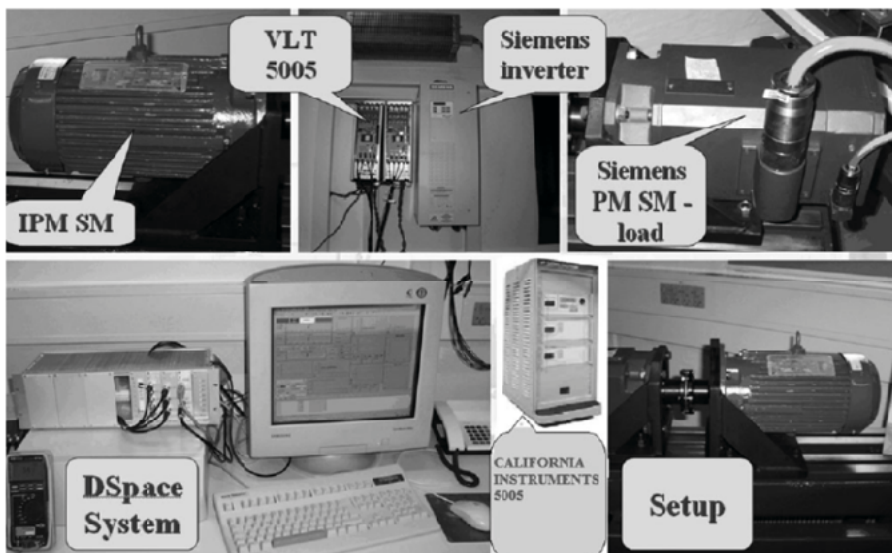


Fig. 9.31 The PMSG testing platform.

Due to its inherent complexity hereby the control system components will be treated one by one. Further on, sample results will be used to illustrate its operation.

### 9.6.1 Grid – side converter control

The grid – side PWM converter control system is depicted in Fig. 9.32.

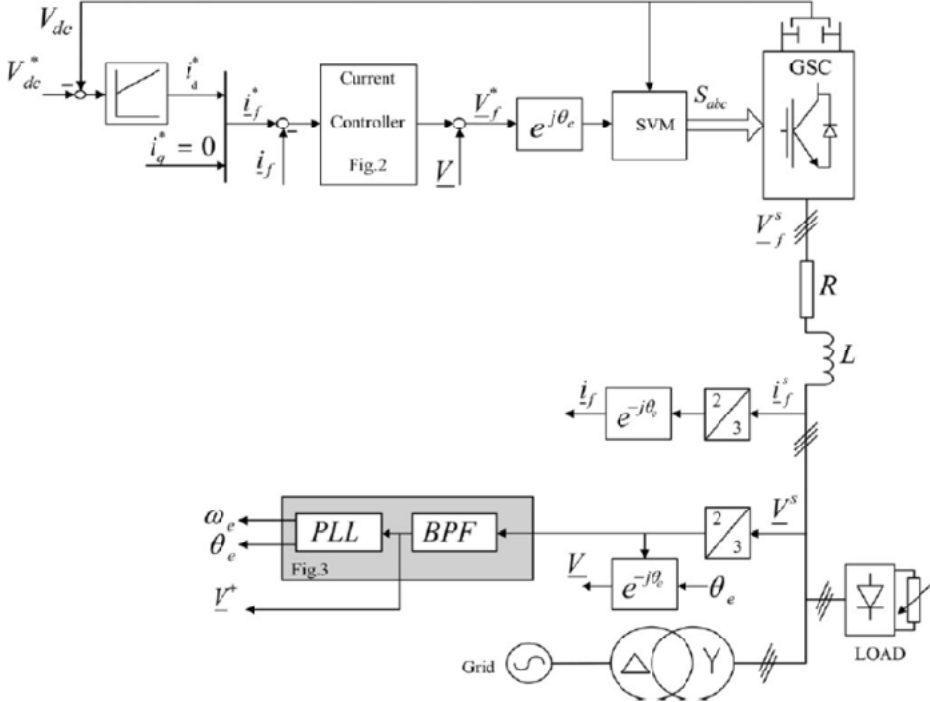


Fig. 9.32 Grid – side PWM inverter control system.

Its main parts are: the PI d.c. link, PI regulator, PI current controllers, band pass filter (BPS) based on D-module filter to extract the positive sequence voltage  $\underline{V}^+$  and the PLL observer for voltage positive sequence and  $\theta_e$ .

The PI d.c. voltage regulator outputs the  $i_d^*$  reference and with  $i_q^* = 0$  (unity power factor at the grid).

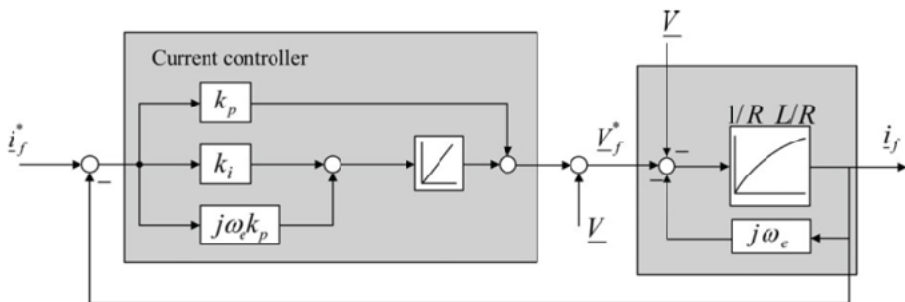


Fig. 9.33 Current  $i_f$  control in synchronous ( $\omega_e$ ) grid voltage reference frame.

The d.c. voltage PI regulator coefficients,  $k_{p\_Vdc}=9.02 \text{ A/V}$ ,  $k_{i\_Vdc}=5 \text{ sec}^{-1}$ , are turned to slow down the  $V_{dc}$  control to avoid interference with current loops. The  $i_f$  current orthogonal loops (Fig. 9.33) provides pole – zero cancellation of the plant by PI controller with cross – coupling cancellation and with feedforward disturbance compensation.

Line voltage positive sequence is identified through a BPF with D module filter [10] in stator coordinates  $\underline{V}^{+s}$  and then a PLL observer yield the positive sequence voltage vector angle  $\theta_e$  and speed  $\omega_e$  [10].

### 9. 6. 2 Standalone PMSG control with harmonic and negative voltage sequence cancellation under nonlinear load.

In standalone operation of PMSG the reduction of harmonics pollution (and additional losses) under nonlinear (say diode rectified) loads which avoids also resonances, interference is paramount. To handle such a challenge, the voltage control is handling distinctly the fundamental and the harmonics (by injecting opposite phase voltage harmonics in the nonlinear load), Fig. 9.34 [10].

The generic scheme (Fig.9.34a) refers to the load (former grid) side converter. Since the negative sequence voltage compensation implies a frequency shift of  $-\omega_{sa}$  voltage, harmonics orders  $k=6n\pm 1$  become  $k=6n$ . P.R. – proportional – resonant type controllers are used for voltage harmonics cancelation.

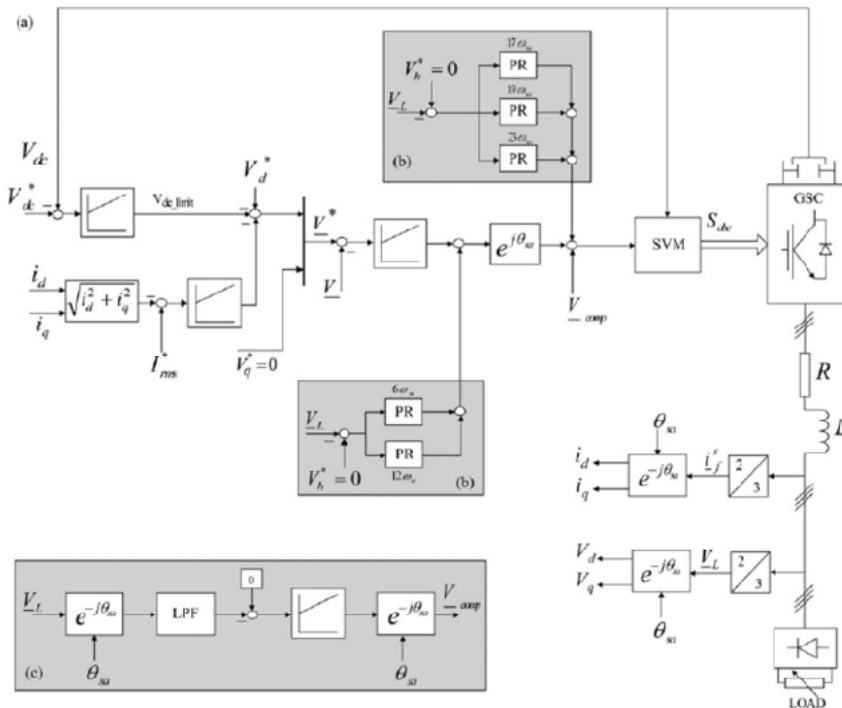


Fig. 9.34 Standalone control with inverse and harmonics voltage compensation: a) generic scheme, b) harmonic voltage compensator, c) negative sequence voltage compensator.

### 9. 6. 3 Smooth transfer from standalone to grid control (and back).

Protection from large voltage and current transients when grid voltage sags occur and when the transfer from grid to standalone operation is required constitutes a formidable challenge in PMSG control.

Figs. 9.35 present the control algorithms put forward [10] for standalone to grid and back transferred.

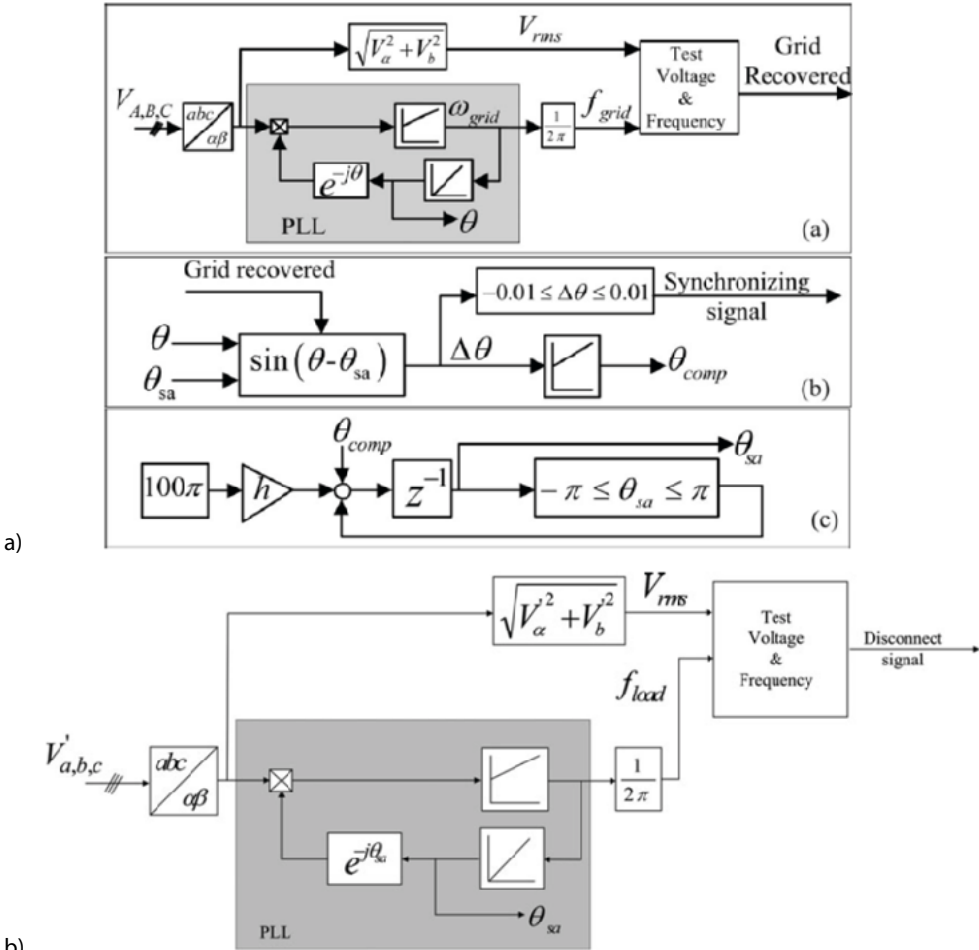


Fig. 9.35 Transfer algorithms: a) from standalone to grid control, b) from grid control to standalone control [10].

When the grid voltage recovers (in amplitude and frequency) a synchronizing signal is generated to match the grid side inverter output to grid voltage phase. The online estimation of phase angle of standalone voltage remains in place even after synchronization to avoid load current interruption in future transfers from grid to standalone nodes (Fig. 9.21a).





The rotor position and speed observer (Fig. 9.36b) has two operation modes:

- \* At start-up and low speed when the position is “activated” from the no load voltage with a PLL.
- \* At load.

The above control system is illustrated here by test results on a laboratory platform with a 12 Nm PMSG with two back to back Danfoss PWM converter and a Simovert Master drive.

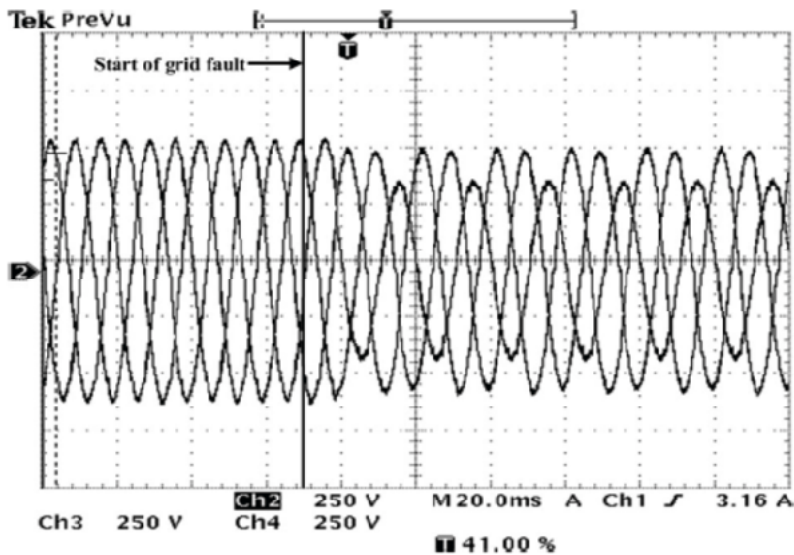
The power grid is replaced by a programmable three phase a.c. source (California instruments, 5005).

A resistive nonlinear load is always connected to the a.c. power source, because the latter is not capable to receive energy.

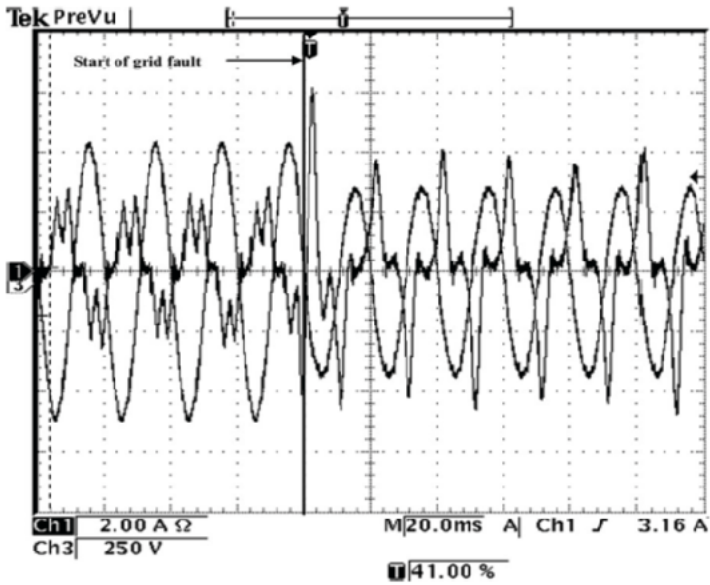
### 9. 6. 5 A single phase voltage sag

From 5.2 s to 5.7 s the a.c. power source is programmed on the primary of the transformer.

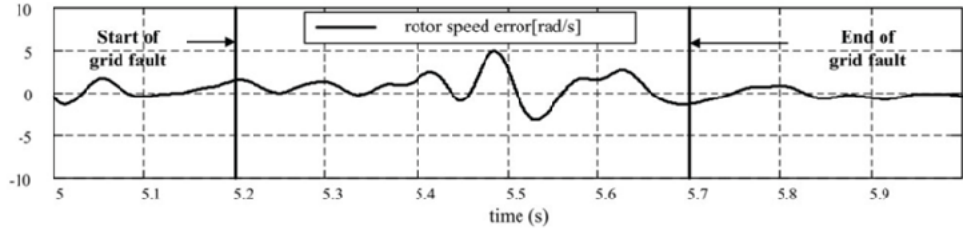
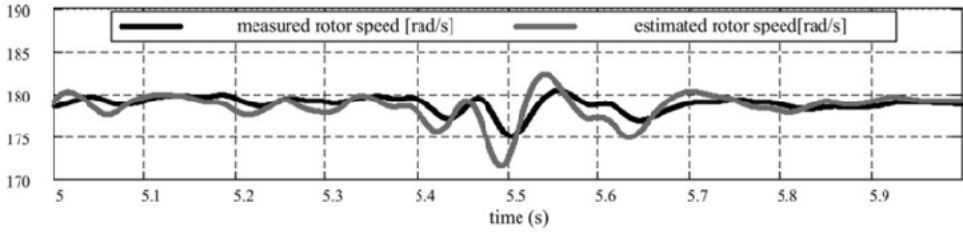
Grid voltages are illustrated in Fig. 9.37a, with phase voltage on Fig. 9.37b and estimated speed in Fig. 9.37c, with generator currents in Fig. 9.37d.



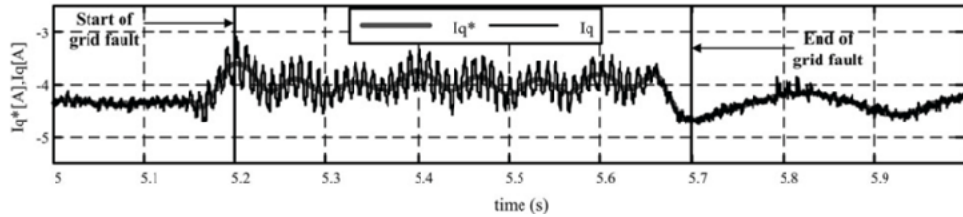
a)



b)



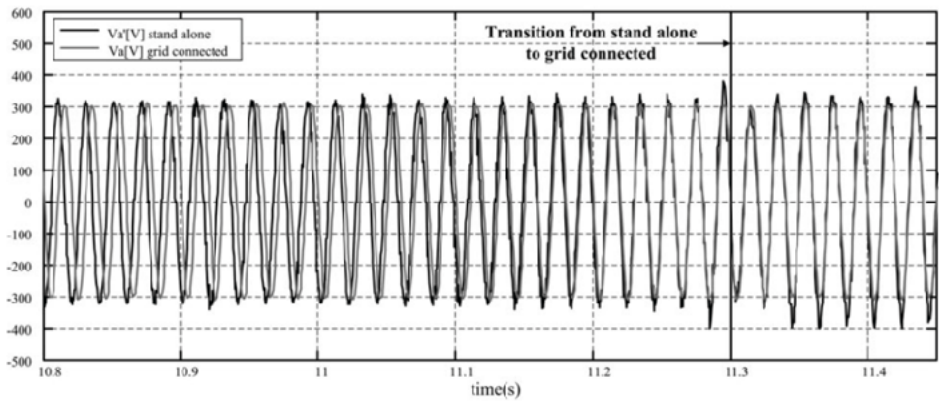
c)



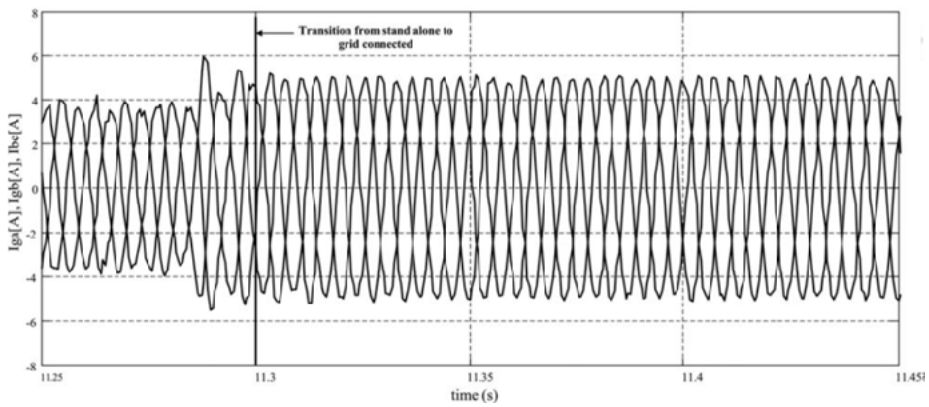
d)

Fig. 9.37 Single phase voltage sag transients: a) transformer secondary voltages, b) voltage and current, c) estimated speed and error, d) generator currents.

Standalone to grid transition transients are illustrated in Fig. 9.38, [10].

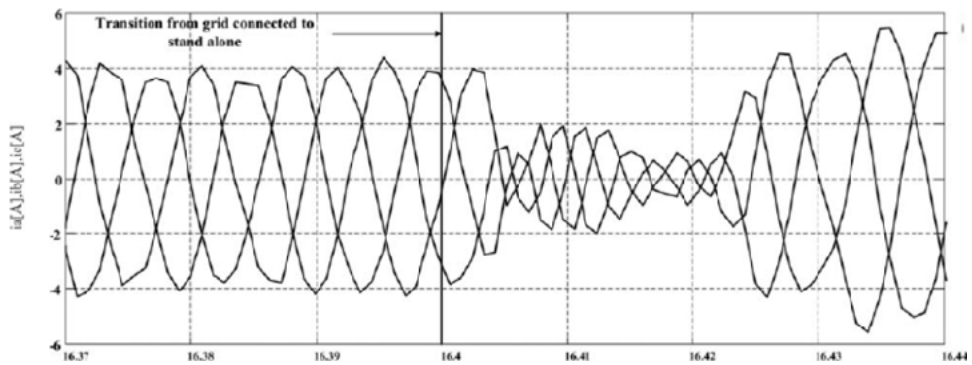


a)

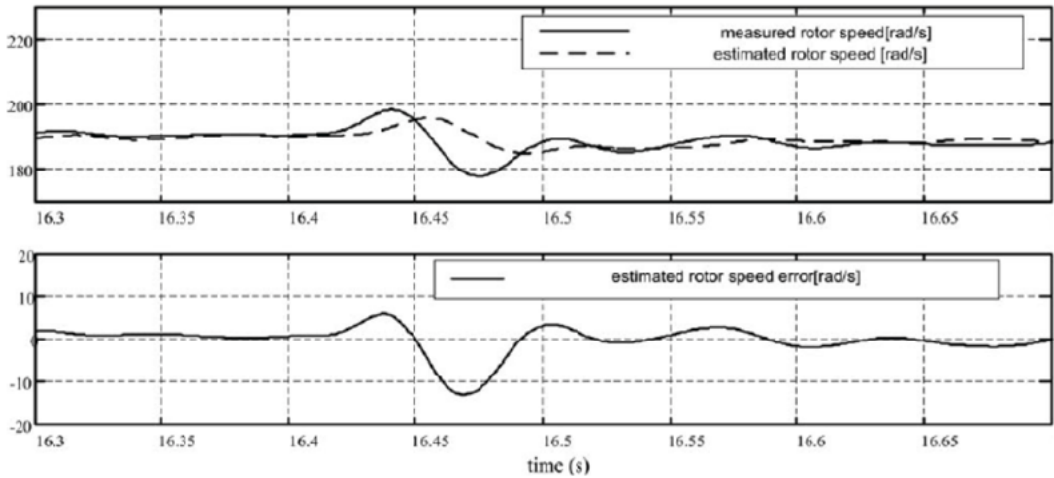


b)

Fig. 9.38 Load voltages, (a) and PMSG currents, (b), and the grid to standalone transition in Fig. 9.39 a, b.



a)



b)

Fig. 9.39 Grid to standalone transition: a) PMSG currents, b) estimated rotor speed and error.

Smooth transients with a reliable estimated speed are visible in the sample test results in Figs. 9.36 - 9.38.

### Conclusion

This chapter discussed in notable detail a few selected contributions in MW range generators for renewable energy: optimal design of d.c. excited SGs and PMSGs, advanced control of CRIGs, DFIGs and PMSGs.

## 9. 7 References

- [1] Boldea, "Electric actuators Handbook" (vol. 1: Synchronous Generators and vol2: Variable speed generators), 2<sup>nd</sup> edition, CRC Press Taylor & Francis, New York, 2016.
- [2] L. N. Tutelea, S. I. Deaconu, I. Boldea, "Classical dc excited synchronous generators for high power direct drive wind turbines: optimal design with FEM validation", *Record of IEEE – EPE – ECCE Europe*, 2015 (IEEEXplore).
- [3] F. Blaabjerg, D. M. Ionel, "Renewable energy devices and systems with simulations in MATLAB and ANSYS", book, Chapter 9 (by Ion G. Boldea, L. N. Tutelea, V. Rallabandi, D. M. Ionel, and F. Blaabjerg), CRC Press Taylor & Francis, New York, 2017.
- [4] Boldea, L. N. Tutelea, F. Blaabjerg, "High power wind generator designs with less or no PMs: an overview", *Record of IEEE – ICEMS*, 2014, China (IEEEXplore).
- [5] Boldea, L. N. Tutelea, A. Popa, "The axial airgap transverse flux PM generator optimal design with FEM validation", *Record of IEEE-ICEM*, 2017, China (IEEEXplore).
- [6] C. Rauti-Bratiloveanu, D.T.C. Anghelus, I. Boldea, "A comparative study investigation of three PM – less MW power range wind generator topologies", *Record of OPTIM -2012* (IEEEXplore)
- [7] L. Mihet-Popa, F. Blaabjerg, I. Boldea, "Wind turbine generator modeling and simulation where rotational speed is the controlled variable", *IEEE Trans.*, vol. IA – 40, no. 1, 2004, pp. 3-19.

- [8] L. Mihet-Popa, I. Boldea, "Dynamics of control strategies for wind turbine applications", *Record of OPTIM* – 2006 (IEEEExplore).
- [9] Serban, F. Blaabjerg, I. Boldea, "A study of double fed wind power generator under power system faults", *Record of EPE – 2003*, Toulouse, France (IEEEExplore).
- [10] M. Fatu, F. Blaabjerg, I. Boldea, "Grid to standalone transition motion–sensorless dual inverter control of PMSG with asymmetrical grid voltage sags and harmonics filtering", *IEEE Trans.*, vol. PE – 29, no. 7, 2014, pp. 3463-3472.
- [11] Fatemi, D.M. Ionel, N.A.O. Demerdash, T.W. Nehl "Fast multi-objective CMODE-type optimization of electric machines for multicore desktop computers", *Record of IEEE-ECCE, 2015*, pp. 5593 – 5600, (IEEEExplore).
- [12] Boldea, L. N. Tutelea, "Reluctance electric machines design and control", book, CRC Press, Florida, Taylor and Francis, New York, 2018, Ch. 12.
- [13] L. Strete, L. N. Tutelea, I. Boldea, C. Martis, I.A. Viorel, "Optimal design of a rotating transverse flux motor (TFM) with permanent magnets in rotor", *Record of ICEM, 2010*, Rome, Italy, (IEEEExplore).
- [14] T. Thiringer, "Grid friendly connection of constant speed wind turbines using external resistors", *IEEE Trans.*, vol. EC – 17, no. 4, 2002, pp. 537-542.
- [15] Boldea, S. A. Nasar, "Electric drives" book, 3<sup>rd</sup> edition, (Chapter 15), CRC Press, Taylor and Francis, New York, 2017.

# FLUX – REVERSAL PM SYNCHRONOUS MOTORS (FR-PMSM) AND GENERATORS AT VARIABLE SPEED

## Abstract

The search for better (higher torque/copper losses) PMSMs (PMSGs) led early (1943-1955) to the idea of using concentrated (stator tooth wound) coil and multiple pole PMs in the stator or in the rotor, embraced by the a.c. stator coils. The term “flux reversal” suggests that the PM flux linkage in the a.c. coils reverses polarity.

Building on this idea references [1]-[4] develop the concept of FR – PMSM for:

- \* Single phase machines [1] with stator PMs
- \* Three phase machines [2, 3] with stator PMs
- \* Three phase machines [4] with rotor PMs

The increase in the number of PM poles for a reduced number of stator large slots and a.c. coils is the key to high torque/copper losses, with applications mainly for small and medium speed (to limit the fundamental frequency to 1kHz range).

Since the introduction of TF-PMSMs (G1) in [1-4], subsequent solid developments have been made worldwide [5-9].

## 10. 1 Introduction

Typical single phase FR – PMSM [1, 2] show 2 (4) a.c. coils with 3 (4, 6) salient rotor poles and 2 PM poles of alternate polarity on each stator large pole (2/4) such stator poles, or slots), Fig. 10.1.

The waveform of the PM flux in a stator coil and its emf reflects the possibility of a sinusoidal – or even trapezoidal – emf to use sinusoidal or trapezoidal current waveform (to reduce torque pulsations). Airgap tapering is needed to secure safe starting (in one direction of motion).

On the other end, a 3 phase FR – PMSM (G), Fig. 10.2 also with stator PMs illustrates again the rather sinusoidal PM flux in the stator coils.

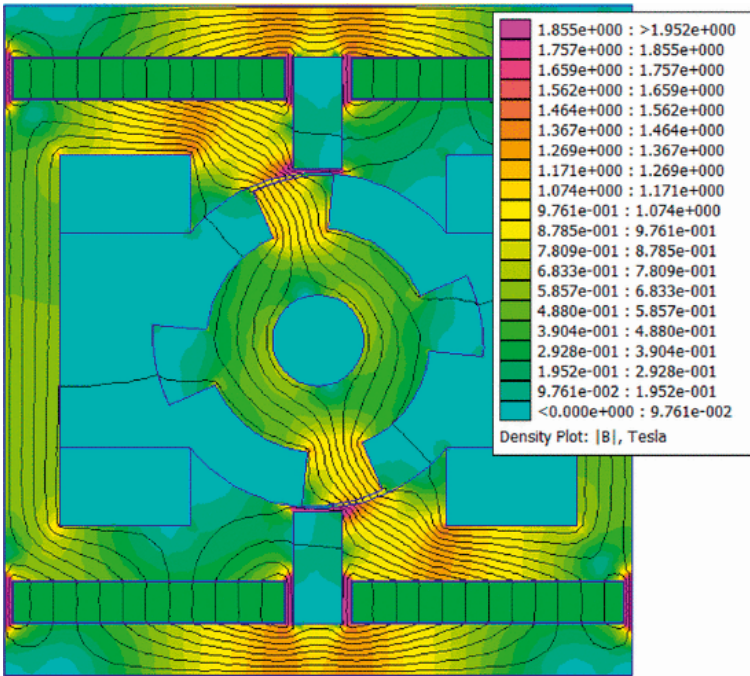
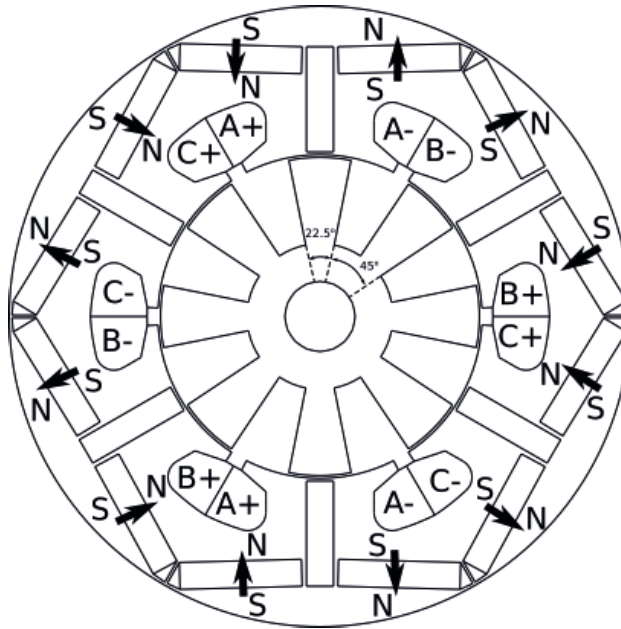


Fig. 10.1 Single phase FR – PMSM with stator PMs and 2 slots/4 poles, after [2].



a)



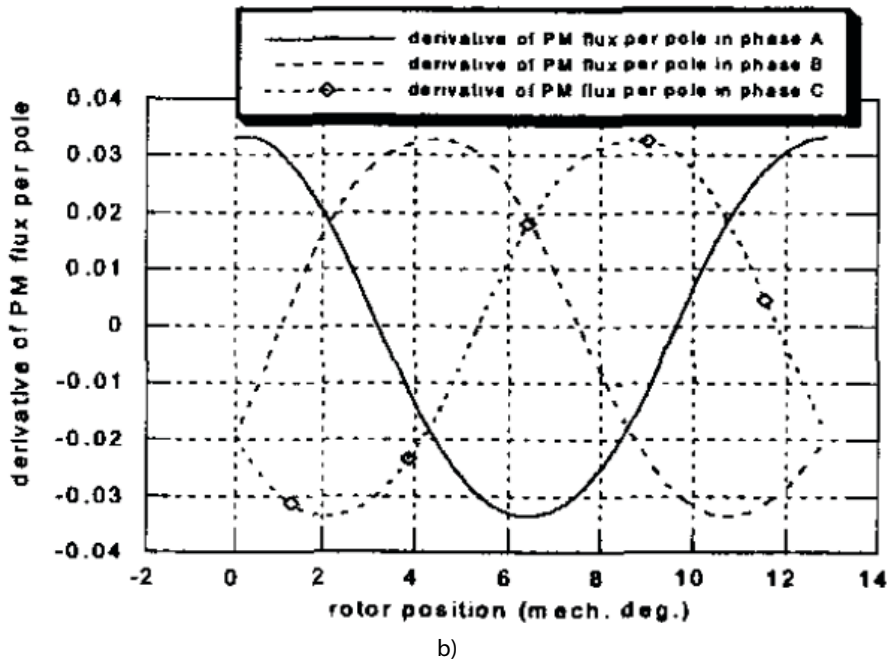


Fig. 10.2 Three phase FR – PMSM (G) with stator PMs: a) typical configuration 6 slots (coils)/8 rotor poles with 2 PM poles/ stator pole, b) 3 phase PM fluxes derivatives versus rotor position, after [2].

It goes without saying that stator slot openings should expand (in general)  $2\tau_{PM}/3$  to secure symmetric emfs and thus reasonably low torque pulsations.

Moreover, it is feasible to interpret FR – PMSM as a PM flux modulation machine and then there is more freedom in choosing the number of stator slots  $N_s$ , rotor poles  $N_r$  and stator mmf pole pairs  $P_a$  such that:

$$P_a = N_r - N_s \tag{10.1}$$

Finally, FR–PMSM acts as a synchronous PM motor with small functional magnetic saliency at the speed  $n_n$  for the rated frequency  $f_{1n}$ :

$$f_{1n} = N_r \cdot n_n \tag{10.2}$$

Therefore, the number of rotor salient poles  $N_r$  “acts” as the number of rotor pole pairs in synchronous operation.

The  $3k$  stator coils (and teeth) may be connected to form a 1, 2, 3 ... pole pair mmf,  $P_a$ .

Based on same principle, another topology of FR–PMSM (G) may be obtained as well, with spoke–shape magnets on the rotor (Fig. 10.3). Now additionally an interior with same shape as the external stator, but stuffed by a PM pole pitch ( $\tau_{PM}$ ), is used [4]. This time the PM flux fringing is smaller and thus the power factor (the main drawback) is increased together with the specific torque/volume.



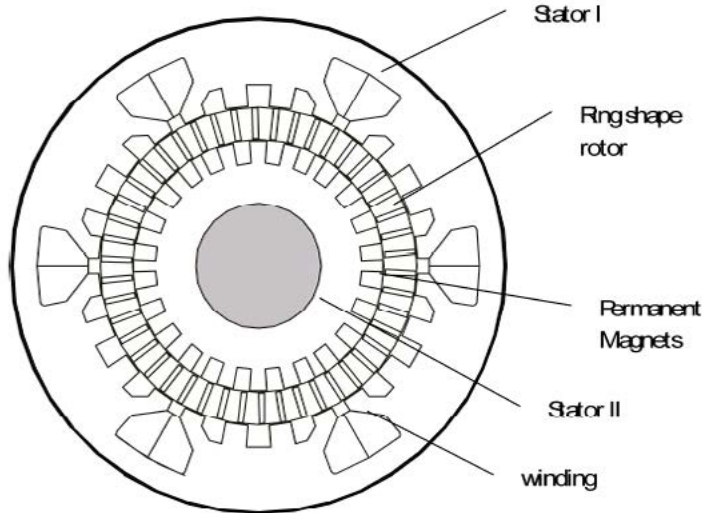


Fig. 10.3 Radial airgap FR – PMSM (G) with spoke – PM – rotor.

In this machine, all PMs are active all the time. It should also be noted that the magnetic cores are built from regular laminations while they may have radial or axial – airgap. In the latter case, the two twin stators both have a.c. coils in slots, with the spoke – PM rotor in between. Core losses occur both in the stator and rotor cores. Also, eddy current losses in the PMs are to be checked and reduced (if needed) simply by dividing the PM – poles into a few smaller PM cubicles.

Note. It should be mentioned that in the stator surface – PM configurations only half of the PMs are active at any time (this is equivalently valid in all stator d.c. (or PM) excitation systems).

Given the simplified topology of FR–PMSM with stator surface PM poles and the better PM utilization in the rotor – PM topology, both will be investigated in some detail, in what follows.

## 10.2 The 3 phase FR – PMSM – stator surface PM pole configuration.

Let us consider [3] a 200 Nm,  $n_n=128$  rpm at  $f_n \approx 60$  Hz 3 phase FR – PMSM with stator surface PMs.

For the initial configuration [3] simply the pole pitch of the rotor saliency  $\tau_{rot}$  is equal to PM pole pitch  $\tau_{PM}$ . The number of rotor salient pole  $N_r$  is:

$$N_s \left( 2n_{np} \tau_{PM} + 2\tau_{PM} / 3 \right) = 2\tau_{PM} N_r \quad (10.3)$$

with  $N_s=12$  stator slots,  $2n_p=4$  PM poles/stator pole,  $N_r=28$  rotor salient poles. From (10.2), the stator frequency  $f_n=N_r \cdot n_n=28 \cdot 128/60=60$  Hz. The cross-section of the three phase motor is shown in Fig. 10.4.

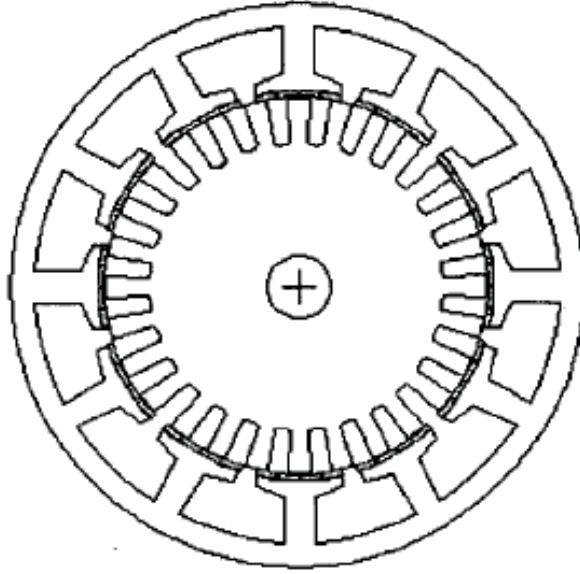


Fig. 10.4 Low speed 3 phase FR – PMSM:  $N_s=12$ ,  $2n_p=4$ ,  $N_r=28$ .

Considering a shear rotor stress  $f_t=2$  N/cm<sup>2</sup> for  $T_e=200$  Nm stator core stack ratio  $\lambda=l_{stack}/D_r=1.055$ , the rotor diameter  $D_r$  is obtained from:

$$T_e = f_t \cdot \pi \cdot D_r \cdot l_{stack} \cdot \frac{D_r}{2}; D_r = 0.182 \text{ m} \quad (10.4)$$

with  $l_{stack}=0.19$  m.

The PM flux per stator coil (one turn),  $\Phi_{PM}$  is:

$$\Phi_{PM} = l_{stack} \cdot B_{gPMi} \cdot k_{fringe} \times \tau_{PM} \cdot n_{pp} \quad (10.5)$$

The ideal airgap PM flux density  $B_{gPMi}$  is:

$$B_{gPMi} = B_r \cdot \frac{h_{PM}}{\frac{h_{PM}}{\mu_{rec}(\text{p.u.})} + g} \approx 1.21 \cdot \frac{2.5}{(2.5 + 0.5)} = 1.00 \text{ T} \quad (10.6)$$

with PM thickness  $h_{PM}=2.5$  mm, airgap  $g=0.5$  mm,  $B_r=1.21$  T,  $H_c=0.91$  MA/m at 25°C.

The  $E_{m1}$  emf per phase  $N_s/3$  coils,  $n_c$  turns per coil (peak value).

$$E_{m1} = \frac{N_s}{3} \cdot n_c \cdot 2\pi n \times l_{stack} \cdot \pi \cdot D_r \cdot k_{fringe} \times \frac{n_{pp}}{2} \cdot B_{gPMi} \quad (10.7)$$

The fringing factor  $k_{fringe}<1$  (to be calculated by FEM) is rather large and depends on the ratios:  $\frac{(g+h_{PM})}{\tau_{PM}}$  and  $\frac{\tau_{PM}}{g}>(3-4)$ . There is an optimum PM thickness for given

motorgeometry which produces a maximum  $B_{gPMi} \times k_{fringe} = B_{gPM}$ , where  $k_{fringe} = 0.4$  (a conservative value). Consequently, the actual PM flux airgap flux density is  $B_{gPM} = 0.4 \text{ T}$ .

But the torque is also:

$$T_e = \frac{3}{2} E_{m1} I_n \sqrt{2} / (2\pi n) \quad (10.8)$$

From (10.8) finally the peak rated ampere turns per coil  $n_c I_n \sqrt{2} = 1.032 \times 10^3$  Aturns/coil. With a slot fill factor of 0.4, 2 coils in a slot,  $i_{con} = 3.5 \text{ A/mm}^2$  the slot area  $A_{slot} = 1.039 \times 10^{-3} \text{ m}^2$  (PM pole pitch  $\tau_{PM} \approx 10 \text{ mm}$ ). Before finishing the analytical sizing, a FEM inquiry is timely.

### 10.2.1 FEM inquiry

The FEM calculated PM flux per coil (1 turn) for the three phases shown in Fig. 10.5, are close to a sinusoidal waveform.

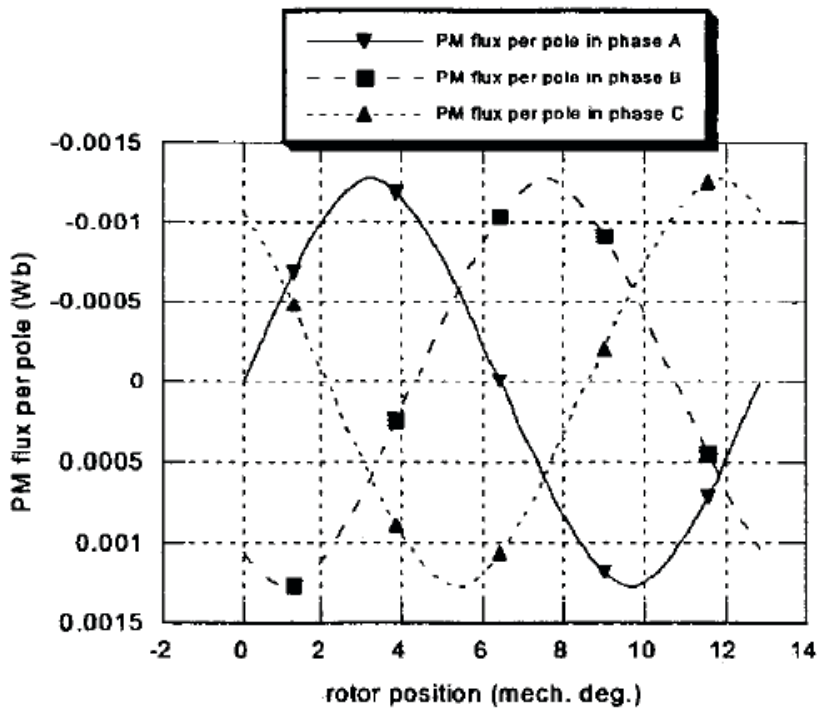
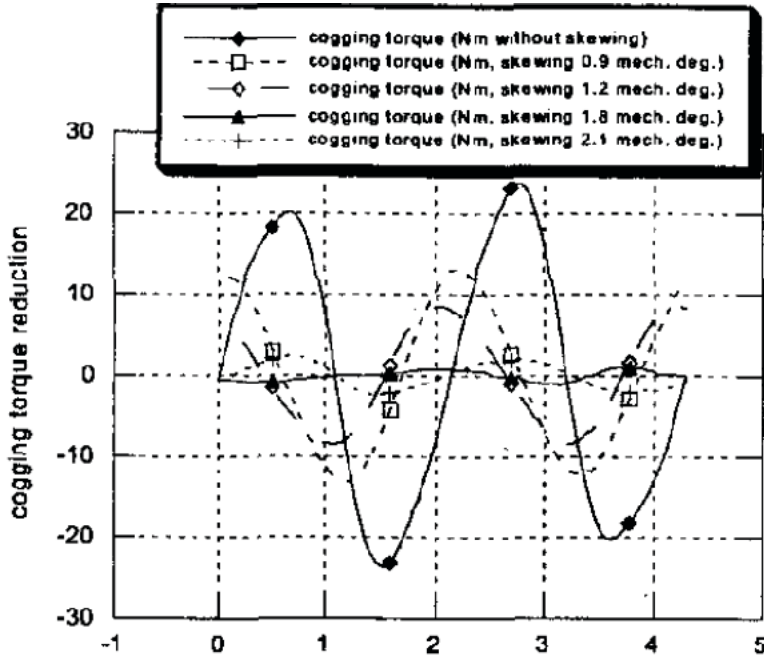
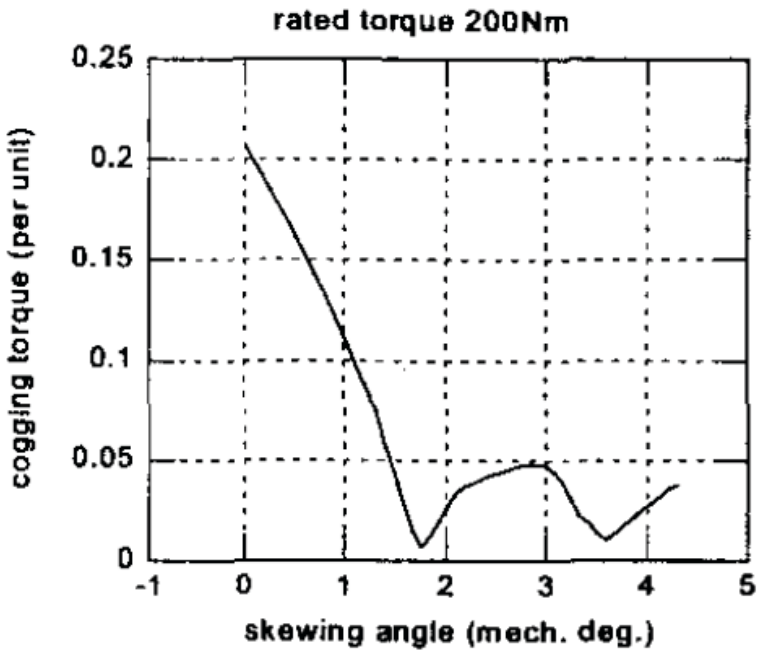


Fig. 10.5 PM flux per coil (one turn) versus rotor position.

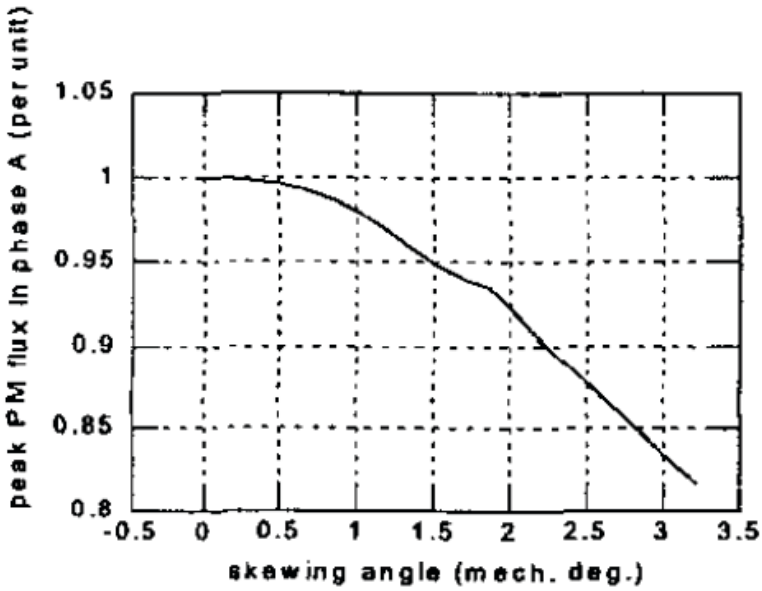
The reduction of cogging torque in Fig. 10.6 indicates spectacular results for 1.8 mechanical degrees rotor skewing for a 6% diminution of PM flux per coil (one turn) amplitude. Their results qualify FR-PMSM for servodrives (1.5% cogging torque).



a)



b)

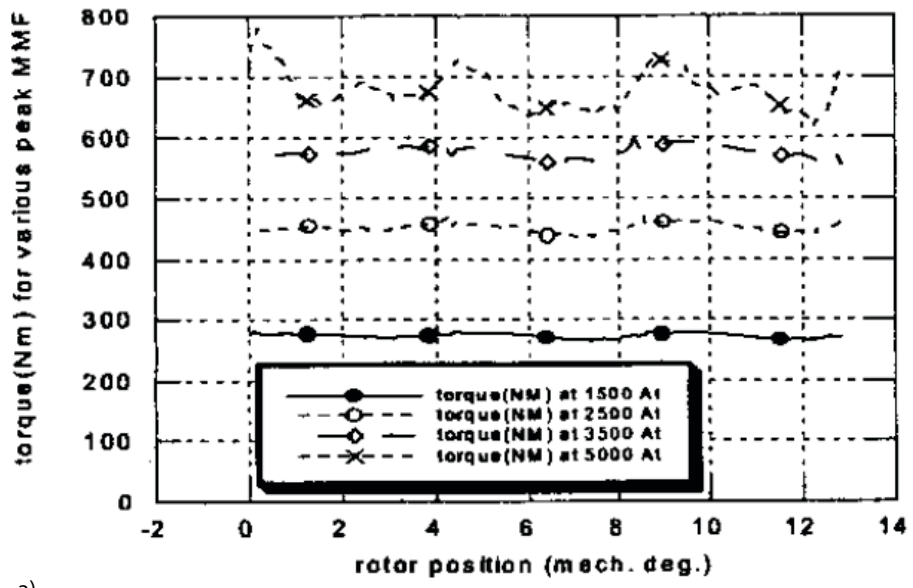


c)

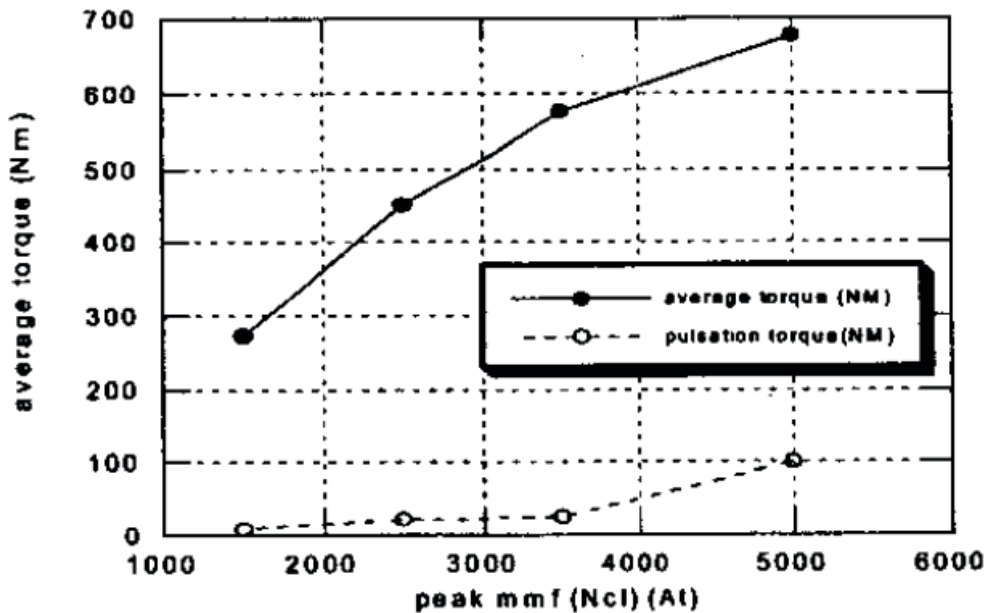
Fig. 10.6 Cogging torque versus skewing a), b) and PM flux per coil reduction, c).

It has to be noticed that skewing not only reduces the phase emf (and torque) but also dephases the emf by up to 30 electrical degrees and thus should be considered in the control system design [3].

The torque for sinusoidal currents in phase with phase emfs ( $i_d=0$ ) is depicted, versus rotor position at 4 coil peak mmf values (1500 At, 2500 At, 3500 At, 5000 At).



a)



b)

Fig. 10.7 Total torque versus rotor position, a) and torque /  $(n_c I\sqrt{2})$  ratio versus peak coil mmf  $N_c I\sqrt{2}$  (At), b).

A few remarks are occasioned by the results so far:

- \* Shear rotor stresses  $f_t$  up to  $7.108 \text{ N/cm}^2$  have been obtained
- \* The current – related torque pulsations increase in % with current
- \* The torque / coil ampere turns (Fig. 10.7b) indicates that for  $n_c I\sqrt{2} > 3500$  Aturns (1000 Aturns is the rated value) the torque/Amp reduces severely due to magnetic saturation ( $h_{PM} = 2.5 \text{ mm}$ ). At 3.5 p.u. load the torque pulsations represent 3%.
- \* The question arises if at  $n_c I\sqrt{2} = 5000$  Aturns (50 p.u. load) the PMs are not in danger of demagnetization. Calculating the radial airgap flux density on the PM surface (Fig. 10.8) demonstrates that this is not the case.

Apparently, the radial PM flux density of this large current as pure  $i_d$  (Fig. 10.8), decreased on the north poles and increased on the south poles is too large, considering PM flux bringing. However, the latter appears away from the magnets and thus reduces the “armature reaction” effect.

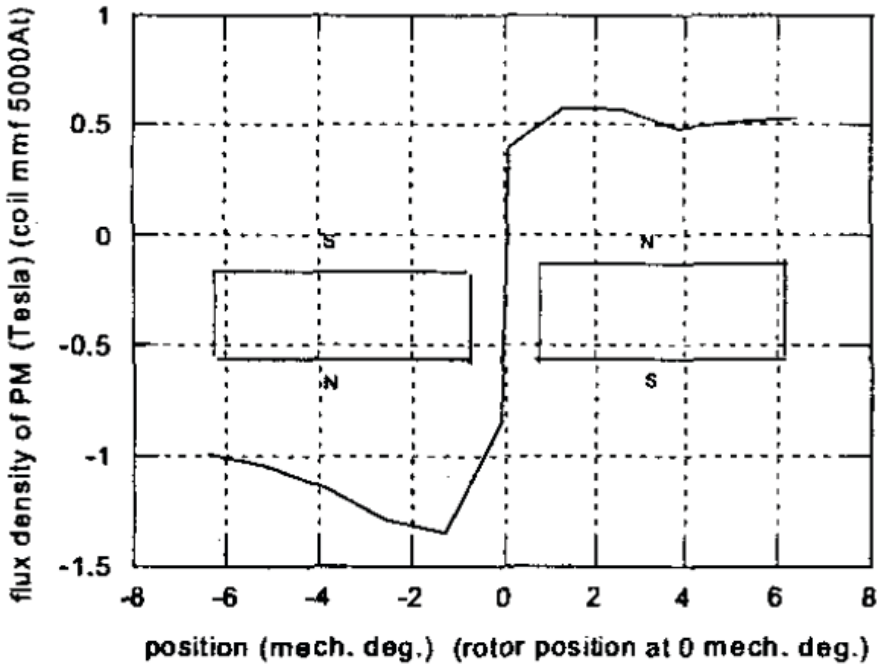


Fig. 10.8 Radial PM flux density versus rotor position at 5000 At/coil (one turn).

### 10.2.2. Calculated performance

With  $j_{con}=3.5 \text{ A/mm}^2$  is calculated as 295.66 W with a turn length  $l_{coil}=0.458 \text{ m}$ , and  $f_t=2.1 \text{ N/cm}^2$  at 200 Nm (rated torque). The rated torque electrical efficiency at  $n_n=128 \text{ rpm}$  and 200 Nm is (with neglected core loss):

$$\eta_e \approx \frac{T_{en} \cdot 2\pi n_n}{2\pi n_n + p_{copper}} = 0.9 \quad (10.9)$$

For a 5/1 p.u. load the efficiency would be only 0.56 and thus the machine would stand it thermally probably less than a few minutes.

Now the self and mutual phase inductances versus rotor position may be FEM calculated and a standard circuit model (with curve fitted emfs and inductances versus rotor position) may be developed for transients and control system design. As this path is standard for all PMSMs, it will not be followed here with this machine capable of about 3.8 Nm/liter (at airgap diameter) at rated torque (200 Nm) and 128 rpm with an efficiency of 0.88 – 0.9.

However, it is to be mentioned that other aspects as PM eddy current losses have to be checked and reduced by making PM poles of  $m \times n$  cubicles if needed.

### 10.3 Radial airgap 3 phase FR – PMSM(G) with spoke – PM rotor and dual stator.

Let us consider the configuration in Fig. 10.3, again for  $n_p \approx 130$  rpm for 50 Hz and  $T_{en} = 150$  Nm, similar in some respect to the case study in paragraph 10.2.

With only 6 coils (stator slots), stator poles sparring 7 PM poles. The rotor results having  $2p_{PM} = 46$ , with 6 stator big poles (and coils).

Again, the preliminary design will be done first, only to be checked by FEM calculations [4].

#### 10.3.1 Analytical preliminary design

The internal diameter of outer stator  $D_{is}$  is:

$$D_{is} = \sqrt{\frac{2 \cdot T_{en}}{\pi f_t \cdot l_{stack}}} = 0.176 \text{m} \quad (10.10)$$

For  $f_t = 6 \text{N/cm}^2$   $l_{stack} = 0.07 \text{m}$ , also  $\tau_{PM} = 12$  mm.

The airgap  $g = 0.7$  mm on each radial side of the PM rotor.

The actual airgap PM flux density is chosen here larger:

$B_{gPM} = 1.1$  T, to allow for at least an armature reaction flux density of  $B_{ag} = 0.76$  T, which when leakage inductance is considered will lead to a power factor above 0.707 for rated torque:

$$\cos \varphi_1 \approx \frac{B_{gPM}}{\sqrt{B_{gPM}^2 + (1.1 \cdot B_{ag})^2}} \approx 0.8 \quad (10.11)$$

The rotor radial height  $h_{rPM}$  is of almost importance and may be calculated from:

$$\frac{h_r}{\tau_{PM}} = \frac{B_{gPM} / B_r}{2k_{fringe} \left( 1 - \frac{B_{gPM}}{B_r} \cdot \frac{2 \cdot g \cdot \mu_{rec} / \mu_0}{h_{PM}} \right)} \approx 0.8 \quad (10.12)$$

Choosing  $\frac{h_r}{\tau_{PM}} = 1.876$  ( $h_r$  includes 2 iron bridges  $h_b = 0.5$  mm above/ below the PMs in

their closed slot:  $h_r = h_{PM} + 2 \cdot h_b$ ), the PM thickness  $h_{PM} = 3$  mm  $= 0.25 \cdot \tau_{PM}$ , with  $k_{fringe} = 0.55$ . An optimal  $h_{PM}$  may be searched here.

The ampere turns per coil (RMS)  $n_c I_c$  are:



$$n_c I_c = \frac{T_{en}}{3\sqrt{2} \cdot p_{PM} \cdot \Phi_{PMcoil(one\ turn)}} = \frac{150}{3\sqrt{2} \cdot 23 \cdot 2.354 \times 10^{-3}} = 655 \text{ Aturns(RMS)} \quad (10.13)$$

$$\Phi_{PMcoil(one\ turn)} = 4 \cdot B_{gPM} \times \tau_{PM} \times l_{stack} \frac{2}{\pi} = 4 \cdot 1.1 \cdot 0.012 \cdot 0.07 \cdot \frac{2}{\pi} = 2.354 \times 10^{-3} \text{ Wb} \quad (10.14)$$

There are 4 PM poles producing max airgap PM flux in the stator coil (one turn) and there are also 2 coils in series per phase.

For an inductance correction  $k_{cor}=0.1$  due to uncalculated leakage component leads to a straightforward stator phase voltage equation:

$$V_1 \sqrt{2} \approx (1 + k_{cor}) \cdot p_{PM} \cdot \frac{2n_c}{\pi} l_{stack} \cdot 4 \cdot B_{gPM} \cdot \tau_{PM} \cdot \frac{\omega_1}{p_{PM}} \sqrt{1 + \left( \frac{1.1 \cdot B_{ag}}{B_{gPM}} \right)^2} \quad (10.15)$$

The only unknown  $n_c$  (the number of turn/coil) is thus obtained (with  $V_1=220$  V (RMS) per phase, star connection) as  $n_c=158$  turns/coil.

Thus the rated current:

$$I_n = n_c \cdot I_n / n_c = 655 / 156 = 4.2 \text{ A} \quad (10.16)$$

The electromagnetic power  $P_{en} = T_{en} \cdot 2 \cdot \pi \cdot n_n = 2041$  W.

However, the total rated apparent power  $S_n$  is:

$$S_n = 3V_1 I_n = 3 \cdot 220 \cdot 4.2 = \frac{P_{cu}}{\eta_n \cdot \cos \varphi_n} = \frac{2000}{\eta_n \cdot \cos \varphi_n} \quad (10.17)$$

Finally,

$$\eta_n \cdot \cos \varphi_n = 0.736 \quad (10.18)$$

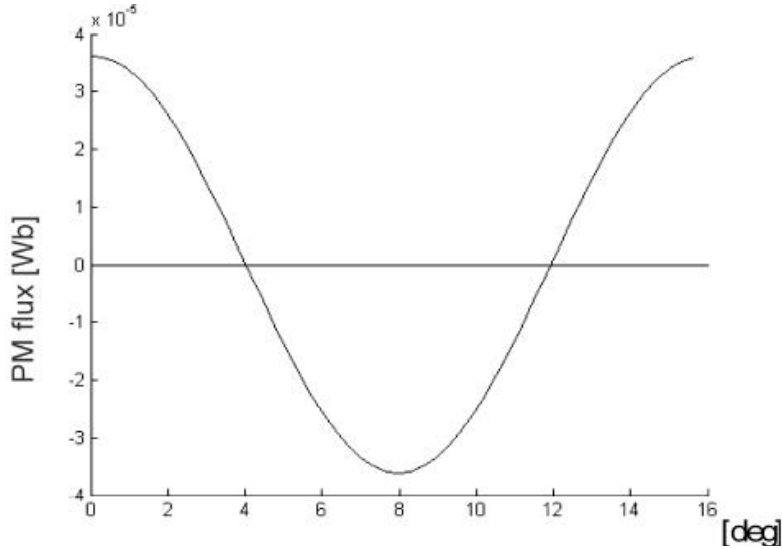
The routine calculations continue to calculate the rated copper losses (at  $j_{con}=6$  A/mm<sup>2</sup>) to 138 W. At 50 Hz the core losses are approximated to  $p_{core}=50$  W and mechanical losses  $p_{mec}=20$  W.

Finally the rated efficiency  $\eta_n=0.92$  and the power factor is calculated as  $\cos \varphi_n=0.8$ .

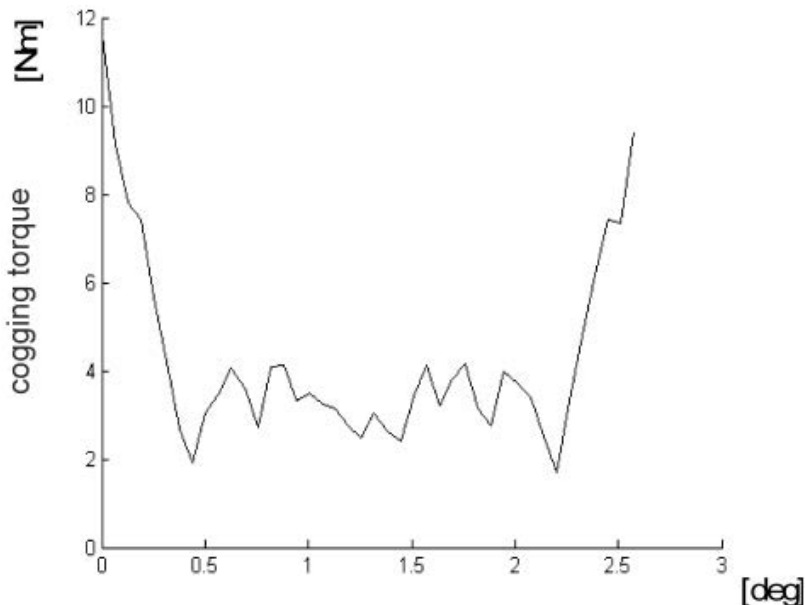
The rated torque/volume at rated airgap diameter is 80 Nm/l notably larger than for the stator – PM FR-PMSM in the previous paragraph.

## 10. 4 FEM analysis

PM flux/phase (one turn per coil) versus mechanical rotor angle shown in Fig. 10.9a seems reasonably sinusoidal. Shifting the interior stator by 0.5 mechanical degree will reduce the cogging torque to less than 4 Nm (3.5%), Fig. 10.9b.



a)



b)

Fig. 10.9 PM flux in a phase (one turn/coil) versus mechanical rotor position, a), cogging torque amplitude versus skewing angle (interior stator angle shifting from  $180^\circ$  electrical degrees position), b).

Finally, the total torque versus position for a few current densities is shown in Fig. 10.10 against mechanical rotor angle (phase emf and current are in phase:  $i_d=0$ ).

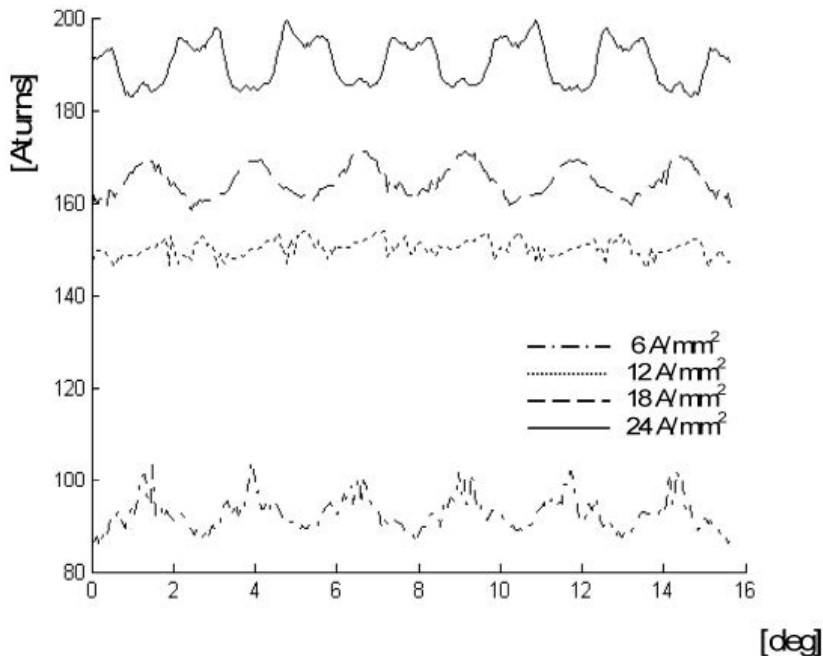


Fig. 10.10 Total torque versus mechanical angle.

## 10.5 Final discussion

The machine torque at 6 A/mm<sup>2</sup> fits the required rated value of 150 Nm. However, in contrast to the surface stator-PM configuration when the current increases to 4 times rated value, the torque only increases to 190 Nm. This is due to the „installation“ of heavy saturation, but mainly due to large armature reaction due to spoke – PM rotor configuration.

However, the performance is good and where heavy over-load is not necessary, this machine may be competitive, and with larger airgap even 150 – 200 % load may be handled.

The reasonable power factor is a sign that the PWM converter kVA and costs will be moderate. Also, the possibility of limited rotation (by a servo) and latching of interior stator for strong PM flux weakening at  $i_d=0$  is tempting.

Final notes. The Vernier dual-stator spoke-PM rotor, developed recently (works somewhat similarly but it takes a distributed stator winding (with long end-coils) and thus higher copper losses).

The axial – airgap FR-PMSM with twin stators and spoke-PM rotor in between analyzed recently [11] may produce even higher torque/volume at better efficiency.

## 10. 6 References

- [1] R.P. Deodhar, S. Andersson, I. Boldea, T.J.E. Miller, "The flux – reversal machine: a new brushless doubly-salient permanent magnet machine", *IEEE Trans.*, vol. IA – 33, no. 4, 1997, pp. 925 – 934.
- [2] I. Boldea, L. N. Tutelea, "Reluctance electric machines design and control", book, CRC Press, Florida, Taylor and Francis, New York, 2018, Ch. 10.
- [3] I. Boldea, J. Zhang, S.A. Nasar, "Characterization of flux reversal machine (FRM) in low speed (direct) servodrives: the pole PM configuration", *IEEE Trans*, vol. IA – 38, no. 6, 2002, pp. 1549 – 1557 (IEEEXplore).
- [4] I. Boldea, L. Tutelea, M. Topor, "Theoretical characterization of three phase flux – reversal machine with rotor – PM flux concentration", *Record of OPTIM – 2012*, pp. 472 – 476 (IEEEXplore).
- [5] D.S. More, H. Kalluru, B.G. Fernandes, "Comparative analysis of flux reversal machine and fractional slot concentrated winding PMSM", *Record of IEEE – IECON – 2008*, pp. 1131 – 1136 (IEEEXplore).
- [6] D. Li, R. Qu, J. Li, "Topologies and analysis of flux – modulation machines", *Record of IEEE – ECCE – 2015*, pp. 2153 – 2160 (IEEEXplore).
- [7] Y. Gao, R. Qu, D. Li, J. Li, Y. Huo, "Design and analysis of a novel flux reversal machine", *Record of IEEE – ECCE – 2016*, pp. 2153 – 2160 (IEEEXplore).
- [8] Y. Gao, R. Qu, D. Li, J. Li, "Design procedure of flux reversal PMSMs", *Record of IEEE – ECCE – 2016*, pp. 1586 – 1592 (IEEEXplore).
- [9] V. Dmitrievskii, V. Prakht, S. Sarapulov, D. Askerov, "A multipole single – phase SMC flux reversal motor for fans", *Record of IEEE – ICEM, 2016*, pp. 55–60 (IEEEXplore).
- [10] D. Li, R. Qu, T. Lipo, "High power factor Vernier permanent magnet machines", *Record of IEEE – ECCE – 2013* (IEEEXplore).
- [11] V. Rallabandi, N. Taran, D.M. Ionel, I. Boldea, "MAGNUS: axial-flux synchronous machines with airgap profiling and very high ratio of spoke rotor poles to stator concentrated cores", *Record of IEEE – IEMDC 2017* (IEEEXplore).

## Abstract

A.c. drives perform electric energy (power, voltage, current, torque, speed, position) control with PWM power electronics at variable voltage amplitude and control in alternative current electric motors or generators.

The myriad of a.c. drives control system may be classified as [1, 2] as:

- \*  $V_1/f_1$  ( $I_1-f_1$ ) control with stabilization/correction close loops but without speed control loop at variable speed in the range of (101100) and with  $\pm$  full torque response time of tens of milliseconds; adequate for general a.c. drives (pumps, compressors, ventilators, etc).
- \* Field oriented control (FOC) decoupled dq stator currents/voltages with 1 to 100 and more variable speed range and with  $\pm$  full torque response in the millisecond range [3]; adequate for servodrives.
- \* Direct torque and stator flux control with servodrive performance but obtained by directly triggering a combination of voltage vectors in the inverter for each  $60^\circ$  electrical degrees sector of stator flux vector, based on the sign  $\pm$  of stator flux and torque error "read" at a given frequency (initially, for IMs, [4, 5], by hysteresis stator flux and torque regulators, later with PI, PI+SM such regulators.
- \* The DTC term has been introduced in 1991 and by ABB (1995) while, in 1988 in [6], the "quick torque response control [4], 1986 and direct self – control [5], 1986, has been generalized for synchronous motors and for current source inverter a.c. drives [17] as torque vector control (TVC). Subsequent papers developed on TVC in IMs [7] and reluctance synchronous motors [8] and then, as DTC in IMs [9-13] and in synchronous motors [14-16] and finally in encoderless (sensorless) IM+SM drives [17 - 19].
- \* DTC implies stator flux observers, and for sensorless control, also rotor position and speed controllers.
- \* So, DTC seems mostly adequate for sensorless control, or for torque mode control as it reduces the on and off line computation effort and increases drive response robustness in comparison with FOC.

Other than that FOC and DTC of a.c. drives may be considered equally capable in terms of speed control range and torque response quickness. This Chapter presents the original TVC concept [6] and current source PWM converters and then introduces very recent contributions in DTC sensorless control of IMs and PMSMs.

## 11.1 Torque vector control (TVC) concept for a.c. machine drives [6]

As inferred in the Abstract, the research for fast torque response in a.c. machine drives led to Field Oriented Control (FOC) first (1972 [3]) and then in an effort to simplify the control system especially for encoderless drives the quick torque response (1986, [4]) and “direct” selfcontrol (DSC), (1988, [5]), has been first introduced for voltage source PWM inverter induction motor drives. The concept of “direct torque control” was generalized as “torque vector control (TVC)” in 1988 [6] for synchronous machines also and for current source PWM inverter a.c. drives. Later on, in 1991 [9] and 1995 [10], the term “DIRECT TORQUE CONTROL” was coined and it has been used ever since, especially due to its commercialization for induction motor drives.

Let us explain here the TVC (later DTC) of induction and synchronous machines with voltage source inverters first and then for current – source inverters afterwards. The concept has been extended toward generator as direct active (torque) and reactive (flux) power control [20].

## 11.2 TVC (DTC) principle for voltage – source inverter fed IMs

There are three main flux linkages in an induction motor:

- \* Stator flux:  $\overline{\Psi}_s$
- \* Magnetization (airgap) flux:  $\overline{\Psi}_m$
- \* Rotor flux:  $\overline{\Psi}_r$

$$\begin{aligned} \overline{\Psi}_s &= L_s \overline{i}_s + L_m \overline{i}_m; L_s = L_{sl} + L_m; \overline{i}_m = \overline{i}_s + \overline{i}_r \\ \overline{\Psi}_m &= L_m \overline{i}_m; \overline{\Psi}_r = L_r \overline{i}_r + L_m \overline{i}_s; L_r = L_{rl} + L_m; L_{sc} \approx L_{sl} + L_{rl} \end{aligned} \quad (11.1)$$

Traditionally, FOC uses rotor orientation ( $\overline{\Psi}_r$ ) and constant rotor flux amplitude for decoupled control the rotor flux (to a constant value in general) and stator current  $i_d$  and the torque current  $i_q$ .

The space phasor model of IM (cage rotor in this case) is:

$$\overline{V}_s = R_s \overline{i}_s + \frac{d\overline{\Psi}_s}{dt} + j\omega_s \overline{\Psi}_s$$

$$0 = R_r \bar{i}_r + \frac{d\bar{\Psi}_r}{dt} + j(\omega_b - \omega_r) \bar{\Psi}_r \quad (11.2)$$

$$T_e = \frac{3}{2} p_1 \operatorname{Re}[j \bar{\Psi}_s \bar{i}_s^*] = -\frac{3}{2} p_1 \operatorname{Re}[j \bar{\Psi}_r \bar{i}_r^*]$$

with:

$$\bar{\Psi}_r = \frac{L_m}{L_r} \bar{\Psi}_s + L_{sc} \bar{i}_s; \bar{i}_s = i_d + j i_q; \bar{\Psi}_r = \Psi_r \quad (11.3)$$

$$i_d = \left( 1 + s \frac{L_r}{R_r} \right) \frac{\Psi_r}{L_m}$$

As  $L_r/L_s \approx 0.1-0.3$  seconds the rotor flux transients are slow with current control.

Considering  $\Psi_r = ct$ :

$$i_q = i_d (\omega_{\Psi_r} - \omega_r) \frac{L_r}{R_r}; i_d = \frac{\Psi_r}{L_m} \quad (11.4)$$

and

$$\bar{\Psi}_s = L_s i_d + j L_{sc} i_q \quad (11.5)$$

The IM space phasor (vector) diagram for steady state is depicted in Fig. 11.1 [23].

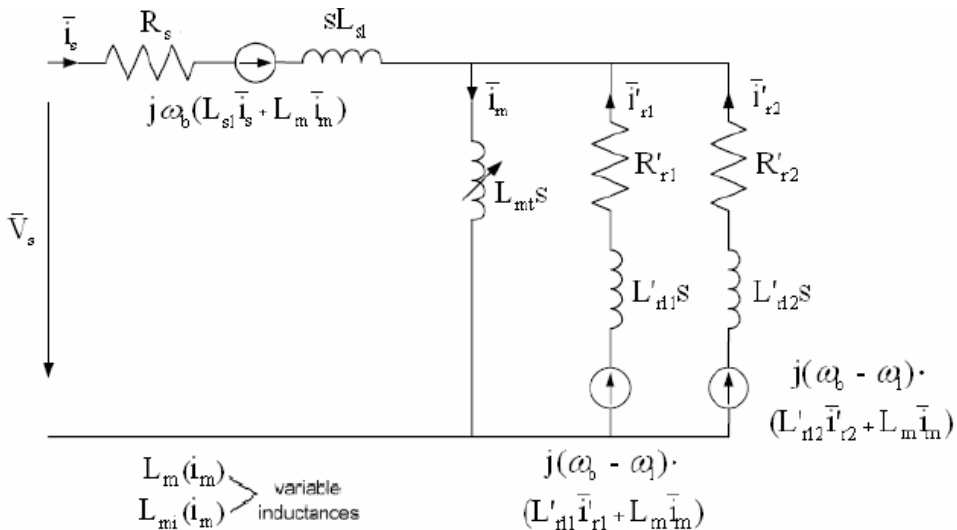


Fig. 11.1 IM vector diagram under steady state for  $R_s \approx 0$ .

From (11.15) and (11.2) the torque expression becomes:

$$T_e = \frac{3}{2} p_1 (L_s - L_{sc}) i_d \cdot i_q \quad \text{or} \quad (11.6)$$

$$T_e = \frac{3}{2} p_1 \frac{(L_s - L_{sc})}{2L_s L_{sc}} \Psi_s^2 \sin 2\delta \quad (11.7)$$

For constant rotor flux – steady state and transients – the torque in (11.6) shows a behavior similar to a reluctance synchronous motor with  $L_d=L_s$  and  $L_q=L_{sc}$  and with the “virtual” rotor magnetic saliency produced by the rotor (torque) currents.

However, it is also feasible to modify the torque by modifying the stator flux amplitude and the torque angle  $\delta$  (11.7).

Accelerating the stator flux vector  $\bar{\Psi}_s^s$  ahead or slowing it down, would make the angle  $\delta$  increase positive and produce more positive torque (motoring) or, respectively, decrease negative  $\delta$  to produce negative (generating) torque.

This is the principle of TVC, but it is to be noticed that the latter is a quasi-scalar control which at the limit reaches vectorial attributes.

In implementing TVC the stator flux equation in stator coordinates is needed:

$$\bar{V}_s^s = R_s \bar{i}_s^s + \frac{d\bar{\Psi}_s^s}{dt} \quad (11.8)$$

with  $R_s \approx 0$ :

$$\frac{d\bar{\Psi}_s^s}{dt} \approx \frac{\Delta\bar{\Psi}_s^s}{\Delta t} = \bar{\Psi}_s^s - \bar{\Psi}_{s0}^s = \int \bar{V}_s^s dt \quad (11.9)$$

Equation (11.9) implies that the stator flux vector variation takes place along the voltage vector  $\bar{V}_s^s$  direction and is proportional to the voltage amplitude. Changing the voltage vector direction and its timing leads to the desired acceleration/deceleration of stator flux and the rise or fall of its amplitude:

$$\int \bar{V}_s^s dt = V_i T_i + V_j T_j + V_0 (T_s - T_i - T_j) \quad (11.10)$$

with  $V_i, V_j$  the neighboring nonzero voltage vectors and  $V_0$  a zero voltage vector in the 3 leg two (multiple) level voltage source inverter. The two level inverter delivers 6 nonzero voltage vectors:  $\bar{V}_1(100)$ ,  $\bar{V}_2(010)$ ,  $\bar{V}_3(001)$ ,  $\bar{V}_4(011)$ ,  $\bar{V}_5(101)$ ,  $\bar{V}_6(110)$ ,  $\bar{V}_0(111)$ ,  $\bar{V}_7(000)$  (Fig. 11.2).

The original principle of TVC (DTC) consisted of triggering directly a certain single voltage vector  $\bar{V}(i) - i=1,2,\dots,6$  in the inverter, based on stator flux error  $\varepsilon_{\Psi_s} = \Psi_s^* - \Psi_s$ , torque error  $\varepsilon_{T_e} = T_e^* - T_e$  sign  $\pm$  and the stator flux vector location in one of the  $\sin 60^\circ$  - wide sectors (Fig. 11.2).



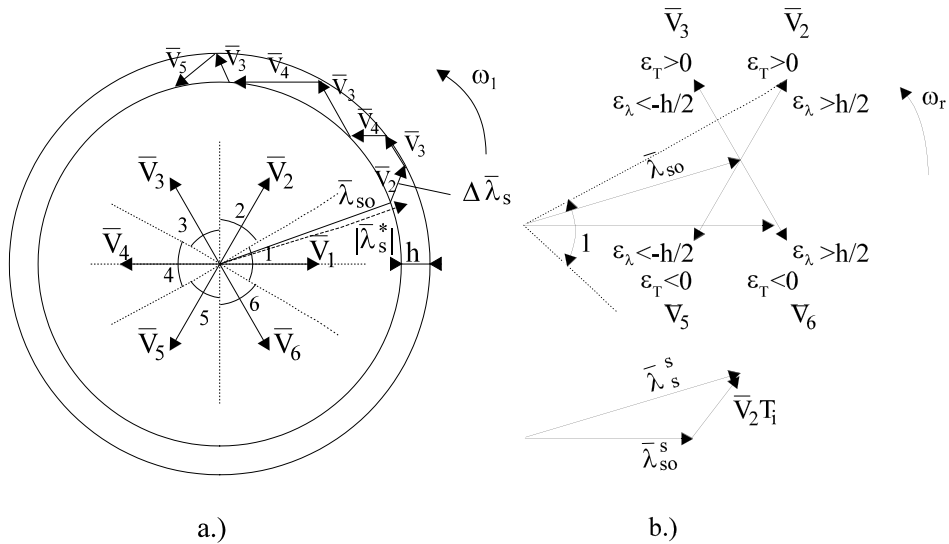


Fig. 11.2 The stator flux hodograph in TVC (DTC), a) and torque pulsations b).

Zero voltage vectors stop the stator flux vector rotation and are used to reduce either flux or torque pulsations but then either  $\epsilon_{T_e}$ ,  $\epsilon_{\Psi_s}$  should be treated as 3 step hysteresis bands.

Using a combination of neighboring voltage vectors (11.10) for every  $60^\circ$  sector –space vector modulation (SVM) also reduces the flux and torque pulsation, however at a larger switching frequency of the SCRs in the inverter.

To develop initial TVC (DTC) solutions for IMs here the adaptations for wide speed range control (with flux weakening) is also developed for 3 main principals:

- \* Maximum torque/stator current: below base speed;
- \* Maximum ideal power factor: below base speed;
- \* Maximum torque/stator flux: towards maximum speed for wide constant power speed range (CPSR).

In essence we use the torque formulae (11.6)-(11.7) to get:

- For maximum torque/stator current:

$$\frac{i_q}{i_d} = 1; \Psi_s^* = \sqrt{\frac{2T_e^* \left( L_s^2 + L_{sc}^2 \right)}{3p_1 (L_s - L_{sc})}}; \Psi_s^* < \frac{V_s}{\omega_1} \quad (11.11)$$

- For maximum power factor:

$$\frac{i_{dm}}{i_{qm}} = \sqrt{\frac{L_{sc}}{L_m}}, \cos \varphi_{1\max} = \frac{1 - L_{sc}/L_s}{1 + L_{sc}/L_s}$$

$$\Psi_s^* = \sqrt{\frac{2T_e^* \left( L_s^2 + L_{sc}L_s \right)}{3p_1 (L_s - L_{sc})}} \sqrt{\frac{L_{sc}}{L_s}} \quad (11.12)$$

for maximum torque per stator flux:

$$i_{dk} = \Psi_s / (L_s \sqrt{2}); i_{qk} = \Psi_s / (L_{sc} \sqrt{2}); \delta_k = \pi / 4 \quad (11.13)$$

$$\Psi_s^* = \sqrt{\frac{4T_e^* L_{sc}}{3p_1 (1 - L_{sc}/L_s)}} \quad (11.14)$$

$$\varphi_1 = \tan^{-1} L_{sc} / L_s + \pi / 4 \quad (11.15)$$

For wide speed range control, the latter may be reconfigured to switch from one strategy to the other as needed accordingly to torque requirements and speed (available voltage in the inverter).

### 11.3 TVC principle for voltage – source inverter fed synchronous machine drives

Synchronous machines make use of distributed (or tooth wound) stator windings on stator and PM or PM assisted anisotropic or magnetically anisotropic (reluctance) or dc. excited or a combination of the above rotors.

For all of them if the emfs are rather sinusoidal and the machine inductances depend sinusoidally on rotor position or they are independent of rotor position the space vector (dq) model may be applied directly.

When used for variable speed drives with voltage – source converters (2 (multiple) level PWM inverters, cycloconverters or matrix converters) no cage on the rotor is necessary.

The space phasor (dq) model of synchronous machines (SMs) in rotor coordinates is as known:

$$\bar{V}_s = R_s \bar{i}_s + \frac{d\bar{\Psi}_s}{dt} + j\omega_r \bar{\Psi}_s; \bar{\Psi}_s = L_d i_d + L_{dm} i_F + jL_q i_q; L_d = L_{fe} + L_{dm} \quad (11.16)$$

$$\bar{V}_F = R_F i_F + \frac{d\bar{\Psi}_F}{dt}; \bar{\Psi}_F = L_{Fe} i_F + L_{dm} (i_d + i_F)$$

$$T_e = \frac{3}{2} \operatorname{Re}[j \bar{\Psi}_s \bar{i}_s^*] = \frac{3}{2} (L_{dm} i_F + (L_d - L_q)) i_q \quad (11.17)$$

Now when PMs are placed instead dc. excitation the latter flux linkage  $L_{dm}I_F$  is replaced by  $\Psi_{PMd}$ , and the field circuit equation (with  $V_F, I_F$ ) is eliminated; also in this case  $L_d < L_q$  (inverse saliency) in contrast, with a strong saliency rotor ( $L_d > L_q$ ) and PM placed in axis q:

$$\Psi_q = L_q i_q - \Psi_{PMq}; \Psi_d = L_d i_d = \frac{3}{2} p_1 \left[ + (L_d - L_q) \cdot i_q \right] i_d \quad (11.18)$$

Also called PM – assisted reluctance synchronous machine (PM-RSM) is obtained. In this case low permanent flux density ( $B_r < 0.6$  T in general) of low costs may be used, mostly to increase power factor and the width of CPSR. Notice that now  $i_d$  is the torque current (that changes polarity to change torque direction).

The vector diagrams of the dc. excited and of PM – RSM are shown for steady state in Fig. 11.3.

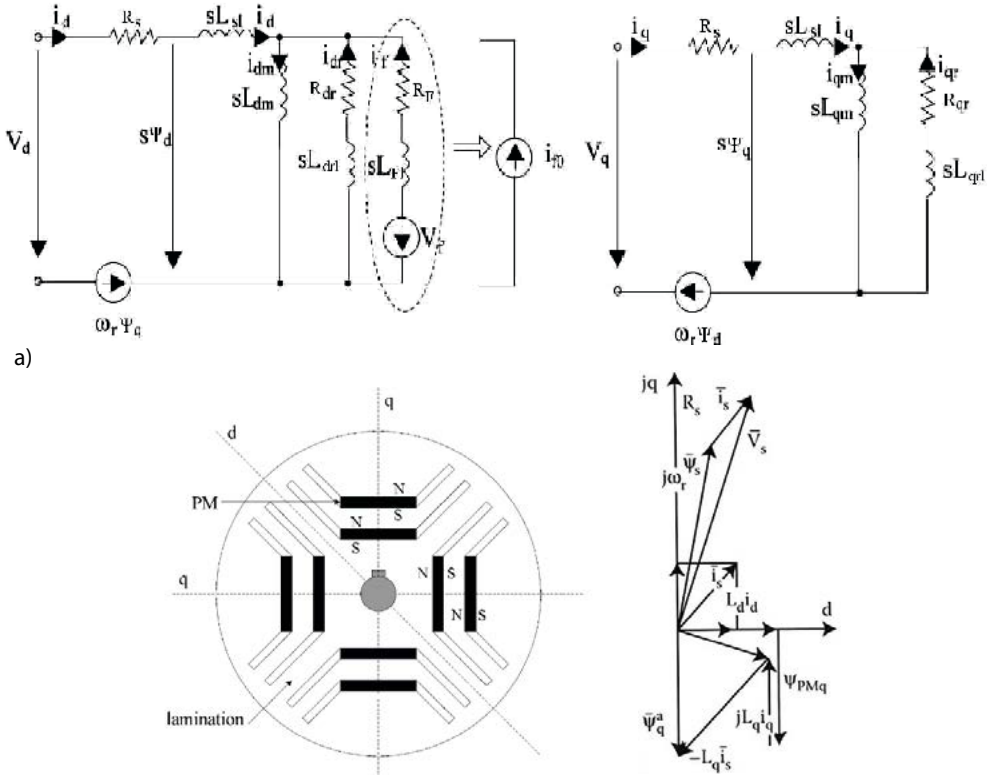


Fig. 11.3 Synchronous machines space vector diagrams in rotor coordinates (steady state): a) d.c. excited  $L_d > L_q$  or d axis PMs ( $L_d \leq L_q$ ), b) PM – RSM: with PMs in axis q and  $L_d \gg L_q$ .

The improvement in power factor brought by PMs in axis q ( $-\Psi_{PMq}$ ) is visible in Fig. 11.3b.

For TVC (DTC) the torque has to be first expressed in terms of stator flux  $\Psi_s$  and flux power angle ( $\delta$ ).

For the d.c. excited (or PM along axis d) rotor (Fig. 11.3a):

$$L_q i_q = \Psi_s \sin \delta; L_{dm} i_F + L_d i_d = \Psi_s \cos \delta \quad (11.19)$$

Consequently, the torque (11.17) becomes:

$$T_{e\text{d0(PM)}}^{\text{SM}} = \frac{3}{2} p_1 \left[ L_{\text{dm}} i_{\text{F}} \frac{\Psi_{\text{s}}}{L_{\text{d}}} \sin \delta + \frac{1}{2} (L_{\text{d}} - L_{\text{q}}) \frac{\Psi_{\text{s}}^2}{L_{\text{d}} L_{\text{q}}} \sin 2\delta \right] \quad (11.20)$$

$$T_{e\text{PMRSM}} = \frac{3}{2} p_1 \left[ \Psi_{\text{PMq}} \frac{\Psi_{\text{s}}}{L_{\text{q}}} \cos \delta + \frac{1}{2} (L_{\text{d}} - L_{\text{q}}) \frac{\Psi_{\text{s}}^2}{L_{\text{d}} L_{\text{q}}} \sin 2\delta \right] \quad (11.21)$$

Notice that in general for PM – RSM1 the flux torque angle  $\delta \leq 0$  while it is positive ( $\delta > 0$ ) for d.c. (PM) SMs.

It is now evident, again, that the torque may be modified by changing stator flux amplitude  $\Psi_{\text{s}}$  and the flux power angle  $\delta$  (as for IMs).

The principle of TVC (DTC) presented for the IM stands in principle. But the typical control systems for wide speed control range (and CPSR) differ from the ones for IMs. They are summarized in what follows:

- \* maximum torque/current for d axis PMs and small rotor saliency ( $L_{\text{d}} \leq L_{\text{q}}$ ) or q axis PMs and high rotor saliency ( $L_{\text{d}} > L_{\text{q}}$ );
  - \* maximum torque/flux (for the motors as above but for wide CPSR);
  - \* unity power factor control ( $\varphi_1 = 0$ ) of d.c. (or hybrid) excited SMs;
  - \* pure  $i_{\text{q}}$  control in d axis d.c. excited or PMSMs at low speeds and high torque;
- For maximum torque/current PMSMs:

$$2 \cdot i_{\text{di}}^2 - i_{\text{di}} \frac{\Psi_{\text{PMd}}}{(L_{\text{d}} - L_{\text{q}})} - i_{\text{s}}^2 = 0; L_{\text{d}} < L_{\text{q}}; i_{\text{di}} < 0 \quad (11.22)$$

Using (11.22) the torque expression (11.17) becomes:

$$T_{\text{e}}^* (i_{\text{s}}^*) = \frac{3}{2} p_1 [\Psi_{\text{PMd}} + (L_{\text{d}} - L_{\text{q}}) i_{\text{di}}] \sqrt{i_{\text{s}}^2 - i_{\text{di}}^2} \times \text{sign}(T_{\text{e}}^*) \quad (11.23)$$

$$\Psi_{\text{s}} = \sqrt{(\Psi_{\text{PMd}} + L_{\text{d}} \cdot i_{\text{di}})^2 + L_{\text{q}}^2 (i_{\text{s}}^2 - i_{\text{di}}^2)}$$

- For maximum torque/flux quite an involuid condition is obtained:

$$(L_{\text{d}} \cdot i_{\text{d}\Psi} + \Psi_{\text{PMd}})^2 \cdot (2L_{\text{d}} - L_{\text{q}}) - L_{\text{d}} L_{\text{q}} \cdot i_{\text{d}\Psi} (\Psi_{\text{PMd}} + L_{\text{d}} i_{\text{d}\Psi}) + (L_{\text{d}} - L_{\text{q}}) \Psi_{\text{s}}^2 = 0 \quad (11.24)$$

The torque and stator flux expressions for this situation correspond to (11.23) but with  $i_{\text{d}\Psi}$  instead of  $i_{\text{di}}$ .

- For unity power factor d.c. excited SMs (Fig. 11.3a)

$$L_q \cdot i_q^* / \Psi_s^* = \sin \delta^* \cos \delta^* = (L_{dm} \cdot i_F^* - L_d |i_d^*|) \Psi_s^* \quad (11.25)$$

$$i_q^* / i_s^* = \cos \delta^*; T_e = \frac{3}{2} \Psi_s^* i_s^*$$

$$\text{So } \delta^* = \tan^{-1} \frac{L_q 2T_e^*}{3p_1 \Psi_s^{*2}}; |i_d^*| = \frac{2T_e^*}{3p_1 \Psi_s^*} \sin \delta^* \quad (11.26)$$

$$i_F^* = \frac{\Psi_s^* \cdot \cos \delta^*}{L_d} + L_d \cdot \frac{2T_e^*}{3p_1 \Psi_s^*} \sin \delta^* \quad (11.27)$$

A unity power factor corrector slower outer loop may be added in front of  $i_F$  (field current) regulator, based on the “reactive torque”, which is frequency rather independent.

$$T_{\text{reactive}} = \frac{Q_1}{\omega_1} = \frac{3}{2} p_1 \text{Re}(\bar{\Psi}_s \times \bar{i}_s^*) \quad (11.28)$$

Note. After presenting the principle of TVC (DTC) for IMs and various SMs, sample implementation case studies are provided.

Key component: the on-line stator flux observer with torque calculator. The TVC (DTC) of wound rotor IM (WRIM) or DFIG, with rotor side dual PWM converter control is similar to the above solutions [20]. And, again, direct active and reactive power (or torques) control of IMs and SMs is similar to TVC (DTC) for drives [20].

## 11. 4 Implementation of TVC (DTC) for CR – Ims

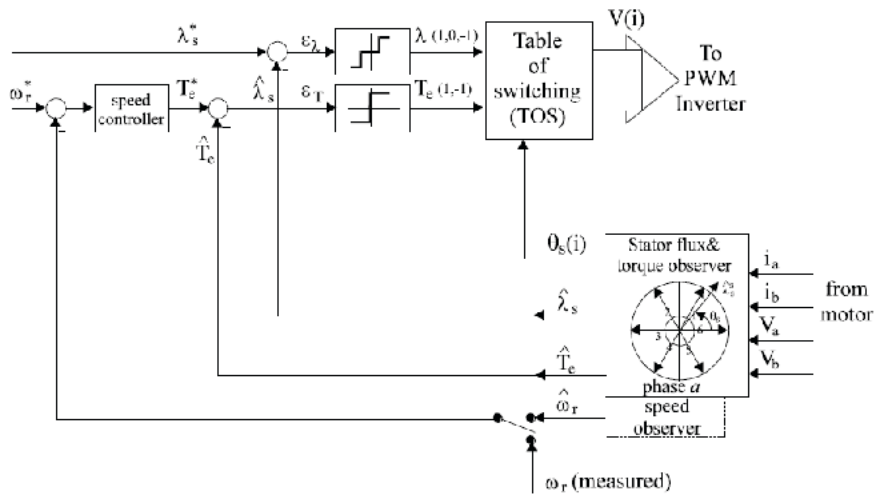
CR – Ims means cage – rotor induction motors. Apparently TVC (DTC) of CR – IMs is simple but during steady state notable torque and flux pulsations occur with the original (single voltage vector command at a time).

Quite a few methods to reduce torque and flux pulsations have been proposed so far for two (multiple) level voltage – source inverter drives.

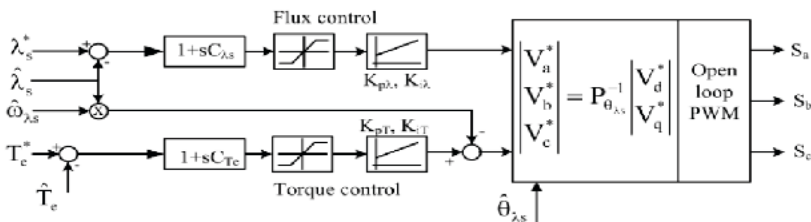
Here the encoderless TVC (DTC) drive with SVM is illustrated [21].

Figure 11.4a, b, shows such a generic control system.

The reference stator flux calculator (versus reference torque  $T_e^*$  and speed), the speed close loop regulator, stator flux and torque PI regulators and SVM structure are all visible in Fig. 11.4.



a)



b)

Fig. 11.4 Sensorless TVC (DTC) IM drive: a) generic scheme, b) SVM controllers and emf compensation.

The main part though is the stator flux observer (Fig.11.5).

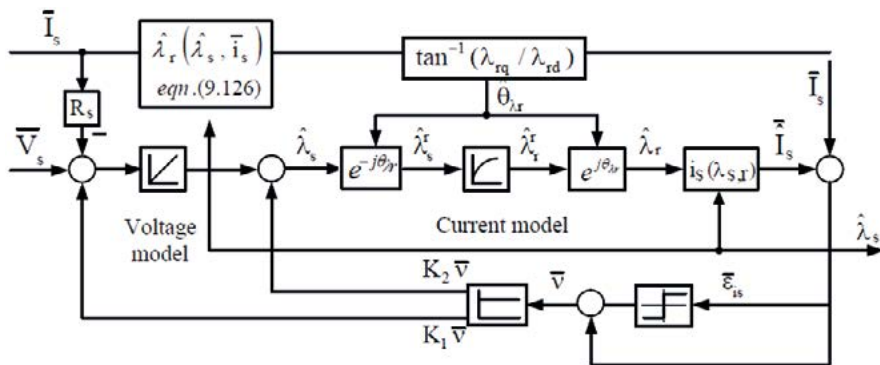


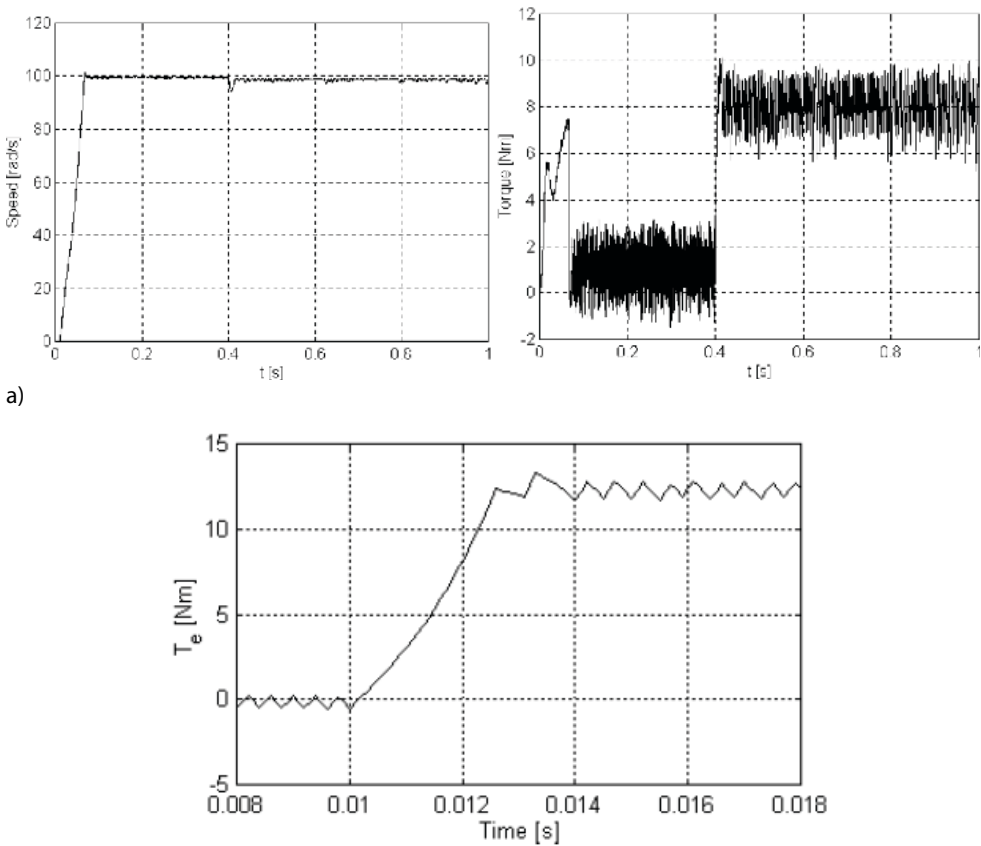
Fig. 11.5 Stator flux  $\Psi_s$  observer [2, 17, 18].

Figure 11.5 illustrates a typical combined voltage-current model observer suitable for a wide speed (frequency) range where the current – model is dominant at low frequencies, while the voltage model dominates at high frequency; some corrections for stator resistance and magnetic saturation may be added. The torque is simply:

$$\hat{T}_e = \frac{3}{2} p \text{Real} \left( j \hat{\Psi}_s \bar{i}_s^* \right) \quad (11.29)$$

where  $\hat{\Psi}_s$  is the flux observer output and  $\bar{i}_s$  is the measured stator current vector. A PLL observer using the equation motions and the estimated torque and rotor flux  $\hat{\Psi}_r$  angle (Fig. 11.5) should secure reliable speed estimation  $\hat{\omega}_r$  down to 3 rpm (0.1 Hz) [18].

No load starting experimental transients in a classical TVC (DTC) IM drive are shown in Fig. 11.6a. With SVM, the torque pulsations are drastically reduced (Fig. 11.6b) [2, 18].



b) Fig. 11.6 TVC (DTC) IM drive starting transients: a) classical; b) SVM.

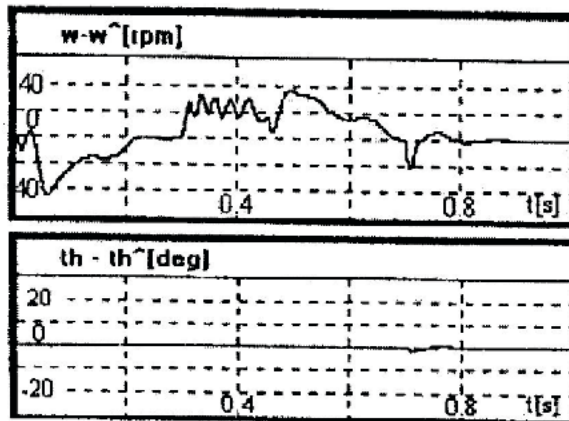
The notable reduction of torque pulsations by SVM without hampering the torque response quickness is evident.



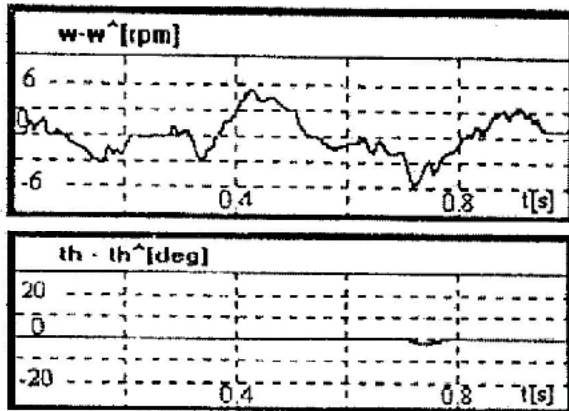


$$\begin{pmatrix} \hat{\theta}_{er} \\ \hat{\omega}_r \\ \hat{T}_{load} \end{pmatrix} = \begin{pmatrix} 0 & 1 & 0 \\ 0 & 0 & -p_1/J \end{pmatrix} \cdot \begin{pmatrix} \hat{\theta}_{er} \\ \hat{\omega}_r \\ \hat{T}_e \end{pmatrix} + \begin{pmatrix} 0 \\ p_1/J \\ 0 \end{pmatrix} \cdot \tilde{T}_e + k \cdot (\hat{i}_s - \hat{i}_s) \quad (11.30)$$

The load torque  $\hat{T}_{load}$  has the step signal class as an exogenous model. The coefficient  $k$  provides predictive correction of desired speed. Convergence and robustness, with  $\hat{T}_s$  estimated in a modified form of the stator flux observer in Fig. 11.7b and with the torque  $\hat{T}_e$  from (11.29). Typical results with such an observer for a PMSM are shown in Fig. 11.8.



a)



b)

Fig. 11.8 Speed & rotor position observer errors: a) at 1000 rpm, b) at 20 rpm [14,16].

Reasonably small errors are reported.

## 11.6 TVC (DTC) of synchronous reluctance machines (RSMs)

TVC (DTC) with SVM has been applied to RSM or PM – RSM as well. Without PMs, the RSM TVC (DTC) control is similar to that of PMSMs, but with  $\Psi_{PM}=0$  and  $L_d \gg L_q$ .

Sample experimental results on such a sensorless motor drive of 2.2 kW,  $L_d=0.32$  H,  $L_q=0.1$  H with standard and SVM TVC (DTC) are shown in Fig. 11.9 [8].

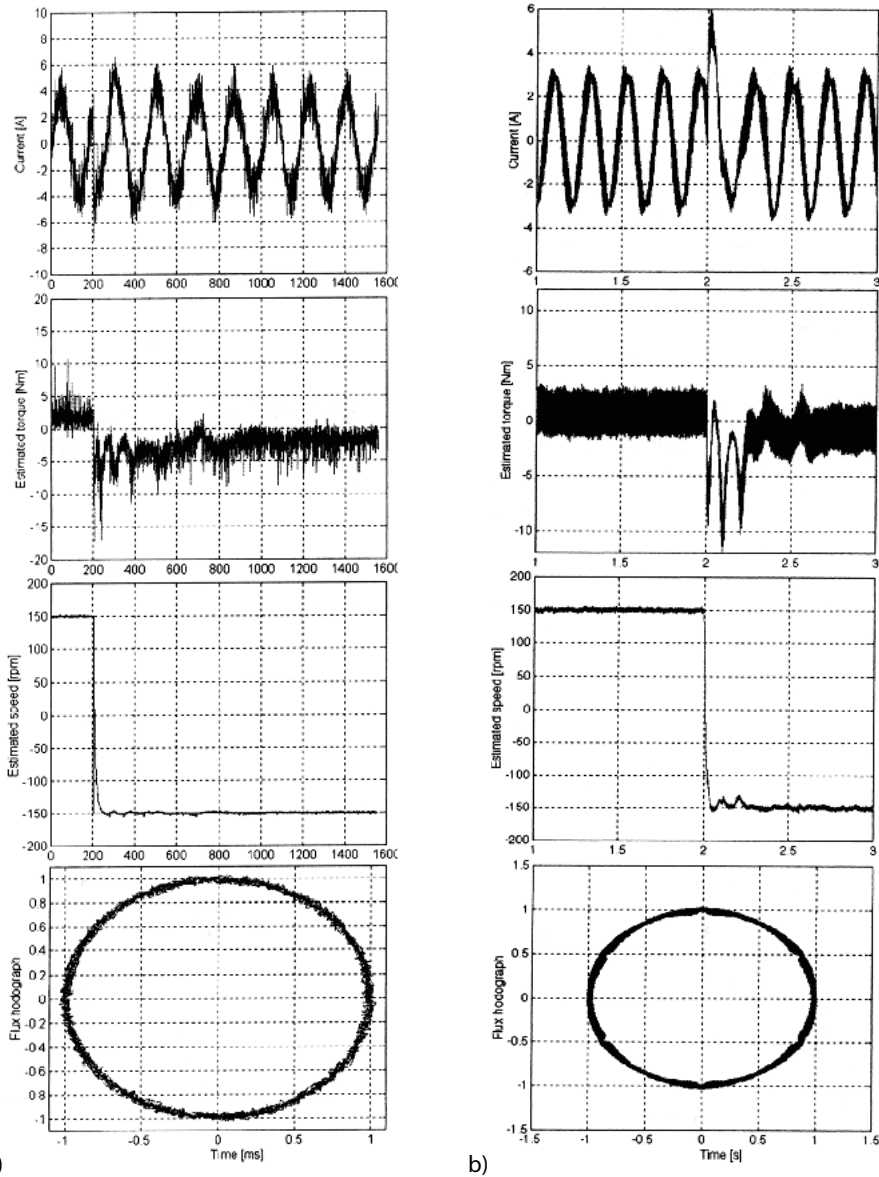


Fig. 11.9 TVC (DTC) of sensorless RSM speed reversal with SVM: a) test results; b) simulation results.

The drive was capable of safe sensorless operation down to 15 rpm [8, 18].



Thus with a subtransient flux  $\bar{\Psi}''$  is:

$$\bar{\Psi}'' = \bar{\Psi}_s - L_c \bar{i}_s \quad (11.31)$$

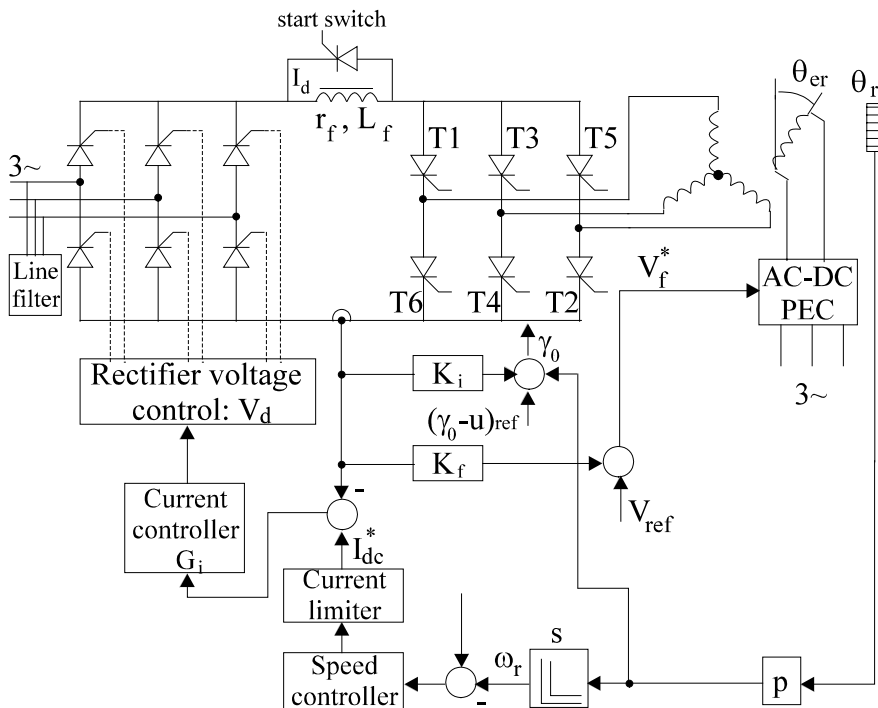
the torque  $T_e$  is:

$$\hat{T}_e = \frac{3}{2} p_1 \operatorname{Re} \left[ j \bar{\Psi}'' \cdot \bar{i}_s^* \right] = \frac{3}{2} p_1 \Psi'' \cdot i_{s1} \sin \gamma_i \quad (11.32)$$

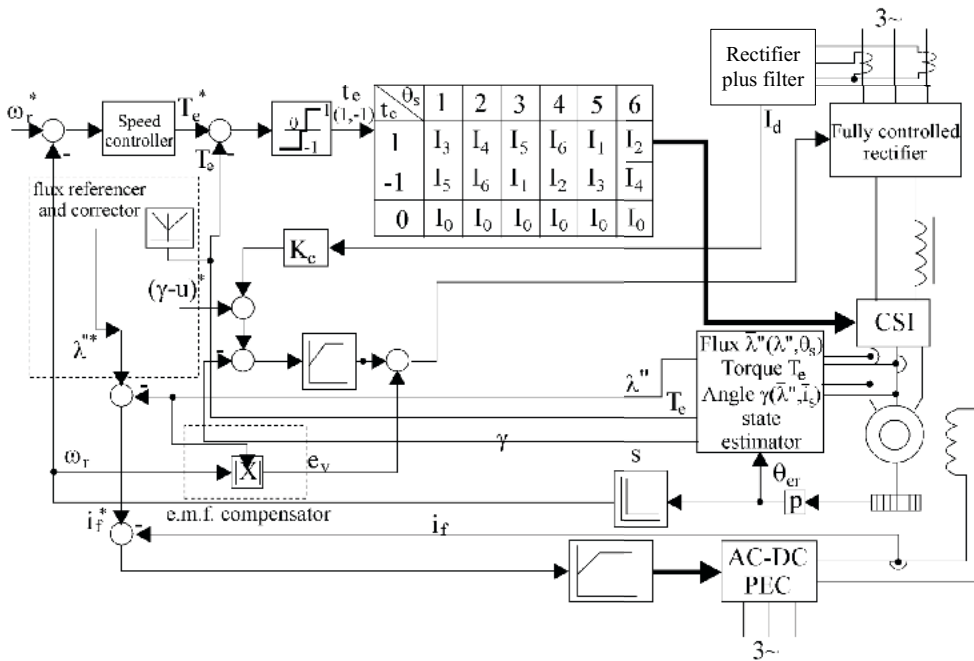
For  $\bar{\Psi}''$  in the first sector, a combination of  $I_1, I_2, I_3$  current vectors (in Fig. 11.11a) may be used to reduce torque pulsation in a kind of current SVM, as long as the flux/current angle  $\gamma_i$  increases.

A table of switching as in Fig. 11.11b is applicable. The generic TVC (DTC) is shown in Fig. 11.11b. The flux error is used to trigger the d.c. link voltage modification. For negative torque, a larger than  $90^\circ$  phase delay in the rectifier is used.

On the other hand, a negative “reactive” torque  $T_{\text{reactive}}^*$  is used in front of field current regulator to secure an interior leading small power factor angle  $\gamma_i$  ( $-(8^\circ-10^\circ)$ ).



a)



b)  
 Fig. 11.11 The current source inverter fed SM, a); block diagram, b).

It should be noticed that the d.c. link voltage reference increases with speed to secure fast d.c. link current response at all speeds.

For a machine to start, the emf is not enough to secure current commutation [23], a separate capacitor commutator in the d.c. link may be provided below 5% of rated speed.

A generic TVC (DTFC) of current inverter fed SM is portrayed in Fig. 11.11b.

### Conclusion

TVC(DTC) of induction and synchronous machines proved practical already in IM drives, while only in the laboratory level for SM drives, especially for encoderless torque, speed (or power) control mode when a state observer is nevertheless required.

## 11.8 References

- [1] I. Boldea, S.A. Nasar, "Vector control of a.c. drives", book, CRC Press, Florida, USA, 1992.
- [2] I. Boldea, S.A. Nasar, "Electric drives", book, 3<sup>rd</sup> edition, CRC Press, Florida, Taylor and Francis, New York, 2017.
- [3] F. Blaschke, "The method of field orientation for induction machine control", Forschungs- und Entwicklungsberichte (in german), 1972, pp. 184-193.
- [4] I. Takahashi, T. Noguchi, "A new quick response and high efficiency control strategy of an induction motor", *Record of IEEE-IAS-1995 and later in IEEE Trans*, vol. IA-22, no. 7, 1986, pp. 820-827.

- [5] M. Depenbrock, "Direct selfcontrol (DSC) of inverter-fed inductin machine", *IEEE Trans*, vol. PE-3, no.4, 1988, pp. 420-429.
- [6] I. Boldea, S.A. Nasar, "Torque vector control: a class of fast and robust torque, speed and position digital controllers for electric drives", *EMPS (now EPCS)*, vol. 15, 1988, pp. 135-147.
- [7] I. Boldea, Al Trica, "Torque vector control (TVC) voltage-fed inductance motor drives – very low speed performance via sliding mode control", *Record of ICEM-1990*, vol. 3, pp. 1212-1217.
- [8] I. Boldea, Z. X. Fu, S.A. Nasar, "Torque vector control (TVC) of axially – laminated anisotropic (ALA) rotor reluctance synchronous motors", *EMPS (now EPCS)*, vol. 19, 1991, pp. 381-398.
- [9] H. Y. Zhong, H. P. Messinger, M. H. Rashid, "A new microcomputer – based for 3-phase induction motor", *IEEE Trans*, vol. IA-27, 1991, pp. 294-298.
- [10] P. Tiitinen, P. Pohjalainen, J. Lalu, "Next generation motion control method: direct torque control (DTC)", *EPE Journal*, vol. 5, no.1, 1995
- [11] I. Boldea, "Torque vector control of a.c. drives", *Record of PCIM – 1992*, Europe, April, 1992, vol. IM, pp.20-25.
- [12] M.P. Kazmierkowski, A.B. Kasprowicz, "Improved direct torque flux control of PWM inverter – fed induction motor drive", *IEEE Trans*, vol. IE – 42, no.4, 1995, pp.344-350.
- [13] D. Casadei, G. Serra, "Constant frequency operation of DTC induction motor drive for electric vehicle", *Record of ICEM 1996*, vol. 3, pp.224-229.
- [14] G.D. Andreescu, "Robust direct torque vector control system with stator flux observer for PMSM drives", *Record of OPTIM*, 1996.
- [15] J. Kaukonen, "Salient pole synchronous motor saturation in a direct torque controlled drive", *Record of ICEM 1998*, Istanbul, Turkey, vol.3, pp.1397-1401.
- [16] I. Boldea, "Direct torque and flux control (DTFC) of a.c. drives: a review", *Record of PEMC - 2000*, Kosice, Slovakia.
- [17] C. Lascu, I. Boldea, F. Blaabjerg, "Variable structure direct torque control—a class of fast and robust controllers for induction machine drives", *IEEE Trans*, vol. IE-51, 2004, pp. 785-792.
- [18] C. Lascu, I. Boldea, F. Blaabjerg, "Direct torque control of sensorless induction motor drives – a sliding mode approach", *IEEE Trans*, vol. IA-40, no. 2, 2004, pp. 582 – 590.
- [19] C. Lascu, I. Boldea, F. Blaabjerg, "Supertwisting sliding – mode control of torque and flux in PMSM drives", *Record of IEEE-IECON*, 2013, Vienna, (IEEExplore).
- [20] I. Boldea, "Variable speed generators", 2<sup>nd</sup> edition, CRC Press, Florida, Taylor and Francis, New York, 2016.
- [21] C. Lascu, I. Boldea, F. Blaabjerg, "A modified direct torque control (DTC) of induction motor sensorless drives", *Record of IEEE-IAS*, 1998, pp. 415-422.
- [22] I. Boldea, L. Janosi, F. Blaabjerg, "A modified direct torque control (DTC) of reluctance synchronous motor sensorless drive", *Journal of EMPS*, vol. 28, no. 2, pp. 115-128.
- [23] I. Boldea, L. N. Tutelea, "Electric machines: steady state, transients and design with MATLAB", book, CRC Press, Florida, 2010.

## Abstract

Linear motion by direct electromagnetic force is produced in linear electric machines (LEMs).

LEMs are obtained by cutting axially and unrolling rotary electric machines. Therefore, in principle, for every rotary electric machine there may be a linear counterpart. The LEMs have numerous applications in industry, from transportation and launchers on wheels and with active magnetic suspension, to linear oscillatory motors for compressor drives with reciprocating motion etc.

Moreover, speakers and microphones everywhere are linear 1 phase oscillatory motors/generators while the solenoid actuators are also linear motors.

Invented already before 1900 (as linear reluctance motors), LEMs have revived with the maturing of power electronics and rotary electric machine control for variable speeds. The elimination of mechanical transmission and the capacity to integrate propulsion and active magnetic suspension (in MAGLEVs) are the main merits of LEMs, with power electronics and motion control.

LEMs have gained wishes of commercialization, there are still R&D strong efforts worldwide to develop them further from improved strategies, modeling optimal design and control for ever more diversified applications [1, 2].

This chapter presents selected UPT contributions from 1970 to 2020, meandering through quite a few different types of LEMs, from those for interurban and urban people movers on wheels and on MAGLEV, to short haul industrial transport plunger solenoids valve actuators and linear oscillatory LEMs for small compressors and for microphones and loudspeakers.

## 12. 1 LEMs classification

LEMs are obtained from rotary machines by cutting and unrolling (Fig. 12.1).

LEMs classification may be done by topology (tubular or flat-single or double sided), by principle, by linear motion nature (progressive or oscillatory) and by application.

By principle, LEMs are classified as:

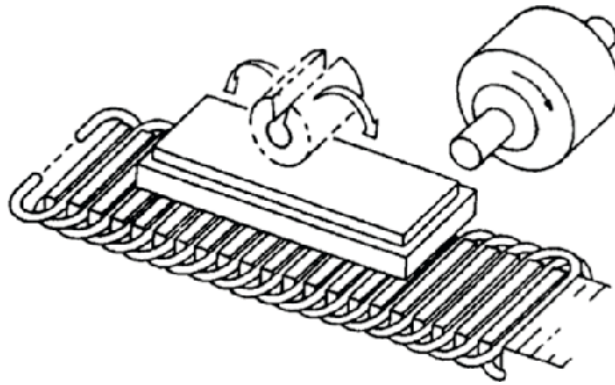


Fig. 12.1 Cutting and unrolling of a rotary machine to obtain a linear counterpart.

- Linear induction motors (LIMs): Fig. 12.2 in a passive guideway (aluminum plate on an iron slab) MAGLEV
- dc. excited linear synchronous motors (LSMs): Fig. 12.3 in an active guideway (long stator) MAGLEV
- Homopolar linear synchronous motors (H-LSMs) MAGLEV: Fig. 12.4
- PM linear synchronous motors (PM-LSMs) MAGLEV: Fig. 12.5a
- Linear dc. Brush PM motors: Fig. 12.5b
- Plunger solenoids: Fig. 12.6
- Linear oscillatory PM compressor motors: Fig. 12.7



Fig. 12.2 Single-sided LIM-LINIMO-MAGLEV in Japan

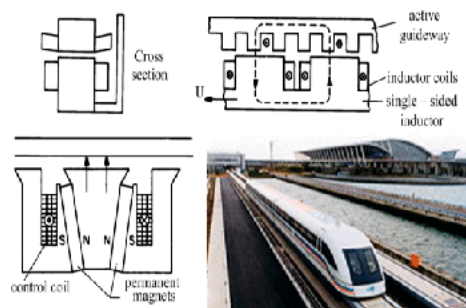
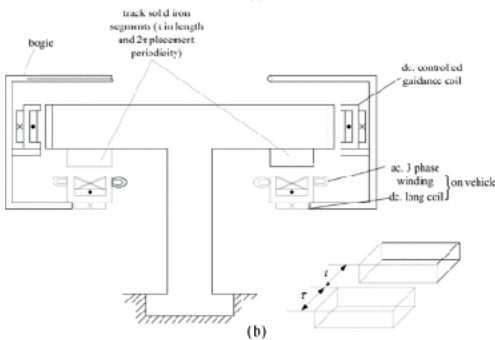


Fig. 12.3 Active guideway d.c. excited LSM MAGLEV vehicle (Transrapid, Germany)



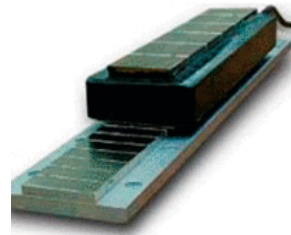


(a)

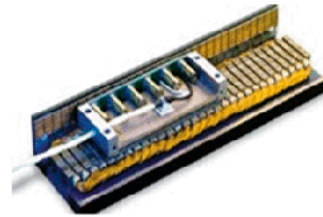


(b)

Fig. 12.4 Homopolar LSM passive guideway MAGLEV (Magnibus RO).



(a)



(b)

Fig. 12.5 Commercial iron-core PM-LSM (double sided) a) and DC brush PM linear motors b).







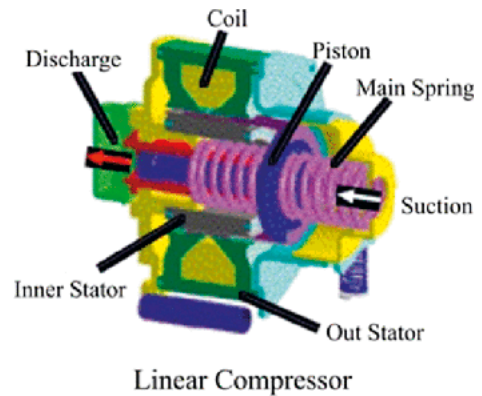
						
	Tubular solenoids	Low profile solenoids	Soft shift solenoids	DC Open Frame	AC Open Frame	Laminates
Solenoid power	Average power consumption; moderate force output.	Average power consumption; high force output.	Average power consumption; moderate force output.	Higher power consumption; moderate force output.	Higher power consumption; moderate force output.	Higher power consumption; highest force output.
Solenoid life	25 million operations for STA models.	1 to 5 million cycles.	10 million cycles.	50,000 to 100,000 cycles.	20,000 to 100,000 cycles.	50,000 to 100,000 cycles.
Solenoid operation	Push/Pull engagement; well suited to lock/latch operations.	Push/Pull engagement; well suited to lock/latch operations.	Quiet operation with 3.5 times the starting force of standard solenoids.	Push-in engagement.	Push-in engagement.	Push-in engagement.
Force	Up to 97.85 N	Up to 335.86 N	Up to 133.05 N	Up to 133.02 N	Up to 133.7 N	Up to 133.05 N
Stroke	1 to 63.5 mm	Up to 9.525 mm (0.75 mm minimum)	Up to 9.525 mm	Up to 25.4 mm	Up to 25.4 mm	Up to 51.75 mm

Fig. 12.6 Sample commercial solenoids.



Linear Compressor

Fig. 12.7 Commercial linear oscillatory PM motor for compressors.

A myriad of topologies for LEMs have been proposed, but in essence they may be treated at low speeds as counterparts of respective rotary electric machines.

However, the open character of their magnetic circuit leads at high speeds (in general above 10 m/s) to dynamic longitudinal effects that reduce thrust normal (levitation) force, power factor and efficiency.

Furthermore, the solid nature of aluminum sheet and solid back iron (slab) in the secondary of LIM warrants the consideration of edge and skin (frequency) effect that influence performances well.

In what follows, reference will be made to various LEMs with respect to notable UPT contributions, noticing first the main scientific works in English and German on the subject since 1968 [2-12].

### 12.2 Linear induction motors

LIMs are in general built with short primaries and excursion-long secondary, mainly flat and single-sided topologies.

The short primary holds a single or 3 phase single layer or double layer windings with  $2p$  or  $(2p+1)$  total numbers of poles[Fig 12.8].

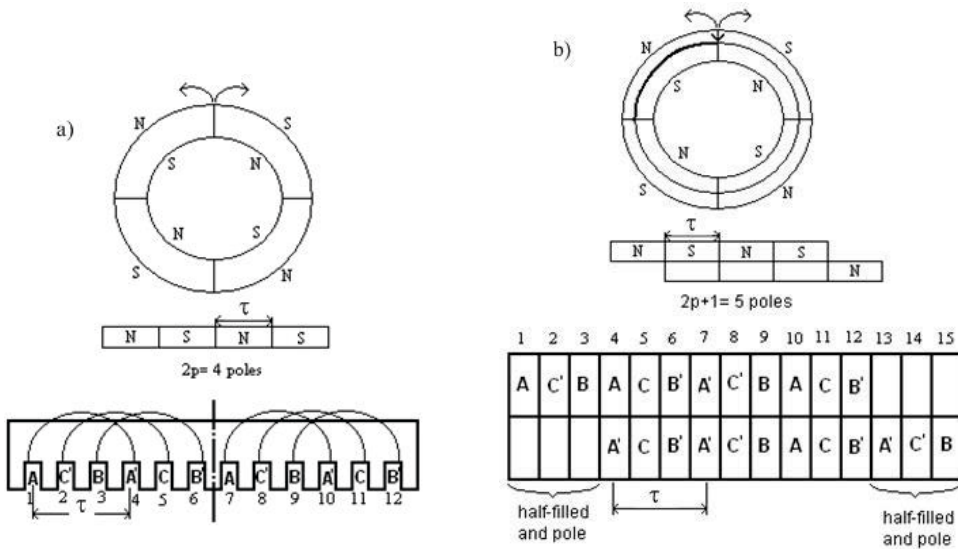


Fig. 12.8 LIM windings: a) single layer  $2p=4$ ,  $q=1$  slot/pole/phase; b) double layer:  $2p+1 = 5$ ,  $q=1$ .

The double layer winding is preferred in large high speed LIMs as shown slightly lower dynamic longitudinal effect (for  $2p+1 >=5$ ) and it is easier to make a lowing also chorded coils, but it uses less completely the core due to half-wound end poles [5]. Technical theories for LIMs, considering dynamic longitudinal effects, have been developed easily [4-7]. However, [5] presents a rather complete such theory including the skin and edge effects, too. First, we shall define an equivalent goodness factor  $G_e$ :

$$G_e = \frac{L_m}{R_2'} \approx \frac{\mu_0 \tau^2 \omega_1 \sigma_{AL} d_{AL}}{\pi K_{tr} K_{skin} g K_c (1 + K_{siron})} \quad (12.1)$$

where:  $L_m$  - cyclic magnetizing inductance,  $R_2'$  - secondary aluminum sheet equivalent resistance,  $K_{tr}$  - transverse flux coefficient;  $K_{tr} = 1.3 - 1.5$  if  $(c - a) \approx \tau / \pi$  (Fig. 12.9); that is a reasonable aluminum overhang is allowed;  $K_{skin}$  - skin effect coefficient  $K_{skin} = 1.05 - 1.2$ , depending on the slip frequency in the secondary;  $g$  - mechanical airgap,  $\omega_1$  - primary frequency,  $\tau$  stator winding pole pitch,  $k_c$  - Carter coefficient,  $K_{siron}$  - magnetic core contribution to "airgap".

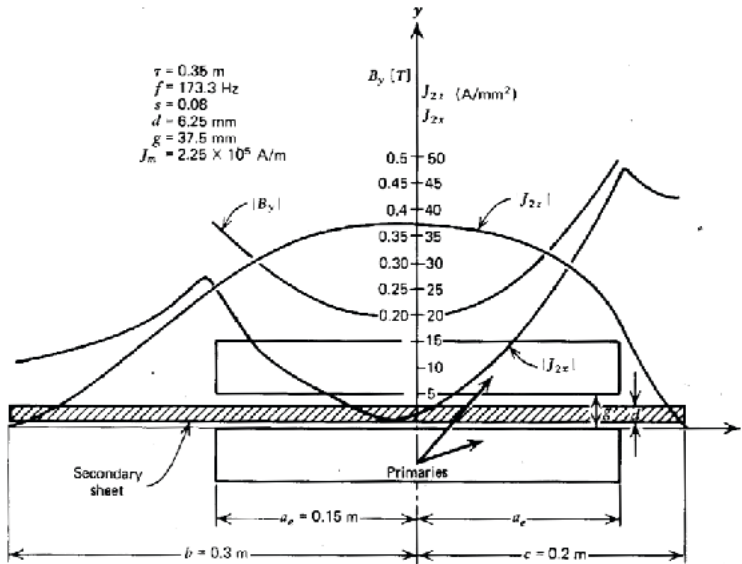


Fig. 12.9 Edge effect on secondary currents and airgap flux density distribution [6] in a double sided LIMaA.

For a single sided LIM, SLIM, the aluminum sheet is placed on a solid back iron slab which experiences magnetic saturation and eddy current that require a complicated theory. However, a simplified solution was obtained by an analytical adoption of (12.1) by replacing  $\sigma_{AL}$  with  $\sigma_{se}$  and  $g_{se}$  to obtain:

$$G_e = \frac{\mu_0 \tau^2 \omega_1 \sigma_{se} d_{AL}}{\pi^2 g_{se}} \quad (12.2)$$

with  $g_{se} = (g + h_{AL})K_c(1 + K_{sat})$  where  $K_{sat}$  allows for the solid iron with variable (12.3) skin effect  $\delta_i$  and variable permeability  $\mu_{iron}$  to the airgap  $g_{se}$ .

Similarly  $\sigma_{se}$  includes the contributions of aluminum sheet ( $d_{al}$  - thick) and solid back iron ( $\delta_i$  - thick) to the secondary equivalent conductivity including also the edge effects [6].

$$\sigma_{se} = \frac{\sigma_{AL}}{K_{trAL}K_{skin}} \left( 1 + \frac{\sigma_{iron}}{\sigma_{AL}} \delta_i \frac{K_{trAL}K_{skin}}{K_{tiron}d_{AL}} \right) \quad (12.3)$$

The above definition of equivalent goodness factor which includes skin edge and magnetic saturation effects allows to develop a quasi-one-dimensional theory for the dynamic-end effect whose principle is illustrated in Figure 12.10.

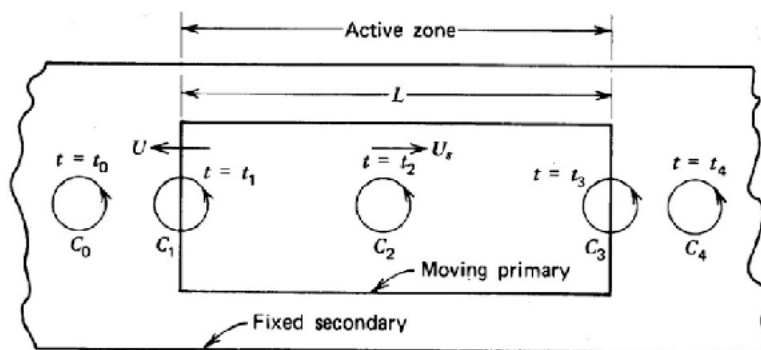


Fig. 12.10 Dynamic end effect in LIM.

The dynamic end (longitudinal) effect is due to new secondary (electrically conductive) sections of long secondary entering and exiting the short stator core and mmf zone consequently, additional current density occurs at the entry zone, mainly, and travels attenuated a length  $L_{ee}$  within the core of similar, though a smaller effect occurs at the primary exit.

In general, if  $L_{ee} \approx 3T_{e2} = 3 \frac{G_e}{\omega_1}$ . The dynamic end effect may be neglected [6,2].

$$L_{ee} \approx 3T_{e2} = 3 \frac{G_e}{\omega_1} \quad (12.4)$$

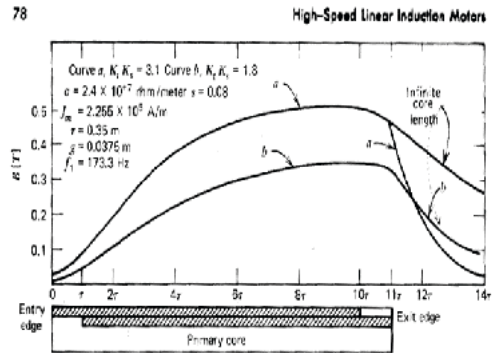
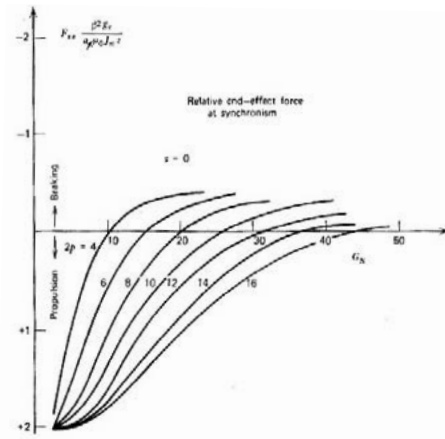
The consequences of dynamic end effect may be summarized as:

- an end effect thrust (positive or negative)  $F_{xe}$  In addition to the conventional thrust  $F_{xc}$  which depends only on the equivalent goodness factor  $G_e$ , slips, pole pairs  $p$  and the stator magneto motive force (mmf)

- the entry end magnetic field wave pole pitch  $\tau_e$  is

$$\frac{\tau_e}{\tau} = \frac{U_{se}}{U} = \frac{2}{\frac{G_e}{2} \left[ \sqrt{1 + \frac{16}{G_e^2 (1-s)^2}} - 1 \right]^{1/2}}$$

and produces a nonuniform total thrust, normal force, airgap flux density, secondary current density distribution along the primary core length (Fig. 12.11a,b).



a)

b)

Fig. 12.11 Dynamic end effect thrust  $F_{xe}$  a) and nonuniform airgap flux density b).

Giving the changing of sign of dynamic end effect force at a certain slip  $s$  for a given LIM with given  $2p(2p+1)$  poles primary and  $G_e$

Ref. [6] defined an optimum equivalent goodness factor  $G_{e0}$ , when, for zero slip ( $s = 0$ ), the dynamic end effect thrust  $F_{xe}$  is:

$$(F_{xe})_{\delta=0} = 0 \Rightarrow G_{e0} \quad (12.6)$$

It turns out that the optimum equivalent goodness factor depends only on the number of poles  $2p$  of the primary winding (Fig. 12.11) [6].

This observation greatly simplifies the design of high speed (above 10m/s) LIMs for industrial, urban, suburban or interurban transport on wheels or in MAGLEVs (see [2] for more details).

### 12.3 Homopolar linear synchronous (H-LSM) motors MAGLEV

The H-LSM topology, illustrated in figure 12.12, evidentiates:

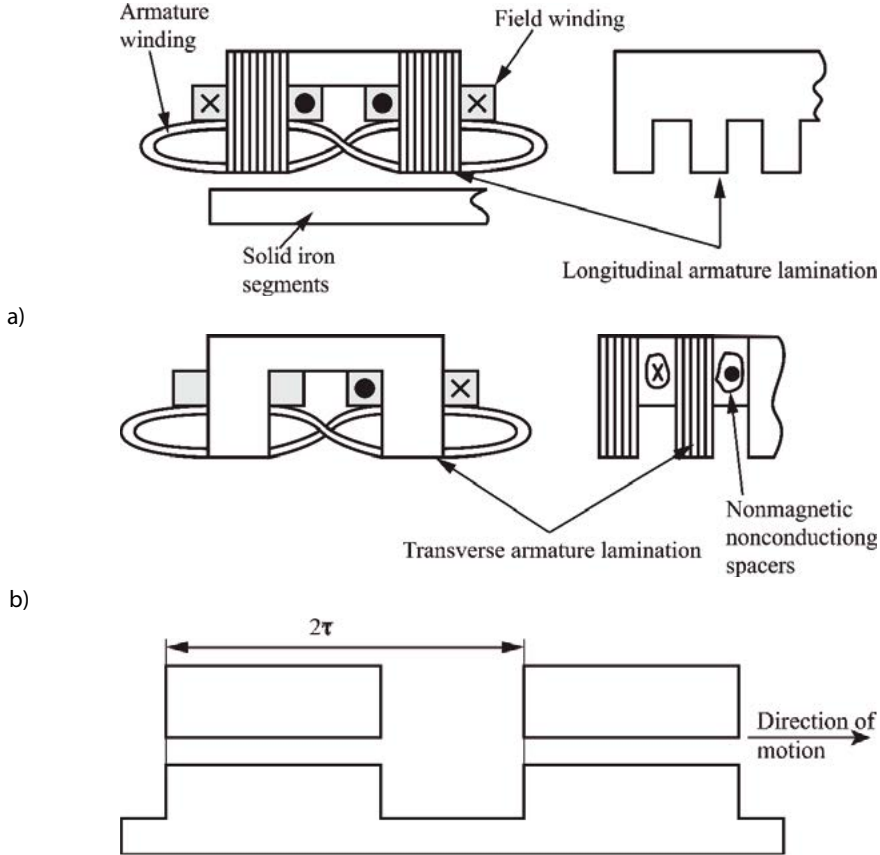


Fig. 12.12 H-LSM layout a) with longitudinal laminations, b) with transversal laminations in the primary core, c) solid segments in the secondary  $2\tau$  – apart.

- The segmented secondary (passive track) made of solid iron (low cost)
- The 8-shape (for separate) a.c coils on the two legs of the core with straight iron segments in the track.
- The d.c (excitation) coils are placed also on the primary behind the a.c coils: they provide a max-min airgap flux density in fact with rotor iron segments, whose fundamental (only) produces emf in the a.c winding for propulsion,  $F_x$ .
- The entire d.c. airgap flux density, although produces attraction, normal, levitation forces,  $F_n$ , which turns to be around:  $F_n \approx 10F_x$ , which for a  $1\text{m/s}^2$  vehicle acceleration requires the H-LIM to represent up to 10% of total vehicle weight, which is quite feasible (Fig. 12.13). This paves the way for integrated propulsion and levitation by H-LSM.

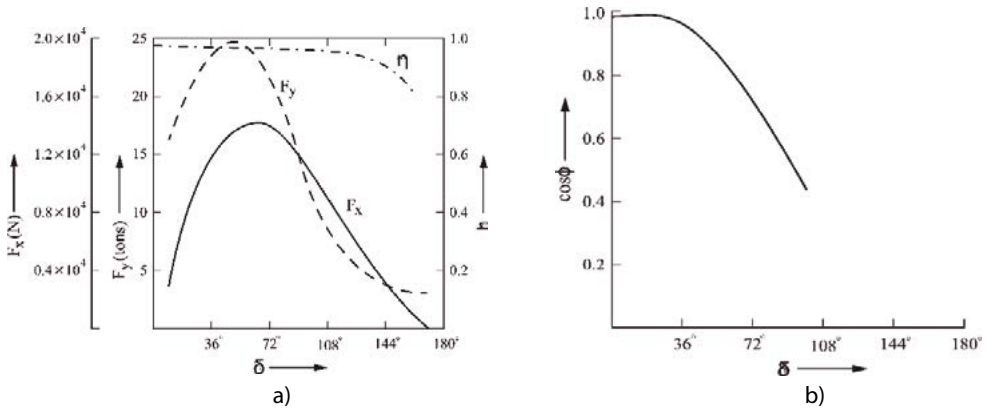


Fig. 12.13 Forces, a) and power factor, b) of angle spread H-LSM ( $U_s = 90\text{m/s}$ ,  $2p = 12$ ,  $\tau = 0.45\text{m}$ ,  $g = 0.02\text{m}$ ,  $2a = 0.25\text{m}$  core legs width,  $w_{\text{fil}} = 30\text{kAturns}$ ,  $v_s = 3\text{kV}$  (RMS); speed  $U_s = 2\tau f_1$  [6]).

- The Magnibus.Ro in figure 12.4[2] makes use of such 4 H-LSMs for integrated propulsion and active suspension (by the control of d.c coils currents). In a single bogie prototype of 4 tons, tested on an 150m long track at UPT (with the generous support of Electropower works Craiova, Romania, from 1970 to 1985), proving at 10m/s a total efficiency of 80% and the power factor (on propulsion) of 0.8,, arguably still the best to our best knowledge.

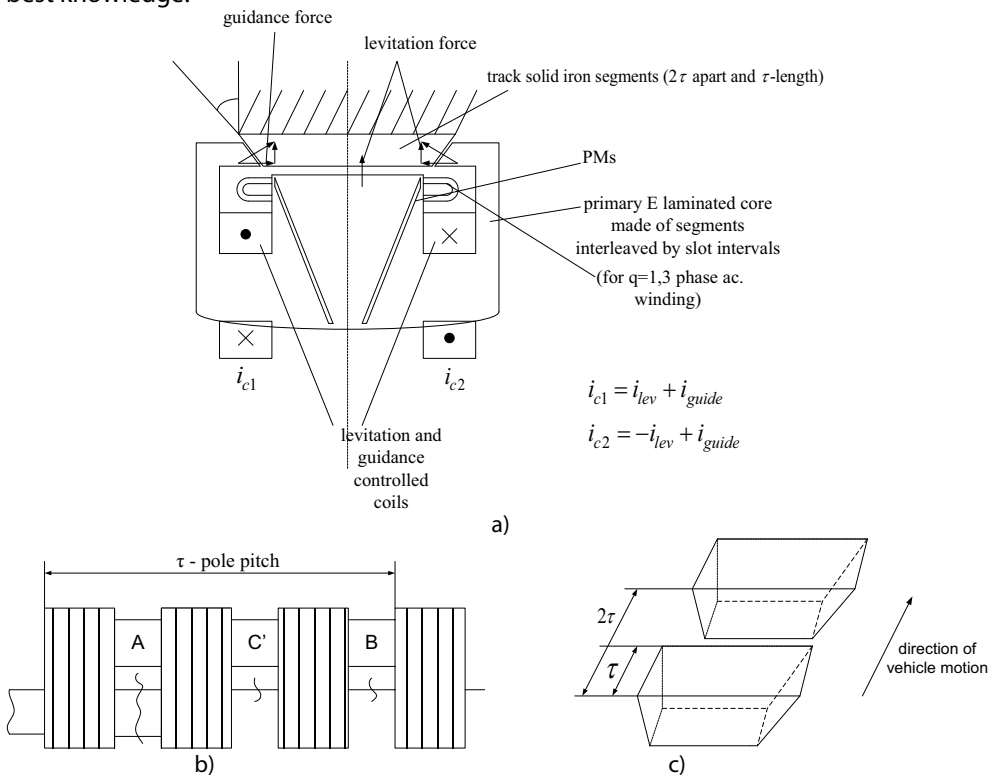


Fig. 12.14 PM assisted H-LSM MAGNIBUS RO concept a) cross section, b) track segments, c) a.c. winding.

- Novel topology (Fig. 12.14) might be capable of integrating levitation, guidance and propulsion by H-LSM in a suspended MAGNIBUS concept when the two d.c. coils are controlled with currents  $i_{c1}$  and  $i_{c2}$  which are different to provide guidance and levitation control:

$$\begin{aligned} i_{c1} &= i_{lev} + i_{guide} \\ i_{c2} &= i_{lev} - i_{guide} \end{aligned} \quad (12.7)$$

## 12.4 PM plunger solenoid for valves actuation

Independent valve actuators for multicylinder internal combustion engines are required to produce fuel consumption at variable load. Besides existing common rail mechanical actuators, individual valve rotary electric actuators with special transmission have been proposed, together with plunger solenoids direct actuation.

However, independent actuation of valves has to meet energy consumption and available volume to install severe limits.

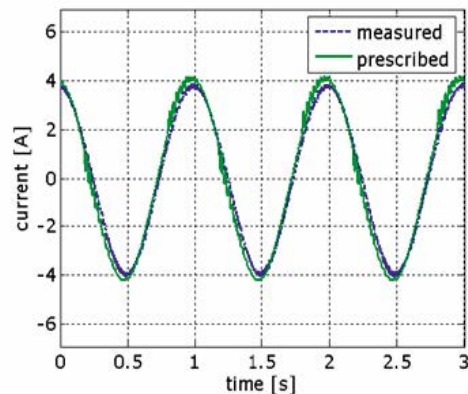
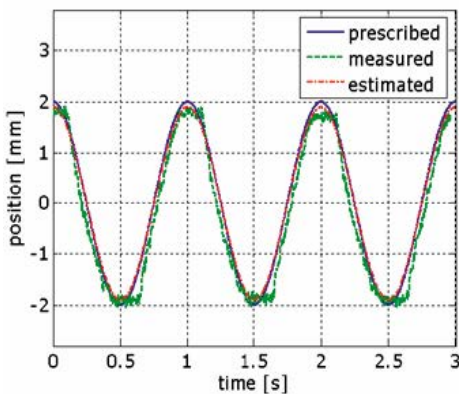
Typical specifications for a medium car ICE engine valves are:

- $F_{x \max} > 300 \text{ N}$
- $a_{\max} \geq 5 \text{ km/s}^2$  (max. acceleration of the valve mover)
- $p_{copper} < 120 \text{ W}$  (average copper losses/valve)
- actuator volume: vol < 0.2 litres.

A PM-assisted plunger solenoid was proposed for the scope (Fig. 12.15)

A rounded study including FEM-based multiphysics optimal design code was used for the scope and an advanced position control – with and without linear encoder was added.

A prototype was built with controlled valve-position sample results as in Fig. 12.16 [2,13].



a)



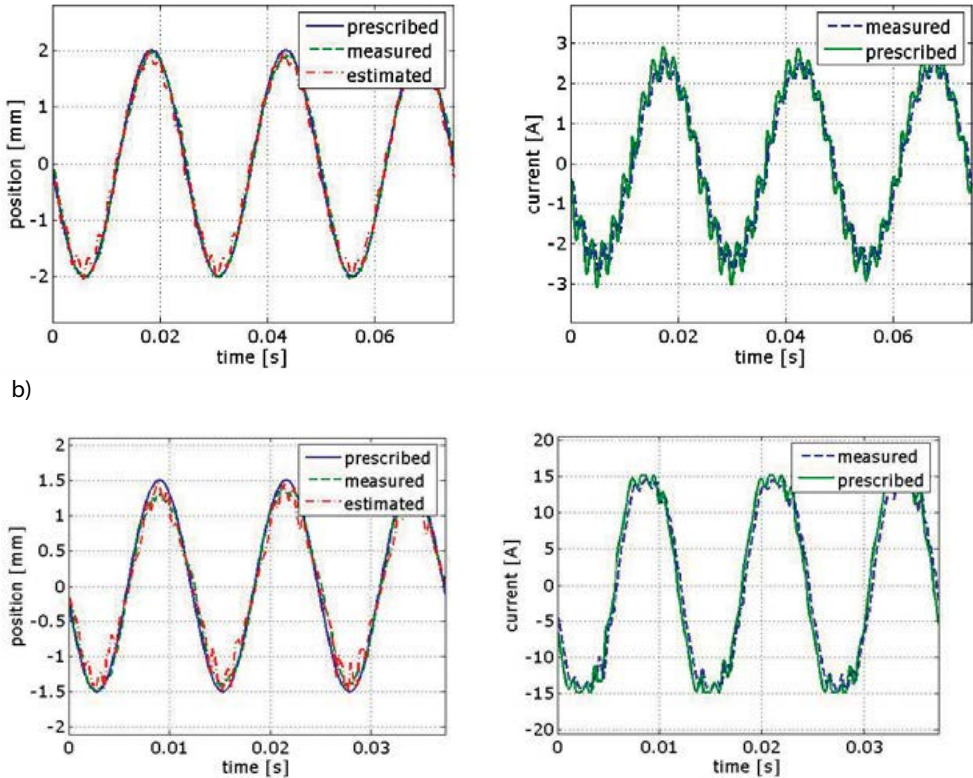


Fig. 12.16 Close loop position encoder-less control of a PM assisted 1 phase linear oscillatory PM motor drive: a) 1Hz, b) 40Hz, c) 80Hz.

Quite a few alternative topologies for liner oscillatory PM machines have been investigated [2]. Among them, one with stator PMs[14,2] and tow with moving PMs [15,2] stand out as competitive. Finally, the elimination of the resonant mechanical spring, by using the cogging force as a spring for resonance was proposed in [16-17].

### 12.5 Springless resonant linear PM oscillomotor

One phase linear oscillatory PM motor operate at resonance- to increase efficiency – by using mechanical springs(flexures) calibrated for the scope such a device may operate line – started (at the power grid) or feed from a single phase inverter.

For frequencies of oscillation in the 50-60Hz, even for powers lower than 1kW, the size of the mechanical spring is larger and its calibration to resonant frequency is tedious.Thus, designing a springless resonant linear PM oscillomotor becomes tempting. Using the cogging of oscillomotor to eliminate the spring has to fulfill the condition that the cogging force is selfcentring and varies linearly with mover position up to the maximum active excursion amplitude. Such a topology obtained through FEM trials is shown in Fig. 12.17 for a 2kW at 40-50Hz, 90% efficiency for 10kg of weight [16, 17].

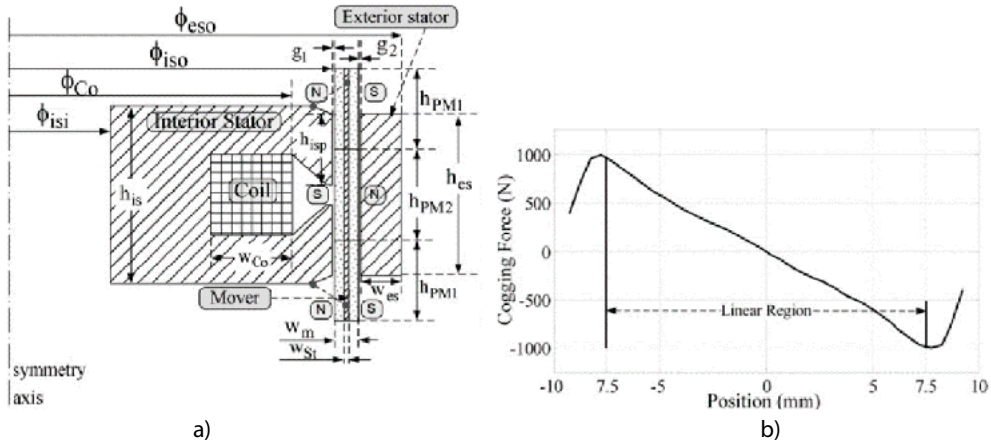


Fig. 12.17 Springless linear PM oscillomotor a) cross-section, b) cogging force versus mover position.

As visible in figure 12.17, the springless configuration contains:

- A single circular-shape coil with a “U shape” SMC core and an axial airgap
- In the axial airgap a disk shape PM magnet mover is placed; the PM mover shows radially 3 magnet poles, if alternate polarity magnetized axially
  - There is another disk-shape stator core to close the PM flux lines
  - The 3 poles (MSM) mover geometry leads to the rather large selfcentring cogging force which varies linearly with radial mover position, exploiting 75% ( $l_{stroke}=15\text{mm}$ ) out of ideal 100% (20mm) stroke length.

It remains now to be seen if this cogging force (magnetic) spring may provide enough springing effect for a resonant frequency in the 40-50Hz for a practical mover total weight (load mover + PM mover).

### 12.5.1 Preliminary design

After a preliminary design, a tentative geometry is obtained for the given specifications.

Let us notice that the “magnet” spring rigidity  $k$  is:

$$K = \frac{F_{cogg \max}}{X_{\max}} = \frac{1000}{0.0075} = 133,333 \quad (12.7)$$

For a PM mover mass of 1.5kg plus 0.5kg for its siluminium fixture:  $m_{mover} = 2 \text{ kg}$ .

The mechanical resonant frequency  $f_m$  is:

$$f_m = \frac{1}{2\pi} \sqrt{\frac{K}{m_{mover}}} = \frac{1}{2\pi} \sqrt{\frac{133,333}{2}} \approx 41,41 \quad (12.8)$$

The average mover speed  $u_{sav}$  for  $l_{stroke} = 15 \text{ mm}$  and  $f_m = 41.41 \text{ Hz}$  is:

$$u_{sav} = 2l_{stroke} f_m = 2.0,015.41,41 = 1,24$$

FEM calculation for a 2400 Atturns (constant) in the coils shows the total thrust (PM and cogging force)  $F_x$  asin Fig. 12.18 [1].

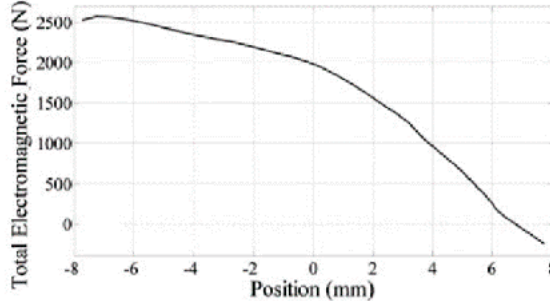


Fig. 12.18 Total thrust versus mover position (zero corresponds to control point at 2400 Atturns (constant) per coil).

It is evident that the total thrust keeps positive for the entire stroke length of 15mm for constant current (mmf) in the coil. In reality, the current may vary trapezoidally (or sinusoidally) with mover position according to the control option.

The circuit model of this one phase PM linear oscillomotor is:

$$V = Ri + \frac{\partial \psi}{\partial i} \frac{di}{dt} + \frac{\partial \psi}{\partial x} \frac{dx}{dt} \quad (12.9)$$

$$m \frac{d^2 x}{dt^2} = F_x - F_{load} - F_{friction} \quad (12.10)$$

$$F_x = \frac{\partial \psi}{\partial x} i + F_{cogg} \quad (12.11)$$

The load force  $F_{load}$  may be considered proportional to speed:

$$F_{load} = K_L \frac{dx}{dt} \quad (12.12)$$

The mechanical load power  $P_m$  is:

$$P_m = \frac{1}{2} K_L (2\pi f_m X_{max})^2 \quad (12.13)$$

So, from given  $P_m$ ,  $K_L = 1017 \text{ kg/s}$  calculated from (12.13) for  $X_{max} = 0.0075 \text{ m}$ ,  $f_m = 41.41 \text{ Hz}$ ,  $P_m = 1937 \text{ W}$ .

Considering sinusoidal oscillatory motion:

$$x(t) = X_{\max} \sin \omega t \quad (12.14)$$

Finally, the machine design parameters are given in table 12.1.

Table 12.1 Linear machine parameters.

Parameter name	Symbol	Value
RMS rated voltage	V	220 V
RMS rated current	I	11.8 A
Rated efficiency	$\eta$	0.91
Average power	$P_m$	1.93 kW
Number of turns	N	152
Armature resistance	R	0.7512 $\Omega$
Average inductance	L	0.0344 H
Mover mass	m	1.97 kg

Due to the magnetic saturation, the family of magnetization curves  $\psi(x, i)$  and  $F_x(x, i)$  are required. They are obtained from FEM (Fig. 12.19).

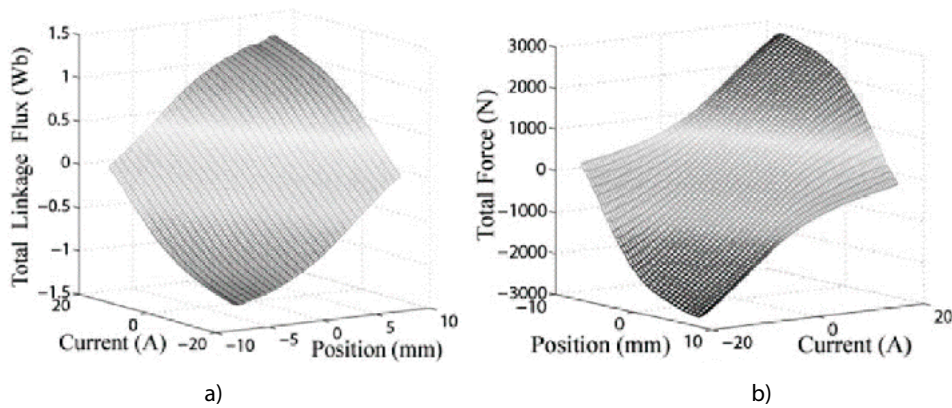


Fig. 12.19 Flux linkage  $\psi$  a), and total thrust  $F_x$  versus current  $i$  and mover position  $X$  (FEM calculated)  $i_{\max} = \pm 17A$ .

In heavy transients the current may go higher (to 50A).

Therefore, further FEM calculation of  $L(x, i)$  and  $d\psi/dx(x, i)$  up to  $\pm 50 A$  are required (Fig. 12.20).

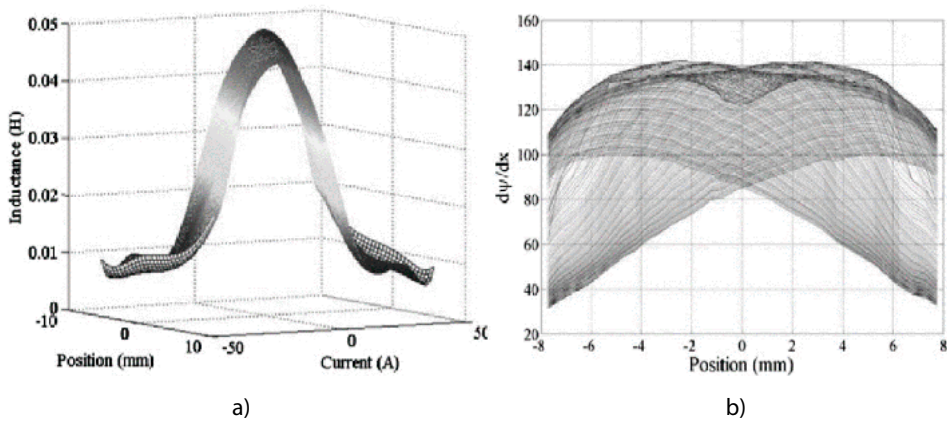


Fig. 12.20 Inductance  $L$  a) and  $d\psi/dt$  b) versus current  $i$  and position  $x$  for up to  $\pm 50A$ .

Fig. 12.20 shows clearly that despite the surface PMs, the inductances varies dramatically for large currents (up to 3 times rated current).

### 12.5.2 The dynamic model and the close loop position control system

The thrust production ( $d\psi/dx$ ) is reduced towards stroke length ( $x_{mx} = \pm 7.5$  mm). Fortunately, there (around ...) a large thrust ... is not needed.

The dynamic circuit model with FEM imputed data from FEM (Fig. 12.14-12.20) is augmented with an additional fictitious spring having a large stiffness  $K_{Ec} = 50$  MN/m. This fictitious strong spring has the role of a slightly elastic wall (material) that accounts for the mover kinetic energy exchanged in the inelastic collision ( $K_{ie} = 4300$  kg/s) that occurs at stoke ends. Also  $K_F = 1.93$  N accounts for kinetic friction for  $F_f$  ( $F_f = K_F = m_{mover} g \mu = 1.97$  kg  $\times$   $4.81$  m/s<sup>2</sup>  $\times$   $0.1 = 1.93$  N).

The core losses are calculated also by FEM [17].

The value of core losses are  $p_{iron} \approx 140$  W.

The steel cylinder in the mover (to keep the rotor) may be placed by a siluminum structure, but it is to be seen if such a change is beneficial (iron losses in the mover amount to 97.5 W out of a total of 140 W). It should be noted that both eddy current losses in the siluminum mover structure and its contribution to reduce the mover weight have to be considered in the comparison with the thin iron cylinder mover fixture.

Finally, the dynamic model of the machine is shown in Fig. 12.21.

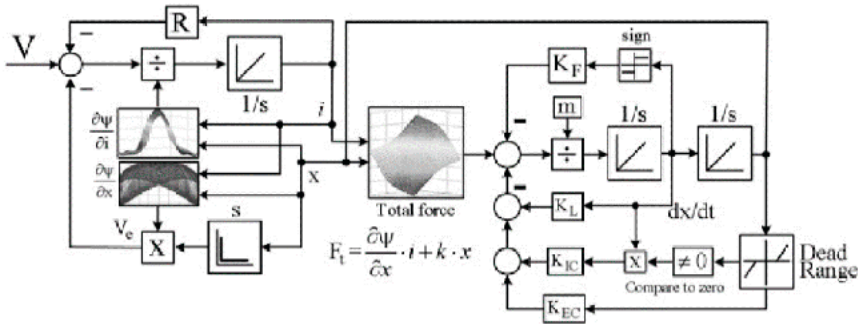


Fig. 12.21 The dynamic model of the springless linear resonant PM oscillomotor.

A cascaded position and current controller (Fig. 12.22).

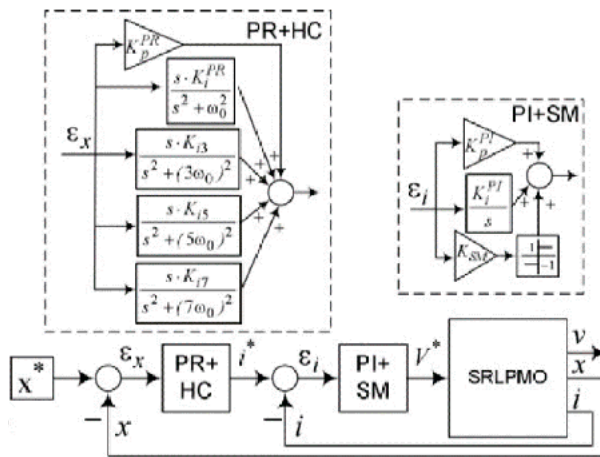


Fig. 12.22 The cascaded position (and current) control system.

Proportional resonant (with harmonics compensation) position control to secure rather sinusoidal position response (Fig. 12.22), while a PI+SM is used for the current control for robustness against machine parameter variations with position and current.

The parameters of the close loop regulators in Fig. 12.22 are:  $K_p^{PI} = 150$ ,  $K_i^{PI} = 573$  with  $K_{sm} = 25$  in the current controller (bandwidth 1.2 kHz) and  $K_p^{PR} = 20$ ,  $K_i^{PR} = 250$ ,  $K_{i3} = 150$ ,  $K_{ir} = 15$  for the PR position controller (bandwidth 270 Hz).

System linearization was performed to check the system stability for close loop operation. When tested against the oscillomotor nonlinear model, the former performed well in critical transients [17].

Finally, sample speed-proportional load force characteristics show good steady state full power performance in voltage, current, speed, position (Fig. 12.13b). The sudden change in load from 50% to 100% in Fig. 12.23c reflects a stable position response with an expected current amplitude increase.



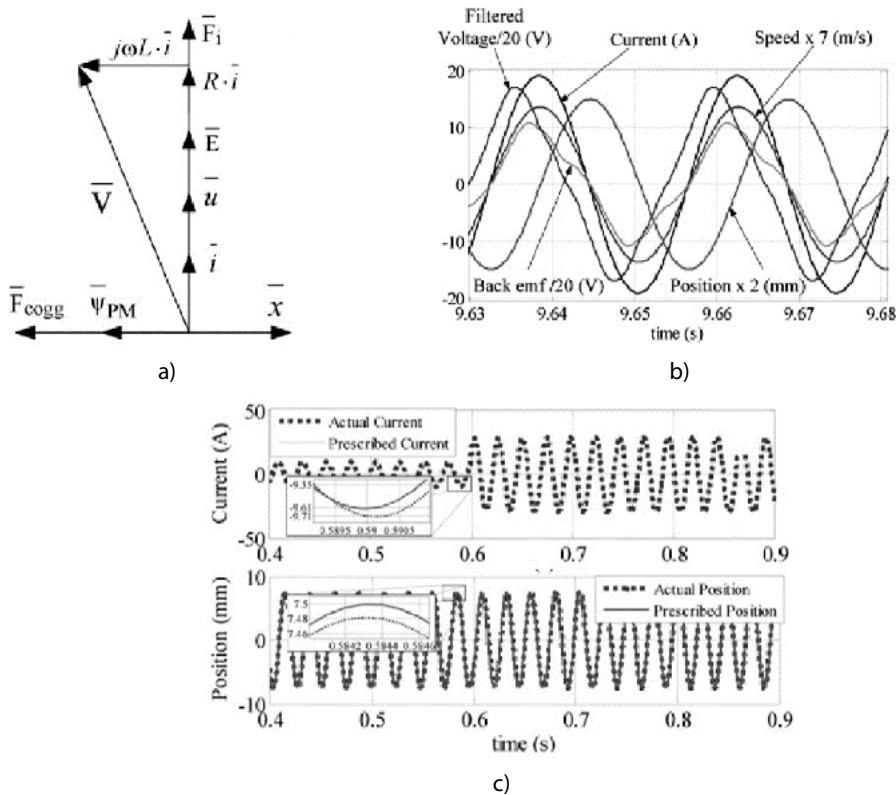


Fig. 12.23 Speed-proportional load force characteristics: a) phasor diagram at resonance (current  $\vec{i}$  in phase with speed  $\vec{u}$  and emf  $\vec{E}$ ); b) Waveforms at full load and steady state; c) 50% to 100% sudden load change responses in current and mover position.

Further steady state characteristics (Fig. 12.24) for efficiency, current amplitude (p.u.) denominated by "position" warm remarks such as:

- As the motion amplitude  $X_{max}$  increases, so does the power and current, while efficiency slightly decreases. Consequently, the power source should vary the voltage amplitude (and eventually adjust the frequency when resonance is lost with a few percents.
- It has been shown that the machine remains stable even if the mechanical resonance frequency (due to PM slight demagnetization) varies by  $\pm 5\%$ . This shows that if designed at power source frequency, only a voltage VARIC is needed for the control of output power (if needed) by voltage reduction to reduce motion amplitude, without notable loss of efficiency.
- The keeping of good efficiency at lower load is explained by the fact that reducing stroke length corresponds to pole pitch continuous reduction in a rotary electric machine; which is similar to modifying frequency (which here stays constant).

- A high immunity to PM demagnetization inductance, resistance and mover mass 20% detuning has been demonstrated [17].

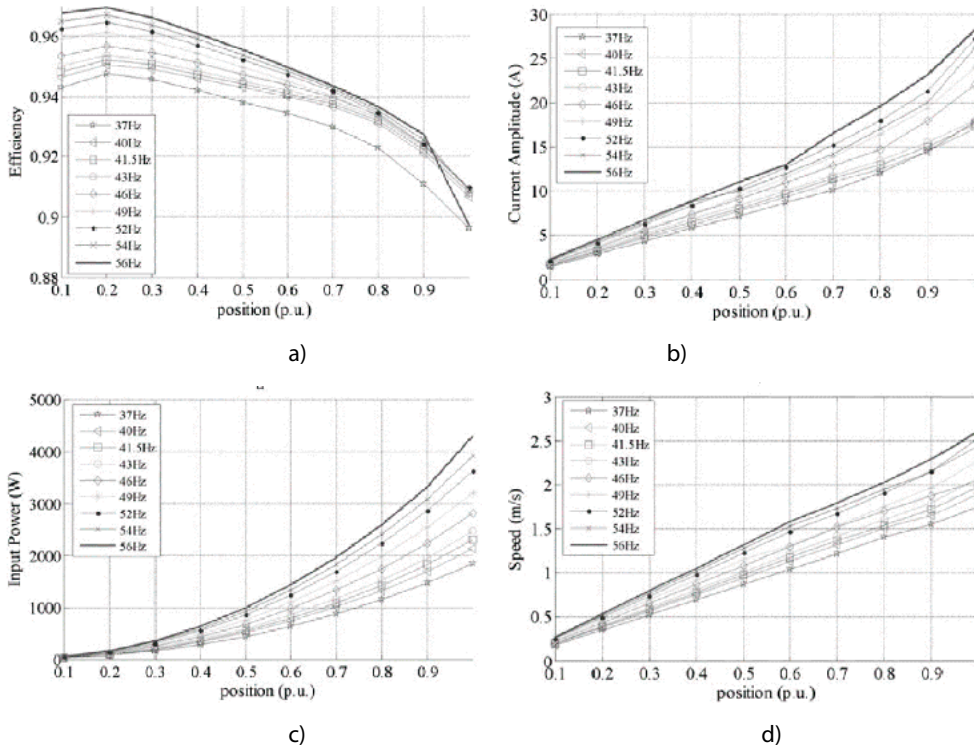


Fig. 12.24 Efficiency a), current amplitude b), input power c) and speed d).

Final Note.

Although the theoretical results (with FEM backing) are promising, only experiments will tell if the springless linear PM oscillomotor presented here is practical.

Active magnetic bearings for motor rotary electric motors may be also assimilated to multiple degree order linear motors with position control [18].

## 12.6 References

- [1] I. Boldea, L. N. Tutelea, W. Xu, and M. Pucci, "Linear electric machines, drives and MAGLEVs: An overview" *IEEE Trans. Ind. Electron.*, vol. 65, no. 9, pp. 7504–7515, Sep. 2018
- [2] I. Boldea "Linear electric machines, drives and MAGLEV Handbook", CRC Press, Florida, USA (2013)
- [3] E. R. Laithwaite "Induction machine for special purposes" book, George Newnes, 1966
- [4] S. Yamamura "Theory of linear induction motors", book, John Wiley & Sons, 1972
- [5] S. A., Nasar, I., Boldea "Linear motion electric machines", book, John Wiley, 1976
- [6] P.K. Budig, A.C. Linear Motors, Veb Verlag Technik, Berlin (in German)



- [7] M. Poloujadoff, Theory of Linear Induction Motors, Oxford University Press, OUP, 1980
- [8] I. Boldea, S., A. Nasar "Linear motors electromagnetic systems", book, John Wiley & Sons, 1985
- [9] J.J. Gieras "Linear induction drives", book, OUP, 1994
- [10] I., Boldea, S., A., Nasar " Linear electric actuators and generators", book, Cambridge University Press, 1997
- [11] J. F. Gieras, J. J. Piech "Linear synchronous motors", book, CRC Press, USA, 2000
- [12] I. Boldea, S., A., Nasar "Linear motion electromagnetic devices", book, CRC Press, Taylor and Francis, New York, 2001
- [13] S.C. Agarlita, I. Boldea, F. Marignetti, L.N. Tutelea "Position sensorless control of linear interior PM oscillatory machine with experiment, *OPTIM – 2010*, pp 689-695(IEEE Xplore)
- [14] I. Boldea, S.A. Nasar, B. Penswick, B. Ross, R. Olan, "New linear reciprocating machine with stationary permanent magnets", *IEEE Trans IAS*, vol 2 pp. 825-829, 1996
- [15] J., Lee, I. Boldea "Linear reciprocating flux-reversal PM machine" US patent No: 6538.344, 25.03.2003
- [16] I. Boldea, S. Agarlita, L. Tutelea "Springless resonant oscillatory PM motors", *Record of LDIA*, Eindhoven 2011
- [17] S, C, Agarlita, L. Tutelea, I. Boldea "Modeling and control of a springless resonant linear PM oscillator", *Trans. On IET*, vol EPA-7, no. 2, pp. 150-158.
- [18] I. Boldea, N, Morcov, Al. Trica, G. Schulhoft " High speed induction motor drive with active magnetic bearings and sliding mode decentralized control", *EMPS(now ECPS journal)*, Vol. 18, pp. 375-382, 1990

# “ACTIVE FLUX” BASED ENCODERLESS FOC, DTFC AND V/F(I-F) WITH STABILIZING LOOPS CONTROL OF A.C. MACHINES

## 13.1 Abstract

Field oriented control (FOC) and direct torque and flux control (DTFC) are now mature technologies that provide fast torque response (in the millisecond range) and precision in torque and speed response of a.c. drives, with encoder feedback, with high efficiency over wide speed range. However, DTFC is commercial only on induction motors

Encoderless FOC and DTFC is commercial, but still torque response quickness, torque and speed control precision, response robustness are open to notable improvements. The key ingredient of encoderless a.c. drives is the complex state observer (stator/rotor flux, torque, rotor position and speed).

In an effort to simplify, but improve the complex state observer in FOC, DTFC [2], but also in slower torque response V/f (I-f) of all a.c. motor/generator drives [3], the “active flux” concept was introduced [1] and then implemented on various synchronous motor drives so far.

The “active flux” concept develops on the “extended flux” [4] and “fictitious PM flux” [5] models to achieve a unitary concept applicable to all induction and synchronous motor/generator drives.

This chapter synthesizes the work so far on the “active flux” principle and its implementation on all a.c. drives.

## 13.2 The “active flux” concept

The active flux vector  $\vec{\psi}_d^a$  may be defined intuitively in two ways:

- from the torque formula in the  $dq$  model
- from the stator flux  $\vec{\psi}_s^s$

According to the first definition, the “active flux” vector  $\vec{\psi}_d^a$  in a.c. machine, aligned with axis  $d$ , is the term that multiplies  $i_q$  in the  $dq$ -model torque formula:

$$T_e = \frac{3}{2} p_1 \left| \bar{\psi}_d^a \right| i_q \quad (13.1)$$

$$\psi_d^a = \psi_{PMd} \quad \text{for SPMSM; } L_d = L_q = L_s$$

$$\psi_d^a = \psi_{PMd} + (L_d - L_q) i_d \quad \text{for IPMSM } L_d < L_q$$

$$\psi_d^a = L_{dm} i_F + (L_d - L_q) i_d \quad \text{for d.c. excited - SM } L_d \geq L_q \quad (13.2)$$

$$\psi_d^a = (L_d - L_q) i_d \quad \text{for RelSyn machines } L_d \gg L_q$$

$$\psi_d^a = (L_s - L_{sc}) i_d \quad \text{for IMs } L_s \gg L_{sc}$$

Axis  $d$  corresponds to rotor pole (PM) axis in all synchronous machines and to the rotor flux axis in induction machines.

Intuitively, again, (13.1) suggests that the machine with an “active flux” concept behaves like a virtually nonsalient-pole machine characterized by a single inductance  $L_q$  or  $L_{sc}$  which “opposes” the change of current:

Consequently:

$$\bar{\psi}_d^a = \bar{\psi}_s - L_s \bar{i}_s \quad (13.3)$$

The space phasor model of stator voltage vector for all a.c. machines is:

$$\bar{V}_s = R_s \bar{i}_s + \frac{d\bar{\psi}_s}{dt} + j\omega_a \bar{\psi}_s \quad (13.4)$$

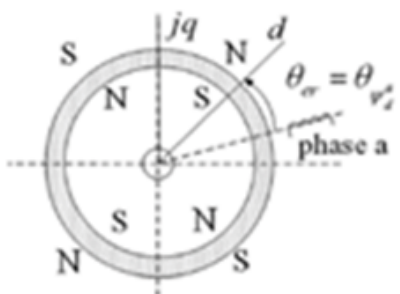
where is the speed of the “active flux” vector, or a general speed.

Using (13.4) in (13.3):

$$\bar{V}_s = R_s \bar{i}_s + (s + j\omega_a) L_q \bar{i}_s + (s + j\omega_a) \bar{\psi}_d^a; s = d/dt \quad (13.5)$$

This equation confirms the “above” situation that the eventual saliency  $L_d \neq L_q$  is “hidden” or “absorbed” into the “active flux” vector, and the machine shows only the inductance.

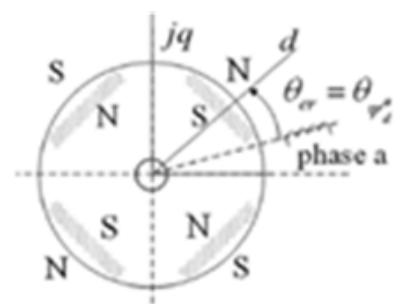
The vector diagrams with “active flux” vector for the steady state of SPMSM, IPMSM, Relsyn, d.c.-excited SM and IM are portrayed in Fig. 13.1, to illustrate the unitary character for all a.c. machines.



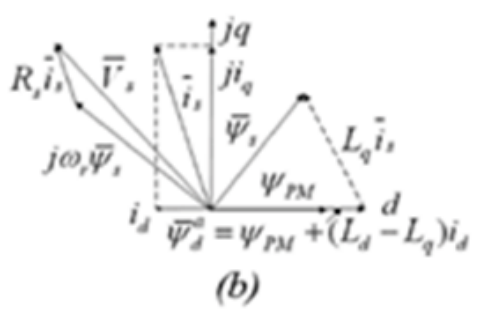
$L_d = L_q = L_s$  (no saliency)



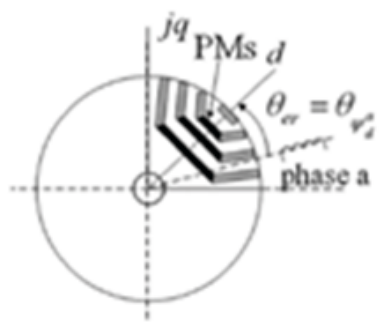
(a)



$L_d < L_q$  (small saliency)



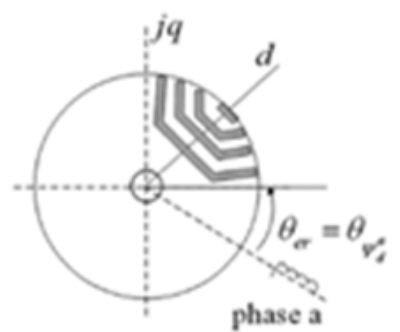
(b)



$L_d \ll L_q$  (high saliency)



(c)



$L_d \gg L_q$



(d)

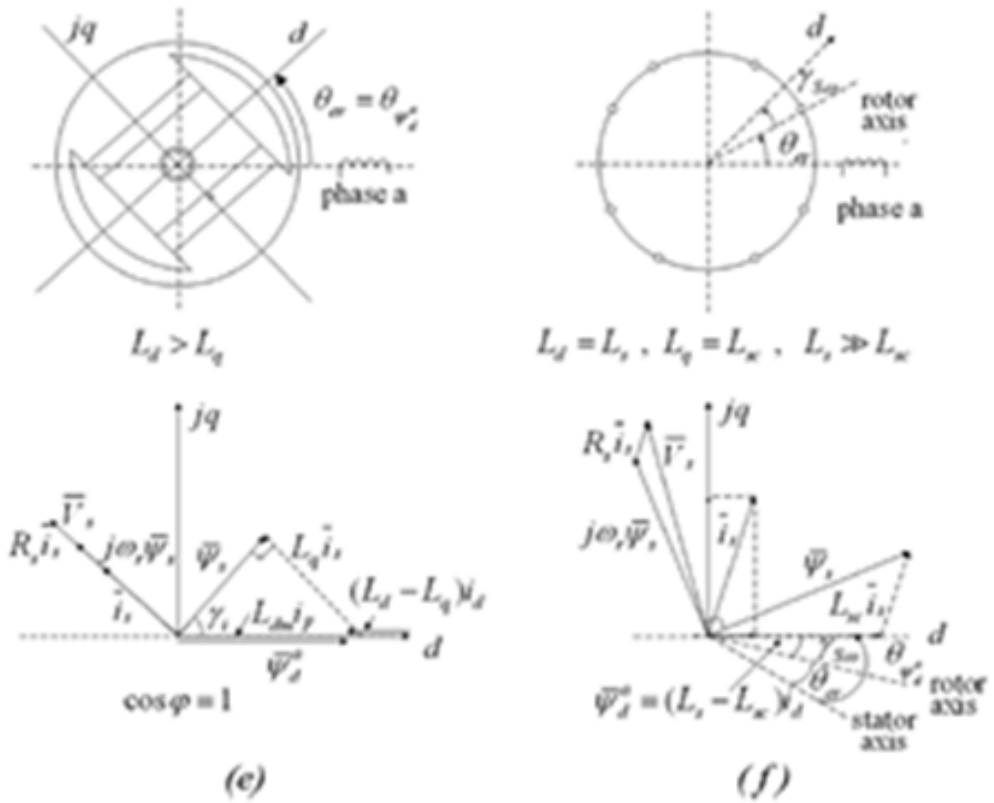


Fig. 13. 1 The vector diagram showing the active flux vector for a) SPMSM, b) IPMSM, c) RelSyn, d) d.c. excited S.M., e) IM.

The “active flux” observer typical structure is summarized in eqn. (13.6):

$$\bar{\psi}_d^{as} = \int (\bar{V}_s = R_s \bar{i}_s + V_{comp}) dt - L_s \bar{i}_s^q \tag{13.6}$$

written in stator coordinates.

The position  $\theta_{\psi_d^a}$  of  $\bar{\psi}_d^a$  (which is rotor position for all synchronous machines, and rotor flux position for IMs) is thus extracted as:

$$\bar{\psi}_d^{as} = \psi_d^a \cos \theta + j \psi_d^a \sin \theta \tag{13.7}$$

The  $V_{comp}$  is related in general to the current model of the respective a.c. machine as shown in Fig. 13.2.

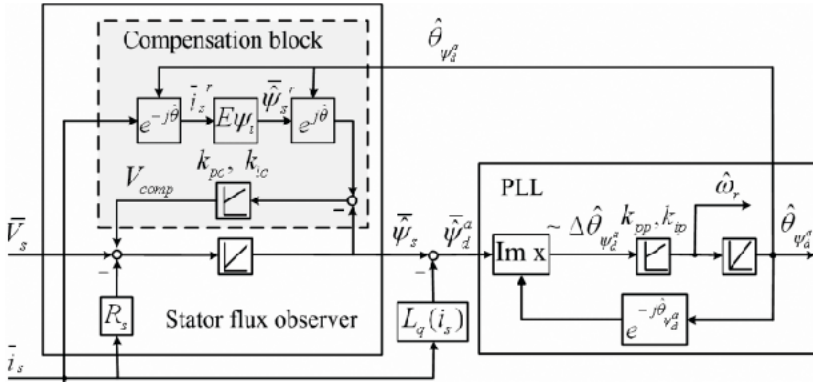


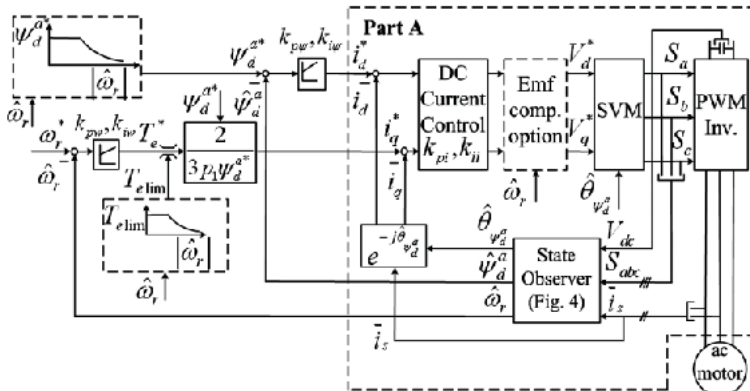
Fig. 13.2 “Active flux” vector observer with position & speed PLL (estimator for PMSM, RelSyn and IM).

It should be noticed that the added current model used for  $V_{comp}$ , to make the observer adequate at small frequency (speed) is “translated” to active flux coordinated first (rotation by  $e^{-j\theta_{\psi_d^a}}$ ) and then back ( $e^{j\theta_{\psi_d^a}}$ ).

The PI regulators in the active flux observer and in the PLL estimator of active flux position  $\theta_{\psi_d^a}$  and speed  $\omega_{\psi_d^a}$  (equal to  $\omega_r$  in SMs and to  $\omega_{\psi_r}$  in IMs).

**13.2.1 Encoderless A.C. Unidrive based on “active flux” FOC (or DTFC) In an encoder unidrive (for PMSM, Relsyn, IM) and dc-excited SM Fig. 13.3 a, b, based on the “active flux” concept, but still using FOC strategy, the amplitude of  $\bar{\psi}_d^a$  has to be planned as a function of reference torque (and or speed) first.**

Then the active flux is regulated in front of the  $i_d$  regulator. A torque limiter with speed is introduced in front of the regulator. Finally, emf computation may be added in FOC.



a)



### 13.3 “Active flux” based encoderless IPMSM FOC and DTFC drives

The heart of “active flux” system is its observer (Fig. 13.2) with measured stator current vector ( $\bar{i}_s$ ) and estimated (or reference) stator voltage vector ( $\bar{V}_s$ ), provided the PM flux linkage  $\psi_{PMd}$  and  $L_d, L_q$  are known precisely (or corrected based on offline or online data).

The current model section in Fig. 13.2 is:

$$\begin{aligned}\hat{\psi}_{si}^s &= [L_d i_d + \psi_{PMd}^a + jL_q (\hat{T}_e) i_q] e^{j\theta_{er}} \\ i_d + j i_q &= \bar{i}_s^s e^{-j\theta_{er}}\end{aligned}\quad (13.8)$$

Again, if parameters are known  $\theta_{er} = \theta_{\psi_d^a}$  in PMSMs.

The compensation voltage  $\bar{V}_{comp}$  is obtained as the output of a PI regulator on the error of stator flux from current and voltage model:

$$\bar{V}_{comp} = \left(k_{pc} + \frac{k_{ic}}{s}\right) (\hat{\psi}_{si}^s - \hat{\psi}_{su}^c) \quad (13.9)$$

The PI compensator in (13.9) eliminates the offset and drifting terms from current measurement chain and the error in integrator initial conditions.

The PI compensator is designed by the pole allocation method and may be added a series sliding mode (SM) component for increased robustness.

At low speeds, the stator resistance may be corrected to secure enough precision, consequence in the  $\hat{\psi}_d^a$  observer. Alternatively, the hot temperature stator resistance may be applied, for simplicity.

To allow only a function of torque while  $L_d$  and  $\psi_{PMd}$  are considered constant. In IPMSM with strong magnets (large emf/voltage) and low magnetic saliency, this assumption holds in practice.

$$L_q = \frac{L_{qu}}{1 + k_T \left| \frac{\hat{T}_e}{T_{en}} \right|} \quad (13.10)$$

Is the unsaturated value  $L_{qu}$  of  $L_q$ ,  $\hat{T}_e$  is the estimated torque and  $T_{en}$  - the rated (base) torque.

A typical illustration of the magnetic saturation influence at 2 rpm on the observer output in speed and position is shown in Fig. 13.4.



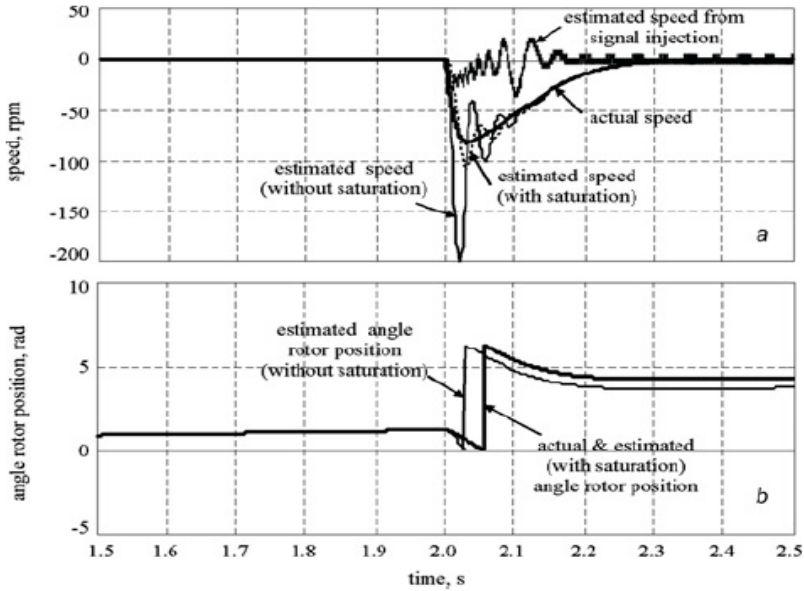


Fig. 13.4 Influence of magnetic saturation of  $L_q$  in the active flux observer at very low speed of 2rpm (0.1Hz) and 100% step-up torque perturbation: actual speed.

The saturation consideration as in (13.10) inflicts a notable improvement on speed estimation by the active flux observer at very low speed (2 rpm).

Fig. 13.2 uses a PLL observer one active flux angle  $\hat{\theta}_{\psi_d^a}$  input to improve  $\hat{\theta}_{\psi_d^a}$  and obtain a smoother speed estimation  $\bar{\omega}_r$ .

If such a PLL observer is eliminated, the speed of active flux vector  $\hat{\omega}_{\psi_d^a} = \hat{\omega}_r$  may be calculated after filtering the expression:

$$\omega_r \approx \frac{\hat{\psi}_{d\alpha}^a - 1\hat{\psi}_{d\beta}^a - \hat{\psi}_{d\beta}^a - 1\hat{\psi}_{d\alpha}^a}{h|\bar{\psi}_d^a|^2}; \hat{\theta}_{er} = \hat{\theta}_{\psi_d^a} = \tan^{-1} \left( \frac{\hat{\psi}_{d\beta}^a}{\hat{\psi}_{d\alpha}^a} \right) \quad (13.11)$$

where  $h$  is the sampling time and “-1” refers to one period before the current sampling cycle.

The low pass filter in speed  $\hat{\omega}_r$ , should have a time constant in the millisecond range ( $T_w = 3.3$  ms in the case of interest here).

While for FOC the estimated rotor position  $\hat{\theta}_{er}$  is used for vector rotations at all speeds, for DTFC the latter appears only in the current model part of the “active flux” observer which is predominant only at low speeds.

Experimental results on a 6 pole 2 kW IPMSM drive, at 2 rpm are shown in Figs. 13.5 and 13.6 [2].

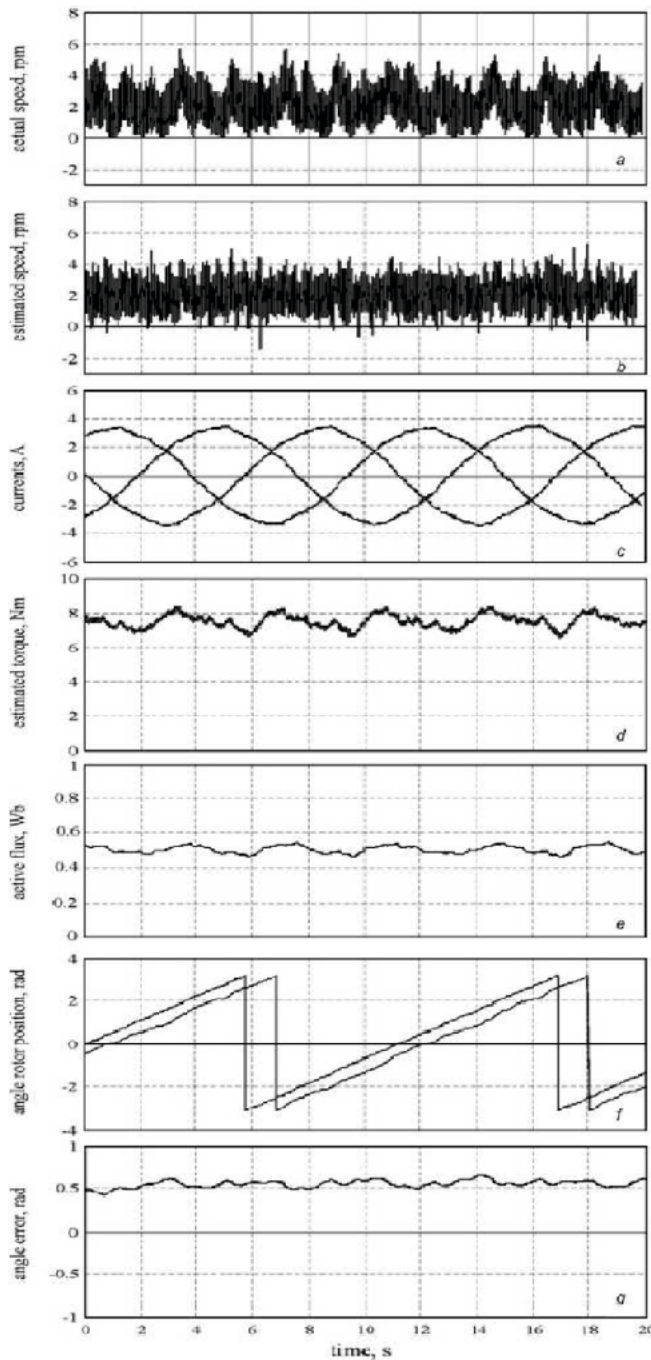


Fig. 13.5 Encoderless IPMSM FOC drive (2.2kW, 6 poles) “active-flux” at 2 rpm in test results: a) actual speed (by encoder); b) estimated speed; c) measured currents; d) estimated torque; e) active flux; f) estimated and actual rotor position; g) rotor position error.

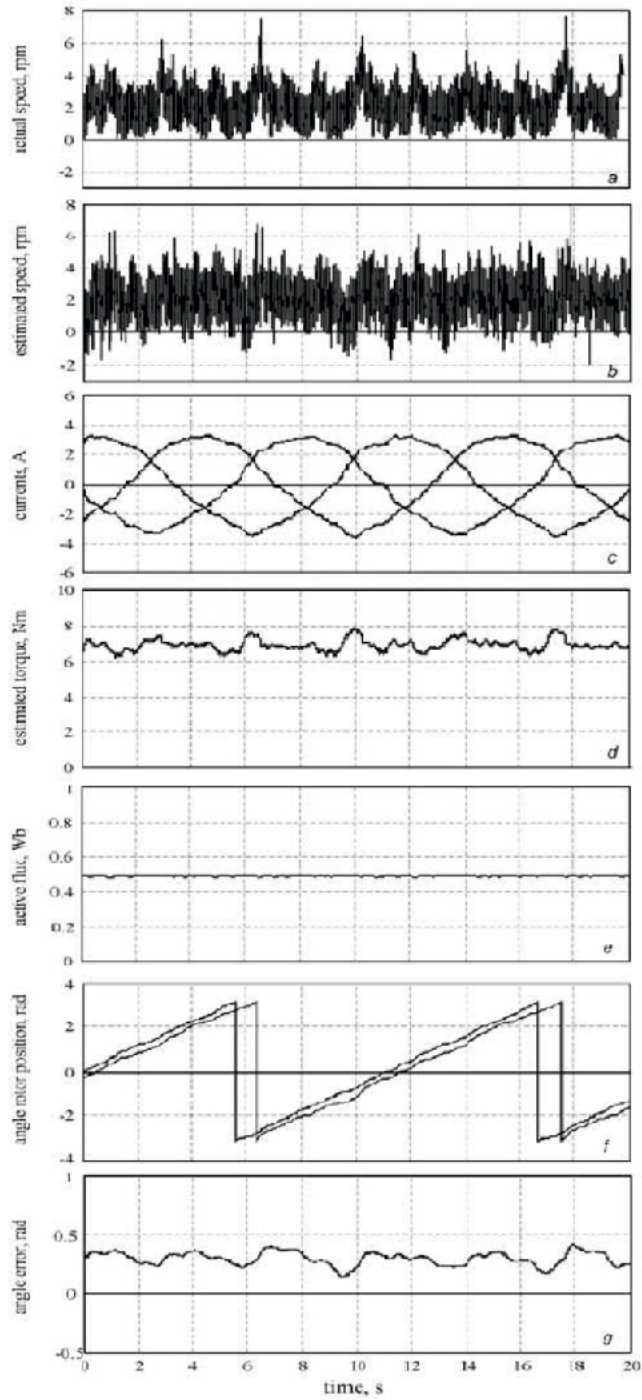


Fig. 13.6 Encoderless IPMSM DTFC (2.2 kW, 6 poles) test results: same as in Fig. 13.5.  
 The test platform is visible in Fig. 13.7.

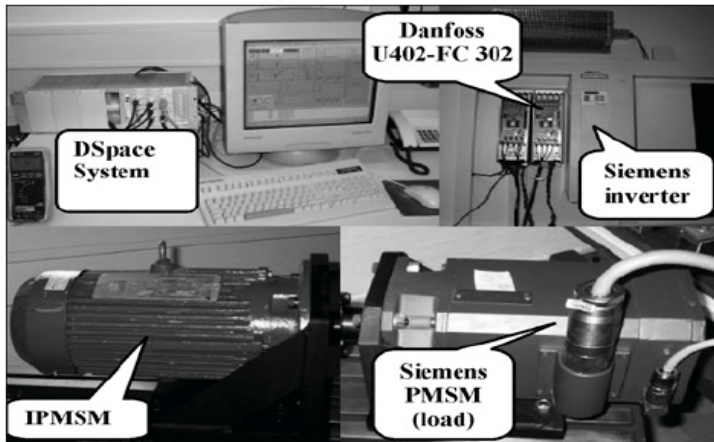


Fig. 13.7 The test platform.

Both FOC and DTFC can handle 2 rpm under load in active flux observer based encoderless drive, but both show a rather constant rotor position error that may be compensated by trial and error versus speed (if needed).

The torque pulsations and estimated active flux are smoother for DTFC.

However, for DTFC, the current waveforms are further away from sinusoids than in FOC for similar average switching frequency in the inverter.

It should be noted that 2 rpm (experimental) is arguably the lowest speed in encoderless control of IPMSM without signal injection.

#### A). Wide constant power speed range (CPSR) control of IPMSM and PM-RSM

Wide CPSR when needed (in transportation spindle drives etc.) requires PM flux weakening operation. The default mode of control in PMSM is the maximum torque/current control which leads to the equation:

$$2i_d^2 - \frac{\psi_{PMd}}{L_d - L_q} - i_s^2 = 0; L_d < L_q \quad (13.12)$$

Using the  $\psi_d^a$  concept eqn. (13.12) translates into:

$$i_d^* = -|i_s| \sqrt{\frac{\hat{\psi}_d^a - \psi_{PMd}}{2\hat{\psi}_d^a - \psi_{PMd}}}; i_q^* = \frac{2}{3p_1} \frac{T_e^*}{|\psi_d^a|}; \hat{\psi}_d^a > \psi_{PMd} \quad (13.13)$$

$i_d^*$  is zero for SPMSMs.

Eqns. (13.13) are much easier to handle in control implementation than eqn. (13.12).

When the voltage limit is met a PI on  $V_s^* - V_{s,max}$  may be used to further increase  $i_d^*$  in the negative direction by  $\Delta i_d^*$ :

$$\Delta i_d^* = -PI(V_s^* - V_{s \max}); \text{ when } V_s^* - V_{s \max} \geq 0 \quad (13.14)$$

The above methodology should provide wide speed range with good efficiency (max. torque/current) and wide CPSR in strong magnet IPMSM with moderate rotor anisotropy.

For PM-RSMs, whose PM flux linkage is small ( $\psi_{PMd}\omega_b/V_{s \max} < 0.3$ ) and the magnetic saliency is large  $L_d/L_q > 3$  (in general) a simplified method for wide speed range control has been developed [8].

The default operation with PMs in axis  $q$  is now for

$$\psi_q = L_q i_{qk} - \psi_{PMq} = 0 \quad (13.15)$$

In this case the torque limit  $T_{ek}$  is:

$$T_{ek} = T_{e \max b} = \frac{3}{2} P_1 \frac{\psi_{PMq}}{L_q} \frac{V_{s \max}}{\omega_b}; \left| \omega_r \right| < \omega_b \quad (13.16)$$

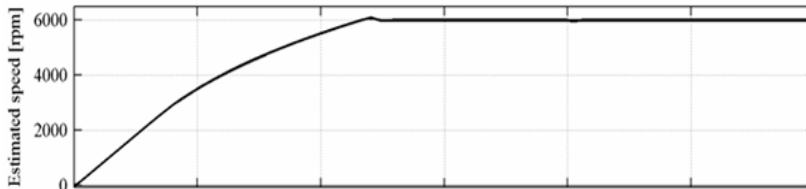
$$T_{ek} = T_{e \max b} \left| \frac{\omega_b}{\omega_r} \right|; \left| \omega_r \right| > \omega_b$$

These conditions will secure operation on the torque-speed envelope. When the reference torque is smaller than  $T_e^*$  the current  $i_q^*$  is modified to

$$i_q^* = i_{qk} \sqrt{\frac{T_e}{T_{ek}}} = \frac{\psi_{PMq}}{L_q} \sqrt{\frac{T_e}{T_{ek}}} \quad (13.17)$$

This “square-root” approximation method will be close to max. torque/current condition with high saliency  $L_d/L_q > (3-5)$  and with weak magnets as in PM-RSM used for wide CPSR because their no load voltage at maximum speed may be designed below 150% of  $V_{s \max}$ . Thus, no overvoltage protection at no load at highest speed is required.

Typical digital simulation results for such a drive [8] are illustrated in Fig. 13.8 (750 W PM-RSM, 4 poles, 1500 rpm, 42 Vdc,  $\psi_{PMq} = 0.011$  Vs/rad,  $L_d = 2.5$  mH (saturated),  $L_q = 0.5$  mH).



a)

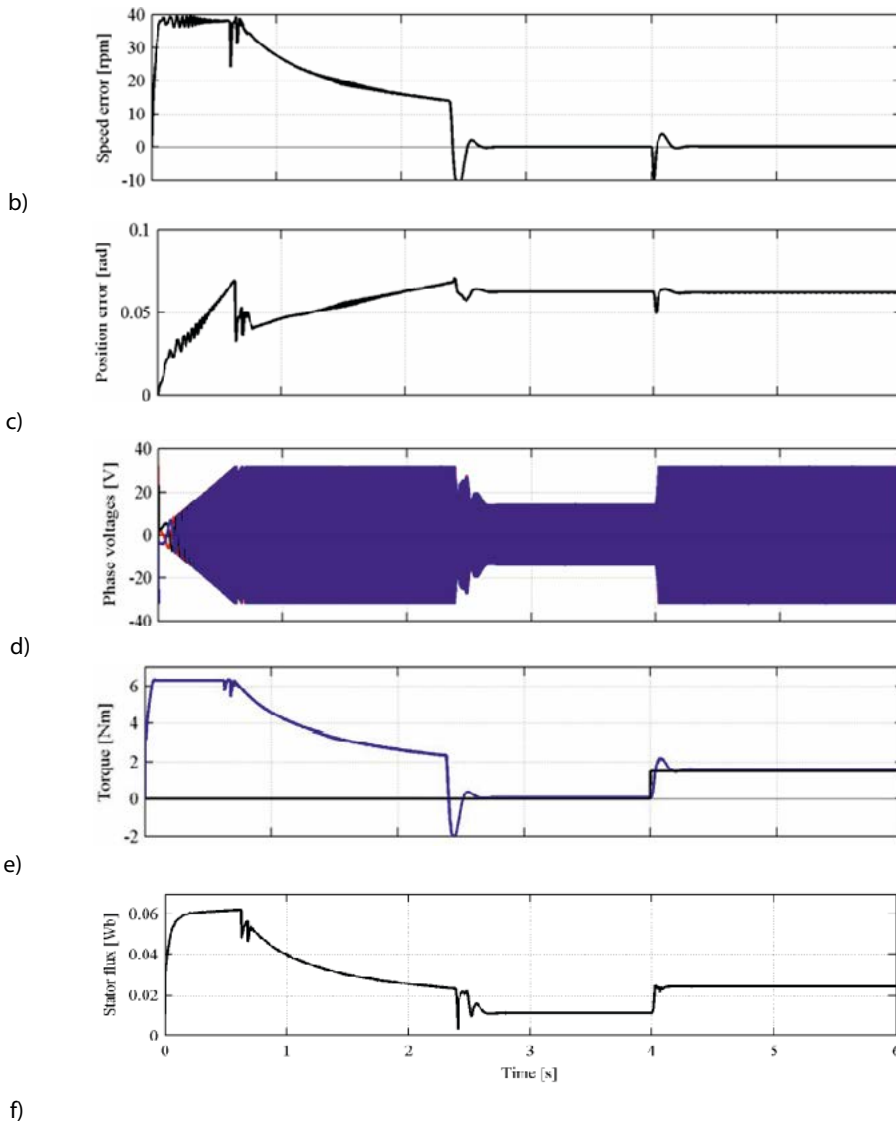


Fig. 13.8 Start-up transients of an PM-RSM with encoder-less FOC and active flux observer (750W, 1500rpm, 42V<sub>DC</sub>), from digital simulations: a) estimated speed, b) speed error, c) position error, d) phase current, e) estimated torque, f) stator flux.

A step load torque of 25 % is applied at  $t=4$  s (Fig. 13.8) to show that the increase in torque occurs too and the response is smooth despite of the fact that at  $t>4$  s the motor is in the flux weakening mode at high speed ( $\omega_{r,max}/\omega_r = 1/4$  (6000 rpm/1500 rpm)).

The reduction of current after the tendency of reducing losses even if by the “square-root” approximation (eqn. (13.17)).

### 13. 4 Active flux based high saliency RSM field-oriented control [9]

The axially laminated anisotropic (ALA) rotor RSM is characterized by rather high magnetic saliency such as a 4-pole small RSM (1Nm rated torque) whose  $dq$  flux/current curves family are measured as in Fig. 13.9 [7].

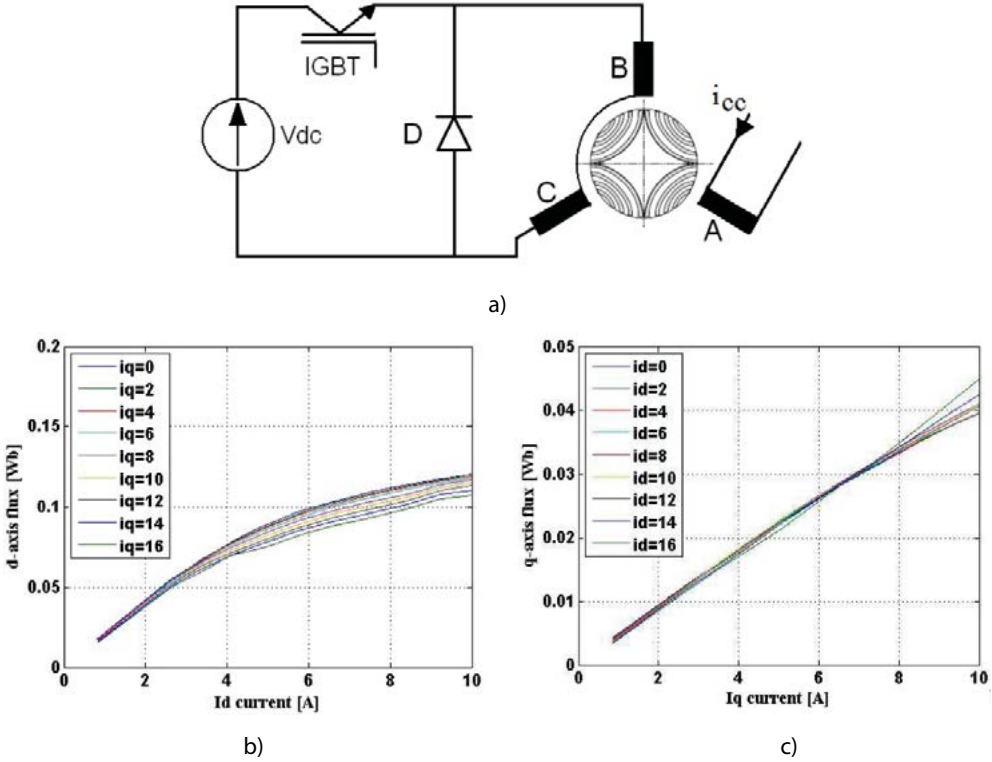


Fig. 13.9 ALA rotor 1Nm RSM: a) d.c. current decay standstill test platform, b)  $\psi_d(i_d, i_q)$ .

c)  $\psi_q(i_d, i_q)$ .

It is evident that there is some, but mild cross coupling effect (rated current  $i_s = 4$  A (peak value)) due to the ALA rotor configuration. Moreover, there is an up to  $L_d/L_q \approx 4.5$ .

The active observer is still the one in Fig. 13.2., but the  $dq$  flux current relationships are now:

$$\begin{aligned} \psi_d &\approx (L_{du} - k_{dd}i_d - k_{dq}i_q)i_d \\ \psi_q &\approx (L_{qu} - k_{qq}i_d)i_d \end{aligned} \quad (13.18)$$

To provide  $\partial\psi_d/\partial i_q = \partial\psi_q/\partial i_d : k_{dq}i_d = k_{dq}i_q$ .

In a first approximation

$$L_d \approx L_{du} - k_d i_d; L_q \approx L_{qu} \quad (13.19)$$

The active flux

$$\bar{\psi}_d^a = (L_d - L_q) i_d; L_d \gg L_q \quad (13.20)$$

It should be noted that even for large overload there is still enough saliency to yield sufficient torque. This merit is mainly due to the ALA rotor.

The position and speed observer is here different. A Luenberger style structure is used in the form of a PLL enhanced with the acceleration information from a mechanical equation (with estimated inertia) for improvements (Fig. 13.10).

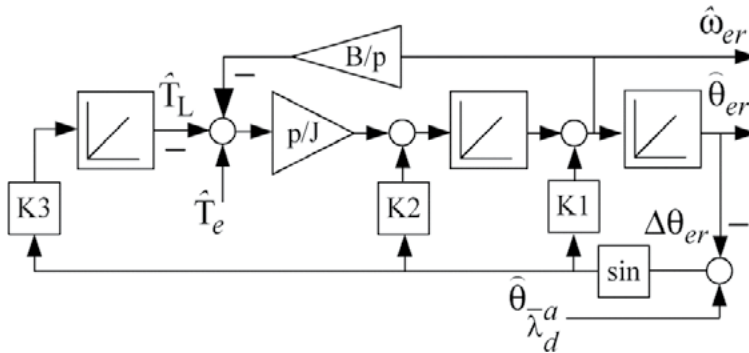


Fig. 13.10 PLL based rotor position and speed observer.

By trial and error for the case in point  $K_1 = 100, K_2 = 5000, K_3 = -15$ , observer damping is 0.707 ( $B = 2 \times 10^{-3}$  Nms/rad and  $J = 21.3 \times 10^{-3}$  Kg/m<sup>2</sup>, and load included).

For very small speeds (from standstill), signal injection is used ( $f_c = 500$  Hz,  $V_c$  varies with speed) on top of the fundamental one (Fig. 13.11). A standard processing of current response at  $f_c$  for saliency is followed.

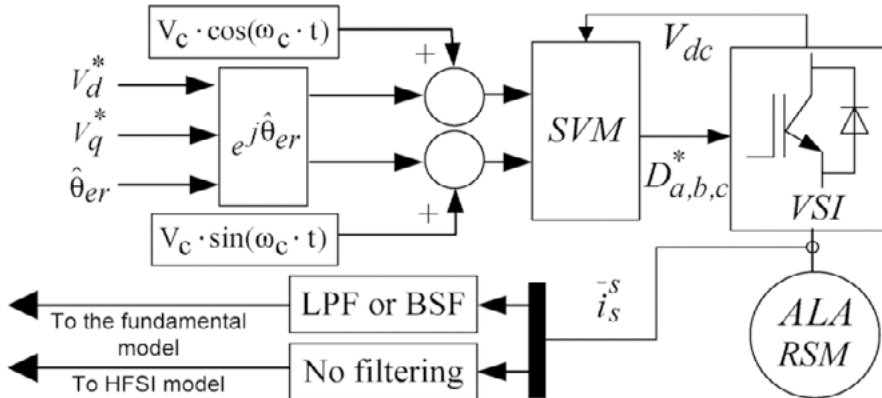


Fig. 13.11 Injection of high frequency voltage along axis d in stationary frame.



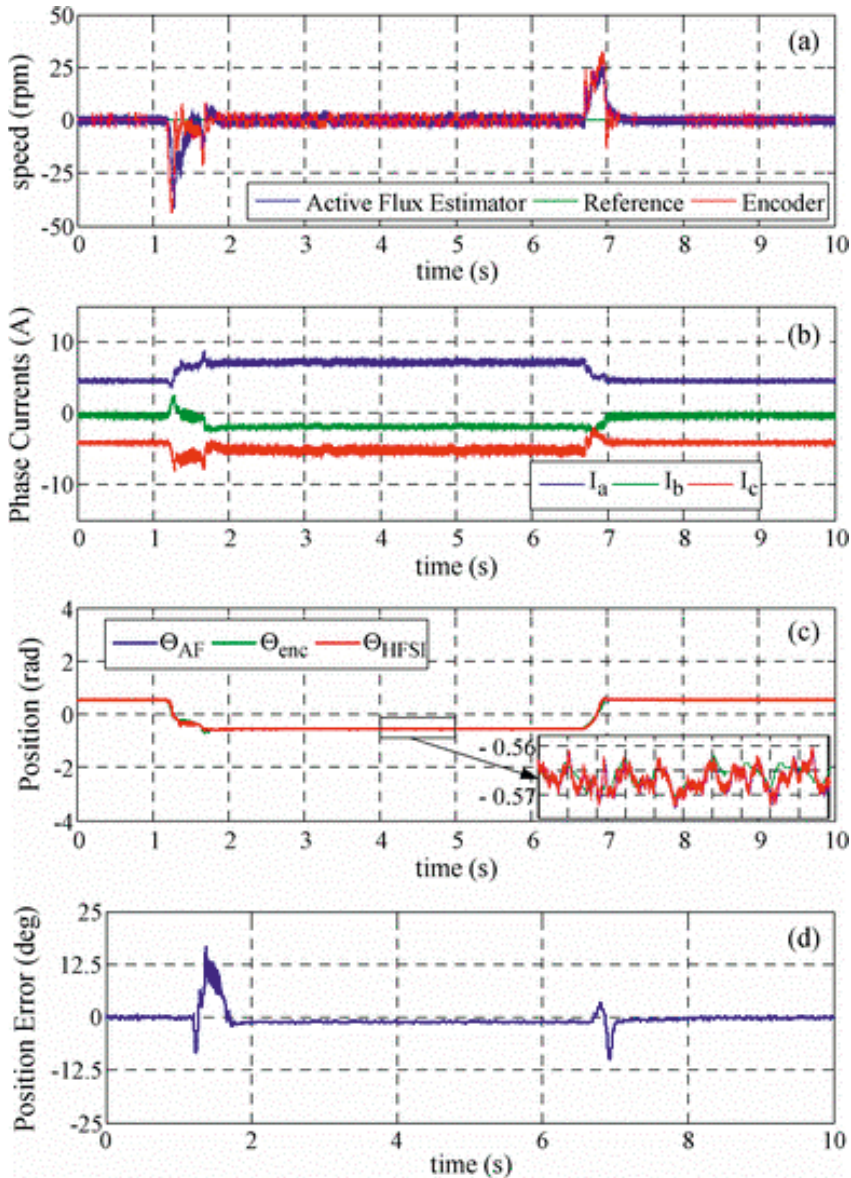


with  $K_{pd} = 12, K_{id} = 83, K_{pq} = 3.55, K_{iq} = 384$ .

It should be noted that because  $L_d \gg L_q$  the current regulator parameters are different from each other.

The zero of the current controllers transfer functions were chosen to cancel the pole of the corresponding electric equation (again damping ratio).

Some experimental results at zero speed (Fig. 13.14-Fig. 13.16.)



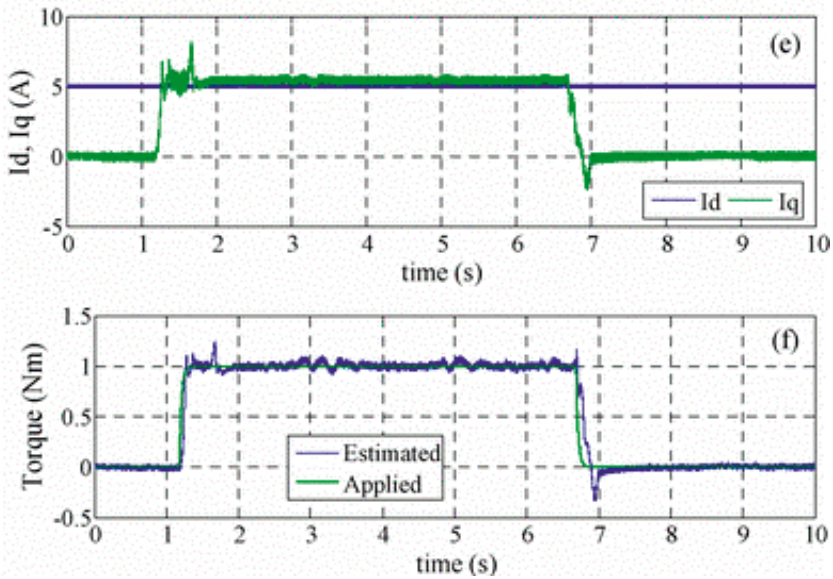
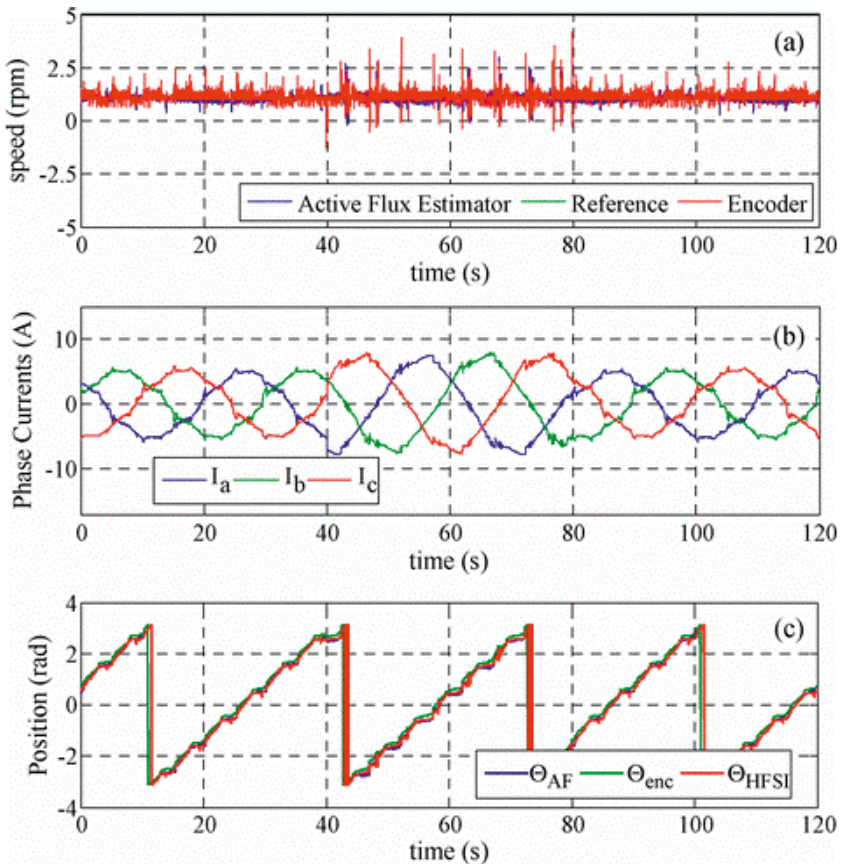


Fig. 13.14 Zero speed RSM encoder-less transients with 1Nm step load torque.





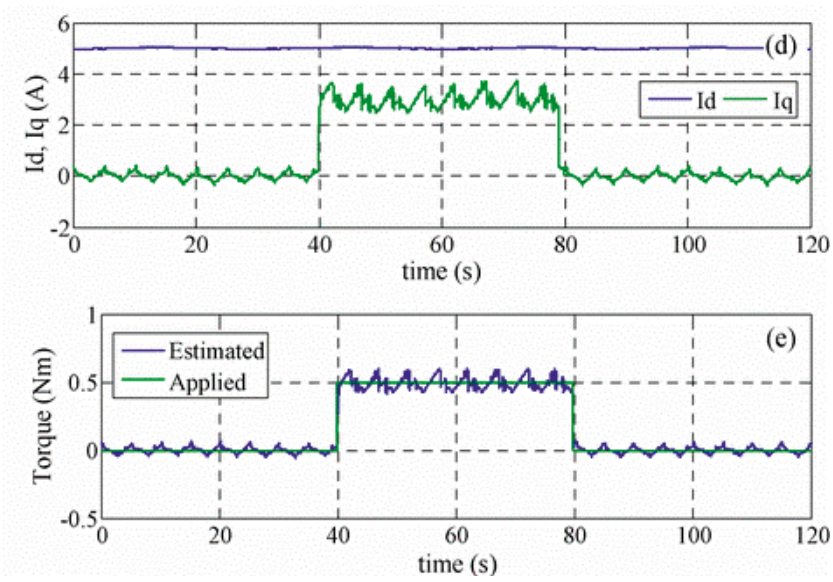
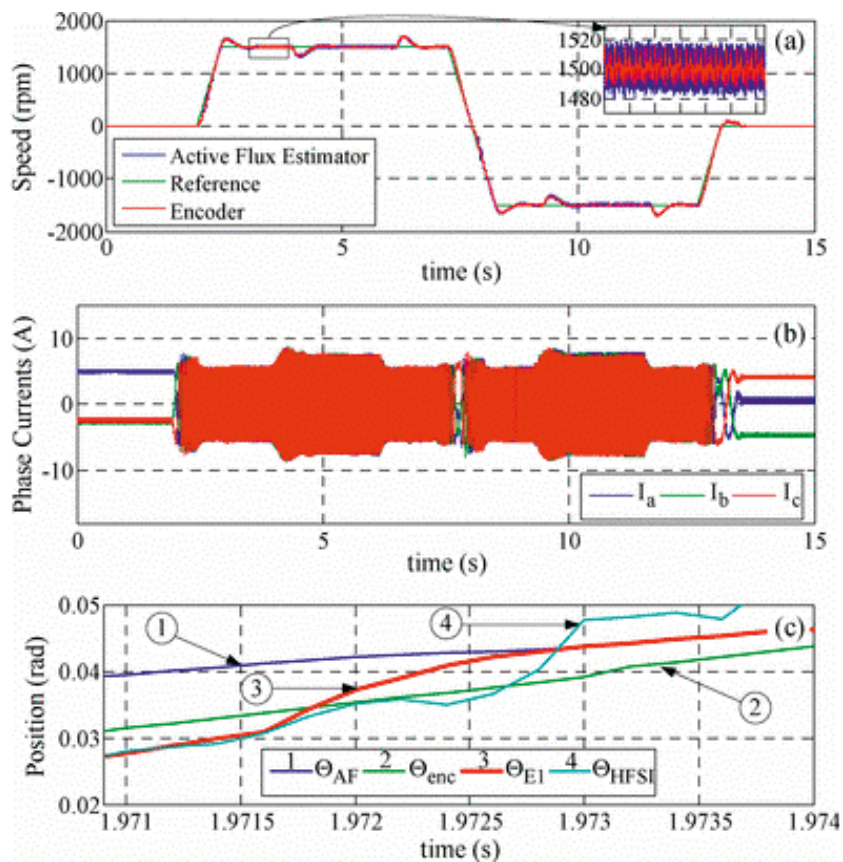


Fig. 13.15 1rpm, 0.5Nm step torque transients.



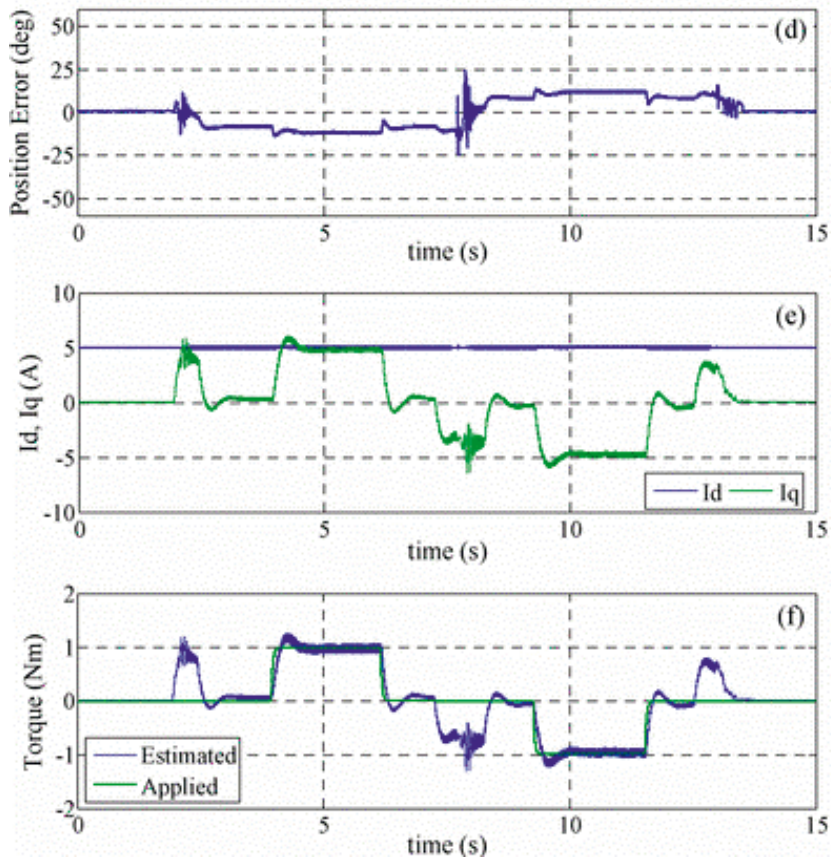


Fig. 13.16 Speed reversal ( $\pm 1500$ rpm) RSM encoder-less transients with 1Nm step load torque at 1500rpm.

A few remarks are in order:

- The drive operates safely at zero speed even with full step torque load mainly due to signal injection rotor position observer contribution.
- Similarly, goal results are obtained at 1 rpm, but this time only 50 % of the full step load for is handled safely.
- Speed reversal from + to - 1500 rpm with 1 Nm step loading at  $\pm 1500$  rpm shows stable behavior.
- Higher speeds may be obtained with more flux weakening with lower than 1 Nm torque.
- The signal injection rotor position observer for a very low speed may be implemented on the same "active flux" observer as at zero speeds, if there is even a small magnetic saliency (10%), still the "active flux" vector is fixed-aligned to the d axis (high inductance) for travelling stator flux injection (Fig.13.17).

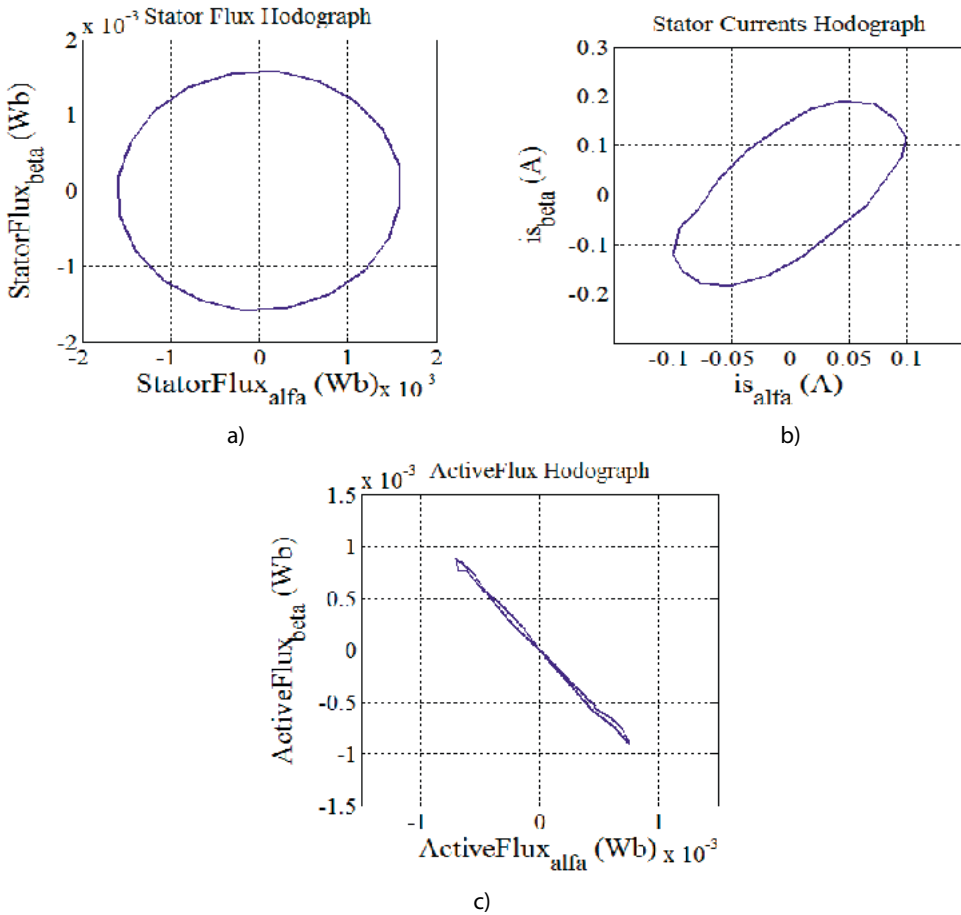


Fig. 13.17 Stator flux, a) stator current, b) and “active flux”, c) vector hodographs traveling voltage vector at zero speed in the RSM for signal injection.

- As shown in Ref. [7], processing “active flux” for signal injection at a very low speed gives better results than processing stator current and inverse component in hunt for magnetic saliency (rotor position).

### 13.5. Active flux encoderless vector control of d.c. excited SM.

The active concept may be easily particularized for FOC (vector control) of d.c. excited SMs as, again:

$$\begin{aligned}
 T_e &= 1.5 p_1 \psi_d^a i_q; \psi_d^a = L_{md} i_F + (L_d - L_q) i_d; L_d > L_q \\
 \bar{V}_s &= R_s \bar{i}_s + \frac{d\bar{\psi}_s}{dt} + j\omega_r \bar{\psi}_s \\
 \bar{\psi}_s &= L_{dm} i_F + L_d i_d + jL_q i_q; \bar{\psi}_d^a = \bar{\psi}_s - L_q \bar{i}_s
 \end{aligned} \tag{13.23}$$

The complete state observer, with the rotor position and speed estimator (Fig. 13.2) with the cross-coupling saturation current flux model of SM (Fig. 13.18) is portrayed in Fig. 13.19 [10].

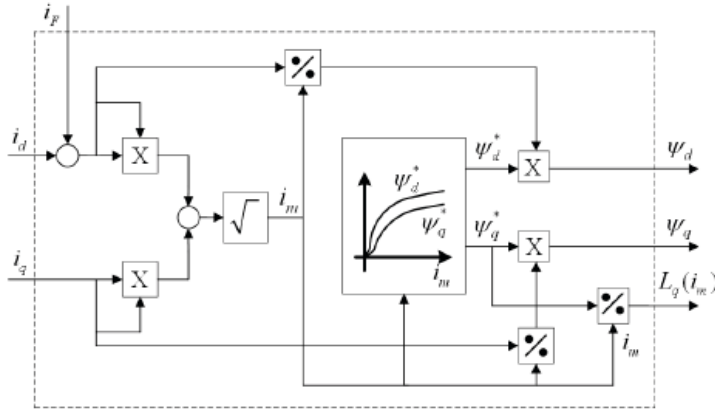


Fig. 13.18 Cross coupling saturation current flux model of d.c. excited SM.

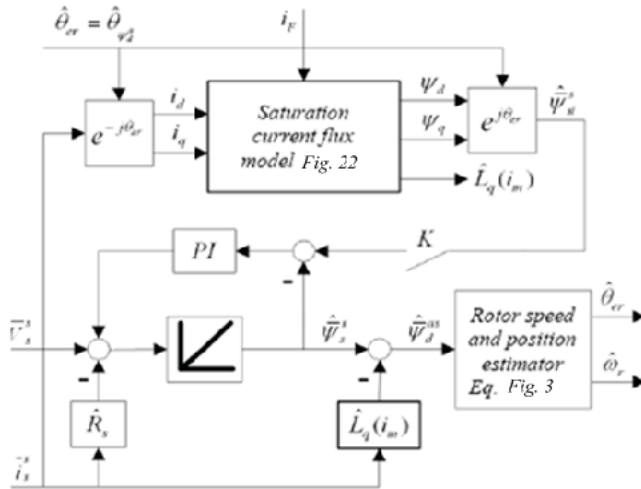


Fig. 13.19 Active flux-based state observer for SM.

The equivalent unique  $dq$  magnetization curves are:

$$\psi_d^* = \psi_d \frac{i_m}{i_d + i_F}; \psi_q^* = \psi_q \frac{i_m}{i_q} \quad (13.24)$$

with

$$L_d = \frac{\psi_d^*}{i_m}, L_q = \frac{\psi_q^*}{i_m}; i_m = \sqrt{(i_d + i_F)^2 + i_q^2} \quad (13.25)$$





The procedure for estimating  $\hat{\theta}_{er}$  is obtained in 3 steps:

- The stator is shortcircuited by applying a zero voltage vector in the inverter ( $V_0(0,0,0)$  or  $V_7(1,1,1)$ ) in 6 switch 2 level voltage source inverters)
- A current ramp is applied to the field circuit
- The induced currents  $i_d(t)$  and  $i_q(t)$  in the stator are recorded. Neglecting the stator resistance influence the stator current vector orientation (at shortcircuit) opposes the rotor d axis position.

Consequently:

$$\hat{\theta}_{er0} \approx -\tan^{-1} \frac{i_\beta}{i_\alpha}; i_\alpha = i_a, i_\beta = (i_a + i_2b)/\sqrt{3} \quad (13.27)$$

During the field current ramping transient, the stator currents are sampled and calculated and an average value  $\hat{\theta}_{er0}$  is calculated after the 25 ms current ramping interval.

A precision of 5° (electrical) has been checked experimentally considering numerous initial rotor position values.

A typical acceleration transient under 100 % load (70 Nm from zero speed, by a friction tightening belt with torque meter) up to 80 rpm is shown in Fig. 13.22 [10].

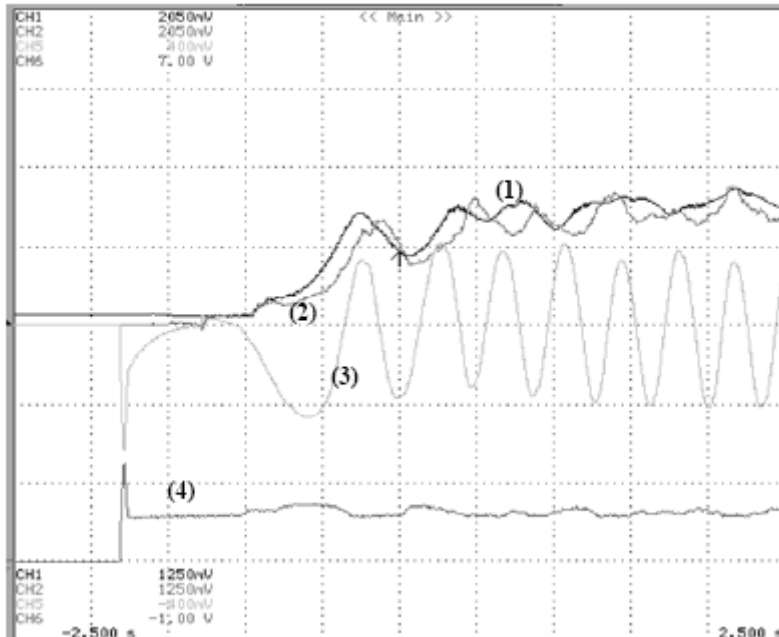


Fig. 13.22 Active flux based FOC of d.c. excited SM: acceleration under full torque (70Nm from zero speed) from zero to 80rpm.

In subsequent tests the same 54 V, 110 A, 4 poles, 70 Nm, 1010 rpm,  $i = 7.5$  A (reduced to the stator  $i_{Fn} = 118$  A),  $R_s = 12m\Omega$  d.c. excited SM drive safe acceleration under full torque from zero speed to 800 rpm has been proven.

It is inferred here that the initial rotor position estimation was kee in safe starting under full load from zero speed.

Final note.

The “active flux” vector concept has been proven instrumental in increasing simplicity, robustness and unification of a.c. motor/generator drives.

### 13.6 “Active flux” based scalar V/f (I-f) control of a.c. machines

V/f (I-f) scalar open loop control in a.c. machines was in fact the first method of control with PWM converters for variable speed. It was also clear from the start that a gentle speed (frequency) referencing with time and voltage amplitude with reference speed (frequency) is required to avoid instabilities and acceleration failures (Fig. 13.23)

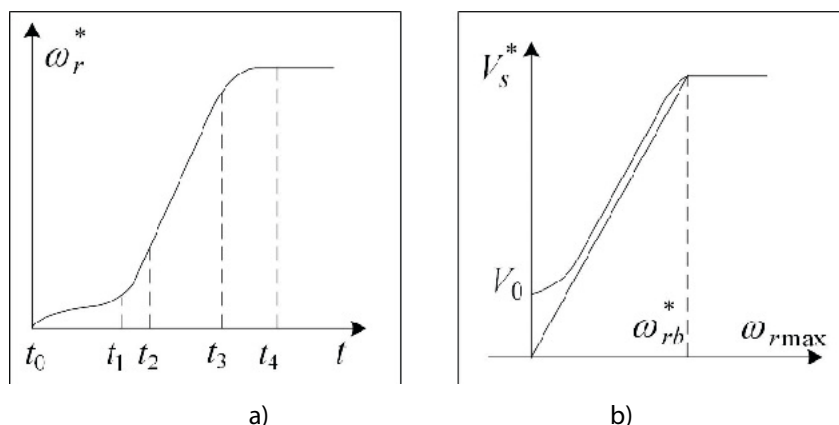


Fig. 13.23 Typical reference speed  $\omega_r^*$  (frequency) versus time, a) and reference voltage amplitude versus  $\omega_r^*$  (frequency).

Involved stability studies have proved that V/f(I-f) control implies slow torque response and that in the absence of a speed close loop regulators and of current regulators, some other stabilizing loops are required to increase the speed control range, the quickness of the torque response and of speed steady state response error (especially in IMs where slip increases with load).

In an effort to solve some of these problems for IM, slip correction was proposed [12-13] and finally frequencies down to 3(1.2) Hz have been reached and sustained from limited slow torque perturbations.

And there is the energy saving during wide speed range control (with flux weakening also) when the stator flux has to decrease with torque and (or) with speed as proved for FOC and DTFC a.c. machine drives.

For what follows “active flux” based V/f (I-f) scalar control methods with d.c. stabilizing loops are introduced to extend the speed range and torque response quickness and precision in both IMs and SMs.

### 13.6.1 An “active flux” based V/f IM control with stabilizing loops

A generic “active flux” based V/f IM control with a single (magnetic energy) close loop is introduced here.

First the active flux  $\bar{\psi}_d^a$  oriented along rotor flux is:

$$(\bar{\psi}_d^a)^{\psi_r} = (L_s - L)i_d; T_e = \frac{3}{2} p_1 \psi_d^a i_q \quad (13.28)$$

The current components  $i_d$  and  $i_q$  are expressed in rotor flux (active flux) coordinates as known.

Here maximum power factor is the default operation:

$$\left(\frac{i_d}{i_q}\right)_{(\cos \varphi)} = \sqrt{\frac{L_{sc}}{L_s}}; \bar{\psi}_s = L_s i_d + jL_{sc} i_q; \bar{\psi}_r = \psi_d^a \frac{L_m}{L_s - L_{sc}} \quad (13.29)$$

with  $L_m$  - cyclic magnetization inductance of IM .

It has been proved that the IM magnetic energy for  $(\cos \varphi)_{\max}$  :

$$(W_m)_{(\cos \varphi)_{\max}} = \frac{3}{2} (L_s i_d^2 + L_{sc} i_q^2) = 3L_{sc} i_q^2 \quad (13.30)$$

The stator flux and active flux estimator of Fig. 13.2 may be used here too. But for  $f_1 > 1$  Hz, the voltage model estimator will suffice:

$$\hat{\bar{\psi}}_s \cong \int (\bar{V}_s - R_s \bar{i}_s) dt \approx \frac{T}{1 + sT} (\bar{V}_s - R_s \bar{i}_s) \quad (13.31)$$

$$\hat{\bar{\psi}}_d^a = \hat{\bar{\psi}}_s - L_{sc} \bar{i}_s \quad (13.32)$$

$$T_e = \frac{3}{2} p_1 \operatorname{Re}(j \hat{\bar{\psi}}_s \bar{i}_s^*) \quad (13.33)$$

Also in stator coordinates  $W_{m\alpha\beta}$  is:

$$W_{m\alpha\beta} = \frac{3}{2} \operatorname{Re}(\hat{\bar{\psi}}_s \bar{i}_s^*) \quad (13.34)$$

Now the reference voltage (as in Fig. 13.23) may be corrected by  $\Delta V$  :

$$\Delta V_{\cos \varphi} = PI(W_{m\alpha\beta} - (W_{mdq})_{\cos \varphi} \max) \quad (13.35)$$

when the voltage limit is met:

$$V_s^* - V_{s \max} \geq 2 \quad (13.36)$$

The  $\Delta V_{\max}$  should consider the case of max torque /flux magnetic energy formula:

$$(W_m)_{flux} = \frac{3}{2} i_{sc} i_q^2 \left(1 + \frac{L_{sc}}{L_s}\right) \quad (13.37)$$

A gradual from  $\Delta V_{\cos \varphi}$  to  $(\Delta V)_{flux}$  should reduce transients.

The generic control scheme depicted above is presented in Fig. 13.24.

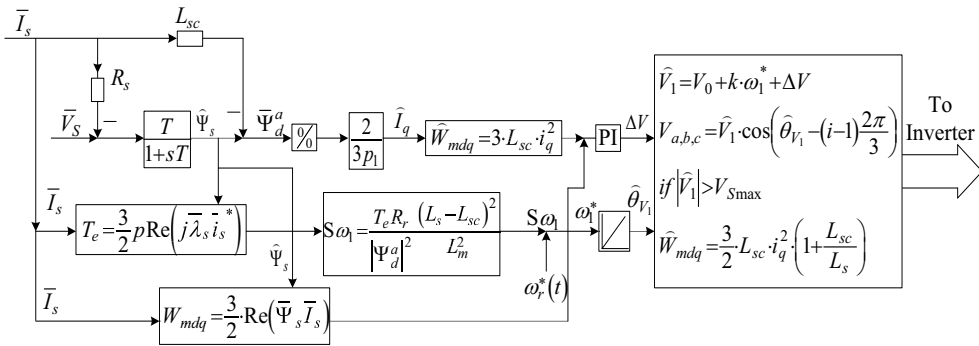


Fig. 13.24 Active flux based V/f IM control with magnetic energy stabilizing loop [3].

The slip frequency  $s w_1$  compensation is feed forwardly compensated to yield the reference frequency and thus the reference voltage phase  $\theta_{v1}^*$  :

$$w_1^* = w_r^*(t) + s w_1; \theta_{v1}^* = \int w_1^* dt \quad (13.38)$$

In depth for the investigations are required to prove the above scheme performance/cost competitive.

### 13.6.2. SPMSM V/f control with stabilizing loops [14]

A similar rationale as above in terms of magnetic energy close loop, but here both voltage amplitude and angle are corrected by  $\Delta V$  and  $\theta_v$  .

In SPMSMs, the active flux  $\psi_d^a = \psi_{PM}$  .

However, the magnetic energy is here for maximum torque per current ( $i_d = 0$ ):

$$(W_{dq})_{i_d=0} = \frac{3}{2}(\psi_d^a i_d + L_{sc} i_s^2) = \frac{3}{2} L_{sc} i_s^2 \quad (13.39)$$

Its reactive power is:

$$(Q_{dq})_{i_d=0} = \frac{3}{2} \omega_r^* L_{sc} i_s^2 \quad (13.40)$$

In (stator) coordinates the reactive power  $(Q_{dq})_{i_d=0}$  is:

$$Q_s = \frac{3}{2} (V_\beta i_\alpha - V_\alpha i_\beta) \quad (13.41)$$

Finally, the correction voltage amplitude  $\Delta V$  is:

$$\Delta \hat{V} = PI(Q_s - Q_{dq(i_d=0)}) \quad (13.42)$$

A similar correction  $\Delta \hat{\theta}_{v1}$  may be calculated after filtering:

$$\Delta \hat{\theta}_{v1} = HPF(\Delta \hat{V}) \quad (13.43)$$

Alternatively the active power pulsations (calculated in the d.c. link with  $V_a^*, V_b^*, V_c^*$  and  $i_a^*, i_b^*, i_c^*$ ) - with a high pass filter -  $\Delta P$  may produce  $\Delta V$  to correct the voltage angle.

Such a control system is shown in Fig. 13.25.

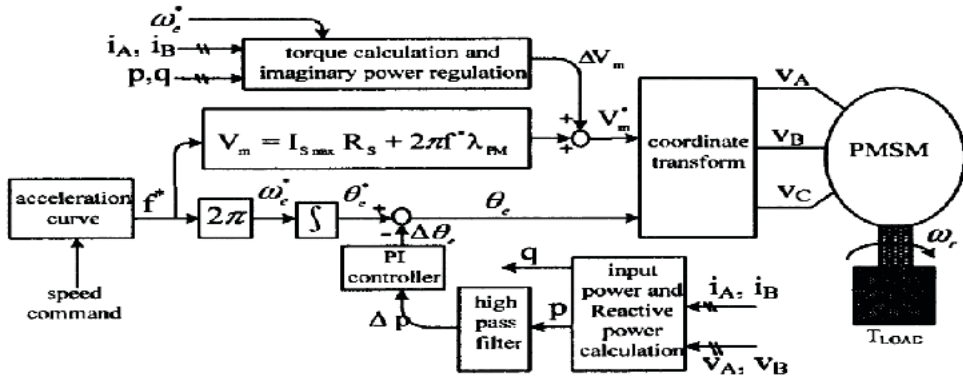
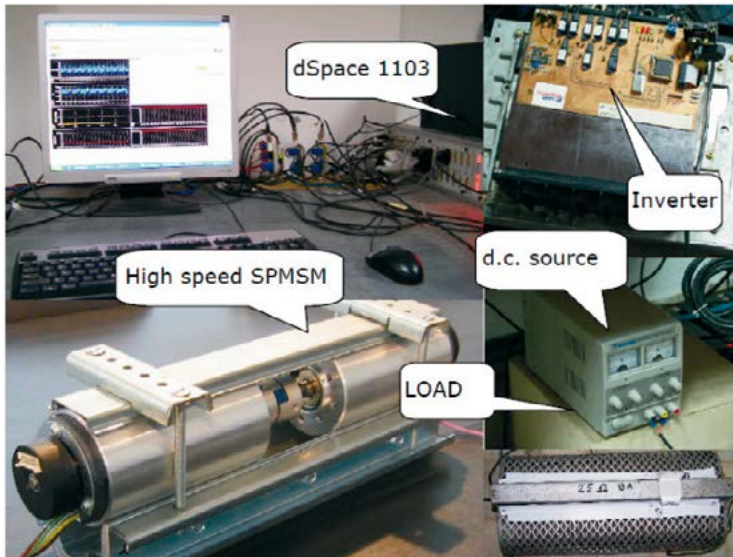
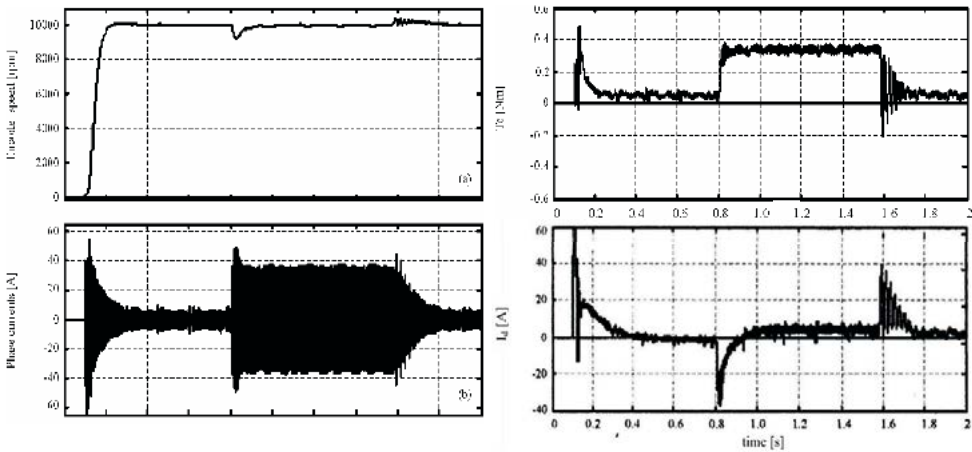


Fig. 13.25 V/f with frequency power modulation and reactive power control of an PMSM.

Acceleration and loading transients for a 14 Vdc inverter fed SPSM (Fig. 13.26.a) shows in Fig. 13.26.b a remarkable behavior. In the sense that a fast acceleration is obtained and when loaded the current increases, a sign that losses are small at small torque (max torque /current) and thus energy savings is included in the control as done in FOC and DTFC.



a)



b)

Fig. 13.26 14V<sub>DC</sub> small PMSM back to back testing platform a) and test transients with V/f and correction loop (as if Fig. 13.25b).

### 13.6.3 IPMSM scalar V/f control and stabilizing loops

Refs [15-16] propose similar V/f control schemes with stabilizing loops for PM-RSMs and IPMSMs based on an “active flux” observer (but, again without speed or current close loops).

Typical experimental such results [16], Fig. 13.27, show operation at 5 rpm (0.25 Hz) which may be considered still a record in V/f a.c. drives.

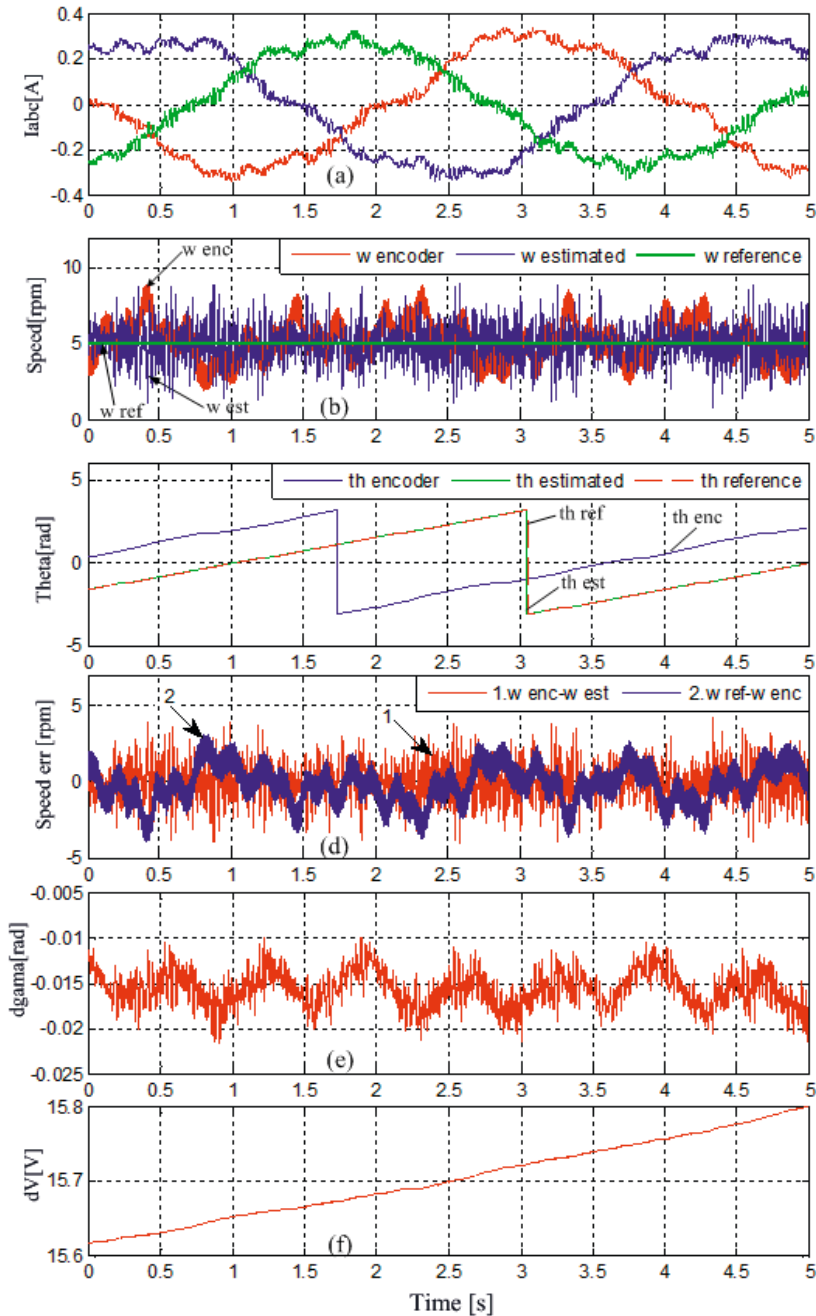
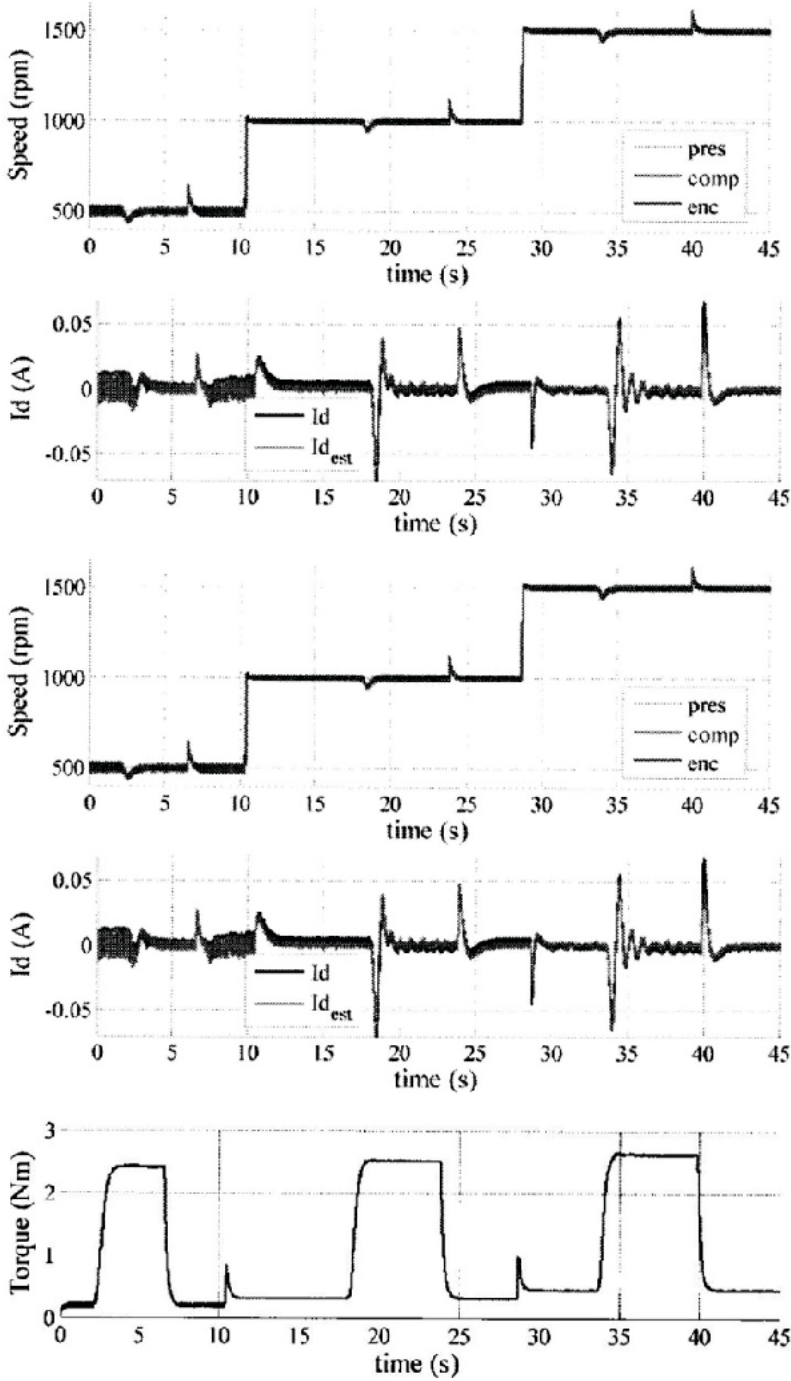


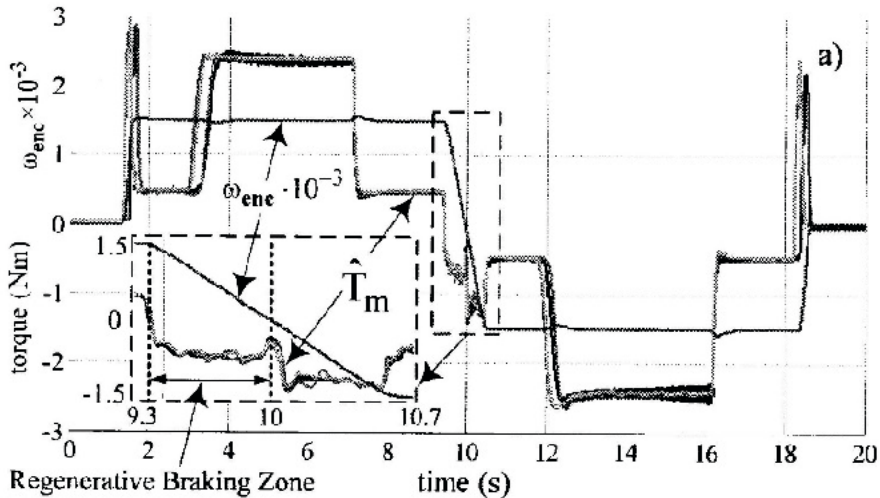
Fig. 13.27 IPMSM V/f control with stabilizing loops: test results at 5rpm on no load.

To illustrate the torque response quickness in V/f control with stabilizing loops even in SPMSM heavy experimental transients are shown in Fig. 13.28 [17], which illustrates “a regenerative braking” episode.



a)





b)

Fig. 13.28 Active flux based SPMSM speed and torque heavy transients in V/f control with frequency modulation and power factor angle stabilizing loop [17]: a) and a regenerative braking episode ( $\omega_r > 0, T_e < 0$ ) b).

Furthermore, I-f control for starting with “active flux” observer FOC of RSM [18] and for single phase BLDC-PM motor [19] have been demonstrated.

In the latter case, again, regenerative braking was performed to certify response quality for wide speed range control of small power single phase BLDC-PM motors.

Final Note.

The developments on V/f (I-f) control of IMs, PMSMs and RSMs showed notable potential in competitiveness (performance/cost), but they may be extended to d.c. excited SMs and to all types of vehicular or power system electric generators that operate at variable speed.

## 13.7 References

- [1] I. Boldea, M. C. Paicu, G. D. Andreescu “Active flux concept for motion sensorless unified ac drives”, *IEEE Trans vol. PE-23*, no 5, 2008, pp. 2612-2618
- [2] I. Boldea, S. C. Agarlita, L. Tutelea “The active flux concept for motion-sensorless unified a.c. drives – a tutorial review”, *record of ACEMP 2011*, Bodrum, Turkey
- [3] I. Boldea, A. Moldovan (Popa) L. Tutelea, “Scalar V/f and I-f control of a.c. motion drives” *Record of ACEMP/OPTIM/Electromotion 2015*, Side, Turkey
- [4] Z. Chen, M. Tomita, S. Ichikawa, S. Doki, S. Okuwa “Sensorless control of IPMSM by extraction of an extended EMF”, *record of IEEE – IAS – 2000*, pp. 1814 – 1819
- [5] S. Koonlaboon, S. Sangwongwanich “Sensorless control of interior PMSMs based on fictitious permanent magnet flux model”, *Record of IEEE-IAS 2005*, vol. 1, pp311-318

- [6] M. Barcaro, M. Morandin, T. Pradella, N. Bianchi, I. Furlan "Iron Saturation Impact on High-Frequency Sensorless Control of Synchronous Permanent-Magnet Motor", *IEEE Trans.* Vol. IA-53, no. 6, 2017, pp. 5470 - 5478.
- [7] M. C. Paicu, F. Blaabjerg, L. Tutelea, C. Lascu, G. D. Radulescu, I. Boldea "Wide speed range sensorless control of PM-RSM via active flux model", *Record of IEEE-ECCE 2009*, pp. 3822-3829
- [8] S. Agarlita, I. Boldea, F. Blaabjerg "High frequency injection assisted active-flux based sensorless vector control of RSM with experiments from zero speed", *IEEE Trans* vol IA-48, no 6, 2012, pp.1931-1939.
- [9] I. Boldea, G. D. Andreescu, C. Rossi, A. Pilati, D. Casadei "Active flux based motion sensorless vector control of a.c. excited synchronous motor" *Record of IEEE-ECCE-2009*, pp. 2496-2503.
- [10] I. Boldea, S. A. Nasar "Unified treatment of core losses and saturation in the orthogonal-axis model of electric machines", *IEE Proc. Vol 134 Pt b*, no. 6, 1987, pp. 355-363
- [11] K. Koga, R. Ueda, T. Sonoda "Constitution of V / f control for reducing the steady state speed error to zero in PMs drive system", *IEEE Trans.* Vol. IA-28, no. 2, 1992, pp. 463-471
- [12] M. A. Garcia, T. A. Lipo, D. A. Novotny "A new IM V/f control capable for high performance regulation at low speeds", *IEEE Trans* vol. IA-34, no. 5, 1998, pp. 813-821.
- [13] R. A. Ancuti, I. Boldea, G. D. Andreescu "Sensorless V/f control for surface PMSM drives", *IET Proc.* Vol 4, No. 3, 2010, pp. 40-57.
- [14] I. Boldea, A. Moldovan, V. Coroban-Schramel, G. D. Andreescu "A class of fast dynamics V/f sensorless AC general drives with PM-RSM as a case study", *Record of OPTIM – 2010 (IEEEExplore)*, pp. 453-459
- [15] A. Moldovan, F. Blaabjerg, I. Boldea "Active flux based V/f with stabilizing loops versus sensorless vector control of IPMSM", *Record of IEEE-ISIE-2011*, pp. 514-519.
- [16] A. Agarlita, C. Coman, G. D. Andreescu, I. Boldea "Stable V/f control system with controlled power factor angle for SPMSMs", *IEE Proc.* Vol. EPA, no. 6, 2013
- [17] S. C. Agarlita, M. Fatu, L. Tutelea, F. Blaabjerg, I. Boldea "I-f starting and active flux based sensorless vector control of RSM, with experiments", *Record of OPTIM-2010 (IEEEExplore)*
- [18] E. I. Iepure, F. Blaabjerg, I. Boldea "Hybrid I-f starting and observer-based sensorless control of single phase BLDC-PM motor drives", *IEEE Trans.* Vol IE-59, no. 9, 2012, pp. 3436 – 3444.

# HIGH PERFORMANCE RELUCTANCE SYNCHRONOUS MACHINES FOR VARIABLE SPEED: MODELING, PERFORMANCE AND DESIGN

## 14.1 Abstract

For general a.c. machine variable speed drives traditionally inverter-fed cage-rotor induction motors (CRIM) are used both for motoring and generating (in wind and small hydro generators in the MW power range).

Lacking the rotor cage (with its cooling problems reluctance synchronous machines (RSMs), but allowing for high magnetic saliency  $L_d/L_q > 5/1$  would increase efficiency with (5-1)% in the 10 kW-1.5 MW range, but produce by (7-10)% the power factor in comparison with IM drives.

High magnetic saliency  $L_{dm}/L_{qm} > 8-10$  has been already obtained in the kW to MW range in 4 pole configurations RSMs with multiple-flux-barrier (MFB) rotors being recently brought to markets from 10 kW to 500 kW and to 1500 kW in 4pole configuration for variable speed.

However, below 10 kW, and in general axially laminated anisotropic (ALA) rotors have been proven capable of much higher magnetic saliency  $L_d/L_q = 16$  (saturated conditions, for a 1.5 kW, 2 pole RSM)[1]. Thus, a record for maximum power factor  $\cos \varphi_{\max} = 0.91$  has been measured. Although ALA rotor fabrication is still considered difficult, the potential performance improvement on existing (MFB) rotors is worth revisiting for 2 and more poles.

This is why ALA-RSM is presented here in detail. A MFB rotor with PMs in the flux barriers (axis q) and field coils on rotor in axis d (BEGA) is also introduced due to the capacity to operate at unity power factor on a wide CPSR (ideally infinite) [2].

A high performance single-phase a.c. PM generator with saturation produced magnetic saliency is presented to further illustrate the possibilities of variable magnetic saliency to improve a.c. machine performance [3].

Finally, a multi-phase reluctance machine (MRM) operating quasi-synchronously with bipolar currents (BLDC) is described as it shows remarkable potential without PMs and without a rotor winding.

## 14.2 ALA rotor RSMs for variable speed drives

Reluctance synchronous motors (RSM) for variable speed are illustrated by Fig. 14.1.

- A distributed stator 3 (or more) phase a.c. winding with  $2p$  poles
- A cage-less rotor with notable magnetic anisotropy along orthogonal d-q axes  $L_{dm} > L_{qm}$
- Tooth-wound a.c. windings have also been tried recently, but the magnetic saliency is notably small and only PM assistance in axis q may lead to acceptable power factor, efficiency and torque density ( $emf_{PM}/V_{s\max} < (0.3 - 0.5)$ ).
- The lack of PMs and of the cage on the rotor leads to notably smaller losses in the rotor and the possibility of heavy safe overloading as long as the magnetic saliency does not diminish dramatically with increasing currents. This property of maintaining notable  $L_d/L_q$  ratio at heavy overload is typical to ALA rotors in distributed a.c. windings ( $q_1 > 2$  slots/pole/phase).

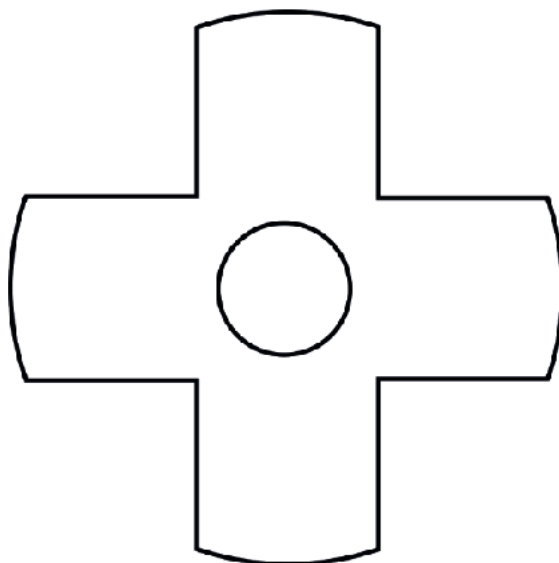


Fig. 14.1 Commercial RSM rotors a) standard ( $2p = 4$ ):  $L_{dm} = L_{qm} < 2$ , b) MFB ( $2p = 4$ ):  $L_{dm}/L_{qm} = 5-8$ , c) MFB ( $2p = 2$ );  $L_{dm} / L_{qm} = 7-10$ .

ALA rotors in  $2p=2$  (shaftless) or  $2p=4$ ,  $\delta \dots$  configurations (Fig. 14.2).

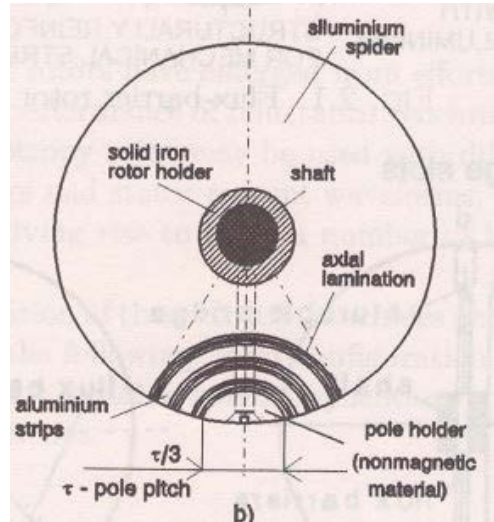
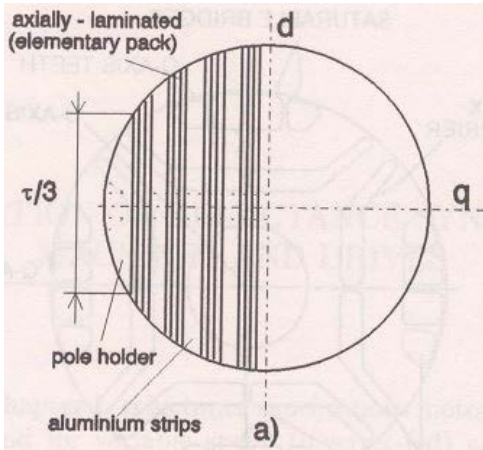


Fig. 14.2 ALA rotors for RSMs a)  $2p = 2$  (shaftless)  $L_{dm} / L_{qm} > 15$ , b)  $2p = 6$   $L_{dm} / L_{qm} > 8 - 10$ .

The absence of lamination bridges in ALA rotors in contrast to MFB rotors increases notably the magnetic saliency  $L_{dm} / L_{qm}$  and makes the RSM more suitable for premium performance.

**Note on ALA rotor fabrication**

So far, the fabrication of 2 pole and multiple pole ( $2p > 2$ ) ALA rotors is still considered difficult. A special fabrication line is justifiable only for mass production.

It is clear from Fig. 14.2 that the ALA rotor may be emulated (approximately by using even a few transverse laminations could do it (Fig. 14.3).

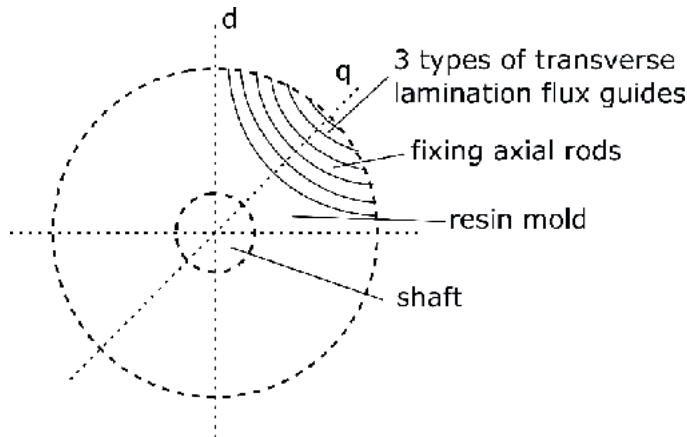


Fig. 14.3 Open MFB rotor for RSM.

The number of lamination types should be limited to perhaps 4(5) per pole.

The magnetic saliency is a bit smaller than that of axial lamination/insulation layer ALA rotor, but it may be easier to fabricate.

The main quality is the absence of flux bridges between flux guides, which results in smaller magnetic saturation influence on reducing  $L_{dm}/L_{qm}$  ratio under heavy overloads.

### 14.3 ALA rotor 2 pole RSM of 1500 W at 3000 rpm case study

To illustrate the performance capability of a small power RSM with ALA rotor, the stator of a 2 pole IM of 1500 W (2HP) at 60 Hz was used with an ALA rotor with alternate axial laminations (0.35 mm thick) and insulation layers (0.2 mm thick) spanning over 66% of the pole pitch.

The rotor ALA composite was fixed with KEVLAR pole caps, with shafts added axially afterwards to form an aligned shaft that allows a 0.3 mm airgap at 3600 rpm [1,2], Fig. 14.4.

Skipping the analytical design methodology of such an RSM [1,2], here only FEM characterization and experimental results are available.



Fig. 14.4 1.5kW, 2pole, 3600rpm ALA rotor RSM prototype, after [1, 2].

Early FEM analysis of magnetic flux paths in axis  $d$  shows they are straight in the rotor, while in axis  $q$  they meander in the rotor and some between the rotor and stator teeth.

Consequently, as expected, the airgap flux densities in axis  $d$  and  $q$  (Fig. 14.6) show high frequency pulsation in axis  $d$  (due to the alternation of lamination /insulation layers in the rotor) and positive and negative values in axis  $q$  over half of a pole pitch; an indication that the magnetic potential of rotor for axis  $q$  is not constant. The  $q$  axis heavy space

harmonics are likely to produce additional rotor core losses in the axial laminations as the flux lines go normally to the former.

Special measures such as 3-5 slots axial suffice to reduce these losses 3-5 times (roughly), Fig. 14.7.

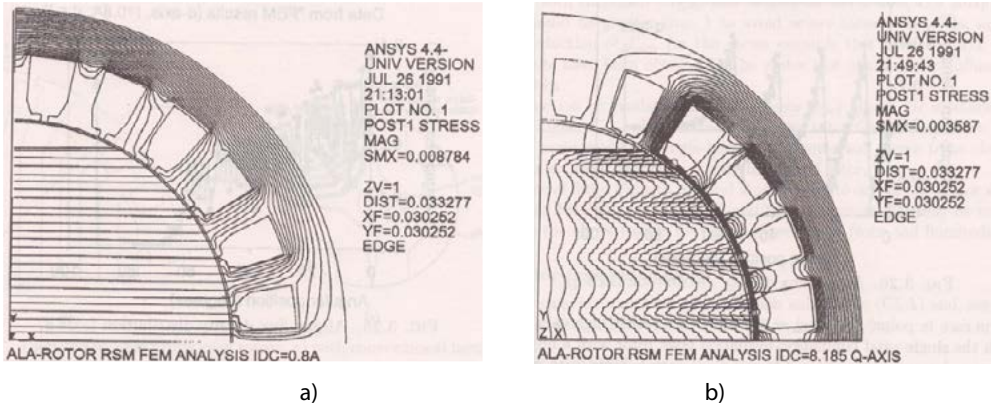


Fig. 14.5 Two pole ALA rotor RSM flux lines a) in axis d, b) in axis q.

$$L_{dm}/L_{qm} = \frac{B_{gd1}}{B_{gq1}} \frac{i_q^2}{i_d \sqrt{3}} \tag{14.1}$$

The magnetization ratio  $L_{dm}/L_{qm} = 30$  with  $L_d/L_q = 16$  ....saturated are obtained with the formula in (14.1), where the ratio  $\frac{2}{\sqrt{3}}$  is due to the 3/2 phase d.c. currents  $i_d, i_q$  in the calculations.

The inductances  $L_d, L_q$  have been measured in a.c. standstill tests ( $d, q$ ) and in no load tests ( $d$ ) –Fig. 14.8.

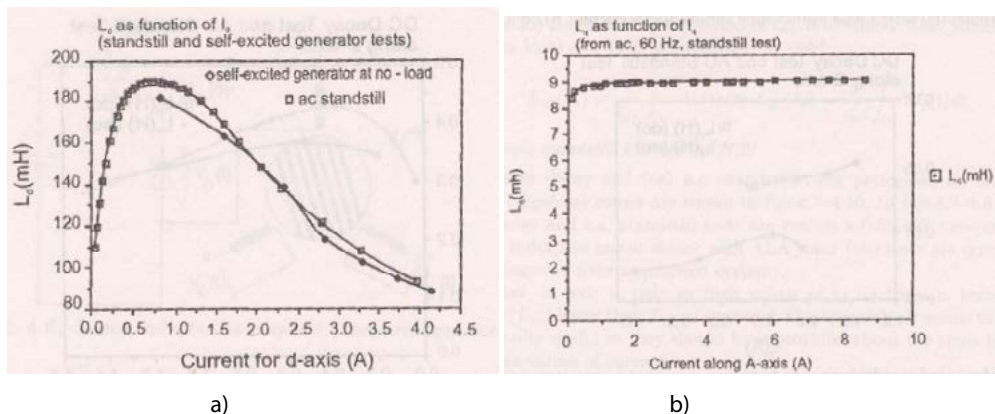


Fig. 14.8 Measured machine inductances a) in axis d, b) in axis q.

A ratio  $L_d/L_q \approx 16$  for rated conditions was also measured.



The  $dq$  model torque of RSM and induction machines are [2]:

$$T_{eiM} = \frac{3}{2} p_1 (L_s - L_{sc}) i_d i_q ; \psi_r = L_m i_d \quad (14.2)$$

(in rotor flux coordinates)

$$L_{dm}/L_{qm} = \frac{B_{gd1}}{B_{gq1}} \frac{i_q^2}{i_d \sqrt{3}} \quad (14.3)$$

(in rotor coordinates).

Moreover, the maximum ideal (zero losses) power factor is calculated for:

$$\cos \phi_{maxi} = \frac{1 - L_q/L_d}{1 + L_q/L_d} = \frac{1 - 1/16}{1 + 1/16} \approx 0.91 \quad (14.4)$$

In reality, due to losses, the maximum power factor is slightly larger for motoring and smaller for generating on account of machine losses.

Direct on load measurements at power grid and variable voltage (through a VARIAC). The synchronization was done by using a d.c. brush motor drive, through the VARIAC. Once the motor voltage was raised enough, the d.c. brush machine was disconnected, only to be used for slow loading as a d.c. brush generator or a variable resistive load.

For each load value, the voltage was varied until maximum power factor was obtained on the digital power analyzer. This way, the results in Fig. 14.9 have been obtained.

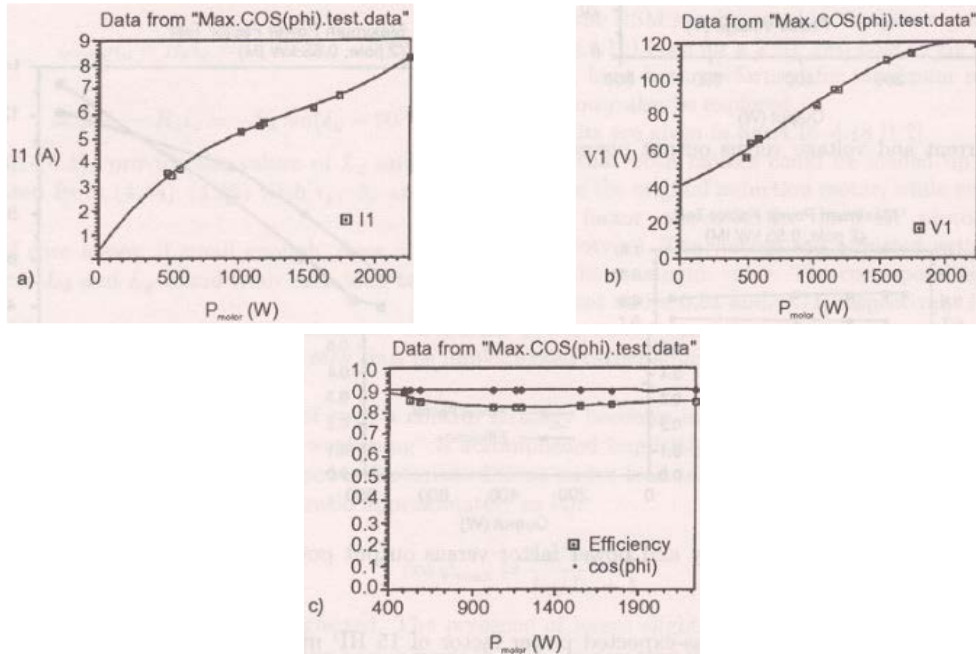


Fig. 14.9 Two pole 1.5kW, 60Hz ALA Rotor RSM performance under load a) current versus power, b) voltage versus power, c) efficiency and power factor.



The power factor was maintained around its calculated 0.91 value for all loads (by voltage variation at 60 Hz) while the efficiency varied, but above 0.86 (at least 4% more than the IM with same stator).

The 0.91 power factor is 7% more than for the original induction motor.

Furthermore, peak power could go safely to 150%, by slow loading under constant frequency (60Hz) and variable voltage.

The machine, with close loop, FOC, DTFC could be heavily overloaded as explained earlier.

Note. At no instant during the experiments the rotor would touch the stator at 3000 rpm for 0.3 mm of airgap.

Advanced FOC and DTFC of ALA rotor RSMs with encoder or encoder less have been successfully tested [3,4-6].

#### 14. 4 BEGA – a biaxial excitation generator for automobiles: a case study

BEGA was proposed for integrated starter-alternator, or for electric propulsion on HEVs.

Bega was proposed for integrated starter-alternator, or for electric propulsion on HEVs and EVs, or as a generator for autonomous applications at constant or for variable speed.

The stator of BEGA is provided with a laminated core with uniform slotting that hosts a distributed 3 phase (or more) a.c. winding.

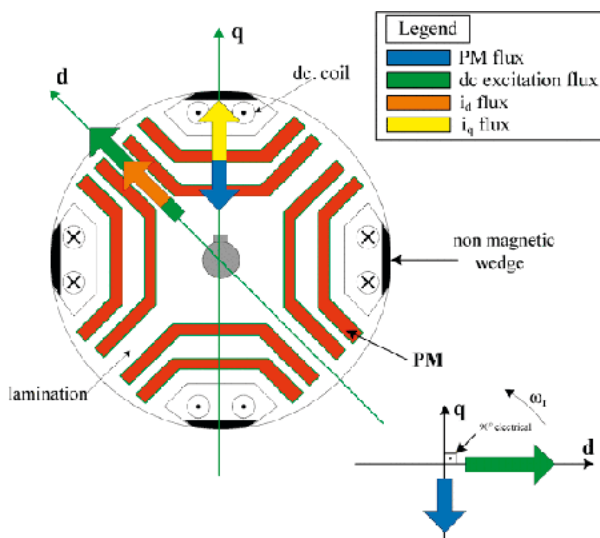


Fig. 14.10 BEGA rotor cross-section.

The rotor (Fig.14.10) is typical for a MFB-RSM, but it allows for big slots in axis q (Fig. 14.10), where d.c. coils are placed. The d.c. excitation coils act on a small airgap large

inductance in axis d and thus it implies low d.c. excitation power to be fed to the rotor through slip rings and brushes (as in standard claw pole alternators).

Or contactless lower power is transmitted to the d.c. excitation on the rotor via an inverter + rotary transformer + high frequency diode rectifier.

The multiple flux barriers are partially or totally filled with PMs so that by control the stator flux in axis  $q\psi_q = 0$  :

$$\psi_q = L_q i_{qk} - \psi_{PMq}; \psi_q = 0, \frac{d\psi_q}{dt} = 0 \quad (14.5)$$

Furthermore, the magnetic saliency should be large, so that  $i_{qk} = i_{sn}$  ( $i_d = 0$  control) for zero  $\psi_q$ .

The PMs are not demagnetized in this situation, because part of  $L_q$  is represented by the leakage inductance an inverter fed BEGA principle.

The mathematical  $dq$  model of BEGA in rotor coordinates is:

$$\psi_q = L_q i_{qk} - \psi_{PMq}; \psi_q = 0, \frac{d\psi_q}{dt} = 0 \quad (14.6)$$

$$\bar{\psi}_s = \psi_d + j\psi_q; \psi_d = L_d i_d + L_m i_F; \psi_q = L_q i_q - \psi_{PMq} \quad (14.6)$$

$$T_e = \frac{3}{2} p_1 [L_m i_F + (L_d - L_q) i_d + \psi_{PMq}] i_q \quad (14.8)$$

$$V_F = R_F i_F + \frac{d\psi_F}{dt}; \psi_F = L_{md} i_d + (L_{Fe} + L_{dm}) i_F \quad (14.9)$$

The rotor current  $i_F, R_F, \psi_F$  and  $V_F$  are already reduced to the stator.

Apparently, the torque  $T_e$  has gained three positive terms with  $L_d > L_q, i_d > 0, i_F > 0$ .

In reality, what limits the torque is magnetic saturation and overtemperatures in the various windings.

The FOC of BEGA may thus provide, by close loop control,  $\psi_q = 0, i_d = 0$  and thus automatically:

$$\bar{\psi}_s = L_{md} i_F; T_e = \frac{3}{2} p_1 L_{md} i_F i_{qk}; \cos \phi_1 = 1 \quad (14.10)$$

$$\text{as } V_F = R_F i_F + \frac{d\psi_F}{dt}; \psi_F = L_{md} i_d + (L_{Fe} + L_{dm}) i_F \quad (14.11)$$

For constant field current (steady state).

This condition allows for ideally infinite CPSR ( $R_s i_q \approx 0$ ) at minimum stator current  $i_{qk} = i_{sn}$ . Consequently, for given large torque below base speed, the inverter KVA rating

is reduced in general by 30 % (from  $\cos\varphi = 0.707$  to  $\cos\varphi = 1$ ). The price to pay is the maximum 5% KVA of the d.c.-d.c. converter that feeds the excitation system. Now, however, the field current  $i_f$  is the “torque” current which is controlled positively and negatively.

### BEGA with diode rectifier output

A BEGA prototype of 1.5 Kw AT 1500 rpm, 42 Vdc (with diode rectifier) was designed [7] for an efficiency of none than 80% for 7.35 kg of active materials.

Typical design parameters are:  $V_s = 20.658$  V/phase (RMS),  $R_s = 0.0577\Omega$ ,  $L_d = 3.33$  mH,  $L_q = 0.48$  mH,  $\lambda_{PMq} = 0.01761$  Wb,  $i_{sn} = 55.6$  A,  $L_{mF} = 31.28$  mH (field armature inductance for actual field current). With generating through a diode rectifier, the d.c. current output is regulated only by the field current (as in the standard claw pole rotor automotive alternators).

In this case, the fundamental power factor is about unity, but this situation corresponds to and  $i_d = 0$  and  $\psi_q = 0$  only in a single situation.

Digital simulation results are shown in Fig. 14.11.

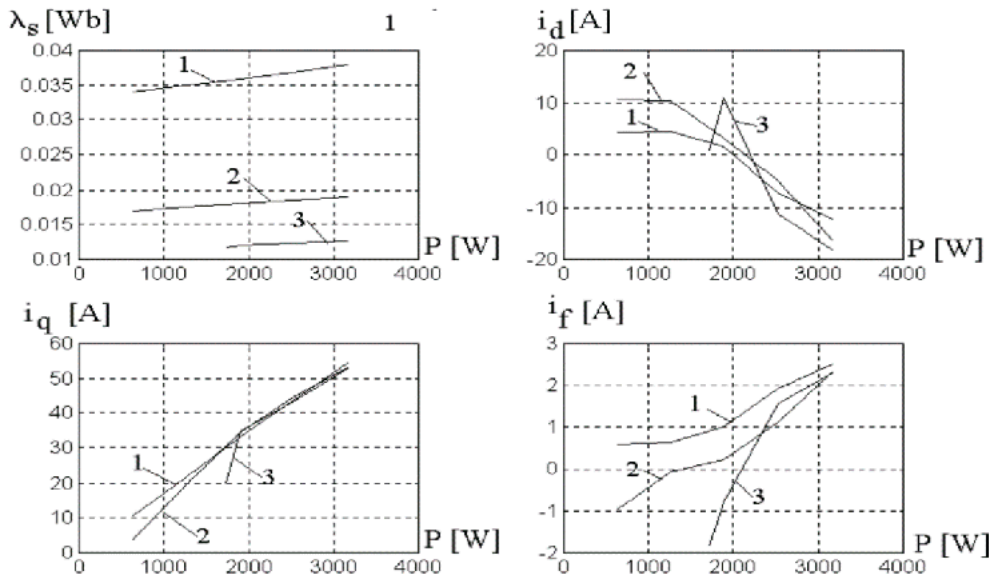


Fig. 14.11 Simulation results: a) Stator flux  $\psi_s$  versus output power; b) d-axis current ( $i_d$ ) versus power; c) q-axis current ( $i_q$ ) versus power; d) field current ( $i_f$ ) versus power; 1, 2, 3 refers to 50Hz, 150Hz, 300Hz (after [7]).

The results in Fig. 14. 11 show that the output power increase with speed (frequency) and by output power if 3 kW may be obtained at 300 Hz (9000 rpm).

Also the zero  $i_d$  condition occurs at different powers for different speeds.

Half rated power (1.5 kW) is delivered at 1500 rpm, while full power (3 kW) is provided from 1650 rpm to 6000 rpm.

At 9000 rpm (Fig. 14.11), with even negative field current, more than 54% rated power is obtained.

**Unity power factor control of BEGA as motor/generator.**

To yield wide constant power speed range at unity power factor for the torque speed envelope  $(T_{ek}(\omega_r)) i_q = i_{qk} = \frac{\psi_{PMq}}{L_q} = const.$  and  $i_d = 0$  by close loop control, but for lower torques  $i_{qk} = i_{sn}$  is too large and may be reduced:

$$i_q^* = i_{qk} \sqrt{\frac{T_e^*}{T_{ek}(\omega_r)}} \tag{14.11}$$

This is an approximation which assures that still the power factor will not decrease too much for lower torque and thus both  $i_q^*$  and  $i_F^*$  are reduced equally as for unity power factor with  $i_d^* = 0$  and  $i_q^* = i_{qk}$ .

Consequently, that current references calculations are shown in Fig. 14.12.

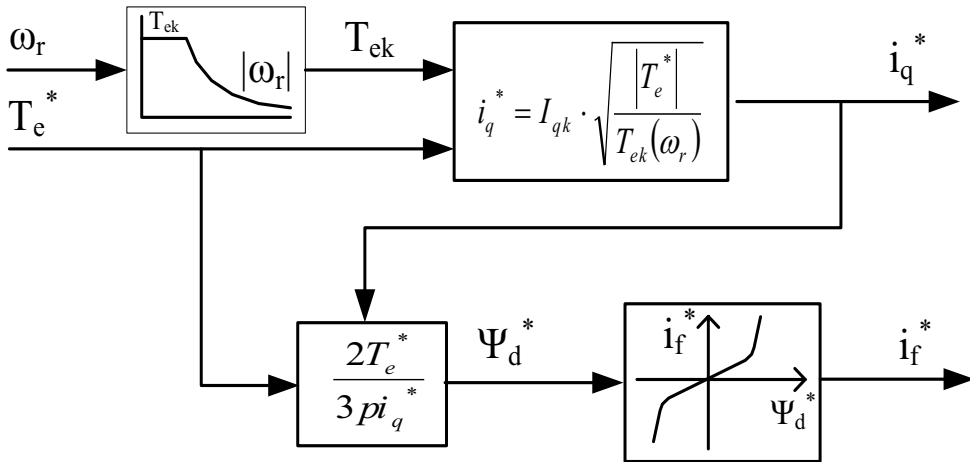


Fig. 14.12 Reference current calculations:  $i_d^*, i_F^*, i_d^* = 0$

The vector control system in Fig. 14.13 makes use of the current reference in Fig. 14.12.

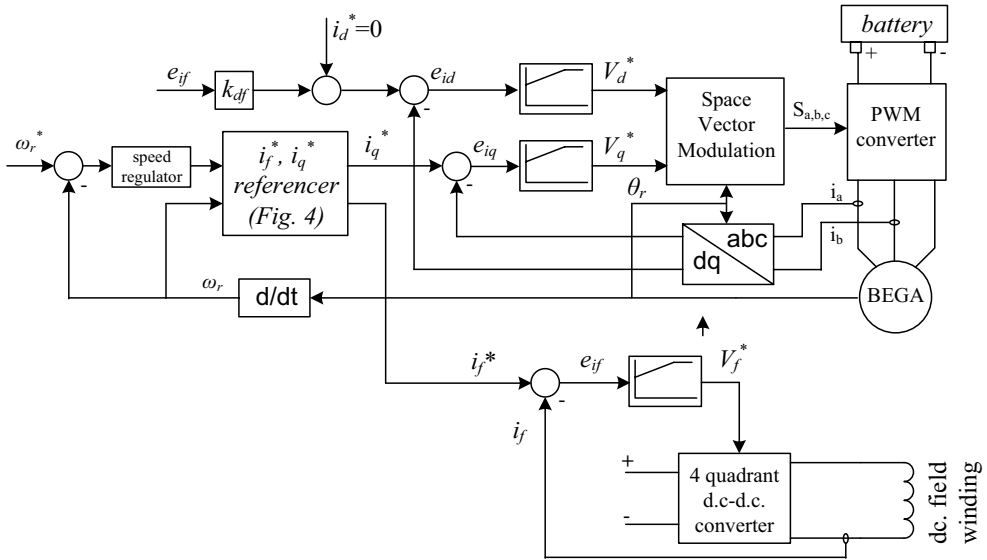


Fig. 14.13 Vector control of BEGA as a motor.

The nonzero  $i_d^*$  intervenes only during transients when the “slowey” field current is advancing to its target value. The torque response will be quickened to 5-6 ms this way.

For the torque/speed envelope ( $\cos \varphi_1 = 0, i_d^* = 0, i_q^* = i_{qk}$ ), the power and torque variations with speed are shown in Fig. 14.14, both in motoring and generating.

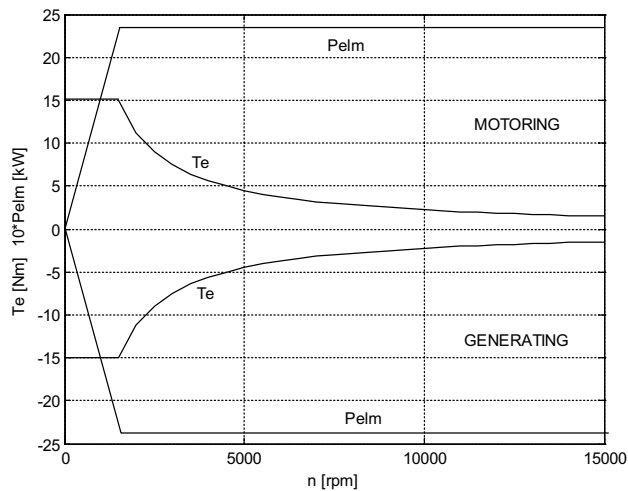


Fig. 14.14  $T_{ek}(\omega_1), P_{elm}(\omega_1)$  versus speed for motoring, generating.

Acceleration from zero to 1500 rpm transients are shown in Fig. 14.15.

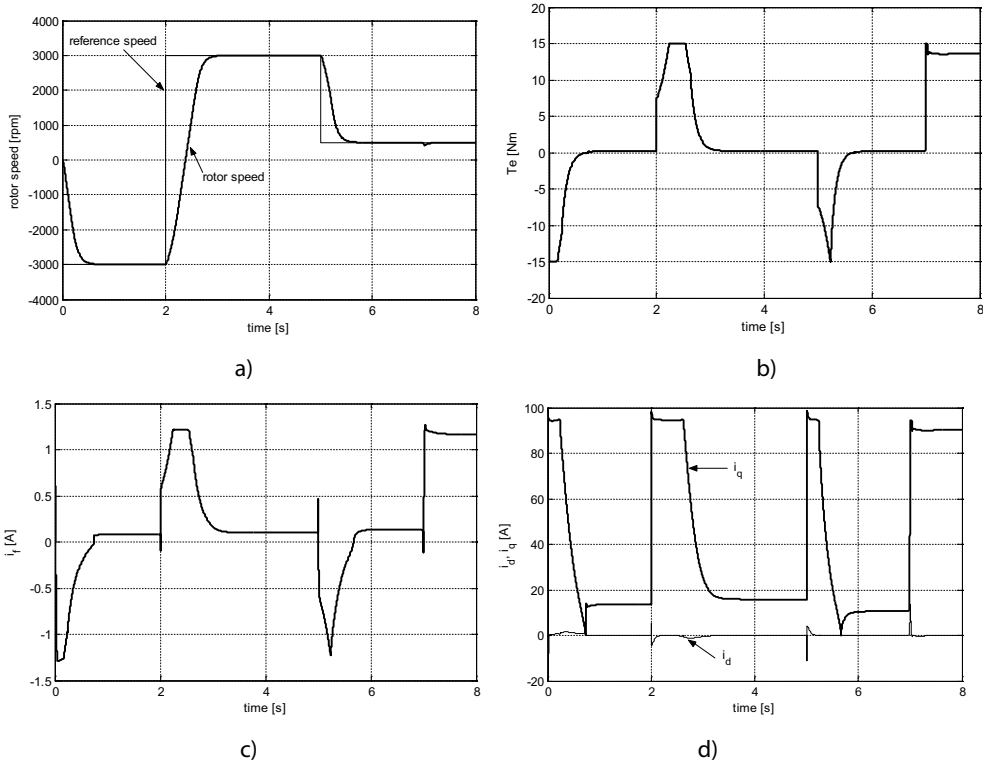


Fig. 14.15 Acceleration from 0 to 1500rpm: a) rotor speed, b) electromagnetic torque c) field current (before reduction to stator), d)  $i_d, i_q$  stator currents ( $i_d^* = 0, i_q^* = i_{qk}$ ).

The speed range for constant, 2.7 Kw, electromagnetic power is very wide (Fig. 14.15b).

An active flux based encoderless FOC of BEGA for variable speed was also conceived and proved performant [9] through tests for the same prototype (Fig. 14.16).



Fig. 14.16 The BEGA prototype: 1500W at 1500rpm, 2p = 4 poles.

## 14.5 1phase a.c. continuous PM generator with saturation caused saliency

Autonomous auxiliary 1 phase a.c. generating, operating at constant speed and 1-3 kW with load cost control, but at high efficiency, are needed for many applications.

Using PMs in such a high efficiency low weight generator is well understood, but planting the PMs on the rotor core surface is easier.

However, to reduce the required reactive power requirements and thus ease the voltage control (regulation), an increase magnetic saliency is needed together with the small p.u. machine reactance secured by surface PMs.

The configuration in Fig. 14.17 is introduced here with its step capacitor voltage control via low cost Triacs, for the scope [11].

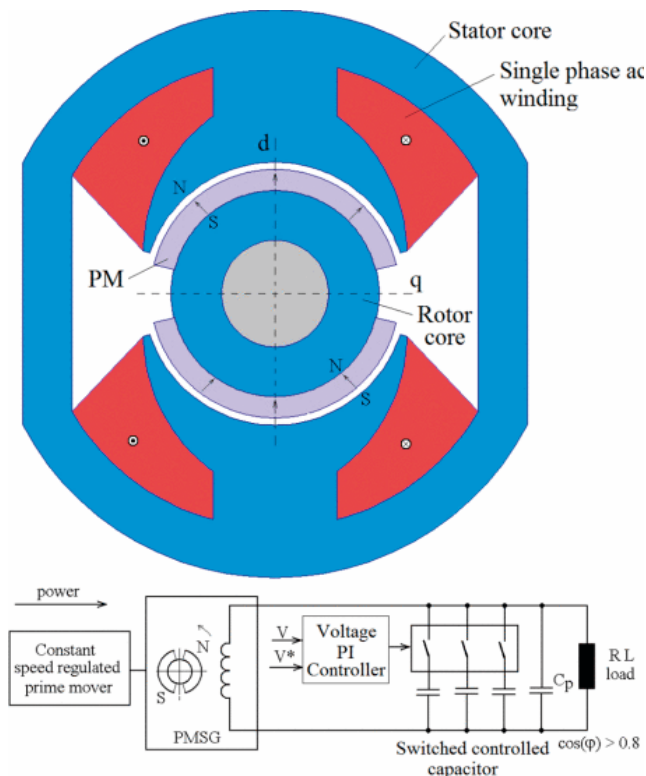


Fig. 14.17 Single phase a.c. PM generator, after [11]. The main problem in the design, besides weight efficiency and cost, is the voltage regulation with sensitive and inductive load (less than 7%).

To obtain this with limited no load overvoltage (+7% at most), inverse saliency ( $L_d < L_q$ ) should be created but also for  $x_d, x_q \leq 1 p.u.$

Let us consider resistive load, in a 3 kW, 3000 rpm, 220 V prototype of 10 Kg with efficiency around 90%.

The voltage equation for steady state (without parallel capacitor) is:

$$\underline{V}_s + R_s \underline{i}_s = \underline{E}_1 - jx_d \underline{I}_d - jx_q \underline{I}_q; x_q > x_d \quad (14.12)$$

For a power and  $\theta_n = 45^\circ$  and a zero load voltage  $E_1 = 1.05V_{sn}$ , from (14.12):

$$\begin{aligned} E_1 - x_d I_{sn} \sin \theta_{sn} &= V_{sn} \cos \theta_{sn} \\ V_{sn} \sin \theta_{sn} &= x_q I_{sn} \cos \theta_{sn} \end{aligned} \quad (14.3)$$

in p.u. values saliency (14.14) yields simply

$$x_d = 0.48 p.u. \quad x_q = 1.0 p.u. \quad (14.4)$$

There is no way to get this results of 5% reduction from  $E_1$  to  $V_{sn}$  for rated sensitive load unless the machine has inverse saliency  $x_d < x_q$  and both smaller than unity in p.u.

The machine has to be designed with heavy magnetic saturation in the stator to provide smaller than unity reactances, avoiding too thick (costly) PMs.

Moreover, the machine inductance under load varies with load and rotor position.

FEM calculated field path with the rotor in axis  $d$  and  $q$  and the inductance variation with rotor position are shown in Fig. 14.18 together with the torque.

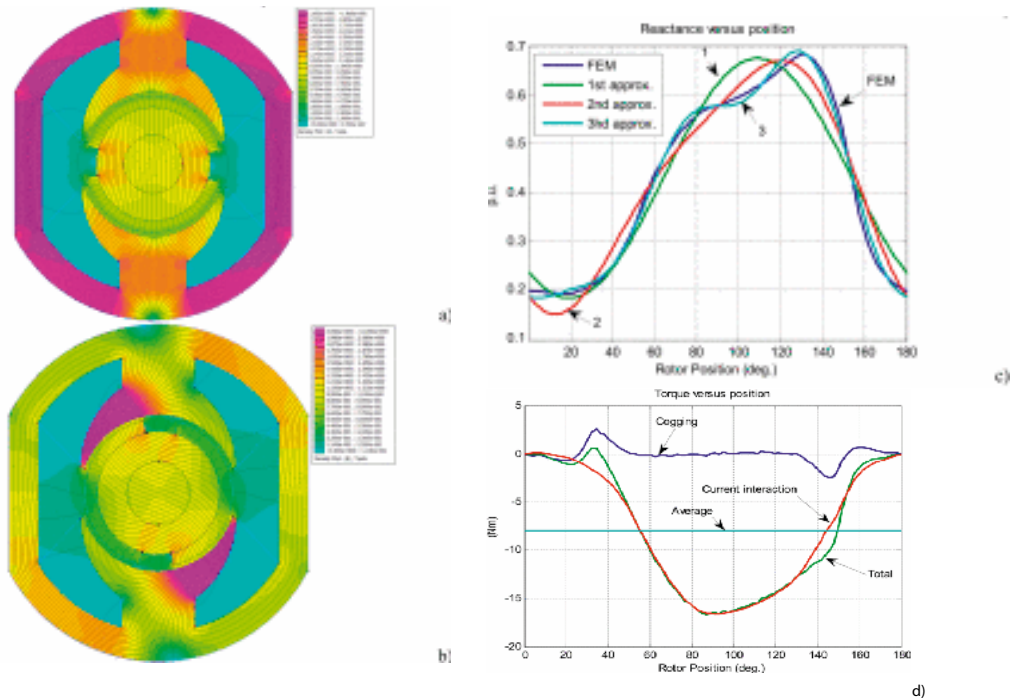


Fig. 14.18 Flux lines for full resistive load a) in axis  $d$ , b) in axis  $q$ , c) machine inductance, d) torque versus rotor position.



As expected in a 1 phase generator, the torque (negative) pulsations from zero to maximum, providing the required 8 Nm average torque.

The step capacitor control system and sample digital simulation load stable transients are visible in Fig. 14.19 a, b.

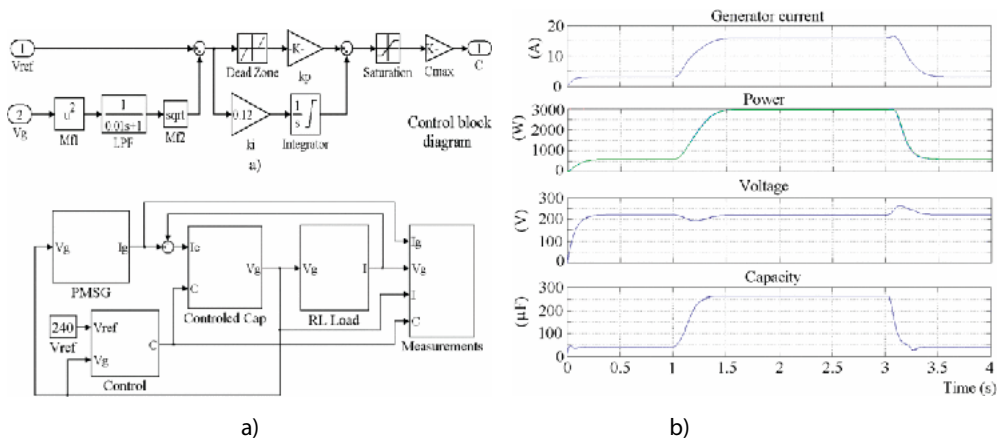


Fig. 14.19 The flux capacitor control system, a) and step load torque transients (from 20% to 100% and back) at 0.8 lagging power factor, b) after [11].

The capacitor variation with load is evident.

Sample prototype test results are visible in Fig. 14.20.

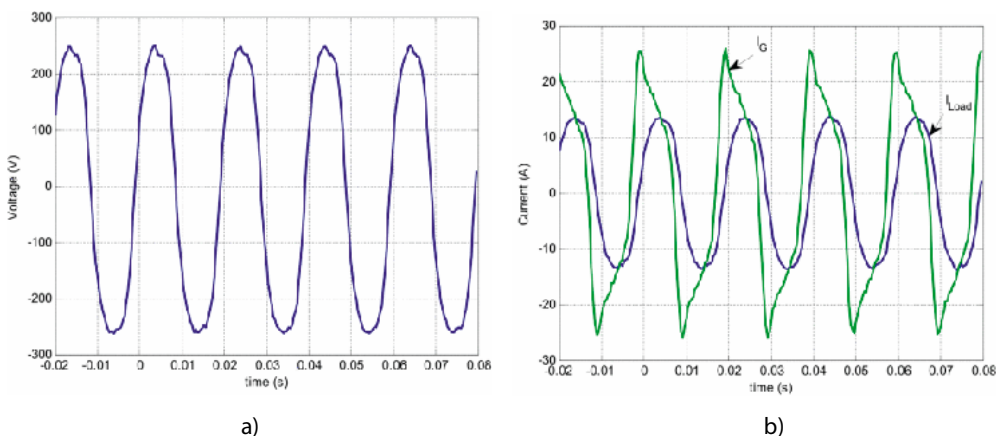
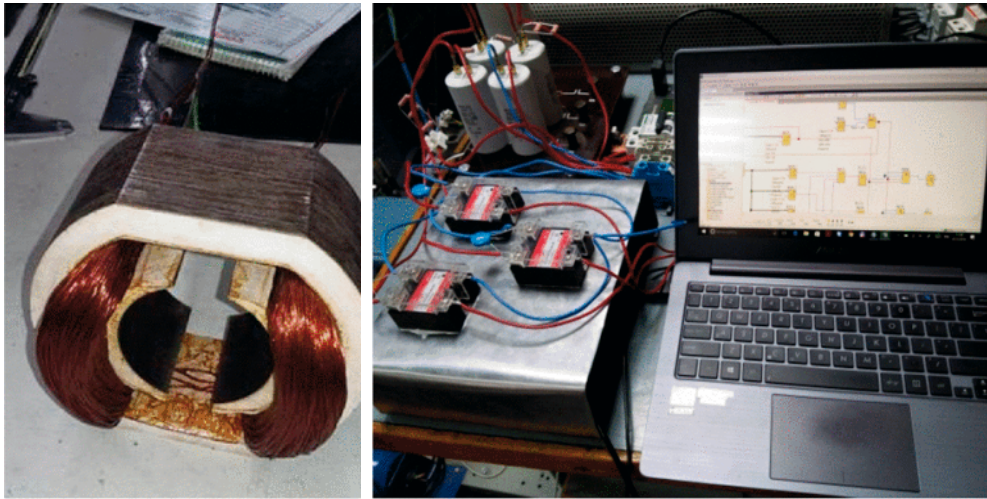


Fig. 14.20 Measured voltage a) generator and load current, b) versus time.

It is clear that the load voltage and current are quite sinusoidal while, due to capacitor current, the generator current is not sinusoidal (Fig. 14.20).

This means that in the machine design such aspects have to be considered, especially in relation to losses.

The test platform is visible in Fig. 14.21.



a)

b)

Fig. 14.21 The test platform: a) the generator-stator, b) the control system.

Final note.

The technique used here, for 1 phase PM generators – to produce inverse saliency with surface PM rotor a.c. generators by magnetic saturation with  $x_d < x_q < 1.0$  may be extended also to 3 phase autonomous PM generator to “induce” low voltage regulation  $\pm 7\%$  from no load to 0.8 power factor (lagging) at full load. High performance efficiency in a small volume comes to complement such solutions.

## 14. 6 BLDC-MRM (brushless multiphase reluctance machines)

Multiphase reluctance machines with bipolar dual flat-top rotor (BLDC-MRM), but with larger airgap, have been recently in an attempt to eliminate PMs and rotor windings.

The recital revival was due to the dramatic rise in PMs price (in view of too much demand for the offer) and to the maturing of multiphase inverter technology with fault tolerance attributes [15-18].

### A). Operation principle of BLDC-MRM

The BLDC-MRM is the inversed (stator: for rotor) d.c. brush machine stripped of excitation circuit with brushes at pole corners and having a MFB stator whose phases between salient poles play the role of field coils ( $i_F$ ), while those under the poles are torque phases ( $i_T$ ); and where the commutation of currents is performed electronically from a multiphase stator feeding (now) the stator  $q=1$  diametrical a.c. multiphase windings (Fig. 14.22a,b,c,d and Fig. 14.23).

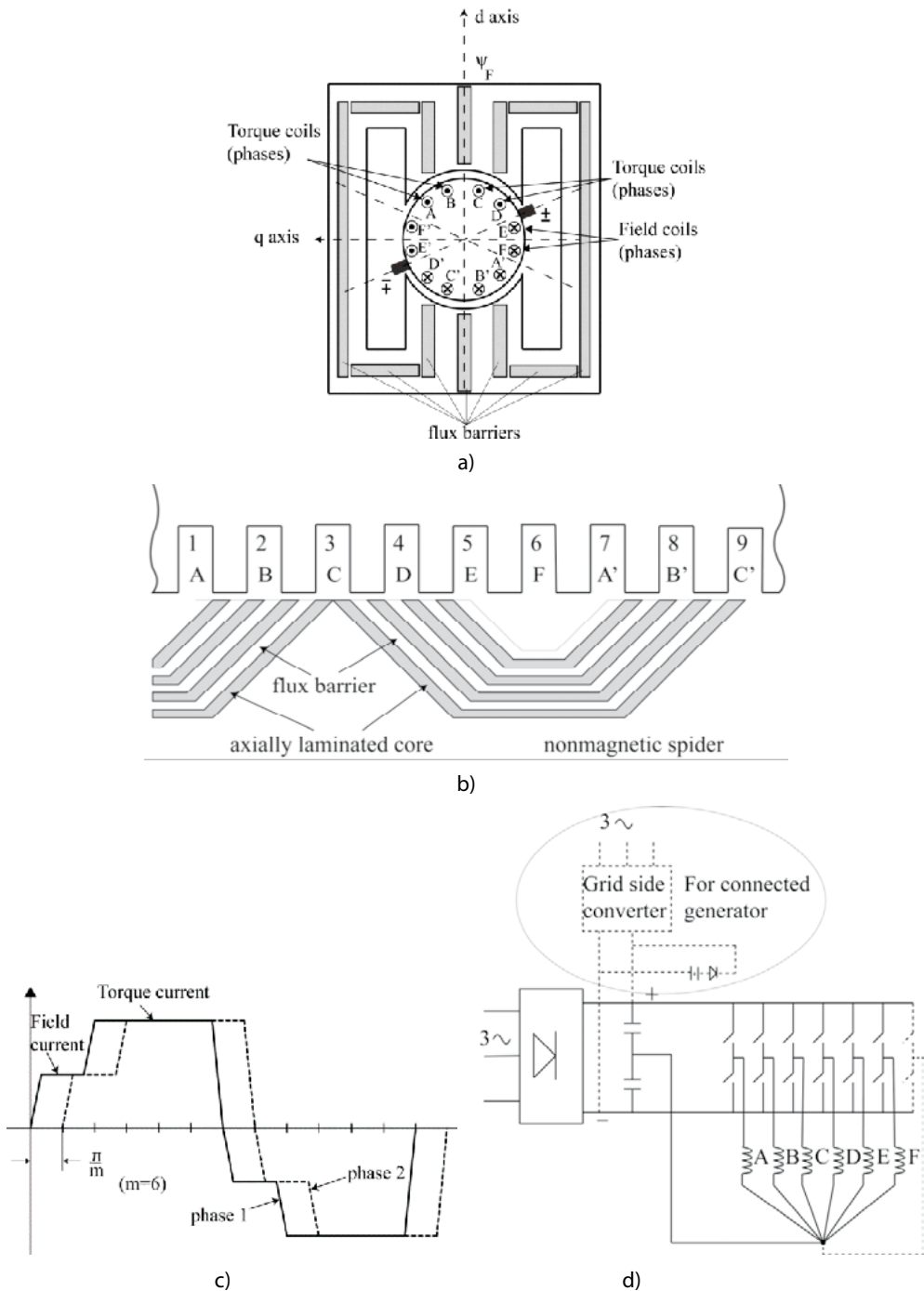


Fig. 14.22 BLDC-MRM: a) equivalent (originally) d.c. brush machine, b) 6 phase rotary (or linear) BLDC-MRM cross-section, c) two phase currents (out of 6,  $m = 6$  phases) waveforms, d) typical 6 phase inverter with individual phase current control and null point voltage control.

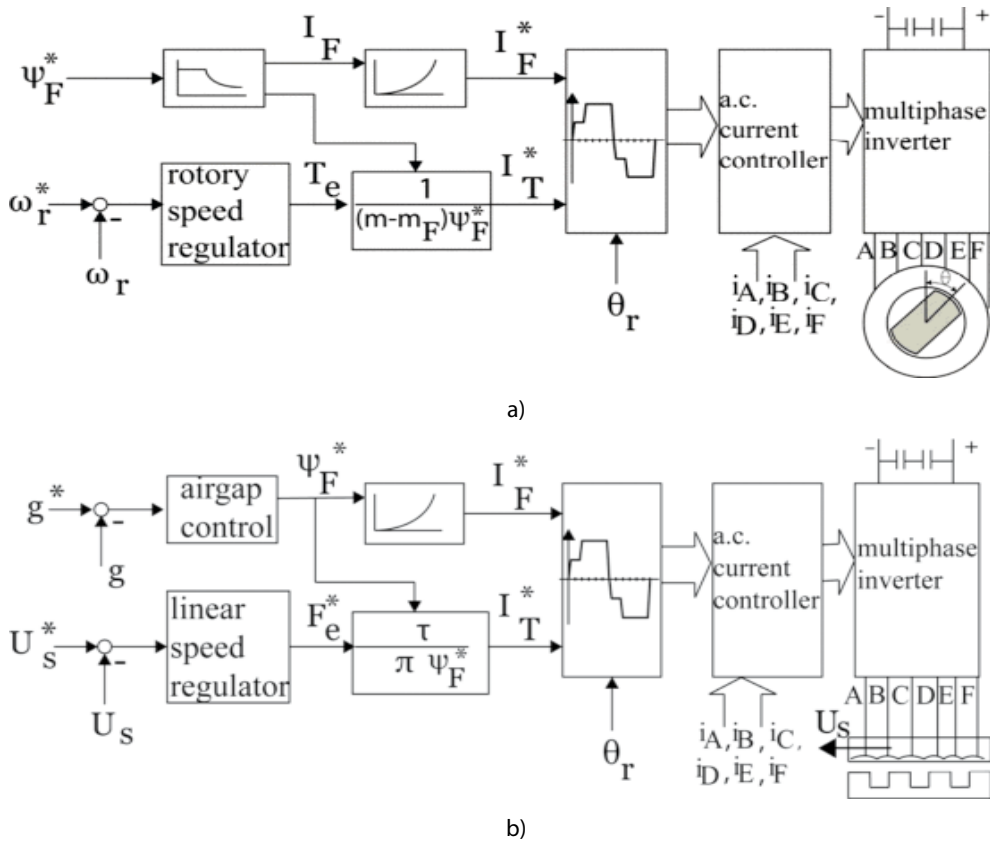


Fig. 14.23 BLDC-MRM: a) rotary machine generic control system, b) Maglev (airgap  $g^*$  and linear speed  $u^*$ ) control.

M machine  $m$  phases are divided into  $m_F = 2, 3, \dots$  excitation phases (placed between rotor MFBA poles) and  $m = m_F = i_F$  torque poles.

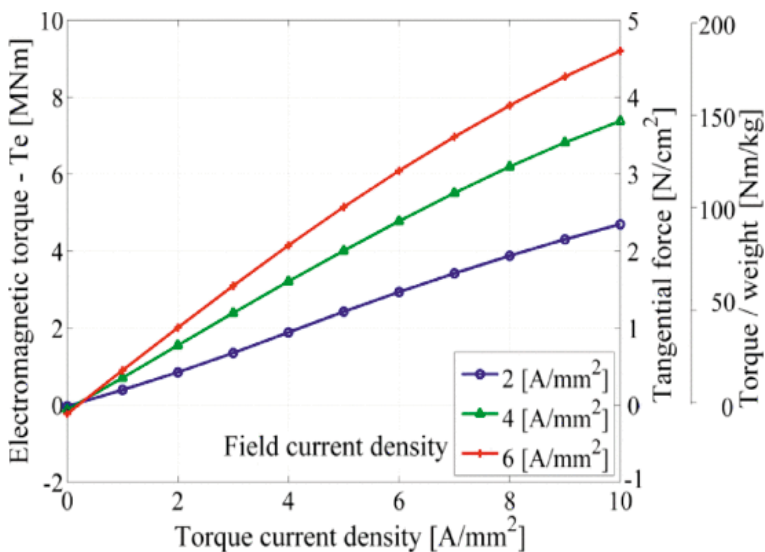
The torque is approximately:

$$T_e \approx k_T (i_F, i_T) m_T i_F i_T$$

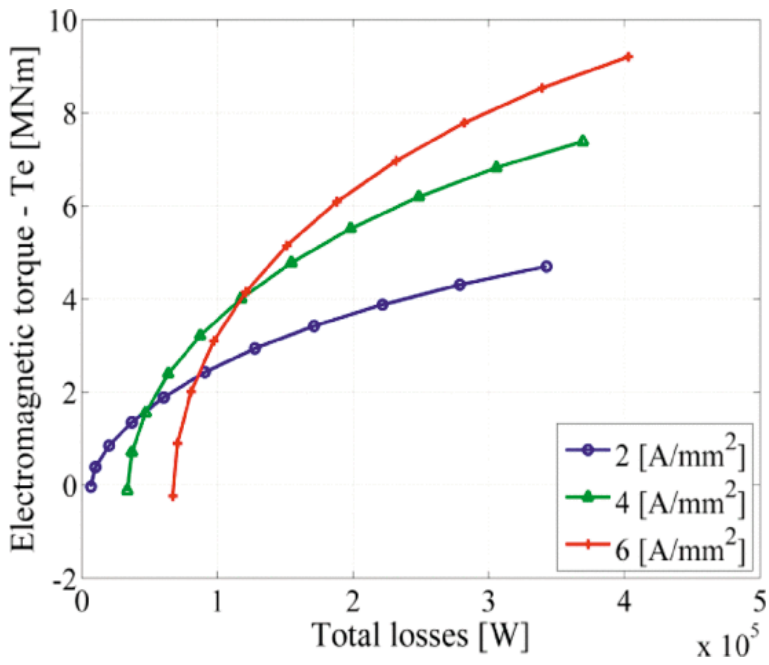
A few remarks are in order:

- The machine has flat double-top bipolar currents that have to commute the appearance of rotor pole corner at their coils slots with at most (in general) one stator seat pitch angle: this limits the maximum speed for given machine geometry, inverter ceiling voltage and torque (the CPSR width)
- Already with  $i_F = i_T$  (the current becomes bipolar and trapezoidal) strong flux weakening with torque reduction occurs, while also meeting the condition of maximum torque per current.

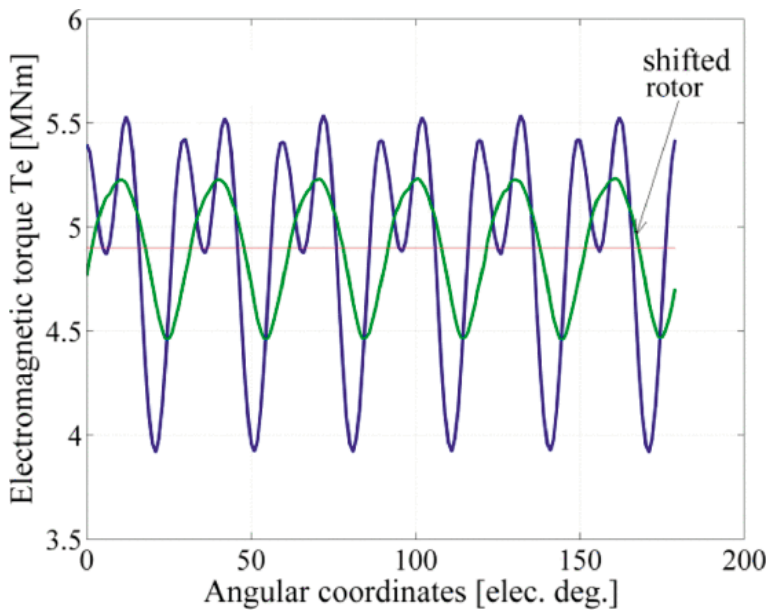
- To brake the machine, the polarity of the torque currents has to be changed again quickly in a angle less than  $m_T$  slot pitch angles.
- The characterization of field  $m_F$  phases flux with the currents of  $m_T$  torque phases takes place at an angle around  $90^\circ$  degrees (electrical), which is optimal but the current commutation at the rotor pole corners is developed by the motion notable induced voltage from the torque phases. To improve (quicken) commutation the airgap of the machine is chosen larger than in reluctance synchronous machine. This may be an advantage in terms of lower mechanical losses and fabrications tolerances, but it implies larger excitation phase currents  $i_F$ .
- Strong flux weakening is obtained by reducing  $i_F$  and thus the core losses at higher speeds machine remain rather constant (for given stator voltage  $V_{s,max}$ ), but the copper losses are decreased; at most, the efficiency is kept as for full flux for wide CPSR in constant to IPMSMs.
- FEM investigations [15] have shown BLDC-MRM potential performance has been investigated by FEM:
  - In a 6 phase 6 pole ALA-rotor configuration for 30 Nm to 20 Nm for up to 6Nm/kg for 800 W copper losses (at 10 A/mm<sup>2</sup>) [15]
  - In a 5 MNm generator for 150 Kw copper losses for 120Nm/kg in a large diameter 6 MW, 1 rpm direct driven wind generator.
  - The torque pulsations are reduced to  $\pm 8\%$  for segmented skewing (2 segments) of rotor (by half a stator slot pitch)[15], Fig. 14.24a,b,c.



a)



b)

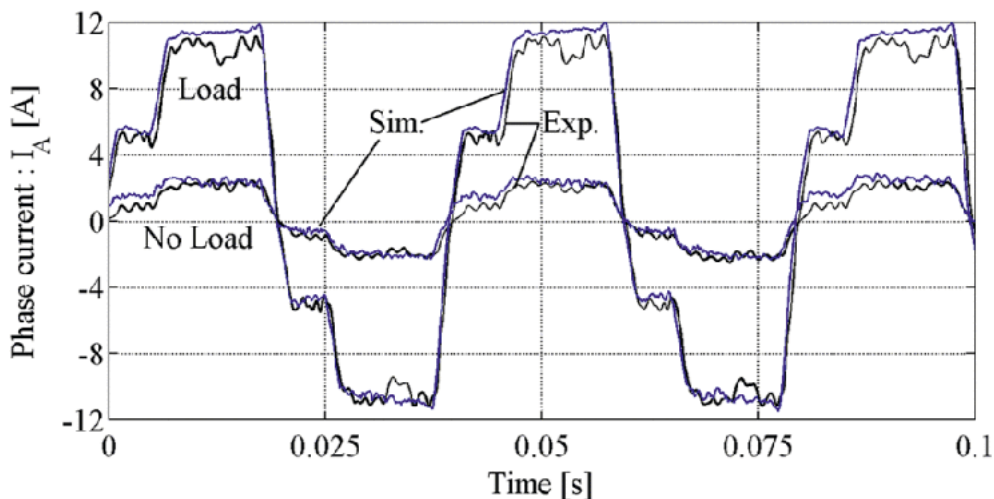


c)

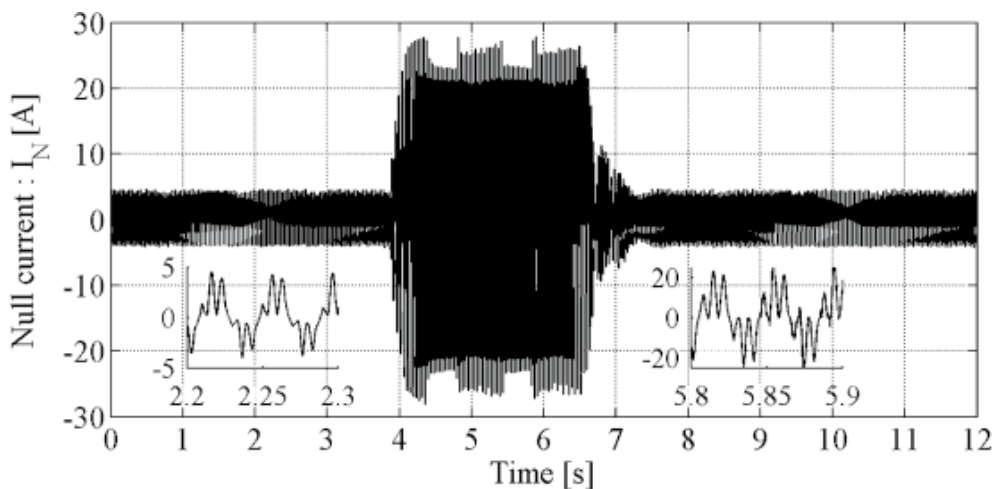
Fig. 14.24 6MW 10rpm BLDC MRM wind generator/motor a) torque and torque density for various current densities, b) total copper loss for given torque and common current density, c) total full torque waveform without and with dual-segmented skewed rotor (by half the stator slot pitch), after [15].

Further investigations into BLDC-MRM FEM +circuit modeling, control [16-17] and its optimal design has revealed promising dynamic and steady state performance in experiments.

Typical measured phase current under no load and load at 500 rpm for a 6 phase, 6 pole ALA-rotor 30-100 Nm BLDC-MRM drive is illustrated in Fig. 14.25[18] together with loading unloading transients at same 500 rpm and transition from no load motoring at loaded generating at 250 rpm (more on RSM with ALA rotor in [19]).

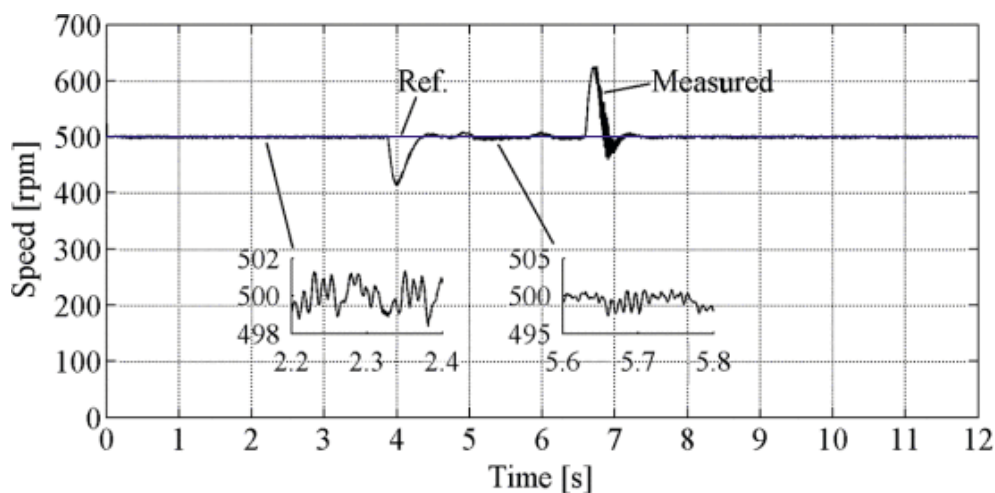


a)



b)





c)

Fig. 14.25 Tests on a 6 phase, 6 pole, 3-100Nm a) steady state one phase current at no load and on load, b) loading and unloading at 500rpm, c) measured speed transients from no load motor to loaded generator at 250 rpm.

Note. Arguably the reluctance synchronous motor with MFBA or ALA rotor may provide similar performance. This is yet to be proved, but if so, still the airgap (and mechanical) losses and rotor ruggedness are larger and a higher switching frequency in the inverter is needed to provide sinusoidal current at highest speed (frequency).

However, the commutation of currents within a slot pitch angle is still a notable limitation.

Moreover, for frequencies below 100 MHz, BLDC-MRM may be tried with confidence from small to high (MNm) torque range applications when a PM-less rugged machine drive is required.

## 14.7 References

- [1] I. Boldea, Z.X. Fu ; S.A. Nasar "Performance evaluation of axially-laminated anisotropic (ALA) rotor reluctance synchronous motors", *IEEE Trans. on Industry Applications*, 1992, Part 1, pp. 212-218.
- [2] I. Boldea, T. Fukao, T. A. Lipo, L. Malesani, T. j. Miller, A. Vagati " Synchronous reluctance motors and drives: a new alternative" *Record of IEEE-IAS-1994-tutorial course*.
- [3] I. Boldea "Reluctance synchronous machines and drives", book, Oxford University Press 1996.
- [4] I. Boldea, Z. X. Fu, S. A. Nasar "Digital simulations of a vector current controlled ALA rotor reluctance synchronous motor servo drives", *EMPS (now ECPS journal)*, vol. 19, 1991, pp. 415-424.
- [5] S. Agarlita, M. Fatu, I. L. Tutuelea, F. Blaabjerg, I. Boldea "I-f starting and active flux based vector control of RSM with experiments", *Record of OPTIM 2010 (IEEEExplore)*.
- [6] A. Yousefi-Talouki, P. Pascetto, G. Pellegrino, I. Boldea "Combined active-flux and high frequency injection for sensorless direct-flux vector control of synchronous reluctance machines", *IEEE Trans* vol. PE 33, no. 3, 2018, pp. 2447-2457.



- [7] I. Boldea, S. Scridon, L. Tutelea "BEGA – a biaxial excitation generator for automobiles", *Record of OPTIM 2000 IEEE IAS* sponsored conference.
- [8] V. Coroban, I. Boldea, G. D. Andreescu, F. Blaabjerg "BEGA – motor/generator vector control for wide constant power speed range", *Record of OPTIM 2006* (IEEEExplore).
- [9] V. Coroban-Schramel, I. Boldea, G. D. Andreescu, F. Blaabjerg "Active flux based motion sensorless vector control of BEGA", *Record of IEEE-ECCE 2009*.
- [10] I. Boldea, E. Ritchie, F. Blaabjerg, S. Scridon, L. Tutelea "Parameters and characteristics of BEGA", *Record of OPTIM-2002*, pp. 20-25 (IEEE sponsored).
- [11] L. Tutelea, N. Muntean, I. Boldea "A step capacitor controlled 1 phase a.c. autonomous PM generator, with experiments" *Record of OPTIM-2017* (IEEEExplore).
- [12] R. Mayer, H. Moseback, U. Schroder, H. Weh "Inverter fed multiphase reluctance machine with reduced armature reaction and improved power density", *Record of ICEM 1986*, Munich Germany, Part 3, pp 1138-1141.
- [13] I. Boldea, G. Papusoiu, S. A. Nasar, Z. X. Fu "A novel series switched reluctance motor" *Record of ICEM 1990*, MIT, USA, Part 3, pp. 1212-1217.
- [14] I. D. Law, A. Chertok, T. A. Lipo "Design and performance of field regulated reluctance machines", *Record IEEE-IAS-1992*, vol. 4, pp. 234-241.
- [15] I. Boldea, L. Tutelea, D. Ursu "BLDC multi-phase reluctance machine for wide range applications: an introduction", *Record of EPE-PEMC 2011*, Novisad, Serbia (IEEEExplore).
- [16] D. Ursu, P. Shamzi, B. Fahimi, I. Boldea "5 phase BLDC-MRM: design, control, FEA and steady state operation experiments", *Record of OPTIM 2013* (IEEEExplore).
- [17] D. Ursu, V. Gradinaru, B. Fahimi, I. Boldea "Six phase BLDC reluctance machines" FEM based characterization and four quadrant control", *IEEE Trans.* Vol. IA-51, no. 3, 2015, pp. 2105-2115.
- [18] D. Ursu, L. Tutelea, D. M. Ionel, I. Boldea "Optimal design of BLDC-MRM for variable speed drives", *Record of OPTIM/ACEMP 2017* (IEEEExplore).
- [19] I. Torac "An analytical approach to the magnetic field computation for the synchronous reluctance motor with axially-laminated rotor", *Record of ICEM-2002*.

## INVERSED CLAW-POLE-ROTOR (OR STATOR) GENERATOR/MOTOR DRIVES FOR AUTOMOTIVE AND ROBOTICS APPLICATIONS

The claw-pole-rotor alternator has been the standard electric energy source on all automobiles since nineteen seventies, when this Lundell invention has surpassed the dc. Brush generator with separate excitation.

Lundell alternator is in fact a synchronous generator with a (multiple  $2p=10-18$ ) solid iron claw-pole rotor core provided with a single dc. Coil supplied through slip rings and brushes. This circular dc. reduced the excitation power a few times with respect to a hetero-polar dc. excitation system with a coil embracing each pole.

Then, the Lundell alternator used a full power diode rectifier that supplies the backup battery on automobiles, trucks etc. To keep the cost volume and price, the efficiency was somewhat sacrificed.

Not so any more when the electric power on vehicles increases by the day as many auxiliary services are provided with electric motor drives.

Here, a Lundell generator at 42 Vdc, with inter-claw PMs to decreased. Coil flux leakage between rotor claws and desaturate the claw poles is shown to deliver up to 8-10 kW to an additional 42 V Li-ion battery during vehicle braking and thus reduce the fuel consumption by 8-10% for in taken standard driving cycles [1].

Furthermore, on the claw-magnets machine is shown capable to provide competitive electric propulsion on HEVs or EVs [2].

Finally, an interior –SMC-claw pole stator PM rotor SM motor design is shown to produce high torque density in a design for humanoid robot ankle –like application.

### 15.1 Inter-claw PM-pole-rotor alternator system (IPM-CPA) for more energy recuperation during vehicle braking

The today's claw-pole Lundell alternator (Lundell alternator) at 14 Vdc on automobile and 28 Vdc on trucks is known to have efficiency below 70% and down to 40% at high speeds, as the latter was sacrificed for power volume and cost [3].

The rotor claw-pole (with  $2p>10$  poles) rotor, in general, runs at small airgap and thus the machine inductance is large but dc. excitation losses are kept low at the price of rather large eddy current losses in the rotor solid forged iron claws induced by the armature (stator) field produced harmonics.

The idea of placing PM between the rotor claws (Fig. 15.1) to reduce dc. coil fringing between rotor poles and desaturate the rotor core was proposed decades ago but considered too an expensive solution then; not so much today.

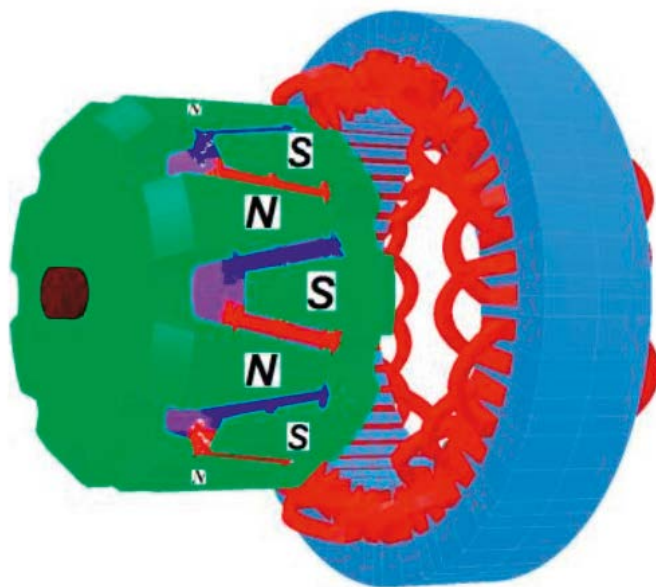


Fig. 15.1 Inter - claw – PM – claw – pole – rotor alternator (IPM-CPA).

The use of such magnets has the merit that at zero stator and dc. excitation rotor currents the no load stator voltage (emf) at high speeds is notably less than the rated voltage and thus no dedicated overvoltage protection is needed.

This is in contrast to the case of using PMs to entirely or partially excite (d.c. excite) the machine.

The idea to reduce fuel consumption by retrieving some of the braking of vehicle kinetic energy through increased power in the alternator has been proposed for one decade on some vehicles but at a small rate, mostly at 14 Vdc and none for 42 Vdc [4].

Such a system with 8-10 kW energy recuperation for 50 seconds braking cycles has been implemented by 2011 with higher efficiency IPM-CPA optimally designed for the purpose at 42 Vdc, with a d.c.-d.c. converter to streamline the power from the 42 Vdc hidden dc. brush (with a Li-ion battery backup) to the regular 14 Vdc battery when needed [5].

Moreover, some electric loads are tied directly to the 42 Vdc hidden bus (the air conditioner's electric drive: 2-25 kW) and supplied in full mainly during the braking intervals by adequate energy management.

To present the system [5] first the 42 Vdc IPM-CPA optimal design to produce (8-10 kW) power, at an efficiency of 80% (10% more than in up to date CPA of 3.2 kW, 14 Vdc), for the braking typical time cycles.

### A). 3D nonlinear magnetic electric circuit (MEC) model of IPM-CPA

A 3D MEC of IPM-CPA with 3D FEM key validation was chosen for modeling the machine for optimal design (Fig. 15.2). The 3D character of flux lines and the flux fringing in tangential and axial direction between rotor claws imposes a 3D modeling methodology.

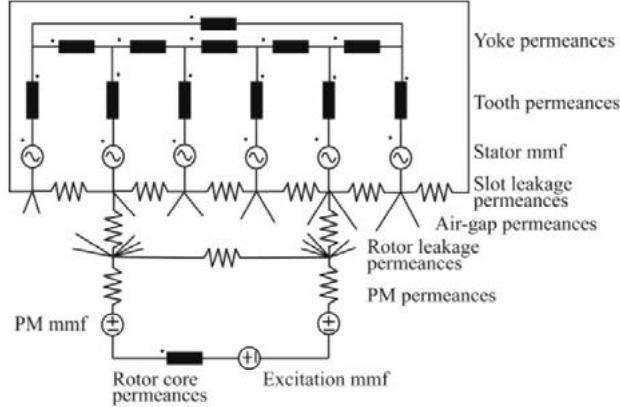


Fig. 15.2 MEC of IPM-CPA (one pole pair).

Analytical expressions for air-gap permeances (variable with rotor position) and variable with magnetic saturation iron permeances (of flux tubes).

First the 3D MEC model was “tested” on an up to date 2.5 kW 14 Vdc CPA without IPMs comparing it with test result curves for dc. output CPA current versus speed for given efficiency values (Fig. 15.3).

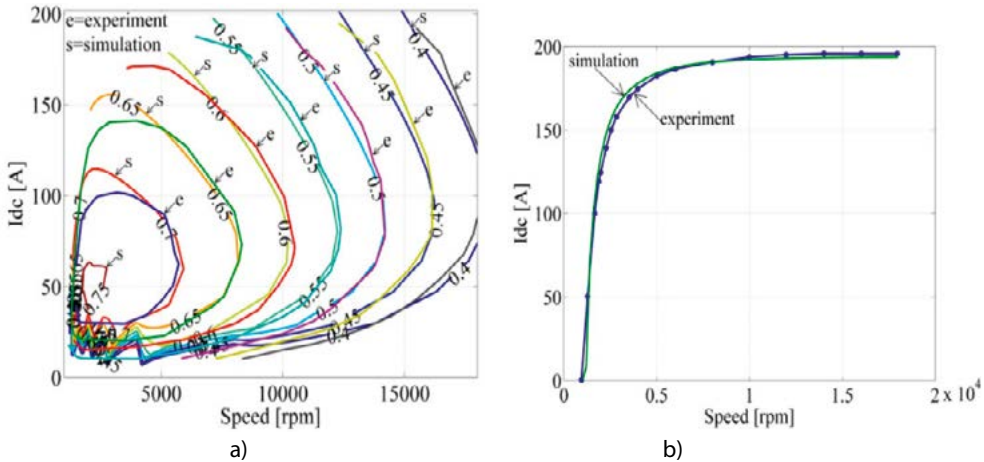


Fig. 15.3 Measured versus calculated  $i_{dc}$  versus speed: a) for given efficiency value, for a commercial competitor, 2.5W, 14V<sub>DC</sub> CPA without IPM; b) maximum  $I_{dc}$  versus speed.

Given the complexity of the CPA 3D geometry, magnetic saturation, skin effect etc, the 3D-MEC is proved to be trustworthy to use in an optimal design code.

**B). Optimal design of IPM-CPA at 42 Vdc for (8-10) kW output in a redesigned 3.2 kW 14Vdc topology**

For constraint design optimization, the 3D MEC was used for modeling while using modified Hooke-Jeeves algorithm.

The variable vector for optimization  $\bar{x}$  is:

$$\bar{x} = \left[ sD_0, sD_i, rD_{ci}, l_c, s_{hy}, s_{tw}, s_{Ms}, h_{ag}, poles, s_{lo}, a_p, w_{rd}, l_{rc}, r_{dcl}, r_{ph}, I_{ext\ max}, k_{ism} \right] \quad (15.1)$$

They are explained in Table 15.1.

Table 15.1 Optimization variables.

sDo	Stator outer diameter
sDi	Stator inner diameter
rDci	Rotor coil inner diameter
lc	Stator core length
shy	Stator core yoke width
stw	Stator tooth width
sMs	Mouth of stator slot
hag	Air-gap length
poles	Number of poles
sb	Turns per coil
ap	Polar cover
rpl	Rotor pole length
wrd	Width of rotor end disk
lrc	Rotor core length
rdcl	Rotor core length variation due disk
rph	Rotor pole height
lexmax	Maximum [A turns] do field coil
kippm	Inter pole PM: 0 –no IPM

The optimal design code reaches the minimum objective function (initial + losses costs with constraints on minimum power on efficiency, etc) is reached in 70 iteration steps.

The final optimum variable vector was:

$$\bar{x}_{optim} = [164, 107, 53.5, 34.5, 12.8, 3, 3, 1, 0.4, 16, 8, 0.81, 34.3, 13.4, 70.5, 4.2, 10, 2780, 0.49] \quad (15.2)$$

The optimal design provided that a maximum of 9 kW of vehicle braking power may be retrieved electrically in the frame of a 3.2 kW, 14 Vdc CPA after it was redesigned for 42 Vdc .

Moreover (as visible in Fig. 15.7), the target 80% efficiency was even surpassed (to 85%) for a small region.

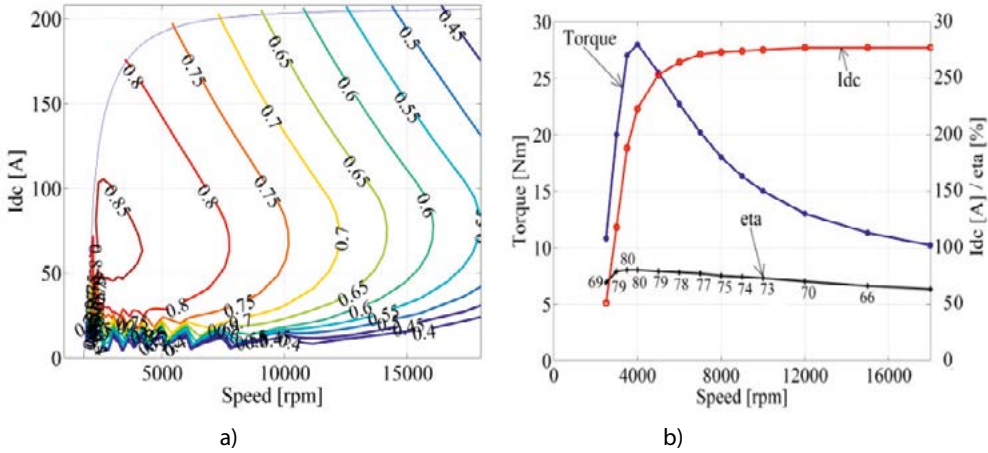


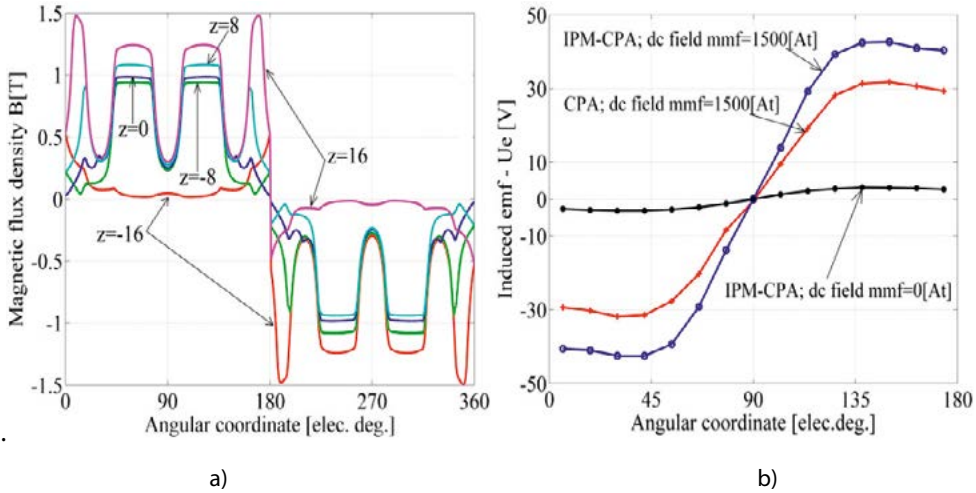
Fig. 15.4 Retrofitted 3.2kW, 14V<sub>DC</sub> CPA:  $I_{DC}$  versus speed a) and efficiency b) from IPM CPA at 43V<sub>DC</sub>.

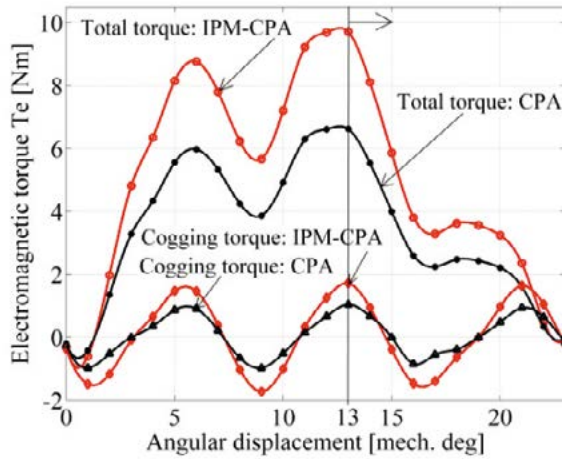
### C). FEM key validation

3D FEM was parsimoniously used for verification after terminating the 3D-MEC-based optimal design code iterations, to save computation time but verify further the latter model.

IPMs were made of NdFeB ( $B_r = 1.13$  T and  $H_r = 860$  KA/m at 20°C).

Typical airgap flux density at no load (Fig. 15.5a) emf (Fig. 15.5b) and torque for sinusoidal rated currents ( $i_d, i_q, i_F$ ), of the optimal design (Fig. 15.5c).





c)

Fig. 15.5 3D FEM results for the optimally designed IPM-CPA: a) airgap flux density at no load (field mmf = 1500Aturns) for a few axial positions  $z$ ; b) emfs with IPMs (and without) and field mmf = 1500A turns and for zero field current; c) Torque and cogging torque versus rotor position in mechanical degrees for  $I_{\max} = I_a = -2I_b = -2I_c = 200A$  and zero speed.

The torque pulsations are notable, but the average torque is 30% more with IPMs(Fig. 15.6).

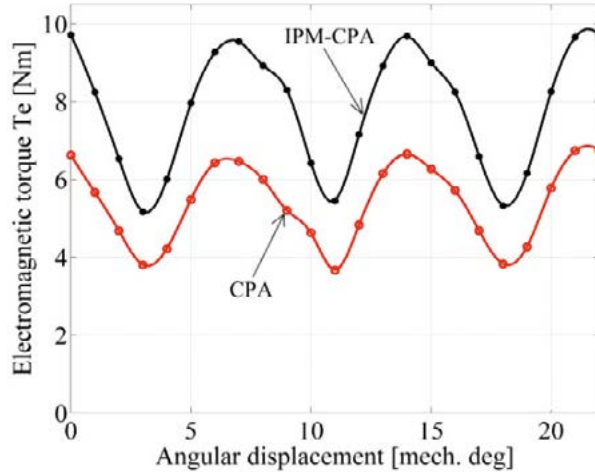


Fig. 15.6 CPA torque pulsations without and with IPMs in details of 3D FEM calculation details (see [1]).

#### D). Vehicle braking energy recuperation scheme and its control

The solution for vehicle braking recuperation-which is limited to 8 kW in a medium size core by the drive comfort -is presented in Fig. 15.7 [1].



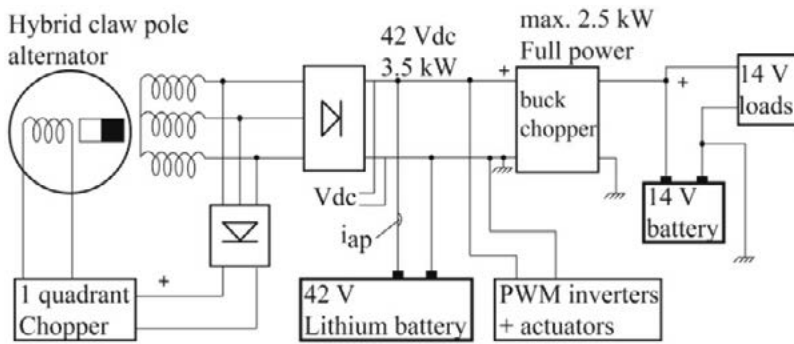


Fig. 15.7 Vehicle power net.

A Matlab/Simulink model of the system which may be triggered only by the IPM CPA field current control based on the SOC of 42 Vdc Li-ion (64 Ah) battery and the power consumption on board of vehicle management system.

Skipping the details [1], typical results for a given speed variation profile during braking (Fig. 15.8a) are illustrated for a large 5 kW load power for SOC=0.8 (Fig. 15.8b,c,d,e). The large SOC value contributed to good performance by a little larger 42 Vdc battery voltage. The battery voltage decreases a little during loading vehicle for a supercapacitor storage system the voltage variation would be very large (50%) to top 75% of stored energy during the braking storage and thus higher initial voltage would be needed to feed an equivalent load.

Final note.

The system summarized here was implemented in an FP7 Grant (EEVERT) between 2009 and 2011 and was later with small changes applied on some commercial european troubles, as it proved the (8-10) % fuel consumption reduction on a regular core in town standard driving, for a limited/reasonable investment somewhere between 1500 EURO to 800 EURO.

## 15. 2 10kW and 100 kW, 6000 rpm IPM-CPA for HEV and EV propulsion optimal design and controlled dynamics

The power of 10 kW would be typical for a mild hybrid electric vehicle (HEV), while 100 KW is a power range typical for a heavy HEV or for an EV.

The CPA, with IPMs might be an adequate solution for HEV (EV) electrical propulsion (partial or integral) because it is already a technology accepted on vehicles due to its low rotor dc. excitation losses.

The crucial question is whether the efficiency/weight/cost can go to values competitive with IPMSMs used today on most HEVs (EVs), with one exception where the copper case induction motor is applied.



As expected, the IPM-CPA is here used as motor and generator at variable speed and thus is inverter-fed (Fig. 15.9) and FOC or DTFC controlled. In addition, a 10 W power rating (5%) d.c.-d.c. converter is used to feed the d.c. circular coil of the claw pole rotor (Fig.15.9).

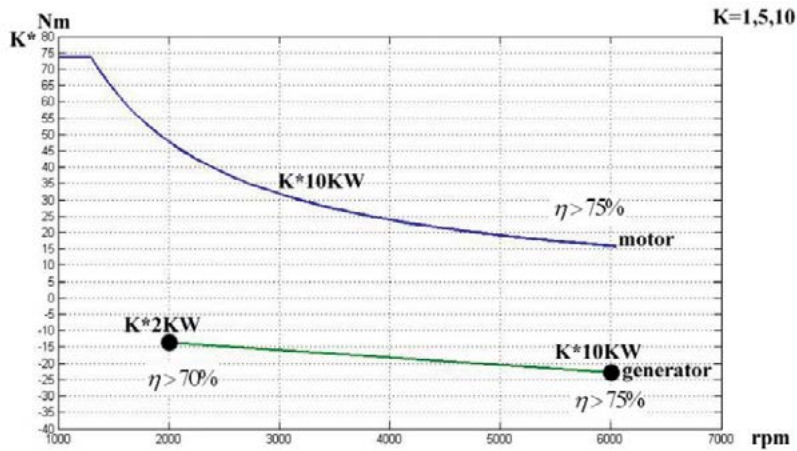


Fig. 15.8 Typical torque speed characteristic.

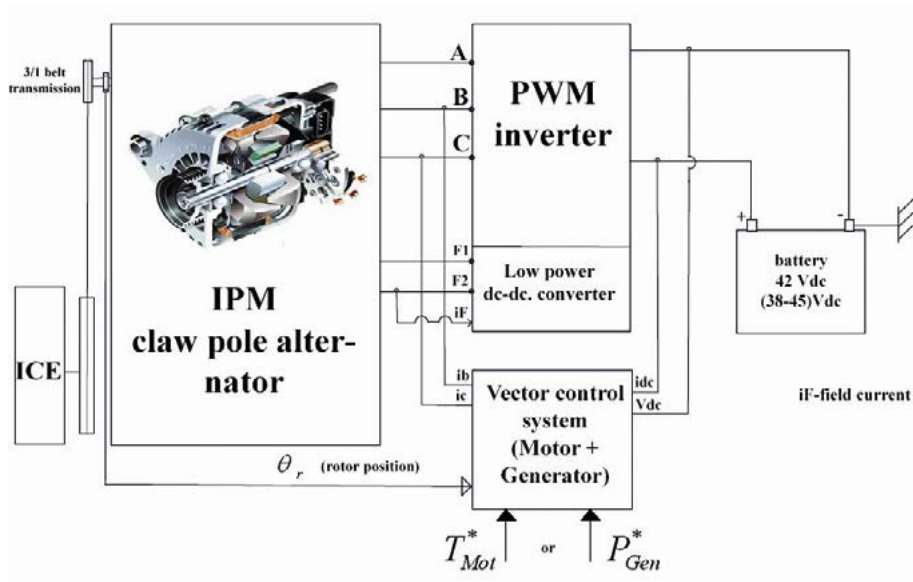


Fig. 15.9 The IPM CPA with inverter control.

The d.c. voltage is 42 Vdc for 10 kW and 500 Vdc for the 100 kW efficiency should be larger than 85% at 6000 rpm and above 70% at 2000 rpm.

### A). Optimal design code

The 3D-MEC model discussed in the previous paragraph has been extended to 10 kW and 100 kW. The objective function is detailed here through:

$$f_{obj} = C_i + C_e + C_p \quad (15.3)$$

$C_i$  - initial cost,  $C_e$  - energy loss cost,  $C_p$  - penalty cost.

The energy efficiency optimization handles the energy losses cost:

$$C_e = \left( \frac{rt_1 \cdot P_{n1} / n_1 + rt_2 \cdot P_{n2} / n_2}{1000 \cdot h_{py} \cdot n_y} \right) P_{energy} \quad (15.4)$$

with  $P_{n1}$ ,  $P_{n2}$  - the powers produced at 3krpm and respectively, 6krpm;  $rt_1$ ,  $rt_2$  - operation time at 3krpm, respectively, at 6krpm;  $h_{py}$ ,  $n_y$  - hours of operation per year, and respectively, years of use.

The penalty function  $C_p$  is related to power unrealisation avoidance:

$$C_p = [P_n / (rt_1 \cdot P_{n1} / n_1 + rt_2 \cdot P_{n2} / n_2 + P_b \cdot rt_b)] k_{pp} \cdot C_i \quad (15.5)$$

The operation time at the chosen base speed.

$P_b$  (power at base speed) may be equal or different from  $P_{n1}$  (rated power that meets overtemperature constraints).

The variable vector is the same as in eqn. (15.1)

Skipping the details sample design optimization results for three CPA variants:

- CPA without IPM (inter-claw pole magnets)
- IPM-CPA with inferred NdFeB magnets
- IPM-CPA with Ferrite magnets
- The variants are illustrated in Table 15.2 and they warrant remarks such as:

Table 15.2 10kW and 100kW CPAs: optimal design.

	10kW CPA			100kW CPA		
	CPA without IPM	IPM-CPA with NdFeB PMs	IPM-CPA with Ferrite PMs	CPA without IPM	IPM-CPA with NdFeB PMs	IPM-CPA with Ferrite PMs
Efficiency at 3000 [rpm] [-]	0.747	0.776	0.7	0.934	0.9468	0.9425
Power produced at 3000 rpm [W]	1230	1975	2250	105280	108500	159260
Efficiency at 6000 [rpm] [-]	0.863	0.877	0.8675	0.9262	0.942	0.9396
Power produced at 6000 rpm [W]	12900	23400	30000	120000	130720	207000
Weight of active materials [kg]	15.66	15.41	12.87	55.03	75.49	62.21
Active material cost [EUR]	60.38	74.77	42.22	132.71	213.98	148.15

	10kW CPA			100kW CPA		
	CPA without IPM	IPM-CPA with NdFeB PMs	IPM-CPA with Ferrite PMs	CPA without IPM	IPM-CPA with NdFeB PMs	IPM-CPA with Ferrite PMs
Airgap length [mm]	1.25	1.05	1.25	1.15	1	1.45
Total objective function [EUR]	24500	23550	23560	296710	307110	296250
Stator outside diameter [mm]	218	209.5	190	395.5	389	388
Stator core length [mm]	33.5	38.5	41.5	36.5	51	47.5

- all three configurations at 10 kW provide enough power for an efficiency larger than 70 % at 3krpm and above 85% at 6 krpm; the lowest initial cost and weight occurs for the IPM-CPA with Ferrite PMs between rotor claws

- even at 100kW all three variants show efficiency above 92% at both 3krpm and 6krpm, but the ferrite IPM-CPA show 1% more efficiency than the simple CPA at 10% more initial cost: the NdFeB IPM-CPA has the highest efficiency (94%) by its initial active materials cost is 50% more than the one with Ferrite PMs.

-the outer rotor diameter is rather large, but the stator stack length is short, as typical for CPAs.

In view of dynamics and control design investigation, the two optimal machines circuit parameters have been calculated (Table 15.3).

Table 15.3 Circuit parameters of optimal design.

		$V_{dc}$ [V]	$R_s$ [ $\Omega$ ]	$R_{ex}$ [ $\Omega$ ]	$L_{md}$ [H]	$L_{mq}$ [H]	$L_{sl}$ [H]	$L_{se}$ [H]
10 KW CPM	No IPM	42	0.032	12.06	$6 \cdot 10^{-5}$	$8.5 \cdot 10^{-5}$	$3.7 \cdot 10^{-5}$	0.098
	NdFeB IPM		0.023	9.6	$4.2 \cdot 10^{-5}$	$7.2 \cdot 10^{-5}$	$2.8 \cdot 10^{-5}$	0.194
	Ferrite IPM		0.0245	4.9	$4.4 \cdot 10^{-5}$	$6.1 \cdot 10^{-5}$	$3.1 \cdot 10^{-5}$	0.0724
100 KW CPM	No IPM	500	0.218	153.27	$14.24 \cdot 10^{-4}$	$11.23 \cdot 10^{-4}$	$3.94 \cdot 10^{-4}$	1.26
	NdFeB IPM		0.216	153.27	$16.37 \cdot 10^{-4}$	$14.03 \cdot 10^{-4}$	$3.41 \cdot 10^{-4}$	4.21
	Ferrite IPM		0.213	142.1	$12.12 \cdot 10^{-4}$	$12.96 \cdot 10^{-4}$	$3.03 \cdot 10^{-4}$	2.09

where  $V_{dc}$  is the d.c. voltage of the battery,  $R_s$  - stator phase resistance,  $R_{ex}$  - field circuit resistance,  $L_{md}$ ,  $L_{mq}$  - d,q magnetization inductances (average saturated values),  $L_{sl}$  - stator phase leakage inductance,  $L_{se}$  - excitation circuit leakage inductance.

## B). Dynamic model and vector control

The general system MATLAB model contains:

- The claw pole MIG model
- The control and vector model with control for various operation modes
- The converter limits
- A more self-explanatory block diagram of the control system is shown in Fig. 15.10.

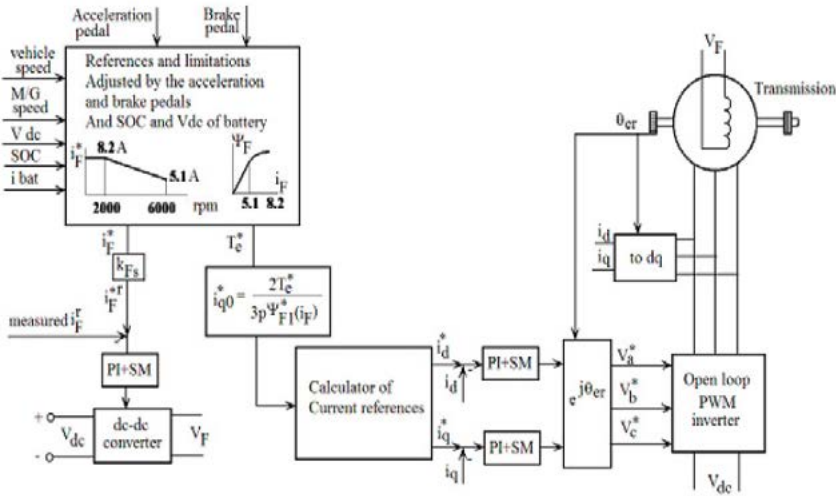


Fig. 15.10 The vector control system with numbers for the 10kW machine.

The  $i_d^*$  and  $i_q^*$  references depend on the sign of the stator voltage difference  $\varepsilon_v = V_s^* - V_{dc} / \sqrt{2}$ . For motoring:

$$\begin{aligned}
 -i_d^* &= 0 \text{ for } \varepsilon_v < 0 \\
 \text{and } -i_d^* &= -\varepsilon_v (k_p + k_i/s) + k_{SM} \text{sign}(\varepsilon_v) \text{ for } \varepsilon_v > 0
 \end{aligned}
 \tag{15.6}$$

For generating:

- for  $\varepsilon_v < 0, i_d^* > 0$  is commanded through same PI+SM loop (15.6); as  $i_q^*$  was calculated in Fig. 15.11 for  $i_d^* = 0$  it has to be corrected a little more that  $i_d^* \neq 0$  :for  $\varepsilon_v > 0$ ; motor or generator and  $i_d^* < 0, |i_q^*|$  is a bit increased while for  $\varepsilon_v < 0$  for generating and  $i_d^* > 0, |i_q^*|$  should be somewhat increased.

For simplicity, the reference field current  $i_F^*$  is given graphically (from design) in Fig. 15.10.

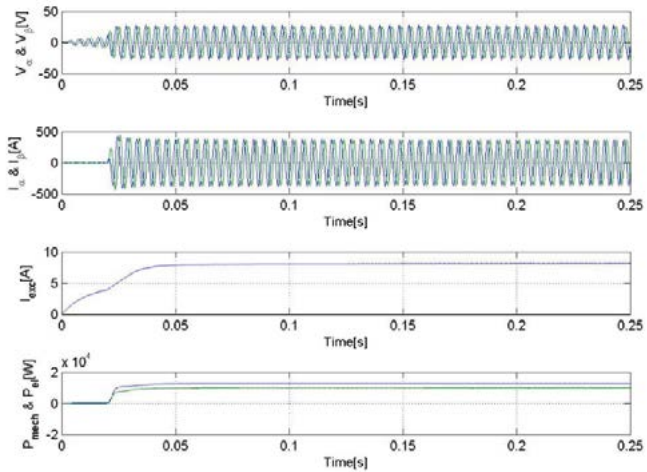
Only Ferrite IPM-CPA controlled dynamics for the 10 kW and 100kW machine motoring and generating are given here:

Fig. 15.11a,b: 10kW motoring and generating at 2000rpm

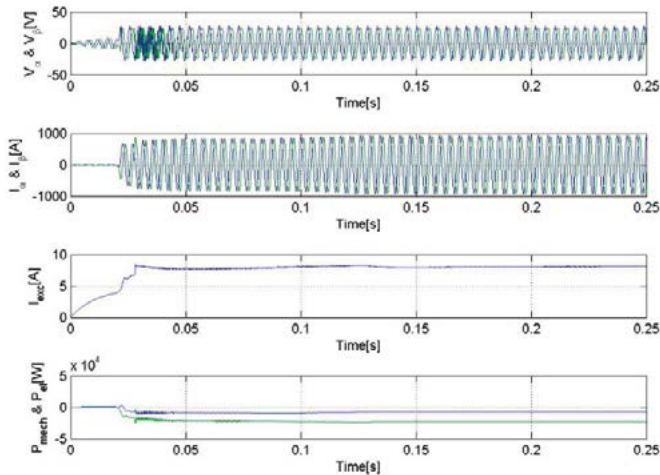
Fig. 15.12a,b: 10kW motoring and generating at 6000rpm

Fig. 15.13a,b: 100kW motoring and generating at 2000rpm

Fig. 15.14a,b: 100kW motoring and generating at 6000rpm

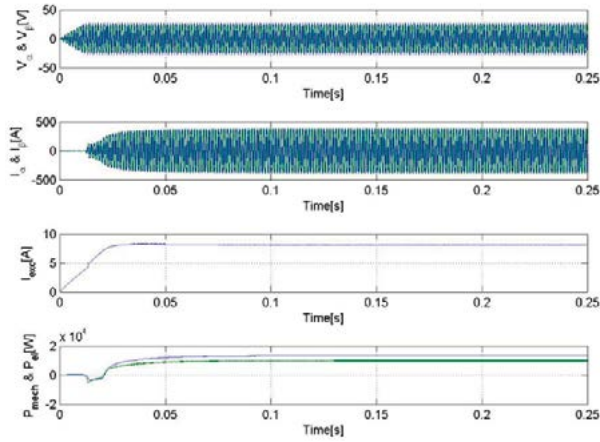


a)

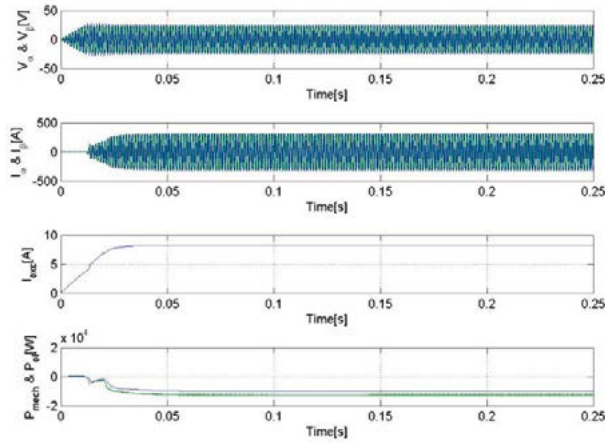


b)

Fig. 15.11 10kW, 2000rpm, 42V<sub>DC</sub>, power transients: a) motoring, b) generating.

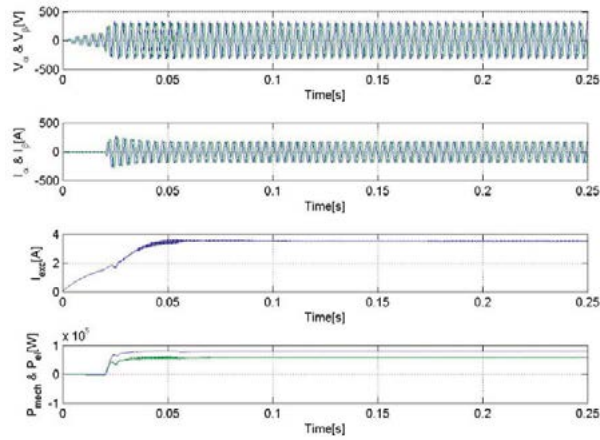


a)

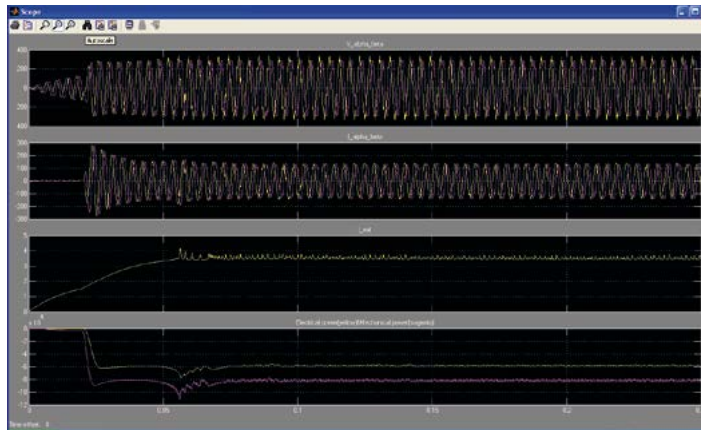


b)

Fig. 15.12 10kW at 6000rpm, 43V<sub>DC</sub> power transients: a) motoring, b) generating.

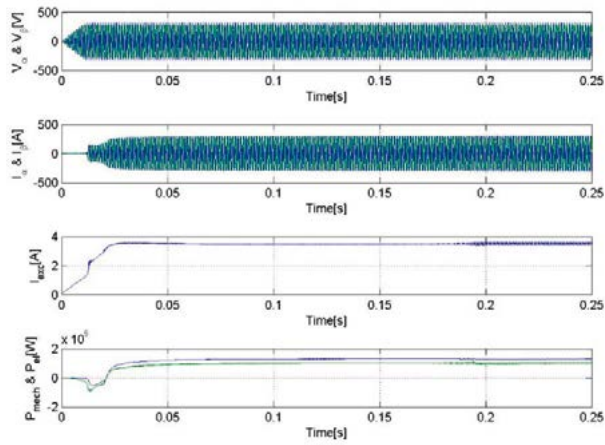


a)

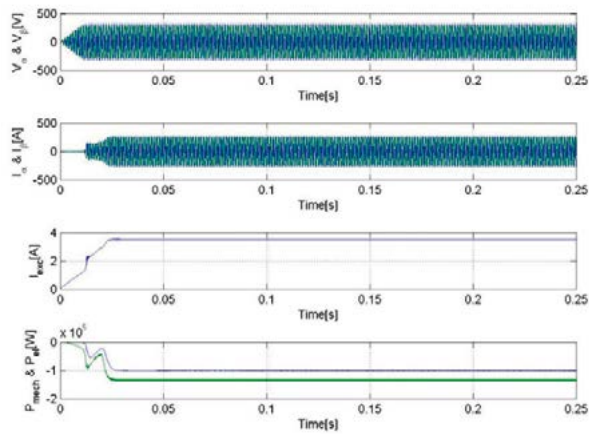


b)

Fig. 15.13 100kW, 2krpm, 500V<sub>DC</sub>, power transients: a) motoring, b) generating.



a)



b)

Fig. 15.14 100kW, 6krpm, 500V<sub>DC</sub> power transients a) motoring, b) generating.



Final Notes:

- Figs. 15.12, 15.13 show the 10kW machine control system capable to produce stable power transient response for four critical operation modes within 50 milliseconds (motoring and generating)
- The same is valid for the 100kW machine control system (Figs. 15.14-15.15), but this time the power response oscillates more before stabilization
- The voltage ceiling of the inverter is observed in all the investigated cases
- With an efficiency of 94% at 100 kW from 2krpm to 6krpm in a 62kg active weight machine, the Ferrite IPM-CPA seems fully competitive for HEV(EV) electric propulsion
- The IPM-CPA may be made brushless by using an inverted (100kHz) – rotary transformer and diode rectifier at less than 3% power rating to feed the circular shape d.c. coil on the rotor. The solution has been already proven feasible for a multi-hetero-polar d.c. excited 100 kW SM for HEV(EV) electric propulsion [6].
- The outer PM rotor SMC claw-pole stator synchronous motor (Fig. 15.15) was recently proposed in multiple configurations as a super high torque-density copper losses solution in small electric actuators for robotics (example: humanoid robot ankle electric actuator); strong R&D efforts in this direction are expected in the near future.
- Finally, using the IPM-CPA configuration, but replacing the dc. excitation coil by a thick disk-shape axially-magnetized bounded NdFeB ( $B_r=0.8T$ ) PM on the rotor. Such a configuration could produce high torque densities such as 55 Nm/liter for an efficiency of around 94% at 3 krpm.

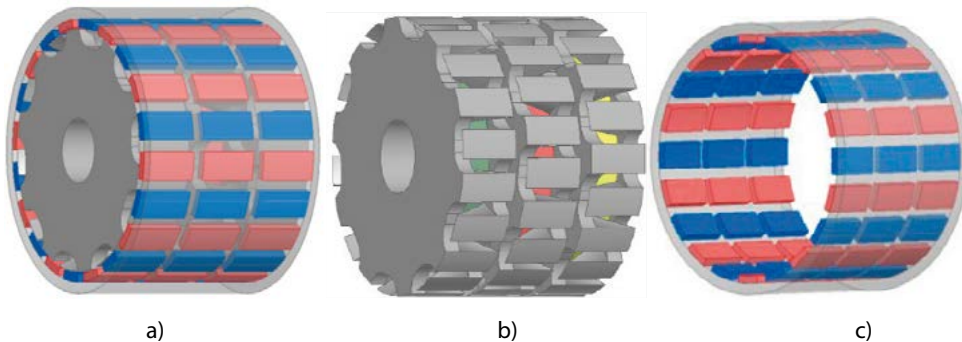


Fig. 15.15 Tentative outer-PM-rotor SMC claw-pole-stator synchronous motor geometry for robotics drivers from 5Nm/120W copper losses short duty cycle (10%): after UPT internal report: a) 3D model, b) claw pole stator, c) outer PM rotor



### 15.3 References

- [1] L. Tutelea, D. Ursu, I. Boldea, A. Agarlita, "IPM claw pole alternator system for more vehicle braking energy recuperation" *Journal of Electrical Engineering*, Vol.12(3), pp. 211-220
- [2] I. Boldea, L. Tutelea, M. Abele, B. Simo, "Comparisons of automotive generators/motors with claw-pole PM-less, NdFeB or Ferrite interclaw pole (IPM) rotors for 10KW and 100KW at 6000rpm: optimal design and vector control dynamics", UPT internal report 2013
- [3] S. Schulte, K. Hameyer "Computation of mutual inductance between rotor and stator of synchronous claw pole alternators regarding claw chamfers", *Record of IEEE-IEMDC-2005*, pp. 1300-1303
- [4] J. G. Kassakian, H. C. Wolf, J. M. Miller, C. H. Hurton, "Automotive electrical systems circa 2005: demands for better fuel economy and more electric power are driving car to multiple higher voltage" *IEEE Spectrum*, No 1, 1999, pp. 12-16
- [5] B. Simkin, R. Marko, C. D. Ambrosio, M. Abele, G. Hener, A. Terre, I. Boldea, S. Scridon, "Improved energy efficiency for conventional vehicles through an enhanced dual voltage architecture and new components with an attractive cost-benefit ratio", *Record of EVER-2011*, Monaco, paper no 70
- [6] C. Stancu, T. Ward, K. Rahman, R. Dawsey, P. Savagian, "Separately excited synchronous motor with rotary transformer for hybrid vehicle application", *Record of IEEE Energy Conversion Congress and Exposition (ECCE)*, 14-18 Sept. 2014, Pittsburgh, PA, USA

## 16.1 Introduction

Despite its simple and robust construction, the motion control for induction generators should take into account the complexity of the dynamic model which is nonlinear and variable in time and that the physical parameters of the machine are not always known with great precision. Under these conditions, the motion control means control of the speed and/or the position, respectively torque control, thus obtaining a faster torque response as the motion control is more efficient. There are two main control strategies: scalar control and vectorial control [1]-[18]. Cage rotor induction generators have been employed to operate as wind turbine generators and small hydroelectric generators in isolated power systems [1], [2], due to their practical advantages related to low maintenance cost, better transient performance, ability to operate without dc power supply for field excitation and brushless construction.

In a split-wound machine, the stator winding consists of two similar but separate three-phase windings wound for the same number of poles. Both stators are fed by the same frequency and the rotor is a standard squirrel cage. The two stator windings are mutually coupled and small unbalances in the supplied voltages generate circulating currents. Furthermore, because of the low impedance of the harmonic currents there is a high level of circulating currents when a non sinusoidal voltage source supply is used, adding losses and demanding larger semiconductor device ratings [3]-[7]. The attractive advantages of this kind of machines are: better controllability in the very low speed range and the flexibility of the output generator characteristics. Since the air-gap flux linkages created by the two stator windings and the induced rotor currents share the same magnetic stator and rotor cores, the main air gap flux saturation phenomenon is more complicated than that of the normal single-stator-winding squirrel-cage induction machine [10]. Because of this complexity, a reconsideration of the main flux linkage saturation effect is required in the design of the machine and in the development and practical implementation of speed/torque control algorithms. To avoid deep magnetic saturation in the stator and rotor cores and rotor and stator teeth, magnetic design methodologies have been suggested both for the dual stator-winding and brushless doubly fed induction machines [9], [10]. An approach that includes the influence of magnetic saturation and iron loss using finite-element analysis in the performance prediction of the brushless doubly fed induction

machine was set. The proposed finite-element model provides very good steady-state predictions and can be used for the sizing and design optimization of the machine.

The dual-stator-winding squirrel-cage induction machine is the most recent innovation in the family of induction machinery. Broadly, there are two designs: the first type has two stator windings wound for the same pole numbers with similar or dissimilar phase numbers, and the second design has two stator windings with dissimilar pole numbers with the same or unequal phase numbers [2], [10]. There is also the brushless doubly fed induction machine that has two stator windings wound for dissimilar pole numbers and a specially designed nested loop rotor structure that couples the two airgap flux linkages derived from the two stator windings. The synchronous mode of operation of this, the machine appears to be the most profitable, particularly for converter-based drive control [10], [13], [18-25].

A new optimal method to identify the parameters of the two stator winding induction machines [10], using only industrial measurement equipment (Voltmeter, Ampere-meter, Power-meter) from standard tests, (no load and two phase short circuit) is proposed. This method does not need mechanical coupling of the induction machine with a load machine and does not need any speed measurement. The method is also able to deal with measurement error.

In this chapter we propose a new scheme and control strategies able to convey active and reactive power across both windings but with a low cost power converter. Moreover, for the dual-stator-winding cage rotor induction generator (DSWIG), the main winding (2/3 slot area) is connected from a dc bus through a roughly 50% rating PWM inverter. The auxiliary winding (1/3 slot area) is connected to a 3 phase capacitor and through a diode rectifier (of 50% power rating) to the dc bus. At low speeds only the main winding works as controlled by the inverter, while at high speeds the auxiliary winding starts delivering active power into the dc bus. This arrangement allows for optimal power (energy) extraction at low and high speeds at reasonably low initial cost and satisfactory energy conversion efficiency [26-35].

## **16.2 Dual Stator Windings Induction Generators (DSWIG): New Proposed Topologies**

There is a large variety of excitation schemes for conventional and DSWIG generators. According to the primary sources (hydro, wind, thermal energies) and to consumer needs, a capacitive reactive current systems [5] may be used for excitation, connected to generator terminals, such as: AC capacitances, synchronous compensator, diode bridge rectifier or inverter. In order to provide better utilization of the copper for DSWIG, a new scheme is proposed here (figure 16.1) which contains an active rectifier (inverter) and a diode rectifier, both designed at half of the rated power. In this configuration, both windings convey active and reactive power through the machine. At low speeds, only the main winding delivers active power to the dc link through the PWM converter, while at

high speeds the auxiliary winding adds more power to the dc link. In general the rating of the PWM converter (active rectifier) is around 50% while the auxiliary winding may add an additional 50% in active power. This arrangement allows for optimal power (energy) extraction at low and high speeds at reasonably low initial cost and satisfactory energy conversion efficiency.

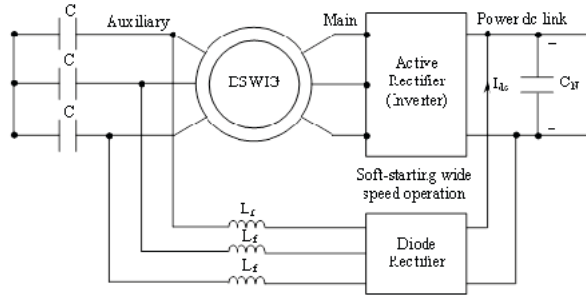


Fig. 16.1 The proposed solution for variable speed wind or hydro energy conversion system [28].

All the induction generator energy is available in the dc circuit while in [2], [12] a part of energy is available only for some ac unpretentious loads that are connected directly to the auxiliary winding (figure 16.2), and as expected the diode rectifier may be eliminated. In the wind turbine applications, the unpretentious load will be connected only when available power is greater than 50% of the rated power, which means a turbine speed that is greater than 80% of the rated speed.

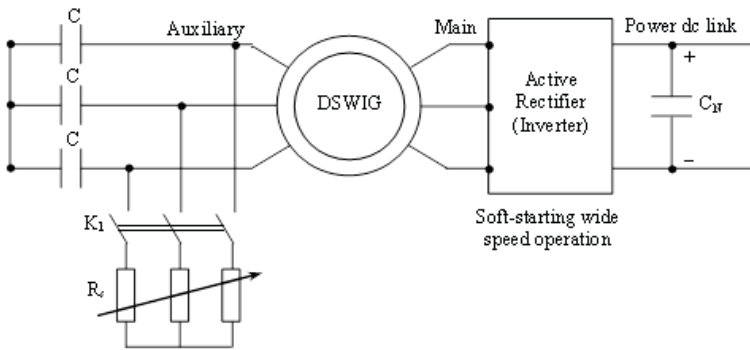


Fig. 16.2 Proposed solutions for unpretentious loads [28].

### 16.3 Analytical Model of DSWIG

The dynamic model of the DSWIG expressed in the complex variable form is set forth as follows [11] when the parameters on the rotor and the excitation windings are all converted to the main winding. The voltage and fluxes equations in the stationary reference frame are given as:

$$\underline{U}_m = R_m \cdot \underline{I}_m + \omega_1 \cdot \underline{\Psi}_m, \quad (16.1)$$

$$\underline{U}_e = R_e \cdot \underline{I}_e + \omega_1 \cdot \underline{\Psi}_e, \quad (16.2)$$

$$\underline{U}_r = R_r \cdot \underline{I}_r + (\omega_1 - \omega_r) \cdot \underline{\Psi}_r, \quad (16.3)$$

$$\underline{\Psi}_m = L_m \cdot \underline{I}_m + L_{me} \cdot \underline{I}_e + L_{mr} \cdot \underline{I}_r, \quad (16.4)$$

$$\underline{\Psi}_e = L_e \cdot \underline{I}_e + L_{me} \cdot \underline{I}_m + L_{mr} \cdot \underline{I}_r, \quad (16.5)$$

$$\underline{\Psi}_r = L_r \cdot \underline{I}_r + L_{mr} \cdot (\underline{I}_m + \underline{I}_e), \quad (16.6)$$

where the subscripts m, e, and r denote the variables associated with the main winding, excitation winding, and the equivalent rotor winding, respectively,  $\omega_1$  is the main electrical frequency,  $\omega_r$  is the angular rotor electrical frequency,  $L_{mr}$  and  $L_{me}$  are the mutual inductance and the amplitude of the mutual leakage inductance between main and excitation windings respectively:

$$L_m = L_{\sigma m} + L_{me} + L_{mr}, \quad (16.7)$$

$$L_e = L_{\sigma e} + L_{me} + L_{mr}, \quad (16.8)$$

$$L_r = L_{\sigma r} + L_{mr}, \quad (16.9)$$

$$\underline{I}_0 = \underline{I}_r + \underline{I}_m + \underline{I}_e, \quad (16.10)$$

where the subscript  $\sigma$  denotes the leakage inductance. From the mathematical model of the DSWG, the equivalent circuit can be shown in fig. 16.3.

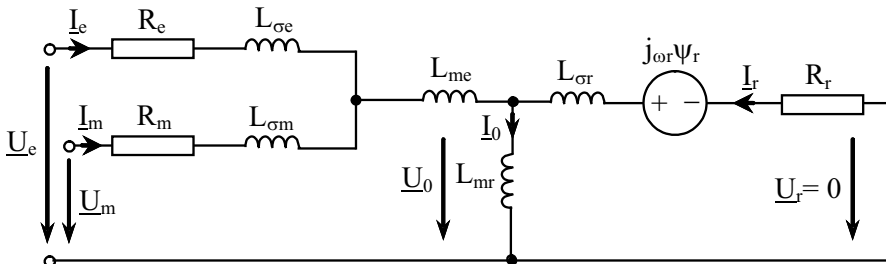


Fig. 16.3 Complex vector model of the DSWG under steady state [13].

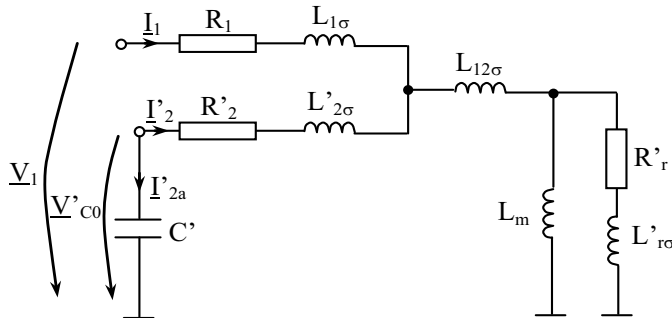


Fig. 16.4 Equivalent circuit of the proposed scheme (figure 16.3) in no load conditions, with capacitor in the auxiliary winding [28].

The equivalent circuit of the DSWG shown in figure 16.4 is using the '1' indices for main winding, '2' for auxiliary winding and 'r' for rotor winding. Auxiliary and rotor windings were reported to the main winding [10], [13], [26].

## 16.4 Optimal Design

The general optimization problem can be divided into three quasi-independent sub-problems: choosing the objective function, choosing the optimization variables and the machine model, and then solving the problem. The optimal design of the DSWG generator is subject to multi-objective criteria and constructive constrains such as: reducing the initial cost, reducing the generator size and weight, improving the efficiency and limiting the temperature of the components to a feasible level. The multi-objective criteria should be aggregated into a single objective function if the design objective is to obtain a unique solution. This could be a total cost function including a penalty for unmet constraints. The objective function,  $C_t$  becomes [6], [13]:

$$C_t = C_i + C_E + C_a + C_p, \quad (16.11)$$

where  $C_i$  is the initial cost,  $C_E$  the cost of the lost energy,  $C_a$  an additional cost to consider the impact of the machine size and finally  $C_p$  is the penalty cost. Sixteen optimization variables are used to control the machine main size dimensions as well as the slot details. The probability to reach the global optimum using the Hooke Jeeves (HJ) algorithm could be increased by starting the algorithm several times from different points of the optimization variable space. A few sample results for the HJ optimization evolution to the best design are shown in figures 16.5, 16.6 and 16.7. Using the optimization program, the variation of the initial cost and total expenses for the machine was observed (for 10 years of functioning) with different numbers of poles,  $2p$ : 8, 12, 16, 18, 20, and 24. These results along with other characteristics are shown in Table 16.1 [13].

Analyzing the results which were obtained, it can be stated that the cheapest machine is the one with 20 poles, the one with the lowest global expenses is the one with 16 poles (which has the highest efficiency), the lightest is the machine with 24 poles; the machine with 8 poles has the best power factor, etc.

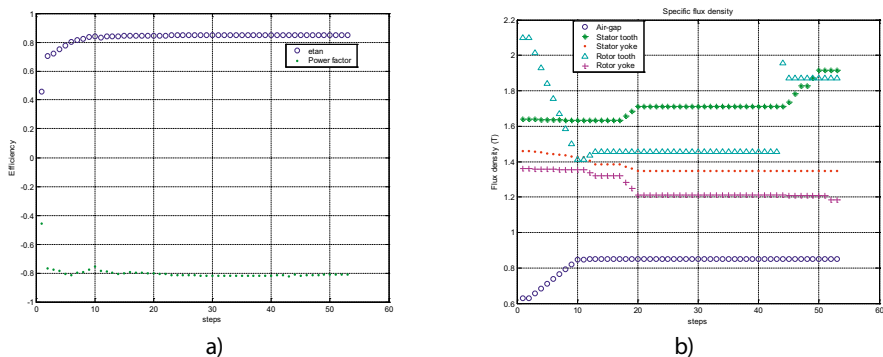
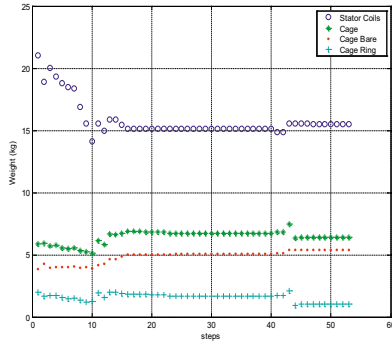
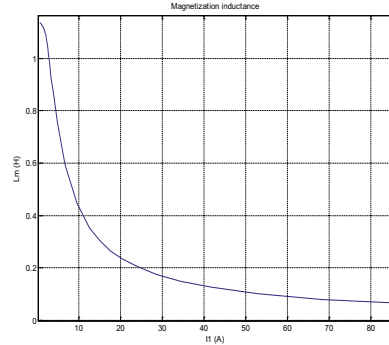


Fig. 16.5 a) Efficiency and power factor; b) specific flux density [34].

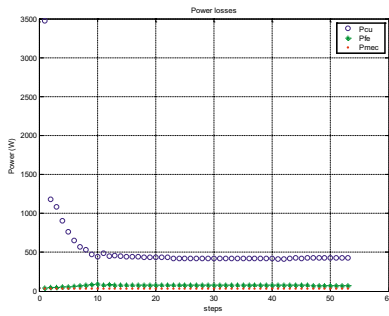


a)

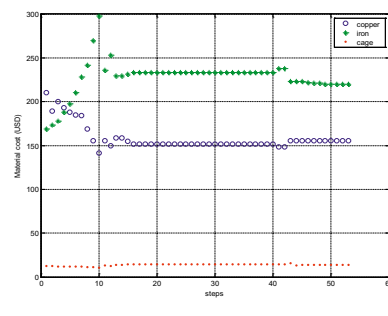


b)

Fig. 16.6 a) Weight; b) magnetization inductance [34].



a)



b)

Fig. 16.7 a) power losses; b) material cost [34].

Table 16.1 Comparative study of DSWG depending on pole number.

	<b>Pole number</b>	<b>2p</b>	<b>8</b>	<b>12</b>	<b>16</b>	<b>18</b>	<b>20</b>	<b>24</b>
Base frequency	$f_n$	[Hz]	15	24	32.5	36.5	40.5	49
Fabrication cost	$i\_cost$	[USD]	512.8	425.1	399.1	398.8	384.7	403.3
Objective function (total cost)	$t\_cost$	[USD]	1478.8	1385.3	1355.8	1367.7	1399.7	1431.2
Efficiency	$\eta_{tan}$		84.83	84.9	84.95	84.79	84.18	84.01
Power factor	$\cos\phi_{in}$		0.81	0.75	0.73	0.72	0.7	0.69
Weight active materials	weight M	[kg]	88.8	68	58.4	55.4	51.8	48.8
Optimization time	sim_time	[s]	10	23.8	12.8	8.9	6.8	10.2
Air-gap	h <sub>ag</sub>	[mm]	0.35	0.35	0.35	0.35	0.35	0.35
Rated current	$I_{1n}$	[A]	5.61	6.05	6.19	6.31	6.54	6.56
Outer stator diameter	$D_{so}$	[mm]	386	409	484	519	533	594
Inner stator diameter	$D_{si}$	[mm]	286.3	319.6	393.9	433.4	450.1	519.7
Length of stator laminations pack	$l_c$	[mm]	139.3	107.1	72.0	65.1	60.2	55.3
Air-gap flux density	$B_{agsp}$	[T]	0.85	0.85	0.83	0.81	0.81	0.73
Specific solenation	el <sub>sp</sub>	[kA/m]	16.22	15.31	15.94	15.0	14.45	13.07

The dual stator winding induction generator could reduce the inverter (active rectifier) KVA with 43% for 8 poles, when the inverter is placed on the excitation winding. The full power rectifier and the dc-dc boost converter required in this case drastically reduce the advantages of this scheme. The converter KVA reductions are smaller (19%) when the inverter is placed on the main windings. In this case the converter power reduction is higher for a large number of poles where the converter for standard induction machine is also larger due to smaller power factor. The method does not require other power electronics, but it requires a capacitor battery on the excitation windings. If the DSWIG is made in the same size as the single winding induction machine, the efficiency will be decreased by around 5%, and that creates cooling problems. The efficiency could be preserved (only 0.5%-1% efficiency reduction) at the cost of increasing the DSWIG size to 10% in diameter which would lead to 29% in the generator weight and about 32%-35% in the active material costs. Economic benefits will be obtained when the full power inverter price is larger than the generator price by more than 50%, which is the case for small power machines. Analytical calculation for parameter optimal identification are given in [35].

## 16.5 2-D FEM Analysis

An approach that includes the influence of magnetic saturation and iron loss using finite-element analysis in the performance prediction of the dual stator winding induction machine was set. The proposed finite-element model provides very good steady-state predictions and can be used for the sizing and design optimization of the machine. Induction machine saturation could be increased at low frequency (required in direct driving) without notable iron loss increases in order to have a larger slot area required in two stator winding or for aluminum winding which could replace the copper winding in low cost machines.

The program starts in Matlab and creates the mesh and run in the FEMM 4.2 software platform. When applied to electrical machines, the problem is usually reduced to cover only one pole or one pole pair with the help of boundary and symmetry conditions, in order to reduce the computation time. In addition, it is often sufficient to reduce the problem to a 2D plane and use the finite element analysis (FEA). The mesh has 47758 nodes and 95129 elements [10]. No load (zero rotor current) FEM investigations at standstill, with dc currents for star connection lead to  $I_{Ae} = I = -2I_{Be} = -2I_{Ce}$ . The total distribution of the flux density for 4 poles is shown in figure 16.8 for excitation current and in figure 16.9 for main winding current [10].

Figure 16.10 shows the air-gap flux density (produced by main and excitation currents) and figure 16.11 shows the flux density space harmonics. The linkage fluxes ( $A_e$  produced by excitation current in excitation winding and  $A_m$  produced by excitation current in main winding) are shown/presented in figure 16.12. Figure 16.13 shows inductances versus current ( $L_{e1}$  excitation phase inductance,  $L_{m1}$  main phase inductance,  $L_{ed}$  excitation d axes inductance,  $L_{mq}$  main q axes,  $L_{em}$ ,  $L_{me}$  coupling inductances between excitation and main winding computed in two ways: linkage flux produced by excitation current in main



winding divided by excitation current respectively linkage flux produced by main current in excitation winding divided by main current). The difference between  $L_{em}$  and  $L_{me}$  are smaller than 0.3% and they should be showing in FEM accuracy [13], [26].

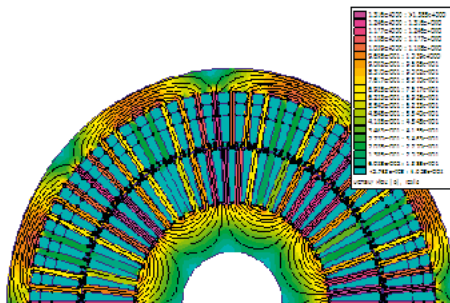


Fig. 16.8 Total flux density at  $I_{Ae}=4.5A$  and  $I_{Am}=0$  [10].

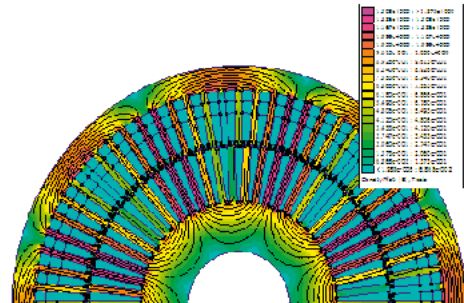


Fig. 16.9 Total flux density at  $I_{Am}=4.5A$  and  $I_{Ae}=0$  [10].

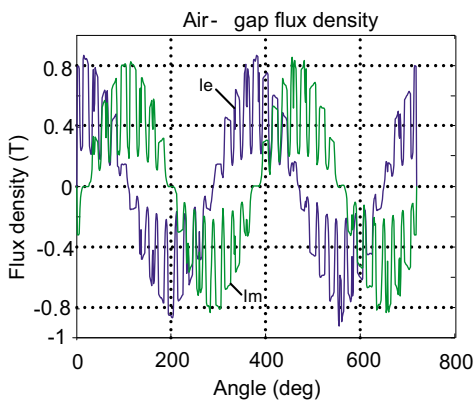


Fig. 16.10 The normal component of air-gap flux density [10].

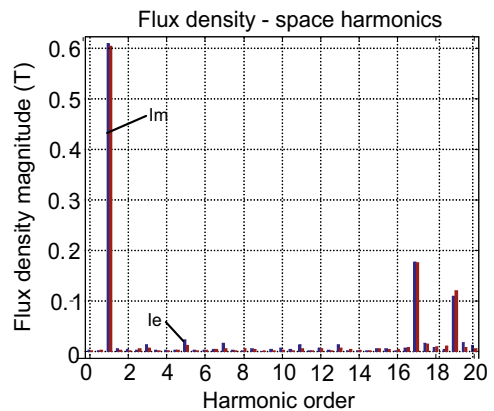


Fig. 16.11 The flux density space harmonics

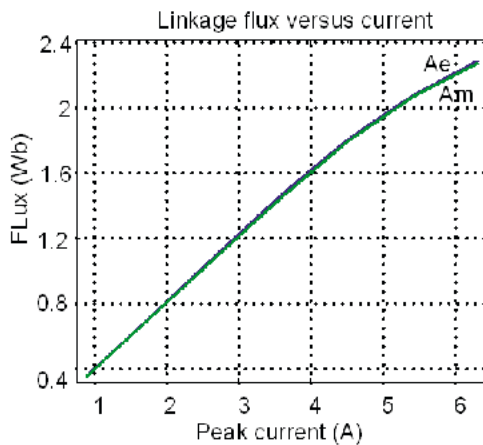


Fig. 16.12 The link. fluxes vs. current [10].

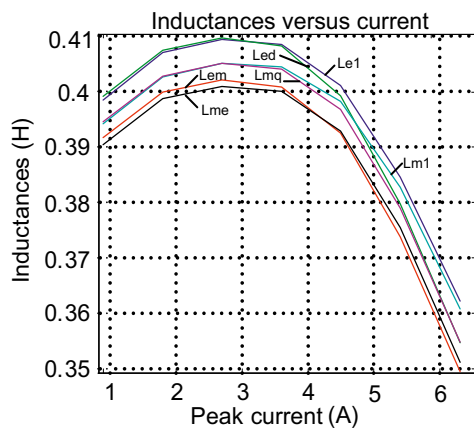
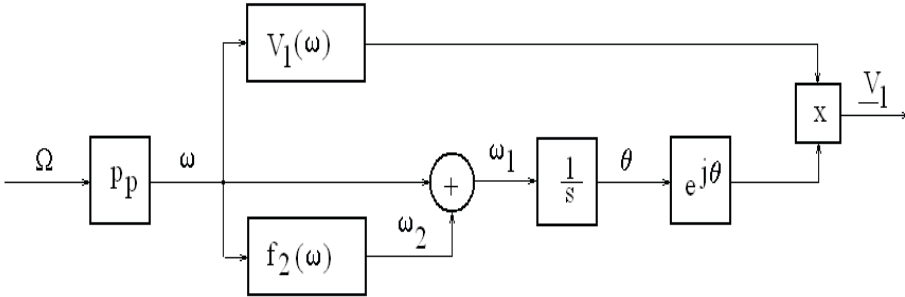


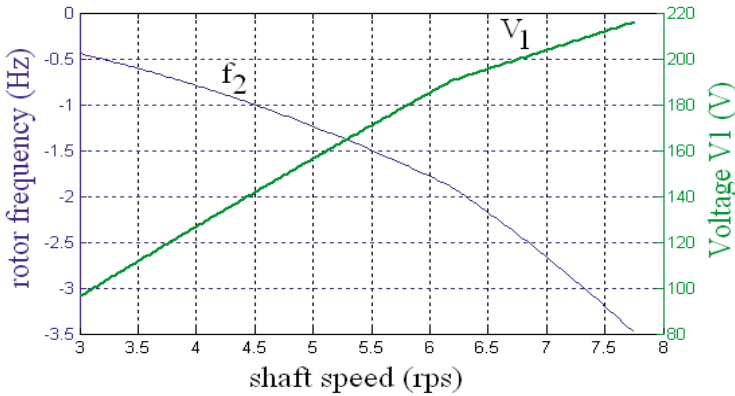
Fig. 16.13 The induct. vs. current [10].

## 16.6 Control model and dynamic simulation

A preliminary feed-forward control shown in fig. 16.14a was implemented to verify the dynamic of proposed topology. The auxiliary winding voltage becomes larger than dc voltage, after 80% of the rated speed and it starts to deliver the power to the dc link. The power in the main winding is maintained constant by controlling the main voltage  $V_1$  as it is shown in fig. 16.14b from [28].



a)



b)

Fig. 16.14 Feed-forward control a) block diagram, b) nonlinear  $V_1$  and  $f_2$  function.

Numerical simulations of the dynamic process are used to proof the proposed control strategy. The matrix form equations (16.12-16.14) in a stator reference frame are used to model the DSWG in transient regime. The main inductances  $L_m$  saturation is considered through an analytical approximation (16.15-16.16) where  $L_{m0}$ ,  $a$ ,  $b_1$ ,  $b_2$  parameters are given from a curve fitting process considering the magnetization inductances values from FEM [35].

$$\begin{pmatrix} \dot{I}_{\alpha 1} \\ \dot{I}_{\alpha 2} \\ \dot{I}_{ar} \end{pmatrix} = L^{-1} \begin{pmatrix} V_{\alpha 1} - R_1 I_{\alpha 1} \\ V_{\alpha 2} - R_2 I_{\alpha 2} \\ -R_r I_{ar} - \omega_r \Psi_{\beta r} \end{pmatrix} \quad (16.12)$$

$$\begin{pmatrix} \bullet \\ I_{\beta 1} \\ \bullet \\ I_{\beta 2} \\ \bullet \\ I_{\beta r} \end{pmatrix} = L^{-1} \begin{pmatrix} V_{\beta 1} - R_1 I_{\beta 1} \\ V_{\beta 2} - R_2 I_{\beta 2} \\ \omega_r \Psi'_{\alpha r} - R_r I_{\beta r} \end{pmatrix} \quad (16.13)$$

$$L = \begin{pmatrix} L_m + L_{1\sigma} + L_{12\sigma} & L_m + L_{12\sigma} & L_m \\ L_m + L_{12\sigma} & L_m + L_{12\sigma} + L_{2\sigma} & L_m \\ L_m & L_m & L_m + L_{r\sigma} \end{pmatrix} \quad (16.14)$$

$$L_m = L_{m0} \cdot \frac{1 + a I_0^2}{1 + b_1 I_0^2 + b_2 I_0^3} \quad (16.15)$$

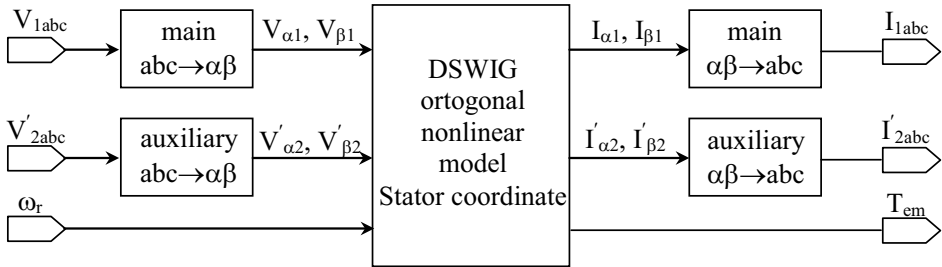
$$I_0 = \sqrt{(I_{\alpha 1} + I'_{\alpha 2} + I'_{\alpha r})^2 + (I_{\beta 1} + I'_{\beta 2} + I'_{\beta r})^2} \quad (16.16)$$

$$\begin{pmatrix} \Psi_{\alpha 1} \\ \Psi'_{\alpha 2} \\ \Psi'_{\alpha r} \end{pmatrix} = L \cdot \begin{pmatrix} I_{\alpha 1} \\ I'_{\alpha 2} \\ I'_{\alpha r} \end{pmatrix} \quad (16.17)$$

$$\begin{pmatrix} \Psi_{\beta 1} \\ \Psi'_{\beta 2} \\ \Psi'_{\beta r} \end{pmatrix} = L \cdot \begin{pmatrix} I_{\beta 1} \\ I'_{\beta 2} \\ I'_{\beta r} \end{pmatrix} \quad (16.18)$$

$$T_{em} = \frac{3}{2} P_1 (\Psi'_{\beta r} \cdot I'_{\alpha r} - \Psi'_{\alpha r} \cdot I'_{\beta r}) \quad (16.19)$$

The DSWG model, based on the previous equations is presented in figure 16.15.



a)

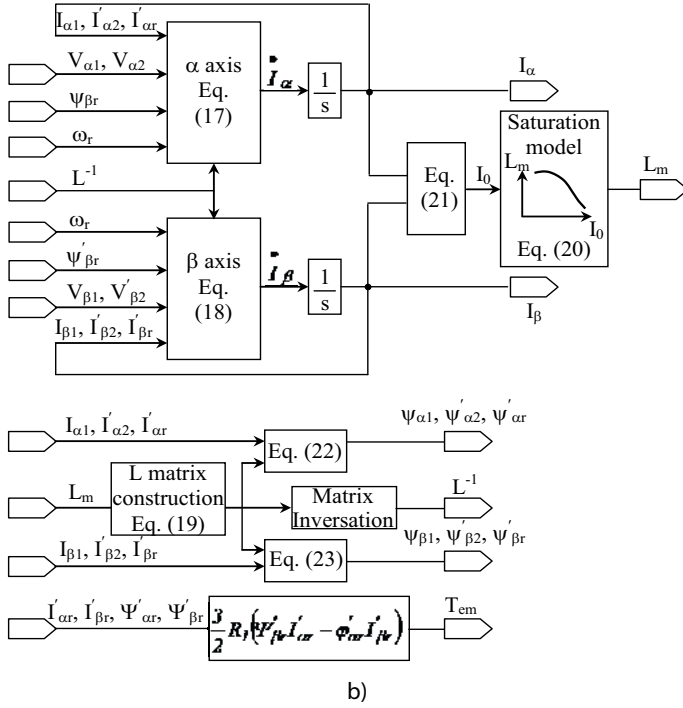


Fig. 16.15 The DSWIG model a) orthogonal transformation; b) orthogonal nonlinear model [28], [35].

Mathematical model of the DSWIG and control is combined with the circuit model in figure 16.16.

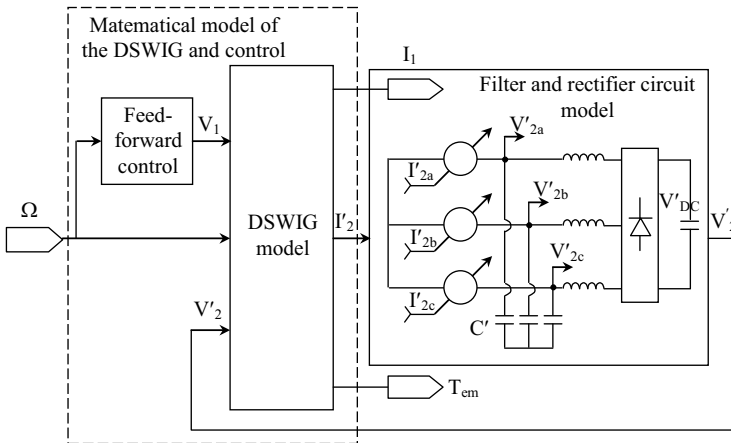


Fig. 16.16 System simulation-block diagram.

The feed-forward control is set to extract electrical power in direct ratio with the cube of the shaft speed. Only the active rectifier is able to extract electrical power at low speed, figure 16.17.a. The iron losses and mechanical losses are not considered in the dynamic simulations and consequently the efficiency, figure 16.17.b, contains only the copper losses.

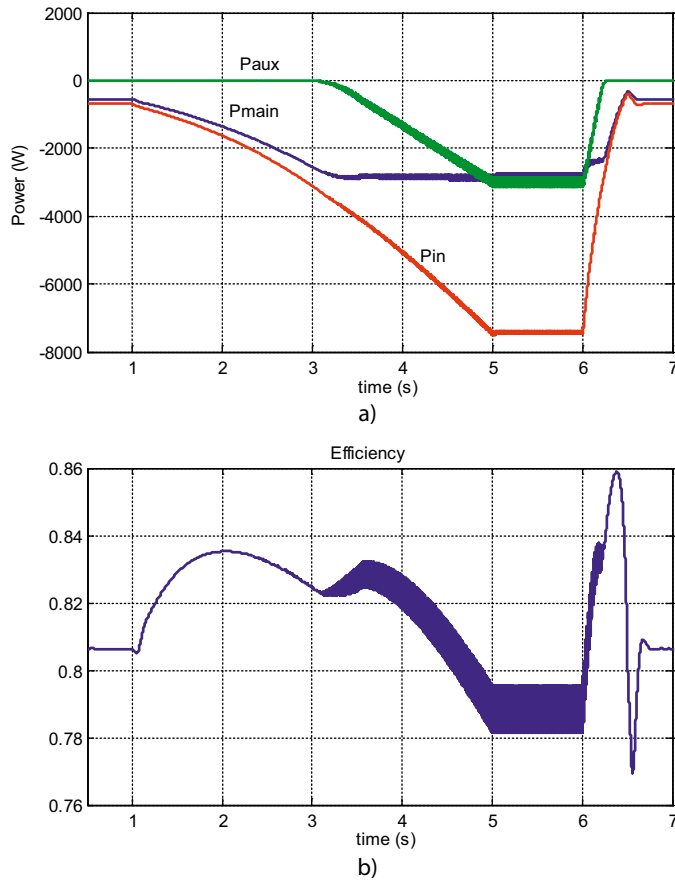


Fig. 16.17 Power (a) and efficiency (b) variation [28].

The prime mover is assumed to rotate the generator with a variable speed and a test variation of the speed is considered in the simulation, figure 16.18. The voltages and current variations considering the test profile of the speed are shown in figure 16.19.

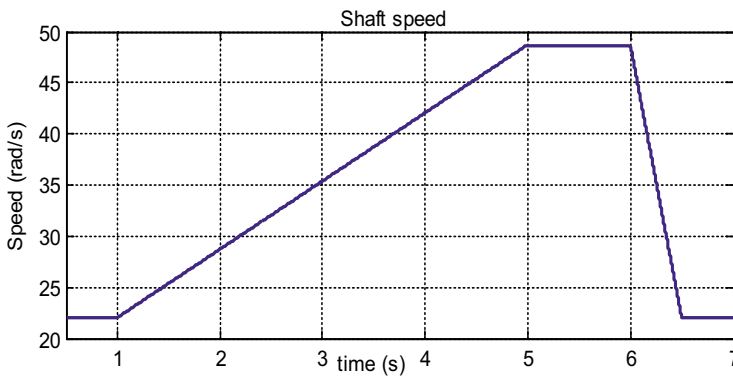


Fig. 16.18 Shaft speed profile [28].

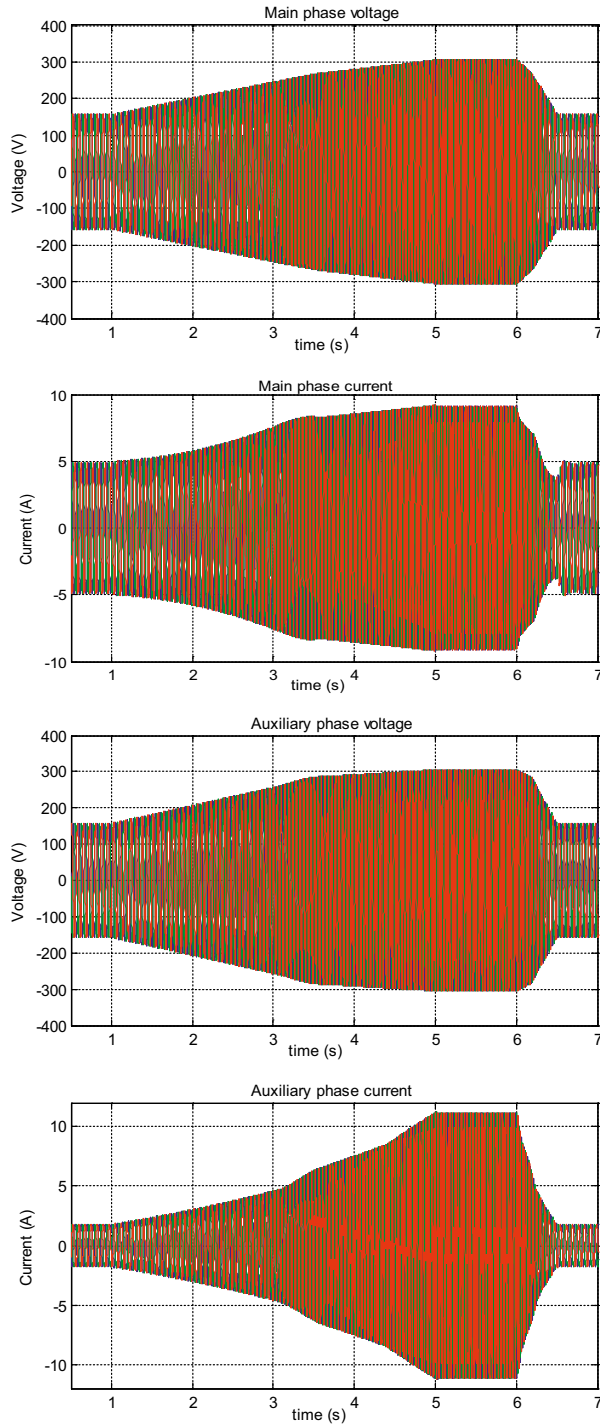
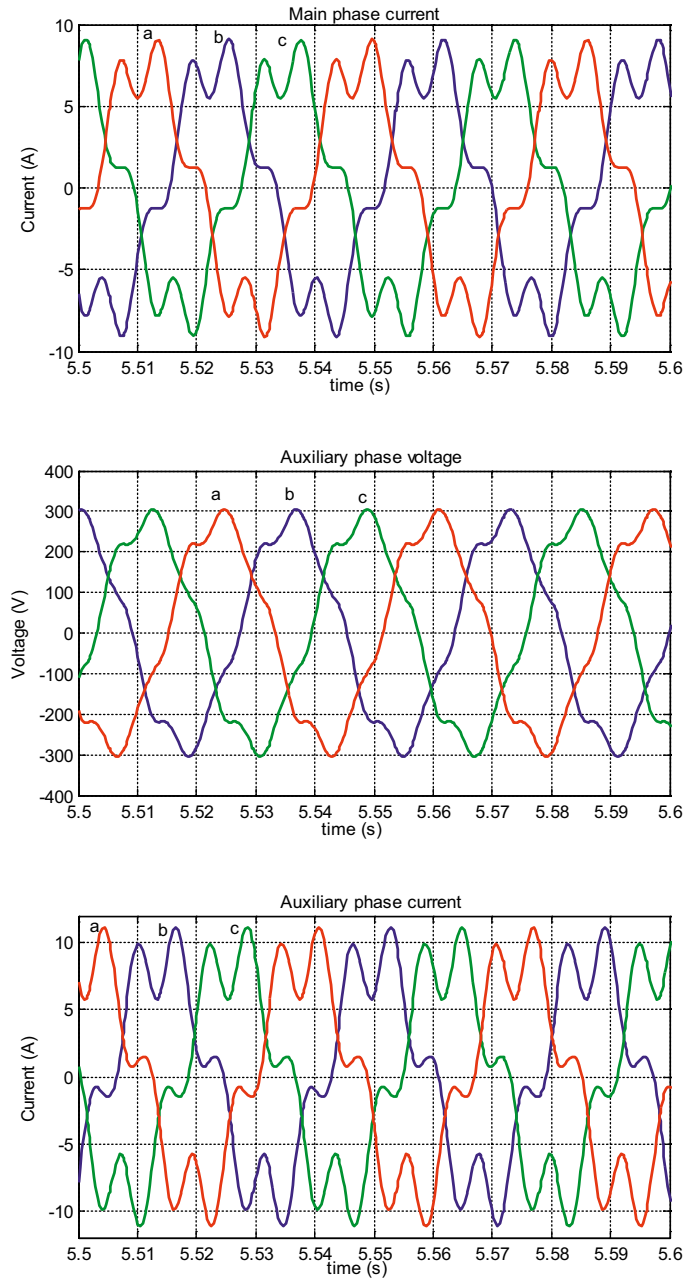


Fig. 16.19 Main and auxiliary voltages and current variations [28].

Only the fundamental harmonics is considered in the voltage applied to the main windings. When the speed is small and the diode rectifier is closed, all the voltages and the currents are sinusoidal. When the diode rectifier is opening, the harmonics are spread in auxiliary current and voltage, but also in the main current as it is shown in fig. 16.20 at the rated power in the auxiliary winding.



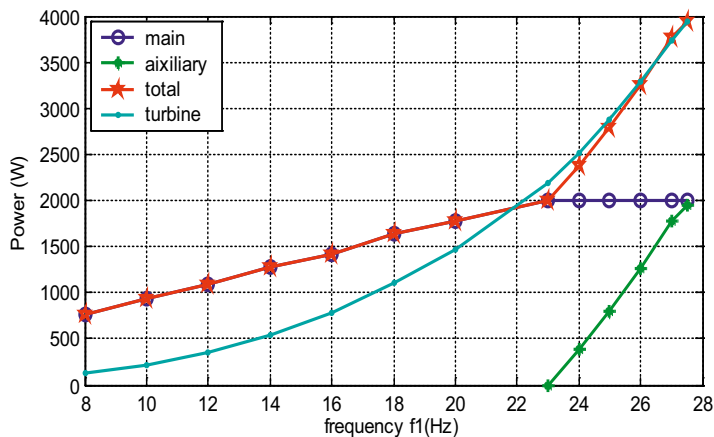




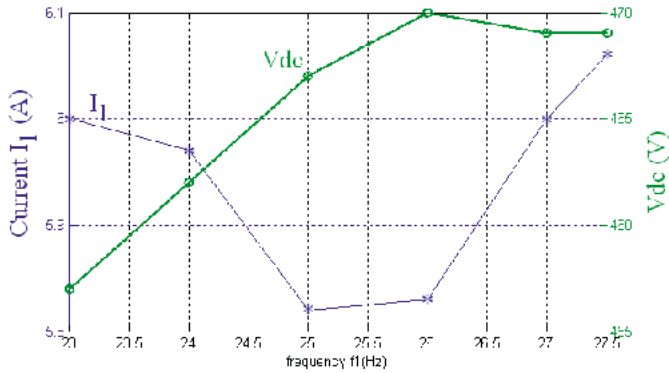
Steady state and dynamic simulation show that in order to connect the diode rectifier to the same dc link, it was necessary an around 1.26 turn's ratio between auxiliary and main winding. The actual DSWIG could be used to prove the principle if the auxiliary winding is connected, trough diode rectifier, to a secondary dc link voltage with the ratio of the dc link voltage and secondary dc voltage equal by 1.26. A bidirectional power flow industrial converter is used to implement the dc link circuit, and equivalent dc load and the active rectifier. The dc link voltage value for the bidirectional industrial power converter is  $V_{DC}=580V$ .

The secondary dc voltage,  $V_{DC2}$ , was set at 460V considering the required ratio between dc link voltage and secondary dc voltage. The secondary dc link voltage was emulated through a variable resistive load connected in parallel with the diode rectifier and controlled through a static contactor to hold the secondary dc voltage at constant value (figure 16.21). The scope of the test was to prove that the maximum power available from a wind turbine could be extracted using the DSWIG proposed scheme. The current harmonics, usually introduced by the diode rectifier, are not presented by using this experimental setup but the control of the active and reactive power flow with a single converter remain. The prime mover is simulated by a three-phase cage-type induction machine driven by an inverter of ABB ACS 800-11. The parameters of the prototype are given above. The winding's cross sections of the existing machine are not the same as it is required for the proposed strategy and then it will be de-rated at 4kW.

The experimental results, figure 16.22.a, prove that DSWIG in the proposed configuration could double the power at high speed where the power in the main winding is constant and the power through the auxiliary winding is increasing with the speed. It could be noticed that by using the active rectifier the power extraction covers all wide speed range. The extraction power capability (at a given rated current 6.2A for main winding) is larger than the power available from a wind turbine.



a)



b)

Fig. 16.22 Preliminary experimental results [28].

Small variation of the rectified auxiliary voltage, figure 16.22b, proves that it is possible to deliver power in constant voltage dc bus. Also it shown that main winding current remain constant. More experimental results were presented in [35].

## 16.8 Conclusions

The optimal design had shown the parameters and performance complex dependence on the number of poles. However, the 16 poles generator is considered the optimum because it has the maximum efficiency, while the active material cost is also near its minimum and the power factor (which influences the power converter cost) is not large. The double stator winding induction generator could reduce the inverter (active rectifier) KVA by between 43% 28% (for 8 to 24 poles), when the inverter is placed on the excitation winding. The power converter reduction decreases when the number of poles is increasing because the inverter has to handle more reactive power with an increasing number of poles. The full power rectifier and the dc-dc boost converter required in this case drastically reduce the advantages of this scheme. The converter KVA reductions are smaller (19% to 30.6%) when the inverter is placed on main windings. In this case, the converter power reduction is higher for a large number of poles where the converter for the standard induction machine is also larger due to smaller power factor. The method does not require other power electronics but it requires a capacitor battery on the excitation windings. If the DSWIG is the same size as the single winding induction machine, the efficiency will be decreased by around 5% and create cooling problems. The efficiency could be reduced (only 0.5%-1% efficiency reduction) at the cost of increasing the DSWIG size by 10%-6.5% (8 -24 poles) in diameter which means 29% to 37.8% in the generator weight and about 32%-35% in the active material costs. Economic benefits will be obtained when the full power inverter price is larger than the generator price by more than 50%, which is the case for small power machines. This chapter presents a new topological variant of the dual stator winding induction machine (DSWIG) operating in generator mode (84% efficiency

at 170 Nm and 250 rpm, 3kW for 1.93 Nm/kg at 8 poles and 3.48 Nm/kg at 24 poles). The dedicated optimal DSWIG design could further reduce the DSWIG oversizing by several percent, but new winding connection topologies and inverter controls could improve further the DSWIG concept in order to be competitive with wind or hydro power plants [35].

A mathematically perfect saturated model should be implemented in flux rotating frame coordinates in so that the transients and steady state magnetization inductance could be considered. In our application, a long simulation time is required, without fast transients. Following this, a simplified version of the model using stator frame coordinate is applied with only the steady state magnetization inductance. The model and simulation results are still accurate despite the large difference between steady state inductance and transient inductances, because the magnetization current magnitude is constant during the fundamental currents and voltages. The dynamic simulation proves that the induction generator is able to start and run with full load without any control and with controlled converter. The active controller is also used to adjust the active power flow in order to extract the maximum energy for a given speed wind. The main advantage of the DSWIG is its improved capability to operate at variable low speeds [35].

It presents an optimal method for induction machine parameter identifications which could be allayed to the classical rotor cage machine with a single three phase winding in the stator and also to a dual stator winding cage-rotor induction machine. The estimate is performed by using an equivalent scheme to the DSWIG and a simple standard test without requiring mechanical coupling of two machines or a mechanical sensor. The model uses constant parameters as they are required in practical applications. The linkage inductance variation with the magnetization current could also be added using no load test points at larger voltage. During the parameter identification the machine speed is also an estimate at each no-load test point. If the speed variation range is small then the mechanical losses distribution in Coulumbian friction, viscous friction and fan friction are poor in precision, but the total mechanical losses (sum of the components) are more precise. For future work, a better thrust weighing factor could be computed considering the unbalanced current level and the short circuit resistance deviation from and to the average value [35].

Digital simulations as well the preliminary experimental results prove that the reduced power active rectifier, able to cover only the rated active power, could be used for a large speed range when the prime mover power increases in direct ratio or more with the speed. The reactive power is produced only by the capacitor battery at rated speed and the active rectifier is able to assist the reactive power at low speed. The proposed configuration is able to run self-excited at full power at rated speed wind in emergence mode (without any power electronics) with the same excited capacitor and at low power with some stability problem at low wind speed. Increasing the capacitor battery by 50% will improve the system stability and self-excited generator power capability at low wind speed [35].

The DSWIG scheme proposed in this paper uses an inverter with apparent power lower than the corresponding generator power. The expected ratio between the inverter power and the generator power is 50% in the case of DSWIG. This is similar to DFIG applications. The advantage of DSWIG is the lack of brushes. DSWIG can be used in variable speed applications. It is possible to extract low power even at low speeds, which cannot be obtained when the generator is directly connected to the grid, or when the generator has an inverter on the excitation winding and a diode bridge on the main winding. The DSWIG typology is an advantageous solution when it supplies unpretentious loads. The inverter on the main winding is used to transfer active power and also reactive power required for generator magnetization at low speeds, when the capacitor could not provide enough reactive power. A method to determine the saturated inductance of the DSWIG was also developed. Digital simulations and experimental results, in good correspondence, prove the validity of the theoretical considerations [35].

## 16.9 References

- [1] R. Alfredo, M.T. Lipo. „Dual stator winding induction machine drive,” *IEEE Transactions on Industry Applications*, Vol. 36, No. 5, September/October 2000, pp. 1369-1379
- [2] O. Ojo, I.E. Davidson, „PWM-VSI Inverter-Assisted Stand-Alone Dual Stator Winding Induction Generator,” *IEEE Transactions on Industry Applications*, Vol. 36, No.6, November/December 2000, pp. 1604-1610
- [3] O. Ojo, Z. Wu, „Modeling of a dual-Stator-Winding Induction Machine Including the Effect of Main Flux Linkage Magnetic Saturation,” *IEEE Transactions on Industry Applications*, Vol. 44, No.4, July/August 2008, pp. 1099-1107
- [4] I. Boldea, „Variable Speed Generators,” CRC Press, Boca Raton, FL USA, 2006
- [5] N. Budisan, „Problems of induction generator systems,” Politehnica Publishing House, Timisoara, Romania, 2003
- [6] L. Tutelea, I. Boldea, „Optimal Design of Residential Brushless D.C. Permanent Magnet Motors with FEM Validation,” *Proceedings of ACEMP*, 2007, pp. 435-439.
- [7] R. Muñoz and T. A. Lipo, “Complex vector model of the squirrel cage induction machine including instantaneous rotor bar currents,” *IEEE Trans. Ind. Appl.*, vol. 35, no. 6, pp. 1332-1340, Nov./Dec. 1999.
- [8] I. Boldea, S.A. Nassar, „The Induction Machine Handbook,” CRC Press Boca Raton FL USA, 2001.
- [9] G. Madescu, I. Boldea, T.J.E. Miller, „An Analytical Iterative Model (AIM) for Induction Motor Design,” *Rec. of IEEE – IAS*, Annual Meeting, 1996, vol. 1, pp. 566 – 573.
- [10] L.N. Tutelea, S.I. Deaconu, I. Boldea, N. Budişan, “Design, control and 2D-FEM validation for an Double Stator Winding Induction Generator,” *IECON 2013*, November 10-13, Vienna, Austria, pp. 2732-2737.
- [11] E. Muljadi, T.A. Lipo, “Series compensated PWM inverter with battery supply applied to an isolated induction generator,” *IEEE Transactions on Industry Applications*, vol. 30, no. 4, Jul./Aug. 1994, pp. 1073–1082.

- [12] F. Bu, W. Huang, Y. Hu, K. Shi, "An Integrated AC and DC Hybrid Generation System Using Dual-Stator-Winding Induction Generator With Static Excitation Controller," *IEEE Transactions on Energy Conversion*, vol. 27, no. 3, Sept. 2012, pp. 810-812.
- [13] L.N. Tutelea, S.I. Deaconu, N. Budişan, I. Boldea, "Double Stator Winding Induction Generator for Wind and Hydro Applications: 2D-FEM Analysis and Optimal Design," *15<sup>th</sup> European Conference on Power Electronics and Application, EPE ECCE Europe*, 3-5 September 2013, Lille, France, 10 pp.
- [14] G. Madescu, A. Trica, N. Budisan, O. Prostean, M. Biriescu, M. Mot, "Performance optimization of low-speed induction generators for direct drive wind turbines," *Electrical Power Conference*, Montreal, Canada, October 2007, ISBN 978-1-4244-1444-4, pp. 166-171.
- [15] D. Panda, T.A. Lipo, "Reduced switch count double converter fed wound rotor induction machine drive for wind energy application," *Electric Machines and Drives Conference*, June 2003, vol.3, ISBN 0-7803-7817-2, pp. 1924-1931.
- [16] F. Bu, W. Huang, Y. Hu, J. Shi, K. Shi, "A Stand-Alone Dual Stator-Winding Induction Generator Variable Frequency AC Power System," *IEEE Transactions on Power Electronics*, vol. 27, no. 1, Jan. 2012, pp. 10-13.
- [17] P. L. Alger, E. H. Freiburghouse, D. D. Chase, "Double windings for turbine alternators," *IEEE Trans.*, vol. 49, pp. 226-244, Jan. 1930.
- [18] F., Bu, W. Huang, Y. Hu, K. Shi, "An Excitation-Capacitor-Optimized Dual Stator-Winding Induction Generator with the Static Excitation Controller for Wind Power Application," *IEEE Transaction on Energy Conversion*, vol. 26, no. 1, March. 2011, pp. 122-131.
- [19] J.O. Ojo, A. Consoli, T.A. Lipo, "An Improved Model of Saturated Induction Machines," *IEEE Transactions on Industry Applications*, vol.26, no.2 March/April, 1990, pp. 212-221.
- [20] T.A. Lipo, "Introduction to AC Machine Design," vol.1, pp.84, WEMPEC – University of Wisconsin, 1996.
- [21] V. Ostovic, "Dynamics of Saturated Electric Machines," Springer Verlag, New York, 1989.
- [22] F. Bu, Y. Hu, W. Huang, S. Zhuang, "Parameter design and static performance of Dual Stator-Winding Induction Generator Variable Frequency AC Generating System with Capacitive and Inductive Loads," *IEEE Transactions on Industrial Electronics*, ISSN 0278-0046, vol. 61, issue 8, 2014, pp. 3902-3914.
- [23] F. Bu, Y. Hu, W. Huang, S. Zhuang, K. Shi, "Control Strategy and Dynamic Performance of Dual Stator-Winding Induction Generator Variable Frequency AC Generating System with Capacitive and Inductive Loads," *IEEE Transactions on Power Electronics*, ISSN 0885-8993, vol. 29, issue 4, 2014, pp. 1681-1692.
- [24] F. Bu, Y. Hu, W. Huang, S. Zhuang, K. Shi, "Wide-Speed-Range-Operation Dual Stator-Winding Induction Generator DC Generating System for Wind Power Applications," *IEEE Transactions on Power Electronics*, ISSN 0885-8993, vol. 30, issue 2, 2015, pp. 561-573.
- [25] W. Huang, Y. Hu, F. Bu, K. Shi, "The magneto motive force of a novel dual stator-winding induction generator," *Proc. IEEE Energy Convers. Cong. Expo.*, 2010, pp.3582-3587.
- [26] L. N. Tutelea, S. I. Deaconu, G. N. Popa, "Reduced Cost Low Speed Wind or Hydro Energy Conversion System with Twin Stator Windings Induction Generators," *16th International Conference on Power Electronics and Motion Control Conference and Exposition, PEMC*, Antalya, Turcia, 21-24 September, pp. 317-324.
- [27] L. N. Tutelea, S. I. Deaconu, G. N. Popa, "Control System for Producing Electricity with Dual Stator Winding Cage-Rotor Induction Generator," *National Electric Drives Conference no. 17*,

October 9-10 2014, Reșița, România, Anals of the Eftimie Murgu University, year XXI, no. 2 , 2014, vol.I, pp. 323-334.

[28] L. N. Tutelea, I. Boldea, N. Muntean, S. I. Deaconu, „Modeling and Performance of Novel Scheme Dual Winding Cage Rotor Variable Speed Induction Generator with dc Link Power Delivery,” *IEEE ENERGY CONVERSION CONGRESS & EXPOSITION, ECCE2014*, September 14-18, Pittsburgh, USA, pp. 271-278.

[29] L. N. Tutelea, I. Boldea, S. I. Deaconu, „Parameter optimal identification of dual three phases stator winding induction machine,” *14th International Conference on Optimization of Electrical and Electronic Equipment OPTIM 2014*, Braşov, 22-24 May, pp. 231-238.

[30] L. N. Tutelea, N. Muntean, S. I. Deaconu, C. D. Cunţan, „Dual stator winding variable speed asynchronous generator: magnetic equivalent circuit with saturation, FEM analysis and experiments,” *IOP Conf. Series: Materials Science and Engineering* 106 (2016) 012029 ISSN: 1757-899X, pp. 1-10.

[31] S. Basak, C. Chakraborty, “Dual Stator Winding Induction Machine: Problems, Progress, and Future Scope,” *IEEE Trans. on Ind. Electronics*, vol.62, no.7, July 2015, pp. 4641-4652.

[32] I. Boldea, L. Tutelea, “Electrical machines – Steady State, Transients, and Design with MATLAB,” CRC Press, 2010.

[33] A. D. Martin, D. L. Vitan, L. N. Tutelea, N. Muntean, „Double Stator Winding Induction Generator for Renewable Energy Conversion System,” *Journal of Electrical Engineering*, vol. 15, no. 3, pp. 1-8.

[34] L. N. Tutelea, S. I. Deaconu, G. N. Popa, „Dual stator winding variable speed asynchronous generator: optimal design and experiments,” *IOP Conf. Series: Materials Science and Engineering* 85 (2015) 012010, ISSN: 1757-899X, pp. 1-9.

[35] L. N. Tutelea, N. Muntean, S. I. Deaconu, “Dual Stator Winding Induction Generator for Wind or Hydro Applications,” Editura Politehnica Timișoara, ISBN 978-606-35-0111-1, 2017, 186 pp.

## 17.1 Introduction

In an effort to simplify the planetary-g geared e-CVT for the parallel HEV or the series HEV we hereby propose to replace the basic two electric machines and their two power converters by a single, axial-air-gap, electric machine central stator, fed by a single PWM converter with dual frequency voltage output and two independent PM rotors capable to deliver independently torque by adequate vector control. This chapter presents a preliminary design with Matlab, an optimal design via Hooke Jeeves method, sample quasi-3D results and dual vector control of a synchronous machine with axial air-gap single stator dual-rotor with permanent surface magnets and different pole pair's number, destined for hybrid electric vehicles (HEV) or electric vehicle (EV) applications.

Recently, axial flux permanent magnet (AFPM) machines, which have high torque density, excellent efficiency and reliability feature, are popular for various applications such as electric ships, hybrid and electric vehicles and airplane propulsion due to their compact construction and high power density. The fractional slot, concentrated winding has shortened end windings compared with those of a distributed winding, resulting in lower power losses and shorter axial frame lengths, but the magneto motive force (MMF) has in general numerous harmonics. Segmented cores have been proposed for this kind of machines [1]-[5].

Basically, a hybrid propulsion system includes two electric machines: one is used for wheel drive; while the other is mainly used for battery charge. Moreover, their locations within the power train represent a drawback from the point of view of volume reduction. Therefore, the integration of both machines into an electromechanical set, in an attempt to improve the compactness and the cost-effectiveness, is currently considered a challenging technology [6]. Dual-rotor machines with toroidally and radially wound stators have been reported recently in [7].

The motor has inner and outer rotors with a stator in between, which is toroidally wound or axially wound with inner and outer slotted stator surfaces. Finite element analysis (FEA) is employed to verify the designs and the Hooke Jeeves algorithm is considered for an optimal design of PMSM for automotive applications [8]-[12].

The present chapter is organized as follows: proposed dual PM rotor machine topology, preliminary and optimal design, quasi 3D FEM validation, proposed dual vector control with dynamic simulations and conclusions.

## 17.2 Proposed machine topology

In an effort to simplify the planetary-gear e-CVT for the parallel HEV or the series HEV, we hereby propose to replace the basic two electric machines and their two power converters by a single axial-air-gap electric machine central stator, fed by a single PWM converter with dual frequency voltage and two independent PM rotors with  $2p_1$  and  $2p_2$  poles, placed on the sides of the central stator provided with  $N_{st}$  slots and a tooth-wound winding (Fig. 17.1), one placed on one side and another on the other side of the slotted magnetic core; the two groups can be connected in parallel or in series.

For the stator magnetic core, a rolled-lamination magnetic core is feasible. However, Soft Magnetic Composites (SMC) are intensively studied for the scope since they are easy to machine and fit well higher frequencies. A surface-mounted PM topology has been considered for the rotors (fig. 17.2). It consists of two rotors with different pole pairs ( $p_1 = 7$ ,  $p_2 = 5$ ) and both shafts are totally independent, so that different operations of the two electric machines could be accessed. The stator is sandwiched between the two rotors, being provided with 12 slots on one side and another in which the phases' coils are introduced, the winding being of fractional concentrated type with winding factors larger than 0.945 for  $p_1=7$  and  $p_2=5$ . An important advantage of using the synchronous axial air-gap single stator dual-rotor permanent magnet machine is represented by its smaller length, the machine allowing to be introduced in the place of the clutch between the motor and the gearbox. Two 3D drawings of the machine are shown in fig. 17.3 [13]-[17].

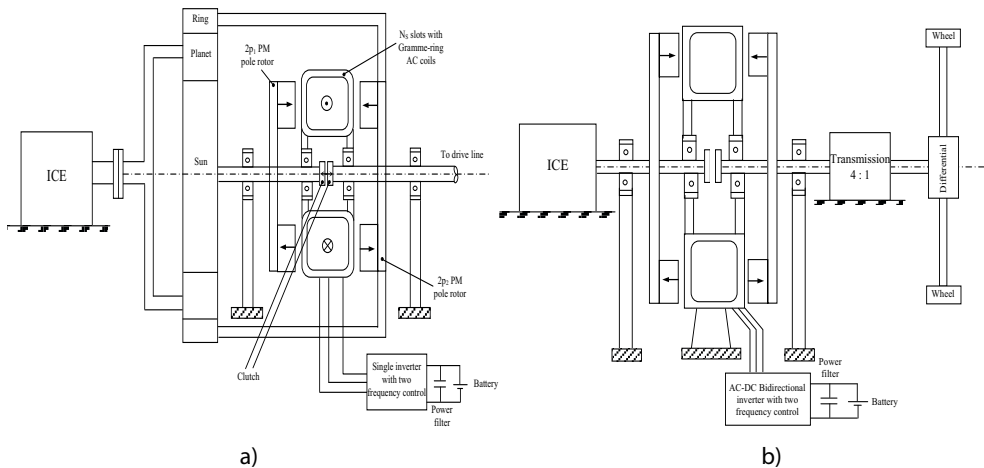


Fig. 17.1 Proposed e-CVT with single electric machine stator and inverter: a) for planetary geared parallel HEV; b) for series HEV.





where  $C_i$  is the initial cost,  $C_E$  the cost of the machine losses,  $C_a$  additional cost to consider the impact of the machine size on the mechanical structure and finally  $C_p$  is the penalty cost. In this example the penalty cost  $C_p$  has the following structure:

$$C_p = C_{Temp} + C_{demag} + C_T + C_{In} , \quad (17.2)$$

where  $C_{Temp}$  is the over-temperature penalty cost;  $C_{demag}$  is the demagnetization penalty cost;  $C_T$  is the lack of torque at maximum speed  $n_{max}$  penalty cost;  $C_{In}$  is the over current at maximum speed  $n_{max}$  penalty cost.

$C_{Temp}$  is computed considering that the surpassing of the maximum allowable winding (and core and PM) temperature leads to immature aging of the equipment. To avoid this, within the optimization algorithm we introduce a penalty cost for over-temperature  $C_{temp}$  in the objective function. The penalty cost  $C_{Temp}$  may vary either linearly or nonlinearly, but monotonously, with the over-temperature. In this case it is computed as in (17.3) [11]:

$$C_{Temp} = \begin{cases} k_T (T - T_{max}) C_i & \text{if } T > T_{max} \\ 0 & \text{if } T \leq T_{max} \end{cases} , \quad (17.3)$$

where  $T$  is the windings temperature;  $T_{max}$  is the windings allowed temperature;  $K_T$  is the proportional constant for over-temperature.

The stator mmf could demagnetize the PMs and then the demagnetization penalty cost was used to reinforce the PMs:

$$C_{demag1,2} = \begin{cases} \left( \frac{I_{t1,2} \cdot k_{s\,demag}}{h_{PM1,2} \cdot H_C} - 0.9 \right) \cdot h_{c\,demag} \cdot C_i, & \text{if } \frac{I_{t1,2} \cdot k_{s\,demag}}{h_{PM1,2} \cdot H_C} > 0.9 \\ 0 & \text{if } \frac{I_{t1,2} \cdot k_{s\,demag}}{h_{PM1,2} \cdot H_C} < 0.9 \end{cases} , \quad (17.4)$$

where  $I_{t1,2}$  – peak of mmf at maximum load for machine 1, 2;  $h_{PM1,2}$  – height of PM for machine 1, 2;  $H_C$  – coercitive field of PM;  $K_{s\,demag}$  – safety factor;  $K_{c\,demag}$  – the proportional constant.

The lack of torque at maximum speed penalty cost,  $C_T$  depends in direct ratio on the lack of torque and on the initial cost  $C_i$  (17.5), (17.6):

$$C_T = C_{T1} + C_{T2} \quad (17.5)$$

$$C_{T1,2} = \begin{cases} \frac{T_{max\,req1,2} - T_{max1,2}}{T_{max\,req1,2}} \cdot C_i, & \text{if } T_{max\,req1,2} > T_{max1,2} \\ 0 & \text{if } T_{max\,req1,2} \leq T_{max1,2} \end{cases} , \quad (17.6)$$

where  $T_{maxreq1,2}$  is required torque at rated constant power and maximum speed for machines 1, 2;  $T_{max1,2}$  is the deliverable maximum torque at  $n_{max}$ .

In order to produce the required torque, the current should be less than 110% rated current. The over current at maximum speed penalty cost (17.7), (17.8),  $C_{In}$  was introduced to secure this requirement:

$$C_{In} = C_{In1} + C_{In2}, \quad (17.7)$$

$$C_{In1,2} = \begin{cases} \frac{I_{smax1,2}^2 - (k_i \cdot I_s)_{1,2}^2}{I_s^2} \cdot C_i, & \text{if } I_{smax1,2} > k_i \cdot I_{s1,2} \\ 0 & \text{if } I_{smax1,2} \leq k_i \cdot I_{s1,2} \end{cases}, \quad (17.8)$$

where  $I_{smax1,2}$  is the stator current (rms value) at maximum required torque for machines 1, 2;  $I_{s1,2}$  is the rated current for machines 1, 2;  $k_i$  is the overloading current factor at  $n_{max}$ .

The machine performance is computed considering the magnetic circuit nonlinearities due to magnetic core saturation. The algorithm was implemented in a MATLAB code using input and output file and graphics user interface. The rated data and results from preliminary design used in optimization of the axial dual PM rotor single stator and the results of optimization are given in Table 17.1. A few sample results for the HJ optimization evolution to the best design are shown in fig. 17.4, 17.5, and 17.6.

Table 17.1 Parameters and Machines Dimensions.

Parameters	Machine M1	Machine M2
Power [kW]	55	110
Base speed [rot/min]	4200	2200
Maximum speed [rot/min]	5500	12000
Rated phase voltage, rms [V]	220	
Pole pairs	7	5
Number of phases	3	
Inner diameter [mm]	220	
Outer diameter [mm]	394	
PM height [mm]	3	6.3
Air-gaps [mm]	2	
Total stator yoke height [mm]	50	
Slot height [mm]	29.5	65
Slot width [mm]	30.2	32.7
Total axial length [mm]	188.1	
Total machine weight [kg]	133	
PM type	Vacodym 677AP $B_r = 1.13T, H_c = 860 \frac{kA}{m}$ at 20°C	

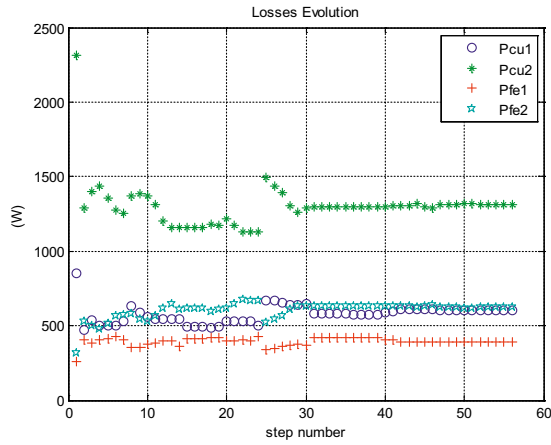


Fig. 17.4 Loss evolution.

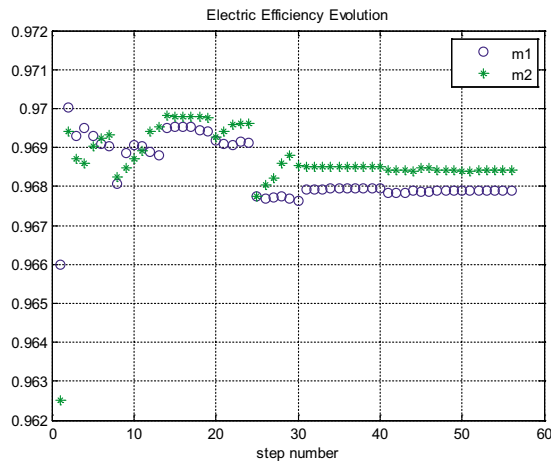


Fig. 17.5 Efficiency evolution m1 – machine1, m2 – machine2.

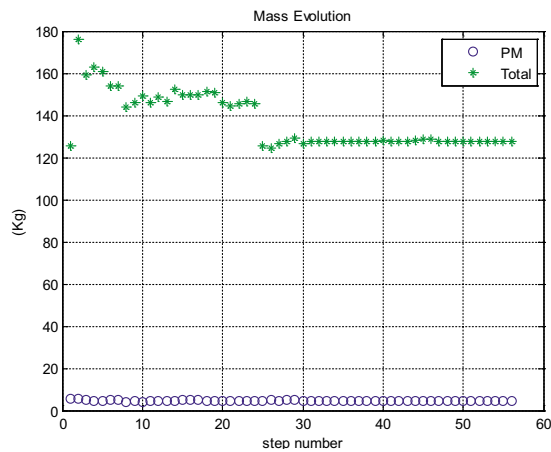


Fig. 17.6 Mass evolution.

The evolution of the losses is presented in fig. 17.4. The electric efficiency (zero mechanical losses) is increasing from around 0.962 and 0.966 respectively to over 0.968 (fig. 17.5) and mass evolution is presented in fig. 17.6.

### 17.4 Quasi 3D FEM Validation

The results obtained with Matlab analytical optimization have been compared with results from quasi 3D FEM validation (Table 17.2). Due to high saturation in rotor disk (yoke) and stator tooth corner, and reduced order of the analytical model, a notable but acceptable difference with respect to quasi 3D FEM could be observed.

Table 17.2 Parameter Comparison.

Parameters	FEM quasi 3D	MATLAB optimization
<b>Torque of machine 1 [N·m]</b>	138.8	125
<b>Torque of machine 2 [N·m]</b>	438.1	477.5
<b>Inductance of machine 1 [mH]</b>	0.5	0.567
<b>Inductance of machine 2 [mH]</b>	0.35	0.398
<b>Linkage PM flux of machine 1 [mWb]</b>	73.8	63.7
<b>Linkage PM flux of machine 2 [mWb]</b>	191.5	206.4

The linkage flux, and machine torque were computed using the Simpson formula on inner, medium and outer layers finite element results. The linkage PM flux are quite sinusoidal (fig. 17.7) despite of fractionary tooth wound windings with surface PM rotors. The largest harmonic is the third harmonic and it represents only 2.21% of fundamental for M1, respectively 0.7% of fundamental for M2. Classical vector control with PWM inverter could be used with good results in order to control proposed machines.

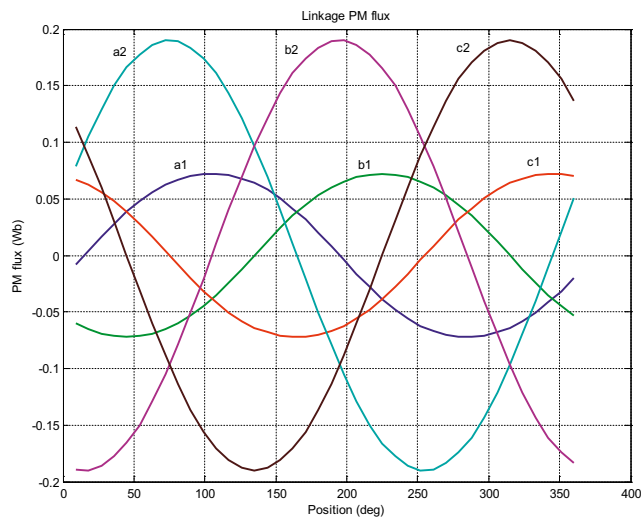


Fig. 17.7 Linkage PM flux for machines 1 and 2 and three phase.

The interaction (PM, stator mmf) torques  $T_1$ ,  $T_2$ , (fig. 17.8) were computed as a difference between total torque and cogging torque from FEM. The cogging torque is acceptable for automotive power drive application: 1.8% for generator (M1) and 2.9% for traction machine (M2). The torque and PM flux computed in FEM ( Table 17.2) are larger than values from analytical model for M1 (about 10% for torque) and they are smaller than values from analytical model for M2 (about 8% for torque).

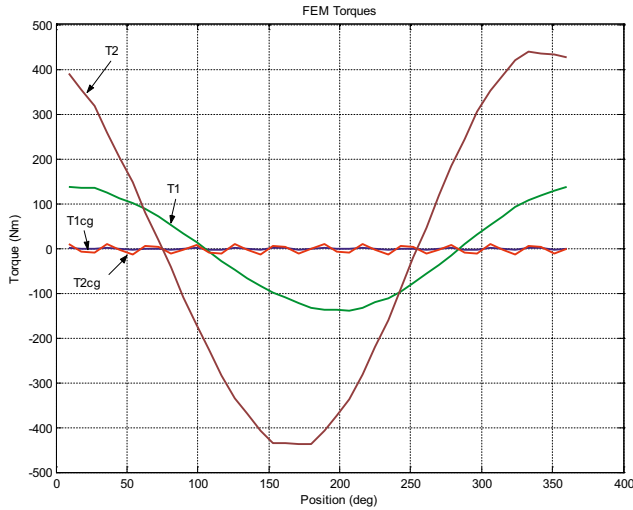


Fig. 17.8 Interaction and cogging torques computed with quasi 3D FEM (  $I_A=100\%$  (p.u.) ,  $I_B=I_C=-50\%$  (p.u.).

## 17.5 Control and Dynamic Simulations

We assume here that the stator windings (if there are two of them) are connected in series and the objective of the dynamic simulation is to evaluate the dynamic and steady state operation of the dual vector control algorithm using two frequency modulation operation. Fig. 17.9 illustrates this vector control strategy.

The classic vector control with two-frequencies is made after the currents  $i_{d1}$ ,  $i_{d2}$ ,  $i_{q1}$ ,  $i_{q2}$  corresponding to the spinning systems with pulsations  $\omega_1$  and  $\omega_2$ . In this case, the stator windings are in series and for control we can use the voltage  $V^*$ . Because there is no possibility to control the four components of the currents, torque components  $i_{q1}$ ,  $i_{q2}$  are closely loop controlled, and components  $i_{d1}$ ,  $i_{d2}$  are quasi zero (and let to vary freely because in case the longitudinal and the transverse inductances are equal ( $L_d = L_q$ ), the components  $i_{d1}$  and  $i_{d2}$  do not produce torque). In fig. 17.10, the fluxes of the permanent magnets ( $\psi_{PM1}$  and  $\psi_{PM2}$ ) and the emf induced voltages ( $u_{e1}$  and  $u_{e2}$ ) in the stator coordinate system ( $\alpha$ ,  $\beta$ ) are presented. The projections of these variables on the two axes have the expressions:

$$\psi_{PM1\alpha} = -\psi_{PM1} \cdot \cos \theta_1, \quad \psi_{PM1\beta} = -\psi_{PM1} \cdot \sin \theta_1, \quad (17.9)$$

$$\Psi_{PM2\alpha} = -\Psi_{PM2} \cdot \cos\theta_2, \quad \Psi_{PM2\beta} = -\Psi_{PM2} \cdot \sin\theta_2, \quad (17.10)$$

$$E_{1\alpha} = -u_{ePM1} \cdot \sin\theta_1 = -\omega_1 \cdot \Psi_{PM1} \cdot \sin\theta_1, \quad E_{1\beta} = u_{ePM1} \cdot \cos\theta_1 = \omega_1 \cdot \Psi_{PM1} \cdot \cos\theta_1, \quad (17.11)$$

$$E_{2\alpha} = -u_{ePM2} \cdot \sin\theta_2 = -\omega_2 \cdot \Psi_{PM2} \cdot \sin\theta_2, \quad E_{2\beta} = u_{ePM2} \cdot \cos\theta_2 = \omega_2 \cdot \Psi_{PM2} \cdot \cos\theta_2. \quad (17.12)$$

The resulting emfs along the two axes have the matrix expression:

$$\begin{pmatrix} u_{e\alpha} \\ u_{e\beta} \end{pmatrix} = \begin{pmatrix} -\sin\theta_1 & -\sin\theta_2 \\ \cos\theta_1 & \cos\theta_2 \end{pmatrix} \begin{pmatrix} \omega_1 \Psi_{PM1} \\ \omega_2 \Psi_{PM2} \end{pmatrix}. \quad (17.13)$$

The electromagnetic torques developed  $T_1$  and  $T_2$  have the expressions:

$$T_1 = \frac{3}{2} p_1 (-\Psi_{PM1} \cdot i_\alpha \cdot \sin\theta_1 + \Psi_{PM1} \cdot i_\beta \cdot \cos\theta_1), \quad T_2 = \frac{3}{2} p_2 (-\Psi_{PM2} \cdot i_\alpha \cdot \sin\theta_2 + \Psi_{PM2} \cdot i_\beta \cdot \cos\theta_2), \quad (17.14)$$

where from the currents  $i_\alpha$  and  $i_\beta$  are deduced:

$$\begin{pmatrix} i_\alpha \\ i_\beta \end{pmatrix} = \frac{1}{\sin(\theta_1 - \theta_2)} \begin{pmatrix} -\cos\theta_2 & \cos\theta_1 \\ -\sin\theta_2 & \sin\theta_1 \end{pmatrix} \cdot \begin{pmatrix} T_1 \\ \frac{3}{2} p_1 \Psi_{PM1} \\ T_2 \\ \frac{3}{2} p_2 \Psi_{PM2} \end{pmatrix}. \quad (17.15)$$

From the previous equations, it is found that the machine can be driven by a single inverter by the currents  $i_\alpha^*$  and  $i_\beta^*$  produced by the voltage  $V^*$ .

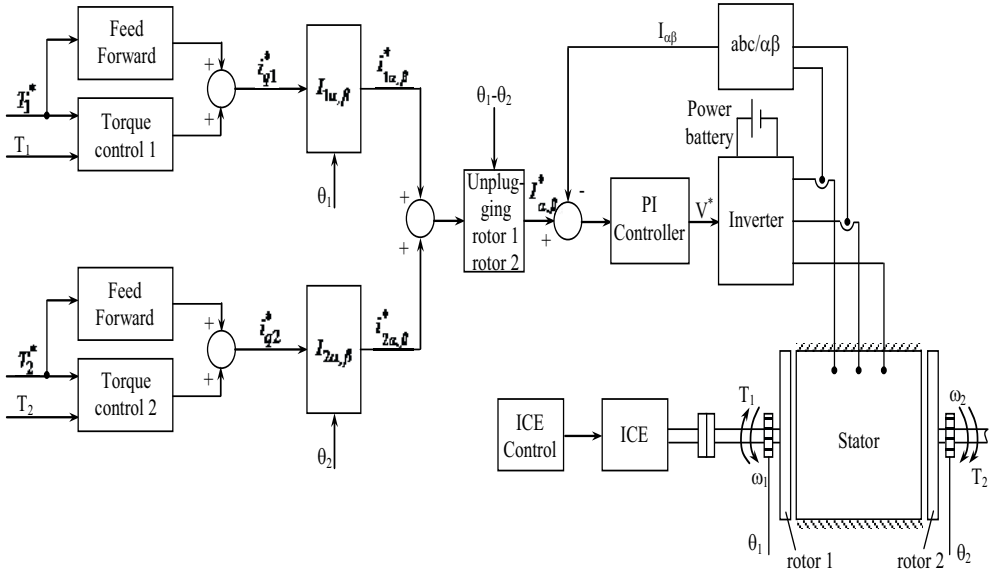


Fig. 17.9 The proposed dual vector control strategy.

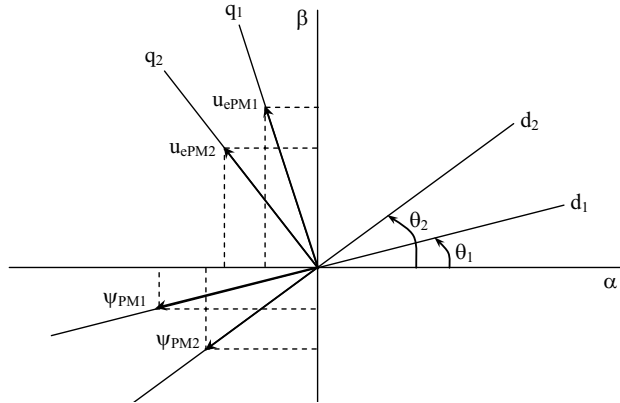


Fig. 17.10 The phase diagram of the permanent magnets' fluxes and the emf induced voltages.

Due to the term  $\frac{1}{\sin(\theta_1 - \theta_2)}$ , it is very difficult to follow the prescribed current that can vary within  $(-\infty, +\infty)$ . Current limitations are introduced while the sinus is monitored by its sign given by the difference  $(\theta_1 - \theta_2)$ . By this, the solution becomes easier to implement and the division by zero is avoided. When the electrical speeds become closer to each other,  $\omega_1$  is equaled with  $\omega_2$  (fig. 17.11a), the systems are rotated until  $\theta_1 - \theta_2 = 90^\circ$  ( $-90^\circ$ ) (fig. 17.11b). In this way the machines are decoupled and can be loaded.

The drive torque of the thermal motor in stationary regime is equal to the electromagnetic torque of rotor 1 (fig. 17.12b). In fig. 17.12a, the torque reference for the rotor 2 and the torque achieved by this are given, observing that the reference is tracked with quite high accuracy. The strongest oscillations that appear both in the torque of rotor 2 and of rotor 1 take place in the moment when the electric speeds of the two rotors become equal to each other (fig. 17.13). The delay between the reference and the achieved value is due to the rank 1 filter with a time constant of 0.2 s. The speed of rotor 1 reaches rapidly the reference value and the speed of rotor 2 depends on the torque reference (fig. 17.13).

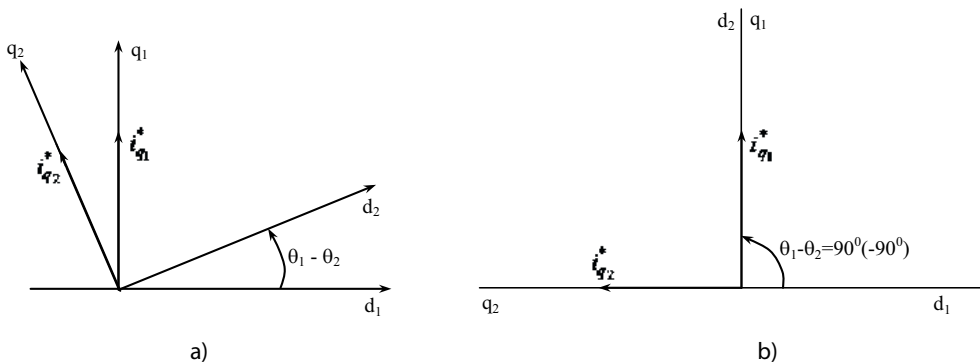


Fig. 17.11 a) systems  $d_1$ - $q_1$  and  $d_2$ - $q_2$  rotating at  $\omega_1 = \omega_2$ ; b) systems  $d_1$ - $q_1$  and  $d_2$ - $q_2$  rotating at  $\omega_1 = \omega_2$  and  $\theta_1 - \theta_2 = 90^\circ$  ( $-90^\circ$ ).



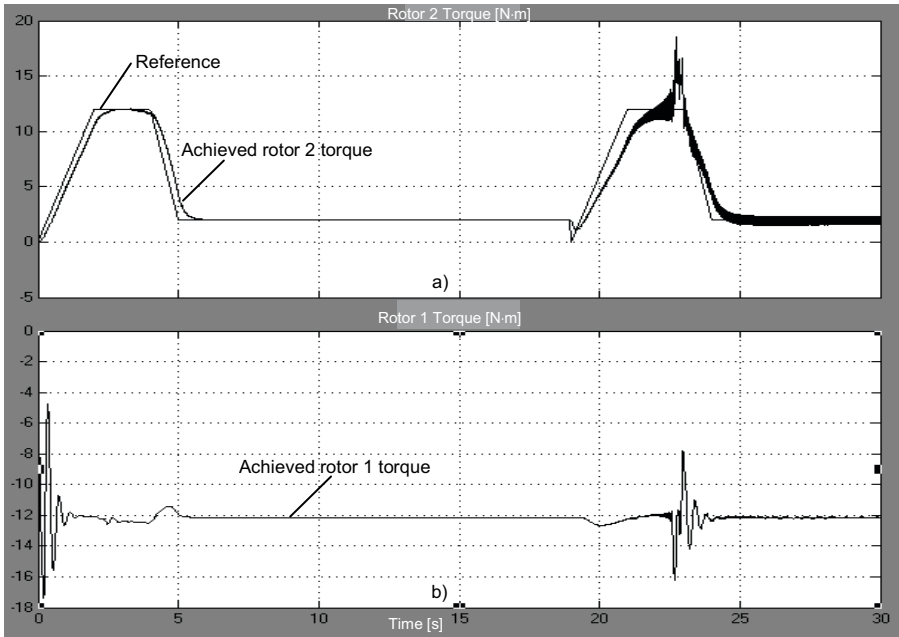


Fig. 17.12 a) Reference and achieved torque by rotor 2; b) achieved torque by rotor 1.

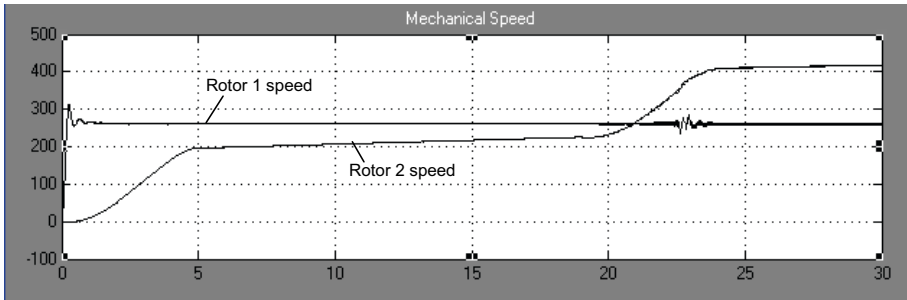
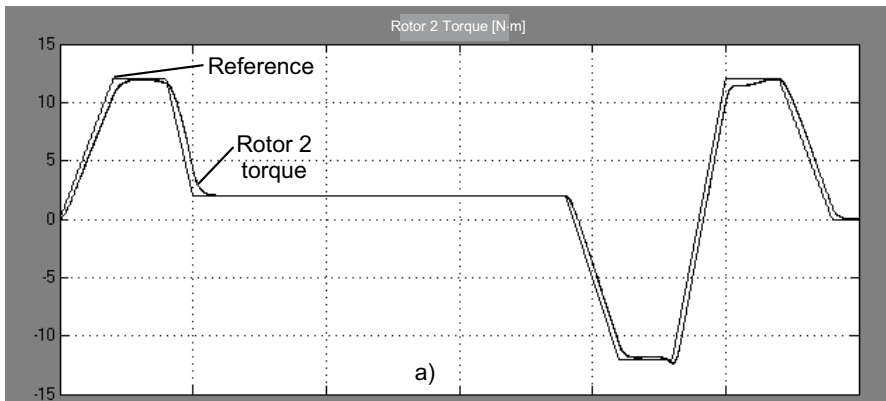


Fig. 17.13 Rotor 1 and rotor 2 mechanical speed.



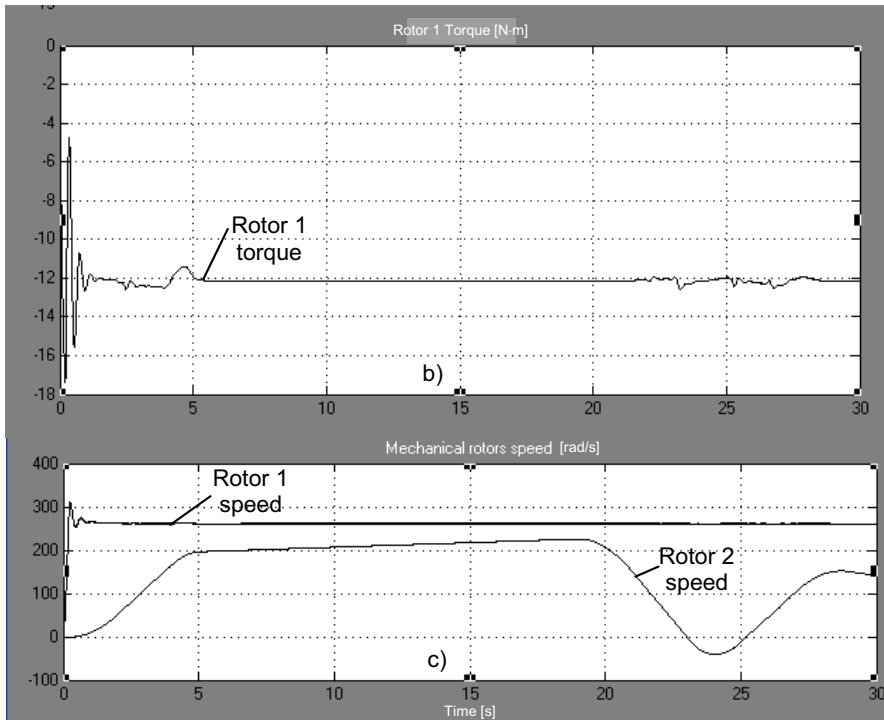


Fig. 17.14 a) Reference and achieved torque by rotor 2 when machine 2 operates both as motor and as generator; b) rotor 1 torque in this case; c) speeds of the 2 rotors in this case.

When the electric speeds are close to each other, an oscillation appears, but passing is made quite easily. In the electric speeds' equalizing area the current shows an increase. The phase currents and voltages modulation is specific to variables that contain two frequencies. It is noticed that the torque pulsation frequency is reduced when electric speeds are close to each other. Fig. 17.14a shows the reference and the realized torque of the rotor 2 if the motor is operating also as generator, while fig. 17.14b, c depicts the torque of rotor 1 and the two speeds for this situation.

Though torque pulsations occur when the two rotors cross through the same electrical speed, the passing is successful (fig. 17.13) and thus the dual vector control is considered adequate for the scope. As an alternative control solution that allows two distinct stator windings (and which leads to some copper loss reduction) a 4-leg PWM inverter control system is reported in [23].

## 17.6 Conclusions

In this chapter, a drive system to produce dual, independent, electromechanical torque output using an axial-air-gap machine with a single stator and two different PM rotors has been introduced in terms of topologies, circuit model, control method, and preliminary quasi 3D-FEM torque production analysis. A novel machine family is proposed in order to

improve machine radial and axial dimensions, torque density and efficiency. The key design equations and procedures of the Single Stator Dual Rotor PMSM have been presented, some design guidelines to achieve the design objectives were given and the influence of the saturation effect on machine inductances was presented. It has been proven the torque production capability of a concentrated winding surface mounted permanent – magnet (PM) machine. As for, the torque average value and ripple amplitude are directly linked to the air-gap MMF profile. Due to its special configuration and principle of operation, this machine can offer the advantages of high torque density and good controllability [24].

Using an analytical design method or the 2D finite element analysis (FEA) only for the average radius on the machine does not generally yield sufficiently accurate computation results. With the 3D FEA, it is possible to take into consideration the actual 3D structure of the machine, but performing the computations is too often time-consuming, especially if the objective is to achieve a preliminary design of the machine. The basic idea of the hereby proposed design method is to firstly subdivide the axial flux machine into a sufficient amount of independent computation plans, then perform the required 2D computations on each plane, and finally compose the overall performance of the machine from the computation results obtained for each design plan [24].

The proposed analytical model was validated by FEM with an accuracy of 8-10% for torque, respectively 13% for inductances. This is acceptable, but it could be further reduced by a complex analytical model. The maximum computed torque versus speed shows that both machines are able to produce the request torque on the entire speed range. This paper shows that it is possible to design an assembly of two machines (generator 55 kW/motor 110 kW) for a hybrid vehicle with a mass of only 133 kg, an outer diameter of 394 mm and an axial length of 188 mm. When the optimization variable vector is large (13 in our case). The Hooke Jeeves algorithm cannot find firmly the global optimum, but however it finds a notably better solution than the initial one. Large values of the initial variation step could improve the HJ chance to find solutions close to the global optimum [24].

A rather extended simulation for two cases was considered (steady state and dynamic). The dual vector speed control for the independent rotors with one common stator is presented and proven to be effective. The next step was the dual vector torque control simulations. The single stator dual-rotors permanent magnet axial synchronous machine can be controlled by a single inverter and two frequencies, the two rotors being able to operate both as motor and as generator in a wide speed range, in the same sense or in different senses. By simulation it is shown that the rotors reach at a certain moment in the situation of equality of the electric speeds, the power transfer between generator and motor being made directly without the inverter and the transitory regime due to this equality is exceeded without important torque oscillations and speed. It is found also that

passing from one operation regime into another (motor-generator or reverse) is made rapidly and more easily [24].

It was introduced a single stator-dual delta-connected three phase winding-two-rotor PMSM fed from a 4 leg inverter with split capacitor. It demonstrates, through digital simulations, wide speed range control with compensated split capacitor-neutral voltage active compensation. It is possible to run one machine at low speed using the current compensation through both inverters. The model allows to study the increasing of machine RMS currents, compared with two symmetrical inverters (with 3 legs, each). An anti-parallel diodes leg was proposed in order to limit the overvoltage on the capacitors. The torque pulsations and power losses of the proposed method are reduced in comparison with those with a single 3-leg inverter where the two windings are considered in series. Both machines could be controlled independently over a wide speed and torque range. The number of active semiconductor devices is still reduced in comparison with two full inverters. In future investigations the use of a split battery system is intended, in order to further reduce the capacitors size in the inverters [24].

## 17.7 References

- [1] D.G. Dorell, M.F. Hsieh, and A.M. Knight, "Alternative Rotor Designs for High Performance Brushless Permanent Magnet Machines for Hybrid Electric Vehicles," *IEEE Transactions on Magnetics*, vol. 48, pp. 835-838, no. 2, February 2012.
- [2] S.L. Ho, S. Niu, and W.N. Fu, "Design and Analysis of a Novel Axial-Flux Electric Machine," *IEEE Transactions on Magnetics*, vol. 47, pp. 4368-4371, no. 10, October 2011.
- [3] M. Ehsani, K. M. Rahman, and H. A. Foliyat, "Propulsion System Design of Electric and Hybrid Vehicles," *IEEE Transaction on Industrial Electronics*, Vol. 44, pp. 19- 27, no 1, February 1997.
- [4] W. Wang, K.W.E. Cheng, K. Ding, and L.C. Meng, "A Novel Approach to the Analysis of the Axial-Flux Permanent-Magnet Generator With Coreless Stator Supplying a Rectifier Load," *IEEE Transactions on Magnetics*, vol. 47, pp. 2391-2394, no. 10, October 2011.
- [5] J. Li, D.W. Choi, C.H. Cho, D.H. Koo and Y.H. Cho, "Eddy-Current Calculation of Solid Components in Fractional Slot Axial Flux Permanent Synchronous Machines," *IEEE Transactions on Magnetics*, vol. 47, pp. 4254-4257, no. 10, October 2011.
- [6] I. Boldea, and S. Scridon, "Electric propulsion systems on HEVs: review and perspective," *EVER 2010*, Monaco, 25-28 March, pp. 1-8, 2010.
- [7] Y.H. Yeh, M.F. Hsieh, and D.G. Dorrell, "Different Arrangements for Dual-Rotor Dual-Output Radial-Flux Motors," *IEEE Transactions on Industry Applications*, vol. 48, pp. 612-622, no. 2, March/April 2012.
- [8] A. Parviainen, "Design of AFPM low-speed Machines and Performance Comparison between Radial-Flux and Axial-Flux Machines," Doctoral Thesis, Lappeenranta University of Technology, Finland, April, 2005.
- [9] O. Wen, D. Zarko, and T.A. Lipo, "Permanent Magnet Machine Design Practice and Optimization," *41st IAS Annual Meeting. Conference Record of the 2006 IEEE*, vol. 4, pp. 1905-1911, October 8-12, 2006.

- [10] S. Wang, X. Meng, N. Guo, H. Li, J. Qiu, J.G. Zhu, Y. Guo, D. Liu, Y. Wang, and W. Xu, "Multilevel Optimization for Surface Mounted PM Machine Incorporating With FEM," *IEEE Trans. On Magnetics*, Vol. 45, pp. 4700-4703, No. 10, October 2009.
- [11] L.N. Tutelea, and I. Boldea, "Optimal Design of Residential Brushless D.C. Permanent Magnet Motors with FEM Validation," *Proceedings of ACEMP*, pp. 435-439, 2007.
- [12] R. Hooke, and J.A. Jeeves, "Direct search solution of numerical and statistical problems," *Journal of ACM*, Vol. 8, No. 2, pp. 212-229, 1961.
- [13] I. Boldea, M. Topor, F. Marignetti, S.I. Deaconu, and L.N. Tutelea, "A Novel, Single Stator Dual PM Rotor, Synchronous Machine: topology, circuit model, controlled dynamics simulation and 3D FEM Analysis of Torque Production," *12th International Conference on Optimization of Electrical and Electronic Equipment OPTIM 2010*, pp. 343-351, May 20-22 2010, Brasov, Romania.
- [14] L.N. Tutelea, S.I. Deaconu, I. Boldea, F. Marignetti, and G.N. Popa, "Quasi-3D FEM Analysis of an Single Stator dual PM Rotors Axial Electric Vehicles," *Electrimacs 2011*, pp. 1-7, June 6-8 2011, Cergy-Pontoise, France.
- [15] I. Boldea, L.N. Tutelea, S.I. Deaconu, and F. Marignetti, "Dual rotor single stator brushless PMSM motor/generator system for full HEVs," *ECAI 2011*, pp. 95-102, 30 June-2 July 2011, Pitesti, Romania.
- [16] L.N. Tutelea, S.I. Deaconu, I. Boldea, F. Marignetti, and G.N. Popa, "Design and Control of a Single Stator Dual PM Rotors Axial Synchronous Machine for Hybrid Electric Vehicles," *EPE 2011*, pp. 1-10, 30 August-02 September 2011, Birmingham, England.
- [17] L.N. Tutelea, I. Boldea, and S.I. Deaconu, "Optimal Design of Dual Rotor Single Stator PMSM Drive for Automobiles," *International Electric Vehicle Conference*, pp. 1-8, March 4-8 2012, Greenville, S.C. USA.
- [18] H.W. Van Der Broeck, and J.D. Van Wyk, "A comparative investigation of a three-phase induction machine with a component minimized voltage-fed inverter under different control options," *IEEE Trans. on Industry Applications*, vol. IA-20, Mar./Apr., 1984, pp. 309-320.
- [19] K. Matsuse, N. Kezuka, and K. Oka, "Characteristics of Independent Two Induction Motor Drives Fed by a Four-Leg Inverter", *IEEE Trans. on Industry Applications*, vol. 47, no. 5, September/October, 2011, pp. 2125-2134.
- [20] T.B. Bashaw, and T.A. Lipo, "B4 Topology Options for Operating Three Phase Induction Machines on Single Phase Grids", *Applied Power Electronics Conference and Exposition, APEC 2005, Twentieth Annual IEEE*, vol. 3, pp. 1894-1902.
- [21] B.A. Welchko, and T.A. Lipo, "A Novel Variable-Frequency Three-Phase Induction Motor Drive System Using Only Three Controlled Switches", *IEEE Trans. on Industry Applications*, vol. 37, no. 6, November/December, 2001, pp. 1739-1745.
- [22] M. Nasir Uddin, T.S. Radwan, and M.A. Rahman, "Fuzzy-Logic-Controller-Based Cost-Effective Four Switch Three-Phase Inverter-Fed IPM Synchronous Motor Drive System", *IEEE Trans. on Industry Applications*, vol. 42, no. 1, January/February, 2006, pp. 21-30.
- [23] L.N. Tutelea, I. Boldea, and S.I. Deaconu, "The Single Stator Dual Rotor PMSM for HEV: Two Windings and 4 Leg Inverter Control," *15th International Power Electronics and Motion Control Conference, EPE PEMC 2012 ECCE Europe*, Novi Sad, Serbia, 4-6 September, 2012, in press.
- [24] L.N. Tutelea, S.I. Deaconu, "Dual rotor single stator permanent magnet motors for hybrid electrical vehicles", Editura Politehnica Timisoara, ISBN 978-606-554-861-9, 2014, 119 pp.



POLITEHNICA UNIVERSITY TIMISOARA  
1920-2020

ISBN: 978-606-35-0319-1